



# Research on Engineering Structures and Materials

[www.jresm.org](http://www.jresm.org)

Volume 10

Issue 3

September 2024



P-ISSN: 2148-9807 E-ISSN: 2149-4088



Research  
Group

The International Journal of **Research on Engineering Structures and Materials (RESM)** is a peer-reviewed open access journal (p-ISSN: 2148-9807; o-ISSN: 2149-4088) published by MIM Research Group. It is published in February, June, September, and December.

The main objective of RESM is to provide an International academic platform for researchers to share scientific results related to all aspects of mechanical, civil, and material engineering areas.

RESM aims the publication of original research articles, reviews, short communications technical reports, and letters to the editor on the latest developments in the related fields.

All expenditures for the publication of the manuscripts are most kindly reimbursed by *MIM Research Group*. Thus, authors do not need to pay for publishing their studies in the journal.

The scope of the journal covers (but not limited to) behavior of structures, machines and mechanical systems, vibration, impact loadings and structural dynamics, mechanics of materials (elasticity, plasticity, fracture mechanics), material science (structure and properties of concrete, metals, ceramics, composites, plastics, wood, etc.), nano-materials performances of new and existing buildings and other structural systems, design of buildings and other structural systems, seismic behavior of buildings and other structural systems, repair and strengthening of structural systems, case studies and failure of structural systems, safety and reliability in structural and material engineering, use of new and innovative materials and techniques in energy systems and mechanical aspects of biological systems (biomechanics and biomimetics).

#### **The topics covered in JRESM include:**

- Structural Engineering
- Mechanical Engineering
- Material Engineering
- Earthquake Engineering
- Nano-technology
- Energy Systems (Focus on Renewable)
- Biomechanics and Biomimetics
- Environment (Material and Engineering System Related Issues)
- Computer Engineering and Data Science (Material and Engineering System-Related Issues)

#### **Abstracting and Indexing**

Please visit <http://www.jresm.org> for more information.

#### **Graphics and Design**

Mehmet Yilmaz

[myilmaz@jresm.net](mailto:myilmaz@jresm.net)



**RESEARCH on  
ENGINEERING STRUCTURES &  
MATERIALS**



# RESEARCH on ENGINEERING STRUCTURES & MATERIALS

## Editorial Board

---

### Editor in Chief

Hayri Baytan Özmen

Usak University

Türkiye

---

### Editors

Canan Kandilli

Usak University

Türkiye

---

Antonio F. Miguel

University of Evora

Portugal

---

Michele Barbato

University of California Davis

USA

---

Alp Karakoç

Aalto University

Finland

---

Faris Tarlochan

Qatar University

Qatar

---

Mehmet Palancı

Arel University

Türkiye

---

Francesco D'Annibale

University of L'Aquila

Italy

---

Samson Olalekan  
Odeyemi

Kwara State University Malete

Nigeria

---

Saifulnizan Jamian

Universiti Tun Hussein Onn  
Malaysia

Malaysia

---

Chitaranjan Pany

Vikram Sarabhai Space Centre

India

---

Daniel Cruze

Hindustan Institute of Technology  
and Science

India

---

Badrinarayan Rath

Wollega University

Ethiopia

---

Taymaz Tabari

Jagiellonian University

Poland

---

Tamer  
Saracyakupoglu

İstanbul Gelisim University

Türkiye

---

## Editorial Office

---

### Publishing Manager

---

Mehmet Yılmaz

MIM Research Group

Türkiye

---

### Language Editors

---

Gaye Kuru

Uşak University

Türkiye

Mete Çal

MIM Research Group

Türkiye

---

---

**Editorial Board Members**

---

Farid Abed-Meraim	Arts et Metiers ParisTech	France
P. Anbazhagan	Indian Institute of Science	India
Raffaele Barretta	University of Naples Federico II	Italy
R.S. Beniwal	Council of Scientific and Industrial Research	India
Antonio Caggiano	University of Buenos Aires	Argentina
Noel Challamel	University of South Brittany	France
Abdulkadir Çevik	Gaziantep University	Türkiye
J. Paulo Davim	University of Aveiro	Portugal
Hom Nath Dhakal	University of Portsmouth	UK
Ali Faghidian	Islamic Azad University	Iran
S. Amir M. Ghannadpour	Shahid Beheshti University	Iran
Ali Goodarzi	Harvard University	USA
Jian Jiang	National Institute of Standards and Technology	USA
Ramazan Karakuzu	Dokuz Eylül University	Türkiye
Arkadiusz Kwiecien	Cracow University of Technology	Poland
Stefano Lenci	Universita Politecnica delle Marche	Italy
Silva Lozančić	University of Osijek	Croatia
Fabio Mazza	University of Calabria	Italia
Yuan Meini	North University of China	China
Stergios A. Mitoulis	University of Surrey	UK
Vinayagam Mohanavel	Anna University	India
Ehsan Noroozinejad Farsangi	Kerman Graduate University of Technology	Iran
Alaa M. Rashad	Shaqra University	Saudi Arabia
Mohammad Mehdi Rashidi	University of Tongji	China
Pier Paolo Rossi	University of Catania	Italy
Neritan Shkodrani	Polytechnic University of Tirana	Albania
Y.B. Yang	National Taiwan University	Taiwan

---

---

**Advisory Board Members**

---

A. Abdelbary	Alexandria University	Egypt
A.A.A. Sheha	Petrogulfmistr Oil Company	Egypt
Aashish Roy	S. S. Tegnoor Degree College	India
Abbasali Sadeghi	Islamic Azad University, Mashhad	India
Abdelbaki Chikh	Ibn Khaldoun University of Tiaret	Algeria
Abdelhalim Bensaada	University of Yahia Fares of Medea	Algeria
Abdel-Hamid Ismail Mourad	United Arab Emirates University	BAE
Abdelkader Fidjah	University of Djelfa	Algeria
Adil Mahdi Jabbar	Wasit University	Iraq
Ahmet Demir	Bolu University	Türkiye
Ahmet Devlet Ozcelik	Istanbul Gelişim University	Türkiye
Alaa M. Rashad	Building Materials Research and Quality Control Institute	Egypt
Aleksandar Savić	University of Belgrade	Serbia
Ali Bagherkhani	Shiraz University of Technology	Iran
Ali Raza	University of Engineering and Technology	Pakistan
Ali Abbar Khleif	University of Technology	Iraq
Ali Goodarzi	Harvard University	USA
Alpay Tamer Erturk	Kocaeli University	Türkiye
Alper Incesu	Karabük University	Türkiye
Ameer Baiee	University of Babylon	Iraq
Amiya Pandit	University College Dublin Ireland	Ireland
Ammar Tawashi	Al-Baath University	Syria
Anjishnu Biswas	Indian Institute of Technology Guwahati	India
Ankang Kan	Shanghai Maritime University	China
Arif Tuncal	General Directorate of State Airports	Türkiye
Arife Kübra Yontar	Ondokuz Mayıs University	Türkiye
Arunkumar K	Kalsalingam Academy of Research and Education	India
Ash-Shu'Ara Marafa Salman	Kwara State University	Nigeria

---

---

Asimina Athanatopoulou	Aristotle University	Greece
Atike İnce Yardımcı	Uşak University	Türkiye
Ayoub Souileh	University Mohammed V	Morocco
Berrin İkizler	Ege University	Türkiye
Billel Rebai	Abbes Laghrour University	Algeria
Breetha Yesudhas Jayakumari	Chennai Institute of Technology	India
Brijesh Singh	National Council for Cement and Building Materials	India
Bülent İmamoğlu	Gedik University	Türkiye
Can Gonenli	Ege University	Türkiye
Catur Harsito	Universitas Sebelas Maret	Indonesia
Chella Gifta Christopher	National Engineering College Kovilpatti	India
Chitaranjan Pany	Vikram Sarabhai Space Centre	India
Chinenye Elizabeth Okere	Federal University of Technology	Nigeria
Chuanjin Yu	Southwest Jiaotong University	China
Daniel Cruze	Mohamed Sathak A J College of Engineering	India
Davide Forcellini	University of San Marino	San Marino
Debasish Sen	Ahsanullah University of Science and Technology	Bangladesh
Deniz Uner	Middle East Technical University	Türkiye
Dhirendra Patel	Kalaniketan Polytechnic College	India
Dilay Uncu	Celal Bayar University	Türkiye
Dipankar Das	Tripura University	India
Diyar Qader	University of Kirkuk	Iraq
Abdul Razak Abdul Karim	Universiti Malaysia Sarawak	Malaysia
Anand Murthy Hc	Adama Science & Tech. University	Ethiopia
Vera Ilyina	Institute of Geology Karelian Research Centre	Russia
Dulce Franco Henriques	Instituto Politécnico de Lisboa	Portugal
Elavenil S	Vellore Institute of Technology	India
Elton Hala	Polytechnic University of Tirana	Albania
Emre Kemer	Usak University	Türkiye

---



---

Enea Mustafaraj	Epoka University, Tirana	Albania
Ercan Isık	Bitlis Eren University	Türkiye
Esra Özer	Tokat Gaziosmanpasa University	Türkiye
Essam Mohamed	South Valley University	Egypt
Fatoş Koç	Ege University	Türkiye
Federico Scafati	University of L'Aquila	Italy
Fokruddin Ahmad	Washington State University	USA
Gaurav Dhadse	G. H. Rasoni Institute of Engineering and Business Management	India
Guobo Wang	Wenzhou University	China
Gururaj Hatti	KLS Vishwanathrao Deshpande Institute of Technology	India
Guy Louarn	Université de Nantes	France
Habibe Demir	İskenderun Teknik University	Türkiye
Hadj Bekki	University Ibn Khaldoun of Tiaret	Algeria
Hakan Sarıkaya	Uşak University	Türkiye
Hakan Ulker	Bursa Teknik University	Türkiye
Halil Murat Enginsoy	Çanakkale Onsekiz Mart University	Türkiye
Halil Yalcin Akdeniz	Eskisehir Osmangazi University	Türkiye
Hasan Ulus	Selcuk University	Türkiye
Hemadri Prasad Raju	Sree Vidyanikethan Engineering College	India
Hints G. Gebremariam	Addis Ababa University	Ethiopia
Hossein Kabir	University of Illinois	USA
Hussein Hamada	Al-Qalam University College	Iraq
I Gede Gegirang Wiryadi	Universitas Mahasaraswati Denpasar	Indonesia
Ibrahim Sharaky	Taif University	Saudi Arabia
Ikram Kouidri	University of Relizane	Algeria
Indra Mawardi	Politeknik Negeri Lhokseumawe	Indonesia
Irakli Premti	Polytechnic University of Tirana	Albania
Isabel Milagre Martins	Laboratório Nacional de Engenharia Civil	Portugal

---

---

Ivana Štimac Grandić	University of Rijeka	Croatia
J. Jenix Rino	Anna University	India
J. Paulo Davim	University of Aveiro	Portugal
Jinxu Mo	Yangtze University	China
Jojok Widodo Soetjipto	Universitas Jember	Indonesia
Josephine Chang Hui Lai	Universiti Malaysia Sarawak	Malaysia
Juan Llorca-Schenk	University of Alicante	Spain
K. Ashwini	Jawaharlal Nehru Technological University Hyderabad	India
Kabiru Mustapha	Kwara State University	Nigeria
Kadir Gunaydın	GE Aviation Marmara Technology Center	Türkiye
Kamel Chaoui	Badji Mokhtar University	Algeria
Kanish Kapoor	Dr B R Ambedkar National Institute of Technology	India
Khairul Nizar Ismail	Universiti Malaysia Perlis	Malaysia
Konstantinos Kalfas	University of Texas at Tyler	USA
Lawrence Zahemen Tuleun	University of Ilorin	Nigeria
Lomesh Mahajan	Dr. Babasaheb Ambedkar Technological University	India
Lyamine Briki	University of Batna2	Algeria
M. Kalil Rahiman	Saveetha School of Engineering	India
Magdalini Titirla	Conservatoire National des Arts et Métiers	France
Maher Chakhari	Tunis El Manar University	Tunisia
Mahesh Gopal	Wollega University, Nekemte	Ethiopia
Maheswaran Chellapandian	Mepco Schlenk Engineering College	India
Mahmoud Mokhtar	Housing & Building National Research Center	Egypt
Majid Pouraminian	Islamic Azad University	Iran
Maria Richert	AGH University of Science and Technology	Poland
Marina Sunara	University of Split	Croatia
Marwa Enneffati	Université Angers	France
Md. Saiful Islam	Universiti Putra	Putra
Mehdi Panji	Islamic Azad University	Iran

---

---

Mehmet Ada	Uşak University	Türkiye
Mehmet Cemal Genes	Eastern Mediterranean University	Cyprus
Mehrab Nodehi	University of California Davis	USA
Mert Göksüzöğlü	SAMPA Advanced Parts for Commercial Vehicles	Türkiye
Mohammad .I Al Biajawi	Universiti Malaysia Pahang Al-Sultan Abdullah	Malaysia
Mohammad Afrazi	Tarbiat Modares University	Iran
Mohammad Naeim Moradi	Amirkabir University of Technology	Iran
Mohammad Saleh Baradaran	Islamic Azad University	Iran
Mohammed Bentahar	Tahar Moulay University of Saida	Algeria
Mohammed Sarhan	Mustansiriyah University	Iraq
Mohsen Hajizamani	Graduate University of Advanced Technology	Iran
Morchid Fatima Ezzahrae	University of Hassan II Casablanca	Morocco
Muhammad Bilal Khan	Ghulam Ishaq Khan Institute of Engineering Sciences and Technology	Pakistan
Mustafa Akpolat	Munzur University	Türkiye
Mustafa H. Omar	Bilad Alrafidain University College	Iraq
Mustafa Ozgunler	Mimar Sinan Fine Arts University	Türkiye
Mustaqqim Abdul Rahim	University Malaysia Perlis	Malaysia
Nadhim Hamah Sor	University of Garmian	Iraq
Nagaraj Ekabote	KLE Technological University	India
Nahida Nazim Musayeva	Azerbaijan National Academy of Sciences	Azerbaijan
Navdeep Singh	Dr. Babasaheb Ambedkar Technological University	India
Nebab - Mokhtar	University Hassiba Benbouali of Chlef	Algeria
Nghia P. Tran	The University of Melbourne	Australia
Nitin Kumar	University of California Davis	USA
Olfa Maalej	Monastir University	Tunisia
Olumoyewa D. Atoyebi	Landmark University	Nigeria
Orhan Gülcan	General Electric Aerospace	Türkiye
Osman M. Ramadan	Cairo University, Giza	Egypt

---

---

Ozgur Avsar	Eskisehir Technical University	Türkiye
Özgür Demircan	Ondokuz Mayıs Üniversitesi	Türkiye
Partheeban Pachaivannan	Chennai Institute of Technology	India
Peng Gao	University of Massachusetts Lowell	USA
Peyman Beiranvand	Razi University	Iran
Piya Chotickai	Kasetsart University	Tailand
Pooja Sharma	Dr. Yashwant Singh Parmar University of Horticulture and Forestry	India
Subash Thanappan	KAAF University College	Ghana
Raif Sakin	Balıkesir University	Türkiye
Rajesh Kumar	KPR Institute of Engineering and Technology	India
Rajesh M.	Hindustan Institute of Technology and Science	India
Ramaswamy Palanivel	Shaqra University	Saudi Arabia
Rami Sldozian	University of Technology-Iraq	Iraq
Rasheed Abdulwahab	Kwara State University	Nigeria
Ravichandran M	K.Ramakrishnan College of Engineering	India
Revathi Srinivasan	Mepco Schlenk Engineering College	India
Riadh Bennai	University Hassiba Benbouali of Chlef	Algeria
Rianti Dewi Sulamet-Ariobimo	Universitas Trisakti	Indonesia
Roberto Nascimbene	School of Advanced Studies IUSS Pavia	Italy
Royal Madan	Chandigarh University	India
S. Ali Faghidian	Islamic Azad University	Iran
Saeid Foroughi	Konya Technical University	Türkiye
Sahar Ismail	Saint Joseph University of Beirut	Lebanon
Sajjad Hassanpour Kasanagh	Middle East Technical University	Türkiye
Salmabanu Luhar	National Taipei University of Technology	Taiwan
Samer Adeeb	University of Alberta	Canada
Samia Bouzouaid	Kasdi Merbah University	Algeria
Samuel Awe	Automotive Components Floby AB	Sweden

---

---

Sangeetha Palanivelu	SSN College of Engineering	India
Sarmila Sahoo	Heritage Institute of Technology Kolkata	India
Sercan Serin	Osmaniye Korkut Ata University	Türkiye
Shaish K. John	College of Engineering Trivandrum	India
Shaohong Cheng	University of Windsor	Canada
Sharmin Reza Chowdhury	Ahsanullah University of Science and Technology	Bangladesh
Sivakumar N	SSN College of Engineering	India
Solomon Olalere Ajamu	Ladoke Akintola University	Nigeria
Somya Ranjan Patro	Indian Institute of Technology Delhi	India
Sonal Thakkar	Nirma University	India
Sophia Immanuel	National Institute of Technology Tiruchirappalli	India
Suliman Khan	NFC Institute of Engineering and Fertilizer Research	Pakistan
Sumanth Ratna Kandavalli	New York University	USA
Surajit Kumar Paul	Indian Institute of Technology	India
Susmita Naskar	University of Southampton	Englang
T.V. Reshma	GITAM School of Technology	India
Taha Rashid	Universiti Teknologi Malaysia	Malaysia
Tamer Saracyakupoglu	TUSAŞ Academy	Türkiye
Taqiy Eddine Boukelia	University of Jijel	Algeria
Tarun Kumar Rajak	Shri Shankaracharya Institute of Professional Management and Technology	India
Tasnia Ahmed	Military Institute of Science and Technology	Bangladesh
Thaer Alrudaini	University of Basrah	Iraq
Thi Loan Pham	Civil Engineering, Hai Phong University	Vietnamese
Thomás L. Resende	Federal University of Jequitinhonha and Mucuri Valleys	Brazil
Thomas Salonikios	The Institute of Engineering Seismology and Earthquake Engineering	Greece
Toufik Sebbagh	University of Skikda	Algeria
Tuan Anh Nguyen	Thuyloi University	Vietnamese

---

---

Upendra K. Mallela	Indian and Toubro Technology	India
Vedat Arda Küçük	Çankırı Karatekin University	Türkiye
Vineeth Kumar T. V.	Siddaganga Institute of Technology	India
Víctor I. Fernandez-Davila	Pontifical Catholic University of Peru	Peru
Victor Rizov	University of Architecture	Bulgaria
Vincent Sam Jebadurai	Karunya Institute of Technology and Sciences	India
Wahyu Dwi Lestari	University of Pembangunan Nasional Veteran Jawa Timur	Indonesia
Waleed A Abbas	University of Technology, Baghdad	Iraq
Yamini Sreevalli I	Vellore Institute of Technology	India
Yang Feng	Xi'an Jiaotong University	China
Yang Yang	Southeast University	China
Yaser Acikbas	Uşak Üniversitesi	Türkiye
Yonatan Ayele Abera	Dilla University	Ethiopia
Yunika Kirana Abdul Khalik	University of Malaysia	Malaysia
Zafer Kaya	Dumlupınar University	Türkiye
Zahid Iqbal Khan	Universiti Teknologi Malaysia	Malaysia
Zikriye Ozbek	Çanakkale Onsekiz Mart University	Türkiye

---

## In This Issue

### Research Article

- 857 **Abeer M. Humad, Ali J. Dakhil, Samer A. Al-Mashhadi, Zainab Al-Khafaji, Zainab Adel Mohammed, Sarah Fadel Jabr**  
Improvements of mechanical and physical features of cement mortar by nano  $Al_2O_3$  and  $CaCO_3$  as additives

### Research Article

- 873 **Peter Ikubanni, Makanjuola Oki, Adeolu Adediran, Sarah Akintola, Adekunle Adeleke, Ikechukwu Anyim, Olanrewaju Adesina, Lawrence Efenovwe**  
Valorized rice husk as green corrosion inhibitor for Al 6061 in 1M HCl

### Research Article

- 885 **Yaser Acikbas**  
Surface plasmon resonance chemical sensor modified with  $\alpha$ -naphthylmethacrylate nano thin film for chloroform detection

### Research Article

- 897 **S Naveena, Govardhan Bhat**  
Parametric study on the effect of temperature on properties of engineered cementitious composites using induction furnace slag as a partial replacement for river sand

### Research Article

- 917 **Gaurav Pandey, Vishal Kumar Mourya, Dharendra Patel, Rajesh Kumar, Suresh Kumar**  
Load sharing behaviour in piled-raft foundations over sand and clay: An experimental investigation

### Technical Note

- 943 **Dinesh Kumar, Satnam Singh**  
Enhancing friction and wear performance in hybrid aluminum composites through grey relational analysis

### Research Article

- 957 **Mohammad Salim Kaiser**  
Results of Sn/Pb solder affected aluminum under wear study

### Research Article

- 973 **Katherine E. Buenaflor, Philip Jun S. Celerinos, Chris Julie P. Del Castillo, Jay Marc R. Gala, Katrina A. Sumatra**  
Effects of sugarcane bagasse ash as partial replacement of cement in the compressive strength and light transmissibility of Litracon blocks

Research Article

- 995 **Venkateswarlu Kuruva, Shirish V. Deo, Meena Murmu**  
Impact of superabsorbent polymer on self-compacting concrete's workability, strength, carbonation and freezing-thawing

Review Article

- 1017 **Dhirendra Patel, Vishal Kumar Mourya, Gaurav Pandey, Rajesh Kumar**  
Advancements in base isolation for seismic mitigation: Perspectives on elastomeric and lead rubber bearings

Research Article

- 1051 **Ilya Lozovsky, Aleksei Churkin**  
Spectral analysis of cross-hole sonic logging data for pile integrity assessment

Research Article

- 1065 **Oguntayo Daniel, Ogundipe Olumide, Aluko Oluwasegun, Babatunde Yusuf**  
RSM based modelling and optimization of Marshall properties of steel-slag and lime-modified asphalt mixtures

Research Article

- 1085 **Enio Deneko, Hüseyin Bilgin**  
Observed failure modes in existing URM buildings after November 26, 2019 earthquake in Albania

Research Article

- 1109 **Youcef Gheid, Abdennacer Chemami, Djamel Gaagaia, Hamza Aouaichia**  
Effects of seawater and acidic environment on mechanical properties of iron powder-loaded glass-epoxy composite laminates: Experimental and analytical investigation

Research Article

- 1125 **Kadapa Hemadri, Ajith Arul Daniel S, Vijayendra Kukanur, Madeva Nagaral**  
Determination of wear rate and coefficient of friction of Al6262 reinforced with different weight percentage of WC/MoS<sub>2</sub> under dry sliding condition



Research Article

- 1139 **Rami J. Sldozian, Alexander E. Burakov, Dhafer Z. M. Aljaboobi, Ali Jihad Hamad, Alexey G. Tkachev**

The effect of multi-walled carbon nanotubes on mechanical properties and water adsorption of lightweight foamed concrete

Research Article

- 1155 **Daniel Cruze, Chandan Sah, Nijampatnam Manikanta, Dharendra Kumar Mandal, Abhinash Kumar Jha, A. Arun Solomon**

Axial compressive behavior of recycled aggregate concrete steel composite columns

Research Article

- 1173 **Gaurav D. Dhadse, Gangadhar Ramtekkar, Govardhan Bhatt**

Thin layer interface: An alternative modeling consideration in soil-structure interaction system

Research Article

- 1195 **Alireza Roshan, Magdy Abdelrahman**

Predicting flexural-creep stiffness in bending beam rheometer (BBR) experiments using advanced super learner machine learning techniques

Research Article

- 1209 **Philip Jun S. Celerinos, Sarah Jayne C. Frigillana, Joshua Jonielle D. Grande, Norfatima G. H. Ali, Jamie Angel C. Navarro**

Influence of seawater exposure at the splash zone on the reliability of the rebound hammer test in estimating concrete compressive strength

Review Article

- 1231 **Suyash Surendra Sagare, Kirthiga R, Elavenil S**

A state of art of review on strengthening of concrete structures using fabric reinforced cementitious matrix

Research Article

- 1261 **Muti Adelodun Akinpelu, Ash-Shu'ara Marafa Salman, Yusuf Ayoola Jimoh, Ibrahim Tunde Yahaya, Hakeem Mayowa Salami**

Impact of treatment temperature of metakaolin on strength and sulfate resistance of concrete

Review Article

- 1281 **Ashish Singh, Denise-Penelope N. Kontoni, Sasankasekhar Mandal**  
Wind-induced torsional loads and responses of tall buildings

Research Article

- 1301 **Mangalapuri Venkateswarlu, T.D Gunneswara Rao**  
Effect of GGBFS and fly ash proportions on fresh, tensile and cracking features of alkali activated concrete with low NaOH concentrations

Research Article

- 1321 **Faouzi Hamza, Ouzine Boussaid, Hamid Hamadache, Abdelmoumene Guedri**  
Experimental investigation and numerical optimization of sheet metal forming limits during deep drawing process of DD14 steel

Free access to tables of content, abstracts and full text of papers for web visitors.

Copyright © 2023

Research on Engineering Structures & Materials

MIM Research Group Publications

P-ISSN: 2148-9807

E-ISSN: 2149-4088

<http://www.jresm.org>



## ABSTRACTING / INDEXING

The international journal of Research on Engineering Structures and Materials (RESM) is currently Abstracted/Indexed by Asos Indeks, CiteFactor, Cosmos, CrossRef, Directory of Research Journal Indexing, Engineering Journals (ProQuest), EZB Electronic Journal Library, Global Impact Factor, Google Scholar, International Institute of Organized Research (I2OR), International Scientific Indexing (ISI), Materials Science & Engineering Database (ProQuest), Open Academic Journals Index, Publication Forum, Research BibleScientific Indexing Service, Root Indexing, Scopus, Ulakbim TR Index (Tubitak), Universal Impact Factor and under evaluation by many other respected indexes.

Check web site for current indexing info, [www.jresm.org](http://www.jresm.org)



Research Article

## Improvements of mechanical and physical features of cement mortar by nano $AL_2O_3$ and $CaCO_3$ as additives

Abeer M. Humad<sup>1,a</sup>, Ali J. Dakhil<sup>2,b</sup>, Samer A. Al-Mashhadi<sup>1,c</sup>, Zainab Al-Khafaji<sup>3,4,\*d</sup>, Zainab Adel Mohammed<sup>5,e</sup>, Sarah Fadel Jabr<sup>6,f</sup>

<sup>1</sup>Civil Eng. Dept., College of Engineering, University of Babylon, Babylon, Iraq

<sup>2</sup>Dept. of Roads and Transport Eng., College of Eng., University of Al-Qadisiyah, Al-Qadisiyyah, Iraq

<sup>3</sup>Dept. of Civil Eng., Faculty of Eng. and Built Environment, Universiti Kebangsaan Malaysia, Malaysia

<sup>4</sup>Imam Ja'afar Al-Sadiq University, Qahira, Baghdad, Iraq

<sup>5</sup>Babel Tower for Studies and Scientific Research com

<sup>6</sup>College of Materials Engineering, University of Babylon, Iraq

### Article Info

### Abstract

#### Article history:

Received 06 Aug 2023

Accepted 10 Dec 2023

#### Keywords:

Cement mortar;  
 $AL_2O_3$  and  $CaCO_3$   
nanoparticles;  
Compressive strength;  
Density;  
Ultrasonic pulse  
velocity

The impact of Nanoparticles of ( $AL_2O_3$  and  $CaCO_3$ ) particles on the features of cement mortar was explored in current research with a mean diameter of ~50nm, and 100nm in three various amounts of 1, 3, and 5% substitution by cement's weight as binary blending materials with fixed water/cement proportion 0.46. Cement mortar's mechanical and physical features (compressive strength, density) were tested after 7 and 28 days. The findings illustrated that utilizing nanoparticles of  $AL_2O_3$  improved the mortar compressive strength at early ages at 7 curing days better than 28 curing days, and 3% of substitution was the optimal proportion. Also, utilizing nano- $CaCO_3$  as a binary blending mixture with substitution proportion (1, 3, 5%) by cement's weight improved mortar compressive strength at early ages at 7 curing days better than 28 curing days. However, there were no apparent effects when nanoparticles of ( $AL_2O_3$  and  $CaCO_3$ ) were replaced on the density and ultrasonic pulse velocity of cement mortar at 7 and 28 days. The interaction impact of substitution 1 and 3 percent of nanoparticles of ( $AL_2O_3$  and  $CaCO_3$ ) particles to cement mortar increased the CS by (28 and 74%) at 7 curing days and (30 and 42%) at 28 curing days, respectively.

© 2024 MIM Research Group. All rights reserved.

## 1. Introduction

Ordinary Portland cement (OPC) is a type of cement that is commonly utilized in concrete and mortar. It is made by heating limestone and clay at high temperatures and grinding the resulting material into a fine powder [1–3]. OPC is the most common type of cement utilized in various applications, including foundations, driveways, sidewalks, and walls. It also creates various structures, including bridges and dams [4,5]. OPC is highly durable and has a long-life span. It is also relatively inexpensive and has a high compressive strength (CS), meaning it can withstand much pressure. OPC concrete is made by mixing OPC with water and aggregate (sand, gravel, or crushed stone). This mixture is then poured into forms and allowed to harden. OPC concrete is strong, durable, and has a long life span, making it a popular choice for construction projects [6].

Portland cement is an essential concrete component, producing significant amounts of CO<sub>2</sub> throughout its manufacturing process [7]. The primary sources of CO<sub>2</sub> emissions come

\*Corresponding author: [p123005@siswa.ukm.edu.my](mailto:p123005@siswa.ukm.edu.my)

<sup>a</sup> [orcid.org/0000-0002-5328-4073](https://orcid.org/0000-0002-5328-4073); <sup>b</sup> [orcid.org/0000-0002-3598-261X](https://orcid.org/0000-0002-3598-261X); <sup>c</sup> [orcid.org/0009-0008-0507-9121](https://orcid.org/0009-0008-0507-9121);

<sup>d</sup> [orcid.org/0000-0002-5450-7312](https://orcid.org/0000-0002-5450-7312); <sup>e</sup> [orcid.org/0009-0003-4910-7482](https://orcid.org/0009-0003-4910-7482); <sup>f</sup> [orcid.org/0009-0001-0203-8956](https://orcid.org/0009-0001-0203-8956)

DOI: <http://dx.doi.org/10.17515/resm2023.43me0806rs>

from burning fossil fuels (coal and natural gas) utilized to heat the rotary kiln and from the calcination process [8,9]. Other sources of emissions include the burning of fuels to drive the grinding and mixing equipment and the movement of materials throughout the cement manufacturing process [10,11]. However, several alternatives to OPC can be utilized in place of it [10-21]. These alternatives include fly ash, slag cement, silica fume, and the Nanomaterials that have recently been utilized in a cement matrix, which involved various types, including Nanoparticles of  $\text{SiO}_2$ ,  $\text{TiO}_2$ ,  $\text{AL}_2\text{O}_3$ , carbon Nano-fibers,  $\text{Fe}_2\text{O}_3$ , and  $\text{CaCO}_3$ . It was detected that the nanomaterials utilized in cement and concrete improve their mechanical, physical, and other features [22].

Ali Nazari et al. [23] explored the impact of  $\text{AL}_2\text{O}_3$  with nanoparticles on the strength of concrete. Nano- $\text{AL}_2\text{O}_3$  with four various amounts of 0.5, 0.1, 1.5, and 2.0 percent by cement's weight. The mean particle size of  $\text{AL}_2\text{O}_3$  with nanoparticles is 15nm, with a water/binder proportion of 0.40. Cubes with a 100mm edge were cast and compacted in two layers on a vibrating table. The CS of concrete made without add had (27.3, 36.8, 42.3) MPa at (7, 28, and 90) days. However, by increasing  $\text{AL}_2\text{O}_3$  nanoparticles to 2.0, the CS had (27.5, 37.7, 42.6) MPa at (7, 28, and 90) days, respectively. It indicates a reduction in CS with no discernible cause. According to the researcher, "it might be since the  $\text{AL}_2\text{O}_3$  nanoparticles greater than the required amount to incorporate with liberated lime throughout the process of hydration, resulting in excess silica leaching out and causing a deficiency in strength as it substitutes some of the cementitious material but does not contribute to strength. Additionally, the weak areas might result from faults created throughout the dispersion of nanoparticles.

Arefi et al. [24] investigated the impact of adding  $\text{AL}_2\text{O}_3$  nanoparticles on cement mortar features.  $\text{AL}_2\text{O}_3$  nanoparticles with a mean particle size of 20nm were utilized with three amounts of 1, 3, and 5 percent by cement's weight—water/binder proportion of 0.42. For compressive tests, cubes of size  $50 \times 50 \times 50$  mm in three layers were cast and compressed by 10 impacts of a steel rod. This study illustrated that CS without add had 11.96MPa at 7 curing days, while concrete made with 1 percent of  $\text{AL}_2\text{O}_3$  with nanoparticles had (17.25 MPa), with 3 percent had (19.54MPa). However, by increasing  $\text{AL}_2\text{O}_3$  nanoparticles to 5 percent, the CS had (10.9 MPa). That means the mechanical features are reduced severely by increasing  $\text{AL}_2\text{O}_3$  nanoparticles to 5 percent. The researcher thinks it may be due to reduced nanoparticle distance and  $\text{Ca}(\text{OH})_2$  crystals since limited space cannot grow to the appropriate size. This factor, along with the agglomerated nanoparticles, causes a reduction in CS.

Liu et al. [25] investigate the impact of nanoparticles of  $\text{CaCO}_3$  on cement paste. Nanoparticles of  $\text{CaCO}_3$  were added to three various substitutions (1, 2, 3 percent) of cement weight and the mean particle size (15-50) nm. The water/cement proportion was 0.45. The CS test was done at 7 and 28 curing days. Samples were cubic bars with the size (20\*20\*80) mm. The result illustrated that the CS in the two ages increased with  $\text{CaCO}_3$  until it reached 20 percent and then reduced when  $\text{CaCO}_3$  was 2 percent; the CS had (111.2 percent and 108.6 percent) at age (7 and 28) curing days, respectively. "Since the consuming and refinement of  $\text{Ca}(\text{OH})_2$  grain, which occurred throughout the hydration of cement, especially at early ages".

Barbhuiya et al. [26] Conducted a study to find the impact of  $\text{AL}_2\text{O}_3$  with nanoparticles on the CS of cement paste at an early age.  $\text{AL}_2\text{O}_3$  with nanoparticles with a mean particle size of 27-43nm were utilized, two various replaced with 2 percent and 4 percent by cement's weight, the water-to-binder proportion of 0.4. Cubes of 50mm size were cast and vibrated on the vibration table. The CS of hydrated cubes was calculated at 1, 3, and 7 curing days. This research illustrated that the CS of cement paste having 2 percent and 4 percent nano- $\text{AL}_2\text{O}_3$  increased slightly at 1 and 7 curing days. It was noticed that adding nano- $\text{AL}_2\text{O}_3$  in

cement paste does not directly impact CS because the changes in CS at 1, 3, and 7 curing days are minimal.

AL Ghabban et al. [27] explored the impact of nanoparticles of  $CaCO_3$  in concrete. Nanomaterials were added in four various substitutions (1, 2, 3, and 4 percent) of cement weight in the concrete mixture, with a water/binder proportion of 0.32. The test samples utilized were cubic with dimensions (150 \*150\*150) mm for the CS test. The result that concretes made with (0, 1, 2, 3, and 4 percent) had (52, 54, 58, 60, and 63) MPa at 28 curing days. It has been detected that an increase in CS (4 percent) at 28 curing days, and the optimal dosages for nanoparticles of  $CaCO_3$  were 4 and 3 percent, respectively, for improving the mechanical features of concrete.

Cosentino et al. [28] conducted to find the impact of nanoparticles of  $CaCO_3$  in cement mortar.  $CaCO_3$  nano partials with a mean diameter of 60nm were utilized with four different substitutions (1, 2, 3, and 7 percent) of cement weight. Cement mortar made without add had 40.16 MPa at 7 and 53.28 MPa at 28 curing days. Substitution of nanoparticles of  $CaCO_3$  with (1, 2, 3, 7 percent) had (40.16, 43, 38, 44.16) MPa respectively at seven days, and (53.28, 55, 51.78, 50.81) MPa respectively at 28 curing days. The CS increased by 7 percent for seven days, but at 28 curing days, the CS reduced. Since poor dispersion and the agglomeration phenomena of the nanoparticles in the slurry and the cement matrix."

Jawad et al. [29] determined the impact of various nanomaterials on the CS of cement mortar. Four amounts of  $AL_2O_3$  with nanoparticles were utilized as a partial substitution of 1, 1.5, 3, and 5 percent by cement's weight. W/C proportion of 0.45. Cubic samples with dimensions 50× 50 ×50mm of cement mortar were produced for CS after 7 and 28 curing days in water. The CS without add had (22, 26) MPa respectively at (7, 28) days. Nevertheless, with (1, 1.50, 3, and 5 percent), the CS recorded (23, 27.7, 32, 33) MPa at seven days and (26.5, 30, 36, 38) MPa, respectively, at 28 curing days. It has been detected that the CS of mortar can be increased gradually by increasing the amount of  $AL_2O_3$  with nanoparticles up to 5 percent by the weight of cement. The increase in CS of cement mortar since the fast consumption of  $Ca(OH)_2$  developed throughout the Portland cement hydration, especially early, is related to the high reactivity of  $AL_2O_3$  with nanoparticles.

Iskra-Kozak and Konkol [30] illustrated the impact of  $AL_2O_3$  with nanoparticles on cement mortar's physical and mechanical features at early and later ages. Four amounts of 1, 2, 3, and 4 percent of  $AL_2O_3$  with nanoparticles, respectively utilized by cement's weight. The water/binder proportion was 0.5, and the binder to the sand proportion was 1:3. Three samples of each additive were made, and the CS of the mortars was tested after 7, 28, and 90 days of curing. The CS without add had (28.2, 36.9, 42) MPa respectively at (7, 28, 90) days. Nevertheless, with (1, 2, 3, and 4 percent) the CS recorded (34.1, 32.4, 31.6, 29.9) MPa, respectively, at seven days, had (39.5, 40.0, 39.6, 36.8) MPa, respectively at 28 curing days and had (47.3, 46.3, 44.6, 44.1) MPa respectively at 90 days. The highest CS of mortars is observed by adding 1 percent  $AL_2O_3$  with nanoparticles. However, with the increase of the addition of nano alumina oxide, the CS of the mortar reduced since the nanoparticles of  $AL_2O_3$  lead to the formation of agglomerates in the structure of the mortar, and this phenomenon findings from the high specific surface area of the  $AL_2O_3$  with nanoparticles.

Muhsin and Fawzi [31] explored the impact of nanoparticles of  $CaCO_3$  on concrete. Nanomaterial was added in three various substitutions (0.75,1,1.5 percent) of cement weight. The mean particle diameter is 100 nm. By utilizing standard cubic samples (50\*50\*50) mm, the findings illustrated that the CS increased (11.4, 39.3, 23.7 percent) at seven days, (5.8, 28.2, and 4.6 percent) at 28 curing days. Also, the result demonstrates that 1 percent of nanoparticles of  $CaCO_3$  give the highest CS at all ages. "Since there is high

surface energy throughout the hydration process, they grow and form a clump with nanoparticles as a nucleus that work on increasing and accelerating the hydration process.

Many studies have been directed toward improving the mechanical features of cement mortar by utilizing nanoparticles, including nanoparticles of ( $AL_2O_3$  and  $CaCO_3$ ) particles. Most researchers noticed that substituting  $AL_2O_3$  with nanoparticles up to 4 percent and 5 percent by cement weight reduces the CS of cement mortar. At the same time, some authors observed that substituting 5 percent of  $AL_2O_3$  with nanoparticles increases the CS, and others observed that substituting  $AL_2O_3$  with nanoparticles did not impact CS. Most researchers noticed that with substitution nano- $CaCO_3$  up to (3,4, and 7 percent) by cement's weight, the CS increased at 7 and 28 curing days, while some observed the CS reduce at 7 and 28 curing days. Previous research found findings inconsistent when utilizing various proportions of nanoparticles of ( $AL_2O_3$  and  $CaCO_3$ ). Therefore, this research aims to study the impact of adding nanomaterials, including [nanoparticles of ( $AL_2O_3$  and  $CaCO_3$ )], to cement mortar and find the best percentage of adding nanoparticles to improve cement mortar's physical and mechanical features.

## 2. Material and Methodology

### 2.1. Materials

#### 2.1.1. Cement

Ordinary Portland cement was utilized; the physical and chemical features are illustrated in Table 1. This work utilized locally available natural sand with a fineness modulus of 2.17 as fine aggregate. The grading of this aggregate was zone 3 as limits of Iraq requirements, No.45/1984.

Table 1. The chemical and physical features of cement.

Chemical composition	Amounts (by weight %)	Limits of Iraqi Requirements NO.5/2019 (42.5 R)
Cao	60.60	---
SiO <sub>2</sub>	19.80	---
AL <sub>2</sub> O <sub>3</sub>	4.80	---
Fe <sub>2</sub> O <sub>3</sub>	3.00	---
MgO	3.50	≤ 5.0 percent
SO <sub>3</sub>	2.22	≤ 2.8 percent if C3A > 3.5 percent
Loss on Ignition (L.O.I.)	3.10	≤ 4.0 percent
The insoluble residue (I.R.)	0.70	≤ 1.5 percent
OPC main compounds (Bogue's Eq.)		
Tricalcium silicate (C <sub>3</sub> S)		59.63
Dicalcium silicate (C <sub>2</sub> S)		11.78
Tricalcium aluminate (C <sub>3</sub> A)		7.64
Tetra calcium alumina-ferrite (C <sub>4</sub> AF)		9.12
Test name	Findings	Limits of Iraqi Requirements NO.5/2019 (42.5 R)
Fineness (Blaine method), (m <sup>2</sup> /kg)	320	≥ 280
Setting time (Vicat's method),	90	≥ 45

Initial setting time (min.)	5	≤ 10
Final setting time (hr.)		
Compressive strength (MPa),		
Early strength (2 days)	24	≥ 20
Standard strength (28 curing days)	43	≥ 42.5

2.1.2. Supplementary Materials

Nano- $AL_2O_3$  with a mean particle size of ~50 nm. The physical and chemical features of  $AL_2O_3$  with nanoparticles are given in Table 2; also, Nano- $CaCO_3$  has a mean particle size of less than 100nm. The features of  $CaCO_3$  with nanoparticles are illustrated in Table 3. Finally, tap water was utilized throughout this work for mixing and curing.

Table 2. Physical and chemical features of nano- $AL_2O_3$ .

Features	Purity	Mean particle size	Density	Ca	K	Cu	Mg	Fe	Mn	Zn	Si
Magnitudes	99.9+ percent (trace metal basis)	50 nm	3.1	<100	<100	<10	<50	<100	<50	<50	<100

Table 3. The physical and chemical features of nano- $CaCO_3$ .

Features	Appearance	Density	Size	Specific area	MgO	Moisture amount	Loss on ignition	Residue on Sieve	$CaCO_3$ amount
Magnitudes	White powder	2.5	>100	≥ 20	≤0.8	≤0.9	44±1	≤0.02	≥96
Features	Alumina + Iron oxide		PH	The insoluble matter with acid		Activation rate		DOP absorbed does	
Magnitudes	≤0.3		8.5-9.7	≤0.3		≥95		35-55	

2.1.3. Sand

Locally available natural sand is applied as a fine aggregate conforming to the requirements of [32]. The fine modulus of 2.42 sulfate content is 0.1% with a density of fine aggregate of 1600 kg/m<sup>3</sup>. The fine aggregate was utilized in the surface's saturated and dry state and has been utilized in the current study. The grading of fine aggregate is demonstrated in Table 4.

Table 4. Fine aggregate grading

Sieve size (mm)	Percent Passing %
10	100
7.75	93.5
2.36	84
1.18	75.5
0.6	50
0.3	20
0.15	4



## 2.2. Mixing Procedure and Samples Preparing

In this study, nine types of mixes were produced to find the impact of nanoparticles of ( $AL_2O_3$  and  $CaCO_3$ ) on the CS of cement mortar. These mixes were [A, B<sub>1</sub>, B<sub>2</sub>, B<sub>3</sub>, C<sub>1</sub>, C<sub>2</sub>, C<sub>3</sub>, B<sub>1</sub>+C<sub>1</sub> and B<sub>2</sub>+C<sub>2</sub>]. Type-A mixture was produced of fine natural aggregate, cement, and water. Types-(B<sub>1</sub>, B<sub>2</sub>, B<sub>3</sub>, C<sub>1</sub>, C<sub>2</sub>, C<sub>3</sub>) were produced with various contest of nanoparticles of ( $AL_2O_3$  and  $CaCO_3$ ) particles. The mixes have been produced with cement substitution (1, 3, 5 percent) by weight. Types- (B<sub>1</sub>+C<sub>1</sub> and B<sub>2</sub>+C<sub>2</sub>) mixtures were produced with nanoparticles of ( $AL_2O_3$  and  $CaCO_3$ ) particles and the cement substitution (1, 3 percent) by weight. In the initial step of mixing the nanomaterials, the binder to the sand of 1:2 and the w\c of 0.46 (water =300 ml and cement =) was mixed in a dry condition for one minute and another two minutes after adding the water. Cubes with size 50 ×50 ×50 mm for the CS tests were cast and compacted in two layers on a vibrating table, where each layer was vibrated for 15 s. The mold was covered for 24 hours. Then, the samples were de-molded and cured in water for the test day. The concrete samples' compressive strength (CS) tests were determined at 7 and 28 curing days (three samples for each mix and the average value). The mixtures with nanoparticles of ( $AL_2O_3$  and  $CaCO_3$ ) are presented in Fig. (1) and Table (5).

The ultrasonic pulse velocity of the high-strength concrete was measured using Pundit Lab+ according to BS:12504 [33] requirements. It had a bandwidth between 24-500HZ. The Ultrasonic pulse velocity (Pundit Lab+) is demonstrated in Fig. 1(b).

The density of the concrete was measured with 150x150x150 mm cubes by the ASTM C 642-13 standard [34]. The dry density of concrete cubes can be determined through a series of steps. Firstly, the specimens are subjected to drying in an oven at a temperature of 110 degrees Celsius for one day. After this, the specimens are submerged in water for another day. Their wet weights are recorded once the specimens have reached a stable state. Finally, the samples are weighed again while submerged in water to obtain the weights. The investigation was conducted at the respective time intervals of 7 and 28 days. The density of cubic concrete samples can be determined by employing the formula outlined in the reference [35].

$$\text{Dry density} = \frac{W_1}{W_2 - W_3} * P_w \quad (1)$$

Where:

$W_1$ : The dry weight of the sample (g),  $W_2$ : The wet weight of the sample (g),  $W_3$ : The immersed Specimen weights in water (g),  $P_w$ : The water density equals (1 g/cm<sup>3</sup>).

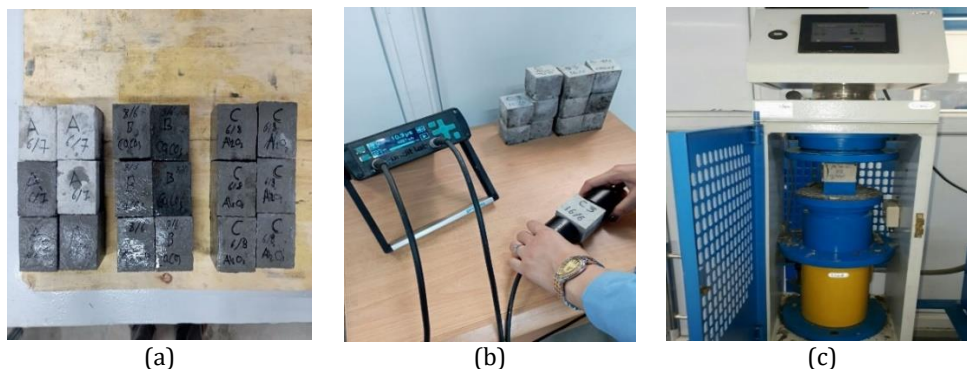


Fig. 1. (a) Various mortar cubes, (b) Test of Ultrasonic pulse velocity, (c) compressive strength test machine.

Table 5. The mixtures of nanoparticles of ( $AL_2O_3$  and  $CaCO_3$ ).

Sample	Cement (gm)	Sand (gm)	Water (gm)	Nano- $AL_2O_3$ (gm), %	Nano- $CaCO_3$ (gm), %	W\C
A (control)	650	1300	300	-	-	0.46
B1	643	1300	300	7, (1 percent)		0.46
B2	630	1300	300	20, (3 percent)		0.46
B3	620	1300	300	30, (5 percent)		0.46
C1	643	1300	300		7, (1 percent)	0.46
C2	630	1300	300		20, (3 percent)	0.46
C3	620	1300	300		30, (5 percent)	0.46
B1+C1	643	1300	300	3.5, (1 percent)	3.5, (1 percent)	0.46
B2+C2	630	1300	300	10, (3 percent)	10, (3 percent)	0.46

where;

A is the cement mortar mix without nanoparticles, B refers to the mixes with  $CaCO_3$  with nanoparticles with various substitution proportions, C refers to the mixes with  $AL_2O_3$  with nanoparticles with various substitution proportions.

(B+C) refers to the mixes of cement mortar and a combination of both nanoparticles with various substitution proportions.

### 3. Result and Discussion

#### 3.1. Mechanical and Physical Features

The CS, density, and ultrasonic pulse velocity (UPV) test of cement mortar with partial substitution of nanoparticles of ( $AL_2O_3$  and  $CaCO_3$ ) by cement's weight are illustrated in Table (6).

Table 6. Result of CS, density, and UPV for cement mortar with nanoparticles of ( $AL_2O_3$  and  $CaCO_3$ ) particles.

Samples	Nano $CaCO_3$ (%)	Nano $AL_2O_3$ (%)	CS (MPa)		Density (kg\m3)		UPV (m\s)
			7 days	28 days	7 days	28 days	28 days
A (control)	0	0	20.5	27	2312	2320	4587
B1		1	31	33	2288	2278	4356
B2		3	38.5	38	2288	2294	4520
B3		5	21	37.5	2282	2309	4383
C1	1		31.6	31	2352	2336	4533
C2	3		37.5	33	2253	2296	4587
C3	5		33	27.5	2285	2329	4385
B1+C1	1	1	26.3	35	2285	2296	4533
B2+C2	3	3	35.7	38.3	2270	2299	4587

Fig. 2 and 3 demonstrate the CS findings of the selected mixtures before and after replacing OPC with different nanoparticles of ( $AL_2O_3$  and  $CaCO_3$ ) proportions, utilizing nano ( $AL_2O_3$ ,  $CaCO_3$ , and  $AL_2O_3+CaCO_3$ ) increase the CS at early ages when utilizing 1 and 3 percent, but

increase the replacement to 5 percent lead to decrease the early ages significantly since creating ettringite at early ages [36], and utilizing  $CaCO_3$  with 3 percent considered best ratio for replacement.

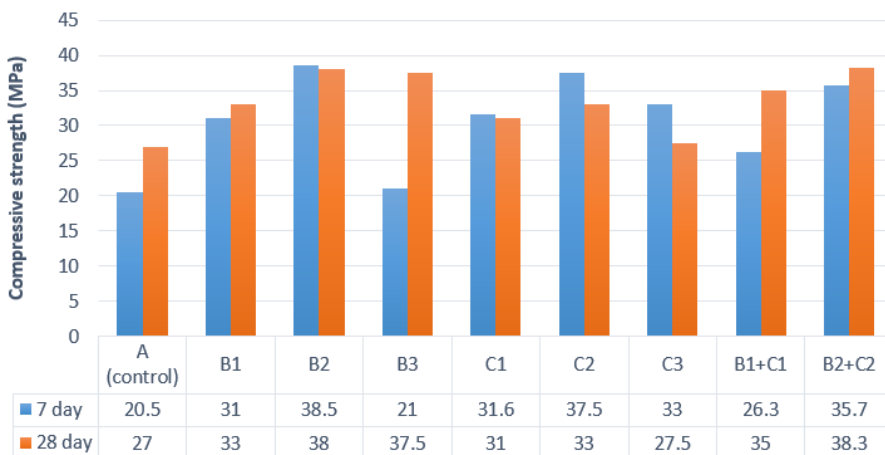


Fig. 2. CS finding various samples at 7 and 28 curing days

Fig. 3 demonstrates the CS findings of the selected mixtures before and after replacing OPC with different nanoparticles of ( $AL_2O_3$  and  $CaCO_3$ ) proportions, utilizing nano- $AL_2O_3$ ,  $CaCO_3$ , and nano- $AL_2O_3+CaCO_3$  increase the CS at 28 ages when utilizing 1 and 3 percent, but increase the replacement to 5 percent lead to decrease the final ages significantly since converting ettringite to cement's get (C-H, C-S-H) at final ages and [36–38], and utilizing nano- $AL_2O_3+CaCO_3$  with 3 percent considered best ratio for replacement at final ages.

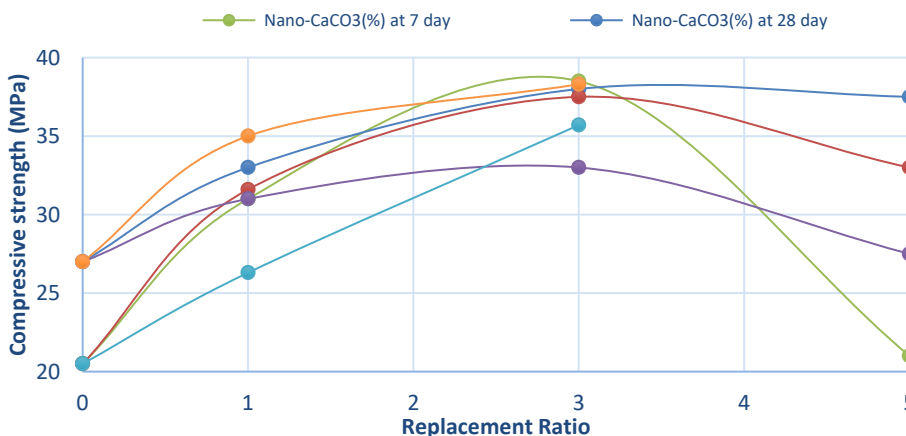


Fig. 3. Influence of replacing OPC with Nano ( $CaCO_3$ ,  $AL_2O_3$ , and  $CaCO_3 + AL_2O_3$ ) on CS at 7 and 28 curing days

Figs. 4 and 5 demonstrate the density findings of the selected mixtures before and after replacing OPC with different nanoparticles of ( $AL_2O_3$  and  $CaCO_3$ ) proportions; utilizing nano- $AL_2O_3$ , increasing the density at 7 and 28 ages when utilizing 1, but increasing the replacement to 3 percent led to a decrease the density of the early ages significantly, utilizing nano- $CaCO_3$ , decrease the density at 7 and 28 ages when utilizing 1, but increase the replacement to 3 percent lead to increase the density of the early ages little and notable

for final ages. While combining nano- $AL_2O_3+CaCO_3$  with 1 and 3 percent reduces the density for both 7 and 28 curing ages, final ages give better findings than early ones.

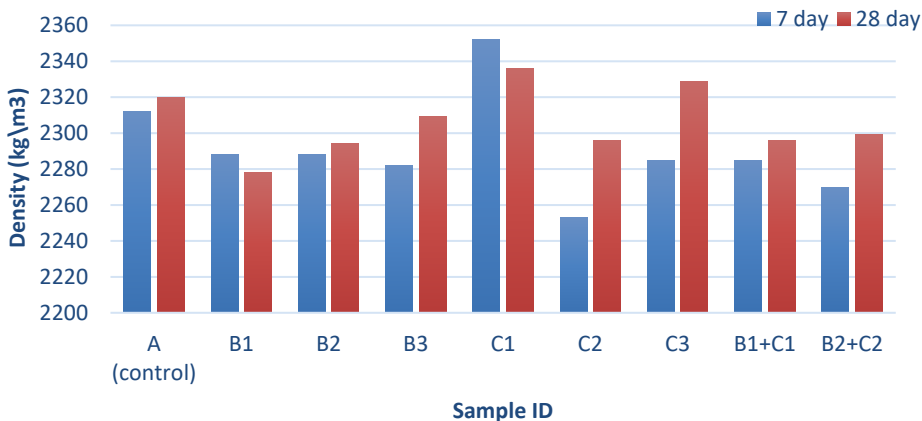


Fig. 4. Density finding for various samples at 7 and 28 curing days

It has been detected that the CS of cement mortar with  $AL_2O_3$  with nanoparticles (1, 3, and 5 percent) (C1, C2, C3) substitution by cement’s weight, the CS increase (54, 82, 61 percent) at 7 curing days and (14, 22, 1 percent) at 28 curing days respectively. It was noticed that utilizing 5 percent  $AL_2O_3$  with nanoparticles reduces the CS to a magnitude near the standard sample (A). It might be because there are more  $AL_2O_3$  nanoparticles present than what is necessary to react with the freed lime throughout the hydration process, resulting in excess silica leaking out and weakening the concrete since it only replaces a portion of the cementitious material. Additionally, the weak areas might result from flaws created throughout the dispersion of nanoparticles [23]. The best CS for all cement mortar mixtures was noticed with substitution of 1 percent and 3 percent of  $AL_2O_3$  with nanoparticles Because the  $AL_2O_3$  had high activity. The presence of nanoparticles in the cementing system leads to the consumption of portlandite  $Ca(OH)_2$  caused by a pozzolanic reaction, filling the capillaries, reducing the pores, and increasing the strength.

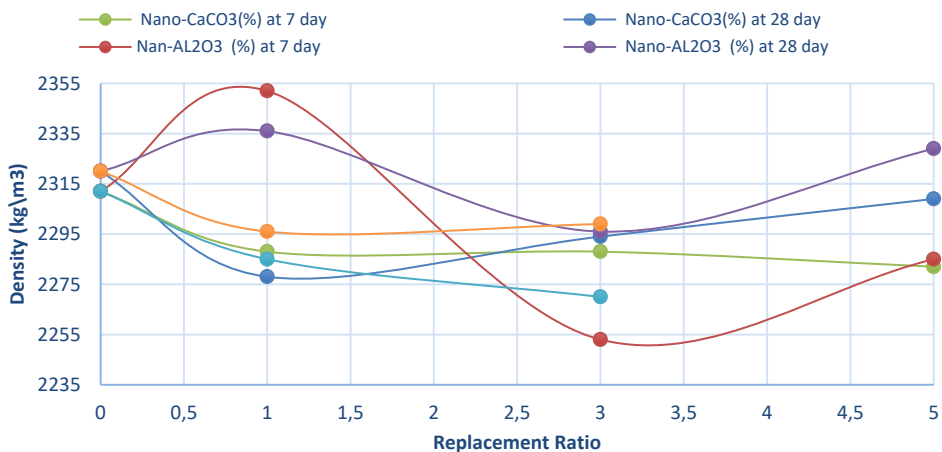


Fig. 5. Influence of replacing OPC by Nano ( $CaCO_3$ ,  $AL_2O_3$ , and  $CaCO_3 + AL_2O_3$ ) at 7 and 28 curing days on density.

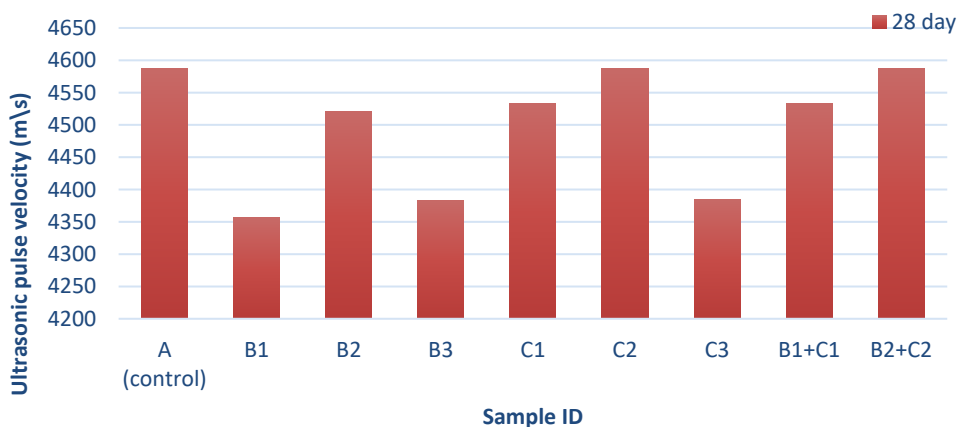


Fig. 6. Ultrasonic pulse velocity finding for various samples at 7 and 28 curing days.

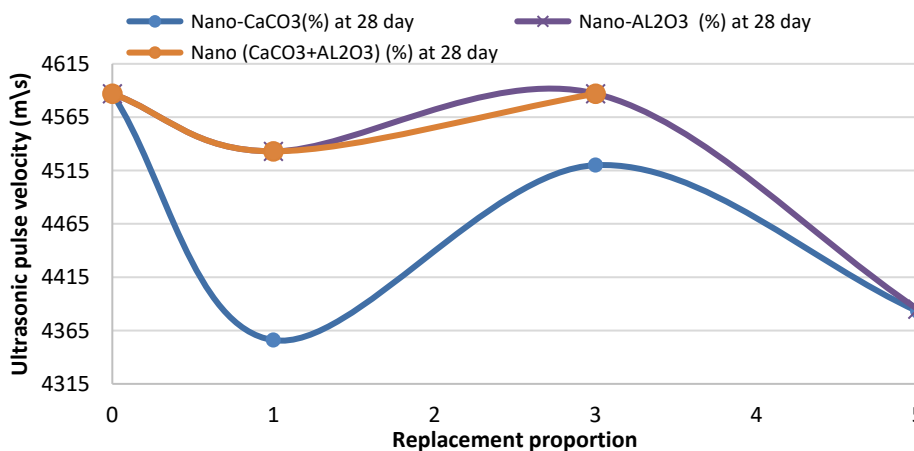


Fig. 7. Influence of replacing OPC by Nano ( $CaCO_3$ ,  $AL_2O_3$ , and  $CaCO_3 + AL_2O_3$ ) at 28 curing days on UPV.

Furthermore, no apparent effects were when replaced nanoparticles of ( $AL_2O_3$  and  $CaCO_3$ ) with (1, 3, and 5 percent) by cement's weight in density and ultrasonic pulse velocity of cement mortar at 7 and 28 curing days, respectively; this probably attributed to the size of cubes were small with dimensions ( $50 \times 50 \times 50$ ) mm as illustrated in Fig. 6 and 7.

For  $CaCO_3$  with nanoparticles replaced by (1, 3, and 5 percent) (B1, B2, B3) by cement's weight, the findings illustrated that the CS increase (51, 87, 2.4 percent) and (22,40,38 percent) at 7 and 28 curing days respectively. It was noted that the increase in CS at (1 percent and 3 percent) because the  $CaCO_3$  with nanoparticles are chemically stable and filled the pores and increased the surface activity.

In the case of a combination of substitution of nanoparticles in cement mortar cubes having combined 1 percent and 3 percent (B1+C1) and (B2+C2) nanoparticles of ( $AL_2O_3$  and  $CaCO_3$ ). The substitution of 1 percent and 3 percent of nanoparticles of ( $AL_2O_3$  and  $CaCO_3$ ) to cement mortar increased the CS (28 and 74 percent) at 7 curing days and (30 percent and 42 percent) at 28 curing days, respectively. Because the  $AL_2O_3$  nanoparticles had high activity, the present nanoparticles in the cementing system led to the consumption of portlandite  $Ca(OH)_2$  caused by a pozzolanic reaction that fills the capillaries, reducing the

pores and increasing the strength. The  $CaCO_3$  with nanoparticles filled the pores and increased the surface activity.

### 3.2. Statistical Analysis of Results

Determining which substitution proportion of nanoparticles significantly affects the explored parameters is possible by utilizing a completely randomized design and implementing two-factor ANOVA without replication. Hence, tests of samples' mechanical and physical parameters (i.e., CS and density) on one sample of each of the nine cement mortar mixes. Table (7) presents the CS and density based on the substitution proportion (treatment) per curing age.

Table 7. Data for two-factor ANOVA without replication analysis.

Treatment	Control	B1 (1 %)	B2 (3 %)	B3 (5 %)	C1 (1 %)	C2 (3 %)	C3 (5 %)	B1+C1 (1 %)	B2+C2 (3 %)
CS (MPa)									
7days	20.5	31	38.5	21	31.6	37.5	33	26.3	35.7
28 curing days	27	33	38	37.5	31	33	27.5	35	38.3
Density (kg/m <sup>3</sup> )									
7days	2312	2288	2288	2282	2352	2253	2285	2285	2270
28 curing days	2320	2278	2294	2309	2336	2296	2329	2296	2299

Tables (8 and 9) demonstrate the main part of the findings of the two-factor ANOVA analysis. The rows relate to the determined factors, and the columns relate to the substitution proportion.

Table 8. Output for two-factor ANOVA analysis for CS (MPa) at a significant level of 0.05.

Source	SS	df	MS	F	p-magnitude
Rows	35.28	1	35.28	1.4796	0.2585
Columns	311.23	8	38.9037	1.6316	0.2521
Error	190.75	8	23.8437		
Total	537.26	17	31.6035		

Table 9. Output for two-factor ANOVA analysis for Density (kg/m<sup>3</sup>) at a significant level of 0.05

Source	SS	df	MS	F	p-magnitude
Rows	1122.25	1	1122.25	4.3360	0.07582
Columns	6487	7	926.7142	3.5805	0.0571
Error	1811.75	7	258.8214		
Total	9421	15	628.0666		

df: the freedom degrees in the source; SS: the sum of squares because of the source; MS: the sum of squares means because of source; F: the *F*-statistic; P: the *P*-magnitude.

As the focus was on the columns factor (substitution proportion) for both explored factors, there was a slight variance between the substitution proportions for the CS (p-magnitude = 0.2521). On the other hand, there was a significant variance between the substitution proportions for the density (p-magnitude = 0.0571), which was inferred to agree with the analysis of the previous findings [39,40].

#### 4. Conclusion

The mechanical features of cement mortar are affected by substituting nanoparticles of ( $AL_2O_3$  and  $CaCO_3$ ) with cement. It has been detected from replacing nanoparticles of ( $AL_2O_3$  and  $CaCO_3$ ) in cement mortar that:

- The compressive strength was improved by (54 82)% and (15 and 22)% when using nanoparticles of  $AL_2O_3$  by (1 and 3)% by cement weight at 7 and 28 curing ages, respectively.
- Increasing the utilized ratio of  $AL_2O_3$  to 5wt% of cement led to a decreased compressive strength improvement rate for the produced mortar at the advanced ages from 61% to 2% only compared with the control sample without additives material. The best compressive value was obtained when using 3wt% of  $AL_2O_3$ .
- The compressive strength was improved by (51, 88, 2)% and (22, 41and 39)% when using nanoparticles of  $CaCO_3$  by (1, 3, and 5)% by cement weight at 7 and 28 curing ages, respectively.
- Increasing the utilized ratio of  $CaCO_3$  to 5wt% of cement decreased the compressive strength of the produced mortar at the advanced ages. The best compressive value was obtained when using 3wt% of  $AL_2O_3$ .
- Substituting 1 percent and 3 percent of binary combination nanoparticles of ( $AL_2O_3$  and  $CaCO_3$ ) to cement mortar increased the CS to (28 percent and 74 percent) MPa at 7 curing days and (30 percent and 42 percent) MPa at 28 curing days, respectively.
- The effects of replacing nanoparticles of ( $AL_2O_3$  and  $CaCO_3$ ) with (1, 3, 5 percent) by cement's weight on density and ultrasonic pulse velocity of cement mortar at 7 and 28 curing days were insignificant.

#### References

- [1] Ali YA, Falah MW, Ali AH, Al-Mulali MZ, AL-Khafaji ZS, Hashim TM, et al. Studying the effect of shear stud distribution on the behavior of steel-reactive powder concrete composite beams using ABAQUS software. Journal of the Mechanical Behavior of Materials 2022;31:416–25. <https://doi.org/10.1515/jmbm-2022-0046>
- [2] Hamad MA, Nasr M, Shubbar A, Al-Khafaji Z, Al Masoodi Z, Al-Hashimi O, et al. Production of Ultra-High-Performance Concrete with Low Energy Consumption and Carbon Footprint Using Supplementary Cementitious Materials Instead of Silica Fume: A Review. Energies 2021;14:8291. <https://doi.org/10.3390/en14248291>
- [3] Al-Masoodi ZO., Al-Khafaji; Z, Jafer; HM, Dulaimi; A, Atherton W. The effect of a high alumina silica waste material on the engineering properties of a cement-stabilised soft soil. The 3rd BUId Doctoral Research Conference, Dubai, AUE: 2017.
- [4] Al-Husseinawi FN, Atherton W, Al-Khafaji Z, Sadique M, Yaseen ZM. The Impact of Molar Proportion of Sodium Hydroxide and Water Amount on the Compressive Strength of Slag/Metakaolin (Waste Materials) Geopolymer Mortar. Advances in Civil Engineering 2022;2022. <https://doi.org/10.1155/2022/591070> 1
- [5] SHUBBAR ALI, Al-khafaji Z, Nasr M, Falah M. Using non-destructive tests for evaluating flyover footbridge: case study. Knowledge-Based Engineering and Sciences 2020;1:23–39. <https://doi.org/10.51526/kbes.2020.1.01.23-39>
- [6] Zhang G, Ali ZH, Aldlemy MS, Mussa MH, Salih SQ, Hameed MM, et al. Reinforced concrete deep beam shear strength capacity modelling using an integrative bio-inspired algorithm with an artificial intelligence model. Engineering with Computers 2020:1–14. <https://doi.org/10.1007/s00366-020-01137-1>
- [7] Al-Khafaji ZS, Al-Naely HK, Al-Najar AE. A review applying industrial waste materials in stabilisation of soft soil. Electronic Journal of Structural Engineering 2018;18:16–23. <https://doi.org/10.56748/ejse.182602>

- [8] Hussain AJ, Al-Khafaji ZS. Reduction of environmental pollution and improving the (Mechanical, physical and chemical characteristics) of contaminated clay soil by using of recycled oil. *Journal of Advanced Research in Dynamical and Control Systems* 2020;12:1276–86. <https://doi.org/10.5373/IARDCS/V12SP4/20201604>
- [9] Al-Masoodi Z, Dulaimi A, Jafer H, Al-Khafaji Z, Atherton W, Safa H. Soft Soil Treated with Waste Fluid Catalytic Cracking as a Sustainable Stabilizer Material. *Iraqi Geological Journal* 2022;54:84–98. <https://doi.org/10.46717/igi.55.1C.4Ms-2022-03-23>
- [10] Hussain AJ, Al-Khafaji ZS. The fields of applying the recycled and used oils by the internal combustion engines for purposes of protecting the environment against pollutions. *Journal of Advanced Research in Dynamical and Control Systems* 2020;12. <https://doi.org/10.5373/IARDCS/V12SP1/20201119>
- [11] Al-Khafaji ZS, Majdi A, Shubbar AA, Nasr MS, Al-Mamoori SF, Alkhulaifi A, et al. Impact of high volume GGBS replacement and steel bar length on flexural behaviour of reinforced concrete beams. *IOP Conference Series: Materials Science and Engineering*, vol. 1090, IOP Publishing; 2021, p. 12015. <https://doi.org/10.1088/1757-899X/1090/1/012015>
- [12] Shanbara HK, Shubbar A, Ruddock F, Atherton W. Characterizing the Rutting Behaviour of Reinforced Cold Mix Asphalt with Natural and Synthetic Fibres Using Finite Element Analysis. *Advances in Structural Engineering and Rehabilitation*, Springer; 2020, p. 221–7. [https://doi.org/10.1007/978-981-13-7615-3\\_20](https://doi.org/10.1007/978-981-13-7615-3_20)
- [13] Majdi HS, Shubbar AA, Nasr MS, Al-Khafaji ZS, Jafer H, Abdulredha M, et al. Experimental data on compressive strength and ultrasonic pulse velocity properties of sustainable mortar made with high content of GGBFS and CKD combinations. *Data in Brief* 2020;31:105961. <https://doi.org/10.1016/j.dib.2020.105961>
- [14] Al-Khafaji ZS, Falah MW, Shubbar AA, Nasr MS, Al-Mamoori SF, Alkhayyat A, et al. The Impact of Using Different Ratios of Latex Rubber on the Characteristics of Mortars Made with GGBS and Portland Cement. *IOP Conference Series: Materials Science and Engineering* 2021;1090:012043. <https://doi.org/10.1088/1757-899x/1090/1/012043>
- [15] Al-Baghdadi HM, Shubbar AAF, Al-Khafaji ZS. The Impact of Rice Husks Ash on Some Mechanical Features of Reactive Powder Concrete with High Sulfate Content in Fine Aggregate. *International Review of Civil Engineering (IRECE)* 2021;12:248–54. <https://doi.org/10.15866/irece.v12i4.19834>
- [16] Tuama WK, Kadhum MM, Alwash NA, Al-Khafaji ZS, Abdulraheem MS. RPC Effect of Crude Oil Products on the Mechanical Characteristics of Reactive-Powder and Normal-Strength Concrete. *Periodica Polytechnica Civil Engineering* 2020. <https://doi.org/10.3311/ppci.15580>
- [17] Falah MW, Hafedh AA, Hussein SA, Al-Khafaji ZS, Shubbar AA, Nasr MS. The Combined Effect of CKD and Silica Fume on the Mechanical and Durability Performance of Cement Mortar. *Key Engineering Materials*, vol. 895, Trans Tech Publ; 2021, p. 59–67. <https://doi.org/10.4028/www.scientific.net/KEM.895.59>
- [18] Shubbar AA, Jafer H, Abdulredha M, Al-Khafaji ZS, Nasr MS, Al Masoodi Z, et al. Properties of cement mortar incorporated high volume fraction of GGBFS and CKD from 1 day to 550 days. *Journal of Building Engineering* 2020;30:101327. <https://doi.org/10.1016/j.jobe.2020.101327>
- [19] Hanoon DS, Sallal AK, Shubbar AA, Al-Khafaji ZS, Nasr MS, Al-Mamoori SF, et al. Early age assessment of cement mortar incorporated high volume fly ash. *IOP Conference Series: Materials Science and Engineering* 2021;1090:012019. <https://doi.org/10.1088/1757-899x/1090/1/012019>
- [20] Shubbar AA, Sadique M, Nasr MS, Al-Khafaji ZS, Hashim KS. The impact of grinding time on properties of cement mortar incorporated high volume waste paper sludge ash. *Karbala International Journal of Modern Science* 2020;6. <https://doi.org/10.33640/2405-609X.2149>



- [21] Shubbar AA, Nasr MS, Islam GM, Al-Khafaji ZS, Sadique M, Hashim K, et al. Early Age and Long-term Mechanical Performance of Mortars Incorporating High-volume GGBS. *Advances in Civil Engineering*, Springer; 2022, p. 267–74. [https://doi.org/10.1007/978-981-16-5547-0\\_26](https://doi.org/10.1007/978-981-16-5547-0_26)
- [22] Mukhopadhyay AK. Next-generation nano-based concrete construction products: a review. *Nanotechnology in Civil Infrastructure* 2011;207–23. [https://doi.org/10.1007/978-3-642-16657-0\\_7](https://doi.org/10.1007/978-3-642-16657-0_7)
- [23] Nazari A, Riahi S, Riahi S, Shamekhi SF, Khademno A. Influence of Al<sub>2</sub>O<sub>3</sub> nanoparticles on the compressive strength and workability of blended concrete. *Journal of American Science* 2010;6:6–9.
- [24] Arefi MR, Javeri MR, Mollaahmadi E. To study the effect of adding Al<sub>2</sub>O<sub>3</sub> nanoparticles on the mechanical properties and microstructure of cement mortar. *Life Science Journal* 2011;8:613–7
- [25] Liu X, Chen L, Liu A, Wang X. Effect of nano-CaCO<sub>3</sub> on properties of cement paste. *Energy Procedia* 2012;16:991–6. <https://doi.org/10.1016/j.egypro.2012.01.158>
- [26] Barbhuiya S, Mukherjee S, Nikraz H. Effects of nano-Al<sub>2</sub>O<sub>3</sub> on early-age microstructural properties of cement paste. *Construction and Building Materials* 2014;52:189–93. <https://doi.org/10.1016/j.conbuildmat.2013.11.010>
- [27] Al Ghabban A, Al Zubaidi AB, Jafar M, Fakhri Z. Effect of nano SiO<sub>2</sub> and nano CaCO<sub>3</sub> on the mechanical properties, durability and flowability of concrete. *IOP conference series: materials science and engineering*, vol. 454, IOP Publishing; 2018, p. 12016. <https://doi.org/10.1088/1757-899X/454/1/012016>
- [28] Cosentino I, Liendo F, Arduino M, Restuccia L, Bensaid S, Deorsola F, et al. Nano CaCO<sub>3</sub> particles in cement mortars towards developing a circular economy in the cement industry. *Procedia Structural Integrity* 2020;26:155–65. <https://doi.org/10.1016/j.prostr.2020.06.019>
- [29] Jawad ZF, Salman AJ, Ghayyib RJ, Hawas MN. Investigation the effect of different nano materials on the compressive strength of cement mortar. *AIP Conference Proceedings*, vol. 2213, AIP Publishing LLC; 2020, p. 20190. <https://doi.org/10.1063/5.0000164>
- [30] Iskra-Kozak W, Konkol J. The Impact of Nano-Al<sub>2</sub>O<sub>3</sub> on the Physical and Strength Properties as Well as on the Morphology of Cement Composite Crack Surfaces in the Early and Later Maturation Age. *Materials* 2021;14:4441. <https://doi.org/10.3390/ma14164441>
- [31] Muhsin ZF, Fawzi NM. Effect of Nano Calcium Carbonate on Some Properties of Reactive Powder Concrete. *IOP Conference Series: Earth and Environmental Science*, IOP Publishing; 2021: 856; 12026. <https://doi.org/10.1088/1755-1315/856/1/012026>
- [32] No A. Specification for aggregates from natural sources for concrete. *Bs* 1992;882:1–14.
- [33] EN TS. 12504-4. Testing concrete–Part 4: determination of ultrasonic pulse velocity. *British Standards Institution* 2004:18.
- [34] ASTM C. Standard test method for density, absorption, and voids in hardened concrete. *C642-13* 2013.
- [35] Al-Khafaji ZS, Falah MW. Applications of high density concrete in preventing the impact of radiation on human health. *Journal of Advanced Research in Dynamical and Control Systems* 2020;12. <https://doi.org/10.5373/IARDCS/V12SP1/20201115>
- [36] Zainab SAK, Zainab AM, Jafer H, Dulaimi AF, Atherton W. The effect of using fluid catalytic cracking catalyst residue (FC3R) as a cement replacement in soft soil stabilisation". *International Journal of Civil Engineering and Technology* 2018;9:522–33.
- [37] Hussain AJ, Al-Khafaji ZS. Experimental investigation on applying waste iron filings in the engineering fields for protection the environment from contamination. *Materials Today: Proceedings* 2021. <https://doi.org/10.1016/j.matpr.2021.09.039>

- [38] Ali AM, Falah MW, Hafedh AA, Al-Khafaji ZS. Evaluation the influence of steel- fiber on the concrete Characteristics. *Periodicals of Engineering and Natural Sciences* 2022;10. <http://dx.doi.org/10.21533/pen.v10i3.3111>
- [39] Fediuk R, Makarova N, Qader DN, Kozin A, Amran M, Petropavlovskaya V, et al. Combined effect on properties and durability performance of nanomodified basalt fiber blended with bottom ash-based cement concrete: ANOVA evaluation. *Journal of Materials Research and Technology* 2023;23:2642–57. <https://doi.org/10.1016/j.jmrt.2023.01.179>
- [40] Cibilakshmi G, Jegan J. A DOE approach to optimize the strength properties of concrete incorporated with different ratios of PVA fibre and nano-Fe<sub>2</sub>O<sub>3</sub>. *Advanced Composites Letters* 2020;29. <https://doi.org/10.1177/2633366X20913882>

Blank Page

## Valorized rice husk as green corrosion inhibitor for Al 6061 in 1M HCl

Peter Ikubanni<sup>\*1,a</sup>, Makanjuola Oki<sup>1,2,b</sup>, Adeolu Adediran<sup>1,c</sup>, Sarah Akintola<sup>3,d</sup>, Adekunle Adeleke<sup>4,e</sup>, Ikechukwu Anyim<sup>1,f</sup>, Olanrewaju Adesina<sup>5,g</sup>, Lawrence Efenovwe<sup>1,h</sup>

<sup>1</sup>Department of Mechanical Engineering, Landmark University, Omu-Aran, Nigeria

<sup>2</sup>Greenfield Creations Ltd., Benue Close, Agbara Industrial Estate, Agbara, Nigeria

<sup>3</sup>Department of Petroleum Engineering, University of Ibadan, Ibadan, Nigeria

<sup>4</sup>Department of Mechanical Engineering, Nile University of Nigeria, Abuja, Nigeria

<sup>5</sup>Department of Mechanical Engineering, Redeemer's University, Ede, Nigeria

### Article Info

### Abstract

#### Article history:

Received 21 Oct 2023

Accepted 15 Dec 2023

#### Keywords:

Corrosion inhibitor;

Rice husk;

Al 6061;

FTIR;

SEM/EDAX;

Gravimetric and

potentiodynamic;

Polarization analyses

This study investigated the inhibition characteristics of rice husk (RH) on corrosion of Aluminum 6061 in 1M hydrochloric acid. Gravimetric analysis and Scanning Electron Microscopy (SEM)/ Energy Dispersive X-ray analysis (EDX) as well as electrochemical studies revealed the potency of RH as a good inhibitor of the corrosion of Al 6061 in 1M HCl. Fourier Transform Infrared Spectroscopy (FTIR) indicated that -OH, C=C, and C=O with signals at (3317.19, 2932.9, 2848.2), (1631.8) and (1105.73, 1030.2, 447.15), respectively in RH were the viable active functional groups which adsorbed on the metal surface to effect reduction of corrosion rates. However, literature suggested the presence of amorphous silica in RH which served as a complimentary corrosion inhibitor. The corrosion current density of Al 6061 was reduced to  $3.46 \times 10^{-7}$  A/cm<sup>2</sup> at 24 h as against  $9.27 \times 10^{-7}$  A/cm<sup>2</sup> at the commencement of the potentiodynamic polarization measurements in inhibited 1M HCl. The control specimens exhibited an average corrosion rate of  $3.86 \times 10^{-6}$  A/cm<sup>2</sup> in HCl solution at the start of this investigation as compared to the corrosion rate of  $3.46 \times 10^{-7}$  A/cm<sup>2</sup> at 24 h of exposure in 5 mg RH- inhibited HCl. The obtained results gave a corrosion inhibition efficiency of about 90 to 92%.

© 2024 MIM Research Group. All rights reserved.

## 1. Introduction

Aluminium alloys are important structural engineering materials and their applications in industries come closely behind those of steel because of their lightweight, relatively high strength, and good corrosion resistance properties [1, 2]. Although highly resistant to atmospheric corrosion, aluminium alloys do undergo serious pitting corrosion in the presence of extraneous ions such as chlorides as may be encountered in process streams [3, 4]. Most of the generally known methods of corrosion control of metals are also suitable for aluminium alloys, however, in process streams as well as in radiators and heat exchangers, it is more appropriate to use inhibitors streams [3 – 6]. Inhibitors are either organic and/or inorganic chemicals that, when added in small quantities to corroding systems, reduce corrosion rates of metals by functioning as anodic, cathodic, or mixed-type inhibitors depending on their molecular structures and some other factors in the

\*Corresponding author: [ikubanni.peter@lmu.edu.ng](mailto:ikubanni.peter@lmu.edu.ng)

<sup>a</sup> [orcid.org/0000-0002-2710-1130](https://orcid.org/0000-0002-2710-1130); <sup>b</sup> [orcid.org/0000-0002-9234-9095](https://orcid.org/0000-0002-9234-9095); <sup>c</sup> [orcid.org/0000-0001-9457-1071](https://orcid.org/0000-0001-9457-1071);

<sup>d</sup> [orcid.org/0000-0003-3146-8039](https://orcid.org/0000-0003-3146-8039); <sup>e</sup> [orcid.org/0000-0002-0301-7698](https://orcid.org/0000-0002-0301-7698); <sup>f</sup> [orcid.org/0000-0003-0123-1110](https://orcid.org/0000-0003-0123-1110);

<sup>g</sup> [orcid.org/0000-0001-5719-2558](https://orcid.org/0000-0001-5719-2558); <sup>h</sup> [orcid.org/0009-0009-5996-7834](https://orcid.org/0009-0009-5996-7834)

DOI: <http://dx.doi.org/10.17515/resm2023.55ma1021rs>

Res. Eng. Struct. Mat. Vol. 10 Iss. 3 (2024) 873-883

environment. Misgivings with inhibitors in current usage are their synthetic routes of production, high costs as well as being hazardous which affect both the environment and humans. These amongst others have made searches for low-cost, biodegradable inhibitors from renewable sources inevitable. Hence, researchers have beamed searchlights on extracts from plants such as *Sabdariffa calyx*, castor oil, and agricultural wastes such as rice husks, hydrolyzed chicken feather, walnut leaf, almond fruit leaves, *Jatropha curcas* leaf, *Cascabela thevetia*, and so on, as alternatives [7 – 11].

A series of studies by various authors [7-14] on the inhibitive effects of extracts of plants and waste farm produce, on acid corrosion of metals, using different electro chemicals, in conjunction with other techniques, indicated that all the extracts inhibited the corrosion process by virtue of adsorption of their phytochemical constituents on the corroding metal surface. Inhibition efficiencies were shown to improve with a concentration of the active constituents. From such studies, the mechanisms of inhibition showed no generalized behaviour, however, it was noted that inhibition efficiencies, in excess of 90 to 95% in many instances, may be an indication that these extracts are suitable candidates for the formulation of non-toxic, environment-friendly corrosion inhibiting materials.

In the current research, rice husk which forms about 25% of wastes from paddy milling [12] was valorized for use as a corrosion inhibitor for Al 6061 in hydrochloric acid. Valorized rice husks contain amorphous silica [13] and organic species such as cellulose [14] and have been severally employed as inhibitors in various environments [14, 15]. The RH was prepared and functional groups were obtained using Fourier transform infrared (FTIR) spectroscopy. The surfaces of the inhibited substrate and uninhibited substrate in 1 M HCl were characterized using scanning electron microscopy with an attachment of energy dispersive X-ray analyzer (SEM-EDX). Both gravimetric and potentiodynamic polarization techniques were employed for the corrosion studies.

## 2. Materials and Methods

Spade-like electrodes were made from Al 6061 sheet metal. The electrodes were etched in 10% NaOH, rinsed in water, de-smutted in 50% HNO<sub>3</sub>, and given a final rinse in water before drying at room temperature. The corrosion medium was 1M HCl with and without 5 mg of valorized rice husk. All chemicals were laboratory-grade reagents from BDH Chemicals, UK.

### 2.1. Preparation of Rice Husks and FTIR Analysis

Spade-like electrodes were made from Al 6061 sheet metal. The electrodes were etched in 10% NaOH, rinsed in water, de-smutted in 50% HNO<sub>3</sub>, and given a final rinse in water before drying at room temperature. The corrosion medium was 1M HCl with and without 5 mg of valorized rice husk. All chemicals were laboratory-grade reagents from BDH Chemicals, UK.

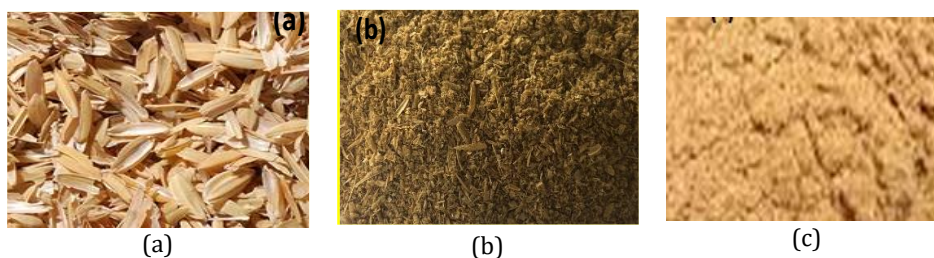


Fig. 1 Rice husk (a) As received (b) Pulverized (c) Powdered

## 2.2. Gravimetric Measurements

The gravimetric analysis was performed in accordance with NACE recommended practice RP-0775 (NACE, 2005) [16] and ASTM G-31-72 (2004) [17] in which cleaned and weighed Al 6061 electrodes were immersed in 100 ml HCl in a 200 ml beaker in the absence and presence of 5 mg RH for periods ranging from 2 h to 16 h. After each period of immersion, the specimens were rinsed in running water, dried under the fan at room temperature for 30 min, and reweighed. For each immersion period, three different measurements were made and the average of the readings were taken as final measurements. From the gravimetric measurements, corrosion rates were obtained with Eq. (1) and % inhibition efficiency, %IE, was calculated with Eq. (2).

$$\text{Corrosion rate, } CR = \frac{K \cdot W}{A \cdot D \cdot T} \quad (1)$$

where CR is the corrosion rate (mm/year), K is a constant ( $8.766 \times 10^4$ ), T is the time of exposure (hr), A is the area (cm<sup>2</sup>), W is the weight loss (mg), and D is the density of Al, (g/cm<sup>3</sup>).

$$IE \% = (CR - CR_i) / CR \times 100 \quad (2)$$

where CR is the corrosion rate in the absence of inhibitor and CR<sub>i</sub> is the corrosion rate in the presence of inhibitor.

## 2.3. Scanning Electron Microscopy (SEM) and Energy Dispersive Analysis of X-Ray (EDX)

Spade-like electrodes immersed for 16 h in 1M HCl in the presence of 5 mg of rice husk extract and without the extract were examined in a Scanning Electron Microscope, Model Pro X, with an Energy Dispersive X-ray analyzer (EDX) attached at high vacuum (HV) mode with 20 kV accelerating voltage.

## 2.4. Electrochemical Measurements

Electrochemical measurements were performed in a conventional three-electrode cell using computer-controlled potentiostat/galvanostat (Autolab PGSTAT 302N). The platinum electrode served as the counter electrode (CE), Ag/AgCl, as the reference electrode (RE), and Al 6061 specimens were employed as working electrodes (WE). The area of WE exposed to the medium was approximately 1 cm<sup>2</sup>. Before each potentiodynamic polarization measurement, the electrode potential was allowed to stabilize while the open circuit potential (OCP) was recorded as a function of time up to about 30 minutes. After this, a steady-state OCP corresponding to the corrosion potential ( $E_{\text{corr}}$ ) of the working electrode was obtained. The potentiodynamic measurements were carried out on the specimens in 1M HCl with and without 5 mg of inhibitor. The potential scans were executed automatically between 200 and -200 mV vs OCP at a rate of 10 mV/s. Fresh HCl solution and Al 6061 samples were used after each potential sweep.

## 3. Results and Discussion

### 3.1. FTIR Analysis

The spectrum generated for the rice husk is displayed in Fig. 2, where it can be observed that -OH, C=C, and C=O had signals at (3317.19, 2932.9, 2848.2), (1631.8), and (1105.73, 1030.2, 447.15), were present respectively. These have electron-rich centers that interact with corroding surfaces to stifle corrosion reactions.

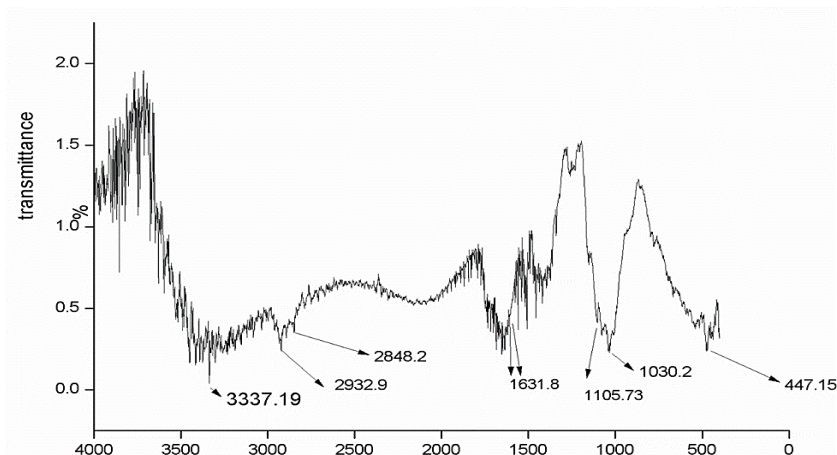


Fig. 2. FTIR spectra for rice husk

However, for C=C, especially when the double bonds are conjugated as in organic moieties found in rice husks, delocalization of electrons occurred in electrolytes leading to interactions with corroding surfaces thereby destabilizing corrosion reactions to reduce corrosion rates. Cellulose in rice husks is a typical reference point with both double bonds and reactive -OH groups. Therefore, such interactions are expected to reduce corrosion while descaling aluminium artefacts and radiators in water cooling systems.

### 3.2. Gravimetric Analysis

The plot for the corresponding corrosion rates in 1M HCl solution at ambient temperature from gravimetric analyses is displayed in Fig. 3. The weight loss in blank HCl was observed to increase steadily with time from about 0.22 mg at 2 h to about 0.56 mg at 16 h of immersion periods with corresponding corrosion rates of  $3.4 \times 10^{-6}$  and  $1.08 \times 10^{-6}$  mm/y, respectively. On the other hand, the inhibited weight loss commenced from a lowly 0.03 mg at 2 h to about 0.14 mg at 16 h of immersion time with corresponding corrosion rates of  $4.63 \times 10^{-7}$  and  $2.7 \times 10^{-7}$  mm/y, respectively. From the foregoing, an inhibition efficiency of about 92% was observed.

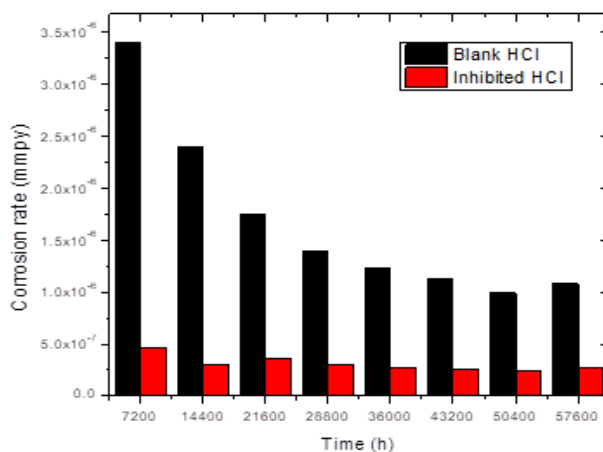


Fig. 3. Corrosion rate versus time in blank and 5 mg inhibited 1M HCl solution

This was expected as adsorption and desorption of inhibiting species occurred with time while the offending species continually interacted with the corroding surface. However, an overall decrease in corrosion rate was observed.

### **3.3. Scanning Electron Microscopy (SEM)/Energy Dispersive Analysis of X-ray (EDX) Analysis**

The scanning electron micrograph of Al6061 specimens immersed in inhibited 1M HCl solution for 16 h is displayed in Fig. 4. It can be observed that there are only two major pits along a scratch line revealed on the surface, which indicated that the inhibitor was effective throughout the exposure period. The EDX revealed a major peak for Al and numerous other elements as displayed in Table 1 along with their percentage occurrences. The other major elements are C at 0.5 %, Si at 1% and Fe at 2.3% as against 0% C, 0.7% Si, and 0.6% Fe in Al6061 [18].

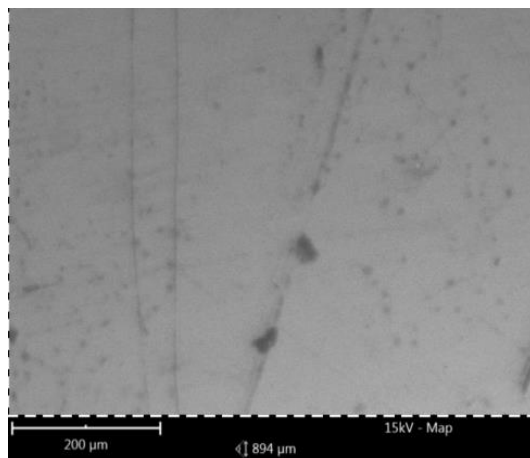


Fig. 4. Scanning electron micrograph of Al 6061 immersed for 16 h in RH inhibited 1M HCl

C is derived from organic components like cellulose in rice husks with active -OH groups at various positions [19], which can adsorb on corroding sites to inhibit corrosion in such areas. The presence of Si at a percentage higher than was expected in Al6061 suggested the interaction of SiO<sub>2</sub> with corroding alloy of interest. Amorphous silica is present in rice husks and is known to be a good corrosion inhibitor separately [14, 15] and in combination with other chemicals [20]. The higher weight percentage of Fe's presence on the inhibited specimen than expected in Al6061 also indicated the interaction of rice husks with the corroding surface. In all, most of the elements detected are also present in rice husks albeit at higher percentages than expected in Al6061.

The scanning electron micrograph of Al 6061 exposed for 16 h in 1M HCl is displayed in Fig. 5, where it can be observed that almost the entire surface was ravaged with pitting corrosion episodes with almost 90 to 95% of the surface covered with pits of various shapes as against 2 to 5% pitting corrosion observed on the inhibited specimen, Fig. 3.



Table 1. Percentage elemental composition of Al6061 exposed to 1 M HCl with 5 mg of rice husks and 1 M HCl only

Element Number	Element Symbol	Al6061 in HCl + 5 mg RH		Al6061 in HCl	
		Atomic Conc.	Weight Conc.	Atomic Conc.	Weight Conc.
13	Al	92.61	88.90	94.68	90.50
26	Fe	1.15	2.29	1.26	2.50
47	Ag	0.43	1.64	0.37	1.41
20	Ca	0.73	1.04	0.77	1.09
41	Nb	0.30	1.01	0.29	0.96
14	Si	1.00	1.00	0.70	0.70
39	Y	0.31	0.99	0.32	1.00
19	K	0.67	0.93	0.54	0.75
16	S	0.61	0.70	0.38	0.44
6	C	1.33	0.57	-	-
22	Ti	0.25	0.42	0.09	0.16
12	Mg	0.44	0.38	0.40	0.34
11	Na	0.16	0.13	0.19	0.15
15	P	0.00	0.00	0.00	0.00

Thus, it can be inferred that components of rice husks adsorbed and performed as corrosion inhibitors on Al6061 in 1M HCl solution. Table 1 presents the elemental composition of the uninhibited specimen. It is interesting to note that Si remained at 0.7 wt.% and C remained at 0 wt.% as in Al 6061 as against 1% and 0.57% on the surface of the inhibited specimen. These further suggest interactions of rice husk components with inhibited specimens in reducing pitting corrosion episodes.

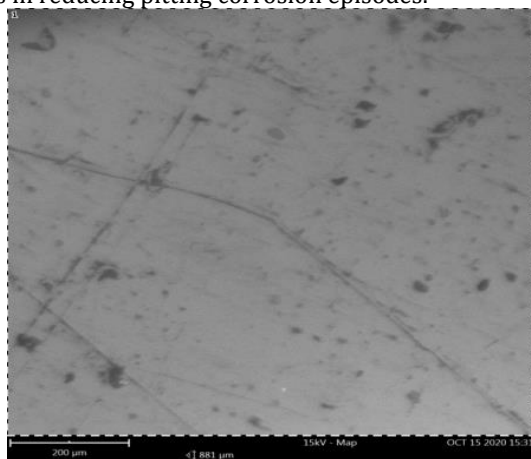


Fig. 5. SEM micrograph of Al 6061 exposed for 16 h in 1M HCl without inhibitor

Niobium and Yttrium present in both specimens may be contaminants present in chemicals employed during the various preparations in carrying out the research. However, since their weight concentrations remained almost constant at about 1%, Nb and Y are more likely to be in the substrate Al alloy.

### 3.4. Electrochemical Analysis

The potentiodynamic curves for Al 6061 in HCl with and without inhibitor are displayed in Fig. 6 and corresponding parameters from the Tafel extrapolations are shown in Table 2, respectively.

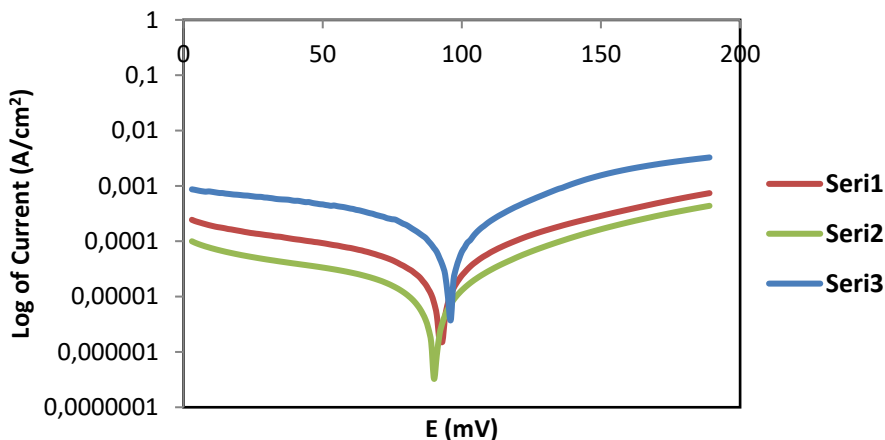
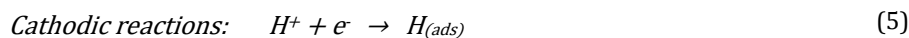
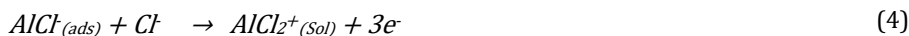
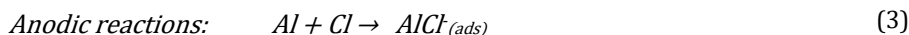


Fig. 6. Potentiodynamic polarization scans of Al 6061 exposed to 1M HCl at 30°C with and without 5 g of RH Inhibitor (Series 1 – OCP/blank; Series 2 – OCP/RH, Series 3 – 24 h/RH)

It has been canvassed in the literature [21,22] that the associated mechanisms with anodic and cathodic reactions for Al as described in Fig. 6 can be written as Eqs. (3-6):



The mechanism of corrosion inhibition of the rice husk on Al substrate in 1M HCl could be described as follows. Corrosion inhibitor causes adsorption on the interface of the metal and 1M HCl aggressive solution. The dissolution of metal and hydrogen gas liberation occurred at the anode and cathode, respectively [23]. The rice husk molecules' adsorption on the surface of the substrate could be attributed to a negatively charged acid anion ( $\text{Cl}^-$ ) from the HCl solution. Hence, the adsorption results in the surface coverage of the metallic material by preventing the corrosion of the substrate [24]. The metal surface protection occurs due to coordinated bond creation between the Al alloy and the rice husk inhibitor molecules [25, 26].

From the foregoing, it is obvious that Al readily reacts in HCl to form the various products observed in Equations 3 and 4. The cathodic polarization curves in the absence and presence of RH appear parallel to each other and the same can be observed for the anodic polarization which suggested that the inhibitor did not change the processes occurring on the electrode surface, it only decreased the rate of reaction to delay corrosion.

From Table 2, the difference in corrosion potentials in the presence and absence of inhibitor is not up to 85 mV suggesting that the inhibitor acted as a mixed type inhibitor. Thus, both anodic and cathodic reactions were slowed down to lower the corrosion rates of the specimens in inhibited HCl. Moreover, it is evident from Table 2, that the corrosion rate was reduced from  $3.8 \times 10^{-6} \text{ A/cm}^2$  to  $3.46 \times 10^{-7} \text{ A/cm}^2$  at 24 h of exposure in the presence of an inhibitor. The % inhibition from these readings was calculated to be about 90% which approximates the values obtained from gravimetric analyses further indicated that RH was an efficient inhibitor capable of strong adsorption on the surface of corroding Al6061

Table 2. Polarization parameters for specimens at attainment of OCP and at 24 h in HCl

Samples	Corrosion			Polarization resistance Rp ( $\Omega$ )	Cathodic constant Bc (V/dec)	Anodic constant Ba (V/dec)
	Corrosion rate, CR (mm/y)	Corrosion current density, Icorr (A/cm <sup>2</sup> )	Corrosion potential, Cp (V)			
@OCP/blank	0.044831	3.86E-06	-0.89735	106.97	0.002653	0.001481
@OCP/RH	0.010774	9.27E-07	-0.92046	548.82	0.002334	0.002353
@24h/RH	0.004022	3.46E-07	-0.9351	1289.4	0.001631	0.00278

Further examination of Table 2 in conjunction with Fig. 6 reveals that the values of Ba and Bc were altered on adding inhibitor to the corroding systems which is more prominent with Bc at 24 h exposure in the inhibited system. This implied that the cathodic hydrogen evolution reaction in the acidic system was impacted more by the adsorption of inhibitor moieties [27].

Various studies [3, 8, 15, 25, 28] on the corrosion inhibition performances of plants' extracts have shown that "x-ray electron spectroscopy (XPS), scanning electron microscopy (SEM), and Fourier transform infrared spectroscopy (FTIR) surface study techniques have all supported the existence of protective layers on the numerous metals studied. These extracts operated as mixed-type inhibitors, according to PDP data. The current research revealed significant findings in the preparation of original, environment-friendly, sustainable inhibitors with high inhibitory power commensurate with findings from the literature.

#### 4. Conclusions

This study is very important to the field of materials with regard to the development of eco-friendly and non-toxic corrosion inhibitors. The green inhibition tendencies of valorized rice husk on Al6061 substrate in 1M hydrochloric acid environment were investigated. Fourier Transform Infra-Red spectroscopy revealed the availability of functional groups, -OH, C=C, and C=O in RH with peaks at various wavelengths of 3317.19, 2932.9, 2848.2, 1631.8, 105.73, 1030.2 and 447.15. These functional groups were variously employed to inhibit corrosion on the Al 6061 substrate. The functional groups adsorbed on the corroding substrate and reduced the pitting corrosion episodes to between 90 and 92%.

The micrographs revealed that the density of pits on the surface of the substrates exposed in an uninhibited environment was reduced from about 100/mm<sup>2</sup> to about 2/mm<sup>2</sup> on the metal surface exposed to the inhibited 1M hydrochloric acid.

The rice husk performed as a mixed-type inhibitor as the difference in the corrosion potentials of the inhibited and uninhibited specimens was less than 85 mV. The corrosion rate of Al6061 was reduced from  $3.8 \times 10^{-6}$  A/cm<sup>2</sup> in blank hydrochloric acid to  $3.46 \times 10^{-7}$  A/cm<sup>2</sup> at 24 h of exposure in rice husk-inhibited hydrochloric acid solution. Thus, rice husk performed as an effective corrosion inhibitor for Al 6061 in 1M hydrochloric acid solution with an inhibition efficiency of between 90 and 92%.

The Tafel constants  $B_a$  and  $B_c$  differed slightly in values which suggested that the electrochemical mechanisms for the corrosion of Al 6061 remained the same in the presence and absence of inhibitor in the aggressive hydrochloric acid over the immersion periods employed in this investigation. The anodic and cathodic corrosion reactions were only slowed down to effect reduction in corrosion rates, without any change in mechanisms. This is an important study to material scientists and engineers based on the promising results obtained.

### **Acknowledgment**

The authors acknowledge the use of facilities at Landmark University, Omu-Aran, Kwara State, Nigeria.

### **References**

- [1] Ikubanni PP, Oki M, Adeleke AA, Ajisegiri ESA, Fajobi MO. Corrosion behavior of Al/SiC/PKSA hybrid composites in 1.0 M H<sub>2</sub>SO<sub>4</sub> environment using potentiodynamic polarization technique. *Acta Metallurgica Slovaca*, 2022a; 28: 169 - 171. <https://doi.org/10.36547/ams.28.4.1561>
- [2] Ikubanni PP, Oki M, Adeleke AA, Adesina OS, Omoniyi PO, Akinlabi ET. Electrochemical studies of the corrosion behaviour of Al/SiC/PKSA hybrid composites in 3.5% NaCl solution. *Journal of Composites Science*, 2022b; 6: 286. <https://doi.org/10.3390/jcs6100286>
- [3] Keramatinia M, Ramezanzadeh B, Mahdavian M. Green production of bioactive components from herbal origins through one-pot oxidation/polymerization reactions and application as a corrosion inhibitor for mild steel in HCl solution. *Journal of Taiwan Institute of Chemical Engineering*, 2019; 105: 134 - 149. <https://doi.org/10.1016/j.jtice.2019.10.005>
- [4] Ramezanzadeh B, Arman SY, Mehdipour M, Markhali BP. Analysis of electrochemical noise (ECN) data in time and frequency domain for comparison corrosion inhibition of some azole compounds on Cu in 1.0 M H<sub>2</sub>SO<sub>4</sub> solution. *Applied Surface Science*, 2014; 289: 129 - 140. <https://doi.org/10.1016/j.apsusc.2013.10.119>
- [5] Loto RT, Olowoyo O. Corrosion inhibition properties of the combined admixture of essential oil extracts on mild steel in the presence of SO<sub>4</sub><sup>2-</sup>-anions. *South African Journal of Chemical Engineering*, 2018; 26: 35 - 41. <https://doi.org/10.1016/j.sajce.2018.09.002>
- [6] Edoziuno FO, Adediran AA, Odoni BU, Oki M, Adesina OS. Comparative analysis of corrosion inhibition effects of mebendazole (MBZ) on mild steel in three different sulphuric acid concentrations. *International Journal of Corrosion and Scale Inhibition*, 2020; 9: 1049 - 1058. <https://doi.org/10.17675/2305-6894-2020-9-3-17>
- [7] Oki M, Adediran AA, Ikubanni PP, Adesina OS, Adeleke AA, Akintola SA, Edoziuno F, Aleem A. Corrosion rates of green novel hybrid conversion coating on aluminium 6061. *Results in Engineering*, 2020; 7: 100159. <https://doi.org/10.1016/j.rineng.2020.100159>
- [8] Adekunle AS, Adeleke AA, Ikubanni PP, Adewuyi OA. Comparative analysis of the inhibitive influence of *Cascabela thevetia* and *Jatropha curcas* leaves extracts on mild

- steel. *Nature Environment and Pollution Technology*, 2020; 19: 923 - 933. <https://doi.org/10.46488/NEPT.2020.v19i03.003>
- [9] Odusote JK, Adeleke AA, Ikubanni PP, Ayanda OS, Abdul JM, Yahya RA. Inhibitive action of *Plukenetia conophora* plant extract on the corrosion of Al-Zn-Cu alloy in acidic media. *International Review of Applied Science and Engineering*, 2020; 11: 269 - 279. <https://doi.org/10.1556/1848.2020.00108>
- [10] Akintola SA, Oki M, Aleem AA, Adediran AA, Akpor B, Oluba O, Ogunsemi BT, Ikubanni, PP. Valorized chicken feather as corrosion inhibitor for mild steel in drilling mud. *Results in Engineering*, 2019; 4: 100026. <https://doi.org/10.1016/j.rineng.2019.100026>
- [11] Olawale O, Ogunsemi BT, Bello JO, Ikubanni PP, Ogunsemi SJ, Abayomi TS. Optimisation and modelling of aluminium corrosion inhibition using almond (*Prunus amygdalus*) fruit leaves extract as green inhibitor in HCl acidic medium. *International Journal of Mechanical Engineering and Technology*, 2018; 9: 1274 - 1285.
- [12] Hossain SKS, Mathur L, Roy PK. Rice husk/rice husk ash as an alternative source of silica in ceramics: A review. *Journal of Asian Ceramic Societies*, 2018; 6: 299 - 313. <https://doi.org/10.1080/21870764.2018.1539210>
- [13] Rivas AL, Vera G, Palacios V, Cornejo M, Rigail A, Solórzano G. Phase Transformation of Amorphous Rice Husk Silica. In: Muruganant M, Chirazi A, Raj B. (eds) *Frontiers in Materials Processing, Applications, Research and Technology*. Springer, Singapore, 2018; 17 - 26. [https://doi.org/10.1007/978-981-10-4819-7\\_2](https://doi.org/10.1007/978-981-10-4819-7_2)
- [14] Olusegun SJ, Alaneme KK, Daramola YS, Afolabi AS. Corrosion inhibition and adsorption characteristics of rice husk extracts on mild steel immersed in 1M H<sub>2</sub>SO<sub>4</sub> and HCl Solutions. *International Journal of Electrochemical Science*, 2015; 10: 3553 - 3567. [https://doi.org/10.1016/S1452-3981\(23\)06561-6](https://doi.org/10.1016/S1452-3981(23)06561-6)
- [15] Pramudita M, Sukirno S, Nasikin M. Rice husk extracts ability to reduce the corrosion rate of mild steel. *International Journal of Chemical Engineering and Applications*, 2018; 9: 143 - 146. <https://doi.org/10.18178/ijcea.2018.9.4.715>
- [16] NACE recommended practice RP-0775, <https://fdocuments.net/reader/full/nace-rp-0775-2005> (Accessed, 14/04/2022).
- [17] ASTM G31-72. (2004). Standard Practice for Laboratory Immersion Corrosion Testing of Metals. ASTM International. [www.astm.org](http://www.astm.org)
- [18] Ekambaram S, Murugan N. Synthesis and characterization of aluminium alloy AA6061-alumina metal matrix composite. *International Journal of Current Engineering and Technology*, 2015; 5: 3211 - 3216.
- [19] Hermawan B, Nikmatin S, Alatas H, Sudaryanto, Sukaryo SG. Molecular analysis on the utilization of oil palm empty fruit bunches fiber as reinforcement for acrylonitrile butadiene styrene biocomposites, *IOP Conference Series: Earth and Environmental Science*, 2017; 65: 012028. <https://doi.org/10.1088/1755-1315/65/1/012028>
- [20] Vu VTH, Dinh TTM, Pham NT, Nguyen TT, Nguyen PT, To HTX. Evaluation of the corrosion inhibiting capacity of silica/polypyrrole-oxalate nanocomposite in epoxy coatings, *International Journal of Corrosion*, 2018; 2018: 6395803. <https://doi.org/10.1155/2018/6395803>
- [21] Prakashaiaha BG, Shetty AN, Amitharania BE. 2-(4-(Diethylamino)-2-hydroxybenzylidene) hydrazinecarboamide as corrosion inhibitor on AA2024-T3 aluminium alloy in 0.5 M hydrochloric acid solution. *Surface Engineering and Applied Electrochemistry*, 2018; 5: 286 - 296. <https://doi.org/10.3103/S1068375518030109>
- [22] Arrousse N, Fernine Y, Al-Zaqri N, Boshala A, Ech-chihbi E, Salim R, El Hajjaji F, Alami A, Touhamie ME, Taleba M. Thiophene derivatives as corrosion inhibitors for 2024-T3 aluminum alloy in hydrochloric acid medium, *RSC Advances*, 2022; 12: 10321. <https://doi.org/10.1039/D2RA00185C>
- [23] Raviprabha K, Bhat RS. Electrochemical and quantum chemical studies of 5-[4-Chlorophenoxy) Methyl]-4H-1,2,4-triazole-3-thiol on the corrosion inhibition of 6061

- Al alloy in hydrochloric acid. *Journal of Failure Analysis and Prevention*, 2020; 20: 1598 - 1608. <https://doi.org/10.1007/s11668-020-00954-2>
- [24] Edoziuno FO, Adediran AA, Odoni BU, Oki M, Ikubanni PP, Omodara O. Performance of methyl-5-benzoyl-2-benzimidazole carbamate (Mebendazole) as corrosion inhibitor for mild steel in dilute sulphuric acid. *Scientific World Journal*, 2020; 2020: 2756734. <https://doi.org/10.1155/2020/2756734>
- [25] Ikubanni PP, Adeleke AA, Odusote JK, Adegoke H, Oki M, Okolie JA. Corrosion control of AISI 1007 steel using hybrid inhibitors of plant extracts, *Chemistry Africa*, 2023. <https://doi.org/10.1007/s42250-023-00704-5>
- [26] Odusote JK, Adeleke AA, Ikubanni PP, Asafa TB, Kolawole SK, Opatola EA, Orhadahwe TA. Corrosion inhibition potential of silver-gold nanoparticles on mild steel in 1.0 M hydrochloric acid. *Chemistry Africa*, 2023
- [27] Mehmeti V. Nystatin drug as an effective corrosion inhibitor for mild steel in acidic media- An experimental and theoretical study. *Corrosion Science and Technology*, 2022; 21: 21 - 31.
- [28] Haleem EA, Eissa ME, Fouda AES. Inhibitive impact of Terfeziaceae plant extract on nitric acid decomposition of copper. *Journal of Chinese Chemical Society*, 2023. <https://doi.org/10.1002/jccs.202300364>

Blank Page



Research Article

## Surface plasmon resonance chemical sensor modified with $\alpha$ -naphthylmethacrylate nano thin film for chloroform detection

Yaser Acikbas

Materials Science and Nanotechnology Engineering Department, Usak University, Usak, Türkiye

### Article Info

### Abstract

#### Article history:

Received 27 Oct 2023

Accepted 15 Dec 2023

#### Keywords:

*$\alpha$ -Naphthylmethacrylate;  
Langmuir-Blodgett nano thin film;  
Surface plasmon resonance;  
Chemical sensor;  
Swelling dynamic*

The research on the rapid and sensitive detection of pollution caused by the products and technologies used has recently attracted attention in the literature. In the detection of volatile organic compounds (VOCs), polymers/monomers are used in the production of sensitive, fast-responding, reversible thin-film gas sensor elements. In this work, the monomer  $\alpha$ -Naphthylmethacrylate was selected as thin film sensor element. The  $\alpha$ -Naphthylmethacrylate-based nano thin films were prepared with technique of LB. Monomer LB thin films fabricated onto gold-coated glass substrate to investigate their vapour sensing properties by using Surface Plasmon Resonance (SPR) optical technique. This prepared monomer-based thin film sensor exposed to five different concentrations of chloroform vapors varying between  $13.98 \times 10^3$ - $69.9 \times 10^3$  ppm and the sensor response values were recorded. Swelling dynamics of this monomer thin film sensor was also illuminated by using Fick's early-time diffusion law. Diffusion coefficients of  $\alpha$ -Naphthylmethacrylate LB thin film sensor materials exposed to the five different concentrations of chloroform vapor were calculated with the help of reflected light intensity graph data and Fick's Law as a function of time. It was determined that the diffusion coefficient values of the first and second slope regions as varying between  $5.72 \times 10^{-17}$ - $21.97 \times 10^{-17}$   $\text{cm}^2\text{s}^{-1}$  and  $3.06 \times 10^{-17}$ - $6.25 \times 10^{-17}$   $\text{cm}^2\text{s}^{-1}$ , respectively. SPR kinetic measurement results showed that  $\alpha$ -Naphthylmethacrylate material is promising for the detection of chloroform vapor.

© 2024 MIM Research Group. All rights reserved.

## 1. Introduction

Volatile organic compounds (VOCs) are the leading chemicals causing environmental pollution [1,2]. These compounds, which have low boiling points and high vapour pressures and can pose very serious health risks, have great negative effects on people's respiratory, circulatory, nervous, excretory and even immune systems [3,4]. It is of great importance that these compounds remain within acceptable limits in the indoor or outdoor environment, and various sensors are being developed for their detection. One of these compounds, chloroform, is harmful to the environment and human health. Chloroform with chemical formula  $\text{CHCl}_3$  is colourless, having a boiling point of  $61^\circ\text{C}$  and it has a density of  $1.48 \text{ g cm}^{-3}$ . Chloroform has very high volatility and very low solubility in water. It is a chemical that can be found at very low levels in some cleaning products and medicines. While short-term exposure can cause central nervous system disorders, long-term exposure can lead to hepatitis, lung disorders, depression and irritability. Exposure to chloroform above 40000 ppm can result in death. Chloroform, which used to be used for anaesthesia, is no longer used for this purpose.

These vapors can be easily detected due to the favourable cavity and host-guest interaction. With their assistance of Quartz Crystal Microbalance (QCM), Surface Plasmon

Corresponding author: [yaser.acikbas@usak.edu.tr](mailto:yaser.acikbas@usak.edu.tr)

orcid.org/0000-0003-3416-1083

DOI: <http://dx.doi.org/10.17515/resm2023.57ma1027rs>

Res. Eng. Struct. Mat. Vol. 10 Iss. 3 (2024) 885-895



Resonance (SPR) and other gas measurement systems, the response of the thin film sensor can be recorded as a function of time when organic vapor is injected into a thin film sensor. Among these techniques, SPR technology provides both the elucidation of the optical properties of thin films and the analysis of the prepared thin film sensors at a low concentration.

Many sensors with different operating mechanisms, fast and sensitive detection of organic volatile compounds in the indoor or outdoor environment can be carried out [5,6]. A thin film layer is usually preferred as the basic gas sensor element in the detection of volatile organic compounds in this field [7-9]. These thin films are designed to have a controlled, homogeneous structure and effective detection capability; researchers are making great efforts to develop gas sensor elements with increased sensitivity, low cost and reversibility [10-12]. Many thin film fabrication techniques such as LB thin film technique [13-15] and spin coating [16-18] are in the focus of researchers' attention in this sense; design, modelling and fabrication of thin films are carried out. These techniques, in which an unlimited number of raw materials can be used for different application areas, contribute to the emergence of thin films suitable for the purpose with their flexibility. There is a limited number of research on the synthesis and characterisation of new raw materials that can offer many of the desired properties at the same time at low cost. The majority of these synthesised raw materials are monomers and polymers.

Polymers are considered as versatile materials that are suitable for an uncountable number of applications due to their controllable properties. The low cost of polymers, which can be produced in various forms and properties, makes them indispensable for many fields [19-21]. In the detection of volatile organic compounds (VOCs), these unique polymers are utilized in the production of sensitive, fast responding, reversible thin film chemical sensors. The main objective of this study is to investigate monomers that can best interact with the volatile organic compounds to be detected and enable the production of efficient chemical sensors [22-24]. It is important to synthesize raw materials that are suitable for the molar volume of the gas to be detected and that can form dipole moments or other secondary interactions with the gas.

Increasing environmental pollution and harmful organic vapors, which are increasingly emitted into the indoor and outdoor environment, can reduce the quality of life of people and cause serious health problems in long-term exposures. Considering the increase in these harmful chemical compounds, the importance of the design and application of reversible gas sensors that can perform fast, sensitive and repetitive detection is understood. For these reasons, this study aims to produce thin films from monomer materials, to elucidate their reactions and interaction mechanisms against harmful organic vapors.

In this study,  $\alpha$ -Naphthylmethacrylate based thin films were prepared by utilizing LB thin film technique onto the gold-coated glass substrates. These LB thin films were exposed to chloroform vapour at different concentrations to investigate their gas sensing abilities. The performance of  $\alpha$ -Naphthylmethacrylate based LB thin film sensor was measured by calculating the values of sensitivity, LOD and diffusion coefficients. The diffusion coefficients of chloroform for  $\alpha$ -Naphthylmethacrylate LB thin films were illuminated with this study.

## **2. Theory**

### **2.1. Method of Surface Plasmon Resonance (SPR)**

SPR is one of the spectroscopic methods used to measure the thickness and refractive index of thin films on metal surfaces. Fig. 1 shows a symbolic presentation of the SPR

measurements. The thickness of LB films and their weakly bound molecular interactions with organic vapors can be studied with the sensitivity of SPR [25,26]. That is, the layer-by-layer production of thin films is controlled in relation to the angle shift in the SPR curve of the molecules attached to the substrate. On the contrary, the thickness of the thin film is kept constant and exposed to organic vapors and the molecular interactions are analysed in relation to the reflected light changes recorded in the photodetector.

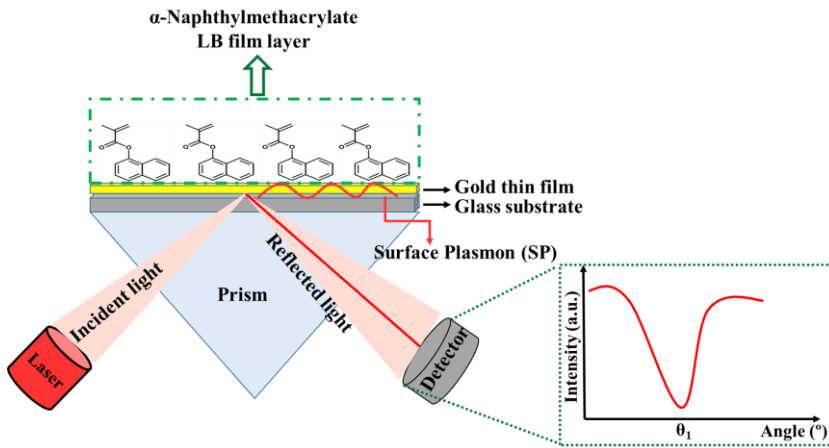


Fig. 1. A symbolic presentation of the SPR measurements

The light intensity reflected of the metal-thin film structure is recorded in the form of an SPR curve given in Fig.1. Surface plasmons (SPs) occurs during interaction between incident light and thin film [27]. The setup of SPR experimental system known as the Kretschmann configuration is shown in Fig. 1. Molecular interactions that cause a change in the refractive index, or an increase in molecular mass, change the intensity of the sensor material and hence the angle of incident light, which translates into a response signal in the detector [28]. This change causes a shift in the minimum of the resonance angle in the SPR graph. For thin films with linearly increasing thickness, the change in the resonance angle increases in direct proportion.

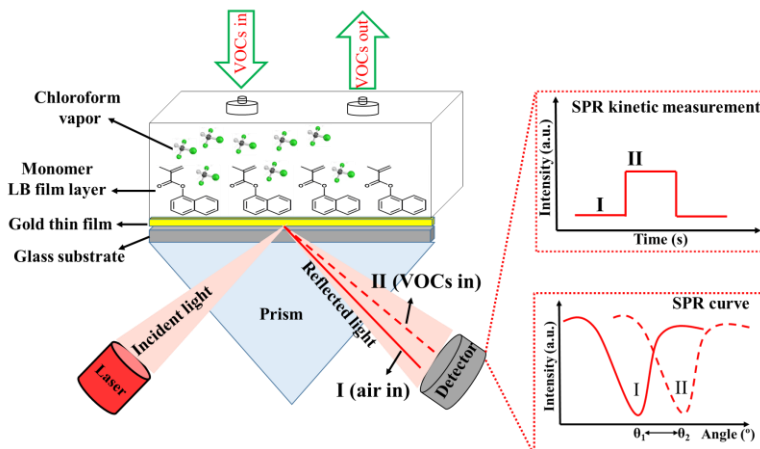


Fig. 2. A schematic demonstration of SPR curves and SPR kinetic measurements

From this data, the thickness of the transferred layers can be determined. Since SPR curve can display the distribution and amount of molecules transferred to a metal surface in real time, its use for the determination of the manufacturability of thin film monolayers is quite common [29]. A schematic representation of the gas cell for SPR kinetic measurements is given in Fig. 2. When the sensor surface is organized to contain selective receptors for specific chemicals or biomolecules, the structure of the newly formed material can be applied in chemical and biochemical sensor fields. SPR spectroscopy is one of the main optical techniques used today for the development of low-cost and high-resolution chemical and biochemical optical sensors [30]. SPR sensing has been receiving increasing attention in the scientific community due to its advantages of real-time monitoring and remarkable sensitivity.

## 2.2. Fick's Law and its Application

The diffusion coefficient ( $D_s$ ) is calculated with the equations of diffusion described in Fick's 2. law. The data of SPR kinetic results obtained in real-time measurements was used during this calculations [31]. In this study, this diffusions' law was applied to calculate the value of diffusion coefficient during chloroform molecule diffuse into the monomer film. The early-time approximation presented in Eq (1) for plane layers [31].  $a_0$  is the initial thickness of the surface layer,  $D$  is the diffusion coefficient,  $M_t$  and  $M_\infty$  represent the amount of material diffusing into the surface layer at times  $t$  and infinity, respectively.

$$\frac{M_t}{M_\infty} = 4 \sqrt{\frac{D}{\pi a_0^2}} t^{1/2} \quad (1)$$

This behavior suggests that the number of saturated vapor molecules  $M_t$  diffusing into the LB thin film should be inversely proportional to  $I_r$  and Eq (1) can be expressed as Eq (2).

$$\frac{M_t}{M_\infty} \cong \left( \frac{I_r(t)}{I_r(\infty)} \right)^{-1} = 4 \sqrt{\frac{D}{\pi a_0^2}} t^{1/2} \quad (2)$$

This new equation states that the ratio of reflected luminous intensity varies in direct proportion to the  $t^{1/2}$ . Using Eq (2) and the plot of the normalized irradiance as a function of the  $t^{1/2}$ , the diffusion coefficients can be calculated.

## 3. Experimental Details

The monomer  $\alpha$ -Naphthylmethacrylate (given in Fig. 3) preferred in preparation of chemical sensor thin films was obtained with the procedure given in previous studies [32,33].

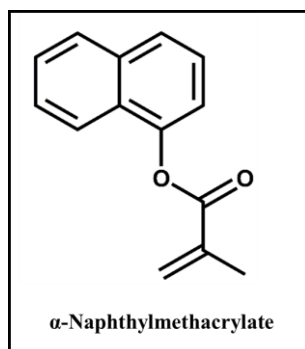


Fig. 3. The chemical structure of  $\alpha$ -Naphthylmethacrylate monomer

In this study, the  $\alpha$ -Naphthylmethacrylate was chosen as thin film element to research its VOCs sensing characteristics. The optimum surface pressure value for the production of  $\alpha$ -Naphthylmethacrylate LB thin film was determined as  $13\text{mN m}^{-1}$  from isotherm graph of this monomer [25] and 10 layers of LB thin film were produced on a gold-coated glass surface for investigating their gas sensing properties.

#### 4. Results and Discussion

Generally, the interaction mechanism between the thin film and organic vapor molecules is known to occur in three steps: surface adsorption interaction, interlayer diffusion and desorption [34,35]. A schematic representation of these steps is given in Fig. 4. When organic vapor is injected into the gas cell, the reason for the rapid increase in reflected light intensity is due to the surface adsorption interaction between the LB thin film and organic vapor molecules. This is followed by the diffusion effect where the organic vapor molecules begin to penetrate into the LB thin film layers. The diffusion process is related to many important physical properties of vapor molecules. Desorption is the removal of organic vapor by injecting fresh air into the gas cell.

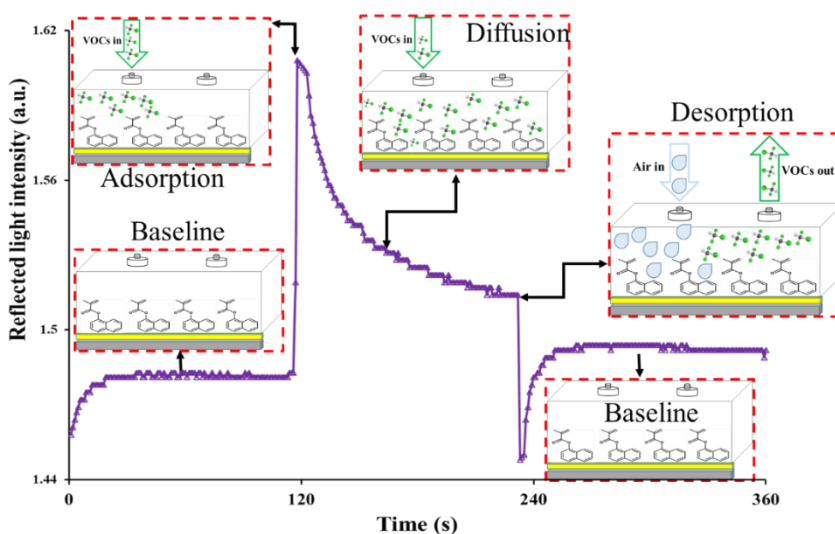


Fig. 4. A schematic representation of the interaction mechanism between monomer thin film and chloroform vapour

From the graph given in Fig. 4, there is fresh air in the environment between 0 and 120 seconds. At 120. Second, when chloroform vapor was introduced into the gas cell, the reflected light intensity increases rapidly and reaches a maximum value. It is noteworthy that the intensity changes rapidly as soon as organic vapor is introduced, indicating that the thin film reacts quickly to chloroform vapor. After a certain change in the reflected light intensity, approximately takes a constant value. The fact that the reflected light intensity remains stable in this period indicates that the thin film interacts with chloroform vapor. After allowing the chloroform vapor to remain in the environment for 2 minutes, air was introduced into the environment at 240. second and the reflected light intensity was observed to return to its previous value. After air introduced to cell, if the value of the reflected light intensity is not return to its previous value, the sensor coated with monomer thin film is not reversible property. Similarly, three times chloroform vapor was sent to cell and the reflected light intensity change was recorded. Fig. 5 displays the responses of monomer-coated SPR sensor to chloroform vapors nearly same.

The interactions of monomer LB thin film sensor with saturated and different concentrations of chloroform organic vapour is shown in Fig. 6. Between 0 - 120 seconds there is air in the environment. At 120 seconds,  $13.98 \times 10^3$  ppm chloroform was introduced into the environment where the monomer LB thin film sensor was located. After the chloroform vapor was kept in the environment for 2 minutes, air was introduced into the environment to remove it from the environment. Then, at 360 seconds,  $27.96 \times 10^3$  ppm chloroform vapor was introduced into the environment and kept in the environment for 2 minutes, and then air was again introduced into the environment and removed from the environment. This process was repeated with  $41.94 \times 10^3$ ,  $55.92 \times 10^3$  and  $69.9 \times 10^3$  ppm chloroform vapour. Fig. 7 shows that the shift in the reflected light intensity increases as the concentration ratio increases. The LB thin film sensor fabricated with monomer was found to be sensitive to harmful chloroform vapor.

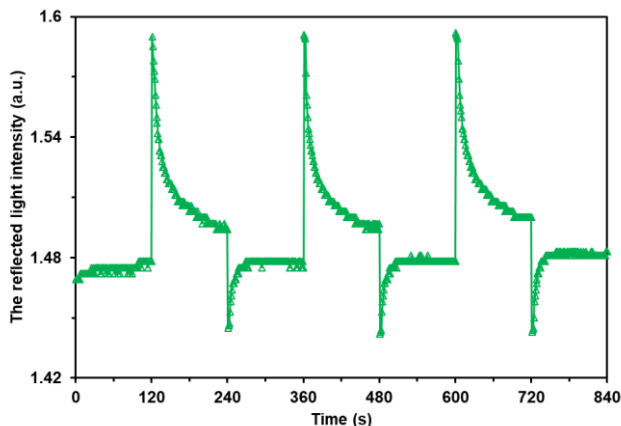


Fig. 5. The response of monomer LB thin film sensor to the saturated chloroform vapour for three cycles

The sensitivity value of the monomer-based SPR optical sensor was obtained from the slope of Fig. 7. This figure explains the relationship between the sensor response and chloroform vapor at distinct concentration. As a result, the sensitivity value of the monomer-based SPR optical sensor is  $1.297 \times 10^{-3} \text{ ppm}^{-1}$  with LOD value of 9.02 ppm.

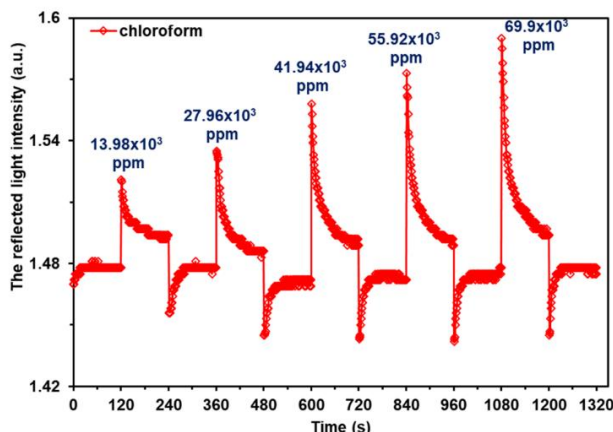


Fig. 6. The response of monomer LB thin film sensor to chloroform vapour at different concentrations

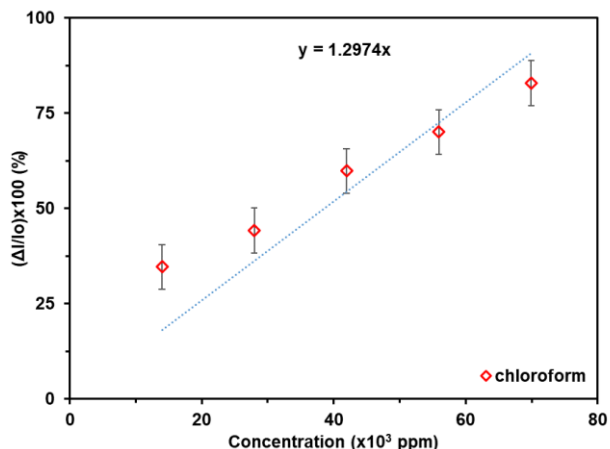


Fig. 7. The linearship relation between chloroform vapour and the change in the reflected light intensity

The chloroform vapour may be interacted with the sensor films by the emergence of hydrogen bonds during interaction between VOC and sensor film. The SPR kinetic result can be also explained in terms of molecular weight of chloroform vapour. Such physical parameters have an impact on the adsorption behavior when vapor molecules bind to sensing films. A larger vapor molecular weight such as chloroform leads to higher sensitivity as reported in previous findings in the literature [36,37]. The diffusion data between 120-240 second obtained from Fig. 4. Using these data, the change in reflected light intensity of the monomer LB thin film for chloroform vapor is obtained as a function of diffusion time shown in Fig. 8. In order to compare the experimental data with each other, the y-axis is arranged as normalized irradiance. The variation of the normalized irradiance value versus time decreases as an exponential function.

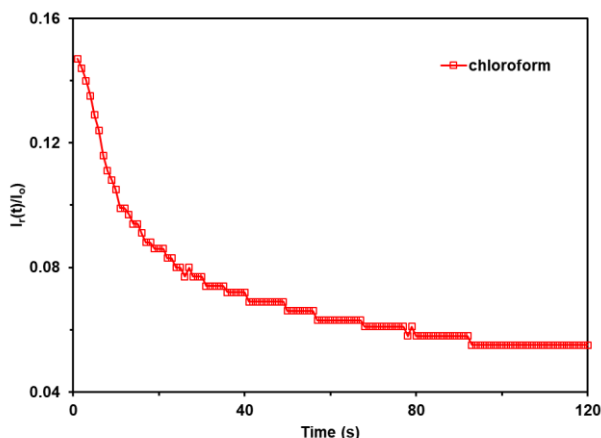


Fig. 8. The normalised responses as a function of time for the interaction of monomer LB thin film and chloroform vapour

In the diffusion interaction process, two different slopes were observed. During the first slope period, rapid surface adsorption interaction occurs as the organic vapor makes initial contact with the monomer LB thin film surface when it is introduced into the gas cell. In the second slope region, the chloroform vapor molecules enter the monomer LB thin film

layers, where they diffuse into the monomer LB thin film structure through physical and/or chemical interactions. This diffusion process can be reversible or irreversible depending on the physical and chemical interactions between the sensitive LB thin film material and the chloroform organic molecules. These interactions are not only dependent on physical properties such as vapor pressure, molar volume, viscosity, etc. [7,15], but also chemical interactions such as host-guest, hydrogen bonding, Van der Waals, etc. [38].

Fick's law is one of the most effective approaches to analyze the diffusion process and calculate diffusion coefficients. When the saturated chloroform vapour (for  $69.90 \times 10^3$  ppm concentration) molecules in the gas cell increases, the amount of material penetrating the monomer LB thin film will increase in both slope regions.

Table 1. The values of diffusion coefficient for the first and second regions at different chloroform concentrations.

Concentration (ppm)	First region $D(\text{cm}^2\text{s}^{-1}) \times 10^{-17}$	Second region $D(\text{cm}^2\text{s}^{-1}) \times 10^{-17}$
$13.98 \times 10^3$	8.23	4.05
$27.96 \times 10^3$	5.72	6.89
$41.94 \times 10^3$	14.64	3.06
$55.92 \times 10^3$	16.14	4.01
$69.90 \times 10^3$	21.97	6.25

From this linear relationship given in Fig. 9, diffusion coefficients for both slope regions were obtained using Eq (2). As shown in the inset in Fig. 9, the values of diffusion coefficient for the first and second regions were determined as  $21.97 \times 10^{-17} \text{ cm}^2\text{s}^{-1}$  and  $6.25 \times 10^{-17} \text{ cm}^2\text{s}^{-1}$ , respectively. The diffusion coefficient values of the first and second slope regions for other concentrations were presented in Table 1.

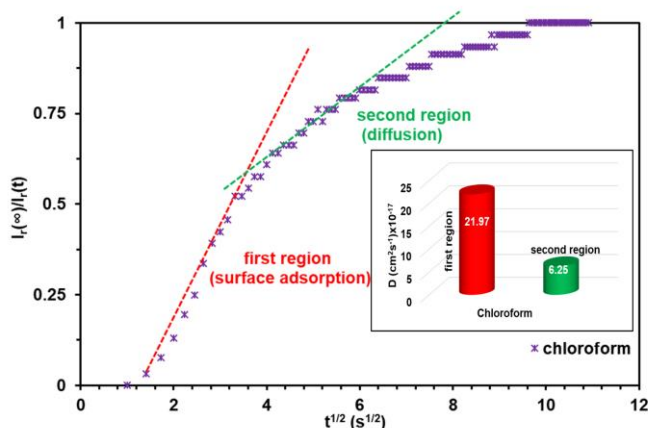


Fig. 9. Plot of  $t^{1/2}$  versus normalized value of  $I_r(\infty)/I_r(t)$  for monomer thin film-chloroform vapour interaction

The pyrene-based (PS) polymer chains, having three different molecular weights (PS1, PS2 and PS3) were prepared via LB thin film technique by Erdogan and his group [22]. The response of PS-based sensor for chloroform vapor at distinct five concentrations by using

QCM technique. The obtained values of diffusion coefficients vary among  $0.2\text{-}3.0 \times 10^{-16}$ ,  $5.0\text{-}13 \times 10^{-16}$ , and  $1.0\text{-}1.6 \times 10^{-15} \text{ cm}^2\text{s}^{-1}$  for the sensor of PS1, PS2, and PS3, respectively. The values of diffusion coefficients for PS1 LB thin film nearly the values for  $\alpha$ -Naphthylmethacrylate LB thin film against to chloroform vapour.

## 5. Conclusions

SPR LB thin film sensors prepared using the monomer  $\alpha$ -Naphthylmethacrylate were exposed to different concentrations of chloroform organic vapors. An increase in reflected light intensity was observed with increasing vapor concentrations. After the SPR LB thin film sensor materials were exposed to saturated chloroform organic vapors, time-dependent measurements were repeated three times and the repeatability capacity of the monomer-based sensor material was measured.

The results obtained for monomer LB thin film sensors indicate that this sensor is self-renewing and has the capacity for multi-use potential. The response of monomer thin film materials was analyzed from SPR kinetic data. The fact that monomer-based SPR sensor material reacted to the chloroform VOC and that their responses to this vapor differed showed that this material have selectivity against chloroform organic vapors.

The illumination of the diffusion process, which is a factor in the sensor interaction mechanism for the selected material, was also studied for the first time in this study. Diffusion coefficients of  $\alpha$ -Naphthylmethacrylate LB thin film sensor materials exposed to the saturated concentration of chloroform vapor were calculated with the help of reflected light intensity graph data and Fick's Law as a function of time. It was determined that the diffusion coefficient values of the first and second slope regions as  $21.97 \times 10^{-17} \text{ cm}^2\text{s}^{-1}$  and  $6.25 \times 10^{-17} \text{ cm}^2\text{s}^{-1}$ , respectively. All diffusion coefficient values of the first and second slope regions as varying between  $5.72 \times 10^{-17}\text{-}21.97 \times 10^{-17} \text{ cm}^2\text{s}^{-1}$  and  $3.06 \times 10^{-17}\text{-}6.25 \times 10^{-17} \text{ cm}^2\text{s}^{-1}$ , respectively. It has been revealed that monomer LB thin films have sensor properties such as sensitive, selective, fast, recyclable and reusable as well as being suitable for use as sensor materials and can be used in this field.

## References

- [1] Sorek A, Atzmon N, Dahan O, Gerstl Z, Kushisin L, Laor Y, Mingelgrin U, Nasser A, Ronen D, Tsechansky L, Weisbrod N, Graber ER. The Use of Trees for Discovering Subsurface Contamination by VOCs. *Environ Sci Technol*, 2008; 42: 536-542. <https://doi.org/10.1021/es072014b>
- [2] Ghanbarian M, Zeinali S, Mostafavi A. A Novel MIL-53(Cr-Fe)/Ag/CNT Nanocomposite Based Resistive Sensor for Sensing of Volatile Organic Compounds. *Sens. Actuators B*, 2018; 267:381-391. <https://doi.org/10.1016/j.snb.2018.02.138>
- [3] Ndiaye AL, Brunet J, Varenne C, Pauly A. Functionalized CNTs-Based Gas Sensors for BTX-Type Gases: How Functional Peripheral Groups Can Affect the Time Response through Surface Reactivity. *J. Phys. Chem. C*, 2018;122: 21632-21643. <https://doi.org/10.1021/acs.jpcc.8b05379>
- [4] Wang Y, Yang Q, Zhao M, Wu J, Su B. Silica-Nanochannel-Based Interferometric Sensor for Selective Detection of Polar and Aromatic Volatile Organic Compounds. *Anal. Chem*, 2018;90: 10780-10785. <https://doi.org/10.1021/acs.analchem.8b01681>
- [5] Acikbas Y, Capan R, Erdogan M, Yukruk F. Characterization and organic vapor sensing properties of Langmuir-Blodgett film using perylendiimide material. *Res. Eng. Struct. Mat*, 2015; 2: 99-108. <https://doi.org/10.17515/resm2015.08ma0514>
- [6] Yang D, Wang J, Cao Y, Tong X, Hua T, Qin R, Shao Y. Polyaniline-Based Biological and Chemical Sensors: Sensing Mechanism, Configuration Design, and Perspective. *ACS*



- Applied Electronic Materials, 2023; 5(2); 593-611. <https://doi.org/10.1021/acsaelm.2c01405>
- [7] Büyükkabasakal K, Acikbas S, Deniz A, Acikbas Y, Capan R, Erdogan, M. Chemical sensor properties and mathematical modeling of graphene oxide Langmuir-Blodgett thin films. IEEE Sensors Journal, 2019; 19(20): 9097-9104. <https://doi.org/10.1109/JSEN.2019.2926367>
- [8] Toudjen NH, Lamri Zeggar, M, Aida, MS, Rouabah, S, Aouabdia, N. Volatile Organic Compound Gas Sensing Applications of n-Type SnO<sub>2</sub> and p-Type CuO Based on Thin Films. J. Electron. Mater. 2023; <https://doi.org/10.1007/s11664-023-10559-8>
- [9] Matavž A, Margot FK, Verstreken MFK, Smets J, Max L, Tietzeand RA. Comparison of Thin-Film Capacitor Geometries for the Detection of Volatile Organic Compounds Using a ZIF-8 Affinity Layer. ACS Sens. 2023; 8:3167-3173. <https://doi.org/10.1021/acssensors.3c00859>
- [10] Şen S, Önder FC, Çapan R, Ay M. A room temperature acetone sensor based on synthesized tetranitro-oxalix [4] arenes: thin film fabrication and sensing properties, Sens. Actuators A Phys, 2020; 315: 112308. <https://doi.org/10.1016/j.sna.2020.112308>
- [11] Çapan İ, İlhan B. Gas sensing properties of mixed stearic acid/phthalocyanine LB thin films investigated using QCM and SPR. J. Optoelectron. Adv. Mater, 2015; 17(3-4): 456-461.
- [12] Shah AY, Choudhury S, Betty CA. Reliable liquified petroleum gas sensing at room temperature by nanocrystalline SnO<sub>2</sub> thin film deposited by Langmuir-Blodgett method. Appl. Phys. A, 2023; 129: 478. <https://doi.org/10.1007/s00339-023-06767-y>
- [13] Moreno-García HM, Sifuentes-Turrubiartes J, Chavez-Veloz SG, Rodríguez A.G. Pb-Bi-S thin films by chemical deposition - optical and electrical properties. Thin Solid Films, 2023; 775(30): 139866. <https://doi.org/10.1016/j.tsf.2023.139866>
- [14] Hasa N, Nguyen TMH, Busse K, Kressler J. Influence of Tacticity on the Structure Formation of Poly(methacrylic acid) in Langmuir/Langmuir-Blodgett and Thin Films. Macromol. Chem. Phys, 2023; 224: 2200428. <https://doi.org/10.1002/macp.202200428>
- [15] Lai YC, Chiu YC, Chuang KW, Ramachandran B, Wu IF, Liao YC. Conformal Conductive Features on Curvilinear Surfaces with Self-Assembled Silver Nanoplate Thin Films. Langmuir, 2023; 39: 9211–9218. <https://doi.org/10.1021/acs.langmuir.3c01031>
- [16] Olumurewa KO, Eleruja MA. Photoelectrical and thermal sensing measurement of spin coated ZnO and ZnO-RGO thin film. Physica B: Condensed Matter, 2023; 650: 414588. <https://doi.org/10.1016/j.physb.2022.414588>
- [17] Pandey V, Siddiqui MS, Munjal S, Ahmad T. Optical analyses of spin-coated Mn<sub>3</sub>O<sub>4</sub> thin film. Materials Today: Proceedings, 2023; <https://doi.org/10.1016/j.matpr.2023.07.025>
- [18] Samal S, Kosjakova O. Surface feature of PMMA films on NiTi alloy substrate by the spin coating method. Ceramics International, 2023; 49: 24370-24378. <https://doi.org/10.1016/j.ceramint.2022.10.152>
- [19] Kondawar,SB, Patil PT. Conducting polymer nanocomposites for sensor applications, 2017; 223-267. [https://doi.org/10.1007/978-3-319-46458-9\\_8](https://doi.org/10.1007/978-3-319-46458-9_8)
- [20] Singh P, Shukla SK. Advances in polyaniline-based nanocomposites. J. Mater. Sci. 2020; 55 (4): 1331-1365. <https://doi.org/10.1007/s10853-019-04141-z>
- [21] Wang Y, Liu A, Han Y, Li T. Sensors based on conductive polymers and their composites: a review. Polym. Int, 2020 69(1): 7-17. <https://doi.org/10.1002/pi.5907>
- [22] Erdogan M, Özbek Z, Capan R, Yagci Y. Characterization of polymeric LB thinfilms for sensor applications. J. Appl. Polym. Sci. 2012; 123: 2414-2422. <https://doi.org/10.1002/app.34793>

- [23] Acikbas Y, Dogan G., Erdoğan M, Çapan R, Soykan C. Organic vapor sensing properties of copolymer Langmuir-Blodgett thin film sensors. *J. Macromol. Sci. Part A*, 2016; 53(8): 470-474. <https://doi.org/10.1080/10601325.2016.1189279>
- [24] Acikbas Y, Cankaya N, Çapan R, Erdoğan M, Soykan C. Swelling behavior of the 2-(4-methoxyphenylamino)-2-oxoethyl methacrylate monomer LB thin film exposed to various organic vapors by quartz crystal microbalance technique. *J. Macromol. Sci. Part A*, 2016; 53(1): 18-25. <https://doi.org/10.1080/10601325.2016.1110453>
- [25] Laurinavichyute VK, Nizamov S, Mirsky VM. The role of anion adsorption in the effect of electrode potential on surface plasmon resonance response, *Chem. Phys. Chem.*, 2017; 18(12): 1552-1560. <https://doi.org/10.1002/cphc.201601288>
- [26] Wang, Y, Shan, X, Wang, H, Wang, S, Tao, N. Plasmonic imaging of surface electrochemical reactions of single gold nanowires, *J. Am. Chem. Soc.*, 2017; 139(4): 1376-1379. <https://doi.org/10.1021/jacs.6b10693>
- [27] Nagata K, Handa H. Real-time analysis of biomolecular interactions, Japan: Springer 2000. <https://doi.org/10.1007/978-4-431-66970-8>
- [28] Sambles JR, Bradbery GW, Yang F. Optical excitation of surface plasmons: An introduction. *Contemp. Phys.*, 1991; 32: 173-183. <https://doi.org/10.1080/00107519108211048>
- [29] Capan R, Göktas H, Özbek Z, Sen S, Özel ME, Davis F. Langmuir-Blodgett thin film for chloroform detection. *Appl. Surf. Sci.*, 2015; 350: 129-134. <https://doi.org/10.1016/j.apsusc.2015.02.109>
- [30] Homola S, Gauglitz G. Surface plasmon resonance sensors: review. *Sens. and Actuat. B*, 1999; 54: 3-15. [https://doi.org/10.1016/S0925-4005\(98\)00321-9](https://doi.org/10.1016/S0925-4005(98)00321-9)
- [31] Crank J. The mathematics of diffusion. London: Oxford University Press., 1970; 26-41.
- [32] Acikbas Y, Özkaya C, Bozkurt S, Çapan R, Erdoğan M, Tetik GD. (2019) Organic vapor sensing properties and characterization of  $\alpha$ -naphthylmethacrylate LB thin films, *J. Macromol. Sci. Part A*, 2019; 56(9): 845-853. <https://doi.org/10.1080/10601325.2019.1612253>
- [33] Chesnokov SA, Kovylin RS, Mamysheva, ON, Fukin GK, Cherkasov VK, Lyssenko KA. The Photopolymerization Kinetics Features of Naphthyl(Meth) Acrylates in Melts. *J. Polym. Res.* 2014; 21: 441-455. <https://doi.org/10.1007/s10965-014-0441-4>
- [34] Huang Y, Fu L, Zou W, Zhang F, Wei Z. Ammonia sensory properties based on single-crystalline micro/nanostructures of perylene diimide derivatives: core-substituted effect. *J. Phys. Chem. C*, 2011; 115(2): 10399-10404. <https://doi.org/10.1021/jp200735m>
- [35] Muzikante I, Parra V, Dobulans R, Fonavs E, Latvels J, Bouvet M. A novel gas sensor transducer based on phthalocyanine heterojunction devices. *Sensors*, 2007; 7(11): 2984-2996. <https://doi.org/10.3390/s7112984>
- [36] Xu LG, Hu X, Lim YT, Subramanian, VS. Organic vapor adsorption behavior of poly(3-butioxythiophene) LB films on quartz crystal microbalance, *Thin Solid Films*, 2002; 417: 90-94. [https://doi.org/10.1016/S0040-6090\(02\)00634-X](https://doi.org/10.1016/S0040-6090(02)00634-X)
- [37] Sun P, Jiang Y, Xie G, Yu J, Du X, Hu J. Synthesis and sensitive properties of poly(bistriethylphosphine)-platinum-diethynylbenzene for organic vapour detection, *J. Appl. Polym. Sci.* 116 (2010) 562-567. <https://doi.org/10.1002/app.31506>
- [38] Bai R, Yang X, Zhao J, Zang Z, Yan X. Phototriggered Formation of a Supramolecular Polymer Network Based on Orthogonal H-Bonding and Host-Guest Recognition. *Chem. Res. Chin. Univ.*, 2023; 39: 777-78. <https://doi.org/10.1007/s40242-023-3056-7>

Blank Page



Research Article

## Parametric study on the effect of temperature on properties of engineered cementitious composites using induction furnace slag as a partial replacement for river sand

S Naveen<sup>a,\*</sup>, Govardhan Bhat<sup>b</sup>

Department of Civil Engineering, NIT Raipur, Chhattisgarh-492010, India

### Article Info

### Abstract

#### Article history:

Received 24 Aug 2023

Accepted 31 Dec 2023

#### Keywords:

River sand;  
Induction furnace steel slag;  
Engineered cementitious composites;  
Elevated temperatures;  
Normalized strength;  
Normalized UPV

This paper studies the effect of temperature on Engineered Cementitious Composites (ECC) properties using induction furnace slag (SS) as a partial replacement for river sand (RS). Replacement percentages are between 5 and 65%, with an increment of 15% by dry weight of RS having various particle sizes (2.36 mm, 1.18 mm and 0.6 mm). The cubes are subjected to various temperatures (200, 400, 600 and 800°C) in a muffle furnace. After heating, visual observations and strength deterioration of RS and SS ECC are assessed. The extent of postfire damage is determined using the UPV test. SEM and XRD are used to identify the changes in the microscopy morphology and the chemical compositions. It is clear from the test findings that with SS partially replacing RS, the heat insulation capacity of ECC is enhanced. Based on test results, the ECC up to 50% SS as an RS alternative performs better at all temperature exposures.

© 2024 MIM Research Group. All rights reserved.

## 1. Introduction

Engineered cementitious composites (ECC), composed of cement, fly ash, fine aggregate, chemical admixture, water and fibres, were developed by Victor Li to overcome the brittleness of traditional cement-based materials. Especially as a fine aggregate microsilica sand used in ECC [1]. Sand size, amount, and roughness impact ECC's properties [2]. ECC is utilised in structural applications, including bridges, high-rise buildings, road pavements, and repair and retrofitting structures [3]. It can also be used in earthquake-resisting structures [4]. ECC enhances structure service life, which reduces maintenance and repair costs [5]. Furthermore, ECC performs much better than conventional concrete when exposed to chemical attacks and various temperatures.

Fire generally has an impact on structural behaviour at various temperatures. Including Polyvinyl alcohol (PVA) fibres in ECC can reduce explosive spalling at various temperatures [6]. Many researchers have studied the performance of ECC at various temperatures, and its performance depends on the materials used (fly ash, fibres, and aggregate). The existing literature on ECC at various temperatures shows that micro silica sand of size < 300 microns is used as fine aggregate [7–9]. Instead of using micro silica sand, quartz sand characterises the behaviour of fibre-reinforced cementitious composites at various temperatures [10]. He et al. [11] investigated high-strength ECC at various temperatures, in which River Sand (RS) with a 2 mm particle size is used. According to

\*Corresponding author: [naveence.viit@gmail.com](mailto:naveence.viit@gmail.com)

<sup>a</sup> orcid.org/0000-0002-5555-9691; <sup>b</sup> orcid.org/0000-0002-8693-1918

DOI: <http://dx.doi.org/10.17515/resm2023.36ma0824rs>

Res. Eng. Struct. Mat. Vol. 10 Iss. 3 (2024) 897-915

experimental studies, the strength loss in high-strength ECC is less than in ECC with normal strength. Mohammed et al. [12] performed a study on nano-silica-modified self-consolidating ECC at various temperatures using fine aggregate as RS with 450 microns size. The residual characteristics of nano-silica-modified self-consolidating ECC decreased as temperature increased from 200°C to 400°C. Cao et al. [13] explored the bonding characteristics of existing concrete and steel-basalt hybrid fibre-reinforced cementitious composite (SBFRCC) at various temperatures. The fine aggregate employed in this investigation is RS with a 0.6mm particle size. The test results show that the SBFRCC performed better at high temperatures than existing concrete. The earlier studies focused on ECC's performance with micro silica sand and RS as a fine aggregate at various temperatures. Still, its performance using steel industry by-products as a fine aggregate at various temperatures is not explored.

The most crucial strategy for resolving sustainability issues in the construction sector is effectively transforming industrial by-products into useful concrete materials. Such an approach also protects the environment from harmful solid waste dumped from industries. Ferrites and Calcium silicates combined with the fused oxides of aluminium, calcium, iron, manganese, and magnesium form a non-metallic steel slag [14]. The expansion in concrete is caused by the Free lime and periclase in SS [15]. Studies related to the tests and methods for volume stability are developed. Mehta et al. described autoclave test evolution history as a critical assessment of its current state, and the widely used performance tests for cement soundness are described [16]. Hydration of crystalline magnesia (periclase) is a primary reason for such volume change. The microstructure and expansive behaviour of cement with varying MgO contents and autoclave expansions are explored [17]. The volume stability of SS aggregate can be assessed by testing the free lime content [18]. Lun et al. developed techniques for enhancing the volume stability of SS as a fine aggregate [19]. Weathering is also the best approach for the volume stability of SS.

The characteristics of the SS produced may vary based on furnace type, processing methods and raw materials used [20]. Induction furnaces have Induction Furnace Steel Slag (SS), a good substitute due to their efficient operation and clean manufacturing process [21]. Over 600 Induction furnace plants exist in India alone, each producing over 15,000 tonnes of slag annually [14]. Netinger Grubesa et al. [22] demonstrated that concrete properties with steel slag are similar to the dolomite concrete up to 600°C. Liang et al. [23] implemented ultra-high-performance concrete with 69% residual strength after being subjected to 1000°C with SS as fine aggregate. Jihad Miah et al. [24] observed that the strength reduction at various temperatures increases when sand is replaced by 100% Steel slag powder. The previous literature focused on cement mortar/concrete with SS as fine aggregate at various temperatures. Still, studies related to ECC behaviour at various temperatures with SS aggregate are not covered in the literature. The properties of ECC with SS as a partial substitute material for RS with 5%, 20%, 35%, 50% and 65% having various particle sizes at various temperatures (200, 400, 600 and 800°C) are evaluated. ECC's chemical composition and microstructural properties are identified with SEM and XRD. The results of ECC with SS at elevated temperatures are beneficial for ensuring stable fire resistance of the structural elements.

## **2. Experimental Work**

### **2.1. Materials**

#### *2.1.1 Cement*

As per IS 269: 2015, Ordinary Portland Cement is utilized in all the mixes. The test findings for cement are given in Table 1, confirming the IS: 269: 2015 specifications.

Table 1. Cement properties

Properties	Values	As per IS:269-2015
Normal consistency	30%	-
Initial setting time	147	>30 min
Final setting time	257	< 600 min
Fineness		
a. Dry sieving	4	Less than 10%
b. Blain's air permeability	310.7	More than 225 m <sup>2</sup> /kg
Specific gravity	3.04	-

### 2.1.2 Fly Ash

Fly ash (FA) confirms the requirements of IS 3812 (Part-1): 2003. The chemical composition of the FA from Energy Dispersive Spectroscopy (EDS) is shown in Table 2.

Table 2. Chemical composition of fly ash from EDS

Chemical composition	Oxide (%)
SiO <sub>2</sub>	62.73
Al <sub>2</sub> O <sub>3</sub>	29.17
Fe <sub>2</sub> O <sub>3</sub>	3.17
MgO	0.68
CaO	0.82
Na <sub>2</sub> O	-
K <sub>2</sub> O	1.23

### 2.1.3 Fine Aggregate

RS and SS are used as fine aggregates in ECC and classified as Zone-II, according to IS 383: 2016. The fine aggregate chemical composition is shown in Table 3. The distribution of particle sizes is shown in Fig. 1. Both RS and SS, particle size distributions, are within the upper and lower bound limit. In Table 4, the engineering properties of RS and SS are listed. SEM images of RS and SS particles are shown in Fig. 2, which indicate that the particles of SS are relatively rough and angular compared to those of RS particles.

Table 3. Chemical composition of fine aggregate (RS and SS) by EDS analysis

Chemical composition	Oxide percentage in RS (%) + Oxide percentage in SS (%)	
SiO <sub>2</sub>	75.11	49.86
TiO <sub>2</sub>	-	0.48
Cr <sub>2</sub> O <sub>3</sub>	-	0.2
Al <sub>2</sub> O <sub>3</sub>	13.18	15.95
Fe <sub>2</sub> O <sub>3</sub>	4.92	24.66
Mn	-	1.92
MgO	0.33	0.76
CaO	1.34	4.52
Na <sub>2</sub> O	-	0.95
K <sub>2</sub> O	5.09	0.65

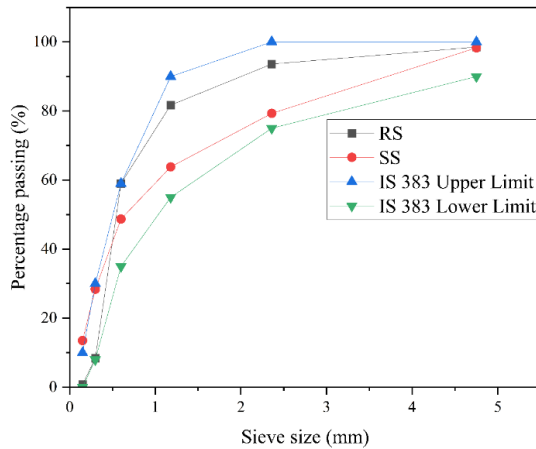
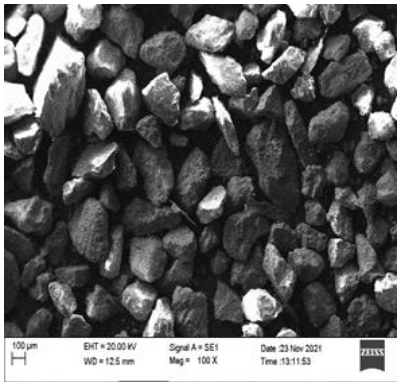


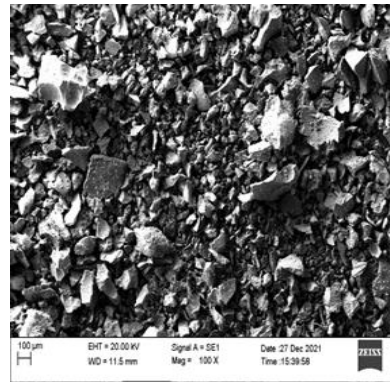
Fig. 1. Distribution of RS and SS particle sizes

Table 4. Fine aggregate Properties

Description	RS	SS
Zone	II	II
Fineness modulus	2.58	2.68
Specific gravity	2.56	2.45



(a)



(b)

Fig. 2. SEM images of (a) RS and (b) SS

#### 2.1.4 Polyvinyl Alcohol (PVA) Fibres

In the current study, PVA fibres coated with a 1.2% hydrophobic oiling agent are utilized, and their features are listed in Table 5. The image of PVA fibres is depicted in Fig. 3. Fibres may decrease the flowability because they may restrict the smooth flow and movement of sand particles and cement paste.

Table 5. Manufacturer-specified properties of PVA fibres

Properties	PVA fibres
Length	12 mm
Fracture elongation	6 %
Modulus of Elasticity	40 GPa
Density	1.30 g/cm <sup>3</sup>
Diameter	40 µm



Fig. 3. PVA fibres

### 2.1.5 Superplasticizer (SP)

Polycarboxylic acid-type superplasticizer is deployed to enhance the flowability and prevents fibre agglomeration, thus regulating the distribution of fibre in the mix.

## 2.2 Mix Proportions

In the ECC mix design, the mix proportion is adopted per Li et al., [25] as shown in Table 6. The standard M45 ECC mix is the most common ECC mix used in practical applications, which has an FA-to-cement ratio of 1.2. It also enhances the flowability of fresh ECC and improves mechanical properties after 90 days. The materials used in preparing ECC mixes are fixed, and the amount of SS varies as a replacement of (5%, 20%, 35%, 50%, and 65%) RS. Based on the past literature available on SS, the percentages are fixed. However, for each percentage, RS or SS particle sizes vary. All mixes are given a specific identity, such as E1, E2 and E3 for control mixes without SS at 2.36 mm, 1.18 mm and 0.60 mm particle sizes. At the same time, E4 - E18 is used for mixes containing 5%, 20%, 35%, 50%, and 65% SS with various particle sizes, respectively. Due to the larger aggregate size in the present research, a higher amount of fibre may lead to fibre clumping; hence, it is only employed at 1% of the volume for all the mixes. Based on the local ingredient conditions to ensure proper fibre dispersion, the superplasticizer and water content are finalized by conducting a marsh cone test. To investigate the influence of SS percentage and size on the properties of ECC, the same constituent proportions but with various particle sizes (2.36mm, 1.18 mm and 0.6 mm) for varying replacement percentages of RS by SS are prepared.

Table 6. Different mix proportions

Mix	Cement	Fly ash	River sand	Steel Slag	Water	SP	PVA fibre, vol%
-----	--------	---------	------------	------------	-------	----	-----------------



E1	1	1.2	0.8	-	0.64	0.015	1
E2	1	1.2	0.8	-	0.64	0.015	1
E3	1	1.2	0.8	-	0.64	0.015	1
E4	1	1.2	0.76	0.04	0.64	0.015	1
E5	1	1.2	0.76	0.04	0.64	0.015	1
E6	1	1.2	0.76	0.04	0.64	0.015	1
E7	1	1.2	0.64	0.16	0.64	0.015	1
E8	1	1.2	0.64	0.16	0.64	0.015	1
E9	1	1.2	0.64	0.16	0.64	0.015	1
E10	1	1.2	0.52	0.28	0.64	0.015	1
E11	1	1.2	0.52	0.28	0.64	0.015	1
E12	1	1.2	0.52	0.28	0.64	0.015	1
E13	1	1.2	0.4	0.4	0.64	0.015	1
E14	1	1.2	0.4	0.4	0.64	0.015	1
E15	1	1.2	0.4	0.4	0.64	0.015	1
E16	1	1.2	0.28	0.52	0.64	0.015	1
E17	1	1.2	0.28	0.52	0.64	0.015	1
E18	1	1.2	0.28	0.52	0.64	0.015	1

### 2.3 Test Methods

The methodology used in the current research is shown in Fig. 4. The flowability of fresh ECC is evaluated using a spread flow test after the mixing process. The ECC mix is poured into a 70.6 mm cube mould. After a day, the specimens are de-moulded and placed in water till the testing age (28 and 90 days). A muffle furnace is used for heating specimens.

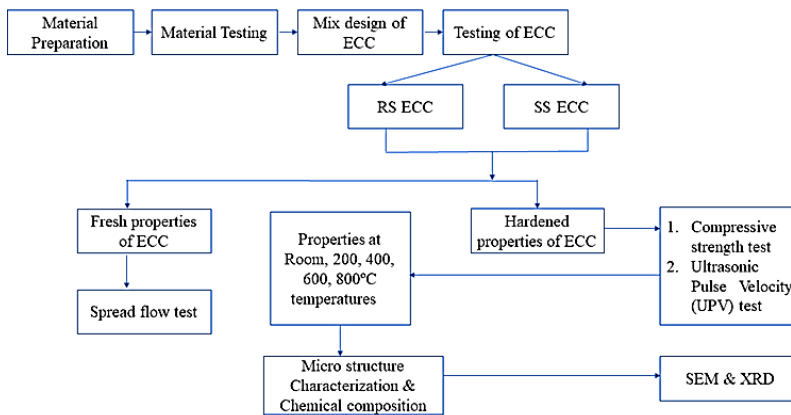


Fig. 4. Methodology for the current study

The exposure time maintained is considered from ISO 834 guidelines [26]. It is calculated based on the formula given in Eq (1), and The ISO 834 curve is shown in Fig. 5 [27]. The exposure temperatures selected from the literature are 200°C, 400°C, 600°C, and 800°C [7]. UPV and compressive strength are evaluated after the heating process. SEM and XRD are used to identify changes in microstructure and chemical composition.

$$T_f = T_0 + 345 \log_{10} (1 + 8t) \tag{1}$$

Where,  $T_f$  = average “furnace” temperature, °C;  $T_0$  = initial temperature °C, and  $T$  = time, min

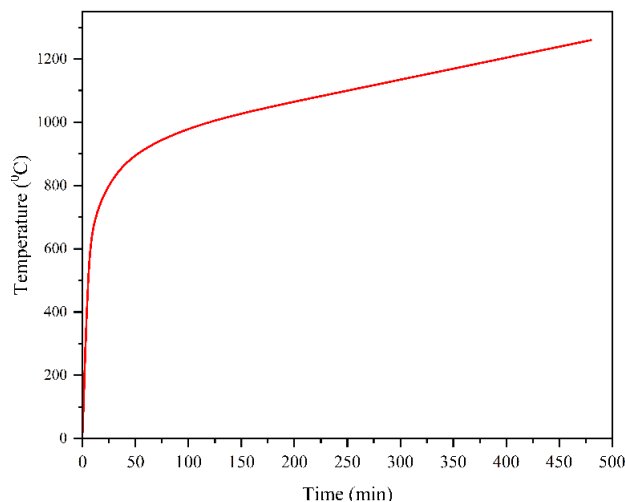


Fig. 5. ISO 834 curve

### 3. Results and Discussions

#### 3.1 Spread flow test

The Flowability of fresh ECC is evaluated using a spread-flow test. Depending on the size of the employed fine aggregate, the flowability of ECC changes. Fresh ECC’s plastic viscosity affects the material’s characteristics [28]. So, the impact of grading on flowability needs to be evaluated. Fig. 6 shows that adding the SS marginally reduces the flowability for ECC. The flowability values of the mixes containing only RS (E1-E3) are about 210-185 mm. When RS partially replaces the SS, the flowability values are 200-135 mm for the E4-E18, respectively. The combination of fibres with SS's angular and rough surface texture (see Fig. 2b) may restrict the smooth flow. The shape of SS aggregates significantly affects flowability; while designing the mix, more care must be taken for the required w/c and proper gradation.

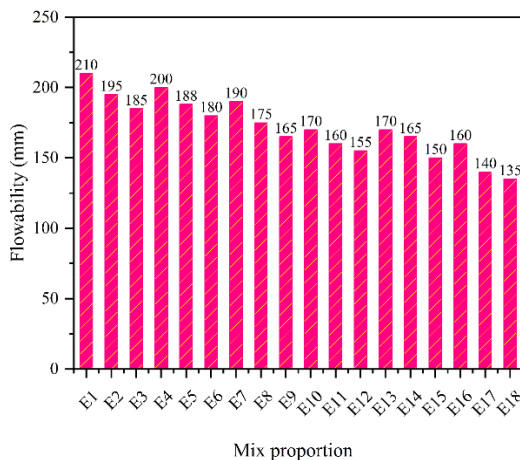


Fig. 6. ECC flowability for different mix proportions

All mixes are prepared with the same dosage of SP and water-to-binder ratio (W/b). The flowability of the SS ECC mixes is not improved Because the same dosage of SP is used for aggregates with different water absorption. However, using SP does not increase the flowability, and it is later noticed that the strength and durability are not affected by the decrease in flowability.

### 3.2 Compressive Strength Test

The compressive strength is determined per IS 516 standards. Fig. 7 indicated that the strength increased significantly with an increase in SS of up to 50% replacement, and after a 50% gradual decrease is observed. As compared with coarser particle mixes (E1, E4, E7, E10 and E13), the finer particle mixes (E3, E6, E9, E12 and E15) show higher strength at all curing periods.

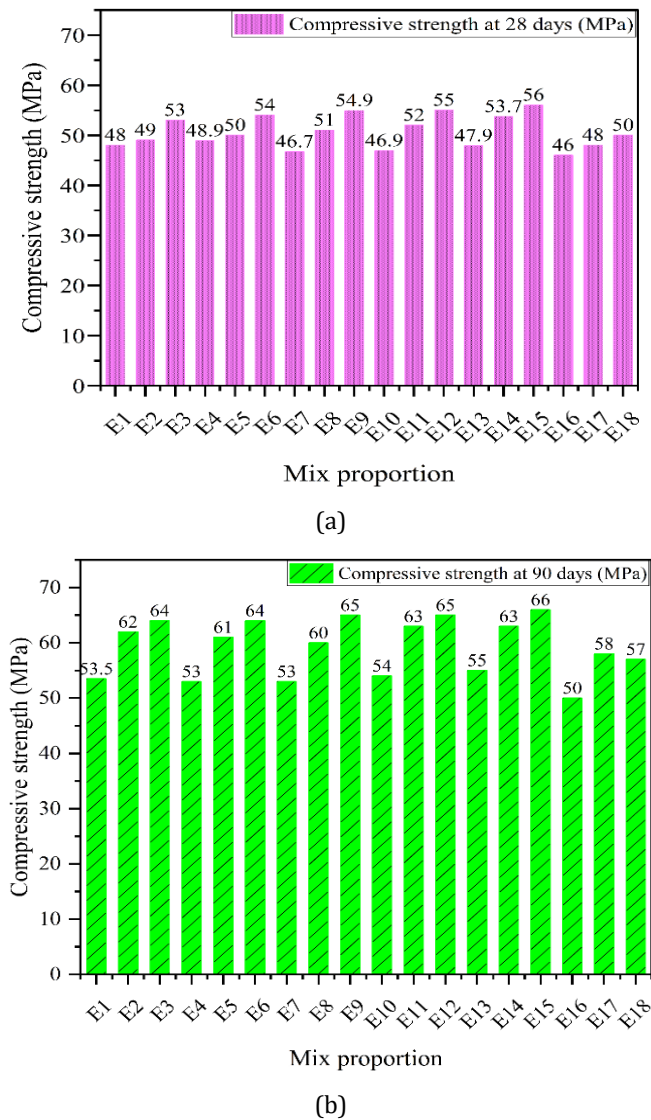


Fig. 7. ECC compressive strength for different mix proportions

Due to the larger proportion of finer particles than RS, mixes that contain 50% SS have an increase in strength, which helps in the development of a denser microstructure. Another reason is the reaction between  $\text{SiO}_2$  and  $\text{Ca(OH)}_2$ . According to Table 3, SS contains about 50% $\text{SiO}_2$ .  $\text{Ca(OH)}_2$  produced on the hydration of cement can react with  $\text{SiO}_2$  to form more C-S-H, which reduces the porosity and enhances the strength. Additionally, the SS employed in this study has a rough surface texture and an angular shape (see Fig. 2 b), which improves the bond between the aggregate and cement paste along with the reduction amount of voids [29].

### 3.3 UPV Test

A non-destructive experiment to check the homogeneity of a specimen is UPV. It calculates the sound wave transmission velocity inside the specimen. In Fig. 8, it is observed that ECC mixes with partial substitution of RS by SS up to 50%; the UPV increases gradually, and after that, it decreases at all curing ages—the reaction of  $\text{SiO}_2$  with  $\text{Ca(OH)}_2$ . According to Table 3, SS contains about 50% $\text{SiO}_2$ .  $\text{Ca(OH)}_2$  produced on the hydration of cement can react with  $\text{SiO}_2$  to form more C-S-H, which reduces the porosity and enhances the strength. Another reason is due to finer particles in SS, which fill the micropores in the composite; E15 exhibits the peak value in UPV.

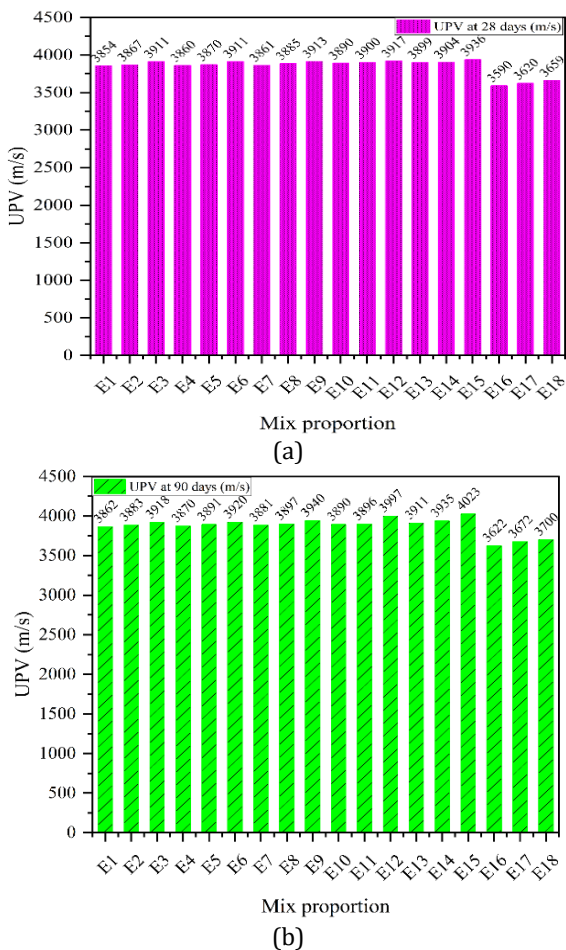


Fig. 8. ECC UPV for different mix proportions

### 3.4 ECC Properties at Various Temperatures

#### 3.4.1 Appearance of the Specimen

A change in the specimen's colour is observed as a result of exposure to various temperatures, as illustrated in Fig. 9. The darker surface of RS ECC specimens at 200°C results from dehydration and water evaporation. As the temperature reaches 400°C, PVA fibres melt, resulting in grey. After 600°C, a light grey colour indicates C-S-H gel dehydration. Yellowish grey at 800°C is related to C-S-H gel decomposition. Similarly, the colour of SS ECC specimens is comparable to that of RS ECC specimens up to 600°C. Grey-white after exposure to 800°C is due to ECC containing SS, which has higher heat-insulation capacity and extends the time it takes for hydration products to decompose.

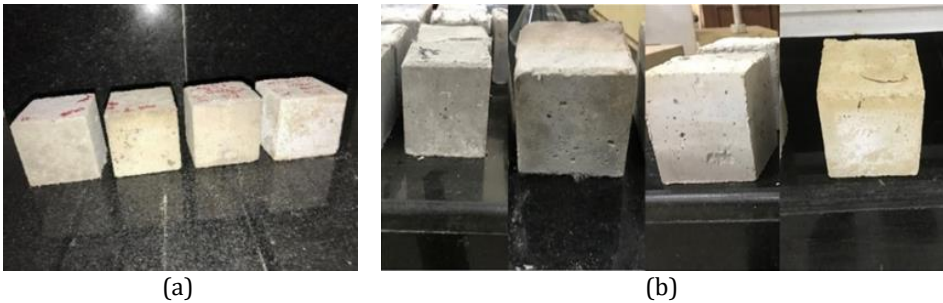


Fig. 9. Appearance of specimens at various temperatures: (a) RS ECC (b) SS ECC

#### 3.4.2 Compressive Strength Test

The ratio of compressive strength at various temperatures ( $f_{CT}$ ) and compressive strength at 28°C ( $f_c$ ) is used to obtain normalized strength ( $f_{CT}/f_c$ ). The  $f_{CT}/f_c$  of ECC at various temperatures for 28 and 90 days are indicated in Fig. 10 and Fig. 11. Fig. 10 shows that after exposure to 200°C, the strength for E1, E2 and E3 is improved by 6.1%, 8.3% and 7.5% for 28 days as compared with specimens at 28°C. A similar phenomenon is observed in another study [30]. It is due to the accelerated pozzolanic reaction, but for 90 days (Fig. 11), it shows a 9%, 6% and 4% reduction in strength.

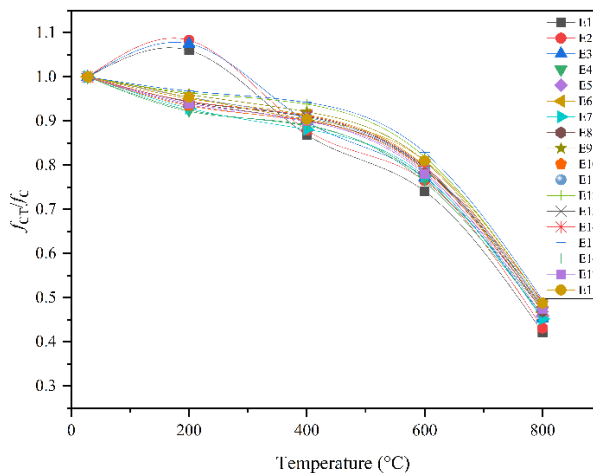


Fig. 10. ECC compressive strength at various temperatures after 28 days

When the temperature rises over 400°C, the strength of ECC mixes decreases, due to the small channels from melted PVA fibres in the matrix (Fig. 18). After exposure to 600°C and 800°C, due to hydrates decomposition, the strength is decreased. Normalized strength for E4-E18 is higher than those of E1-E3 regardless of the curing period because of the denser structure and heat-insulation capacity of the SS [31]. As mentioned below, C-S-H would decompose at 800°C, and Fig. 16 clearly shows that E3 contained significantly less C-S-H than E15. The C-S-H is responsible mainly for the ECC strength. So, the strength loss is greater when C-S-H is very low. A similar trend is observed (Fig. 11) for 90 days.

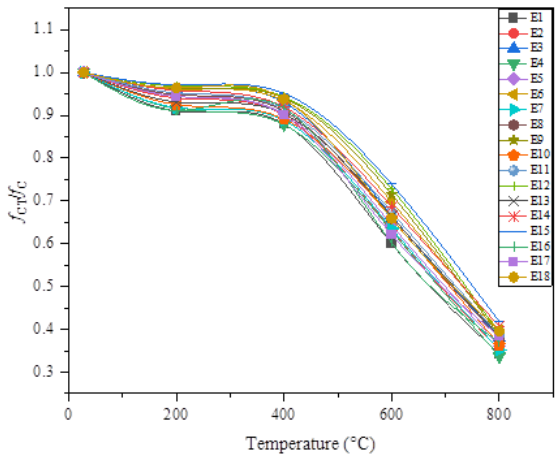


Fig. 11. ECC compressive strength at various temperatures after 90 days

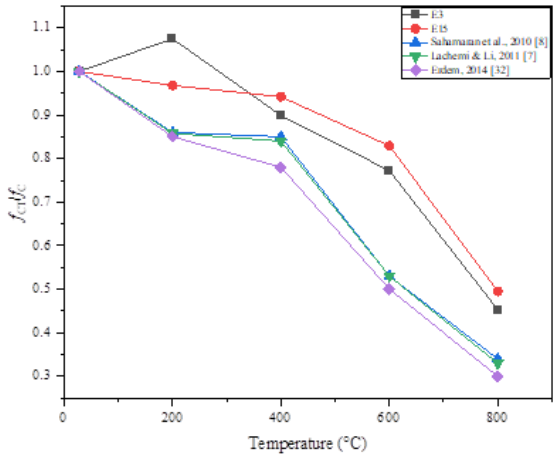


Fig. 12. Normalized compressive strength comparison with literature

The normalized compressive strength of M45 ECC obtained from the literature is compared in Fig. 12 [8][7][32]. The normalized strength of E15 is higher at all temperatures when compared to the results of earlier research. The reaction between SiO<sub>2</sub> and Ca(OH)<sub>2</sub>. According to Table 3, SS contains about 50%SiO<sub>2</sub>. It is well known that the silicates can react with Ca(OH)<sub>2</sub> produced during cement hydration to form additional C-S-H compounds, which reduce the porosity and enhance the strength. Another reason is that ECC containing SS, which has higher heat-insulation capacity, delays the decomposition of hydration products even at 800°C.

### 3.4.3 UPV Test

The ratio of UPV at various temperatures ( $U_T$ ) and UPV at 28°C ( $U$ ) is used to obtain normalized UPV ( $U_T/U$ ). The  $U_T/U$  of ECC at various temperatures for 28 and 90 days are presented in Fig. 13 and Fig. 14. Up to 400°C, the formation of small channels in the specimens due to the melted fibres causes the percentage variation in UPV. At high temperatures (600°C and 800°C), more pores are formed in ECC, extending the pulse wave travel distance and lowering the UPV values. ECC developed with SS (E4-E18) suffered less internal damage at various temperatures than ECC made with RS (E1-E3), because of the stable chemical composition of SS. However, E15 stands out best because of its denser structure and stronger heat insulation capacity.

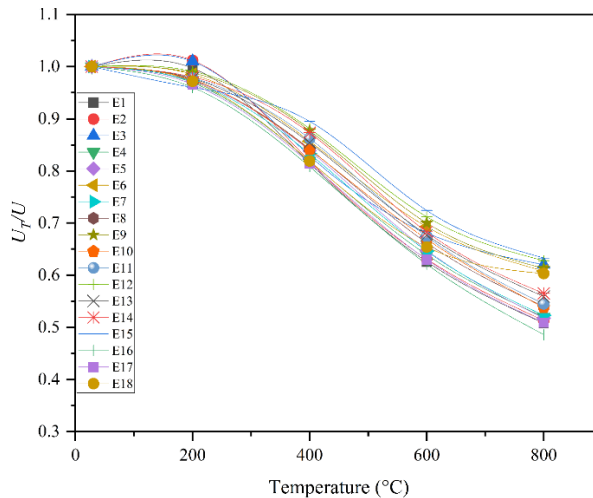


Fig. 13. ECC UPV at various temperatures after 28 days

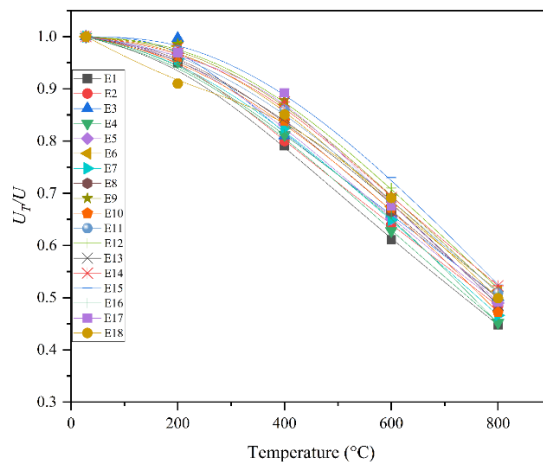


Fig. 14. ECC UPV at various temperatures after 90 days

### 3.4.4 Stress-Strain Curves at Various Temperatures

The stress-strain curves of E3 and E15 specimens at various temperatures (T0, T1, T2, T3 and T4 represent the 28°C, 200°C, 400°C, 600°C and 800°C) at 90 days are shown in Fig.

15. The decrease of peak stress of the curves are observed for both RS and SS ECC specimens with an increase of temperature up to 800°C. But, higher peak stress and strain values are observed for E15 compared to E3 at various temperatures. The peak strain is relatively high at 28°C because the PVA fibres prevent cracks from forming and expanding. The PVA fibres melted at 200°C, increasing the porosity. As the temperature rises, more cracks form and the peak strain is attained at a higher rate. With increased temperature, the ductile nature of both RS and SS ECC specimens becomes brittle.

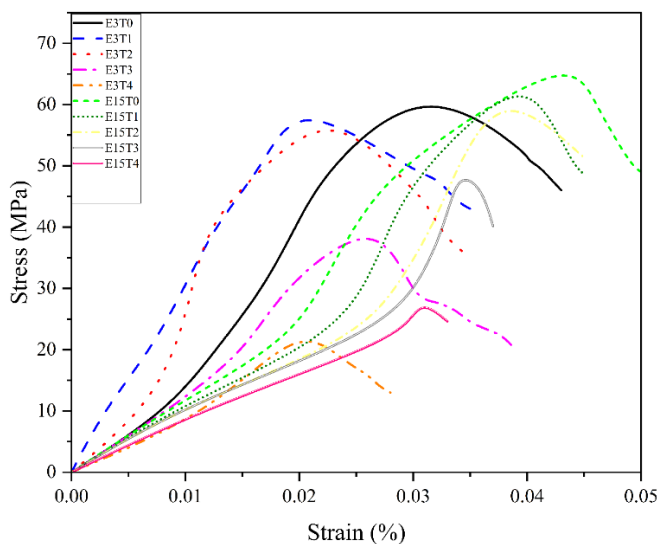


Fig. 15. Stress-strain curves at various temperatures after 90 days

#### 3.4.5 Chemical Composition at Various Temperatures

A study on various mixes at various temperatures is conducted on cube specimens. XRD analysis is performed on the samples collected after the compressive testing process to identify the chemical composition of ECC. Among all, better properties are observed in E3 and E15. So, the XRD pattern of E3 and E15 at various temperatures is highlighted in Fig. 16. At 28°C, hydration products like Calcium Silicate Hydrate (C-S-H) and Portlandite ( $\text{Ca(OH)}_2$ ) are identified for both E3 and E15.

The dehydration process is initiated at various temperatures. For E3, at 200°C, the decreased peak value of  $\text{SiO}_2$  is observed, as indicated in Fig. 16 (a), but it increases when ECC is subjected to 400, 600 and 800°C. For E15, the peak of  $\text{SiO}_2$  is higher at 28°C and becomes lower after exposure up to 800°C (Fig. 16 (b)), resulting in more C-S-H gel formation than E3. The C-S-H phase is still identified at 800°C for E15 and not observed for E3. At 200°C and 400°C, part of  $\text{Ca(OH)}_2$  starts to decompose ( $\text{Ca(OH)}_2 \rightarrow \text{CaO} + \text{H}_2\text{O}$ ), at 600°C and 800°C, is not observed in E3 and E15. In general,  $\text{Ca(OH)}_2$  decomposition is completed at about 530°C [33]. At 800°C, Dicalcium Silicate ( $\text{Ca}_2\text{SiO}_4$ ) and Tricalcium Silicate ( $\text{Ca}_3\text{SiO}_5$ ) are identified, which are formed due to hydration products decomposition for E3, along with  $\text{Ca}_2\text{SiO}_4$  and  $\text{Ca}_3\text{SiO}_5$ , the Magnesium Ferrite ( $\text{MgFe}_2\text{O}_4$ ) is found for E15. The  $\text{MgFe}_2\text{O}_4$  is formed due to a chemical reaction between magnesium oxide ( $\text{MgO}$ ) and ferric oxide ( $\text{Fe}_2\text{O}_3$ ).



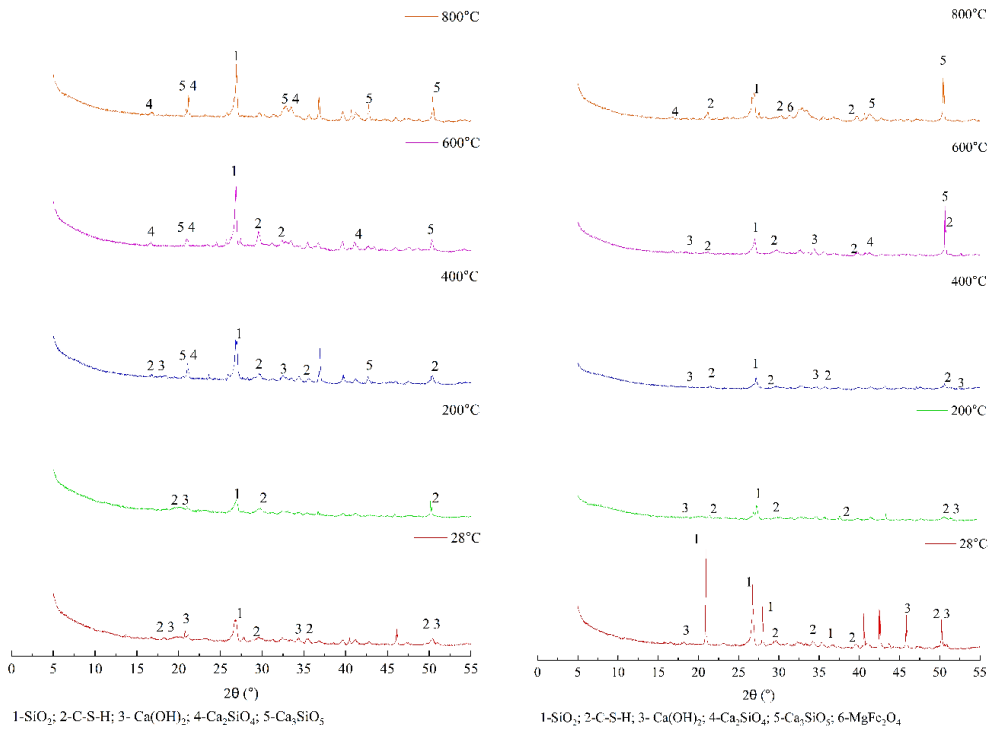
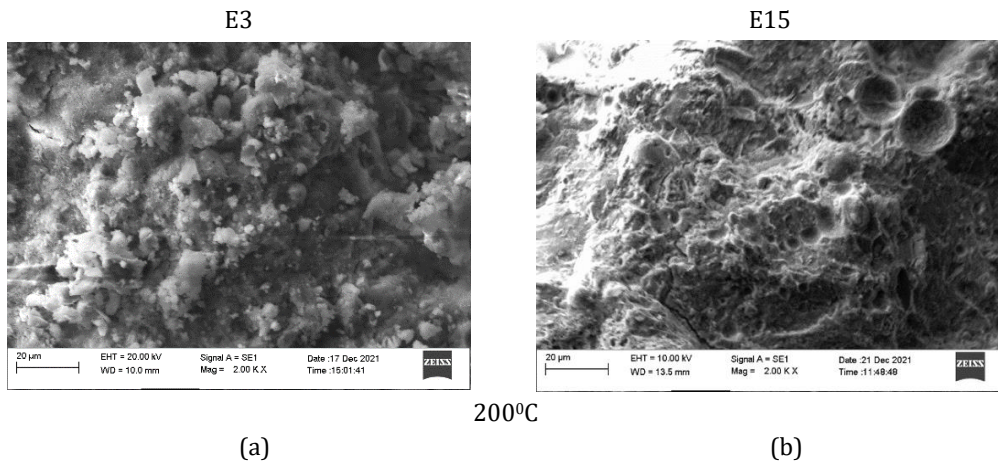


Fig. 16. XRD pattern for ECC at various temperatures: (a) E3, (b) E15

### 3.4.6 Microstructure at various temperatures

The microstructure of E3 and E15 at various temperatures is shown in Fig. 17. At 200°C; both mixes show a change in the morphology of the fibres (Fig. 18). Therefore, PVA fibres Shrinkage may result in matrix separation and a loss of strength. At 400°C, when compared to the E3, the E15 exhibits a compacted matrix with a lower availability of unreacted FA.



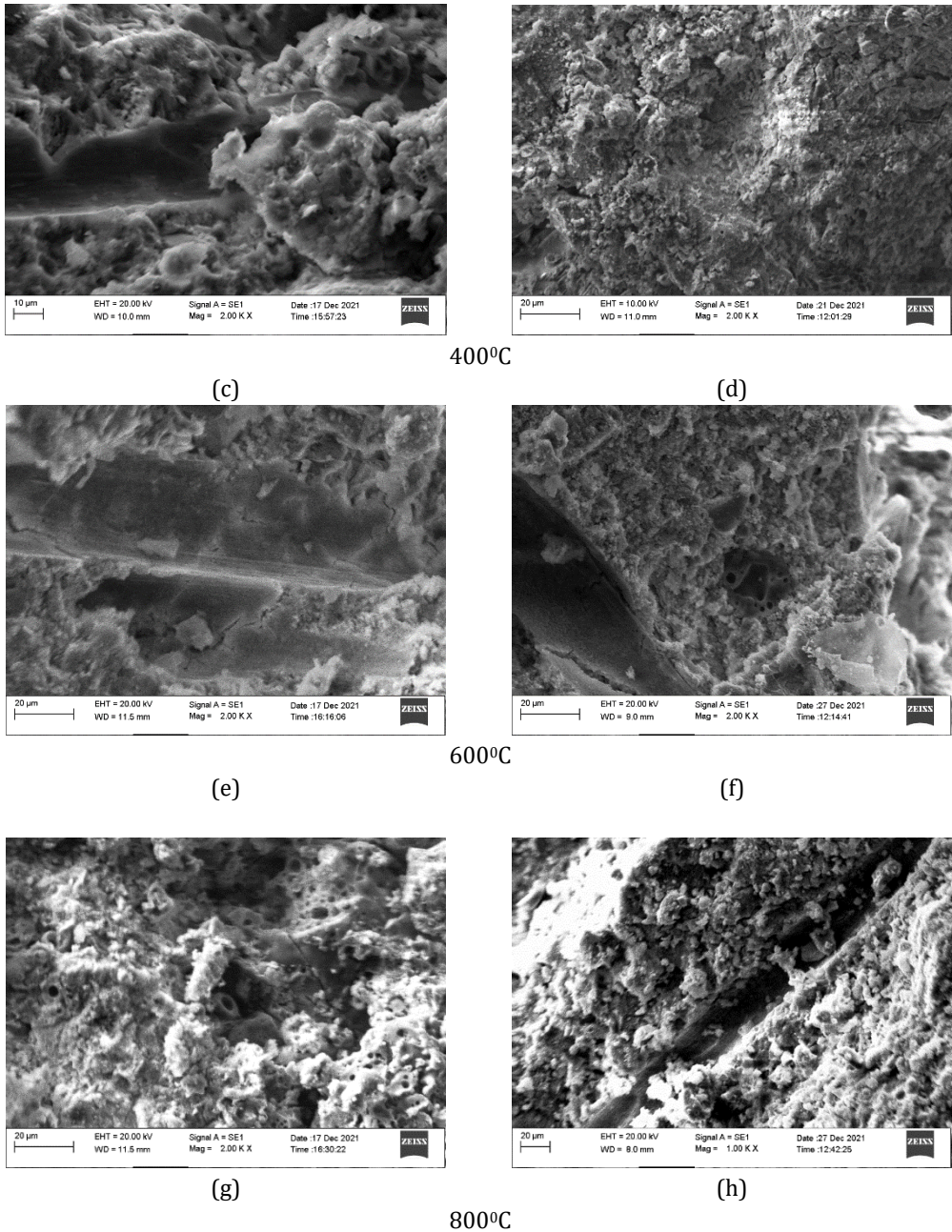
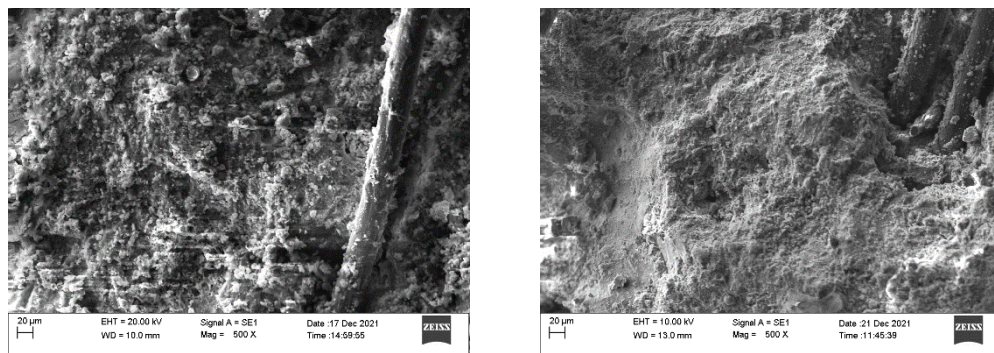
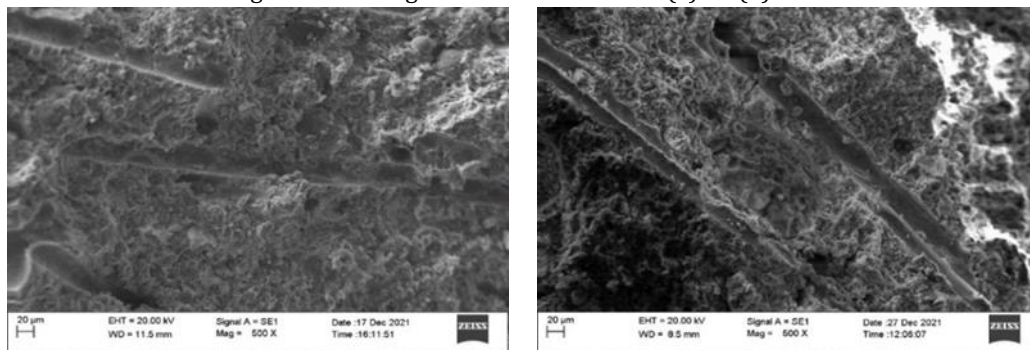


Fig. 17. Microstructure of E3 and E15 at various temperatures

In RS and SS ECC, the PVA fibres helped reduce pore pressure and prevent spalling through melting (seen in Fig. 9 and Fig. 19). At 600°C, irregular bush-like structures are observed due to thermophysical reactions. Strength loss in both mixes occurred at 800°C due to matrix deterioration, hydration product decomposition, and cracking. In contrast to E3, however, E15 exhibits a lesser loss in strength because of the denser structure and heat insulation capacity of the SS.



(a) (b)  
 Fig. 18. Shrinking of PVA fibres at 200°C (a) E3 (b) E15



(a) (b)  
 Fig. 19. Melted PVA fibres after 400°C (a) E3 (b) E15

#### 4. Conclusions

The effect on the characteristics of ECC at elevated temperatures is experimentally studied. The following conclusions are formed in perspective with test findings:

- The reduction in flowability is observed when SS partially replaces the RS. The RS ECC mixes flowability is about 210-185 mm, and SS ECC mixes vary from 200-135 mm. Combining fibres with SS's angular and rough surface texture may restrict the smooth flow.
- The rise in compressive strength and UPV at all ages is observed with the replacement of the RS by SS up to 50%. Among all in the E15 mix, better improvements in strength and quality are noticed. Ca(OH)<sub>2</sub> produced on the hydration of cement can react with SiO<sub>2</sub> to form more C-S-H, which reduces the porosity and enhances the strength and quality.
- The spalling behaviour is not observed in both RS and SS ECC at elevated temperatures.
- The darker surface of RS ECC at 200°C results from dehydration and water evaporation. As the temperature reaches 400°C, PVA fibres melt, resulting in grey. After 600°C, a light grey colour indicates C-S-H gel dehydration. Yellowish grey at 800°C is related to C-S-H gel decomposition. Similarly, the colour of SS ECC specimens is comparable to that of RS ECC specimens up to 600°C. Grey-white after exposure to 800°C is due to ECC containing SS, which has higher heat-insulation capacity and extends the time it takes for hydration products to decompose.

- UPV test is used to understand the developments of voids and cracks in the ECC. The higher and lower values depend on the evolution of cracks in ECC. Thus, UPV tests have revealed that the E15 has better resistance to the evolution of cracks under elevated temperatures.
- The normalized strength of SS ECC is higher than that of RS ECC at elevated temperatures. The E15 specimens provided higher normalized strength even at the 800°C.
- The higher peak stress and strain values are observed for E15 compared to E3 at various temperatures. The peak strain is relatively high at 28°C because the PVA fibres prevent cracks from forming and expanding. The PVA fibres melted at 200°C, increasing the porosity. As the temperature rises, more cracks form and the peak strain is attained at a higher rate.
- The XRD results revealed that The C-S-H phase is still identified at 800°C for E15 and not observed for E3. At 800°C, MgFe<sub>2</sub>O<sub>4</sub> is found in E15.
- The SEM images showed that the increase in temperature, the voids and cracks increased in the RS ECC. However, at elevated temperatures, SS ECC retained a better-compacted structure than RS ECC due to the greater heat insulation capacity of the SS.

## 5. Future Scope

The performance of SS ECC reinforced with higher temperature-resistant fibres, including steel, carbon, and basalt fibres, should be studied. The durability property of hardened ECC in terms of volume stability has to be investigated.

## Acknowledgement

The authors thank HIRA GODAWARI POWER & ISPAT, Sika India Pvt—Ltd, and Ultra Tech Cement for their support.

## References

- [1] Li Y, Li J, Yang EH, Guan X. Investigation of matrix cracking properties of engineered cementitious composites (ECCs) incorporating river sands. *Cem Concr Compos.* 2021;123(July):104204. <https://doi.org/10.1016/j.cemconcomp.2021.104204>
- [2] Bahraq AA, Maslehuddin M, Al-Dulaijan SU. Macro- and Micro-Properties of Engineered Cementitious Composites (ECCs) Incorporating Industrial Waste Materials: A Review. *Arab J Sci Eng.* 2020;45(10):7869-95. <https://doi.org/10.1007/s13369-020-04729-7>
- [3] Li VC, Bos FP, Yu K, McGee W, Ng TY, Figueiredo SC, et al. On the emergence of 3D printable Engineered, Strain Hardening Cementitious Composites (ECC/SHCC). *Cem Concr Res.* 2020;132(April):106038. <https://doi.org/10.1016/j.cemconres.2020.106038>
- [4] Gu D, Pan J, Mustafa S, Huang Y, Luković M. Shear transfer mechanism in reinforced engineered cementitious composite (ECC) beams: Quantification of V<sub>s</sub> and V<sub>c</sub>. *Eng Struct.* 2022;261(April). <https://doi.org/10.1016/j.engstruct.2022.114282>
- [5] Chung KL, Ghannam M, Zhang C. Effect of Specimen Shapes on Compressive Strength of Engineered Cementitious Composites (ECCs) with Different Values of Water-to-Binder Ratio and PVA Fiber. *Arab J Sci Eng.* 2018;43(4):1825-37. <https://doi.org/10.1007/s13369-017-2776-8>
- [6] Liu JC, Tan KH. Mechanism of PVA fibers in mitigating explosive spalling of engineered cementitious composite at elevated temperature. *Cem Concr Compos.* 2018;93(May):235-45. <https://doi.org/10.1016/j.cemconcomp.2018.07.015>

- [7] Lachemi M, Li VC. Effect of Fly Ash and PVA Fiber on Microstructural Damage and Residual Properties of Engineered Cementitious Composites Exposed to High Temperatures. 2011;23(December):1735-45. [https://doi.org/10.1061/\(ASCE\)MT.1943-5533.0000335](https://doi.org/10.1061/(ASCE)MT.1943-5533.0000335)
- [8] Sahmaran M, Lachemi M, Li VC. Assessing mechanical properties and microstructure of fire-damaged engineered cementitious composites. *ACI Mater J*. 2010;107(3):297-304. <https://doi.org/10.14359/51663759>
- [9] Wang Z, Sun P, Zuo J, Liu C, Han Y, Zhang Z. Long-term properties and microstructure change of engineered cementitious composites subjected to high sulfate coal mine water in drying-wetting cycles. *Mater Des*. 2021;203:109610. <https://doi.org/10.1016/j.matdes.2021.109610>
- [10] Zeng D, Cao M, Ming X. Characterization of mechanical behavior and mechanism of hybrid fiber reinforced cementitious composites after exposure to high temperatures. *Mater Struct Constr*. 2021;54(1):1-11. <https://doi.org/10.1617/s11527-021-01622-z>
- [11] He J, Wang Q, Yao B, Ho J. Impact of Elevated Temperatures on the Performance of High-Strength Engineered Cementitious Composite. *J Mater Civ Eng*. 2021;33(9):1-17. [https://doi.org/10.1061/\(ASCE\)MT.1943-5533.0003812](https://doi.org/10.1061/(ASCE)MT.1943-5533.0003812)
- [12] Mohammed BS, Achara BE, Liew MS, Alaloul WS, Khed VC. Effects of elevated temperature on the tensile properties of NS-modified self-consolidating engineered cementitious composites and property optimization using response surface methodology (RSM). *Constr Build Mater*. 2019;206:449-69. <https://doi.org/10.1016/j.conbuildmat.2019.02.033>
- [13] Cao K, Li H, Liu G, Huang Z, Wu G. Bonding properties between steel-basalt hybrid fibers reinforced cementitious composites and existing concrete at high temperatures. *J Build Eng*. 2023;70(December 2022):106371. <https://doi.org/10.1016/j.jobe.2023.106371>
- [14] Chandru P, Karthikeyan J, Sahu AK, Sharma K, Natarajan C. Performance evaluation between ternary blended SCC mixes containing induction furnace slag and crushed stone as coarse aggregate. *Constr Build Mater*. 2021;267:120953. <https://doi.org/10.1016/j.conbuildmat.2020.120953>
- [15] Chandru P, Karthikeyan J, Sahu AK, Sharma K, Natarajan C. z. *Constr Build Mater*. 2021;270:121483. <https://doi.org/10.1016/j.conbuildmat.2020.121483>
- [16] Mehta PK. History and Status of Performance Tests for Evaluation of Soundness of Cements. Vol. STP 663, ASTM Special Technical Publication. 1978. p. 35-56. <https://doi.org/10.1520/STP35785S>
- [17] Kabir H, Hooton RD, Popoff NJ. Evaluation of cement soundness using the ASTM C151 autoclave expansion test. *Cem Concr Res*. 2020;136(May). <https://doi.org/10.1016/j.cemconres.2020.106159>
- [18] Dong Q, Wang G, Chen X, Tan J, Gu X. Recycling of steel slag aggregate in portland cement concrete: An overview. *J Clean Prod*. 2021;282:124447. <https://doi.org/10.1016/j.jclepro.2020.124447>
- [19] Lun Y, Zhou M, Cai X, Xu F. Methods for improving volume stability of steel slag as fine aggregate. *J Wuhan Univ Technol Mater Sci Ed*. 2008;23(5):737-42. <https://doi.org/10.1007/s11595-007-5737-3>
- [20] Hemalatha T, Sindu BS. Experimental Studies to Investigate Efficacies of Slag as Fine Aggregate Substitute. *ACI Mater J*. 2020;(117). <https://doi.org/10.14359/51725981>
- [21] Agalit H, Zari N, Maaroufi M. Thermophysical and chemical characterization of induction furnace slags for high temperature thermal energy storage in solar tower plants. *Sol Energy Mater Sol Cells*. 2017;172(January):168-76. <https://doi.org/10.1016/j.solmat.2017.07.035>
- [22] Netinger Grubeša I, Jelčić Rukavina M, Mladenović A. Impact of High Temperature on Residual Properties of Concrete with Steel Slag Aggregate. *J Mater Civ Eng*. 2016;28(6):04016013. [https://doi.org/10.1061/\(ASCE\)MT.1943-5533.0001515](https://doi.org/10.1061/(ASCE)MT.1943-5533.0001515)

- [23] Liang X, Wu C, Su Y, Chen Z, Li Z. Development of ultra-high performance concrete with high fire resistance. 2018;179:400-12. <https://doi.org/10.1016/j.conbuildmat.2018.05.241>
- [24] Jihad Miah M, Kawsar Ali M, Lo Monte F, Chandra Paul S, John Babafemi A, Šavija B. The effect of furnace steel slag powder on the performance of cementitious mortar at ambient temperature and after exposure to elevated temperatures. Structures. 2021;33(December 2020):2811-23. <https://doi.org/10.1016/j.istruc.2021.06.047>
- [25] Li M, Li VC. Rheology, fiber dispersion, and robust properties of engineered cementitious composites. Mater Struct Constr. 2013;46(3):405-20. <https://doi.org/10.1617/s11527-012-9909-z>
- [26] Nuaklong P, Worawatnalunart P, Jongvivatsakul P, Tangaramvong S, Pothisiri T, Likitlersuang S. Pre- and post-fire mechanical performances of high calcium fly ash geopolymer concrete containing granite waste. J Build Eng. 2021;44(July):103265.
- [27] ISO:834. Fire-resistance tests- Elements of building construction. 1975;1975.
- [28] Yang EH, Sahmaran M, Yang Y, Li VC. Rheological control in production of engineered cementitious composites. ACI Mater J. 2009;106(4):357-66. <https://doi.org/10.14359/56656>
- [29] Abd El-Hakim RT, Elgendy GM, El-Badawy SM, Amin M. Performance evaluation of steel slag high performance concrete for sustainable pavements. Int J Pavement Eng. 2021;0(0):1-19.
- [30] Li Q, Gao X, Xu S, Peng Y, Fu Y. Microstructure and Mechanical Properties of High-Toughness Fiber-Reinforced Cementitious Composites after Exposure to Elevated Temperatures. 2016;28(11):1-11. [https://doi.org/10.1061/\(ASCE\)MT.1943-5533.0001647](https://doi.org/10.1061/(ASCE)MT.1943-5533.0001647)
- [31] Zhuang X, Liang Y, Ho JCM, Wang YH, Lai M, Li X, et al. Post-fire behavior of steel slag fine aggregate concrete. Struct Concr. 2022;(September 2021):1-24.
- [32] Erdem TK. Specimen size effect on the residual properties of engineered cementitious composites subjected to high temperatures. Cem Concr Compos. 2014;45:1-8. <https://doi.org/10.1016/j.cemconcomp.2013.09.019>
- [33] Huang Z, Liew JYR, Li W. Evaluation of compressive behavior of ultra-lightweight cement composite after elevated temperature exposure. Constr Build Mater. 2017;148:579-89. <https://doi.org/10.1016/j.conbuildmat.2017.04.121>

Blank Page

## Load sharing behaviour in piled-raft foundations over sand and clay: An experimental investigation

Gaurav Pandey<sup>\*,a</sup>, Vishal Kumar Mourya<sup>b</sup>, Dhirendra Patel<sup>c</sup>, Rajesh Kumar<sup>d</sup>, Suresh Kumar<sup>e</sup>

Department of Civil Engineering, Indian Institute of Technology (BHU) Varanasi, India

### Article Info

#### Article history:

Received 17 Jul 2023

Accepted 25 Dec 2023

#### Keywords:

Piled-raft;

Experimental analysis;

Settlement;

Load sharing

### Abstract

Piled-raft foundations have gained increasing popularity in the past few decades, providing a viable alternative to traditional raft and pile foundations. Despite this, designers are reluctant to apply them frequently in practice due to their complex behaviour and the lack of well-defined guidelines specific to piled-raft foundations. Previous studies have demonstrated that piled-rafts are more effective in reducing settlement and can sustain heavier loads from superstructures. Experimental investigations have been conducted in the present study to ascertain the load-sharing behaviour in piled-raft foundations under vertical loading. Since experimental research on piled-rafts, especially over clay, is quite sparse, small-scale lab tests were conducted on piled-rafts over both sand and clay. Experimental comparisons of unpiled rafts and rafts with piles have been established for a better understanding of the individual and collective response of piles and rafts. Moreover, the effects of a few geometric parameters on the load-bearing capacity of the foundation have been observed. The results showed a significant contribution of the raft to load sharing in piled-raft foundations. It was also observed that the individual load-bearing capacities of the raft and the piles, when summed together, differ from that of the piled-raft foundation due to the interactions between the soil and the foundation components. Observations also supported the fact that increasing the length and number of piles enhances the load-bearing capacity of the foundation. The load-sharing ratio and load improvement ratio increase with the number of piles. Eventually, it can be concluded that piled-rafts are better at minimizing settlement and simultaneously carrying heavier loads.

© 2024 MIM Research Group. All rights reserved.

## 1. Introduction

There is an increasing need for high-rise constructions due to the rising global population and fast urbanization. The foundations of such constructions are often subjected to tremendous stresses, yet there might not always be a rigid stratum everywhere to sustain them. Hence, they must be placed on soft soils, where settlement, especially differential settlement, is a major problem. The raft foundation has proven to be a good basis for overcoming bearing capacity restrictions, although it may still exceed the permissible differential settling. The conventional pile foundation might restrict the settlement to a permissible limit and transmit the superstructure load to deeper strata.

The conventional pile foundation design does not consider the raft's contribution to load sharing, and hence, several piles may be used to serve the purpose. Consequently, a combination of pile and raft foundations has become popular in recent years as a rational

\*Corresponding author: [gauravp.rs.civ16@iitbhu.ac.in](mailto:gauravp.rs.civ16@iitbhu.ac.in)

<sup>a</sup> [orcid.org/0009-0008-3750-3097](https://orcid.org/0009-0008-3750-3097); <sup>b</sup> [orcid.org/0009-0009-4348-9911](https://orcid.org/0009-0009-4348-9911); <sup>c</sup> [orcid.org/0009-0004-1633-2437](https://orcid.org/0009-0004-1633-2437);

<sup>d</sup> [orcid.org/0000-0001-5145-588X](https://orcid.org/0000-0001-5145-588X); <sup>e</sup> [orcid.org/0000-0002-5528-0260](https://orcid.org/0000-0002-5528-0260)

DOI: <https://dx.doi.org/10.17515/resm2023.41me0714rs>

Res. Eng. Struct. Mat. Vol. 10 Iss. 3 (2024) 917-942



and economical foundation system. Such foundations have commonly been known as piled-rafts or piled-raft foundations. Piled-rafts can be used whenever the raft or pile foundation alone is not sufficient to counteract the upcoming stresses.

Since their introduction by Burland et al. [1] as settlement reducers, piled-raft foundations have drawn a lot of attention as an economical foundation system. Following that, several studies have extensively employed this approach [2-6]. In such an approach, the bearing capacity of the raft is utilized to withstand the applied load, and piles are used to reduce settlements, particularly differential settlements, to a reasonable limit. Another approach is the conventional pile design wherein the piles resist the entire load, and the contribution of the pile cap is completely ignored.

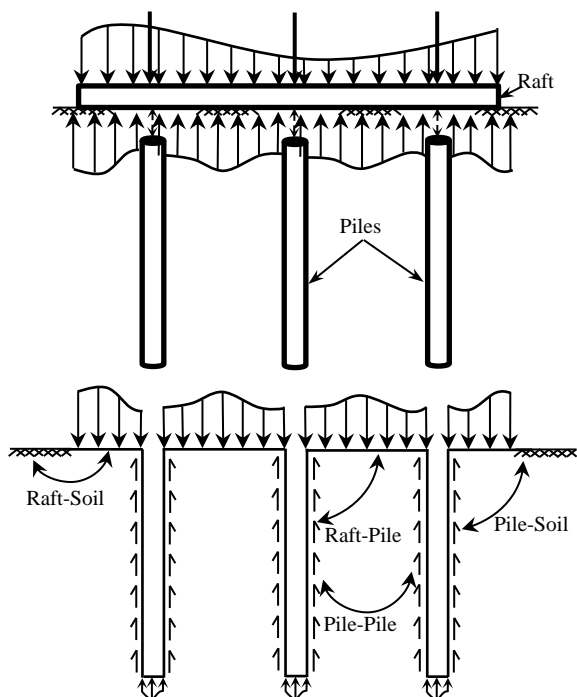


Fig. 1. Interaction mechanism in piled-rafts

High-rise constructions may be assured of having a safe and economical foundation by utilizing a midway strategy that makes use of both the raft and piles' load-bearing capacity. The load-sharing between piles and the raft in such an approach can be more advantageous in the case of strategically employed geometries and soil characteristics. With growing popularity, this approach has been adopted by several scholars [7-9]. Studies on the load-sharing behaviour of piled-rafts have primarily focused on the geometry and stiffness of the foundations [10, 11]. The load-sharing behaviour in piled-raft changes with the settlement as its load-bearing capacity depends on a specific settlement. Hence, it is necessary to consider the non-linear load response of the piled-rafts as well as the interactions between supporting soil and the foundation elements. Following that, a normalized load response model was proposed by Lee et al. [9].

Recent times have witnessed a growing exploration of eco-friendly practices. Rouhanifar [12] explores sustainable sand-rubber mixtures, focusing on mechanical behaviour parameters for low compaction efforts. Similarly, Fareghian [13] proposes recycling waste

tire textile fibre (WTTF) to enhance soil properties, reflecting a broader shift toward environmentally conscious practices in the field.

Due to the interactions between soil and the foundation elements, it becomes very complex to understand the load distribution behaviour in piled-rafts (Fig. 1). However, it becomes feasible with modern technologies and high-speed computers to numerically analyse them through available commercial codes. Viggiani [4] broadly classified piled-raft foundations into small and large piled-rafts. Small piled-rafts refer to those in which the raft lacks the necessary bearing capacity to withstand the overall load. Piles are hence affixed to attain a reasonable level of safety. Due to the high rigidity of rafts in small piled-rafts, differential settlement is not a serious issue. Alternatively, those in which the raft alone carries the applied load satisfactorily and needs piles only for reducing the settlement are called large piled-rafts.

The strategic location of piles plays a key role in improving the load-bearing capacity of the raft and also serves to minimize the total and differential settlement. Moreover, due to recent technological advancements, piled-rafts are now not only limited to high-rise structures but can also find their application in bridges, thermal power plants, offshore structures, residential buildings, and oil storage tanks [14, 15]. Various approaches to piled-raft analysis have been briefly reviewed in the subsequent section.

## **2. Literature Review**

Several approaches to piled-raft analysis have been developed since its inception. The initial theories viewed a raft as a plate or a succession of strips supported over spring. [16, 17]. Later on, simplified approaches have been developed. It includes a manual calculation approach by Poulos and Davis [18] which assumed a tri-linear load-settlement curve. Randolph [2] established approximate equations for the stiffness of piled-rafts that were mostly acceptable for traditional pile design.

For complex problems, researchers started using commercial codes based on numerical methods like BEM, FEM or their combinations. Finally, to validate the numerical results and evaluate the performance of piled-rafts under real-world conditions, experimental trials have been conducted. The most frequently used methodologies nowadays are the numerical techniques which may comprise of the finite difference method, finite element method, boundary element method or a hybrid amalgamation of these. The emergence of high-speed computing technology and the various commercial codes generated over time has boosted the use of these strategies. Researchers have used tools like PLAXIS, FLAC, and ABAQUS to simulate the complicated 2D and 3D problems involving interaction problems of piled-raft foundations. A benefit of 3D simulation is its capacity to analyse even the most complicated scenarios. Although using 2D simulation is quicker and easier than using 3D simulation, the underlying 3D problem must first be adequately simplified.

Reul and Randolph [19] conducted parametric investigations on piled-rafts exposed to uneven vertical loads using finite element analysis. de Sanctis & Mandolini [8] performed a 3D analysis to figure out the failure load coefficients that consider the interaction between the piled-raft components. A non-linear 3D study on piled-rafts supported over soft and stiff clay was done by Cho et al. [20]. The widely spaced piles were found more productive at lowering the average settlement. It was observed that the loading type mostly influences the differential settlement, whereas the pile geometries significantly affect both the average and differential settling. Sinha and Hanna [21] investigated the variations in soil properties and piled-raft geometry using a 3D model. Similarly, several other articles on numerical analysis of piled-rafts are listed in their references.

Case studies on piled-rafts over Frankfurt clay have been the focus of numerous investigations [22, 23]. Yamashita [24] examined certain constructions on piled-rafts in Japan that were subjected to seismic loading. Additionally, Japan has released a design standard for piled-raft foundations [25]. Reports on the behaviour of piled-rafts under actual structures have also been published [26, 27].

In contrast to numerical analysis, there is limited information available about experimental studies on piled-rafts, especially those supported over clayey soil. It is evident from the literature that experimental studies of piled-rafts can be conducted either using small-scale model tests or centrifuge tests.

Unsever et al. [28] conducted experimental studies on a piled-raft in the sand under combined loadings. Lateral and vertical tests were carried out on a piled-raft with three piles and the results were later verified using PLAXIS 3D software. It was evident that the interaction between raft and piles has a significant impact on how a piled-raft behaves. Kumar [29] studied the impact of raft size, pile length, and number of piles on the settlement of a foundation system in dry sandy soils with relative density of 70% through an experimental study. Deb et al. [30] analysed two variations of small-scale piled raft models are created, featuring  $2 \times 2$  and  $3 \times 3$  pile configurations. The experimentation involves modifying the spacing between piles and the thickness of the clayey soil to explore diverse scenarios. Chandiwala & Vasanwala [31] investigates a 160 mm x 160 mm pile-raft model, revealing that optimal pile spacing and length enhance bearing capacity while reducing raft settlement. The findings suggested that careful consideration of pile spacing and length in pile-raft systems has the potential to markedly impact lateral load distribution, presenting a more cost-effective and efficient foundation option for skyscrapers.

Piled-raft behaviour in the sand was analysed experimentally in the laboratory using small model foundations by Elwakil & Azzam [32]. It was discovered that the percentage of load shared by raft increased with a reduction in pile numbers and lengths. Moreover, the optimum performance of settlement-reducing piled-raft was achieved at a settlement ratio of 0.7% and the percentage of load taken by raft was 39%. Kumar and Kumar [33] experimentally examined the piled-raft behaviour in which the relative density of sand was varied. The differential settlement ratio was observed to decrease while the load improvement ratio increased with the number of piles. It was determined that the raft in combination with piles was found to be very effective in reducing the settlements.

Variations in relative density and number of piles were also investigated by Sosahab et al. [34] through lab experiments on piled-rafts. In contrast to the pile numbers, the former parameter proved to be more influential. Besides, the load improvement ratio was noticed to be more pronounced in the case of loose sands. A study on load eccentricity was conducted and it was revealed that the ultimate bearing capacity of the piled-raft gets reduced when the eccentricity of load increases.

Bajad & Sahu [35] performed 1g laboratory model tests to examine the effects of interaction among the raft and piles in a vertically loaded piled-raft supported on locally available soft clay. Mandal & Sengupta [36] inspected the behaviour of piled-rafts on soft clay under eccentric loading. For the same  $e/B$  ratio, the average settlements for rafts with piles were lowered significantly when compared to unpiled-rafts. Additionally, it was determined that piled-rafts were quite beneficial in minimizing the differential settlement. Hoang & Matsumoto [37] studied the long-term consolidation in clays. Although ground creep caused the foundation to continue settling, the load supported by the raft and piles remained steady.

A number of centrifuge tests were performed by Park and Lee [38] to explore several interaction effects of piled-rafts over silica sand. Load-displacement curves demonstrated that the response of a piled-raft first resembled that of piles and with the later settlement, it became more comparable to those of rafts. According to load response, the influence of raft-pile interaction was more pronounced in the upper soil zone. Azizkandi et al. [39] conducted centrifuge tests in the sand to examine the impact of relative density on the interaction between two piles. The findings indicated that the relative density of soil has a significant impact on the interaction coefficients. Consequently, the consideration of the relative density to modify the Randolph and Wroth equation proved to outperform the earlier approaches.

A parametric study using a centrifuge test was also conducted on connected and non-connected piled-rafts by Rasouli et al. [40]. The parameters involved were pile spacing, pile numbers and thickness of the granular layer. Several centrifuge experiments were performed by Sahraeian et al. [14] to analyse an oil tank over piled-raft foundation on dry and saturated sand. It was observed that using piled-rafts to support an oil tank can effectively lessen the tank settlement and rocking motion.

Horikoshi et al. [41] and Nakai et al. [42] performed dynamic centrifuge model tests to examine the dynamic response of pile groups and piled-rafts. Shake-table tests were performed by Matsumoto et al. [43] to examine the response of piled-rafts beneath a superstructure. The effect of moments and lateral loads have also been observed on a piled-raft in the sand by Sawada and Takemura [44] using centrifuge tests. Due to the raft's contact with the supporting soil, the horizontal resistance of piled-raft was found to be greater as compared to group piles. Cyclic lateral loading tests were conducted by Hamada et al. [45] to investigate the behaviour of vertical load during the seismic activity. The findings demonstrated that the majority of the lateral forces were resisted due to the friction of the raft when there was significant earth pressure below it. Horikoshi et al. [41, 46] examined load sharing in laterally loaded piled-rafts over loose sand while considering various pile head fixities.

In the current paper, the performance of piled-rafts in sandy and clayey soil was investigated under vertical loading. Several small-scale tests were performed on a raft, group piles and piled-rafts to observe the load-sharing behaviour under vertical loading. For this purpose, an experimental setup was prepared and several trials were conducted using a model raft with piles of three different lengths, namely, 160mm, 260mm, and 360mm. The number of piles used to perform parametric analysis on sand and clay varied from 1 to 9. Finally, the load improvement ratio (*LIR*) and the load sharing ratio were evaluated with the number of piles.

### 3. Test Materials and Equipment

The expense of large field tests makes it challenging to conduct several trials in a brief amount of time. For this reason, laboratory tests have traditionally been prevalent. Further, it is easier to monitor and achieve desired soil characteristics under controlled laboratory circumstances. With a proper understanding of the model's behaviour, it can be more feasible to apply it in the field reliably and cost-effectively.

The objectives of the current study focus on the load-settlement behaviour of piled-rafts with various layouts. The following sections provide details on test materials, model configurations, and testing techniques that have been used.

Several numbers of test-trials were performed on both sand and clay to attain the objectives of the study. To verify the outcomes, the tests were repeated twice wherever required. The dimensions of the box used for the tests were chosen in a way such that the

boundaries shouldn't have any impact on the test results. Hence, it was decided to use a soil bin with a depth at least twice the longest pile length [21]. Also, the bin width was assumed to be five times the raft width.

### 3.1 Test Soils

Locally available Son River sand and clay from the Ganga basin were used in the current investigation. The Son River is one of the Ganges' largest tributaries, and its sand is widely used in civil engineering purposes across India. The sand particles are yellowish-brown and coarser in size. The used sand and clay were collected from the nearest construction site. Undesirable materials such as roots, plastics or organic wastes were physically removed from the soils and were completely dried. Fig. 2 displays the clay and sand samples that were used.



Fig. 2. Sand and clay

The Index properties of soils used in engineering establish their classification and identification. Table 1 lists some of the key index properties of the soil utilised in the current research. **Hata! Başvuru kaynağı bulunamadı.**3 shows the particle size distribution curves of the used sand. Such a curve represents the distribution of the soil sample into different fractions depending on their sizes. Fig. 4 graphically illustrates the relationship between the density index and the voids ratio for the sand.

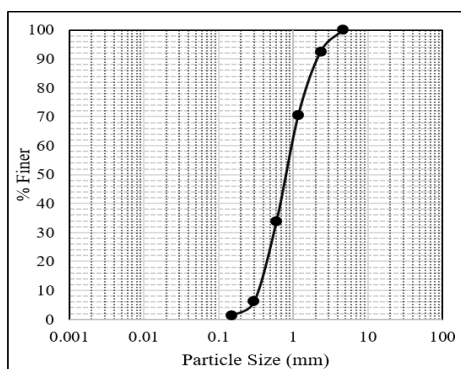


Fig. 3. Particle size distribution curve of sand

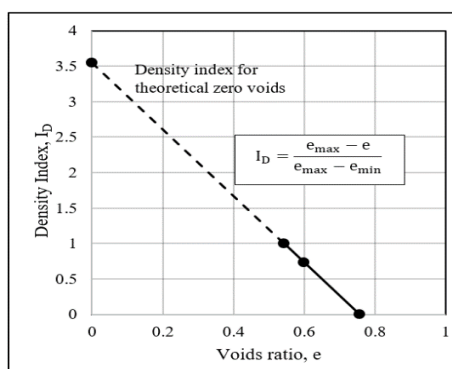


Fig. 4. Density index v/s voids ratio

The coefficient of uniformity ( $C_u$ ) and coefficient of curvature ( $C_c$ ) were obtained as 2.71 and 0.91, respectively. Consequently, the sand sample can be categorized as poorly graded sand (SP) as per IS1498-1970 [47]. Direct and triaxial shear tests are widely adopted methods to determine the shear parameters [48]. Shear parameters of sand were computed using direct shear tests and triaxial tests as per IS 2720 (Part 13)-1986 and IS

2720 (Part 11)-1993 [49], respectively. The friction angle was found approximately to be 39°. Specific gravity was obtained to be 2.67 using the Pycnometer method. The minimum and maximum dry unit weights of the sand sample were determined as per IS 2720 (Part 14)-1983 as 1.52 and 1.73. Finally, the relative density of sand was discovered to be 65%, indicating dense sand.

Table 1. Physical properties of sand and clay

Parameters	Sand	Clay
Specific Gravity ( $G$ )	2.67	2.58
Minimum dry unit weight, $\gamma_{d,min}$ (kN/m <sup>3</sup> )	14.90	-
Maximum dry unit weight, $\gamma_{d,max}$ (kN/m <sup>3</sup> )	16.96	-
$D_{10}$ (mm)	0.35	0.004
$D_{30}$ (mm)	0.55	0.015
$D_{60}$ (mm)	0.95	0.075
Uniformity Coefficient ( $C_u$ )	2.71	18.75
Coefficient of Curvature ( $C_c$ )	0.91	0.75
Liquid Limit ( $w_L$ )	-	40.50%
Plastic Limit ( $w_P$ )	-	22.68%
Soil Type	Poorly graded sand (SP)	Intermediate plasticity clay (CI)

In the case of clay, sieve analysis and hydrometer analysis were performed in accordance with IS 2720 (Part 4)-1985. The corresponding curves are illustrated in Fig. 5 and Fig. 6. The liquid limit and plastic limit tests were performed using procedures mentioned in IS 2720 (Part 4)-1985 [49] and were found to be 40.50% and 22.68%. Finally, according to IS1498-1970 [47], the Casagrande plasticity chart identified the used clay as clay with intermediate plasticity (CI).

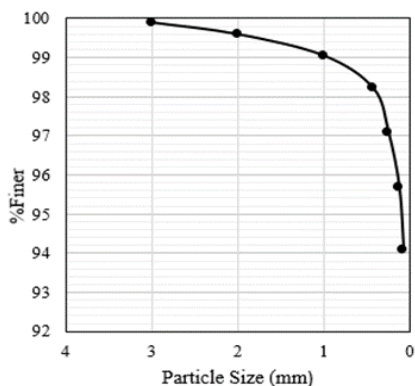


Fig. 5. Sieve analysis

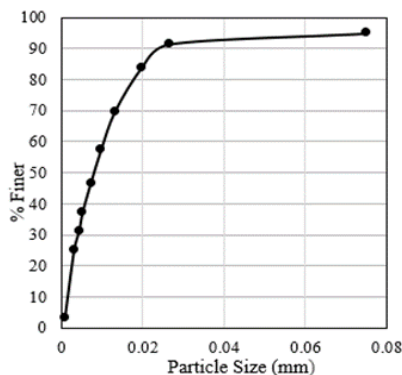


Fig. 6. Hydrometer analysis

### 3.2 Raft and Piles

A square steel plate with sides of 150mm and a thickness of 10mm was used to model the raft. To fasten the model piles in prescribed layouts, 9 similar holes with 50mm spacings were made. Depending on the required configurations, the piles were fastened to these holes and tightened using the nuts through threads. The threaded portion in the piles is confined to the upper section, leading to a minimal impact on the overall behaviour of the

system. The bolts were used to plug holes in the raft. Fig. 7 depicts a model piled-raft with 9 piles attached in a proper arrangement. The current investigation used 1, 4, 5 and 9 piles with lengths of 160mm, 260mm, and 360mm. The cross-sections of all 27 model piles were circular, with a diameter of 12mm. Elastic modulus and Poisson’s ratio of the piles were found to be 200GPa and 0.28, respectively.



Fig. 7. Model piled-raft

Table 2 provides other mechanical properties of the model steel piles. These piles were threaded on the upper side and attached to the raft using nuts. To achieve total fixity, the bolts were provided on both sides of the raft and tightened with a wrench. The different configurations of model piled-rafts used in the study are shown in Fig. 8.

Table 2. Mechanical properties of the steel piles

Parameters	Values
Unit weight (kN/m <sup>3</sup> )	72.43
Minimum yield strength (N/mm <sup>2</sup> )	355.53
Minimum ultimate strength (N/mm <sup>2</sup> )	511.62
Minimum % elongation	23.33

Based on the relative stiffness factor ( $K_{rc}$ ), Poulos and Davis [18] categorised piles into two types: rigid and flexible. Mathematically, the relative stiffness factor  $K_{rc}$  is defined as follows in Eq (1):

$$K_{rc} = \frac{E_p I_p}{E_s L^4} \tag{1}$$

Here,  $E_p$  represents the elastic modulus of the model pile and  $E_s$  denotes the secant modulus of the supporting soil.  $L$  denotes the embedded length of pile and  $I_p$  represents the moment of inertia of the model pile. A pile is considered rigid if  $K_{rc}$  is greater than ( $10^{-2}$ ) and while it is classified as flexible if  $K_{rc}$  is less than ( $10^{-2}$ ). With L/D ratios of 13.33, 21.67, and 30, the piles considered for the present study fall into the category of flexible piles.

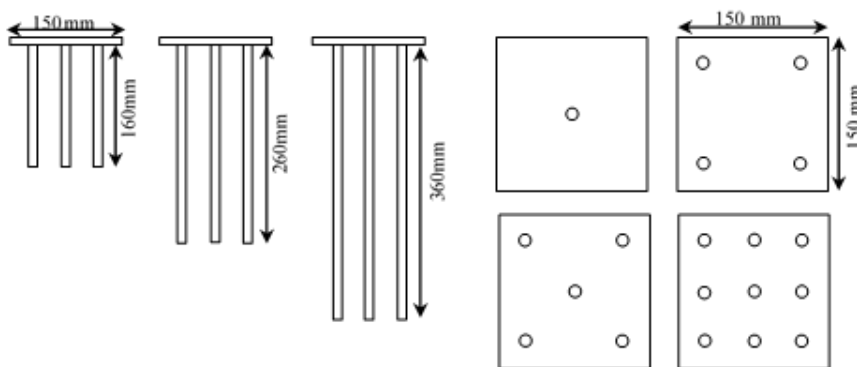


Fig. 8. Different configurations of model piled-raft

### 3.3.1. Scaling Law

The dimensions and proportions of the model need to be adjusted to accurately represent the prototype. To achieve this, scaling is performed using specific scaling laws. Various researchers have suggested scaling laws to imitate the prototype using an equivalent experimental model. Both laboratory and prototype models exhibit direct proportionality in dimensions such as length and width. However, parameters like moment of inertia and flexural rigidity cannot be directly scaled proportionally. Hence, distinct scaling laws are utilized to accommodate these variations. The present study applies the scaling law proposed by Alnuaim et al. [50], which can be represented in Eq (2) and Table 3 below.

$$(EI)_p = n^{3.64}(EI)_m \tag{2}$$

Table 3. Scaling factors used in the present study

Parameters	Scaling factors
Pile length	1/n
Pile diameter	1/n
Raft thickness	1/n
Density	1
Flexural rigidity, $(EI)_m$	$(EI)_p/n^{3.64}$
Stress	1/n
Strain	1

Here,  $EI$  represents the flexural rigidity of the pile, while  $p$  and  $m$  denote the prototype and model, respectively. The scaling factor is denoted by 'n'. It is important to note that the primary objective of this paper is not to replicate a specific prototype. Instead, it aims to investigate and analyse the behaviour of piled rafts within layers of sand and clay. Moreover, the existing literature on experimental analysis has utilized raft dimensions of 150mm × 150mm [29] and 300mm × 300mm [30]. Therefore, it is reasonable to justify the adoption of a square raft with dimensions of 150mm × 150mm in the current paper.

### 3.3 Soil Bin

The entire experimental work was carried out in a soil bin with dimensions of 750mm × 750mm × 800mm. Wooden plies were used to construct the bin and an iron



framework was used to stiffen the bin. The framework was made up of multiple iron rods that were welded together and wrapped around the wooden bin to prevent the connections from opening. The dimensions of the bin were chosen to ensure that the influence zone of the foundation remained within the boundaries.

### 3.4 Loading Mechanism

A manually operated hydraulic jack was used to load the foundation model. The mechanism of the hydraulic jack is designed to pull self-lubricating fluid from its reservoir and release it into a cylinder that further applies the loads. This fluid being incompressible helps in creating pressure between the reservoir and the cylinder through a pump plunger. On each stroke, the plunger assists in drawing the fluid from the reservoir via a suction valve. The fluid is then released into the cylinder after being pushed via a check valve. The suction valve closes after the fluid has passed through the check valve, creating oil pressure inside the cylinder. This oil pressure pushes the cylinder to exert loads.

To measure the amount of load applied, a proving ring with a maximum capacity of 15kN was mounted at the centre of the raft. Two dial gauges of accuracy 0.01mm were attached to the raft to determine its vertical settlement. Dial gauge comprised of a gauge for assessing the displacement that the needle has gone through during the entire process. The gauge was fixed to steel rods to adjust the position and height of the needle. Needles of dial gauges were placed at the extreme corners of the raft and the gauge was clamped using a magnetic base.

## 4. Test Procedures

The following sections cover all of the test procedures for the current experimental investigation. The unpiled-raft was investigated first, then the piled-raft, and finally the group piles. Figs. 9 and 10 illustrate the schematic diagram and the actual experimental arrangement.

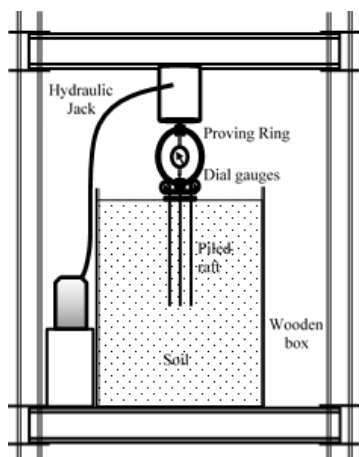


Fig. 9. Schematic diagram of the experimental arrangement



Fig. 10. Actual experimental arrangement

### 4.1 Preparation of Soil Bed

Soil bed preparation is a crucial step in conducting experimental analyses of small-scale model piled rafts. It involves meticulous planning and execution to ensure accurate representation of real-world soil conditions. The soil is carefully selected based on its

gradation and properties, such as particle size, shape, and angularity, to closely resemble the target soil profile. The soil is then evenly spread and compacted layer by layer, ensuring uniform density throughout the bed. The behaviour of small-scale model piled rafts under various loading situations can be thus precisely modelled in an experimental setup by carefully preparing the soil bed.

The soil bed was prepared using the dry pluviation method, where the soil was allowed to fall freely from a predetermined height at a consistent rate. By employing a pluviation height of 750mm, a relative density of 70% was achieved. To create the sand bed, regular intervals were marked within the container, and a measured amount of sand was added up to each marking to maintain the desired density. A 4.9kgs circular plate with a diameter of 150mm and a thickness of 25mm was used to compact the sand. This activity was repeated until the bin's full height of 750mm was reached. The top 50mm of the soil bin was left empty to prevent any overflow during loading. The respective densities were maintained throughout the soil bin with a tolerance of 0.5%. The topmost layer of the soil surface was properly levelled and verified using a spirit level to ensure the proper placement of the raft. The aforementioned process was repeated for each set of tests.

The clay bed preparation followed a procedure similar to that described by Rao et al. [51]. The clay was combined with the appropriate amount of water in a separate mixing tank until it reached a consistency ( $I_c$ ) of 0.30, representative of the clay used in the study. The same procedure was adopted for clay as discussed above for sand in order to compact the clay in layers. Measurements were taken of the water content, density, and undrained shear strengths at different depths within the soil bed to confirm homogeneity.

#### 4.2 Driving of Piled-Raft

The model foundation was positioned at the centre and slowly inserted into the soil using the hydraulic jack. In the case of piled-rafts, the process was continued until the raft's bottom came into contact with the soil and thus completely supported over it. Likewise, the raft was kept 30mm above the surface in the case of group piles

#### 4.3 Taking Observations

The jack was lowered until it came in contact with the proving ring and dial gauges started responding. Further, the readings in all the dial gauges were corrected to zero. Centring of the raft was done using a plumb bob suspended through the centre of the jack to ensure no eccentricity. Concentric vertical loading was hence employed through the jack in increments. The load was continued till the full extension of the jack length. Since the loading was concentric and rotation of the raft was not allowed, hence the dial gauge readings were nearly identical.

The load readings were observed at every 5 divisions of the proving ring having a calibration factor of 1.18. Corresponding settlements in dial gauges were noted down. These dial gauge readings were averaged to acquire the average settlement. Ultimately, the load versus settlement curves were plotted for each model configuration.

### 5. Results and Discussion

The following sub-sections discuss the behaviour of piled-rafts with different configurations. In the current experimental investigations, the variation in pile lengths and pile numbers is analysed and plotted as load-settlement curves.

El-Garhy et al. [52] used 10mm and 25mm as the index parameters for the experimental study. Bowles [53] adopted the ultimate load capacity as the load at 60mm of settlement. However, the load-settlement curves in the present study do not show a considerable change at the initial phases of settlement and the change may be better noticed in the later

stages. Besides, the observations are restricted to 50mm due to the limitation of dial gauges. As a result, a higher settlement of 40mm has been chosen as the index parameter in the current research.

### 5.1 Effect of Number of Piles

The model raft was initially rested on the foundation soil, and its behaviour was assessed. It was important to examine the raft's behaviour to compare it with the behaviour of model piled-rafts. To analyse the effectiveness of attached piles, the number of piles ( $n_p$ ) varied from 1 to 9.

Fig. 11 and Fig. 12 indicate that as the number of piles increases, the load-bearing capacity of the piled-raft also increases. It was observed that an unpiled-raft in the host sand has a load-bearing capacity of 3.6kN at 40mm settlement. This capacity increased to 4.5kN, 8kN, 10kN, and 14kN, when the number of piles affixed to the raft varied, measuring 1, 4, 5, and 9, respectively. Similarly, the load capacity improved from 3.6kN to 5.2kN, 7.9kN, 8.8kN and 10.2kN, in the case of clay. The results are anticipated as the additional piles begin interacting with the underlying soil over a wider surface area. Consequently, the piles can resist a greater amount of the load. It can be confirmed by the literature reported [30].

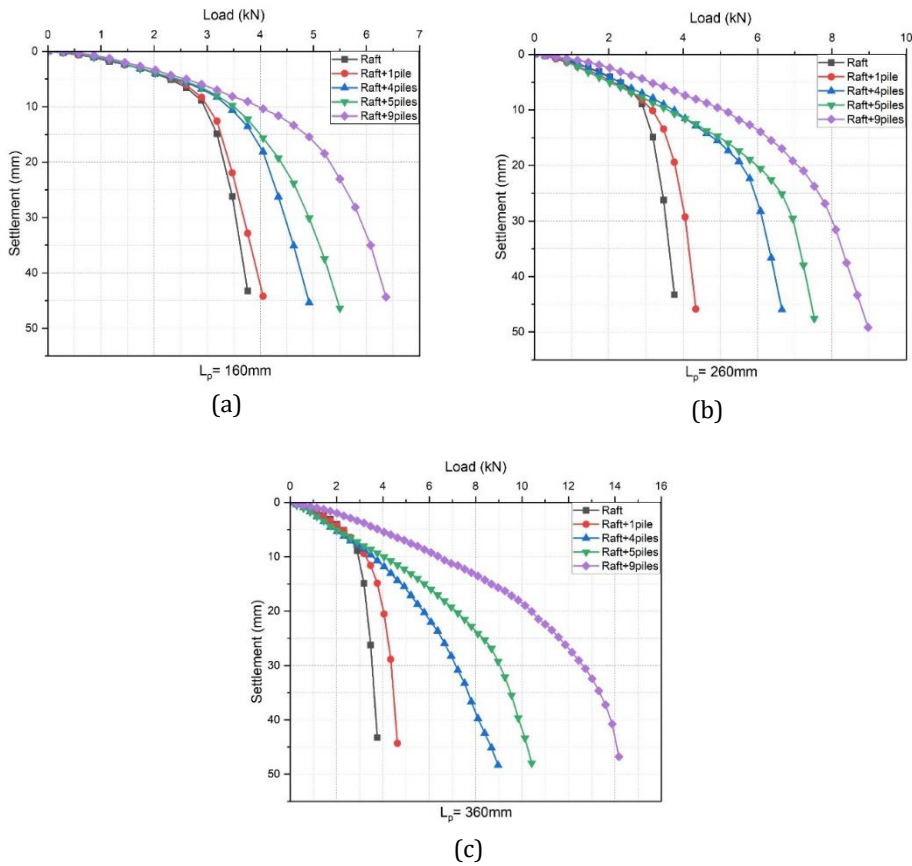


Fig. 11. Effect of number of piles in sand

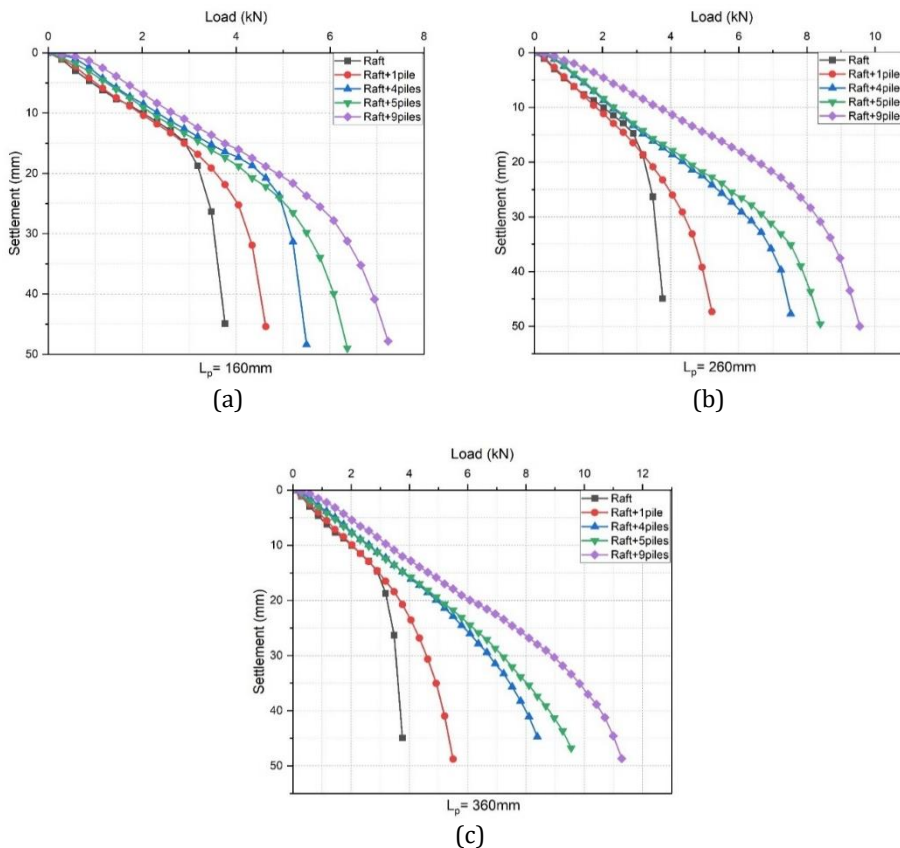


Fig. 12 Effect of number of piles in clay

However, Poulos [54] noted that adding more number of piles to improve the performance of a piled-raft foundation may not always be advantageous. This is due to the fact that once a certain threshold is crossed, very little benefit is observed, and this could result in an uneconomical decision.

### 5.2 Effect of Pile Length

The impact of varying pile lengths has been presented using load-settlement curves in Fig. 13 and Fig. 14. The experimental setup involved the unscrewing of one set of piles while substituting them with piles of different lengths attached to the raft. As the pile length increased, we observed a corresponding improvement in the overall load-carrying behaviour. This relationship is indicative of the enhanced support and structural stability provided by longer piles.

The increased pile length contributed to a more substantial interaction with the underlying soil, effectively distributing and transmitting loads more efficiently. This phenomenon led to a higher load-bearing capacity as longer piles exhibited improved resistance to settlement and deformation. As the length of the piles ( $L_p$ ) affixed to the raft varied, measuring 160mm, 260mm, and 360mm, the load capacity in the case of sand further improved to 6.2kN, 8.5kN, and 13.8kN, respectively at 40mm settlement. Although this load capacity is for a piled-raft with 9 piles, similar increases can be noticed for different numbers of piles as well. It can also be observed that piled-rafts over sand and clay with

any number of piles exhibit a similar trend, and the load capacity in the clay case also enhanced by almost 92%, 150%, and 192%, respectively.

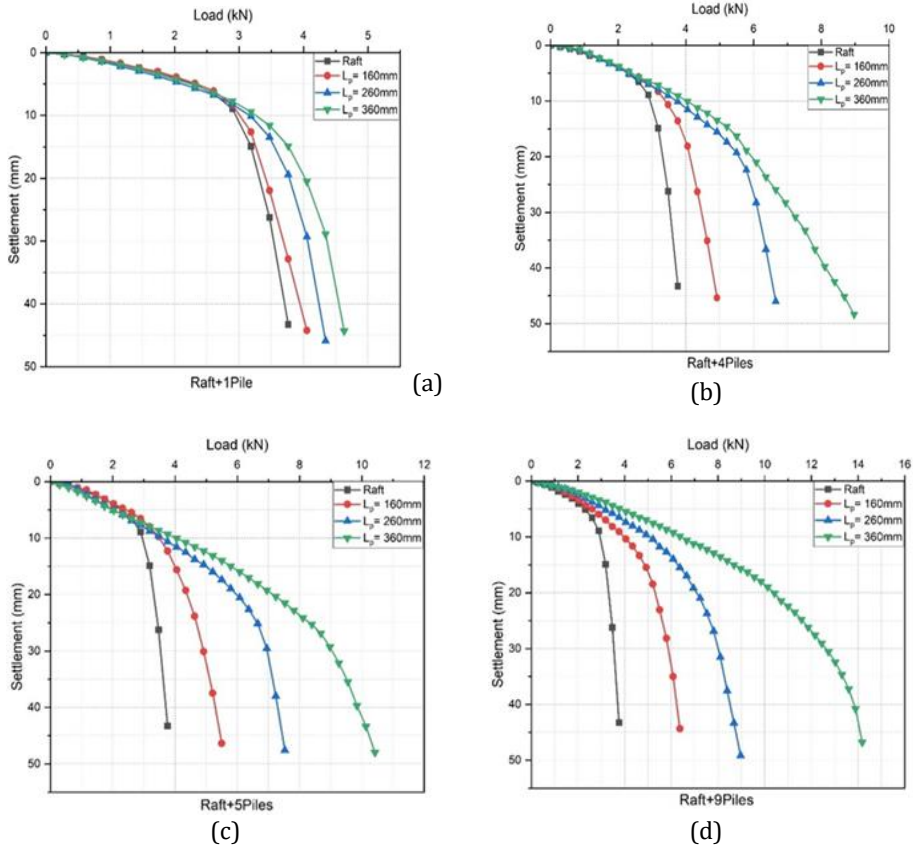
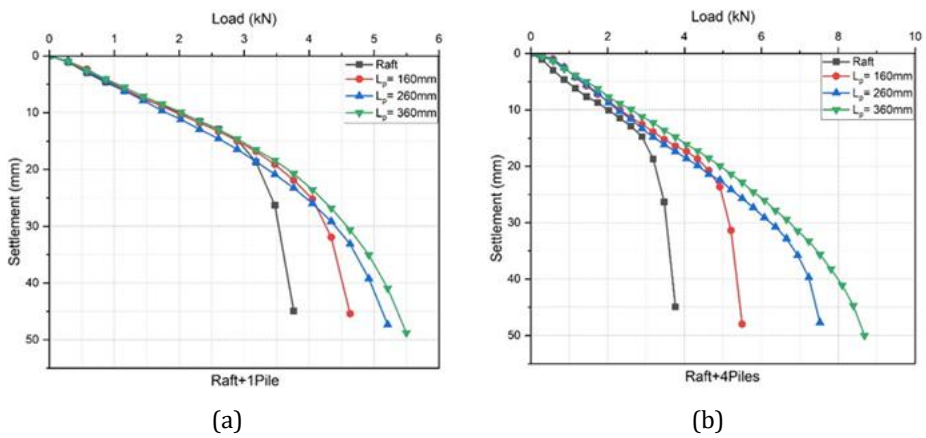


Fig. 13. Effect of pile length in sand



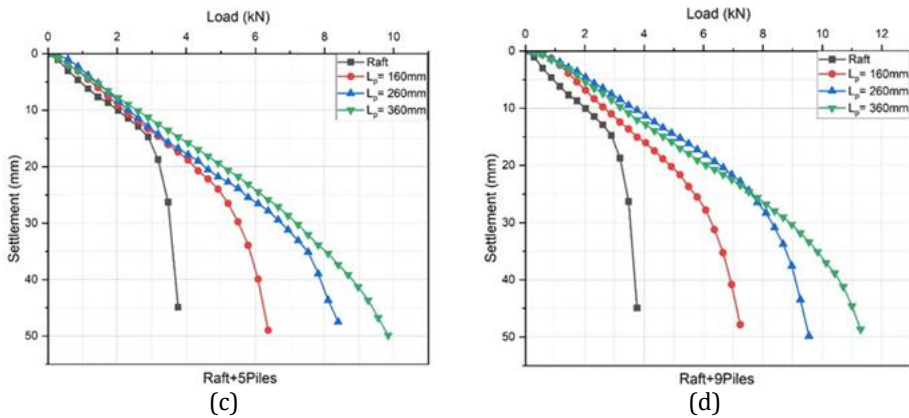


Fig. 14. Effect of pile length in clay

It is evident that when pile lengths increase, surface area increases as well. It suggests an improvement in shear strength and eventually an increase in the load capacity. This supports the findings that have been documented in the literature [34] reporting that piled-rafts with longer piles sustain greater loads.

### 5.3. Effect of Pile Numbers in Pile Groups

The behaviour of pile groups was first studied to compute the load sharing in piled-rafts. Fig. 15 illustrates the comparison of model pile foundations with different numbers of piles. The pile length of 360mm was only considered. The pile foundation model was inserted into the soil such that the raft serving as the pile cap was not in contact with the soil surface and raised 30mm above it.

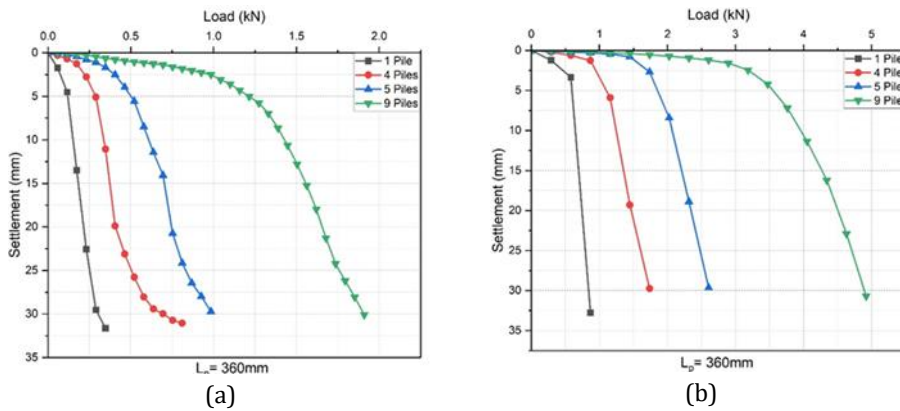


Fig. 15. Effect of pile numbers in pile group in (a) sand and (b) clay

Using 25mm as the reference settlement level in the pile group over sand and clay, the single pile carried a load of 0.25kN and 0.75kN, respectively. It was found that the pile group comprising of 9 piles carried more than 7 and 6 times higher load than a single pile. Similar to the piled-raft case, it was also found that the load-bearing capacity of the pile group gets improved with an increase in the number of piles. Moreover, the deviation in the curve after 30mm settlement indicates that the raft has made contact with the soil surface, and has started taking loads.

### 5.4. Comparison Between Raft, Piles and Piled-Raft

To study the combined behaviour of the raft and piles in a piled-raft, load-settlement curves depicting raft and group piles are individually plotted and then compared with the piled-raft. In the case of group piles, it was ensured that the piles are freestanding and that the bottom surface of the raft does not touch the supporting soil. When the raft was unpiled, it was resting directly over the supporting soil, without any piles attached to it. It was discovered from Fig. 16 and Fig. 17 that the combined load-bearing capacity of the raft and group piles does not equal the piled-raft's capacity. It can also be supported by the observation in literature [34] that the load carried by piled-raft exceeds or is equal to the combined load carried by the raft and the pile. This indeed results from the interactions between the foundation components and the supporting soil. Mathematically, the load-bearing capacity of piled-raft system can be given by Eq (3).

$$Q_{PR} = Q_R + Q_P = \alpha_{pr}Q_{UR} + \alpha_{rp}Q_{PG} \tag{3}$$

Here,  $Q_R$  and  $Q_P$  represents the load that the raft and the piles are carrying.  $\alpha_{pr}$  and  $\alpha_{rp}$  are the interaction factors that characterize interactions between pile and raft and vice-versa, respectively.

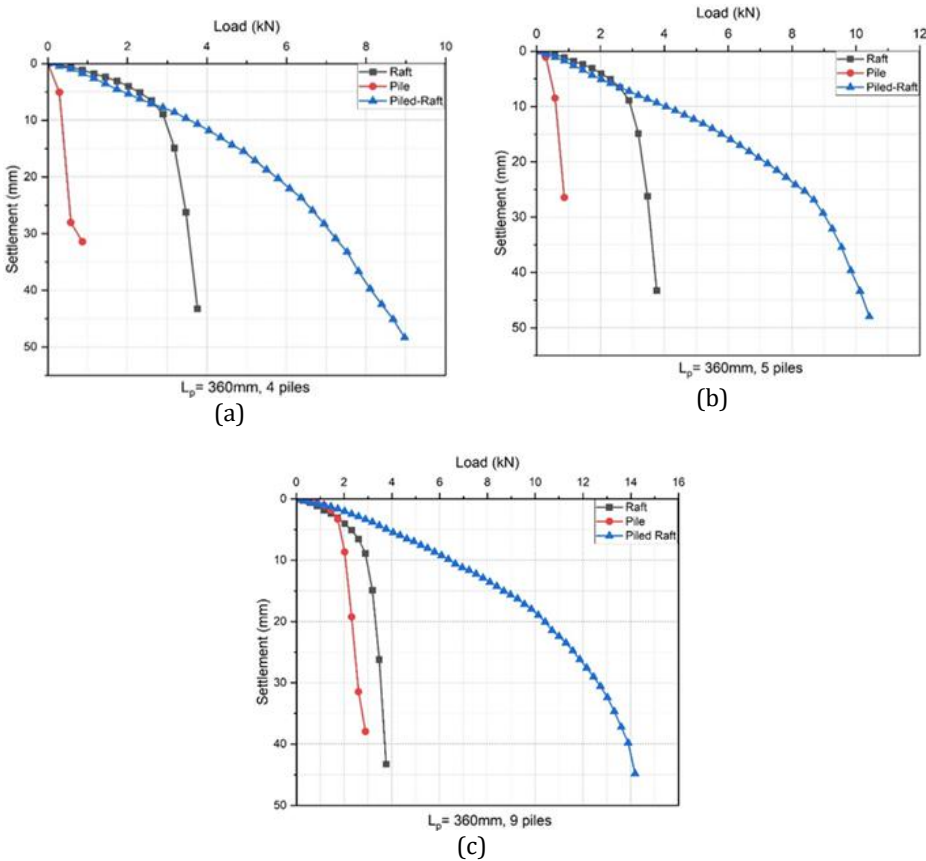


Fig. 16 Comparison between raft, pile group and piled-raft in sand

The subscripts  $UR$ ,  $PG$ , and  $PR$  stand for unpiled-raft, pile group, and piled-raft, respectively, whereas  $Q$  represents the load capacity. The current study, however, is

limited to the load sharing in piled-rafts over sand and clay and does not include the evaluation of these interaction factors. The future objectives of the study could include assessing such interaction factors.

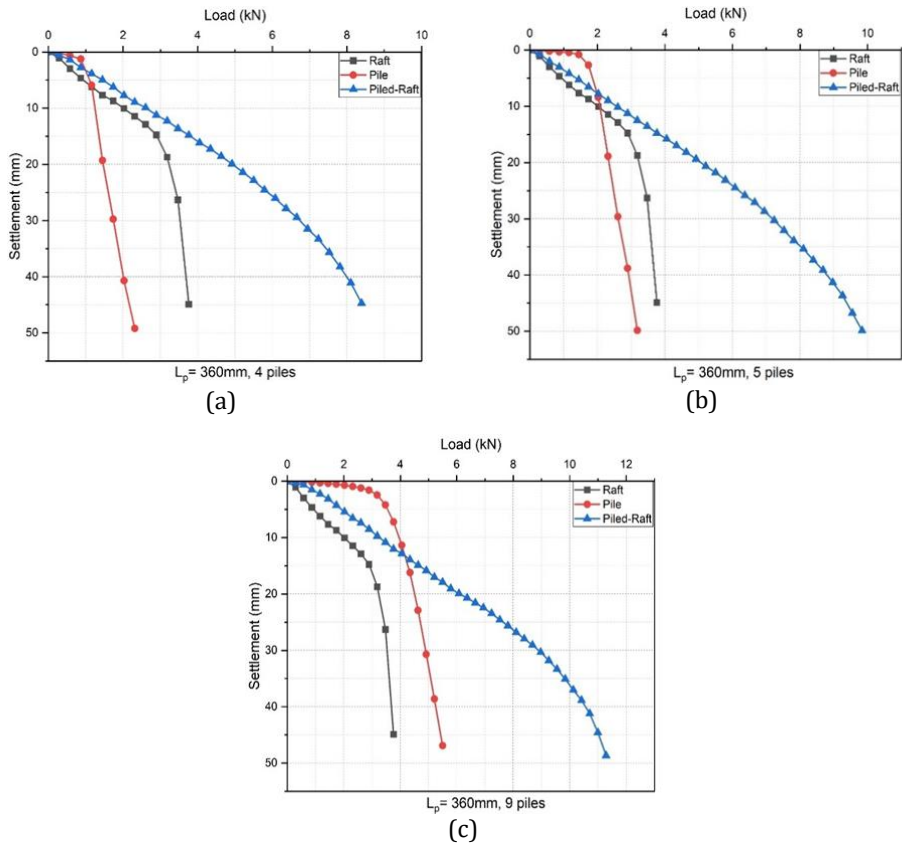


Fig. 17. Comparison between raft, pile group and piled-raft in clay

### 5.5. Load Improvement Ratio

An increase in the load-bearing capacity of the foundation due to the addition of piles can be defined by a dimensionless parameter, known as load improvement ratio (*LIR*). It is expressed as the ratio of the load carried by piled-raft ( $Q_{PR}$ ) to that by the unpiled-raft ( $Q_{UR}$ ) at constant settlement.

$$LIR = \frac{Q_{PR}}{Q_{UR}} \tag{4}$$

Fig. 18 shows the variation of *LIR* with the settlement in the case of sandy and clayey soil. It is observed that with an increase in the number of piles, *LIR* increases. Also, the *LIR* value is high at the early stages and decreases with an increase in settlement value. In the case of sand, the piled-rafts with higher pile numbers show a sudden decrease initially and finally after a certain value, such decrease becomes gradual. This implies the mobilization of piles after initial loading, leading to a reduction in *LIR*. Similar outcomes can be observed in earlier pieces of literature [34, 55]. Moreover, in the case of clay, the *LIR* values converge to roughly the same value regardless of the number of piles and do not significantly vary in later phases.



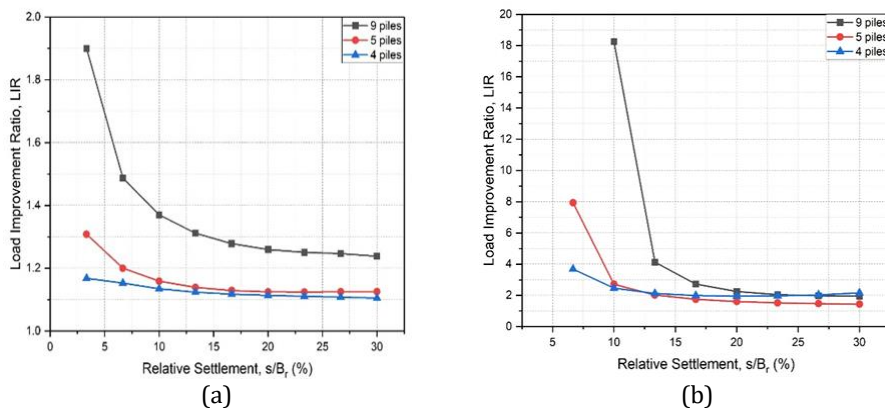


Fig. 18. Variation of load improvement ratio in (a) sand and (b) clay

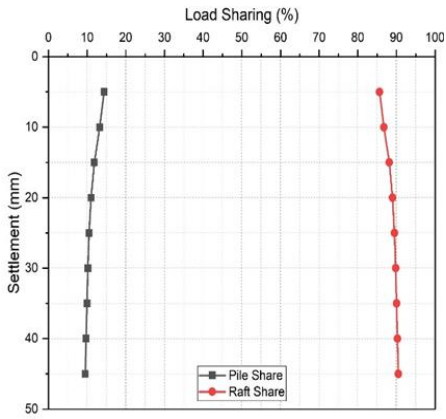
### 5.6. Load Sharing Ratio ( $\alpha_p$ )

It is now widely accepted that in pile-raft foundations, the anticipated load from the superstructure is shared among the piles and the raft. Such a complex load-sharing mechanism is governed mostly by load sharing ratio. Load sharing ratio represents the load-sharing behaviour in piled-rafts and is usually defined as the percentage of the total load imposed on piled-raft ( $Q_{pr}$ ) that is carried by piles ( $Q_p$ ). It can be defined by the following equation:

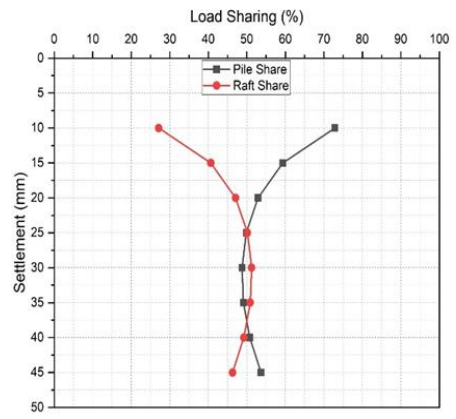
$$\alpha_p = \frac{Q_p}{Q_{pr}} = 1 - \frac{Q_r}{Q_{pr}} \tag{5}$$

where  $Q_r$  and  $Q_p$  denotes the load resisted by raft and piles, respectively. The variation of load sharing ratio for the present case of sand and clay with the settlement is depicted in Fig. 19 and Fig. 20, respectively. Individual share of load carried by piles and the raft is presented for different configurations. The load share of a raft on sand is initially high and rises until it reaches a fixed limit. Even when there are higher number of piles, the piles share of load is comparatively better but still less than the rafts share. Thus, it can be inferred that neglecting the load shared by rafts in the analysis process will not be a wise decision.

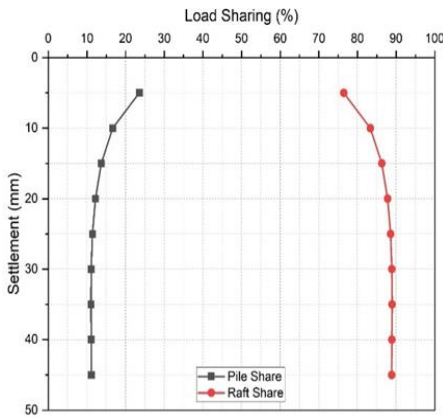
It is evident that in the case of clay, initially the load share of piles is high and gradually the load is transferred to the raft at higher settlements. At initial settlement, the bottom of the raft had inadequate contact with the supporting clayey soil and hence lesser raft share is observed. On the contrary, since the piles are in direct contact with the soil, it leads to confinement of soil and results in a higher proportion of pile share during initial settlement. The density of the soil beneath the raft increases as the piled-raft model settles more. As a consequence, the raft and soil make better contact with each other, increasing the raft's share of the load. A higher percentage of load sharing ratio can also be observed initially in the case of the piled-raft with a greater number of piles due to the greater resistance offered by them.



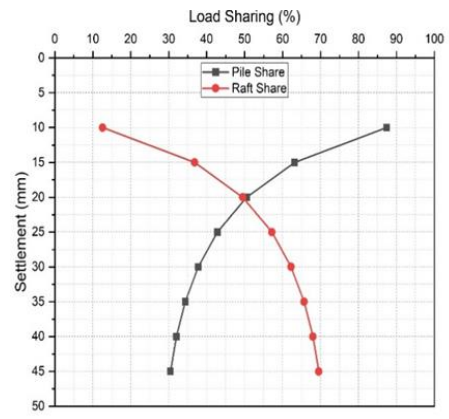
(a)  $n_p = 4$



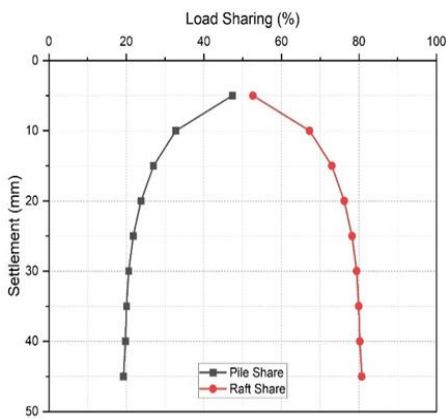
(a)  $n_p = 4$



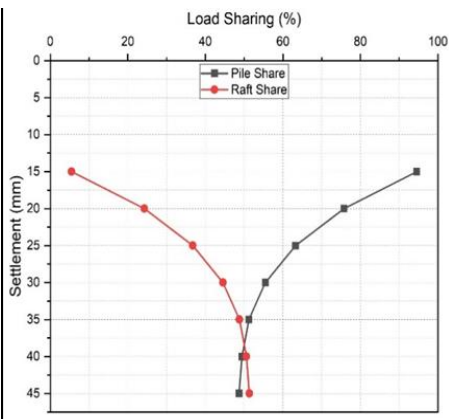
(b)  $n_p = 5$



(b)  $n_p = 5$



(c)  $n_p = 9$



(c)  $n_p = 9$

Fig. 19. Variation of load sharing in sand

Fig. 20. Variation of load sharing in clay

## 6. Validation with Numerical Results

In response to the formidable challenges arising from the cost and time limitations inherent in laboratory or in-situ testing, the scientific community has embraced numerical modelling techniques as a practical alternative. Various commercial codes, such as PLAXIS, FLAC, ABAQUS, and others, have been developed to assist the creation of numerical models [56]. These codes play a crucial role in accurately simulating complex scenarios, with a specific focus on piled raft foundations supported over soil.

The present study uses PLAXIS 3D to validate the experimental study. The dimensions of both the soil continuum and the piled-raft model were matched with those of the experimental model. The test sand was simulated using the elasto-plastic Mohr-Coulomb model obtained from the PLAXIS library. Two models, an unpiled raft and a piled-raft with four piles, were created to validate the experimental findings. The square raft was represented as a plate element, while the pile was modelled as an embedded beam element. The properties of the soil and piled-raft were consistent with those observed in laboratory tests. A medium mesh was generated, comprising 7686 elements and 12450 nodes for the raft and 8019 elements and 13009 nodes for the piled-raft model supported on soil. To mitigate boundary effects, the width of the soil model was set to five times the raft size, and the depth was more than twice the pile length. Fixed boundary conditions were applied to the bottom, while lateral movement was restricted on the sides. Incremental loading was applied to the foundation system through the imposition of vertical pressure.

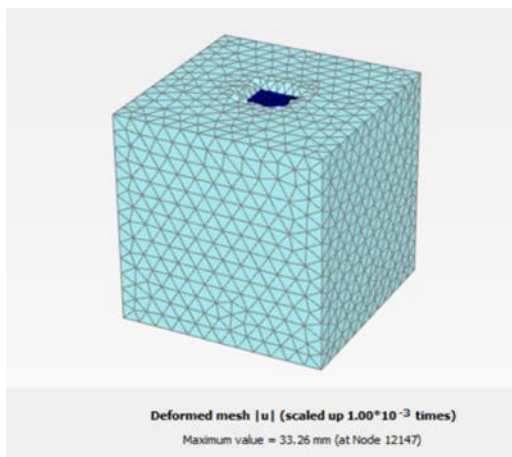


Fig. 21. Numerical model of piled-raft in PLAXIS 3D

In the numerical simulation, the soil-pile interface was modelled with fictitious thickness elements, displaying elasto-plastic behaviour under Coulomb's failure criteria. A strength reduction mechanism, determined by the factor ( $R_{inter}$ ), was applied to the interface elements [57]:

$$\tan\phi_i = R_{inter} \times \tan\phi_{soil} \tag{6}$$

This comprehensive approach ensures that the numerical models closely mimic real-world conditions, providing a robust foundation for validating the experimental results. Figure 21 illustrates the deformed mesh of the current numerical model utilized for validation. The results obtained from the numerical simulation were systematically compared with the experimental data derived from laboratory tests, as depicted in Figure 22. Notably, the

plot demonstrates a good level of agreement between the numerical and experimental results.

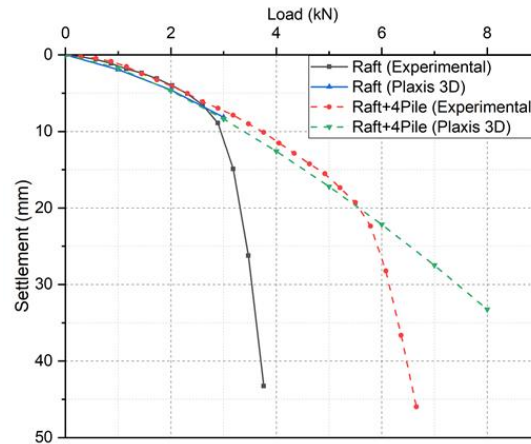


Fig. 22. Validation of the experimental model

## 7. Limitations of the Experimental Study

The limitations of the present experimental study encompass several factors:

- **Dimensional Scaling:** Scaling down model pile and raft dimensions from real-world counterparts can introduce inaccuracies due to the behaviour of physical phenomena at smaller scales, potentially affecting findings' applicability to full-scale scenarios. The study adheres to scaling laws, necessitating the use of scaled-down models. While valuable, these models may not fully replicate real-world behaviour at full scale, possibly leading to scale-dependent discrepancies.
- **In-situ Stress Representation:** Replicating in-situ stress conditions accurately in the testing tank is challenging. Differences between the laboratory setup and actual field conditions can impact the realism and relevance of experimental data. Soil density variations across test scenarios may introduce uncertainties, affecting result comparability.
- **Material Differences:** The use of steel piles in experiments may not perfectly mimic the behaviour of commonly used reinforced concrete (RC) piles. Material property differences can impact the accuracy of findings related to RC pile foundations.
- **Deviation from Natural Soil Conditions:** Experiments conducted in a controlled laboratory setting may not fully capture the complexities of real-world scenarios, and the use of artificial soil substitutes could introduce deviations from natural soil conditions, potentially impacting the study's ability to replicate the intricate properties of real soils.
- **Exclusion of Pore Pressure Effects:** Pore pressure effects, which significantly influence soil behaviour, are omitted from the experiments. This simplification may limit the study's ability to account for the full range of factors influencing piled-raft behaviour in practical applications.

Acknowledging these limitations is essential for interpreting the study's results accurately and for considering the applicability of its findings to real-world engineering scenarios.

## **8. Future Scope**

The findings underscore the need for future research in several key areas. These include:

- **Effect of soil variability:** The behaviour of piled rafts exhibits notable variations contingent upon the specific type of soil, its inherent properties, and the underlying stratigraphy. Even the present study underscores significant distinctions in the behaviour of piled rafts above sandy and clayey soils. Consequently, there arises a compelling necessity to investigate and comprehend the behaviour of piled rafts in soils characterized by different properties.
- **Emphasis on Total Settlement vs. Differential Settlement Models:** Current studies on piled rafts tend to concentrate on overall or total settlement, often overlooking differential settlement, which refers to differential movements between different parts of the foundation. By focusing more on differential settlement models, researchers can gain insights into how non-uniform settling might affect the performance of the foundation and surrounding structures, especially in uneven or complex soil conditions.
- **Dynamic loading:** The current study focuses solely on piled raft foundations under static loads. However, it's essential to recognize that numerous structures experience dynamic and cyclic loading conditions. Therefore, future research endeavours should delve into the analysis of piled-raft foundations subjected to dynamic loads and assess their response to such forces.
- **Complexity of Numerical Models vs. Simplified Analytical Models:** While advanced 3D numerical models have been developed to capture the intricate behaviour of piled rafts, there is a lack of simplified analytical models and standardized guidelines. This absence hinders the adoption of new design approaches and techniques. Developing simplified yet accurate analytical models and codified guidelines can bridge the gap between complex numerical simulations and traditional design methods, making advanced analyses more accessible and applicable in practical engineering design.

Furthermore, there is a need for more field monitoring and testing to validate the performance of piled raft foundation in real-world applications. With continued research in these areas, piled raft foundation systems can become even more reliable and efficient, providing a sustainable and economical solution for various construction projects.

## **9. Conclusions**

The current experimental research provides the analysis of piled-raft foundation systems employing small-scale model tests. Notably, the absence of standardized practices in this domain prompted our investigation. There was a lack of comprehensive studies, particularly in the local region, focusing on load-sharing behaviour in both sand and clay soils. By conducting experiments in both sand as well as clay, our study broadens the scope of knowledge regarding piled-raft foundations' effectiveness as a choice for load-sharing. The inclusion of both soil types enhances the applicability of the findings to diverse geological conditions. Load improvement and load-sharing behaviour were then studied in those cases.

Based on the current experimental investigations, the following conclusions could be inferred:

- The observations of the present lab experiments showed that the piled-rafts substantially reduce the settlement and resist more as compared to the raft foundations. The reason behind this is that the piles alone resisted the majority of the load in piled-rafts.

- Even a few piles added to the raft enhance the load-bearing capacity of the foundation. Also, such enhancement gets stronger with an increase in pile numbers. In both the sand and clay cases, the observed raft capacity against 40mm reference settlement was found to be around 3.6kN. In the case of sand, improvements of up to 4.5kN, 8kN, 10kN, and 14kN, respectively, can be seen for 1, 4, 5, and 9 piles. The corresponding load capacity in clay was found to improve from 3.6kN to 5.2kN, 7.9kN, 8.8kN and 10.2kN.
- Piled-rafts with longer piles typically exhibit greater bearing capacity. The present case showed up to a 300% increase in the load-bearing capacities for the longest length of pile. In comparison to the unpiled-raft carrying a load of 3.6kN, piled-raft having 9 piles and 360mm pile length resisted about 13.8kN and 10.6kN for the sand and clay case, respectively.
- The load improvement ratio has been noticed to rise as the number of piles increases. The load improvement ratio (*LIR*) was found to be larger in the early phases and decreases with an increase in settlement value, suggesting the mobilization of piles after the initial loadings.
- The findings also demonstrated that the raft significantly contributed to the load sharing in piled-raft foundations; as a result, its significance in the analysis and design process cannot be unappreciated.
- In the majority of cases, piled-rafts over clay exhibited patterns resembling those over sand. However, it was found that the raft contributed a larger portion of the load in the sand than in clay. Raft's share of the load in sand reached about 90% when piles were lesser, and decreased as the pile numbers increased. In the clay case, the influence of the piles on load sharing was higher, and the raft's share improved with the settlement.
- The experimental findings also revealed that the load-bearing capacity of the combined piled-raft system is greater than the simple addition of the load capacities of the raft and the piles, hence proving its complex behaviour of load-sharing. Such complexity arises due to the interactions between soil and the foundation components. Moreover, these interactions have a considerable impact on the behaviour of piled-rafts.
- To restrict the maximum settlement, an optimization of the piled-raft geometries should be established to prevent an irrational and uneconomical design.
- Since the current study is only capable of testing the piled-raft behaviour at 1g, centrifuge tests could provide a more comprehensive analysis.
- The soil-dependent nature of load-sharing in piled-raft foundations necessitates further exploration within distinct soil types until region-specific guidelines are established for these foundation systems.
- Furthermore, a concise literature survey on several experimental studies on piled-raft foundations has also been provided.

## References

- [1] Burland JB, Broms BB, de Mello VFB. Behaviour of foundations and structures. Proc Int Conf Soil Mech Found Eng Tokyo, Japan, 1977; 2:495–536.
- [2] Randolph M. Design methods for pile groups and piled rafts. In: Proc. XIII ICSMFE: 5, New Delhi, India, 1994; pp 61–82.
- [3] de Sanctis L, Mandolini A, Russo G, Viggiani C. Some Remarks on the Optimum Design of Piled Rafts. Deep Found, 2002; 405–425. [https://doi.org/10.1061/40601\(256\)30](https://doi.org/10.1061/40601(256)30)
- [4] Viggiani C. Analysis and design of piled foundations. Riv. Ital. Geot., 2001; 47–75.
- [5] Poulos HG. Piled raft foundations: Design and applications. Geotechnique, 2001; 51:95–113. <https://doi.org/10.1680/geot.51.2.95.40292>

- [6] Poulos H. Methods of analysis of piled raft foundations: A report prepared on behalf of technical committee TC18 on piled foundations. *Int Soc Soil Mech Geotech Eng*, 2001; 46.
- [7] Clancy P, Randolph MF. Simple design tools for piled raft foundations. *Geotechnique*, 1996; 46:313–328. <https://doi.org/10.1680/geot.1996.46.2.313>
- [8] de Sanctis L, Mandolini A. Bearing Capacity of Piled Rafts on Soft Clay Soils. *J Geotech Geoenvironmental Eng*, 2006; 132:1600–1610. [https://doi.org/10.1061/\(asce\)1090-0241\(2006\)132:12\(1600\)](https://doi.org/10.1061/(asce)1090-0241(2006)132:12(1600))
- [9] Lee J, Park D, Choi K. Analysis of load sharing behavior for piled rafts using normalized load response model. *Comput Geotech*, 2014; 57:65–74. <https://doi.org/10.1016/j.compgeo.2014.01.003>
- [10] Horikoshi K, Randolph MF. Centrifuge modelling of piled raft foundations on clay. *Geotechnique*, 1996; 46:741–752. <https://doi.org/10.1680/geot.1996.46.4.741>
- [11] Clancy P, Randolph MF. An Approximate Analysis Procedure for Piled Raft Foundations. *Int J Numer Anal Methods Geomech*, 1993; 17:849–869
- [12] Rouhanifar S, Afrazi M, Fakhimi A, Yazdani M. Strength and deformation behaviour of sand-rubber mixture. *International Journal of Geotechnical Engineering*. 2021 Oct 21;15(9):1078-92.
- [13] Fareghian M, Afrazi M, Fakhimi A. Soil reinforcement by waste tire textile fibers: small-scale experimental tests. *Journal of Materials in Civil Engineering*. 2023 Feb 1;35(2):04022402.
- [14] Sahraeian SMS, Takemura J, Seki S. An investigation about seismic behaviour of piled raft foundation for oil storage tanks using centrifuge modelling. *Soil Dyn Earthq Eng*, 2018; 104:210–227. <https://doi.org/10.1016/j.soildyn.2017.10.010>
- [15] Yamashita K, Shigeno Y, Hamada J, Chang DW. Seismic response analysis of piled raft with grid-form deep mixing walls under strong earthquakes with performance-based design concerns. *Soils Found*, 2018; 58:65–84. <https://doi.org/10.1016/j.sandf.2017.12.002>
- [16] Poulos HG. An approximate numerical analysis of pile–raft interaction. *Int J Numer Anal Methods Geomech*, 1994; 18:73–92. <https://doi.org/10.1002/nag.1610180202>
- [17] Poulos HG. Analysis of piled strip foundations. In: *International conference on computer methods and advances in geomechanics*, 1991; 183–191.
- [18] Poulos HG, Davis EH. *Pile foundation analysis and design*, 1980.
- [19] Reul O, Randolph MF. Design Strategies for Piled Rafts Subjected to Nonuniform Vertical Loading. *J Geotech Geoenvironmental Eng*, 2004; 130:1–13.
- [20] Cho J, Lee JH, Jeong S, Lee J. The settlement behavior of piled raft in clay soils. *Ocean Eng*, 2012; 53:153–163. <https://doi.org/10.1016/j.oceaneng.2012.06.003>
- [21] Sinha A, Hanna AM. 3D Numerical Model for Piled Raft Foundation. *Int J Geomech*, 2016; 1–9. [https://doi.org/10.1061/\(ASCE\)GM.1943-5622.0000674](https://doi.org/10.1061/(ASCE)GM.1943-5622.0000674)
- [22] Poulos HG, Small JC, Ta LD, et al. Comparison of some methods for analysis of piled rafts. In: *Proc. XIV ICSMFE: 2*, Rotterdam: Balkema, 1997; 1119–1124.
- [23] Reul O, Randolph MF. Piled rafts in overconsolidated clay: comparison of in situ measurements and numerical analyses. *Géotechnique*, 2003; 53:301–315. <https://doi.org/10.1680/geot.53.3.301.37279>
- [24] Yamashita K, Hamada J, Tanikawa T. Static and seismic performance of a friction piled raft combined with grid-form deep mixing walls in soft ground. *Soils Found*, 2016; 56:559–573. <https://doi.org/10.1016/j.sandf.2016.04.020>
- [25] Architectural Institute of Japan. In: *Recommendations for design of building foundations*, 2001.
- [26] Yamashita K, Yamada T, Hamada J. Investigation of settlement and load sharing on piled rafts by monitoring full-scale structures. *Soils Found*, 2011; 51:513–532. <https://doi.org/10.3208/sandf.51.513>
- [27] Yamashita K. Field measurements on piled raft foundations in Japan, 2012; 79–94.

- [28] Unsever YS, Matsumoto T, Özkan MY. Numerical analyses of load tests on model foundations in dry sand. *Comput Geotech*, 2015; 63:255–266. <https://doi.org/10.1016/j.compgeo.2014.10.005>
- [29] Kumar K, Dahale PP, Hiwase PD. Experimental Studies on Settlement Search of Piled Raft System. *International Journal of Recent Technology and Engineering (IJRTE)*. 2019;8(2):472-5.
- [30] Deb P, Debnath B, Reang RB, Pal SK. Structural analysis of piled raft foundation in soft soil: An experimental simulation and parametric study with numerical method. *Ocean Engineering*. 2022 Oct 1;261:112139.
- [31] Chandiwala A, Vasanwala S. Experimental Study of Lateral Loading on Piled Raft Foundations on Sandy Soil. *International Journal of Engineering*. 2023 Jan 1;36(1):28-34. <https://doi.org/10.5829/IJE.2023.36.01A.04>
- [32] Elwakil AZ, Azzam WR. Experimental and numerical study of piled raft system. *Alexandria Eng J*, 2016; 55:547–560. <https://doi.org/10.1016/j.aej.2015.10.001>
- [33] Kumar V, Kumar A. An experimental study to analyse the behaviour of piled - raft foundation model under the application of vertical load. *Innov Infrastruct Solut*, 2018; 1–17. <https://doi.org/10.1007/s41062-018-0141-8>
- [34] Sosahab JS, Chenari MJ, Chenari RJ, Fard MK. Physical and Numerical Modeling of Piled Raft Foundation in Chamkhaleh Sand. *Int J Civ Eng*, 2018. <https://doi.org/10.1007/s40999-018-0365-1>
- [35] Bajad SP, Sahu RB. An experimental study on the behaviour of vertically loaded piled raft on soft clay. In: *The 12th International Conference of International Association for Computer Methods and Advances in Geomechanics*, 2008; 84–91.
- [36] Mandal S, Sengupta S. Experimental Investigation of Eccentrically Loaded Piled Raft Resting on Soft Cohesive Soil. *Indian Geotech J*, 2017; 47:314–325. <https://doi.org/10.1007/s40098-017-0235-9>
- [37] Hoang LT, Matsumoto T. Long-term behaviour of piled raft foundation models supported by jacked-in piles on saturated clay. *Soils Found*, 2020; 60:198–217. <https://doi.org/10.1016/j.sandf.2020.02.005>
- [38] Park D, Lee J. Comparative Analysis of Various Interaction Effects for Piled Rafts in Sands Using Centrifuge Tests. *J Geotech Geoenvironmental Eng*, 2015; 141:1–10. [https://doi.org/10.1061/\(asce\)gt.1943-5606.0001183](https://doi.org/10.1061/(asce)gt.1943-5606.0001183)
- [39] Azizkandi AS, Baziar MH, Modarresi M. Centrifuge modelling of pile-soil-pile interaction considering relative density and toe condition. *Sci Iran*, 2014; 21:1330–1339.
- [40] Rasouli H, Saeedi Azizkandi A, Baziar MH. Centrifuge modeling of non-connected piled raft system. *Int J Civ Eng*, 2015; 13:114–123. <https://doi.org/10.22068/IJCE.13.2.114>
- [41] Horikoshi K, Matsumoto T, Hashizume Y. Performance of Piled Raft Foundations Under Static Horizontal Loads. *Int J Phys Model Geotech*, 2003; 2:37–50. <https://doi.org/10.1680/ijpmg.2003.030204>
- [42] Nakai S, Kato H, Ishida R, Mano H. Load Bearing Mechanism of Piled Raft Foundation during Earthquake. *Proc Third UJNR Work Soil-Structure Interact* 18, 2004.
- [43] Matsumoto T, Fukumura K, Kitiyodom P. Experimental and analytical study on behaviour of model piled rafts in sand subjected to horizontal and moment loading. *Int J Phys Model Geotech*, 2004; 3:01–19.
- [44] Sawada K, Takemura J. Centrifuge model tests on piled raft foundation in sand subjected to lateral and moment loads. *Soils Found*, 2014; 54:126–140. <https://doi.org/10.1016/j.sandf.2014.02.005>
- [45] Hamada J, Tsuchiya T, Tanikawa T, Yamashita K. Lateral loading tests on piled rafts and simplified method to evaluate sectional forces of piles. *Geotech Eng*, 2015; 46:29–42.
- [46] Horikoshi K, Matsumoto T, Hashizume Y, Watanabe T. Performance of Piled Raft Foundations Subjected to Dynamic Loading. *Int J Phys Model Geotech*, 2003; 2:51–62



- [47] IS: 1498. Classification and identification of soils for general engineering purposes, 1970.
- [48] Afrazi M, Yazdani M. Determination of the effect of soil particle size distribution on the shear behaviour of sand. *Journal of Advanced Engineering and Computation*. 2021 Jun 30;5(2):125-34.
- [49] IS: 2720 (Part 13). Methods of test for soils, Part 13: Direct shear test, 1986.
- [50] Rao SN, Ramakrishna VGST, Rao MB. Influence of rigidity of laterally loaded pile groups in marine clay. *J. Geotech. Geoenvironmental Eng*, 1998; 124, 542–549.
- [51] Alnuaim AM, El Naggar H, El Naggar MH. Evaluation of piled raft performance using a verified 3D nonlinear numerical model. *Geotech. Geol. Eng.*, 2017; 35(4), 1831- 1845. <https://doi.org/10.1007/s10706-017-0212-1>
- [52] El-Garhy B, Galil AA, Youssef AF, Raia MA. Behavior of raft on settlement reducing piles: Experimental model study. *J Rock Mech Geotech Eng*, 2013; 5:389–399. <https://doi.org/10.1016/j.jrmge.2013.07.005>
- [53] Bowles JE. *Foundation Analysis and Design*, 1997.
- [54] Poulos H. *The Piled Raft Foundation for The Burj Dubai - Design & Performance*. IGS-Ferroco Terzaghi Oration, 2008.
- [55] Lee J, Park D, Park D, Park K. Estimation of load-sharing ratios for piled rafts in sands that includes interaction effects. *Comput Geotech*. 2015; 63:306–314. <https://doi.org/10.1016/j.compgeo.2014.10.014>
- [56] Nowroozi V, Hashemolhosseini H, Afrazi M, Kasehchi E. Optimum design for soil nailing to stabilize retaining walls using FLAC3D. *Journal of Advanced Engineering and Computation*. 2021 Jun 30;5(2):108-24.
- [57] Lee S, Moon JS. Effect of interactions between piled raft components and soil on behaviour of piled raft foundation. *KSCE Journal of Civil Engineering*. 2017 Jan;21:243-52.

## Enhancing friction and wear performance in hybrid aluminum composites through grey relational analysis

Dinesh Kumar<sup>\*,a</sup>, Satnam Singh<sup>b</sup>

Department of Mechanical Engineering, National Institute of Technology Kurukshetra, India

### Article Info

### Abstract

#### Article history:

Received 12 Oct 2023  
Accepted 08 Jan 2024

#### Keywords:

Al-6061 alloy;  
Graphene;  
Silicon carbide;  
Hardness;  
Tensile strength;  
Friction;  
Wear;  
GRA

Hybrid aluminum metal matrix composites (AMMCs) include qualities including being lightweight, very effective, and highly resistant to wear, and corrosion. The process used in this study to maximize friction and minimize wear of hybrid AMMCs involves applying grey relational analysis (GRA) to optimize the process features. Stir-casting was used to create hybrid AMMCs of the Al-6061 alloy reinforced with graphene (Gr) and silicon carbide (SiC). The experiment used Taguchi's  $L_{27}$  design, and three process parameters—normal load, sliding distance, and sliding speed—were combined with GRA to produce the maximum coefficient of friction and lowest wear rate. Al-6Gr-6SiC obtained the maximum hardness of 128 VHN and 253 MPa as tensile strength, further coefficient of friction, and wear were analyzed for the same composite., respectively. The ideal mixture of graphene (6 weight percent) and silicon carbide (6 weight percent) as reinforcement in Al-6061 alloy obtained the optimum value of frictional coefficient (0.29766) and wear (0.002588 mm<sup>3</sup>/m), respectively.

© 2024 MIM Research Group. All rights reserved.

## 1. Introduction

Aluminum alloys are extensively used as matrix materials in producing metal matrix composites (MMCs). These composites use the advantageous qualities of aluminum alloys while integrating reinforcing elements to attain improved mechanical, thermal, or other distinct performance characteristics. Due to their higher mechanical qualities compared to monolithic materials, aluminum alloys are deemed to be the most appropriate materials in the aerospace and automotive sectors. Aluminum alloys are popular among researchers for the creation of novel materials with improved properties because of their affordability and ease of supply [1]. A composite is a multi-stage construction that is created by combining reinforcements and a matrix. When metal is employed as the matrix material during the production process, the created composite is referred to as a Metal Matrix Composite (MMC) [2]. Aluminum alloys and two or more reinforcements are combined to create hybrid aluminum metal matrix composites (AMMCs), which have exceptional mechanical and tribological qualities [3]. Due to its high magnesium and silicon content, the aluminum alloy 6XXX series has already been utilized in the transportation and automotive industries. Due to its castability, the Al-6061 alloy is discovered to be the most popular alloy in the 6XXX family. Al-6061 alloy is used to make lightweight automobile components as well [4]. Al-6061 was used as the matrix in the current experiment, with Gr and SiC particles serving as reinforcement. Using Taguchi's  $L_{27}$  experimental design, the friction and wear of manufactured AMMCs were measured under ASTM standards [5]. The ideal set of process parameters at which the friction and wear values reach their optimum

\*Corresponding author: [dinesh.61900120@nitkkr.ac.in](mailto:dinesh.61900120@nitkkr.ac.in)

<sup>a</sup> orcid.org/0000-0003-1885-2431; <sup>b</sup> orcid.org/0000-0002-5648-6113

DOI: <http://dx.doi.org/10.17515/resm2024.05ma1012tn>

Res. Eng. Struct. Mat. Vol. 10 Iss. 3 (2024) 943-956

levels was found using the GRA approach [6]. A hybrid composite was formed by including graphene (Gr) and silicon carbide (SiC) as dual reinforcements in the aluminum matrix. The present literature has yet to extensively investigate the combination of graphene (Gr) and silicon carbide (SiC). Research publications often demonstrate the use of either SiC or graphene as a sole reinforcement or in combination with other reinforcements such as Al<sub>2</sub>O<sub>3</sub>, CNT, TiC, etc. [7]–[11]. The limited availability of literature on the particular combination of silicon carbide and graphene highlights our work's originality and unique character, enhancing the overall comprehension of hybrid composites with the capacity to reveal new synergies between these two reinforcing elements. The amount of reinforcement can be used up to 20% in metal matrix composites to avoid negative effects on the mechanical properties of the composite. Excessive amounts of reinforcement material can lead to poor bonding between the reinforcement and matrix, resulting in reduced ductility and toughness. The decision to restrict the experimentation to 12% for (6% graphene and 6% silicon carbide) despite the observed increase in hardness with higher percentages of these reinforcements may be attributed to several factors. While higher hardness is generally preferred for improved wear performance in certain applications, such as Parts like pistons, cylinder liners, and connecting rods will benefit from improved hardness and wear resistance. While higher percentages of reinforcement materials beyond 12% lead to agglomeration of the reinforcement particles.

## 2. Materials and Methods

### 2.1. Materials Used

In this investigation, Al-6061 alloy is used as the matrix or base alloy and its composition is shown in Table 1. Figure 1 shows the EDAX analysis of Al-6061 alloy that gives the elemental composition of the material. The graphene and silicon carbides are used as reinforcements and their properties are mentioned in Table 2.

Table 1. Matrix material composition

Elements	Aluminum	Magnesium	Silicon	Copper	Iron
Wt. %	97.2	1.00	0.6	0.25	0.40
Elements	Chromium	Zinc	Titanium	Manganese	
Wt. %	0.195	0.125	0.125	0.080	

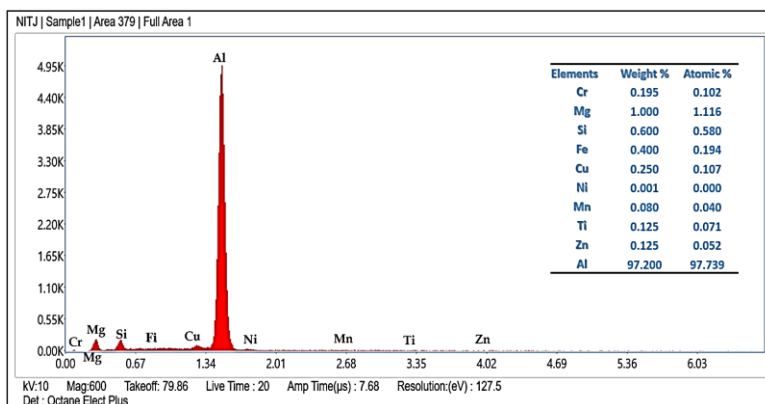


Fig. 1. EDAX analysis of Al-6061 alloy

Table 2. Reinforcement particle specifications

Reinforcement	Melting Point (°C)	Particle size	Density (g/cm <sup>3</sup> )
Gr- Powder	3650	5 nm	2.30
SiC- Powder	2700	220 μm	3.20

## 2.2. Methodology

### 2.2.1 Fabrication of Hybrid Composite

The manufacture of MMCs may be done using several different methods, most of which can be divided into liquid-state and solid-state methods [6]. In this study, Gr and SiC particles were used as reinforcements while Al-6061 was used as the matrix to create the hybrid AMMCs. With the use of a high-frequency induction heater, solid metal is first heated to 750°C in a graphite crucible until it melts or becomes semi-solid [12]. The reinforcements (graphene and silicon carbide) were then applied to the molten metal matrix after preheating. Figure 2 (a) shows the experimental setup of the stir-casting process and Figure 2 (b) shows the fabricated samples.



Fig. 2. Experimental setup and fabricated samples

To achieve the homogeneous mixing of reinforcements into the molten matrix material, a graphite stirrer was employed. Mg and Zr are utilized in quantities of 2wt% for improved reinforcement wettability in the matrix [13]. Tetrachloroethane degasser is used to take carbon dioxide, nitrogen, and hydrogen out of the aluminum melt. To avoid melt oxidation, the entire procedure is carried out under an environment of inert gas, namely Argon. The melt is poured into the die, let to harden, and then removed to be processed further. The nomenclature of fabricated samples is mentioned in Table 3.

Table 3. Nomenclature of fabricated hybrid composites

S. No	Material	Composition
1	Al-6Gr-4SiC	90% Al + 6% Gr + 4% SiC
2	Al-4Gr-6SiC	90% Al + 4% Gr + 6% SiC
3	Al-6Gr-6SiC	88% Al + 6% Gr + 6 % SiC

### 2.2.2 Dry Sliding Wear

According to the ASTM G99 standard, the samples' wear behavior was examined using pin-on-disc wear test equipment [14]. The counter plate was constructed using EN31 steel,

which has a hardness of 62 HRC. The revolving steel counter circle is held against the wear test pins, which are made of composite materials and have dimensions of 10 mm in width and 30 mm in length. Between testing, the counter disc and the samples are meticulously cleaned to remove any worn material that may have adhered to the disc or sample. To make sure the level surface connected with the steel circle before testing, the surfaces of the pin tests were scrubbed against emery paper. The weight of the example is calculated using a computerized weighing offset with a high accuracy of 0.0001g after washing with the  $C_3H_6O$  solution. The weight loss is used to calculate the wear rate, which is expressed as wear volume loss per unit sliding distance [15].

### 2.2.3 Taguchi-Grey Relational Analysis

Using Taguchi's L27 experimental design, the friction and wear of manufactured AMMCs were measured following ASTM G-99 [16]. The ideal set of process parameters at which the friction and wear values become optimal was determined using the GRA approach with three process parameters; Load (N), distance (m), and speed (m/s). The levels of the process parameters are shown in Table 4.

Table 4. Selection of process parameters

S. No	Material	Load	Distance	Speed
1	Al-6Gr-4SiC	20	1000	1.5
2	Al-4Gr-6SiC	40	2000	3
3	Al-6Gr-6SiC	60	3000	4.5

## 3. Results and Discussion

### 3.1. Morphology of Fabricated Samples

The morphology of the manufactured samples, namely the aluminum stir-cast hybrid composites reinforced with silicon carbide and graphite particles, has a significant impact on their structural features and subsequent performance in different applications. SEM study of the base alloy (Al-6061) is shown in Figure 3(a), revealing the microstructure of the unaltered aluminum matrix. Figure 3(b) specifically examines the scanning electron microscopy (SEM) examination of Al-6Gr-4SiC samples, which shows a clear concentration of the reinforcing particles. The clustering seen may be ascribed to causes such as uneven distribution during the stirring process or inadequate dispersion of the graphite (Gr) and silicon carbide (SiC) particles inside the aluminum matrix. The observed clustering has the potential to affect the mechanical and tribological characteristics of the composite, hence impacting parameters like hardness and wear resistance.

The SEM examination of Al-4Gr-6SiC samples in Figure 3(c) reveals a surface that is much smoother in comparison to Figure 3(b). The enhanced smoothness of the Al-4Gr-6SiC samples may be ascribed to the enhanced dispersion and uniform distribution of the graphite and silicon carbide particles inside the aluminum matrix. The enhanced dispersion is probably due to the optimized processing settings used during the stir-casting process, resulting in a more homogeneous integration of the reinforcement phases. The SEM examination of Al-6Gr-6SiC samples, as shown in Figure 3(d), reveals a surface where reinforcement particles are evenly distributed throughout the aluminum matrix. The uniform dispersion seen in this picture is likely due to many variables that enhance the efficiency of processing and mixing during the stir-casting process.

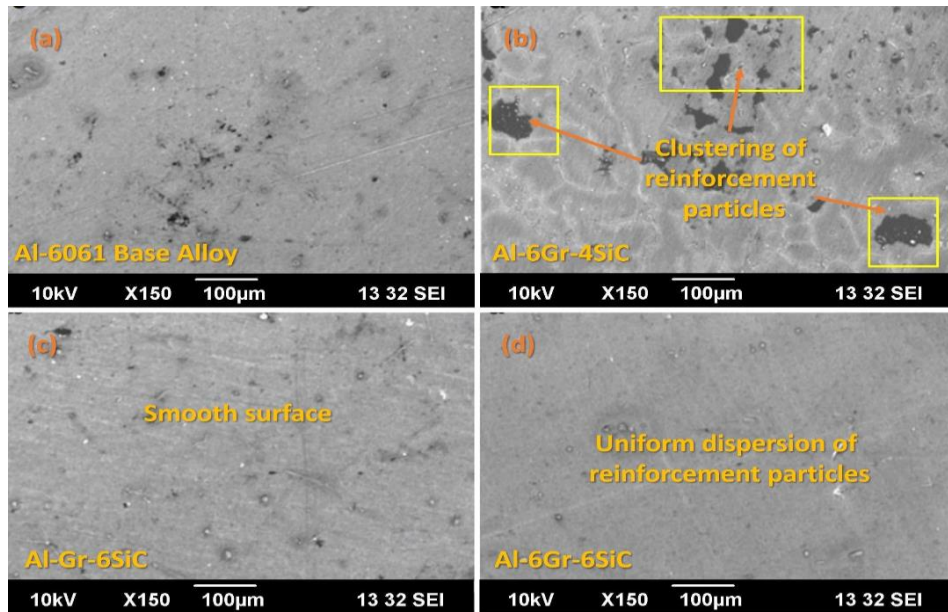


Fig. 3. Morphology of fabricated samples

### 3.2. Hardness and Tensile Strength

Hardness is a material property that measures its resistance to deformation, particularly when subjected to an indentation or applied load. The Vickers hardness test is a popular method that uses a diamond-shaped indenter. The hardness value is determined by measuring the diagonals of the resulting indentation. The Vickers Hardness Number (VHN) is calculated based on the applied force (200 gf) and the surface area of the indentation. Based on the hardness measurements the hardness value of the sample (Al-6Gr-4SiC) is measured to be 102 VHN. The hardness value of the sample (Al-4Gr-6SiC) is recorded as 116 VHN. The sample composed of aluminum, graphite, and silicon carbide (Al-6Gr-6SiC) has the maximum recorded hardness, with a value of 128 Vickers Hardness Number (VHN). As Table 5 indicates it is evident that the sample (Al-6Gr-6SiC) exhibits the highest level of hardness among the three samples. This finding indicates that, within the scope of this particular comparison, the composite denoted as "Al-6Gr-6SiC," which has a greater concentration of silicon carbide (SiC), exhibits the highest level of hardness among the materials subjected to testing. The heightened level of hardness may prove to be beneficial in scenarios where the ability to withstand wear and maintain hardness is of utmost importance, particularly in components that are exposed to abrasive environments.

Table 5. Mechanical properties of hybrid composites

S. No	Samples	Hardness (VHN)				Tensile Strength (MPa)			
		VHN1	VHN2	VHN3	Mean	TS1	TS2	TS3	Mean
1	Al-6Gr-4SiC	103	101	102	102	212	216	214	214
2	Al-4Gr-6SiC	114	116	115	116	235	239	237	237
3	Al-6Gr-6SiC	126	130	128	128	251	253	255	253

In a similar vein, it can be seen that the sample (Al-6Gr-6SiC) exhibits the highest value of tensile strength when compared to the other two samples as shown in Figure 4 (a). This

finding indicates that, within the context of this particular comparison, the composite denoted as "Al-6Gr-6SiC," which has a greater concentration of silicon carbide (SiC), demonstrates the greatest level of tensile strength. The heightened tensile strength is beneficial in scenarios where materials must endure substantial stretching or pulling pressures without experiencing considerable deformation or fracture. This observation suggests that the composite material being referred to exhibits the highest level of strength when compared to the other materials that were evaluated within the given context. Figure 4 (a and b) shows the tensile test samples before and after testings.

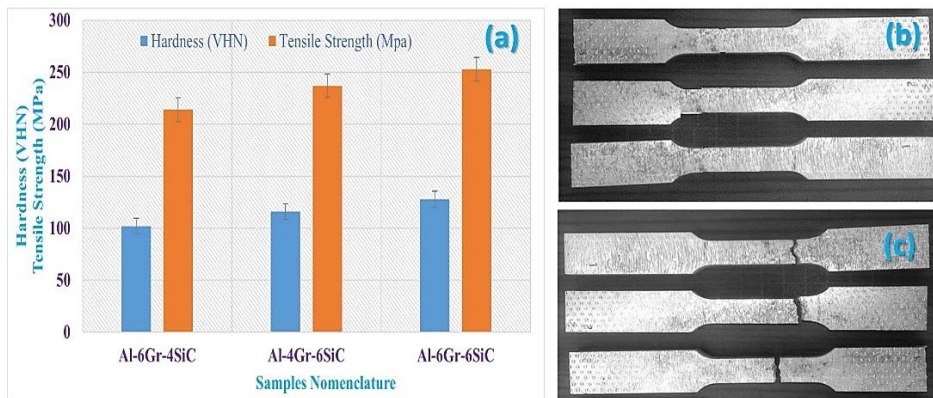


Fig. 4 Graphical representation of hardness and tensile strength

### 3.3. Wear and Friction Measurement

Sample No. 3 (Al-6Gr-6SiC) is selected for conducting the dry wear and friction tests due to its superior hardness and tensile strength compared to the other two samples. An increase in hardness generally signifies enhanced resistance to wear, whereas a higher tensile strength implies increased strength and endurance under applied stresses. The performance of Sample 3 is assessed in settings where friction and wear are significant variables by the implementation of dry wear and friction tests. This testing methodology has the potential to provide significant insights into the material's performance in practical scenarios, particularly when subjected to abrasive or sliding contact with various surfaces. The measured values of wear and friction are represented in Figure 5.

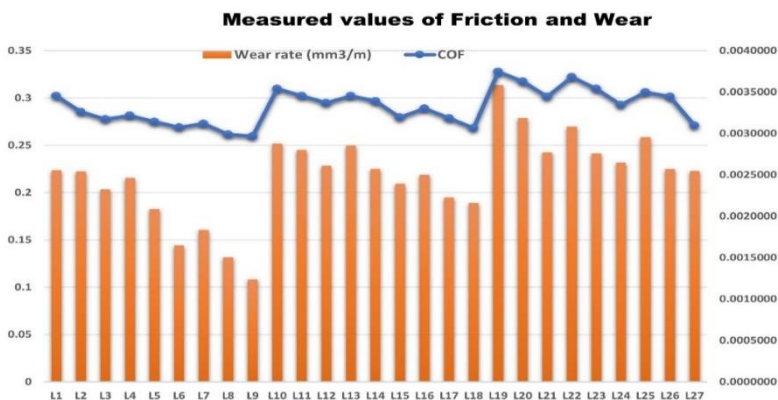


Fig. 5. Measured values for wear and friction

### 3.5. Optimization using the GRA Approach

Table 6 shows the orthogonal array with experimental observation after the wear test on the Pin-on-disc apparatus. In the grey relational analysis, the real several outputs were reduced to a single output. In this method, the final stage of grading was given to the output values as shown in Table 7. Getting the normalized values from the response data is the first stage in the procedure. The second stage involves calculating the departure from the sequence, and the third involves determining the grey relationship coefficient. The grey relational grades (GRG) are created in the next step by calculating the mean of the GR coefficient, and the highest rank is then used to determine the best combination of answer values [17]–[19].

Table 6. Orthogonal Array with experimental observation

S. No	Orthogonal Array	Load (N)	Speed (m/s)	Distance (m)	COF	Wear rate (mm <sup>3</sup> /m)
1	L <sub>1</sub>	20	1.5	1000	0.3023	0.0026
2	L <sub>2</sub>	20	1.5	2000	0.2852	0.0025
3	L <sub>3</sub>	20	1.5	3000	0.2776	0.0023
4	L <sub>4</sub>	20	3	1000	0.2814	0.0025
5	L <sub>5</sub>	20	3	2000	0.2748	0.0021
6	L <sub>6</sub>	20	3	3000	0.2691	0.0016
7	L <sub>7</sub>	20	4.5	1000	0.2729	0.0018
8	L <sub>8</sub>	20	4.5	2000	0.2615	0.0015
9	L <sub>9</sub>	20	4.5	3000	0.2596	0.0012
10	L <sub>10</sub>	40	1.5	1000	0.3098	0.0029
11	L <sub>11</sub>	40	1.5	2000	0.3023	0.0028
12	L <sub>12</sub>	40	1.5	3000	0.2947	0.0026
13	L <sub>13</sub>	40	3	1000	0.3023	0.0029
14	L <sub>14</sub>	40	3	2000	0.2966	0.0026
15	L <sub>15</sub>	40	3	3000	0.2795	0.0024
16	L <sub>16</sub>	40	4.5	1000	0.2890	0.0025
17	L <sub>17</sub>	40	4.5	2000	0.2786	0.0022
18	L <sub>18</sub>	40	4.5	3000	0.2681	0.0022
19	L <sub>19</sub>	60	1.5	1000	0.3278	0.0036
20	L <sub>20</sub>	60	1.5	2000	0.3174	0.0032
21	L <sub>21</sub>	60	1.5	3000	0.3013	0.0028
22	L <sub>22</sub>	60	3	1000	0.3222	0.0031
23	L <sub>23</sub>	60	3	2000	0.3098	0.0028
24	L <sub>24</sub>	60	3	3000	0.2928	0.0026
25	L <sub>25</sub>	60	4.5	1000	0.3060	0.0030
26	L <sub>26</sub>	60	4.5	2000	0.3013	0.0026
27	L <sub>27</sub>	60	4.5	3000	0.2710	0.0025



Table 7. Grey relational analysis

S. No	Normalized value		Deviation Sequence		GR Coefficient		GRG	RANK
1	0.625	0.560	0.375	0.440	0.571	0.532	0.552	10
2	0.375	0.554	0.625	0.446	0.444	0.529	0.487	16
3	0.264	0.462	0.736	0.538	0.404	0.482	0.443	20
4	0.319	0.519	0.681	0.481	0.424	0.510	0.467	17
5	0.222	0.361	0.778	0.639	0.391	0.439	0.415	22
6	0.139	0.174	0.861	0.826	0.367	0.377	0.372	25
7	0.194	0.254	0.806	0.746	0.383	0.401	0.392	24
8	0.028	0.114	0.972	0.886	0.340	0.361	0.350	26
9	0.000	0.000	1.000	1.000	0.333	0.333	0.333	27
10	0.736	0.695	0.264	0.305	0.655	0.621	0.638	4
11	0.625	0.664	0.375	0.336	0.571	0.598	0.585	8
12	0.514	0.583	0.486	0.417	0.507	0.545	0.526	13
13	0.625	0.687	0.375	0.313	0.571	0.615	0.593	7
14	0.542	0.566	0.458	0.434	0.522	0.535	0.529	12
15	0.292	0.490	0.708	0.510	0.414	0.495	0.454	18
16	0.431	0.535	0.569	0.465	0.468	0.518	0.493	15
17	0.278	0.421	0.722	0.579	0.409	0.463	0.436	21
18	0.125	0.392	0.875	0.608	0.364	0.451	0.407	23
19	1.000	0.997	0.000	0.003	1.000	0.993	0.997	1
20	0.847	0.828	0.153	0.172	0.766	0.744	0.755	3
21	0.611	0.651	0.389	0.349	0.562	0.589	0.576	9
22	0.917	0.784	0.083	0.216	0.857	0.698	0.778	2
23	0.736	0.646	0.264	0.354	0.655	0.586	0.620	6
24	0.486	0.599	0.514	0.401	0.493	0.555	0.524	14
25	0.681	0.729	0.319	0.271	0.610	0.649	0.629	5
26	0.611	0.566	0.389	0.434	0.563	0.535	0.549	11
27	0.167	0.556	0.833	0.444	0.375	0.530	0.452	19

3.5.1. ANOVA for GRG's

ANOVA was used to examine each process parameter's percentage contribution and its significance at a 95% confidence level [20]. The acquired findings of the GRGs' ANOVA are displayed in Table 6.

Table 8. Analysis of variance for GRG's

Source	DF	Adj SS	Adj MS	F-Value	P-Value
Load (N)	2	0.240204	0.120102	13.90	0.000
Speed (m/s)	2	0.127637	0.063818	7.38	0.004
Distance (m)	2	0.006978	0.003489	0.40	0.673
Error	20	0.172867	0.008643		
Total	26	0.547685			

R<sup>2</sup> = 68.44% R<sup>2</sup>(adj) = 58.97 %

The findings indicated that load, distance, and sliding speed percentages contributed 61.505%, 25.124%, and 13.371%, respectively, to the ideal values of friction and wear [21]–[23]. According to Table 8, all of the criteria were found to be relevant. Figure 6 shows the residual plots for Grey Relational Grades.

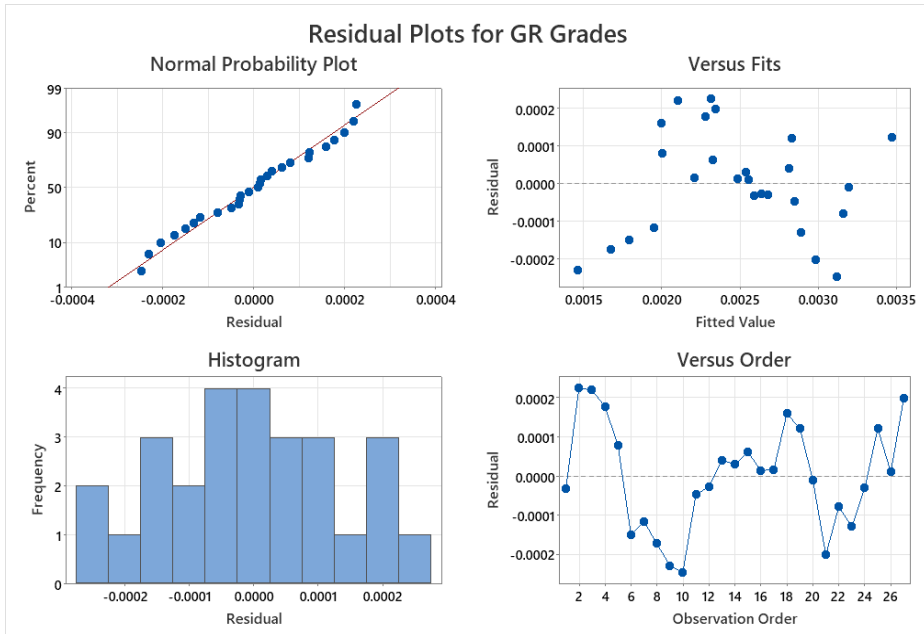


Fig. 6 Residual plots for Grey Relational Grades

### 3.5.2. Regression Equations

#### 3.5.2.1 Coefficient of Friction

$$0.290917 - 0.01488 \text{ Load (N)}_{20} + 0.00028 \text{ Load (N)}_{40} + 0.01460 \text{ Load (N)}_{60} + 0.01112 \text{ Speed (m/s)}_{1.5} + 0.00112 \text{ Speed (m/s)}_{3.0} - 0.01225 \text{ Speed (m/s)}_{4.5} + 0.01060 \text{ Distance (m)}_{1000} + 0.00102 \text{ Distance (m)}_{2000} - 0.01162 \text{ Distance (m)}_{3000} = 0.29776$$

#### 3.5.2.2 Wear Rate (mm<sup>3</sup>/m)

$$0.002492 - 0.000470 \text{ Load (N)}_{20} + 0.000062 \text{ Load (N)}_{40} + 0.000408 \text{ Load (N)}_{60} + 0.000314 \text{ Speed (m/s)}_{1.5} + 0.000008 \text{ Speed (m/s)}_{3.0} - 0.000322 \text{ Speed (m/s)}_{4.5} + 0.000253 \text{ Distance (m)}_{1000} - 0.000020 \text{ Distance (m)}_{2000} - 0.000233 \text{ Distance (m)}_{3000} = 0.002588 \text{ mm}^3/\text{m}$$

Figure 7 represents the effect of wear testing parameters on wear rate. The function of load is major, accounting for a substantial portion (61.505%) of the observed variation in GRG. The high F-value (13.90) and low p-value (0.000) suggest that the load has a substantial impact on the friction and wear performance of the hybrid composites, making it a highly relevant factor. Variations in load levels have a significant influence on the results. Velocity is an additional crucial factor, making a substantial contribution (25.124%) to the total variation in GRG. The F-value of 7.38 and the p-value of 0.004 indicate the statistical importance of speed. Changes in the speed at which objects slide against one another have an impact on their frictional behavior, highlighting the significance of speed in attaining the best possible performance. Distance, while it contributes to the variation (13.371%), has a lesser influence in comparison to load and speed. The F-value of 0.40 and the p-value of 0.673 indicate that distance has a relatively weak statistical significance in impacting

GRG. Variations in the distance of sliding have a relatively lesser effect on the observed tribological results. The aggregate impact of load, speed, and distance explains a significant proportion (about 68.44%) of the observed variation in GRG. The small p-values for load and speed show a strong degree of confidence in their importance, confirming their essential roles in attaining ideal tribological features. Distance, while it has an impact, is statistically less important in the context of this research.

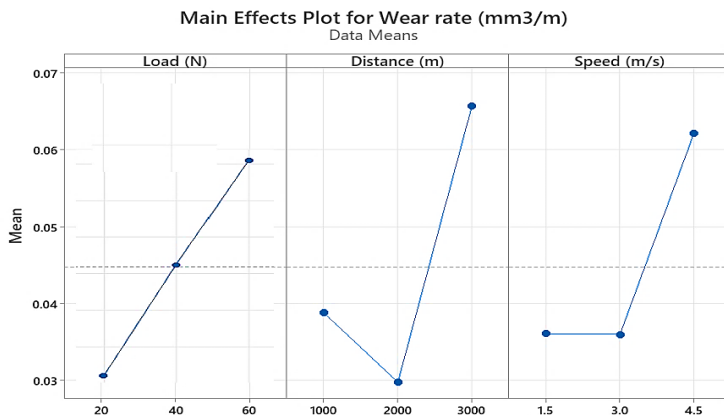


Fig. 7. Effect of process parameters on wear rate

### 3.6. Micrographs of Worn-Out Surfaces After Wear Test

The friction and wear of the synthesized hybrid AMMCs supplemented with graphene and silicon carbide particles are depicted in Figure 5 [24]–[26]. After the inclusion of hard reinforcement particles and their uniform dispersion in the matrix material, an increase in friction and a decrease in wear rate were noted [27]–[29]. The examination of sliding wear behavior included a comprehensive analysis under different situations, with specific attention given to worn surfaces using scanning electron microscope observations. Out of all the factors that were evaluated, the applied load was shown to be the most relevant influence on wear rate. As a result, worn-out surfaces were examined while being subjected to applied stresses of 20 N, 40 N, and 60 N.

Distinct characteristics, including peeled-off particles, delamination, and abrasive wear, were seen at a load of 20 N (Figure 8a) [30]–[32]. The impact intensified when subjected to a 40 N force (Figure 8b), exposing features such as oxidation and adhesive wear. At 60 N load, there was clear evidence of delamination and the appearance of tiny particles (Figure 8c) [33]–[35]. The inclusion of cerium oxide particles significantly improved the hardness and wear resistance of the produced specimens. Nevertheless, an increase in the hardness of the surfaces in contact resulted in the deterioration and wearing away of the material. Sliding wear may lead to the formation of a heterogeneous dispersion layer, which in turn produces debris consisting of particles of aluminum, iron, carbon, and silicon oxide. The inclusion of planar surfaces and increased rigidity, caused by plastic deformation, led to a reduction in the wear rate of the composites. The observation shows that the lowest wear rate of 0.002588 mm<sup>3</sup>/N-m when subjected to a 60 N load, sliding over a distance of 1000 m, and at a velocity of 1.5 m/s.

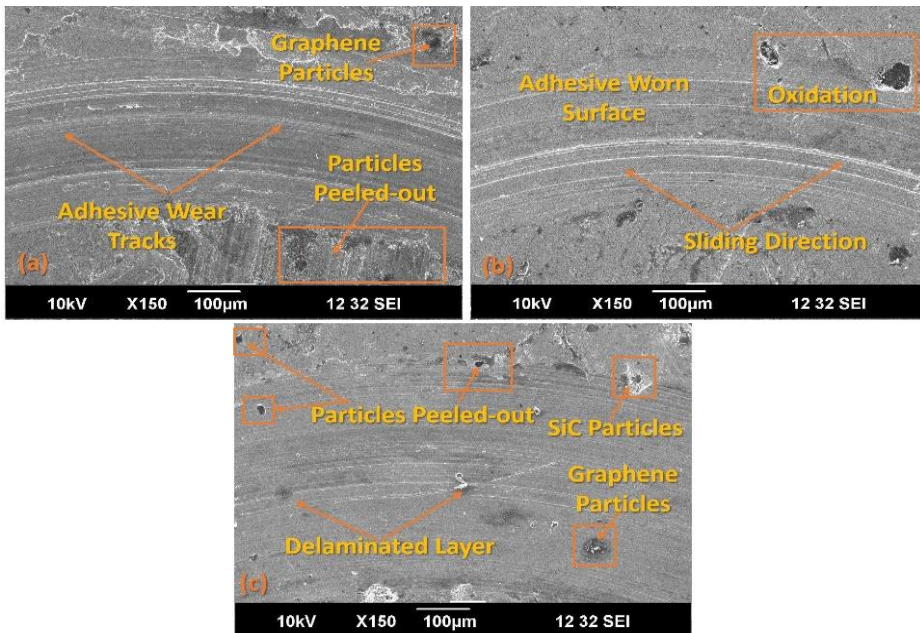


Fig. 8. (a, b, and c) SEM Morphology of Worn-out surfaces after Wear test

#### 4. Conclusions

The main aim of the current study was to find the optimized set of stir-casting parameters using grey relational analysis, which simultaneously affects the friction and wear of the fabricated AMMCs. The conclusions of the study are mentioned below:

- The research effectively optimized the fabrication parameters for hybrid aluminum metal matrix composites (AMMCs) by using grey relational analysis (GRA) and Taguchi's  $L_{27}$  design.
- The Al-6Gr-6SiC composite proved to be the most favorable combination, demonstrating exceptional hardness (measured at 128 Vickers Hardness Number) and tensile strength (measured at 253 MPa).
- The use of both graphene (Gr) and silicon carbide (SiC) as reinforcements in the Al-6061 matrix resulted in enhanced tribological characteristics of the hybrid AMMCs.
- The chosen composite exhibited improved resistance to friction, with a coefficient of friction of 0.29766, and reduced wear rates, measuring  $0.002588 \text{ mm}^3/\text{m}$ .
- The tribological behavior of AMMCs is significantly influenced by the parameters of load, sliding speed, and sliding distance. The research highlighted the crucial roles they play in attaining ideal mechanical and frictional characteristics.
- The analysis of variance (ANOVA) findings highlighted the significant impacts of load (61.505%), speed (25.124%), and distance (13.371%) on achieving optimal friction and wear values.
- Analysis using scanning electron microscopy (SEM) of the manufactured samples showed clear microstructural traits that have an impact on the mechanical and tribological properties.
- The arrangement and spread of reinforcing particles were seen to influence hardness, resistance to wear, and the overall performance of the composite.
- The optimized composite (Al-6Gr-6SiC) shows promise for use in applications that need exceptional wear resistance and durability.

## Acknowledgment

The authors acknowledge that this study is supported by the National Institute of Technology Kurukshetra, India.

## References

- [1] Jawalkar CS, Singh A, Suri NM. Fabrication of Aluminium Metal Matrix Composites with Particulate Reinforcement : A Review. *Materials Today: Proceedings*. 2017;4(2):2927-2936. <https://doi.org/10.1016/j.matpr.2017.02.174>
- [2] Samal BP, Khuntia SK. Corrosion Behavior of Al-Mg-SiC Composite produced by Modified Stir casting method. 2019;14(12):2821-2823.
- [3] Kumar D, Singh S, Angra S. Dry sliding wear and microstructural behavior of stir-cast Al6061-based composite reinforced with cerium oxide and graphene nanoplatelets. *Wear*. 2023;516-517:204615. <https://doi.org/10.1016/j.wear.2022.204615>
- [4] Kumar H, Kumar V, Kumar D, Singh S. Wear Behavior of Friction Stir Processed Copper-Cerium Oxide Surface Composites. *EVERGREEN Joint Journal of Novel Carbon Resource Sciences & Green Asia Strategy*. 2023;10(01):78-84. <https://doi.org/10.5109/6781043>
- [5] Chowdhury MA, Kumar UD, Kchaou M, Shuvho BA, Rahman A, Kumar BR. Correlation between experimental and analytic approaches to study the erosion rate of aluminum-metal matrix composites. *Journal of Engineering Research (Kuwait)*. 2022;10(1):295-315
- [6] Engineering M, Kavary T, Nadu ST. Tribological And Corrosion Behaviour Of Al 6063 / SiC Metal Matrix Composites. *International Journal of Advanced Engineering Technology*, VII(II), 2016;2-7.
- [7] Hashim FA, Abdulkader NJ. Corrosion Behavior of Recycling Al- Alloy Based Metal Matrix Composites Reinforced by Nano particles. *Kurdistan Journal of Applied Research*. 2017; 2(3): 279-283.
- [8] Saravanan C, et al. Investigation on the mechanical, tribological, morphological and machinability behavior of stir-casted Al/SiC/Mo reinforced MMCs. *Materials Today: Proceedings*. 2020;21:1-10.
- [9] Mercado-Lemus VH, et al. Wear Dry Behavior of the Al-6061-Al2O3 Composite Synthesized by Mechanical Alloying. *Metals*. 2021;1-17. <https://doi.org/10.3390/met11101652>
- [10] C Mk. Effect of Carbon Nanotube in Aluminum Metal Matrix Composites on Mechanical Properties. *Journal of Engineering Science and Technology* 2020;15(2):919-930.
- [11] Wei L, Liu X, Gao Y, Lv X, Hu N, Chen M. Synergistic strengthening effect of titanium matrix composites reinforced by graphene oxide and carbon nanotubes. *Materials and Design*. 2021;197:109261. <https://doi.org/10.1016/j.matdes.2020.109261>
- [12] Suresh R. Comparative study on dry sliding wear behavior of mono (Al2219 / B 4 C ) and hybrid ( Al2219 / B 4 C / Gr ) metal matrix composites using statistical technique. *Journal of the Mechanical Behavior of Materials* 2020;57-68. <https://doi.org/10.1515/jmbm-2020-0006>
- [13] Kumar D, Angra S, Singh S. Effect of reinforcements on mechanical and tribological behavior of magnesium-based composites : a review. *Material Physics and Mechanics* 2022;50(3):439-458.
- [14] Kumar D, Angra S, Singh S. High-temperature dry sliding wear behavior of hybrid aluminum composite reinforced with ceria and graphene nanoparticles. *Engg Failure Analysis*,2023;151(May):107426. <https://doi.org/10.1016/j.engfailanal.2023.107426>
- [15] Sharma VK, Kumar V, Joshi RS. Experimental investigation on effect of RE oxides addition on tribological and mechanical properties of Al-6063 based hybrid composites  
Experimental investigation on effect of RE oxides addition on tribological and

- mechanical properties of Al-6063 based hybrid composites. *Materials Research Express* 2019; Vol. 6, PP.1-18, <https://doi.org/10.1088/2053-1591/ab2504>
- [16] Ravichandran G, Rathnakar G, Santhosh N, Suresh R. Wear characterization of hnt filled glass-epoxy composites using taguchi's design of experiments and study of wear morphology. *Composites Theory and Practice*. 2020;20(2):85-91.
- [17] Khatkar SK, Verma R, Kharb SS, Thakur A, Sharma R. Optimization and Effect of Reinforcements on the Sliding Wear Behavior of Self-Lubricating AZ91D-SiC-Gr Hybrid Composites. *Silicon*, 2021;1461-1473. <https://doi.org/10.1007/s12633-020-00523-0>
- [18] Vedabouriswaran G, Aravindan S. Wear Characteristics of Friction Stir Processed Magnesium RZ 5 Composites. *Journal of Tribology*. 2019;141(4). <https://doi.org/10.1115/1.4042039>
- [19] Kumar A, Arafath Y, Gupta P, Kumar D, Mustansar C, Jamwal A. Materials Today: Proceedings Microstructural and mechano-tribological behavior of Al reinforced SiC-TiC hybrid metal matrix composite. *Materials Today: Proceedings*. 2019;8-11. <https://doi.org/10.1016/j.matpr.2019.08.186>
- [20] Begum Y, Bharath KN, Doddamani S, Rajesh AM, Kaleemulla KM. Optimization of Process Parameters of Fracture Toughness Using Simulation Technique Considering Aluminum-Graphite Composites. *Transactions of the Indian Institute of Metals*. 2020;73(12):3095-3103. <https://doi.org/10.1007/s12666-020-02113-5>
- [21] Okumus M. Study of microstructural, mechanical, thermal and tribological properties of graphene oxide reinforced Al - 10Ni metal matrix composites prepared by mechanical alloying method. *Wear* 2022;511(September). <https://doi.org/10.2139/ssrn.4082693>
- [22] Hamada ML, Alwan GS, Annaz AA, Irbhayim SS, Hammood HS. Experimental Investigation of Mechanical and Tribological Characteristics of Al 2024 Matrix Composite Reinforced by Yttrium Oxide Particles. *Korean Journal of Material Research* 2021;31(6):339-344. <https://doi.org/10.3740/MRSK.2021.31.6.339>
- [23] Al MMA, Allam QIM, Patel F, Samad A. Tribological Performance of Sub - Micron - Al 2 O 3 - Reinforced Aluminum Composite Brake Rotor Material. *Arabian Journal for Science and Engineering*. 2021;46(3):2691-2700. <https://doi.org/10.1007/s13369-020-05179-x>
- [24] Chak V, Chattopadhyay H, Dora TL. A review on fabrication methods, reinforcements and mechanical properties of aluminum matrix composites. *Journal of Manufacturing Processes*. 2020;56(May):1059-1074. <https://doi.org/10.1016/j.jmapro.2020.05.042>
- [25] Ramadoss N, Pazhanivel K, Ganesh Kumar S, Arivanandhan M, Anandan P. Effect of B4C and SiC nanoparticle reinforcement on the wear behavior and surface structure of aluminum (Al6063-T6) matrix composite. *SN Applied Sciences*. 2020;2(5):1-16. <https://doi.org/10.1007/s42452-020-2712-5>
- [26] Nyadongo ST. Analysis of Dry Sliding Wear Performance of Tribaloy T-800 / Tungsten Carbide Coating Deposited via Laser Cladding Assisted with Preheating. *Journal of Materials Engineering and Performance*. 2022; 32(12), 5435-5449. <https://doi.org/10.1007/s11665-022-07493-x>
- [27] Kumar D, Angra S, Singh S. Mechanical Properties and Wear Behaviour of Stir Cast Aluminum Metal Matrix Composite: A Review. *International Journal of Engineering, Transactions A: Basics*. 2022;35(4):794-801. <https://doi.org/10.5829/IJE.2022.35.04A.19>
- [28] Vageshappa LS, Channabasappa M. Effect of addition of TiC nanoparticles on the tensile strength of Al7075-graphene hybrid composites *Research on Engineering Structures and Materials*, 9(1), 19-30, 2023. <https://doi.org/10.17515/resm2022.486ma0725>
- [29] Singh C, Kumar V, Manna A. Experimental study on developed electrochemical micro machining of hybrid MMC. *Indian Journal of Engineering & Materials Sciences* 2020;27(June):579-589. <https://doi.org/10.56042/ijems.v27i3.45055>

- [30] Khan MM, Dey A, Hajam MI. Experimental Investigation and Optimization of Dry Sliding Wear Test Parameters of Aluminum Based Composites. *Silicon* 2022;4009-4026. <https://doi.org/10.1007/s12633-021-01158-5>
- [31] Jagannatham M, Saravanan MSS, Sivaprasad K, Babu SPK. Mechanical and Tribological Behavior of Multiwalled Carbon Nanotubes-Reinforced AA7075 Composites Prepared by Powder Metallurgy and Hot Extrusion. *Journal of Materials Engineering and Performance*. 2018;27(11):5675-5688. <https://doi.org/10.1007/s11665-018-3681-3>
- [32] Bhoi NK, Singh H, Pratap S. Developments in the aluminum metal matrix composites reinforced by micro / nano particles - A review. *Journal of Composite Materials* 2019. <https://doi.org/10.1177/0021998319865307>
- [33] Singh S, Pal K. Influence of Texture Evolution on Mechanical and Damping Properties of SiC/Li<sub>2</sub>ZrO<sub>3</sub>/Al Composite through Friction Stir Processing. *Journal of Engineering Materials and Technology, Transactions of the ASME*. 2020;142(2):1-9. <https://doi.org/10.1115/1.4045495>
- [34] Kubit A. The Effect of Adhesive Type on Strength of Inter-Layer Joints in Fiber Metal Laminate Composites. *Composites Theory and Practice*. 2017;17(3):162-168.
- [35] Ra'ayatpour M, Emamy M, Rassizadehghani J. Influence of Hot Extrusion on the Microstructure, Tensile and Wear Properties of Mg-5Sb-xSiC Hybrid Composites. *Metals and Materials International*. 2021; 28(3), 679-694. <https://doi.org/10.1007/s12540-020-00936-x>

## Results of Sn/Pb solder affected aluminum under wear study

Mohammad Salim Kaiser<sup>a</sup>

Innovation Centre, International University of Business Agriculture and Technology, Bangladesh

### Article Info

### Abstract

#### Article history:

Received 29 Oct 2023

Accepted 02 Jan 2024

#### Keywords:

Al- alloy;  
Corrosive;  
Micrographs;  
Sn- Pb solder;  
Tribology;  
Worn surfaces

Nanostructured Al-Sn and Al-Pb alloys are effectively used to improve their wear characteristics. Taking this into consideration, the wear properties of aluminum have been studied while affected by both elements Sn-Pb solder at a lower level to explore its reusing potentials. In this purpose a common pin-on-disk device is used in which different dry, wet and corrosive sliding environments are applied. Additionally, pure Al, Al-Sn and Al-Pb alloys are also considered for recovering the clarification and to separate elemental effects on wear properties. The worn surfaces of the samples are examined using optical and scanning electron microscopy, both before and after wear. Surface roughness also is a measure to assess the wear properties under different environments. The findings revealed that minor solder has a great impact on the wear properties of Al with Sn playing a better role than Pb. Solid solution strengthening is the main reason for improved wear behavior in terms of the low wear rate and coefficient of friction. Both Sn and Pb do not form any intermetallic with Al but with impurities it can easily occur particularly with Sn resulting in better wear properties. This phenomenon is more prominent in corrosive environment than wet due to the protective oxide layer on the surfaces. In dry sliding conditions, numerous large wear particles, oxide debris and grooves can be seen on the worn surface, but smoother wear tracks are seen in wet and corrosive environments as form oxide film and thumbs down somewhat direct contact on the moveable surfaces. SEM analysis also reveals higher abrasive wear and plastic deformation on the worn surface produced under dry sliding conditions where minor added alloys indicating that reinforcing particles effectively influence the properties.

© 2024 MIM Research Group. All rights reserved.

## 1. Introduction

From the beginning, aluminum has been one of the popular materials in many industries due to its excellent physical, mechanical, electrical, and chemical properties such as light density, high strength, wear, and corrosion resistance [1-3]. Its properties are enhanced many times when it is alloyed with other elements. Alloying has a limitation in that improving one property it may affect other properties. In the book by S. Sivashankaranto provides ample information about the effects of alloying elements on aluminum [4]. More precisely Si lowers the melting point, cumulative fluidity, and Cu provides precipitation hardening and strength, while reducing ductility as well as corrosion resistance. Mn enhances work hardening rate, but prevents cracking during stress corrosion., correspondingly Fe can enhance hardness and decrease tensile strength in addition to corrosion resistance. Ni addition improves strength at high temperature, at the expense of electrical conductivity. For grain refining as well as thermal stability minor Zr also added into the Al-alloys [5-7]. Sometimes aluminum alloys give better strength by heat treatment. Plastic deformation is another method of increasing the strength of aluminum and its alloys [4, 8, 9]. The favorable point of aluminum is that it can be recycled again and again

<sup>a</sup>Corresponding author: [dkaiser.res@iubat.edu](mailto:dkaiser.res@iubat.edu)

<sup>a</sup>orcid.org/0000-0002-3796-2209

DOI: <http://dx.doi.org/10.17515/resm2024.59ma1029rs>

Res. Eng. Struct. Mat. Vol. 10 Iss. 3 (2024) 957-972



without losing its major character. The process involves just re-melting and it is much less expensive along with energy-intensive than making new aluminum from its original source. Recycling it also has significant environmental benefits by eliminating air and water pollution which need to process raw materials [10, 11]. Aluminum is extensively used in the manufacturing of electronic and microelectronic components, and in some countries for power lines. It is widely used in the manufacture of transformers, low-voltage rotors, motor capacitors and sometimes also used for antenna and radar construction [12]. Hence, Al-alloys are also claimed to be suitable for the aerospace industry [13, 14].

When used in this electrical sector, Al wires or parts are to be joined. Soldering is applied to the joining process. In this case the recycled aluminum content is a small amount of solder alloy [15, 16]. The best option is reusing the scraped materials at their leftover state for appropriate engineering applications. At earlier stages Sn-Pb solder alloys are mostly used. Therefore, cast aluminum will contain minor amounts of Sn and Pb. From this perspective, reused or melted scraped Al requires characterization of the properties achievable with special attention to surface behavior. Abrasion and friction properties of materials are the main component failures causing surface deformation and reduced durability [17, 18]. Some have reported the effect of Sn or Pb on the wear behavior of Al alloys where the levels of such elements were high [19, 20]. There is no work reported where Sn or Pb is used in small amounts as well as both elements simultaneously. Additionally, sufficient information on the tribological behavior of these alloys under water or saline environments is also lacking. Al-based bearings and associated fittings are preferred in corrosive environments, so it is necessary to have reliable data on friction and wear properties when alloys are applied to noncorrosive stainless steel counter bodies. Therefore, a significant effort has been taken to investigate these properties of Sn-Pb solder affected Al under different sliding conditions as mentioned above for applications in the marine sector.

## 2. Materials and Methods

The objective was to study the wear behavior of Sn-Pb solder affected Al under different conditions. Extensively old Al electrical wire and different soldered connecting electrical components were melted conventionally using a resistance heating furnace. From the chemical composition of melt aluminum, it contained the minor amount of 1.0~1.5wt% Sn and 1.0~1.5wt % Pb. To establish the influence separately of tin and lead in the Al, depending the minor elements another three more samples like pure Al, binary Al-Sn, Al-Pb were chosen. Commercially pure grade Al, Sn and Pb were taken for developing those alloys where mild steel mould of 155 x 45 x 35 mm size was used. The cast alloys were then subjected to homogenization and solutionizing at 450°C for 12 h and 530°C for 2 h respectively. The developed four samples consist the following elements analyzed by Optical Emission Spectroscopy as in Table 1. Additionally, Cu, Mg, Mn, Zn, Ni, Cr, Ti etc, were also present in the alloys as trace impurities.

Table 1. Alloys chemical composition by wt.%

Alloy	Sn	Pb	Fe	Si	Al
Pure Al	0.002	0.002	0.202	0.280	Bal
Al-Sn	1.512	0.012	0.314	0.335	Bal
Al-Pb	0.002	1.275	0.335	0.345	Bal
Al-Sn-Pb	1.433	1.201	0.406	0.435	Bal

For the physical, mechanical and wear test the cast and heat-treated alloy samples were machined to 145 x 40 x 32 mm size for skin out the oxide layer. Then the bar was cold

rolled by 80% with a 10HP rolling mill where the 40 mm thick portion under gone to 8 mm. For wear study, size of 12 mm in length and 5 mm in diameter were machined from the cold rolled alloys. Alloy densities were calculated from the chemical composition. The alloys are aged at 100°C for one hour becoming the better strength [21]. The microhardness of the aged samples was measured using a Micro Vickers Hardness testing machine. One kg load and ten seconds dwell time were used there. Tensile testing was carried out according to ASTM E8 specification at room temperature in an Instron testing machine. The wear and frictional properties of tested alloys were investigated following ASTM standard G99-05 where a pin-on-disc type apparatus was used [22, 23]. As the counter surface material 309s stainless steel disc with 100 mm semi-dia and 15 mm thick was used. The hardness and roughness of the disc was around HRB 85 and was 0.39  $\mu\text{m}$  respectively. The 20 N load, that is calculated contact pressure 1.02 MPa was used for wear study. Furthermore, 5 to 50 N loads were used for other experiments. During the wear study the disc was rotated at 200 rpm where the pin samples stay on a track diameter of 49 mm as a result the calculated sliding speed was 0.51 m/s. All the tests were completed in ambient conditions of 70% humidity and at 22 °C temperature. For an individual data five tests were carried out and the average of these values were considered. The specimens were first subjected to dry sliding conditions and then chronologically to the distilled water and then 3.5% NaCl saline water. For both the wet and corrosive environments, drip-type single-point at the contact interface of the sample and the steel counter plate was maintained with a constant rate of discharge throughout the experiment. The discharge rate was five drops per minute as controlled by the regulator. The specific wear rate was calculated from the measured weight loss ( $\Delta W$ ), the running distance in the test (S.D.), and the normal load (L) applied to the samples [23]. The sliding distances were calculated from the track diameter and speed of rotation of the disc. The load cell reading (F) was normalized by the load applied, L to find out the friction coefficient ( $\mu$ ). The mathematical relations to obtain the weight loss, specific wear rate (S.W.R.) and the friction coefficient are stated by equations as follows:

$$\Delta W = W_{initial} - W_{final} \quad (1)$$

$$S.W.R. = \frac{\Delta W}{S.D. \times L} \quad (2)$$

$$\mu = \frac{F}{L} \quad (3)$$

The worn surface and wear debris of the specimens from the test were put under microstructural observation using USB digital microscope. In some cases, SEM analysis was used by JEOL scanning electron microscope.

### 3. Results and Discussion

#### 3.1. Physical and Mechanical Properties

Table 2 displays the experimental results of physical and mechanical properties of commercially pure Al, binary Al-Sn, Al-Pb and solder affected ternary Al-Sn-Pb alloys including density, hardness, tensile strength and percent elongation. Pure Al exhibit lowest density, while Al-Sn shows higher for addition of 1.51 wt.% Sn. Similarly, 1.28wt% Pb is added to Al-Pb to continue the trend, and it is evident that the alloy with the highest density, Al-Sn-Pb, contains both added elements. The density of Al, Sn and Pb are 2.7gm/cm<sup>3</sup>, 7.3gm/cm<sup>3</sup> and 11.34gm/cm<sup>3</sup> respectively. Hardness of the alloyed samples is higher due to the solid solution strengthening. Sn has the BCC crystal structure but Pb has the FCC structure as Al. As a result, Sn shows the higher hardness than Pb added alloy. Furthermore, both Sn and Pb elements do not form any intermetallic with Al but form

intermetallic with trace impurities resulting in additional hardness with respect to Sn. Solder added alloys exhibit the result of two elements [24, 25].

The solder-affected Al shows the highest tensile strength in the aforementioned reason, followed by alloys containing Sn and Pb, and pure Al, which shows the lowest tensile strength. A small variation is observed in case of percentage of elongation. Maximum fraction of precipitates occurs into the solder affected alloy which hinders the dislocation movement so the lower elongation. For the same reason the result of elongation conforms the sequence of Al-Sn followed by Al-Pb and pure Al [26, 27].

Table 2. Physical and Mechanical properties of the experimental alloys

Alloy	Density, gm/cm <sup>3</sup>	Hardness, VHN	UTS, MPa	% Elongation
Pure Al	2.709±0.008	51.4±1.5	114.4±4.5	10.7±1.1
Al-Sn	2.801±0.025	62.3±2.5	137.3±7.5	9.6±0.7
Al-Pb	2.826±0.025	52.8±2.3	123.8±6.5	10.2±0.7
Al-Sn-Pb	2.889±0.031	63.5±3.1	147.0±8.0	9.5±0.6

### 3.2. Wear Behavior

Figure 1 displays the average weight losses of pure Al, Al-Sn, and Al-Pb, as well as the weight loss of the Al-Sn-Pb alloy, with respect to sliding distance. The dry sliding conditions were maintained at a pressure of 1.02 MPa and a velocity of 0.51 m/s. As expected, weight loss was observed for all samples, but the degree of weight loss varied. As the sliding distance increased, the contact period between the rotating disk and the sample face also increased, leading to further weight loss. The variation in weight loss can be attributed to material properties such as hardness, density, and softening behavior, as shown in Table 2, while increases tensile strength, weight loss decreases [28, 29].

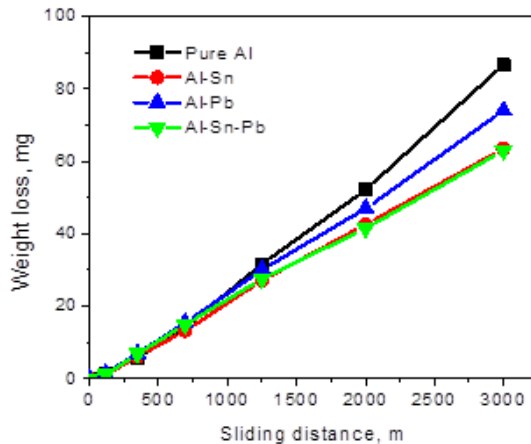


Fig. 1. Variation of the weight loss with sliding distance in dry sliding environment

Using Equations 1 and 2 calculated wear rates of investigated alloys mentioned above are plotted against the sliding distance. Whereas Fig. 2, 3 and 4 show the difference in wear rates in dry, wet and corrosive environments respectively. From the Fig. 2, it may be said that under dry sliding condition wear rate increase to certain distance followed by tends to a constant value. The increase in wear rate can be attributed to frictional heat by excessive pressure as prolonged intimate contact between the two mating surfaces and

softening of materials [30]. So, it occurs more effectively. The highest wear rate is raised for pure Al trailed by Pb added alloy, Sn added alloy and finally the solder affected alloy. According to the Archard's theory wear rate in dry sliding condition of alloys is found to decrease with the increased hardness and found to be consistent with the result [31]. Besides, during wear tests, the generation of an intermediate oxide layer between mating surfaces is also one of the probable reasons for decreasing wear rate. Average values of two opposite effects are displayed in the graphs. For long time sliding contact the surfaces with air forms thick oxide layers which control the wear rate and favorable to the constant wear rate [23].

When sliding in distil water environment, the wear rate decreases some extend for all the alloys (Fig. 3). Throughout sliding the water by hydrogen attack form oxide which is relatively stable on the surface. Minor added alloys form higher oxides as protect the surface from wear. Once more, Sn oxide is more stable than that of Pb oxide as a result slightly the lower wear rate for Sn added as well as solder affected alloy [32]. More specifically in the case of ternary solder affected alloy the role of lower stable oxide of Pb dominates in high wear rates with sliding distance.

Except for pure Al more decreasing nature of wear rate is observed in case of corrosive 3.5% NaCl sliding environment. The wear rate radically reaches a constant value with the sliding distance (Fig. 4). In this case the corrosive wear serves as a clear indicator. Pure Al affected by corrosive attack, dissolute continuously or uniformly detached it wears out more quickly in the corrosive environment. In case of minor added alloys again, it is known that the foreign particles into the alloy is attacked more by the corrosion or oxidization. It may be noted that corrosive products are thought to be more stable on surfaces than when they form oxides in wet environment, resulting in lower wear rate [33]. The overall presence of wear rate variation with sliding distance in corrosive environments first increases then decreases and then increases again. The reason behind this increase in wear rate is due to the corrosive attack, next formation of passive films on the surface of the sample which acts as a barrier against further corrosion hence the wear rate is low. After some time, the wear rate increases due to the gradual breakdown of the progressively thicker passive films [34].

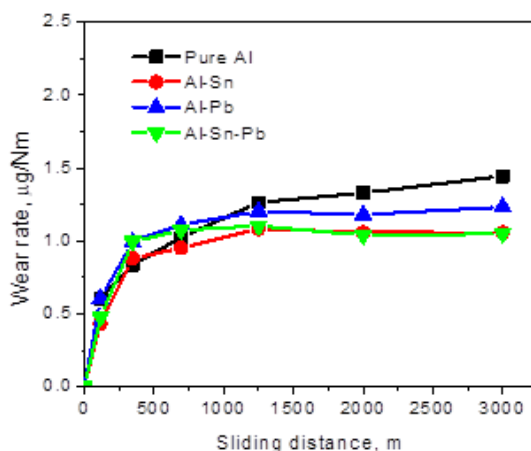


Fig. 2. Variation of wear rate with sliding distance in dry sliding environment

The results of the friction coefficient with different sliding distances are shown in Figures 5-7 for four specimens under dry, wet and corrosive tested environment, respectively. In all cases the friction coefficient is initially low and then rises with increasing sliding

distance. The friction coefficient values are initially low due to the contact between the rough layers on the specimen and the disc material. Within a short sliding distance, the friction coefficient increases. This is because the cracking and removal of the surface oxide layer leading to metal-to-metal contact increases the coefficient of friction. With increasing sliding distance, interface temperatures can develop which can promote surface oxidation thereby reducing the direct contact of the surfaces hence slightly reducing the friction coefficient [35].

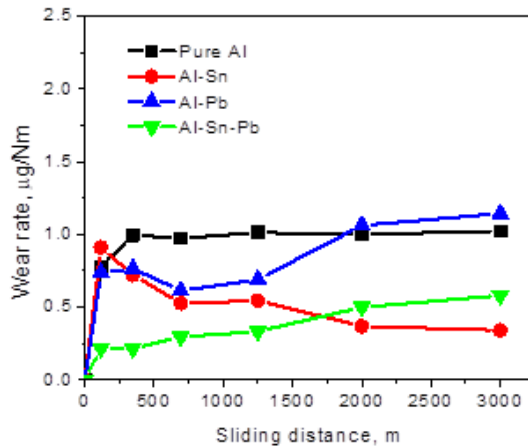


Fig. 3. Variation of wear rate with sliding distance in wet sliding environment

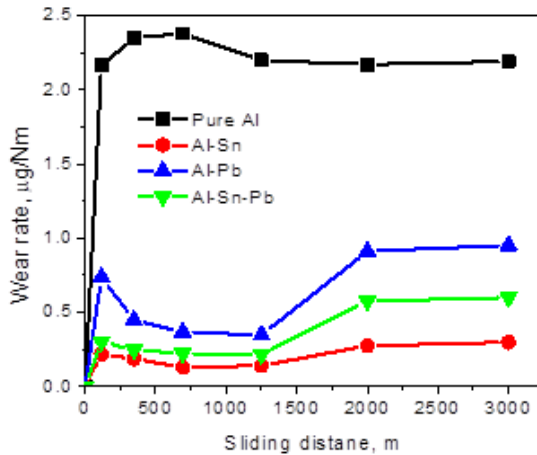


Fig. 4. Variation of wear rate with sliding distance in corrosive sliding environment

The coefficient of friction for all the alloys in the dry environment is much greater than under wet and corrosive environment. The cause of this friction reduction is the “Sealing Effect”, which reduces the roughness of the surfaces in contact [36, 37]. In all the cases the coefficient of friction of commercially pure aluminum shows the highest and solder affected Al-Sn-Pb alloy the lowest followed by tin added Al-Sn and then lead added Al-Pb alloy and the result is in good agreement with the observed microhardness value of the alloys. Differences in the extent of localized plastic deformation at real contact areas may lead to the deficiencies in friction coefficient. The solder affected alloy exhibits the lowest friction as it is the hardest one and undergo lowest plastic deformation [38]. Furthermore, solid solubilities of Sn and Pb in Al are less than 0.02 and 0.026 wt% at room temperature,

therefore, the soft Sn and Pb phase can form compact structure particles in the Al-matrix and act as solid lubricants. Some deviation is observed under water and saline environment as controlled by the oxidization and corrosion created by the minor added elements on the surfaces [24, 39]. The initial friction coefficient for all alloys is high due to the high roughness created by the dense saline particles as well as the rough matting surface. After some time, the corrosive product fills the voids and acts as a sealing effect.

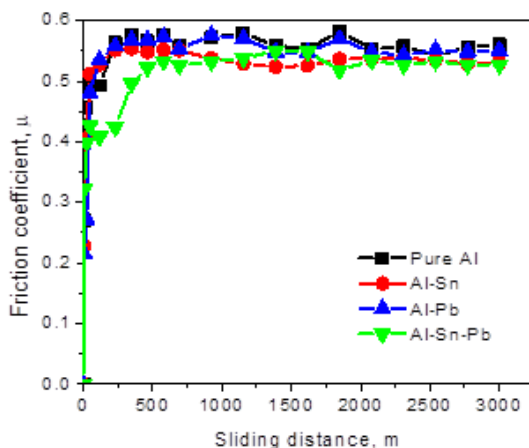


Fig. 5. Variation of the coefficient of friction with sliding distance in dry sliding environment

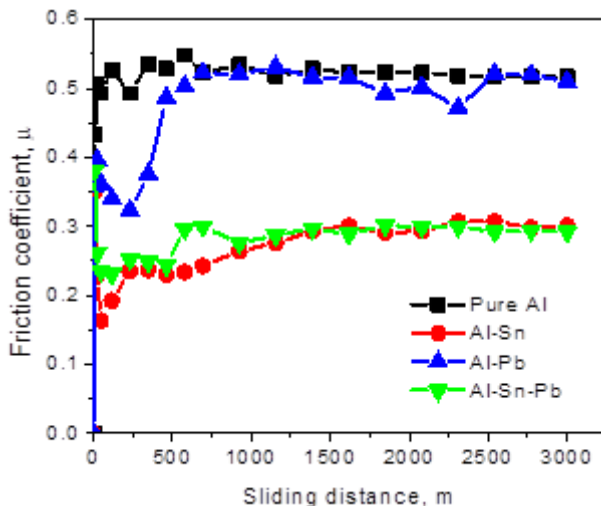


Fig. 6. Variation of the coefficient of friction with sliding distance in wet sliding environment

The nature of friction under different loads and environments at a constant velocity of 0.51 m/s is presented in Figures 8, 9 and 10. The friction coefficient in dry sliding condition shows a normal nature of decreasing trend as it may be related to the development of oxide layers (Fig. 8). But beyond a certain load the coefficient increases and pure Al exhibits the lowest coefficient and solder affected Al shows the highest followed by alloys containing Sn and Pb. Alloys soften due to stress and temperature effects under high level loads

whereas alloys with first Sn and then Pb binary inclusions reflect higher coefficients for their lower melting temperatures. Both alloy effects show the highest intensity with the solder affected alloy.

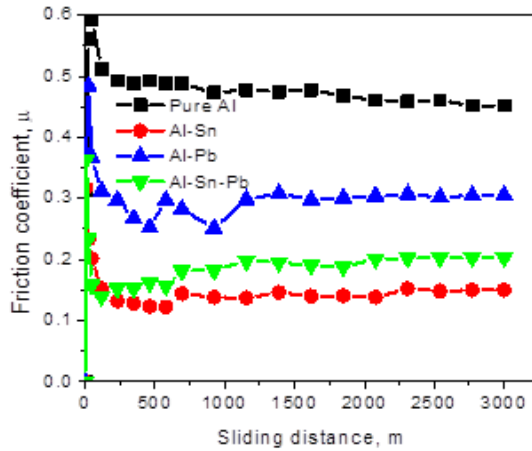


Fig. 7. Variation of the coefficient of friction with sliding distance in corrosive sliding environment

However, under wet sliding condition all the samples show the decreasing trends of coefficient of friction with the applied loads (Fig. 9). In this case higher loads produces some oxide layer due to presence of water but it inhibits the heat generation as a result lower friction. The oxide layer formation of the individual alloys along with sealing effects reduces these coefficients.

Additionally, under corrosive condition, the level of friction coefficient fully controlled by the saline water (Fig. 10). Stable oxide layer forms by the Sn is higher than that of Pb as a result lower friction and both elements effects with higher oxide formation is reflected on the solder added alloy. The sealing effect also more active with high dense of this thin lubricating film of water on the surfaces [40, 41].

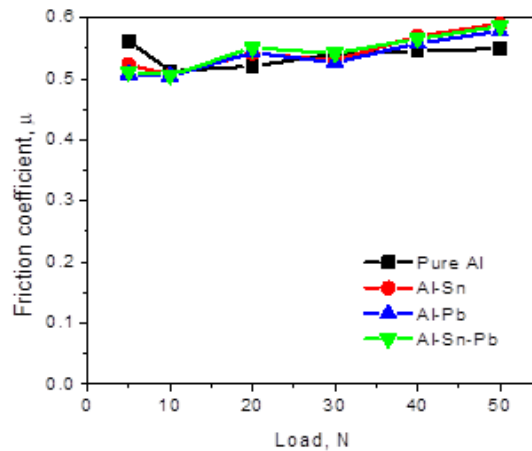


Fig. 8. Nature of friction coefficient in the dry sliding environment with loads

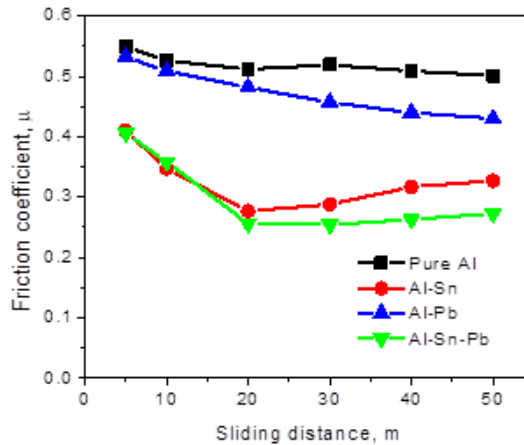


Fig. 9. Nature of friction coefficient in the wet sliding environment with loads

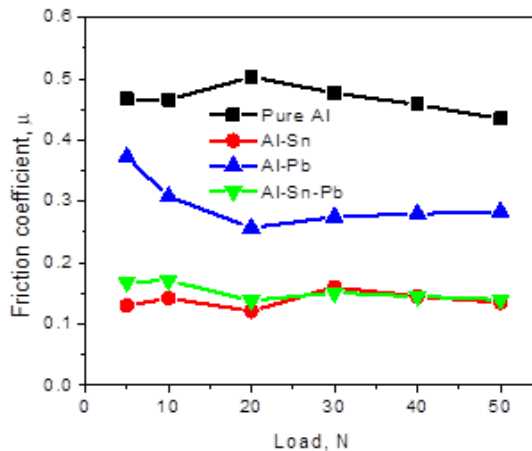


Fig. 10. Nature of friction coefficient in the corrosive sliding environment with loads

### 3.3 Optical Microscopy

Optical images of worn surfaces of pure Al, Al-Sn and Al-Pb and solder affected Al-Sn-Pb alloys before and after wear under dry, wet and corrosive sliding environments are presented in Figure 11. A pressure of 1.02 MPa applied throughout, a sliding velocity of 0.51m/s and a sliding distance of 3000m were used. The worn surfaces before wear demonstrate some scatter mark throughout the direction to polish as created by the metallographic polishing paper. Additionally, the surfaces display some different tones since various levels of alloying elements are present in alloys. Normally, this type of alloy consists of  $\alpha$ -Al phase along with the second phases depending on the element present into the materials. Trace impurities also form intermetallic into in the interdendritic region. Without etching, the polished microstructure does provide the enough information without some color changes depending on the elements present [42].

When the alloys are tested under dry sliding conditions numerous large wear particles, oxide debris and the furrows are shown in the figure. Furthermore, the plastic deformation



and numerous significant cracks can be seen. A significant amount of material is seen to be delaminating. It can also be observed from the figure, polish marks in the worn surfaces are fully absent on the surfaces as the delamination are occurred through removing the particles. The worn surface of solder affected along with minor added alloys show the surface morphology of low cracks but higher oxide layer indicating the white color on the surface compare to base metal pure Al. The wear scars and fragments show how abrasive wear, delamination wear, and oxidation wear all contribute to wear [43].

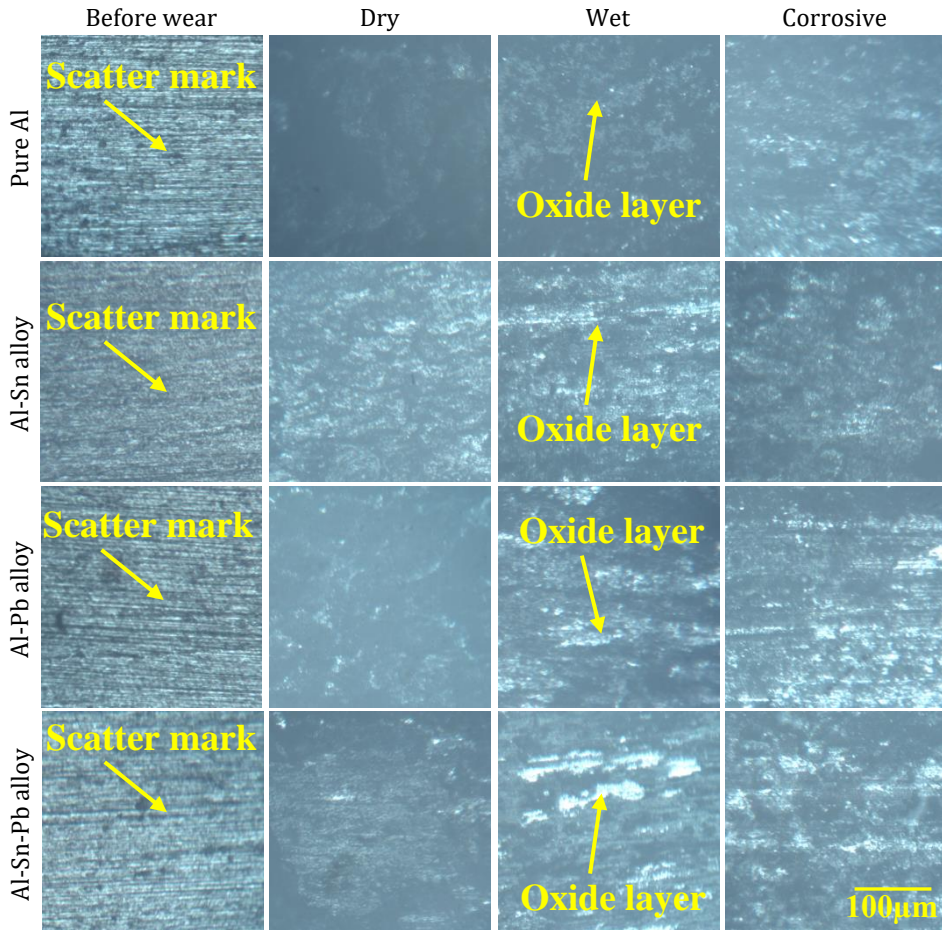


Fig. 11. Optical micrograph of polished surfaces of experimental alloys before and later wear in the condition of dry, wet and corrosive sliding for 3000m at applied pressure of 1.02 MPa

In contrast, the wear tracks visible on the worn surface are smoother in a wet environment. Hardly any cracks are visible. In addition, the debris and grooves are only visible in a few places. Additionally, due to the lubricating and cooling effects, some dark areas can be seen. The liquid environment reduced the heat concentration, local stress, and friction of shear, which prevented the formation of cracks and debris. Furthermore, during the sliding process, the majority of particles and debris are washed away by water, minimizing abrasive wear. As a result, the liquid environment's frictional characteristics are much better than those of the surrounding air. However, in the 3.5% NaCl corrosive environment, the wear mechanism is altered. Actually, the corrosion-wear that occurred in the corrosive fluid is what produced the oxidation film. During the wear testing, the

oxides are subsequently broken down, and wear debris is produced. Additionally, heat from the friction is produced at the interface, which prompts the growth of more oxides. Change of surfaces color also confirms it. The size of the debris and particles is smaller than that of the dry sliding condition, and there are no signs of a crack or plastic deformation [43].

Figure 12 shows the dust particles that were created during the wear test of four experimental alloys when they were sliding in a dry environment. Granular alloy dust is present, and some of the chips are composed of stainless-steel discs. For each alloy, the quantity of steel chips in the dust varies. Pure Al dust has very little chips because of its low hardness. Sn-containing alloy dust has more chips than Pb-containing alloy dust, which results in a higher hardness. For maximum hardness, the majority of chips are produced in solder-affected alloy [44].

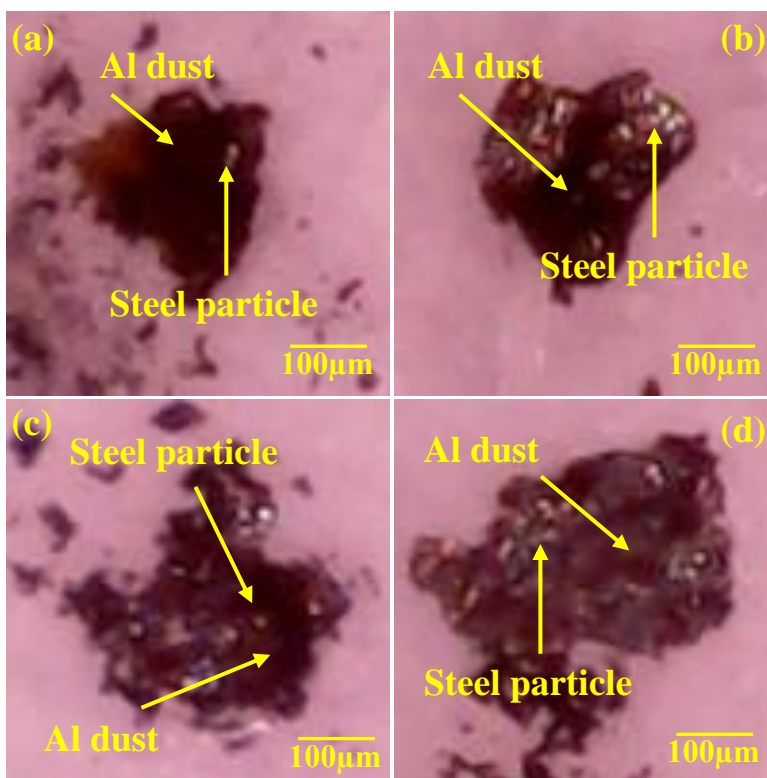


Fig. 12. Optical micrograph of generated dust from the different samples wear under dry sliding condition (a) pure Al (b) Al-Sn, (c) Al-Pb and (d) Al-Sn-Pb alloys

### 3.4. Scanning Electron Microscopy

Again, an attempt has been made for better understanding, SEM microphotographs of the worn surfaces of four samples after dry sliding wear at a distance of 3000 m are presented in Fig. 13. All the pure Al along with other binary Al-Sn, Al-Pb and ternary solder affected Al-Sn-Pb alloys clearly suggesting abrasive wear. The worn surfaces after the wear tests of pure Al showed a two-body abrasive wear with predominance of plow groove regions, indicating abrasive wear by plastic deformation, and some regions with adhesive wear, featured by a rough aspect due to the occurrence of delamination (Fig. 13a). In case of Sn and Pb added alloy, the corresponding phases are present in respected worn surfaces (Fig.

13b and 13c). The solder affected alloy obviously indicates both the phases which dominate the wear properties (Fig. 13d) [45].

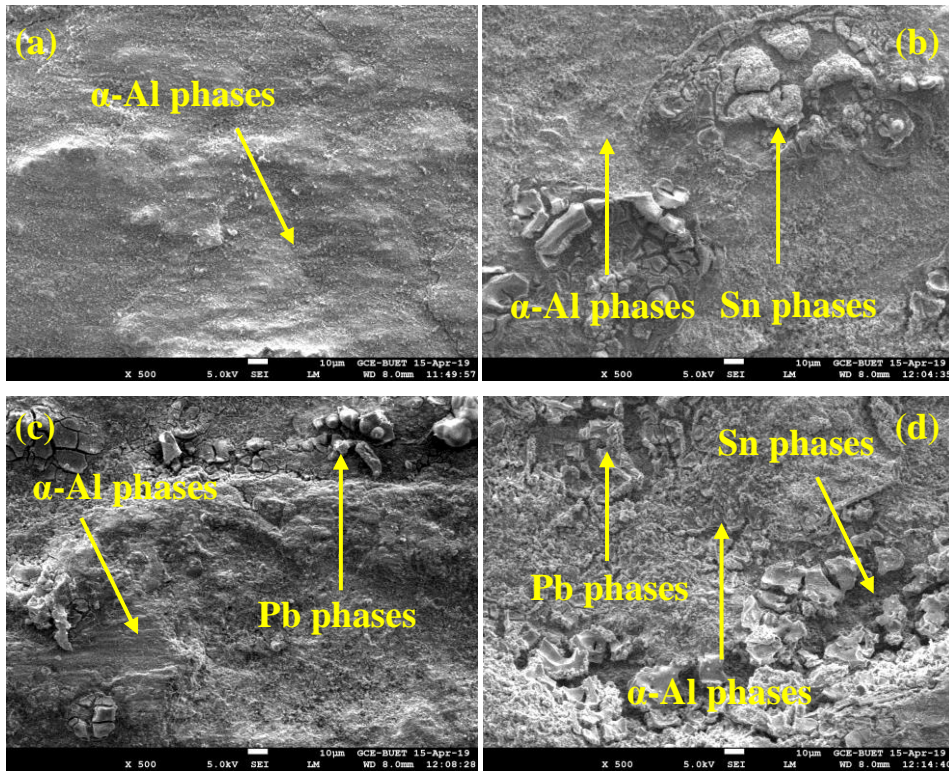


Fig. 13. SEM images of worn surfaces after dry sliding wear under 1.02 MPa pressure for a distance of 3000 m, a) pure Al, b) Al-Sn, c) Al-Pb and d) solder affected Al-Sn-Pb alloys

### 3.5. Roughness

Dry, wet and corrosive environments are used to compare the roughness levels of all four alloys. Figure 14 displays a bar graph of the results. In the dry sliding condition, pure Al exhibits the highest relative roughness, while Pb and Sn add-on alloy resemble those with solder. It is evident that the surface's softness causes more wear marks. This is connected to this phenomenon. Table 2 has been made available to demonstrate the hardness and other properties of materials. When exposed to water in wet environments, the alloy's roughness decreases due to a reduction in direct contracting between matting surfaces. Consequently, there are not enough differences between alloys. In contrast, corrosive wear can result in the presence of NaCl corrosion product on surfaces. Under pressure and temperature, the surface becomes smooth. Consequently, the roughness in this corrosive environment is inferior and entirely depends on the occurrence of rust [34, 46].

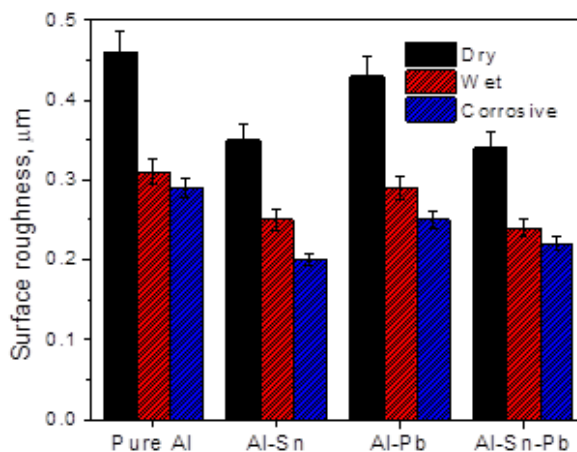


Fig. 14. Surface roughness of the samples worn surfaces under different sliding conditions

#### 4. Conclusions

This study investigated the wear characteristics of commercially pure aluminum affected by Sn-Pb solder and compares the influence of wet and corrosive with the dry sliding condition and the conclusions can be drawn from the study as follows.

- When affected by Sn/Pb solder the tribological characteristics of commercially pure Al improves in terms of low specific wear rate and friction coefficient. Where tin plays a better role compare to lead. Solid solution strengthening is the key reason for better wear performance. Both Sn and Pb do not form any intermetallic with Al but with impurities it can easily ensnare for Sn resulting in better wear properties.
- The highest wear rate is observed under dry sliding conditions due to thermal softening of the material but under distilled water sliding condition wear rate decreases as it holds back the heat generation to prevent the softening of contact materials. The decreasing nature continued in 3.5% NaCl saline water environment due to the formation of stable oxide layer on the surfaces along with the reduced direct contact.
- The friction coefficient is solder affected alloy is the lowest than Al followed by Sn added and Pb added alloy due to better strength, as the low plastic deformation of the material at real contact areas may lead to the lack of friction coefficient. However, in a wet sliding environment every coefficient of friction decreases due to the sealing effects and corrosive environment in addition to the corrosive oxide layer as controlled the friction.
- Optical microscopy confirms the visible wear tracks on worn surfaces are smoother in a wet and corrosive environment than in a dry sliding environment due to avoid softening and preventing direct contact between the two mating surfaces.
- SEM analysis indicates higher abrasive wear and plastic deformation on the worn surfaces wear under dry sliding condition. Whereas minor added alloys show Sn and Pb phase particles in this matrix then perform by way of solid lubricants.
- The solder affected alloy exhibits the lowest relative roughness followed by Sn, Pb and Al due to less wear marks resulting in higher surface hardness. In a wet sliding environment, alloys roughness is reduced due to reduced direct contact between

the matting surfaces. Under saline environment smooth corrosive products fill-up, the gap between wear mark on the surface which further reduces the roughness.

## Acknowledgement

It is acknowledged that the Miyan Research Institute of International University of Business Agriculture and Technology, Dhaka, provided financial support for the project work. The author would like to express his appreciation to Prof. Selina Nargis, the Director of Administration, for all of the helpful support and encouragement she has made available in advancing research activities at the university.

## References

- [1] ASM Handbook Committee. Properties and Selection: Nonferrous Alloys and Special-Purpose Materials. ASM International; 1990.
- [2] Wang F, Li Y, Chen X, Zhao H, Yaqoob K, Du Y, Wang Z, Song M. Superior strength-ductility combination in Al alloys via dislocation gradient structure. Materials Research Letters. 2023;11(5):347-353. <https://doi.org/10.1080/21663831.2022.2151851>
- [3] Ashkenazi D. How aluminum changed the world: A metallurgical revolution through technological and cultural perspectives. Technological Forecasting and Social Change. 2019;143:101-113. <https://doi.org/10.1016/j.techfore.2019.03.011>
- [4] Sivasankaran S. Aluminium Alloys - Recent Trends in Processing, Characterization, Mechanical Behavior and Applications. IntechOpen; 2017. <https://doi.org/10.5772/68032>
- [5] Kaiser MS, Sabbir SH, Kabir MS, Soummo MR, Nur MA. Study of mechanical and wear behaviour of hyper-eutectic Al-Si automotive alloy through Fe, Ni and Cr addition. Materials Research. 2018;2(4):1-9. <https://doi.org/10.1590/1980-5373-mr-2017-1096>
- [6] Kaypour H, Gholamipour R, Khodabandeh A, Sabet H, Tayebi M. Work Hardening and Kinetics Analysis of Al<sub>0.3</sub>MnCrCoFeNi High-Entropy Alloy. The Journal of The Minerals, Metals & Materials Society (TMS). 2023;75:4171-4181. <https://doi.org/10.1007/s11837-023-06040-w>
- [7] Kaiser MS. Solution treatment effect on tensile, impact and fracture behaviour of trace Zr added Al-12Si-1Mg-1Cu piston alloy. Journal of The Institution of Engineers (India): Series D. 2018;99(1):109-114. <https://doi.org/10.1007/s40033-017-0140-5>
- [8] Ng CH, Yahaya SNM, Majid AAA. Reviews on aluminum alloy series and its applications. Academia Journal of Scientific Research. 2017;5(12):708-716.
- [9] Kaiser MS, Datta S, Roychowdhury A, Banerjee MK. Age Hardening Behavior of Wrought Al-Mg-Sc Alloy. Materials and Manufacturing Processes. 2007;23(1):74-81. <https://doi.org/10.1080/10426910701524600>
- [10] Paraskevas D, Ingarao G, Deng Y, Duflou JR, Pontikes Y, Blanpain B. Evaluating the material resource efficiency of secondary aluminium production: A Monte Carlo-based decision-support tool. Journal of Cleaner Production. 2019;215:488-496. <https://doi.org/10.1016/j.jclepro.2019.01.097>
- [11] Luo AA. Recent advances in light metals and manufacturing for automotive applications. CIM Journal. 2021;12(3):79-87. <https://doi.org/10.1080/19236026.2021.1947088>
- [12] Davis JR. Alloying: Understanding the Basics. ASM International; 2001. <https://doi.org/10.31399/asm.tb.aub.9781627082976>
- [13] Saraçyakupoğlu T. Failure analysis of J85-CAN-15 turbojet engine compressor disc. Engineering Failure Analysis. 2021;119(104975). <https://doi.org/10.1016/j.engfailanal.2020.104975>

- [14] Saracıyapupoğlu T. Fracture and failure analysis of the trainer aircraft rudder pedal hanger. *Engineering Failure Analysis*. 2021;122(105254). <https://doi.org/10.1016/j.engfailanal.2021.105254>
- [15] Guan Q, Hang C, Li S, Yu D, Ding Y, Wang X, Tian Y. Research progress on the solder joint reliability of electronics using in deep space exploration. *Chinese Journal of Mechanical Engineering*. 2023;36(22):1-13. <https://doi.org/10.1186/s10033-023-00834-4>
- [16] Kaiser MS. Effect of trace impurities on the thermoelectric properties of commercially pure aluminium. *Materials Physics and Mechanics*. 2021;47(4):582-591.
- [17] Davim JP. *Tribology for Engineers: A Practical Guide*. Elsevier Science; 2011. <https://doi.org/10.1533/9780857091444>
- [18] Katiyar JK, Ruggiero A, Rao TVVLN, Davim JP. *Industrial Tribology*. CRC Press, Taylor & Francis; 2022. <https://doi.org/10.1201/9781003243205>
- [19] Zhu M, Gao Y, Chung CY, Che ZX, Luo KC, Li BL. Improvement of the wear behaviour of Al-Pb alloys by mechanical alloying. *Wear*. 2000;242(1-2):47-53. [https://doi.org/10.1016/S0043-1648\(00\)00397-5](https://doi.org/10.1016/S0043-1648(00)00397-5)
- [20] Liu X, Zeng MQ, Ma Y, Zhu M. Wear behavior of Al-Sn alloys with different distribution of Sn dispersoids manipulated by mechanical alloying and sintering. *Wear*. 2008;265(11-12):1857-1863. <https://doi.org/10.1016/j.wear.2008.04.050>
- [21] Kaiser MS. Trace impurity effect on the precipitation behaviour of commercially pure aluminium through repeated melting. *European Journal of Materials Science and Engineering*. 2020;5(1):37-48. <https://doi.org/10.36868/ejmse.2020.05.01.037>
- [22] ASTM G99-05, Standard Test Method for Wear Testing with a Pin-on-Disk Apparatus. American Society for Testing and Materials; 2010.
- [23] Khan AA, Kaiser MS. Wear Studies on Al-Si Automotive Alloy under Dry, Fresh and Used Engine Oil Sliding Environment. *Research on Engineering Structures and Materials*. 2023;9(1):1-18. <https://doi.org/10.17515/resm2022.505ma0816>
- [24] McAlister AJ. The Al-Pb (Aluminum-Lead) system. *Bulletin of Alloy Phase Diagrams*. 1984;5:69-73. <https://doi.org/10.1007/BF02868728>
- [25] McAlister AJ, Kahan DJ. The Al-Sn (Aluminum-Tin) System. *Bulletin of Alloy Phase Diagrams*. 1983;4:410-414. <https://doi.org/10.1007/BF02868095>
- [26] Xu P, Luo H, Li S, Lv Y, Tang J, Ma Y. Enhancing the ductility in the age-hardened aluminum alloy using a gradient nanostructured structure. *Materials Science and Engineering: A*. 2017;682:704-713. <https://doi.org/10.1016/j.msea.2016.11.090>
- [27] Ard PM, Uthaisangsuk V, Tosangthum N, Sheppard P, Wila P, Tongsri R. Fe-Sn Intermetallics Synthesized via Mechanical Alloying-Sintering and Mechanical Alloying-Thermal Spraying. In *Key Engineering Materials*. 2015;659:329-334. <https://doi.org/10.4028/www.scientific.net/KEM.659.329>
- [28] Kaiser S, Kaiser MS. Comparison of wood and knot on wear behaviour of pine timber. *Research on Engineering Structures and Materials*. 2020;6(1):35-44. <https://doi.org/10.17515/resm2019.115ma0207>
- [29] Baser E, Incesu A, Sismanoglu S, Gungor A. Wear performance investigation of AlSi8Cu3Fe aluminum alloy related to aging parameters. *Research on Engineering Structures and Materials*. 2019;5(2):99-105. <https://doi.org/10.17515/resm2018.64is0829>
- [30] Prabhudev MS, Auradi V, Venkateswarlu K, Siddalingswamy NH, Kori SA. Influence of Cu Addition on Dry Sliding Wear Behaviour of A356 Alloy. *Procedia Engineering*. 2014;97:1361-1367. <https://doi.org/10.1016/j.proeng.2014.12.417>
- [31] Archard JF. Contact and rubbing of flat surfaces. *Journal of Applied Physics*. 1953;24:981-988. <https://doi.org/10.1063/1.1721448>
- [32] Duan XY, Li JR, Chang LM, Yang CW. A comparison of electrochemical oxidation performance of PbO<sub>2</sub> and SnO<sub>2</sub> electrodes. *Journal of Water Reuse and Desalination*. 2016;6(3):392-398. <https://doi.org/10.2166/wrd.2016.150>

- [33] Farooq SA, Raina A, Haq MIU, Anand A. Corrosion Behaviour of Engineering Materials: A Review of Mitigation Methodologies for Different Environments. *Journal of The Institution of Engineers (India): Series D*. 2022;103:639-661. <https://doi.org/10.1007/s40033-022-00367-5>
- [34] Kaiser MS, Sabbirb SH, Rahman M, Kabir MS, Nur MA. Effect of Fe, Ni, and Cr on the Corrosion Behaviour of Hyper-eutectic Al-Si Automotive Alloy in 3.5% NaCl Solution at Different Temperature and Velocity. *Journal of Mechanical Engineering, The Institution of Engineers, Bangladesh*. 2018;48(1):11-17. <https://doi.org/10.3329/jme.v48i1.41083>
- [35] S. Dhanasekaran and R. Gnanamoorthy. Dry sliding friction and wear characteristics of Fe-C-Cu alloy containing molybdenum di sulphide. *Materials and Design*. 2007;28(4):1135-1141. <https://doi.org/10.1016/j.matdes.2006.01.030>
- [36] Meyer WE., Walter JD. Frictional Interaction of Tire and Pavement, STP 793. American Society for Testing and Materials, USA.1983. <https://doi.org/10.1520/STP793-EB>
- [37] Davim JP. *Progress in Green Tribology: Green and Conventional Techniques*. De Gruyter; 2017. <https://doi.org/10.1515/9783110367058>
- [38] Moore, A. J. W., & Tegart, W. J. M. (1952). Relation between friction and hardness, *Proceedings of the Royal Society of London. Series A. Mathematical and Physical Sciences*, 212(1111), 452-458. <https://doi.org/10.1098/rspa.1952.0234>
- [39] X. Liu, M.Q. Zeng, Y. Ma, M. Zhu. Wear behavior of Al-Sn alloys with different distribution of Sn dispersoids manipulated by mechanical alloying and sintering, *Wear*, Volume 265, Issues 11-12, 2008, Pages 1857-1863. <https://doi.org/10.1016/j.wear.2008.04.050>
- [40] R. Tyagi, D. S. Xiong, J. Li and J. Dai. "Effect of load and sliding speed on friction and wear behavior of silver/h-BN containing Ni-base P/M composites. *Wear*, vol. 270, no. 7-8, pp. 423-430, 2011. <https://doi.org/10.1016/j.wear.2010.08.013>
- [41] Zmitrowicz A. Wear debris: A Review of properties and constitutive models. *Journal of Theoretical and Applied Mechanics*. 2005;43(1):3-35.
- [42] Kaiser MS, Qadir MR, Dutta S. Electrochemical corrosion performance of commercially used aluminum engine block and piston in 0.1M NaCl. *Journal of Mechanical Engineering*. 2015;45(1):48-52. <https://doi.org/10.3329/jme.v45i1.24384>
- [43] Kaiser MS, Matin MA, Shorowordi KM. Role of magnesium and minor zirconium on the wear behavior of 5xxx series aluminum alloys under different environments, *Journal of Mechanical and Energy Engineering*. 2020;4(3):209-220. <https://doi.org/10.30464/jmee.2020.4.3.209>
- [44] Rahman MM, Ahmed SR. Dry Sliding Friction and Wear of SnPb-Solder Affected Copper against Stainless Steel Counter Surface. *Iranian Journal of Materials Science and Engineering*. 2021;18(4):1-12.
- [45] Billur CA, Gerçekcioglu E, Bozoklu M, Saatçi B, Ari M, Nair F. The electrical, thermal conductivity, microstructure and mechanical properties of Al-Sn-Pb ternary alloys. *Solid State Sciences*. 2015;46:107-115. <https://doi.org/10.1016/j.solidstatesciences.2015.06.005>
- [46] Davim JP. *Wear of Advanced Materials*. John Wiley & Sons; 2013. <https://doi.org/10.1002/9781118562093>

## Effects of sugarcane bagasse ash as partial replacement of cement in the compressive strength and light transmissibility of Litracon blocks

Katherine E. Buenaflora<sup>a</sup>, Philip Jun S. Celerinos<sup>\*,b</sup>, Chris Julie P. Del Castillo<sup>c</sup>, Jay Marc R. Gala<sup>d</sup>, Katrina A. Sumatra<sup>e</sup>

Civil Eng. Dept., School of Engineering and Architecture, Ateneo de Davao University, Davao City, Philippines

### Article Info

### Abstract

#### Article history:

Received 02 Nov 2023

Accepted 15 Jan 2024

#### Keywords:

Compressive strength;  
Light transmissibility;  
Litracon blocks;  
Partial replacement;  
Sugarcane bagasse ash

Living up to a culture of sustainability and efficiency, the Light Transmitting Concrete or Litracon came to its prominence recently. Aside from that, the increase in the production of cement for building structures to facilitate various social dynamics has contributed to the world's exponentially increasing carbon emissions. Thereby, this study acts upon both phenomena by partially replacing the cement in the concrete mix for producing Litracon blocks using an agricultural waste material called Sugarcane Bagasse Ash or SCBA while aiming to improve their structural performance. The study used five (5) mix designs of 2.5%, 5%, 7.5%, and 10% replacements, and a controlled mix with no replacement. Three (3) cubic samples of 150 mm side dimension for each mix were subjected to the light transmissibility test before the compressive strength test. Results showed that the illumination values in lux of 103 to 120 were at par with the Philippine illumination guidelines for interior rooms, from 100 to 150. Moreover, the highest recorded compressive strength result with SCBA percentage replacement was the 5% design mix at 28.81 MPa, and the 2.5% design mix had the lowest recorded compressive strength of 23.51 MPa. The results further showed that even with no significant relationship between the percentage replacements and compressive strength values from the two-tailed T-test, no significant difference between such strength values was found using the One-way ANOVA test. Thus, this supports the claim that SCBA can partially replace the cement used for the concrete mix of Litracon blocks.

© 2024 MIM Research Group. All rights reserved.

## 1. Introduction

The world is recently aiming for producing innovative materials and practicing efficient energy consumption. Heeding such a call is an important step towards building a sustainable future. This is in line with the Sustainable Development Goal (SDG) 9 of the United Nations, which focuses on promoting the use of renewable sources, efficient use of energy, and reducing pollution, when it comes to constructing structures [1]. This is due to the need to create healthy environments and spaces upon which people can thrive and foster conducive areas of innovation for continuous social development. In this regard, Litracon has the potential to encapsulate what the SDG stands for. The Light Transmitting Concrete or Litracon is a concrete block with optic fibers that span its entire thickness. It can be stacked together as blocks that become a light-transmitting load-bearing partition, with the purpose of increasing the illumination of a room upon which it is contained. With

\*Corresponding author: [piscelerinos@addu.edu.ph](mailto:piscelerinos@addu.edu.ph)

<sup>a</sup> [orcid.org/0009-0007-6204-7954](https://orcid.org/0009-0007-6204-7954); <sup>b</sup> [orcid.org/0009-0009-3919-2357](https://orcid.org/0009-0009-3919-2357); <sup>c</sup> [orcid.org/0009-0008-0731-2433](https://orcid.org/0009-0008-0731-2433);

<sup>d</sup> [orcid.org/0009-0002-2767-4171](https://orcid.org/0009-0002-2767-4171); <sup>e</sup> [orcid.org/0009-0001-9885-8667](https://orcid.org/0009-0001-9885-8667)

DOI: <http://dx.doi.org/10.17515/resm2024.66ma1102rs>

Res. Eng. Struct. Mat. Vol. 10 Iss. 3 (2024) 973-994



this, it aims to reduce the amount of lighting and the resulting energy required to light up habitable spaces [2], [3].

Since this concrete block can reduce energy consumption, the study conducted by Navabi et al. [4] supported the idea of developing light transmitting concrete. Consequently, their study analyzed the light transmittance and energy efficiency of using Litracon blocks as partitions in structures that were built in some of the world's highly urbanized cities. Hence, the Canadian City of Vancouver has reported an almost 30% savings for structures with Litracon partitions compared to the global average. Similarly, the state capital of Arizona, USA, City of Phoenix and the capital of Iran, City of Tehran, despite being on opposite sides of the world, recorded an almost 46% reduction in electricity cost upon utilizing Litracon partitions compared to regular structures. These findings imply that Litracon supports the fulfillment of the aforementioned SDG by being an innovative construction material that promotes efficient energy consumption for illumination purposes.

Having recently been invented in the year 2001, the concrete block has left some gaps unaddressed, particularly in the need to improve its performance in terms of compressive strength. The study of Navabi [5] found that there was an inversely proportional relationship between the volume of optic fibers used and the resulting compressive strength. The addition of optic fibers reduced the compression area in which concrete showed greater resistance. Aside from that, various studies arrived at a consensus that calls for the improvement of the compressive strength of Litracon [6]-[8]. This is because it can be subjected to compressive stress when used as materials for exterior walls which carry loads from beams and slabs [9]. Hence, the conventional Litracon blocks can achieve a compressive strength of 15 MPa [10] or up to 19 MPa [11], which makes the block suitable only for use in architectural partition walls.

Moreover, since Litracon is composed of cement, the production of this block also aimed to lessen the cement usage in the construction industry, apart from attempting to solve the problem of excessive energy consumption from illumination. Various construction projects globally, particularly in the Philippines that used reinforced concrete structures, have been a common sight, which has led to an increase in cement production [12]. In an article by Mangi et al. [13], it was stated that cement production was accountable for almost 5% of the total metric tons of human-induced carbon dioxide pollution annually. This implied that for every ton of cement produced, a tenth of a ton of carbon dioxide was released. Given the essence of cement, it would be important to note that its production needs not to be eliminated; rather, there should be efforts to not contribute to its pollution.

In addressing the aforementioned problems, it is where the use of Sugarcane Bagasse Ash (SCBA) as partial cement replacement had been drawn from. In the province of Cotabato, Philippines, it has a thriving sugar industry that is also involved in tropical fruits, vegetables, and livestock. The province is hailed as Mindanao's Food Basket and is one of the major sugar-producing provinces in the Philippines [14]. Henceforth, the province is home to numerous sugarcane production facilities, where burning of the bagasse, from which sugarcane juice is extracted, is a necessary step to facilitate the reduction of such extracted concentration to produce raw sugar [15]. It was said that for every bagasse, the resulting volume of ash would be equivalent to around 8% of the original bagasse volume [16]. This in turn, leaves behind a lot of SCBA, which can consume valuable spaces and be harmful to the environment through polluting water bodies and affecting the air quality [17]. This has been a recurring concern for those facilities, especially the Philippine Department of Environment and Natural Resources (DENR) through its Solid Waste Management Act and Clean Water Act [18]. Thus, the problems implied the need for initiatives to lessen its accumulation while maximizing its use. For this reason, the study

came up with the idea of utilizing it to partially replace cement in the production of Litracon. Not only did it lessen the amount of cement to be used, but it also reduced the cost required to produce cement [15]. In addition, the pozzolanic nature of SCBA can be used as an advantage which improved Litracon blocks' structural performance.

One theory that supported the potentiality of using SCBA as partial cement replacement is its silica content and how it aids in the compressive strength performance of concrete. It can be noted that it consists of a lot of silica, which is an important component of cement that aided in binding the compositions of the concrete mix and created better bonds during the concrete hardening process. The use of SCBA was promoted in the study of Mangi et al. [13], wherein cylindrical concrete blocks having concrete mixtures with 5% and 10% replacements using SCBA, exhibited a better compressive strength performance compared to a regular concrete sample with no SCBA replacement. Another study by Hussien & Oan [19] revealed that the 5% cement replacement using SCBA for a cylindrical concrete block showed the optimum compressive strength that was beyond that of the controlled sample, as well as those with 7.5% and 10% replacements. Other studies, such as the one conducted by Bahurudeen et al. [20] used cubic samples of 150 mm side dimension with 5%, 10%, 15%, 20%, and 25% cement replacement percentages with SCBA. They found out that even with just marginal differences in compressive strength values, such differences were insignificant, which implied that concrete with SCBA can compete with the controlled sample.

Delving deeper into the performance of concrete blocks with SCBA replacements, another study by Garrett et al. [21] incorporated the SCBA with another pozzolanic material using Rice Husk Ash (RHA). It investigated the compressive strength of the samples when cured using seawater for 28<sup>th</sup> days and 6<sup>th</sup> months. Such a study found out that all samples, with 10%, 20%, and 30% replacements each of SCBA and RHA, exhibited minimal variance in terms of the resulting compressive strength. This meant that the controlled and uncontrolled samples have insignificant differences in the compressive strength. Also, the study of Kumar Reddy et al. [22] investigated the impact of sulfate attack for concrete blocks with SCBA as partial cement replacement by curing the samples in a 5% magnesium sulfate solution. It was found that the samples with SCBA fared better than the controlled sample in the compressive strength performance.

Contextualizing the idea in those existing literatures [13], [19]-[22], it can be implied that the use of SCBA for partial replacement of cement in Litracon blocks further enhanced the sustainability by lessening the use of cement. Hence, no partial replacement of cement in the existing studies pertaining to the concrete mix has been conducted to produce Litracon blocks. Thus, this study particularly sought to address the need to improve its compressive strength performance, from the conventional strength as specified in the study of Swain et al. [10] and Loganayagan et al. [11], since the SCBA is abundant in silica content and has a pozzolanic nature. This also lessened the buildup of agricultural waste that otherwise would have consumed valuable spaces, harmed surrounding ecosystems, and contributed to the exponentially increasing carbon emissions caused by the production of cement. Conversely, light transmissibility was further investigated to enhance the light transmittance considering the improvement of compressive strength of the Litracon block. Thus, it aspired to turn Litracon blocks into a more innovative and sustainable construction material that responded to the call for climate action to benefit the environment and people and helped the sugar industry deal with SCBA waste accumulation.

This present study aimed to determine the compressive strength and light transmissibility of Litracon blocks with partial replacement of cement using SCBA. The study specifically aimed to develop such blocks using five (5) cement replacement percentages by mass

which are 2.5%, 5%, 7.5%, and 10%, including 0% as controlled replacement using SCBA, which were subjected to compressive strength and light transmissibility tests. With those tests, the study determined the compressive strength and light transmissibility of the Litracon blocks, subsequently comparing the results with standard illumination ranges as per the Philippine Department of Energy guidelines [21]. It also discussed how optic fibers were bonded with the concrete mix and how their placement was secured through the Scanning Electron Microscopy (SEM) Interpretation. Lastly, the study also determined the significant difference in the results of the compressive strength test and their correlation through two (2) statistical tools, namely, One-way ANOVA (Analysis of Variance) and two-tailed T-test.

## 2. Methodology

### 2.1. Cement, Coarse Sand, Sugarcane Bagasse Ash, Plastic Optic Fiber, and Cubic Mold Materials

The quantity of materials, particularly cement and coarse sand, had adopted the mortar-based concrete ratio as concrete block samples in this study [24]. The design of Litracon blocks has uniform dimensions with a side measurement of 150 mm for all samples, as shown in Figure 1. The use of the 150 mm thickness followed the minimum architectural convention regarding the thickness of exterior and interior walls, which was the recommended use as a product of this study.



Fig. 1. Litracon samples before failure stage

Generally, Ordinary Portland Cement of grade 33 was used in making the Litracon samples for this study. It was commercially sourced from a local supplier in Tugbok District, Davao City, Philippines using bags that contain 40 kilograms (kg). To ensure the use of good quality cement, the test procedures included the determination of specific gravity through ASTM C188 [25] and unit weight through ASTM C138 [26]. It was carried out at the laboratory of the Civil Engineering Department at Ateneo de Davao University, Davao City, Philippines, wherein a unit weight of 1090 kilograms per cubic meter (kg/cu.m) and a specific gravity of 3.15 were found. Table 1 shows the properties of the Ordinary Portland Cement.

Table 1. Properties of ordinary portland cement

Materials	Grade	Weight (kg/bag)	Unit Weight (kg/cu.m)	Specific Gravity (SSD)
Cement	33	40	1090	3.15

The coarse sand aggregates were quarried from Matalam, Cotabato Province, Philippines. The purpose behind using this kind of aggregate was to explore its potential for being used in Litracon blocks. Most of the related literature pertaining to Litracon involved either the use of only fine sand for mortar-based ones [5], [6], [27] or fine sand and gravel [28] for structural concrete. Hence, this present study intended to contribute new knowledge by exploring the possibilities of using coarse sand for Litracon blocks. Apart from washing these aggregates, these test procedures were conducted to determine if the material was at par with ASTM standards in ensuring the production of good quality Litracon samples. The coarse sand material underwent tests which involved sieve analysis and fineness modulus with ASTM D2487 [29] as the reference standard, as well as specific gravity, water absorption, and unit weight based on the ASTM C128 [30]. The mentioned tests were performed at the laboratory of the Civil Engineering Department at Ateneo de Davao University, Davao City, Philippines. Table 2 shows the results of the conducted quality tests for coarse sand to determine its properties.

Table 2. Properties of coarse sand

Materials	Specific Gravity (SSD)	Unit Weight (kg/cu.m)	Water Absorption (%)	Fineness Modulus
Coarse Sand	2.80	27.47	1.43	6.30

The Sugarcane Bagasse Ash (SCBA), as shown in Figure 2, was sourced out from the Cotabato Sugar Central Company, Incorporated at the town of Matalam, Cotabato Province, Philippines. Similar to the coarse sand used in this study, this material also underwent test procedures to determine the specific gravity, unit weight, water absorption, and fineness modulus. Investigating those properties was of prime importance, as this material would be the main subject of this study. Besides, it is common knowledge in the field of Civil Engineering that cement also contains Silica, which usually ranges from a fifth to a quarter of its mass [24]. The study theorized that SCBA aided in introducing better bonds between the components of the concrete mix while the samples were being cured, as implied by the study of Bahurudeen et al. [20].



Fig. 2. Bagasse Ash used for this study

As previously discussed, a lot of studies have supported the use of SCBA to partially replace cement due to its Silica content and pozzolanic nature. Thereby, its silica content was also determined, and it was done using Gravimetry Analysis. The Gravimetry Analysis was performed in the Chemistry Analytical and Research Laboratory at Ateneo de Davao University, Davao City, Philippines, and the determination of SCBA properties was still

conducted in the Civil Engineering Laboratory at Ateneo de Davao University, Davao City, Philippines. The study of Norsuraya et al. [31] stated that the silica content of some agricultural waste materials such as SCBA typically ranged from 50% to 95%, but a 95% result was highly suggested for studies that aimed to take advantage of its silica content. However, this entailed burning them in a furnace to a thousand degrees Celsius (1000 °C) for four (4) hours, apart from outsourcing them as ashes from factories. With the study aiming to help the sugarcane industry in the Cotabato Province of the Philippines to eliminate the accumulation of SCBA, it was decided that the ashes would be outsourced as is. It did not undergo another type of process for this study to determine if such state of the SCBA would still be deemed enough to partially replace cement and act upon the accumulation of ashes. Table 3 shows the results of the properties of SCBA with 59.78% silica content.

Table 3. Properties of Sugarcane Bagasse Ash

Materials	Specific Gravity (SSD)	Unit Weight (kg/cu.m)	Water Absorption (%)	Fineness Modulus	Silica Content (%)
SCBA	2.14	21.02	366.67	2.95	59.78

Furthermore, optic fibers as light illumination materials were purchased from a local hardware store in Davao City, Philippines. The fibers used were 3 mm diameter, each measuring 200 mm in length, shown in Figure 3. With each sample containing 36 fibers, the total length used for one sample was 7.2 m. The use of 36 fibers was in accordance with the limitations set by this study regarding the percentage of fibers (POF) being limited to one percent of the sample's surface area. The excess length had been accounted for in this measurement, with the purpose of having an allowance for gripping them to eliminate potential sag and straightening them during concrete pouring and tamping. This also highlighted the reason behind using only 36 optic fibers per sample, as it made it easier to manage their placement inside the mold. The said excess length was cut with the use of a cable cutter after the samples were removed from their molds, being a variable of light transmissibility.

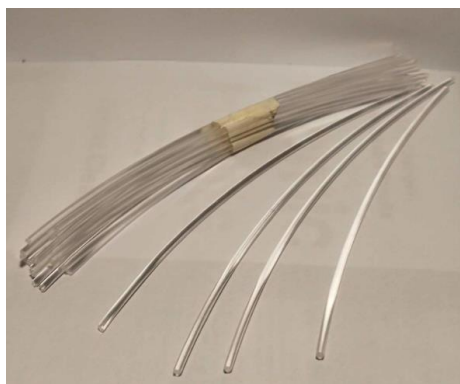


Fig. 3. Optic Fibers used for this study

The verification and legitimacy of the locally purchased optic fibers were supported by the Scanning Electron Microscopy-Energy Dispersive X-Ray or SEM-EDX Analysis. After samples were subjected to the compressive strength test, a portion of one of them was analyzed through a microscope. This was to have a detailed and magnified view as to how the optic fibers bonded with the concrete mix after it had reached the failure stage. Simultaneously, the elemental composition of the sample was determined while the SEM

images were being produced. The elements occupying each pixel were identified to determine their respective percentage. Of the entire image, 37.44% of it was identified as an element of optic fiber. Table 4 shows such composition, with the three rows showing elements that verified the legitimacy of the optic fibers procured for this study. The analysis was conducted in the Chemistry Analytical and Research Laboratory at the Ateneo de Davao University, Davao City, Philippines.

Table 4. Elements of optic fiber

Elements	App. Con	Intensity	Weight (%)	Weight (%) Sigma	Atomic Percent
Fluorine (F K)	332319.50	0.2013	44.25	1.35	36.54
Aluminum (Al K)	11170.29	0.6598	0.45	0.05	0.26
Silicon (Si K)	32979.42	0.7702	1.15	0.07	0.64

Lastly, the Litracon samples were of uniform dimensions, with a side dimension of 150 mm and were molded in a half-of-an-inch thick phenolic board, as shown in Figure 4. Using such material for casting the concrete mix for this study provided a smooth surface for the blocks produced. Since Litracon blocks were stacked into partitions, plumbness or straightness was achieved when the blocks were mortared and installed by adhesion. Furthermore, compared to other ordinary casting materials, its durability and moisture resistance make a good formwork material to ensure that no external factors can affect the concrete block hardening process [32].



Fig. 4. Molds using phenolic board

## 2.2. Litracon Block Samples and Design Mixtures

This study produced twenty (20) Litracon blocks, which were then grouped into five (5) based on the design mixtures. To determine the structural performance of each design mixture, three (3) repetitions of tests were conducted [32]. Additionally, the researchers included one (1) extra sample for each design mix, as a precaution in case any samples from the three (3) test repetitions were exposed to unforeseen conditions. Thus, of the 20 samples, only fifteen (15) were subjected to the tests and statistical analysis. Moreover, the design mixture used in every Litracon block employed a 1:2 ratio of cement-coarse sand materials. This ratio was based on class-A mortar-based concrete with a mix ratio of one part cement to two parts coarse sand. This study used 0.45 water-cement (W/C) ratio for every volume of concrete block sample in each design mixture [24], as shown in Table 5.

Table 5. Quantities and Ingredients of Litracon Block

Mix Designs	Volume (m <sup>3</sup> )	W/C Ratio	Water (kg)	Cement (kg)	Coarse Sand (m <sup>3</sup> )	SCBA (kg)	Optic Fibers (m)
Control Mix (0% SCBA)	0.003375	0.45	1.094	2.43	0.003375	0	7.2
Design Mix - A (2.5% SCBA)	0.003375	0.45	1.094	2.369	0.003375	0.0675	7.2
Design Mix - B (5% SCBA)	0.003375	0.45	1.094	2.308	0.003375	0.1215	7.2
Design Mix - C (7.5% SCBA)	0.003375	0.45	1.094	2.248	0.003375	0.1822	7.2
Design Mix - D (10% SCBA)	0.003375	0.45	1.094	2.187	0.003375	0.243	7.2

This study employed five (5) varied replacement percentages of cement based on its mass. The following were 2.5%, 5%, 7.5%, and 10%; however, the design mixture also included 0% replacement as controlled design mixture. In the study of Mangi et al. [13] and Hussien & Oan [19], the percentages ranged from 0% to 10%, with the 5% sample exhibiting the optimum compressive strength. For this reason, this present study wanted to investigate the results if a 2.5% increment would be implemented, hence the inclusion of the 2.5% and 7.5% replacement percentages. Moreover, tap water that was free from objectionable matter was used to mix the dry materials of Litracon blocks. The partial cement replacement took place by subtracting the percentage to be replaced by SCBA. Also in Table 5 were the calculated quantities of design mixtures used for each one (1) concrete block sample which also considered the multipliers to quantify each mixture. The volume of the sample was taken as the volume of the coarse sand used while the multiplier of 18 and the 40-kilogram constant were multiplied with the volume to get the required mass for cement.

**2.3. Litracon Blocks Making, Curing Procedure, and Series of Tests**

*2.3.1. Production of Litracon Blocks and Workability Test*

After preparing all the materials needed to make Litracon blocks, the sample-making process proceeded by following all the provided design mixtures listed in Table 5. Subsequently, all the materials were mixed and blended in a 500-liter capacity one-bagger mixer. Generally, the mixing process of concrete involved blending the bagasse ash with cement and coarse sand based on its percentage of replacement, which was often added to make a uniform and cohesive mixture. All samples were produced in only one (1) batch of mixture for each design mix to ensure adequate results for the series of tests conducted. The sample-making was performed at Tugbok District, Davao City, Philippines.

Thereafter, each batch of mixes after mixing all materials was subjected to the slump test in compliance with the ASTM C143 [33] to determine its workability. Once the workability in each design mixture was determined, the mixes were poured onto their respective molds, shown in Figure 5. The samples were then left undisturbed for twenty-four (24) hours before being submerged in a water bath for curing, which lasted for twenty-eight (28) days. The curing procedure was in accordance with ASTM C31 [33], and all samples were submerged in a curing pond where the sample-making was conducted.



Fig. 5. Samples casted on the molds

### 2.3.2. Light Transmissibility Test

When the curing period for the 28<sup>th</sup> day was over, samples were tested for light transmissibility before they were subjected to the compressive strength test. This study adopted the light transmissibility test performed in the study of Tahwia et al. [34]. In this test, the illumination values in lux were recorded using a lux meter, as presented in Figure 6. The study tested the light transmissibility of one (1) sample per percentage replacement of Litracon block and compared it to the standard illumination ranges provided by the Department of Energy (DOE) illumination guidelines in the Philippines [23].

A clear image of the entire setup has not been captured because it was conducted in a dark area for accurate results. With this, Figure 7 is presented to show the setup of the light transmissibility test, which was performed in Tugbok District, Davao City, Philippines. In the study conducted by Tahwia et. al [34], about the translucent self-compacting concrete (TSCC), Litracon block samples were subjected to light transmittance test using a Light-Dependent Resistor (LDR) setup as an electrical circuit to measure the current corresponding to the total amount of light passing throughout the specimens. The electrical circuit was set with a 100-ohm resistance and a uniform DC voltage of ten volts (V), but only in the event of voltage variation did the 10V uniform voltage had become 20V and 30V, respectively. Three (3) incandescent lights with wattages (W) of 9W, 20W, and 35W were placed in the middle of each Litracon block sample to demonstrate the fluctuation in light source to attain the desired degree of light intensity. In this present study, a lux meter was used to measure the intensity of light transmittance.



Fig. 6. Lux meter used for the Light Transmissibility Test



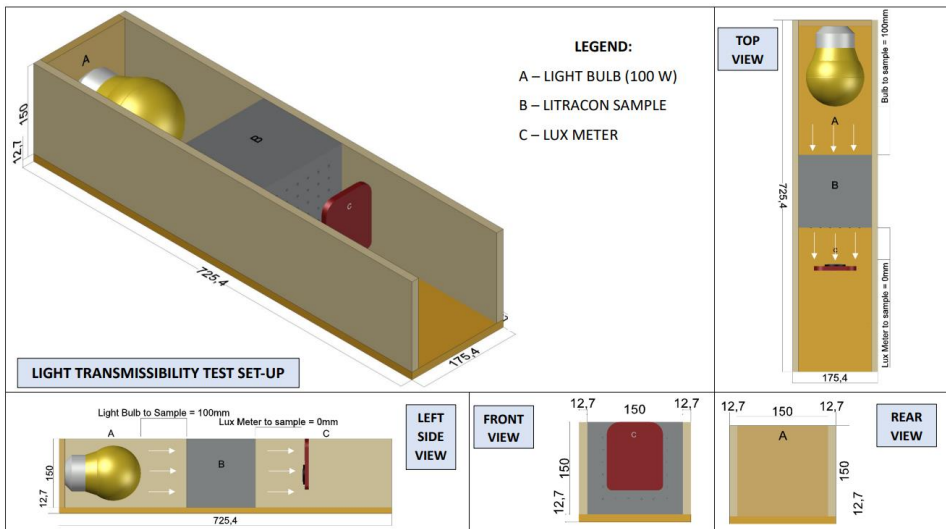


Fig. 7. Illustration of the Light Transmissibility Test setup

It is important to note that a reference standard cannot be found when it comes to this specific test, which is why this study resorted to following the setup of the study by Tahwia et al. [34]. Hence, such setup was set forth for optimum light transmittance during light transmissibility test. Furthermore, the dimensions were restricted to encapsulate the sample, light bulb, and lux meter only. It was made out of phenolic board of the same thickness similar to the formwork material molds used to cast the samples. The actual setup is presented in Figure 8.



Fig. 8. Light transmissibility test setup without the sample, cover, and lux meter

To commence the test, the researchers placed each sample 100 mm from the light source as presented in Figure 9. Afterwards, the sample was covered with another phenolic board, leaving a small hole to insert the lux meter, and recorded the reading when the values have no longer fluctuated. With this, the test needs not to be conducted at a time or place with lighting that can be deemed sufficient to affect the readings from the lux meter. Thereby, the test took place in a dark area at night, around 7 in the evening, with the hole for inserting the lux meter further covered with paper and cloth to eliminate the passage of external light rays that would have otherwise affected the data.



Fig. 9. Light transmissibility test setup without the sample, cover, and lux meter

The results were then compared to the standard illumination ranges by the DOE [23]. However, no statistical analysis was conducted to interpret the results apart from indicating upon which range of values the obtained results fall onto for certain occupancy types such as exterior rooms, tropical public spaces, and interior rooms. The reason behind was that the optic fiber in every sample remained constant, and no variation was made to produce the Litracon blocks in this present study. Moreover, a study about Litracon could not be completed without conducting a light transmissibility test, as its light transmittance was its essence, which made it unique among other types of blocks used for constructing structural partitions.

### 2.3.3. Compressive Strength Test

After conducting the light transmissibility test, the compressive strength test for each sample was then followed to determine the compressive structural performance of each design mixture. With the recent invention of Litracon in the year 2001, a reference specification for testing its compressive strength was yet to be standardized. The relevant studies cited to have either adopted their country's national standard [35] or used the testing procedures by widely accepted standards such as ASTM C39 [36] and ASTM C109 [8], [37]. In this study, the samples were of uniform measurements with 150 mm side dimension in accordance with IS 516-1959 [38] to conform to the minimum requirement for exterior structural partitions [24]. Thus, the compressive strength test conformed to the procedure outlined in ASTM C109, but the dimensions were in accordance with IS 516-1959. This test was executed at AC JOYO Design and Technical Services in Davao City, Philippines.

### 2.3.4. Scanning Electron Microscopy (SEM) Interpretation

The Scanning Electron Microscopy (SEM) Interpretation was conducted subsequent to the compressive strength test, where the samples underwent failure. This was meant to demonstrate the placement of the optic fibers and their binding capability with other components of the concrete mix. High-resolution images were provided and interpreted thereafter. The sample with high compressive strength result was selected for further evaluation through SEM analysis. Hence, a small-sized specimen was cut, shown in Figure 10, and the optic fiber was exposed to analyze the bond characteristic within the concrete mix. The standard area of the specimen for SEM Analysis ranges from approximately 1 cm to 5 microns in width, and the specimen was obtained from the samples with the optimum percentage for replacing cement with SCBA. The result was done and interpreted, wherein no parameters were measured or compared, but the images were presented to understand the sample's mode of failure. This test was conducted in the Chemistry Analytical and Research Laboratory at the Ateneo de Davao University, Davao City, Philippines.

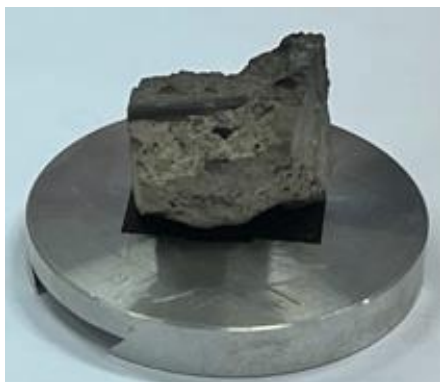


Fig. 10. Portion of the Sample for SEM-EDX Analysis

## 2.4. Statistical Analysis

The study utilized two (2) statistical tools to evaluate the response of the variables considered. The two-tailed T-test and the One-way Analysis of Variance (ANOVA) were employed with 95% confidence level ( $p < 0.05$ ). For the T-test, the means of the resulting compressive strength results as dependent variable for all design mixtures, as well as their corresponding slump measurement as dependent variable, were compared vis-a-vis the partial cement replacement percentages as independent variable in the design mixture. This test determined whether there is a significant relationship, or there is no significant relationship between the former mentioned dependent variable, and the latter mentioned independent variable. In contrast, for the One-way ANOVA test, it determined if there is a significant difference between the results obtained after all samples were subjected to the compressive strength test.

The T-test formulated two hypotheses in this study. First, the null hypothesis, which stated that there is no significant relationship between the partial cement replacement percentages versus the slump measurement and compressive strength results. Second, the alternative hypothesis, which connoted a significant relationship between those variables. For the One-way ANOVA, the null hypothesis is that there is no significant difference between the compressive strength values, while a significant difference is anticipated for the alternative hypothesis. The statistical analysis was accomplished using the IBM® SPSS® statistics software version 22.0 [39] at the University Information Technology Office in Ateneo de Davao University, Davao City, Philippines.

## 3. Results and Discussion

### 3.1. Workability of Design Mixtures

The parameter used to describe the workability of the design mixtures tested in this study was the slump distance in accordance with ASTM C143 [33], with the exception that no coarse aggregate was used in the concrete mix. Table 6 shows the results of the slump test conducted, wherein an increased slump distance was observed as the percentage replacement also increased. The highest value was obtained for the 10% mix design with a slump distance of 6.8 inches. On the other hand, the lowest slump distance was recorded of 2 inches by the controlled mix.

Table 6. Results of the slump test

Mix Designs	Slump Distance (in.)
Control Mix (0% SCBA)	2.00
Design Mix-A (2.5% SCBA)	3.70
Design Mix-B (5% SCBA)	4.50
Design Mix-C (7.5% SCBA)	6.60
Design Mix-D (10% SCBA)	6.80

It was important to note that the results of the slump test were within the limits set forth by ASTM C143 [33]. Regardless of the type, it must neither have too high nor too low slump values, as the compressive strength was inversely proportional to the workability. However, the need for a workable concrete was necessary in this study for the samples to be easily placed and avoid segregation, which attained the desired design strength. For this reason, the slump distance of 2 inches was within the standard limit, which meant that despite being the least workable among the other design mixtures, it still satisfied the need to be easily molded. Similar to that of the 10% mix design with a slump distance of 6.8 inches, it was still covered by the upper limit set forth by the reference standard. It was the most workable, yet it was not to the point that the components of the concrete mix became segregated.

With the results presented in the same table, it can be interpreted that there was a directly proportional relationship between the slump values and the replacement percentages. It was observed that an increase in cement replacement by SCBA had led to a concrete mix that became consolidated and properly placed without segregation while the samples were being cured. The obtained slump values ranged from 2 inches to 6.8 inches and were within the limits of the reference standard. It can be interpreted that all samples, regardless of the design mixture, exhibited the required plasticity and cohesion while they were being poured onto their respective molds.

It was also discussed in the study of Mangi et al. [13] that the partial replacement of cement by SCBA decreased the necessary amount of moisture for the concrete mix. With this, as more SCBA was added to each design mixture, the friction between the components of the mix was minimized, which resulted in an entire mixture behaving more like a fluid. Thus, SCBA provided additional plasticity to the consistency of concrete, and the use of superplasticizers may not be necessary. In addition, the use of a 0.45 W/C ratio, as a constant ratio in all design mixes, also allowed for SCBA to increase the fluidity of the concrete mix, which resulted in a linear increase within the standard range. Thus, the results of the slump test for the workability of concrete used in the Litracon blocks in this study implied that the SCBA contributed to a workable concrete with a watery texture without resistance to shear stress or too stiff that would lead to the formation of honeycombs and air voids in concrete.

### 3.2. Compressive Strength of Litracon Blocks

Testing the durability of concrete on its compressive strength was an important parameter for the structural performance of the Litracon blocks, as discussed herein. In Table 7, it can be seen that for a 28<sup>th</sup>-day curing period, the highest strength was attained by the controlled mix with 29.18 MPa, closely followed by the 5% design mix with 28.81 MPa, and the least value was achieved by the 2.5% design mix with 23.51 MPa. It was found that the obtained compressive strength in all mixtures was above the conventional compressive strength of Litracon blocks from 15 MPa [10] to 19 MPa [11], which could be categorized as a partition wall for architectural use. It can also be observed that the obtained compressive strength results for all design mixtures in this study were above the minimum

requirement of 21 MPa (3000 psi) for structural concrete as per ACI 318 [40], considering that all Litracon blocks had no coarse aggregate in the design mix; hence it was classified as mortar-based.

Table 7. Results of the compressive strength test

Mix Designs	Sample 1 (MPa)	Sample 2 (MPa)	Sample 3 (MPa)	Average (MPa)
Control Mix (0% SCBA)	24.27	27.06	36.22	29.18
Design Mix-A (2.5% SCBA)	21.42	22.06	27.06	23.51
Design Mix-B (5% SCBA)	25.51	29.23	31.68	28.81
Design Mix-C (7.5% SCBA)	22.49	24.30	26.97	24.59
Design Mix-D (10% SCBA)	21.41	23.87	29.04	24.77

Although the 2.5% design mix exhibited the lowest compressive strength, it managed to attain such a minimum requirement and was still feasible for the concrete mix used to make Litracon blocks. Likewise, the 5% design mix, which was neither the lowest nor highest replacement percentage, exhibited the greatest strength among all mix designs with SCBA replacement. This also indicated that such a percentage was the optimum amount required to replace cement with SCBA for better structural performance in terms of compressive strength. Moreover, the average of all compressive strength per design mix can be understood that no relationship could be drawn from the results.

Noticeably, a differed results in the 0% to 5% samples can also be observed, while there was small variation for the remaining replacement percentages. The results indicated that regardless of whether or not a Litracon block has its cement component partially replaced by SCBA, it still performed as good as its controlled counterpart in terms of compressive strength. It might just be that smaller replacement percentages would have greater advantages in such a parameter, as indicated by Mangi et al. [13] and Hussien & Oan [19]. They mentioned in their respective studies that the 5% replacement exhibited the greatest compressive strength. Their findings were similar to the results of this study, with the only difference being that 5% was the optimum replacement percentage. However, both this present study and the mentioned studies observed a similar decreasing trend for replacement percentages greater than 5%. Hussien & Oan [19] have indicated that the sudden increase of compressive strength on the 5% replacement can be attributed to the pozzolanic interaction of the SCBA between the rest of the components of the concrete mix. They also mentioned that this pozzolanic interaction could be minimized for samples with SCBA replacement percentages greater than 5%. In the Litracon's compressive strength, Dos Henriques et al. [6] stated that the presence of voids in the optic fiber-concrete mix interface was accountable for the eminent compressive failure of Litracon blocks. They mentioned that the addition of optic fibers increased the air-void ratio around that interface.

Contextualizing those statements in the present study also indicated that the SCBA had contributed its pozzolanic ability to introduce pozzolanic interaction during the concrete hardening process. It may just be insufficient to strengthen the cementitious bonds in the optic fiber-concrete mix interface. Thus, it still presented a potential for increasing the compressive strength of any concrete mix for any purpose it may serve. Overall, these compressive strength values indicated that Litracon blocks with SCBA can be an effective partial cement replacement to lessen the amount of accumulated SCBA. Furthermore, understanding each sample's mode of failure mechanism showed similar patterns, as presented in Figure 11. As further noticed, the cracks primarily outlined the placement of the optic fibers. This was supported by the study of Dos Henriques et al. [6], wherein the first areas to crack were usually those that were near the optic fiber-concrete mix interface

due to the existence of microscopic air voids enveloping the optic fiber surface. As discussed in the compressive strength test results, the pozzolanic action contributed by SCBA was not enough to counteract such an effect.

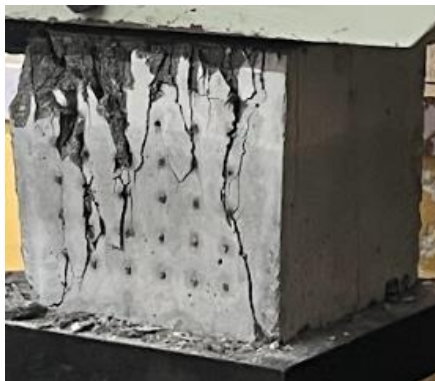


Fig. 11. Litracon block subjected to the compressive strength test

### 3.3. Light Transmissibility of Litracon Blocks

The results of the light transmissibility test were presented in Table 8, wherein a non-linear and inconclusive values were observed, similar to the results of the compressive strength test. Comparing them became irrational as the fiber optic was kept constant at 1%, with the 36 fibers on one sample placed in the same manner as in the other samples. Thus, results of little to no marginal differences were expected for this parameter. Hence, the obtained results ranged from 103 lux to 120 lux, which were interpreted by comparing them with the standard illumination ranges by the DOE [23]. Based on the guidelines, all the lux values for all samples were within the standard range of illumination. The minimum lux for open public spaces was 50 lux. On the contrary, for interior rooms, it ranged from 100 to 150 lux.

Table 8. Results of the light transmissibility test

Mix Designs	Luminance (Lux)
Control Mix (0% SCBA)	105
Design Mix-A (2.5% SCBA)	103
Design Mix-B (5% SCBA)	103
Design Mix-C (7.5% SCBA)	120
Design Mix-D (10% SCBA)	109

The results showed that the produced Litracon blocks can be good partitions for interior rooms since the results ranged from 103 to 120 lux. It can be noted that the lux meter was placed tangentially (Figure 7) to one sample's exterior surface to generate the readings. Since there was no reference standard for this test, using such a method of recording was deemed enough to represent the light transmissibility of the entire structural partition. Even though the light transmissibility results were not subjected to any statistical procedure, the marginal difference between the values obtained was deemed to be insignificantly different. It was highly attributed to the 1% configuration of optic fibers among all samples.

This marginal difference also indicated that the optic fibers of one sample transmitted light illumination in a similar manner as in the other samples, as demonstrated in Figure 12. Contrary to the study of Navabi et al. [4], sensors were used to record the light

transmittance and were placed in multiple areas, not just concentrated in one area that fronted one sample, as compared to the present study. Their light transmittance obtained from 300 lux to 1000 lux was greater compared to this present study, which ranged from 103 lux to 120 lux. Hence, their study also employed varying percentage of optic fiber (POF) ranging from 3% to 15%, compared to this study by only 1%. Nonetheless, this present study provided higher precedence on the structural performance of the compressive strength of the Litracon blocks while lessening the amount of cement to be utilized and acting upon the accumulation of SCBA simultaneously. However, this finding did not imply that the light transmissibility test results were obsolete, as conducting such a procedure would ensure that each produced Litracon block would not have eliminated its light-transmitting nature.

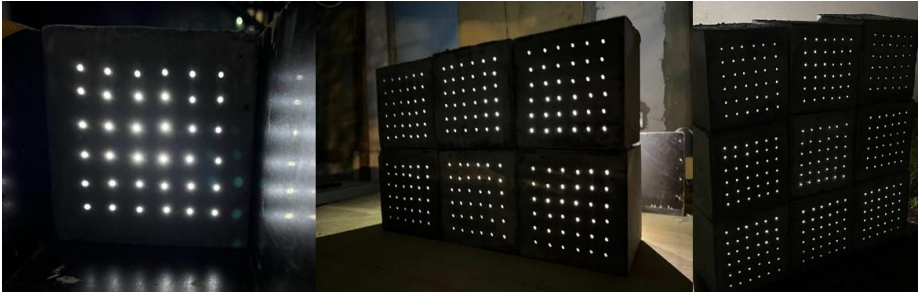


Fig. 12. Litracon block subjected to the compressive strength test

### 3.4. Interpretation between concrete and optic fiber

The Scanning Electron Microscopy (SEM) Interpretation was used to evaluate the microstructure of the concrete. This test was done after compressing the samples into failure during the compressive strength test. Thereafter, cracks were evident in the samples (Figure 11), and small specimens (Figure 10) were collected from these cracked areas for SEM analysis to investigate the bond between the concrete and optic fiber. Accordingly, it was the design mix with 5% SCBA that obtained the optimum compressive strength results for all design mixes with SCBA replacement.



Fig. 13. Micro image of bond between concrete and fiber optic

Interpreting the SEM images for this study involved coming up with inferences pertaining to what was seen in the optic fiber-concrete mix interface. In Figure 13, it showed that the optic fiber had a scratched texture due to the roughness of the concrete. These images demonstrated that the roughness between the fiber optic and the concrete bonded effectively, which obtained in all compressive strength results above the minimum standard for structural concrete. On the other hand, these results had no significant effect

on the optic fiber's light transmittance since the results of the light transmissibility test were within the standard range of illumination. Thus, it could still transmit light, considering the scratched texture defining its circumference.

Additionally, the surface area was negligible compared to the abundantly available volume of optic fiber in the Litracon blocks for transmitting light from one face to its opposite. Correspondingly, Figure 14 presented the optic fiber-concrete mix interface, which showed specks of concrete on the optic fiber's surface. The study interpreted this as evidence of some areas wherein concrete was bonded onto the optic fiber's surface. The contribution of SCBA's cement replacement to strengthening the cementitious bonds within that space was very prominent. This finding was also agreed in the study of Hussien & Oan [19]; however, the optic fiber-concrete mix interface provided minimal micro air voids, which potentially affected the compressive strength of the sample. Dos Henriques et al. [6] stated that achieving optimal concrete performance required minimal presence of air voids.

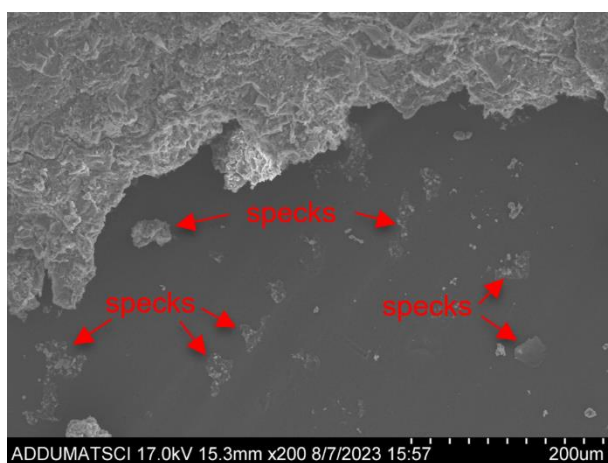


Fig. 14. Specks of concrete on the surface of optic fiber

The results herewith evidently adhered with minimal air voids, which achieved to all design mixes the best concrete performance on its compressive strength. Overall, the optic fibers have greatly provided a medium for transmitting light, which was also bonded on concrete with cement that was partially replaced with SCBA without compromising its integrity and effectiveness. Thus, Litracon blocks were not only aesthetically pleasing, but also a good construction material since there were no gaps or air voids produced when optic fibers and concrete bonded together.

### 3.5. Implications of the Obtained Slump and Compressive Strength Values

This section determined the true relationship between the incremental increase of cement replacement percentages by SCBA and the slump distance and compressive strength values, as well as the significant differences between the obtained results for both parameters. The IBM® SPSS® statistics software was used to determine the  $p$ -values and come up with a decision pertaining to the acceptance or rejection of the formulated hypotheses. Table 9 presented the results of the One-way ANOVA and T-test for the incremental increase of cement replacement percentages versus the slump values and compressive strength.

The  $p$ -value of 0.004 for the first comparison was obtained using the two-tailed T-test, which indicated that it was less than the significance level. Thus, there was a significant



relationship between the partial cement replacement percentages and the resulting slump distance. This supported the claim that the addition of SCBA led to higher values for slump. This was also expressed in the study of Hussien & Oan [19] about using sugarcane waste in concrete for cylindrical blocks. What this implied was that adding SCBA led to concrete mixes that were workable and able to be cast onto their molds without impeding segregation between the components of the mix itself.

Table 9. Implications of the Obtained Slump and Compressive Strength Values

Variables	$p$ -value vs. $\alpha$ -value	Remarks
T-Test for Workability Independent: SCBA Percentages Dependent: Obtained Slump Values	$p = 0.004$ $\alpha = 0.05$ $p < \alpha$ , reject the null hypothesis in favor of the alternative hypothesis	There is a significant relationship between the increasing cement replacement percentages with SCBA and the resulting slump distance.
T-Test for Compressive Strength Independent: SCBA Percentages Dependent: Compressive Strength	$p = 0.4281$ $\alpha = 0.05$ $p > \alpha$ , accept the null hypothesis	There is no significant relationship between the increasing cement replacement percentages with SCBA and the resulting compressive strength.
ANOVA for Compressive Strength Independent: SCBA Percentages Dependent: Compressive Strength	$p = 0.3289$ $\alpha = 0.05$ $p > \alpha$ , accept the null hypothesis	There is no significant difference between the resulting compressive strength values.

For the second comparison, the  $p$ -value of 0.4281 was attained, which indicated a greater value than the confidence level considering the two-tailed T-test. With this, there was no significant relationship between the partial cement replacement percentages and the resulting compressive strength. This supported the claim about the compressive strength results wherein a nonlinear and inconclusive trend could be drawn from the individual results indicated per cement replacement percentage. However, the same table also showed that a  $p$ -value of 0.3289 was obtained in the ANOVA, which also signified that there was no significant difference between the compressive strength values. This also further implied that the marginal differences between each compressive strength value supported the findings that the partial replacement of cement by SCBA would not significantly provide a huge difference on the attained compressive strength on the structural performance of Litracon blocks.

#### 4. Conclusions and Recommendation

The use of SCBA as a partial cement replacement percentage with optic fibers to produce Litracon blocks shows an optimum compressive strength of 28.81 MPa for the 5% design mix. The lowest compressive strength value was attained in the 2.5% design mix of 23.51 MPa. However, all samples were able to achieve above the minimum specified compressive strength of concrete on the 28<sup>th</sup> day of curing despite not being classified as structural concrete. The results of this study support the idea that using SCBA as partial cement replacement would entail reasonable compressive strength results not just for Litracon blocks but for other structures as well. These findings can also serve as a benchmark for enhancing the compressive strength of Litracon blocks by partially replacing the cement

with bagasse ash by burning the bagasse at higher temperatures to achieve 95% pozzolanic materials. Hence, this study only utilized 59.78% silica content of the bagasse ash and has not been conducted to use SCBA with silica content greater than 95%. In addition, it is recommended to open the possibility for further research regarding the use of other pozzolanic agricultural waste materials.

Moreover, the SEM analysis further exhibited that the optic fiber-concrete mix interface had evidently provided an adequate bond, which strengthened the idea that SCBA, as a partial cement replacement, is effective. However, considering the results of the compressive strength, the design mixes have not affected the light transmissibility performance of Litracon blocks since the results have ranged from 103 lux to 120 lux and are within the standard range. The results of this study indicate further that Litracon blocks can be used as a good partition wall, achieving more than the required structural strength for load-bearing blocks. Hence, this result is beneficial to the construction industry by using this block without sacrificing the light transmissibility results. Also, the Litracon block in this study is capable of illuminating lights in living spaces within the Philippine Standard. Similarly, the resulting illumination values from the light transmissibility test fall under the range of illumination guidelines; this study can also be a benchmark for other researchers to explore different methods and mechanisms to better actualize the light-transmitting nature of Litracon blocks.

Overall, this study promoted the use of agricultural waste to produce a structural partition which also aided in the required illumination and energy consumption of habitable spaces. The aim to fulfill the mission of one of the United Nations' SDGs, which is about the innovative infrastructure and materials for construction, has been fulfilled by this study. This is because it produced a concrete block for structural partitions that aided in lessening the accumulation of SCBA. This is particularly important given that the material is a byproduct of the sugar industry in Matalam, Cotabato Province, Philippines, and is otherwise considered as an agricultural waste. By partially replacing cement with bagasse ash, this study shows promising results in terms of reducing both waste and energy consumption while also improving the compressive strength of Litracon blocks. In addition, it can be understood that reducing the use of cement promotes the sustainability of construction materials by dealing with accumulated agricultural waste such as sugarcane bagasse ash. Lastly, this study hopes that further research will be conducted to take advantage of other agricultural waste while building sustainable communities that foster places of innovation and thriving cultures around the world.

### **Acknowledgement**

The researchers would like to acknowledge the different laboratory testing centers, the University Information Technology Office, and the Civil Engineering Department at Ateneo de Davao University.

### **References**

- [1] Lyonsdown. Sustainable development goals, and the construction industry. 2020 Oct 19. <https://17globalgoals.com/sustainable-development-goals-and-the-construction-industry/>. Access Date: 2023 Jan 31.
- [2] Altomate A, Alatshan F, Mashiri F, Jadan M. Experimental study of light-transmitting concrete. *Int J Sustainable Build Technol Urban Dev*. 2016;7(3-4):133-139. <https://doi.org/10.1080/2093761X.2016.1237396>
- [3] Ravivarman S, Mageswari M, Kanagalakshmi AS. Experimental Study of Litracon. *IOSR J Mech Civ Eng*. 2015;12(6):7-13. <https://doi.org/10.9790/1684-12610713>

- [4] Navabi D, Amini Z, Rahmati A, Tahbaz M, Butt TE, Sharifi S, et al. Developing light transmitting concrete for energy saving in buildings. *Case Studies in Construction Materials*. 2023 Jul;18:e01969. <https://doi.org/10.1016/j.cscm.2023.e01969>
- [5] Navabi D, Javidruzvi M, Hafezi MR, Mosavi A. The high-performance light transmitting concrete and experimental analysis of using polymethylmethacrylate optical fibers in it. *J Build Eng*. 2021. <https://doi.org/10.1016/j.jobbe.2020.102076>
- [6] Henriques Tdos, Dal Molin DC, Masuero B. Optical fibers in cementitious composites (LTCM): Analysis and discussion of their influence when randomly arranged. *Constr Build Mater*. 2020;244:118406. <https://doi.org/10.1016/j.conbuildmat.2020.118406>
- [7] Li Y, Li J, Guo H. Preparation and study of light transmitting properties of sulfoaluminate cement-based materials. *Mater Des*. 2015;83. <https://doi.org/10.1016/j.matdes.2015.06.021>
- [8] Ahmed Salih S, Hamodi Joni H, Adnan Mohamed S. Effect of Plastic Optical Fiber on Some Properties of Translucent Concrete. *ETJ*. 2014 Nov 1;32(12):2846-61. <https://doi.org/10.30684/etj.32.12A.1>
- [9] Chiew SM, Ibrahim IS, Mohd Ariffin MA, Lee H, Singh JK. Development and properties of light-transmitting concrete (LTC) - A review. *Journal of Cleaner Production*. 2021 Feb;284:124780. <https://doi.org/10.1016/j.jclepro.2020.124780>
- [10] Swain C, Moharana R, Dash A, Hrudayjeet P, Sahoo C. Transparent Concrete (LiTraCon). *IJRASET*. 2022 May 31;10(5):874-80. <https://doi.org/10.22214/ijraset.2022.42360>
- [11] Loganayagan S, Mohanraj A, Hariharan V, Praveen N. Experimental Study on Light Transmitting Concrete Using Plastic Optical Fiber. *Sustainable Materials and Smart Practices: NCSMSP-2021*. 2022 Jun 15;23:1. <https://doi.org/10.21741/9781644901953-1>
- [12] Crismundo K. Cement Industry Feeling 'build build build effect'. *Philippine News Agency*. 2018. <https://www.pna.gov.ph/articles/1048887>. Access Date: 2023 Jan 27.
- [13] Mangi SA, Jamaluddin N, Wan Ibrahim MH, Abdullah AH, Abdul Awal AS, Sohu S, Ali N. Utilization of sugarcane bagasse ash in concrete as partial replacement of cement. *IOP Conf Ser Mater Sci Eng*. 2017;271:012001. <https://doi.org/10.1088/1757-899X/271/1/012001>
- [14] Special Area for Agricultural Development. North Cotabato - Special area for agricultural development. [https://saad.da.gov.ph/priority\\_provinces/region-xii/north-cotabato](https://saad.da.gov.ph/priority_provinces/region-xii/north-cotabato). Access Date: 2023 Oct 25.
- [15] Memon SA, Javed U, Shah MI, Hanif A. Use of Processed Sugarcane Bagasse Ash in Concrete as Partial Replacement of Cement: Mechanical and Durability Properties. *Buildings*. 2022 Oct 21;12(10):1769. <https://doi.org/10.3390/buildings12101769>
- [16] Chindaprasirt P, Rattanasak U. Eco-production of silica from sugarcane bagasse ash for use as a photochromic pigment filler. *Sci Rep*. 2020;10(1). <https://doi.org/10.1038/s41598-020-66885-y>
- [17] World Wildlife Fund. Sugarcane farming's toll on the environment. <https://www.worldwildlife.org/magazine/issues/summer-2015/articles/sugarcane-farming-s-toll-on-the-environment>. Access Date: 2023 Oct 25.
- [18] Ranjo M. Legal procedures on environmental violations and cases. <https://weap-phil.org/wp-content/uploads/2023/02/2023-WEAP-LEGAL.pdf>. Access Date: 2023 Oct 25.
- [19] Hussien NT, Oan AF. The use of sugarcane wastes in concrete. *J Eng Appl Sci*. 2022;69(1). <https://doi.org/10.1186/s44147-022-00076-6>
- [20] Bahurudeen A, Kanraj D, Gokul Dev V, Santhanam M. Performance evaluation of sugarcane bagasse ash blended cement in concrete. *Cement and Concrete Composites*. 2015 May;59:77-88. <https://doi.org/10.1016/j.cemconcomp.2015.03.004>
- [21] Garrett TD, Cardenas HE, Lynam JG. Sugarcane bagasse and rice husk ash pozzolans: Cement strength and corrosion effects when using saltwater. *Current Research in*

- Green and Sustainable Chemistry. 2020 Feb;1-2:7-13. <https://doi.org/10.1016/j.crgsc.2020.04.003>
- [22] Nithin Kumar Reddy G, Vardhan GH, Bhaskar Reddy SV. Partial replacement of cement in concrete with sugarcane bagasse ash and its behaviour in aggressive environments. *IOSR J Mech Civ Eng.* 2016;16(53):29-35. <https://doi.org/10.9790/1684-16053012935>
- [23] Department of Energy Guidelines. [https://www.doe.gov.ph/sites/default/files/pdf/downloads/guidelines\\_cdbus.pdf](https://www.doe.gov.ph/sites/default/files/pdf/downloads/guidelines_cdbus.pdf). Access Date: 2023 Mar 31.
- [24] Fajardo M. *Simplified Construction Estimates*. 3rd ed. Quezon City: 5138 Merchandising; 2000.
- [25] Padhi S. Density test of hydraulic cement - ASTM C188. <https://civilblog.org/2015/10/14/density-test-of-hydraulic-cement-astm-c-188/>. Access Date: 2023 Oct 25.
- [26] Clason L. ASTM C138: Unit weight, yield, and gravimetric air content of concrete. <https://owlcation.com/humanities/ASTM-C138-Unit-Weight-Yield-and-Gravimetric-Air-Content-of-Concrete>. Access Date: 2023 Oct 25.
- [27] Henriques TdS, Dal Molin DC, Masuero ÂB. Study of the influence of sorted polymeric optical fibers (POFs) in samples of a light-transmitting cement-based material (LTCM). *Construction and Building Materials.* 2018 Feb;161:305-15. <https://doi.org/10.1016/j.conbuildmat.2017.11.137>
- [28] Shenoy A, Nayak G, Tantri A, Shetty KK, Shendkar MR. Annual Transmittance Behavior of Light-Transmitting Concrete with Optical Fiber Bundles. *Materials.* 2023 Nov 4;16(21):7037. <https://doi.org/10.3390/ma16217037>
- [29] Kelechava B. ASTM D2487 Unified soil classification system. <https://blog.ansi.org/2018/03/unified-soil-classification-astm-d2487-17/#gref>. Access Date: 2023 Oct 25.
- [30] TeamCivil. ASTM C128 Obtain specific gravity and absorption of fine aggregate. <https://www.civilengineeringforum.me/astm-c128-obtain-specific-gravity-and-absorption-fine-aggregate/>. Access Date: 2023 Oct 25.
- [31] Norsuraya S. Sugarcane Bagasse as a Renewable Source of Silica to Synthesize Santa Barbara Amorphous-15 (SBA-15). <https://doi.org/10.1016/j.proeng.2016.06.627>
- [32] Alsina. What is phenolic plywood for construction and what are its benefits. <https://www.alsina.com/en/what-is-phenolic-plywood-for-construction-and-what-are-its-benefits/>. Access Date: 2023 Oct 25.
- [33] Clason L. ASTM Standard Test Method C143: Slump of Hydraulic Cement Concrete. <https://owlcation.com/humanities/ASTM-C143-The-Concrete-Slump-Test>. Access Date: 2023 Feb 10.
- [34] Tahwia AM, Abdelaziz N, Samy M, Amin M. Mechanical and light transmittance properties of high-performance translucent concrete. *Case Studies in Construction Materials.* 2022 Dec;17:e01260. <https://doi.org/10.1016/j.cscm.2022.e01260>
- [35] Chiew SM, Ibrahim IS, Mohd Ariffin MA, Lee HS, Singh JK. Assessment of natural light transmittance of light-transmitting concrete incorporated with Plastic Optical Fibre: An experimental study. *SSRN Electronic Journal.* 2022. 4268889. <https://doi.org/10.2139/ssrn.4268889>
- [36] The Constructor. Compressive strength of concrete - cube test, procedure, results. <https://theconstructor.org/concrete/compressive-strength-concrete-cube-test/1561/>. Access Date: 2023 Oct 25.
- [37] Shenoy A, Nayak G, Tantri A, Shetty KK. Thermal transmission characteristics of plastic optical fibre embedded light transmitting concrete. *Materials Today: Proceedings.* 2022;65:1759-73. <https://doi.org/10.1016/j.matpr.2022.04.798>

- [38] Civil Allied Gyan. Cube test of concrete as per IS 516-1959. <https://www.civilalliedgyan.com/2020/03/compressive-strength-test-of-concrete-cube.html>. Access Date: 2023 Oct 25.
- [39] IBM. SPSS statistics for Windows. Version 22.0. Armonk, NY: IBM; 2013.
- [40] Lysett T. Concrete strength explained - cor-tuf. <https://cor-tuf.com/2022-everything-you-need-to-know-about-concrete-strength/>. Access Date: 2023 Oct 25.

## Impact of superabsorbent polymer on self-compacting concrete's workability, strength, carbonation and freezing-thawing

Venkateswarlu Kuruva<sup>\*a</sup>, Shirish V. Deo<sup>b</sup>, Meena Murmu<sup>c</sup>

Dept. of Civil Engineering, National Institute of Technology Raipur, India

### Article Info

#### Article history:

Received 09 Oct 2023  
Accepted 28 Dec 2023

#### Keywords:

Super absorbent polymer;  
Self-compacting concrete;  
Compressive strength;  
Flexural strength;  
Freezing - Thawing test;  
Carbonation;  
Scanning electron microscopy

### Abstract

Superabsorbent Polymer, an internal curing material, is a significant development in concrete technology. Self-compacting concrete is popular due to high flowability or pumpability. However, the higher quantity of cementitious materials required higher moisture consumption to complete the hydration. Further moisture unavailability leads to shrinkage increment. External curing cannot give proper moisture to cementitious material at higher depth. Hence, internal curing with super absorbent polymer is an economical solution for this problem. This study examines the impact of super absorbent polymer on the mechanical and durability properties of concrete. Laboratory tests were conducted to evaluate the workability, mechanical characteristics of the concrete, such as compressive strength and flexural strength. In addition, freezing-thawing tests and carbonation tests were conducted to investigate the durability performance of concrete. Scanning electron microscopy images were also used to observe the concrete's microstructure after freezing-thawing cycles. The findings demonstrate that Compressive strength and flexural strength values decreased in water curing while in air curing, those were increased. Additionally, it was discovered that the freezing-thawing cycles decreased the compressive strength of reference concrete in standard water curing. However, compressive strength increased after freezing-thawing cycles in air-curing super absorbent polymer mixes. Scanning electron microscopy images have confirmed that the microstructure of air-curing super absorbent polymer mixes was improved.

© 2024 MIM Research Group. All rights reserved.

## 1. Introduction

There are drawbacks to the external concrete curing method, including time requirements, resource waste, and subpar curing results. As a result, internally cured concrete technology is being developed gradually (1). Super absorbent polymer (SAP) is a macromolecular substance with strong water retention and super water absorption capabilities. It can effectively increase the volume stability of concrete and prevent issues like micro-cracks and shrinkage. The effect of SAP on the operating performance, mechanical performance, volume stability, and durability of concrete was investigated under low water-cement (w/c) ratio circumstances (2) (3). It was also feasible to ascertain how the SAP and curing age affected the distribution of concrete pores using 3D volume analysis (4). The evolution law was also studied, along with the effects of time-varying damage brought on by various internal curing agents, on concrete's macro and micro characteristics. Zhutovsky et al. (5) demonstrated about the same compressive strength (for 0.33 w/c) with pumice and a 10% drop in compressive strength for w/b of 0.21,0.25 concretes for low water binder concretes. Moreover, SAP reduces compressive strength during the early stages but

\*Corresponding author: [kvenkateswarlu.phd2018.ce@nitrr.ac.in](mailto:kvenkateswarlu.phd2018.ce@nitrr.ac.in)

<sup>a</sup> orcid.org/0000-0001-7712-8457; <sup>b</sup> orcid.org/0000-0003-3371-2082; <sup>c</sup> orcid.org/0000-0002-4509-9185  
DOI: <http://dx.doi.org/10.17515/resm2024.10ma1009rs>

Res. Eng. Struct. Mat. Vol. 10 Iss. 3 (2024) 995-1015

increases it later in life. As SAP content increases, compressive strength falls. This is the result of the breakdown of SAP leaving behind huge holes (6)–(7). In contrast, SAP has been shown in other experiments to progressively increase compressive strength above the control mix at 28 days (8). The compressive strength of SAP mixture samples is greater than that of the control mix even at later ages (9)(10). Due to the lengthier hydration of the higher cementitious material by SAP's entrained water, this benefit is likely greater in SCC. As mentioned earlier, the research has revealed that there is debate regarding the impact of SAP on concrete strength (11,12) and that SAP can significantly increase the durability (13)(14)(15). Aggressive ions are transported via the micro gaps that SAP creates, yet internal curing effect produces a denser microstructure and increases durability (1). Reinhardt et al. (3) also show that SAP enhances the resistance to water penetration and oxygen permeability. By increasing SAP dosage up to 0.6%, Benshausen et al. (13) verified that SAP can reduce carbonation depth and chloride ion penetration depth. Other researchers also noted that the increased hydration of the binder by SAP-released water resulted in a reduction of the carbonation depth and chloride penetration (1). To better understand how SAP affects concrete performance, the morphology of the hydrated product, pore structure, and mineral composition were considered.

Additionally, it was investigated (16–18) how the concrete's pore parameters affected the antifreeze performance. From a micro perspective, it was explained that SAP could increase the concrete's durability and resistance to frost (4) (17). When vapor-filled pores are created, the internal relative humidity of a sealed system decreases, a process known as self-desiccation (5). SAP enhances flexural joints' performance by preventing this self-desiccation (19).

Flowability of SCC has decreased by SAP in dry condition (20)(21). The impact of SAP depends on absorption of SAP, size of SAP, dosage of SAP on properties of self-compacting concrete (SCC). Nevertheless, further clarification is required because it is still being determined. Additionally, there have been few quantitative studies on how much SAP has improved the durability of concrete. It is also necessary to conduct more research on how SAP affects the flexural strength of concrete. More investigation is necessary to ascertain the extent and mechanism of the micro-pore features of SAP-influence concrete on compressive strength. More research is required on how freezing-thawing affects the internally cured concrete with SAP regarding mass loss and compressive strength loss. It also required to study how internally cured concrete affects the carbonation depth and microstructural changes, which caused the change in durability and strength.

This paper investigated the effect of SAP on Workability, freezing-thawing performance, carbonation depth, flexural strength, and compressive strength of SCC with three different curing regimes on internally cured SCC mixtures. Also, microstructural analysis was conducted on SCC samples which were collected after freezing-thawing testing. In addition, the internal curing effect of SAP on SCC made up of Portland Pozzolana Cement (PPC) and Portland Slag Cement (PSC) was studied.

The Novelty of the research is an attempt to solve inadequate curing problems in India's hot climate and improve the strength, durability, and microstructural properties of self-compacting concrete. This parametric study is to meet the shrinkage reduction, durability, compressive strength and flexural strength by SAP as an internal curing agent. A literature review has been done to search for suitable and effective internal curing agents for reducing the shrinkage problem of Self compacting concrete in high-temperature climates. The super absorbent polymer can give a solution to the reduction of shrinkage in self-compacting concrete and improper curing in hot weather conditions.

## 2. Experimental Program

### 2.1. Materials

The experimental study used PPC and PSC with specific gravities of 2.90 and 2.98, respectively. Table 1 displays the PPC and PSC's chemical compositions. The coarse aggregate was consisted of crushed granite with a maximum particle size of 10 mm and a specific gravity of 2.7. Sand from the Kharun River, with a specific gravity of 2.62, served as the fine aggregate. Concrete mixtures were mixed with tap water. The Superplasticizer Master Glenium 8632, manufactured by BASF, is based on polycarboxylate ether and contains a viscosity-modifying ingredient. It can ensure the workability of reference concrete with a 650 mm to 750 mm slump flow diameter by flow table test. The Superplasticizer has a specific gravity of 1.08. The chemical compositions of superabsorbent polymer (SAP, Innovative Agro India) were shown in Table 1. The bulk density of SAP is 0.65-0.80 g/cm<sup>3</sup>. SAP before and after water absorption is shown in Figure 1. Commercially available Sodium based Poly acrylate was used as super absorbent polymer. Water absorption capacities of SAP is 36g/g and 170g/g in cement solutions (prepared solution with w/c=5.0) and tap water respectively calculated by Tea bag method which was given by Schröfl et al. (18). Higher ionic concentration of Ca<sup>2+</sup>, Na<sup>+</sup> present in cement solution may decrease the water absorption of SAP. Hence SAP won't affect the concrete properties directly because it absorbs and desorb the water based on humidity conditions. Based on Bentz formula dosage of SAP calculated in the previous work (22). Theoretically, the amount of SAP required to achieve full hydration for 533.33 kg/m<sup>3</sup> cement is 0.219 kg/m<sup>3</sup>. Due to this the dosage of SAP starts from 0.05% cement which 0.27 kg/m<sup>3</sup> as shown in the Table 2.

Table 1. Chemical composition of PPC, PSC, and SAP

Components	CaO	SiO <sub>2</sub>	Al <sub>2</sub> O <sub>3</sub>	Fe <sub>2</sub> O <sub>3</sub>	MgO	SO <sub>3</sub>	Na <sub>2</sub> O + K <sub>2</sub> O	Na	O <sub>2</sub>	C
PPC	50.00	26.33	11.45	1.75	8.97	-	1.41	-	-	-
PSC	56.64	22.15	10.23	2.65	6.37	1.95	-	-	-	-
SAP	-	-	-	-	-	-	-	33.03	55.78	11.19

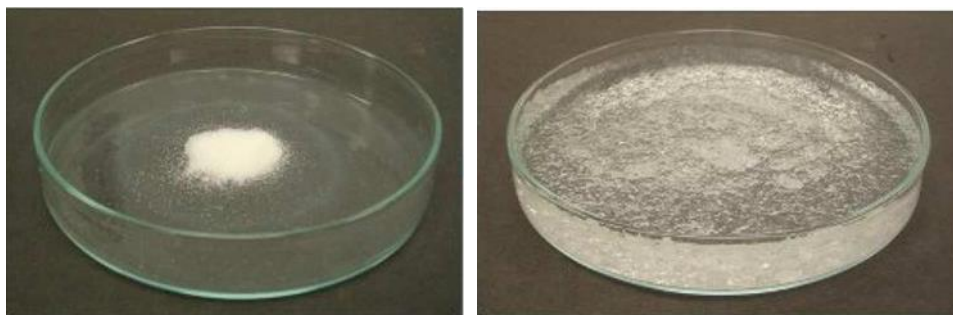


Fig. 1. Image of SAP before and after swelling by water absorption

### 2.2. Mix Proportion and Specimen Preparation

According to the IS 10262:2019 (23), the mix proportions of SCC were designed with PPC and PSC cement. PPC and PSC mix proportions are shown in Table 2 and Table 3, respectively. The w/c ratio of the reference concrete mixture varied from 0.30 to 0.40. P30, P35, and P40 are PPC mixes with 0.30, 0.35, and 0.40 w/c ratios, respectively. S30, S35, and S40 are the PSC mixes with 0.30, 0.35, and 0.40 w/c ratios, respectively. S0, S5, S10,



and S15 are the dosages of SAP at 0%, 0.05%, 0.10%, and 0.15% of cementitious materials, respectively.

Table 2. Mix proportions of PPC in kg/m<sup>3</sup>

Mixes	Cement	W/B	Water	Sand	Coarse aggregate	SAP	SP
P30-S0	533.33	0.3	160	863.33	821.26	0	8
P30-S5	533.33	0.3	160	863.33	821.26	0.27	8
P30-S10	533.33	0.3	160	863.33	821.26	0.53	8
P30-S15	533.33	0.3	160	863.33	821.26	0.8	8
P35-S0	471.43	0.35	165	886.77	843.55	0	7.1
P35-S5	471.43	0.35	165	886.77	843.55	0.24	7.1
P35-S10	471.43	0.35	165	886.77	843.55	0.47	7.1
P35-S15	471.43	0.35	165	886.77	843.55	0.71	7.1
P40-S0	425	0.4	170	902.65	858.66	0	6.4
P40-S5	425	0.4	170	902.65	858.66	0.21	6.4
P40-S10	425	0.4	170	902.65	858.66	0.43	6.4
P40-S15	425	0.4	170	902.65	858.66	0.64	6.4

Table 3. Mix proportions of PSC in kg/m<sup>3</sup>

Mixes	Cement	W/B	Water	Sand	Coarse aggregate	SAP	SP
S30-S0	533.33	0.3	160	870.06	827.65	0	8
S30-S5	533.33	0.3	160	870.06	827.65	0.27	8
S30-S10	533.33	0.3	160	870.06	827.56	0.53	8
S30-S15	533.33	0.3	160	870.06	827.56	0.8	8
S35-S0	471.43	0.35	165	892.72	849.21	0	7.1
S35-S5	471.43	0.35	165	892.72	849.21	0.24	7.1
S35-S10	471.43	0.35	165	892.72	849.21	0.47	7.1
S35-S15	471.43	0.35	165	892.72	849.21	0.71	7.1
S40-S0	425	0.4	170	908.01	863.76	0	6.4
S40-S5	425	0.4	170	908.01	863.76	0.21	6.4
S40-S10	425	0.4	170	908.01	863.76	0.43	6.4
S40-S10	425	0.4	170	908.01	863.76	0.64	6.4

Each specimen was cast, held indoors for 24 hours, and then molded with a number. Reference concrete and internal curing concrete specimens were cured using room air, Gunny bags, and normal water. Concrete specimens that were air-curing in the room were set up in the lab setting. In the process of gunny bag curing, specimens were covered entirely in wet gunny bags, and water was applied twice daily. The water-curing ponds held the conventional water-curing concrete examples.

## 2.3. Testing Methods

### 2.3.1 Workability

One of the physical characteristics of concrete that affects strength is workability. Concrete is transportable, installable, and compactable when done correctly, without bleeding or isolation. Slump flow, the V-funnel test, the L-box test, and the sieve segregation test can

all be used to gauge workability. In this article discussion of workability done based on Slump flow test (Slump flow time and Slump Flow diameter), V-Funnel test. These tests performed according to IS: 10262-2019 (23). Figure 2 shows the slump flow diameter of SCC.



Fig. 2. Slump flow diameter of fresh SCC

### *2.3.2 Compressive Strength Test*

The Compressive strength was measured by applying a Compressive load on 100mm\*100mm\*100mm concrete cubes with a Compressive strength testing machine (CTM). Cube specimens' compressive strength was studied on 28 days after casting and curing in three curing regimes. The cube specimens are tested on a CTM machine per IS: 516-2018 (24). The highest load applied to the specimen during the test is recorded once the load is increased until the specimen fails. The figures 4 and 5 shows test set up of compressive strength and tested cubes respectively.



Fig. 3. Compressive strength testing machine apparatus



Fig. 4. SCC specimens after compressive strength testing

### 2.3.3 Flexural Strength Test

On concrete beams that were 500mm\*100mm\*100mm, a four-point bending test was used to determine flexural strength. In three different curing regimes, the flexural strength of beam specimens was examined 28 days after casting. According to IS: 516-2018(24), the beam specimens were evaluated using a flexural strength testing apparatus. The peak load applied on the specimen is recorded during flexural testing. Figure 5 shows SCC specimens after Flexural strength testing.



Fig. 5. SCC specimens after Flexural strength testing

### 2.3.4 Carbonation Test

The carbonation resistance test was performed following the IS 516-2018 (24) standard test procedure for ordinary concrete's long-term performance and durability. For each batch, three specimens measuring 100 mm cubes were evaluated. The specimens underwent a 28-day curing process under the appropriate curing conditions. The specimens were left for 48 hours to dry before the test. The specimen's top and bottom surfaces were sealed to ensure horizontal CO<sub>2</sub> diffusion that could occur. The specimens were positioned in an accelerated carbonation chamber which was set at  $(20 \pm 2)^\circ\text{C}$  of temperature,  $(70 \pm 5)\%$  of relative humidity and  $(20 \pm 3)\%$  of CO<sub>2</sub>. After that break the specimens into two parts and applied phenolphthalein indicator on the broken surfaces. Further measure the depth of non-colored length from the surface of cube.

### 2.3.5 Freezing-Thawing Test

According to ASTM C666-08 (25), each mixture's quick freezing-thawing durability was evaluated. Three samples measuring 150 mm\*150 mm\*150mm cubes were cast for each mixture to examine the resistance to quick freezing-thawing. The specimens were removed from the molds after  $24 \pm 2$  hours and cured for 28 days at three different curing regimes. Then specimens were taken out and kept in water to achieve the target internal thaw temperature ( $+4^{\circ}\text{C}$ ) for testing. After taking initial measurements, the specimens were put in a water-filled pan so that all faces were completely covered at all times of water during the freezing-thawing cycles. The water-filled pans and the concrete samples were then put in a chamber that underwent freeze-thaw cycling, which involves gradually dropping the temperature of the samples from  $+4^{\circ}\text{C}$  to  $-18^{\circ}\text{C}$  throughout 4 to 5 hours and then gradually raising it back to  $-18^{\circ}\text{C}$  to  $+4^{\circ}\text{C}$ . At the desired thaw temperature, samples were taken out and evaluated until they had undergone 100 cycles.

### 2.3.6 Scanning Electron Microscopy

Scanning Electron microscopy (SEM) Analysis can be used for qualitative purposes but not for quantitative assessment. Both reference concrete and internal curing concrete underwent SEM analysis. Utilizing SEM, the precipitates in the concrete cube's cracks were also examined. After being tested for compressive strength, the broken piece of a 28-day-cured concrete cube specimen was used for this analysis. Acetone was applied to these cubes to stop the process of further hydration. Before being examined, the samples were coated with carbon using sputter coating Emitech K575.

## 3. Results and Discussions

### 3.1 Workability

Test methods used to study the attributes of fresh concrete include the Slump flow test and V-funnel test. These tests were led to decide the filling capacity, and passing capacity and resistance to the isolation of the SCC mix. All SCC mixtures were produced with PPC and PSC with w/c ratios of 0.30, 0.35, and 0.40. For three Water cement ratios, every mix exhibits a slump flow diameter range from 600mm to 760mm, which shows workability varying from class SF1 to SF3 as per IS 10262:2019. When mixing and casting cubes, neither bleeding nor segregation are seen in the SCC mixes. For a more thorough study and comprehension of the workability and rheology of SCC, the tests carried out are the slump flow test, V-funnel test, L-Box test, sieve segregation test and rheometer test.

#### 3.1.1. Slump Flow Time (T500) Test

The slump flow time values of PPC and PSC mixes were observed in the medium range of workability. Figure 6 show the variations of T500 values of PPC and PSC mixes of 0.3, 0.35 and 0.4 w/c ratio. It is observed that the 5%, 8%, and 12% increment in T500 values with the addition of SAP of 0.05%, 0.1%, and 0.15% of the mass of cement as compared to control SCC of 0.3 w/c ratio PPC mixes. Similarly, in 0.35 w/c ratio PPC mixes, the increment observed was 4%, 7% and 10%. In 0.4 w/c ratio PPC mixes, this increment was 5.3%, 8.7%, and 12.7% as compared to control SCC.

While in 0.3 w/c ratio PSC mixes, the increment was 4.5%, 7.5% and 11.5% as compared to control SCC. Similarly, in 0.35 w/c ratio PSC mixes, the increment observed was 3.5%, 6.5% and 9.5%. In 0.4 w/c ratio PSC mixes, this increment was 4.9%, 8.2%, and 12.2% as compared to control SCC.

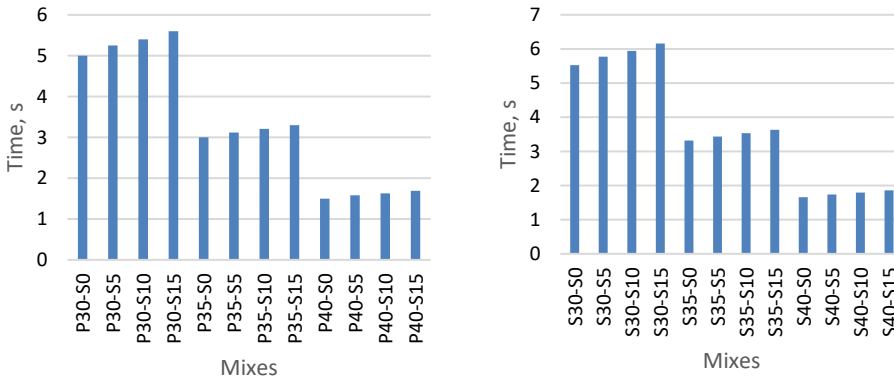


Fig. 6. T500 values of PPC and PSC mixes

### 3.1.2 Slump Flow Diameter Test

The slump flow diameter values of PPC and PSC mixes were observed in the medium range of workability. Figure 7 show the variations of slump flow diameters of PPC and PSC mixes of 0.3, 0.35 and 0.4 w/c ratio. It is observed that the 2.9%, 5.9%, and 8.8% reduction in slump flow diameters with addition of SAP of 0.05%, 0.1%, and 0.15% of mass of cement as compared to control SCC of 0.3 w/c ratio PPC mixes. Similarly, in 0.35 w/c ratio PPC mixes, the reduction observed was 2%, 4.7% and 6.8%. In 0.4 w/c ratio PPC mixes, this reduction was 2.6%, 5.3%, and 7.9% as compared to control SCC. While in 0.3 w/c ratio PSC mixes, the reduction was 3.1%, 6.2% and 9.2% as compared to control SCC. Similarly, in 0.35 w/c ratio PSC mixes, the reduction observed was 1.4%, 4.3% and 5.7%. In 0.4 w/c ratio PSC mixes, this reduction was 2.8%, 5.6%, and 6.9% as compared to control SCC.

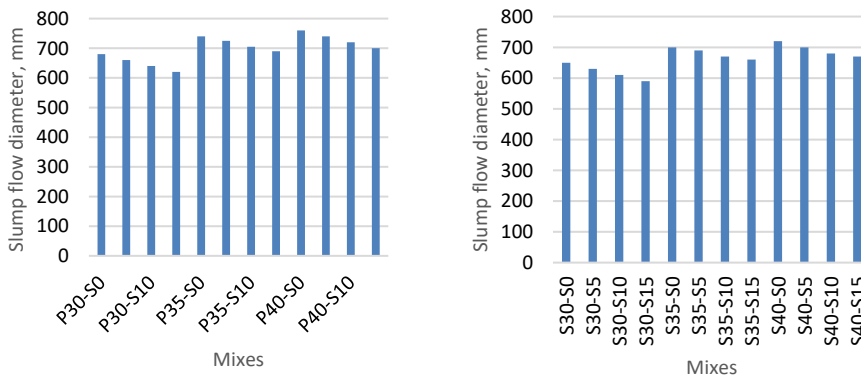


Fig. 7. Slump flow diameters of PPC and PSC mixes

### 3.1.3 V-funnel Test

The V-Funnel time values of PPC and PSC mixes were observed in the medium range of workability. Figure 8 shows the variations of V-Funnel values of PPC and PSC mixes of 0.3, 0.35 and 0.4 w/c ratios. It is observed that the 7%, 12.8%, and 19.8% increment in V-Funnel values with addition of SAP of 0.05%, 0.1%, and 0.15% of mass of cement as compared to control SCC of 0.3 w/c ratio PPC mixes. Similarly, in 0.35 w/c ratio PPC mixes, the

increment observed was 6.6%, 14.5% and 22.4%. In 0.4 w/c ratio PPC mixes, this increment was 7.7%, 15.4%, and 23.1% as compared to control SCC. While in 0.3 w/c ratio PSC mixes, the increment was 6%, 11.8% and 18.7% as compared to control SCC. Similarly, in 0.35 w/c ratio PSC mixes, the increment observed was 5.6%, 14.5% and 22.4%. In 0.4 w/c ratio PSC mixes, this increment was 8.7%, 16.4%, and 24.2% as compared to control SCC.

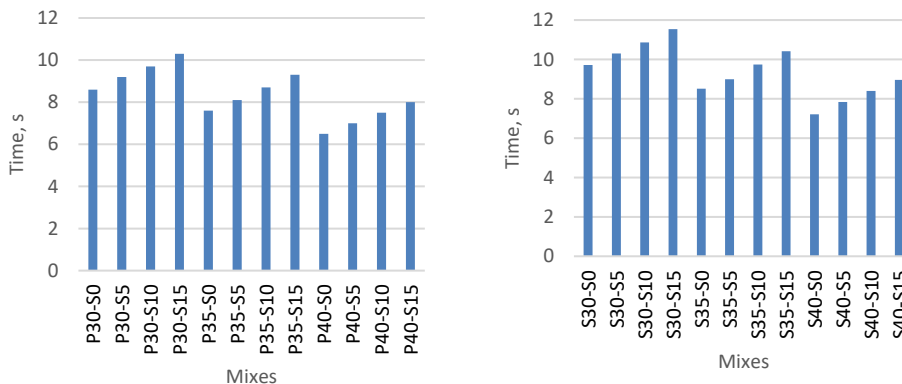


Fig. 8. V-Funnel times of PPC and PSC mixes

From the figures 6 and 8, it is clear that the Slump flow times and V-funnel times of SAP concrete have increased. After observing above workability tests SAP decreases the flowability of SCC. However, this may be due to the absorption of water from the mix by dry SAP. At a time, segregation and bleeding were decreased if additional water is not added which is in accordance with previous researchers(26).

### 3.2 Compressive Strength

Figure 9 shows the results of the compressive strength tests of the control SCC and internal curing mixes with additions of SAP at 0.05%, 0.10%, and 0.15% with PPC and PSC, respectively. Experimentation was conducted on w/c ratios of 0.30, 0.35, and 0.40 and curing regimes of water, air, and gunny bag for 28 days of curing period.

Compressive strength of PPC mixes of 0.3 w/c ratio in water curing was decreased by 2.6%, 5.2% 7.8% for the SAP dosage of 0.05%, 0.10%, and 0.15% respectively with respect to control concrete in the water curing. While compressive strength in air curing was increased by 17.7%, 33.9%, 24.6% for the SAP dosage of 0.05%, 0.10%, and 0.15% respectively with respect to control concrete in the air curing. In the gunny bag curing it was increased by 6.25%, 16.67%, and 12.5% for the SAP dosage of 0.05%, 0.10%, and 0.15% respectively with respect to control concrete in the gunny bag curing.

Compressive strength of PPC mixes of 0.35 w/c ratio in water curing was decreased by 2.3%, 4.7% 7.0% for the SAP dosage of 0.05%, 0.10%, and 0.15% respectively with respect to control concrete in the water curing. While compressive strength in air curing was increased by 16.7%, 30.6%, 22.2% for the SAP dosage of 0.05%, 0.10%, and 0.15% respectively with respect to control concrete in the air curing. In the gunny bag curing it was increased by 5.0%, 9.1%, and 6.6% for the SAP dosage of 0.05%, 0.10%, and 0.15% respectively with respect to control concrete in the gunny bag curing.

Compressive strength of PPC mixes of 0.40 w/c ratio in water curing was decreased by 2.8%, 5.6% 8.3% for the SAP dosage of 0.05%, 0.10%, and 0.15% respectively with respect

to control concrete in the water curing. While compressive strength in air curing was increased by 16.3%, 38.4%, 23.2% for the SAP dosage of 0.05%, 0.10%, and 0.15% respectively with respect to control concrete in the air curing. In the gunny bag curing it was increased by 6%, 14%, and 8% for the SAP dosage of 0.05%, 0.10%, and 0.15% respectively with respect to control concrete in the gunny bag curing.

It can be observed that the compressive strength of all mixtures in the water curing regime decreased with SAP. Whereas compressive strength in air curing and gunny bag curing regimes increased with SAP. The reduction in compressive strength in the water curing regime can be attributed to several macro voids in the microstructure due to SAP hydrogel not being utilized by 100% relative humidity in curing ponds. The humidity meter was arranged in air curing chamber and gunny bag curing chamber to check the humidity percentage variation. In air curing regime, the compressive strength has enhanced from 43.33 MPa for control concrete to 58 MPa for best SAP mix. Here best SAP mix means the strength properties were high at this dosage. The enhancement in compressive strength in the air curing regime can be attributed to the absence of macro voids in the microstructure due to SAP hydrogel being utilized by having less than 60% relative humidity in the surrounding air. In the Gunny bag curing regime, the compressive strength has increased from 48 MPa to 60 MPa for SAP 0% to SAP 0.1%. It may be due to the relative humidity in gunny bag curing varying between 60% and 90%. Hence SAP has yet to release water from SAP hydrogels to the full extent.

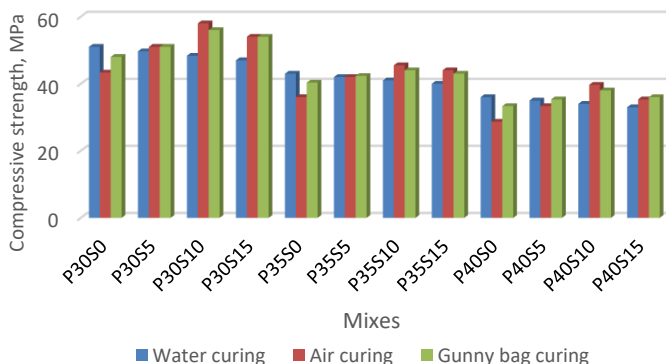


Figure 9. Compressive strength of PPC-based SCC mixes with and without super absorbent polymer in different curing regimes

The compressive strength results of PSC-based reference and internally cured mixtures with 0.30, 0.35, and 0.40 w/c ratios are shown in Figure 10. Compressive strength of PSC mixes of 0.3 w/c ratio in water curing was decreased by 3%, 7.2% 9.6% for the SAP dosage of 0.05%, 0.10%, and 0.15% respectively with respect to control concrete in the water curing. While compressive strength in air curing was increased by 9.7%, 26.2%, 17.9% for the SAP dosage of 0.05%, 0.10%, and 0.15% respectively with respect to control concrete in the air curing. In the gunny bag curing it was increased by 6.2%, 8.1%, and 7.1% for the SAP dosage of 0.05%, 0.10%, and 0.15% respectively with respect to control concrete in the gunny bag curing.

Compressive strength of PSC mixes of 0.35 w/c ratio in water curing was decreased by 2.8%, 6.9% 9.4% for the SAP dosage of 0.05%, 0.10%, and 0.15% respectively with respect to control concrete in the water curing. While compressive strength in air curing was increased by 17.2%, 28.9 %, 21.9% for the SAP dosage of 0.05%, 0.10%, and 0.15%

respectively with respect to control concrete in the air curing. In the gunny bag curing it was increased by 6.8%, 15.9%, and 13.6% for the SAP dosage of 0.05%, 0.10%, and 0.15% respectively with respect to control concrete in the gunny bag curing.

Compressive strength of PSC mixes of 0.40 w/c ratio in water curing was decreased by 2.4%, 4.9% 8.1% for the SAP dosage of 0.05%, 0.10%, and 0.15% respectively with respect to control concrete in the water curing. While compressive strength in air curing was increased by 21.2%, 48.5%, 36.4% for the SAP dosage of 0.05%, 0.10%, and 0.15% respectively with respect to control concrete in the air curing. In the gunny bag curing it was increased by 16.2%, 25%, and 19.8% for the SAP dosage of 0.05%, 0.10%, and 0.15% respectively with respect to control concrete in the gunny bag curing.

The results of PSC mixtures followed the pattern of PPC-based mixtures. In water curing, the compressive strength has decreased from 55.33 MPa to 50MPa for SAP 0% to SAP 0.15%, and the reduction is around 10%. In air curing, the compressive strength has increased from 48 MPa to 61 MPa, and in gunny bag curing, strength has increased from 53 MPa to 59 MPa. These increments are up to SAP 0.10% which is best SAP dosage. The compressive strength in PPC and PSC mixtures increased with best SAP dosage in air curing in the range of 10% to 15% as compared to control mixes in water curing. This improvement most probably higher in SCC because of the longer hydration of higher cementitious material by entrained water of SAP. Previous studies (27)(28)(29) also confirms that the increment of compressive strength in concrete by adding SAP to the concrete mix.

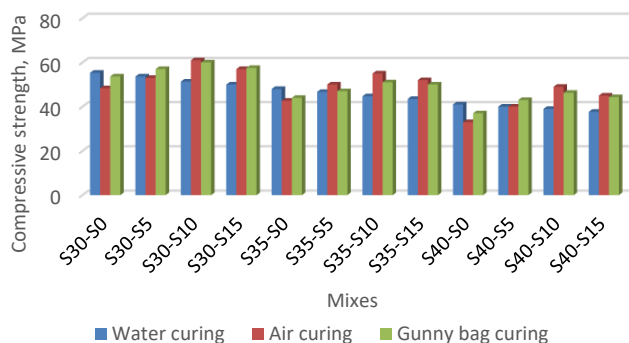


Fig.10. Compressive strength of PSC-based SCC mixes with and without super absorbent polymer in different curing regimes

### 3.3 Flexural strength

The material is under the most significant stress when it is about to give, which is represented by flexural strength. The flexural strength results of SCC mixtures with varying SAP dosages in three curing regimes with w/c ratios of 0.30, 0.35, and 0.40 were shown in Figures 11 and 12 for PPC and PSC-based mixes, respectively.

Flexural strength of PPC mixes of 0.3 w/c ratio in water curing was decreased by 2.2%, 3.3% 5.5% for the SAP dosage of 0.05%, 0.10%, and 0.15% respectively with respect to control concrete in the water curing. While flexural strength in air curing was increased by 6.8%, 18.2%, 11.4 % for the SAP dosage of 0.05%, 0.10%, and 0.15% respectively with respect to control concrete in the air curing. In the gunny bag curing it was increased by 4.5%, 12.4%, and 6.7% for the SAP dosage of 0.05%, 0.10%, and 0.15% respectively with respect to control concrete in the gunny bag curing.



Flexural strength of PPC mixes of 0.35 w/c ratio in water curing was decreased by 3%, 6.1% 9.1% for the SAP dosage of 0.05%, 0.10%, and 0.15% respectively with respect to control concrete in the water curing. While flexural strength in air curing was increased by 19.4%, 27.4 %, 22.6% for the SAP dosage of 0.05%, 0.10%, and 0.15% respectively with respect to control concrete in the air curing. In the gunny bag curing it was increased by 7.9%, 20.6%, and 14.3% for the SAP dosage of 0.05%, 0.10%, and 0.15% respectively with respect to control concrete in the gunny bag curing.

Flexural strength of PPC mixes of 0.40 w/c ratio in water curing was decreased by 1.8%, 3.5% 7% for the SAP dosage of 0.05%, 0.10%, and 0.15% respectively with respect to control concrete in the water curing. While flexural strength in air curing was increased by 9.1%, 18.2%, 12.7% for the SAP dosage of 0.05%, 0.10%, and 0.15% respectively with respect to control concrete in the air curing. In the gunny bag curing it was increased by 5.4%, 10.7%, and 8.9% for the SAP dosage of 0.05%, 0.10%, and 0.15% respectively with respect to control concrete in the gunny bag curing.

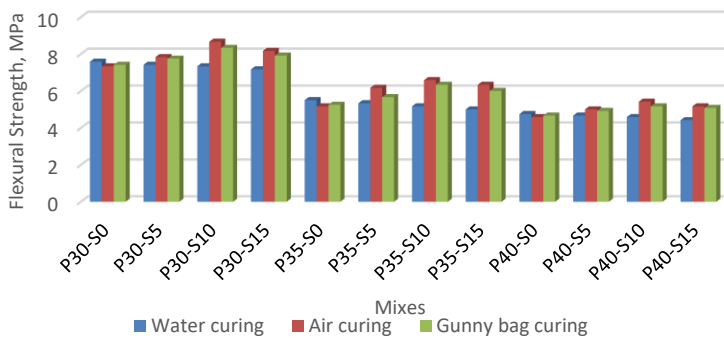


Fig. 11. Flexural strength of PPC-based SCC mixes with and without super absorbent polymer in different curing regimes

Flexural strength of PSC mixes of 0.3 w/c ratio in water curing was decreased by 2.7%, 4.2 % 7.3% for the SAP dosage of 0.05%, 0.10%, and 0.15% respectively with respect to control concrete in the water curing. While flexural strength in air curing was increased by 6.3%, 17.1 %, 9.3 % for the SAP dosage of 0.05%, 0.10%, and 0.15% respectively with respect to control concrete in the air curing. In the gunny bag curing it was increased by 3.5%, 7.4%, and 10.4% for the SAP dosage of 0.05%, 0.10%, and 0.15% respectively with respect to control concrete in the gunny bag curing.

Flexural strength of PSC mixes of 0.35 w/c ratio in water curing was decreased by 3.5%, 6.4% 10.4% for the SAP dosage of 0.05%, 0.10%, and 0.15% respectively with respect to control concrete in the water curing. While flexural strength in air curing was increased by 18.8%, 24.7 %, 19.7% for the SAP dosage of 0.05%, 0.10%, and 0.15% respectively with respect to control concrete in the air curing. In the gunny bag curing it was increased by 7.4%, 19.5%, and 12.7% for the SAP dosage of 0.05%, 0.10%, and 0.15% respectively with respect to control concrete in the gunny bag curing.

Flexural strength of PSC mixes of 0.40 w/c ratio in water curing was decreased by 2.2%, 4.4% 8.7% for the SAP dosage of 0.05%, 0.10%, and 0.15% respectively with respect to control concrete in the water curing. While flexural strength in air curing was increased by 8.6%, 17.1%, 10.7% for the SAP dosage of 0.05%, 0.10%, and 0.15% respectively with respect to control concrete in the air curing. In the gunny bag curing it was increased by

4.9%, 9.7%, and 7.4% for the SAP dosage of 0.05%, 0.10%, and 0.15% respectively with respect to control concrete in the gunny bag curing.

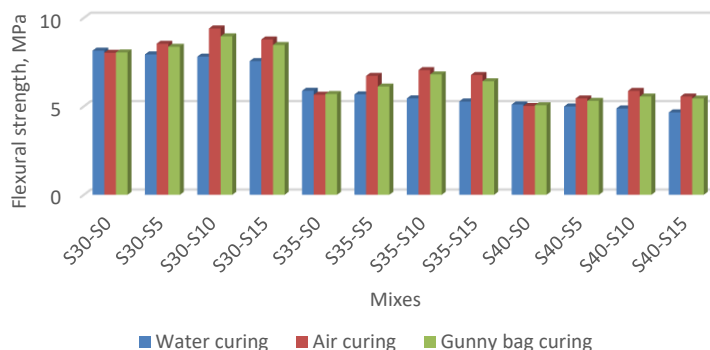


Fig. 12. Flexural strength of PSC-based SCC mixes with and without super absorbent polymer in different curing regimes

It can be observed that the flexural strength of all mixtures in the water curing regime decreased. In comparison, flexural strength in air and gunny bag curing regimes has increased. The flexural strength in air and gunny bag curing increased to SAP with 0.1% SAP dosage which is best. The flexural strength in PPC and PSC mixtures has been increased with best SAP dosage in air curing in the range of 14% to 20% as compared to control mixes in water curing. Previous researchers (30)(31) also confirms that the increment of flexural strength in concrete by adding SAP to the concrete mix. The bending strength is lower in water-curing SAP combinations than in air-curing and gunny-curing SAP mixtures because these mixtures contain more air voids and macropores. Previous research (1) investigated the effect of the total air voids and macro pores in the tensile plane's cross-sectional area on the composite's bending strength. The macro pores will result in a localized loss of strength, possibly reducing the strength in the water curing regime.

### 3.4 Carbonation Depth

Concrete is an alkaline substance with a higher pH. Concrete's pH value decreases due to carbonation, making it easier for the reinforcement to corrode in reinforced concrete. Therefore, concrete carbonation testing is crucial in determining the concrete's endurance. The carbonation test is conducted on PPC and PSC mixtures for w/c ratios of 0.30, 0.35, and 0.40. In addition, for each curing regime 100 mm cubes were casted and cured in respective regime for 28 days. The concrete carbonation test results for each of the three w/c ratios are shown in Figures 13 and 14. The depth of carbonation of reference concrete in air and gunny bag curing regimes increased compared to the water curing regime. However, an air curing regime with best SAP dosage of internal curing mixtures was shown the reduction of carbonation depth as compared to reference concrete. This may be due to denser interfacial transition zone (ITZ) formed in the internal curing mixtures. Concrete's carbonation resistance is correlated with the matrix's degree of compactness (29)(32). The water from the SAP was released into the environment when the concrete hardened, promoting further hydration of the cement matrix and enhancing the compactness of the concrete. These results aligned with compressive strength and flexural strength results. Depth of carbonation decreased by 4-8% in best SAP mixes in air curing compared to

control mix in water curing. Other studies (29)(13)(17)(33) also confirm that decrement in the carbonation by adding the SAP to concrete mix.

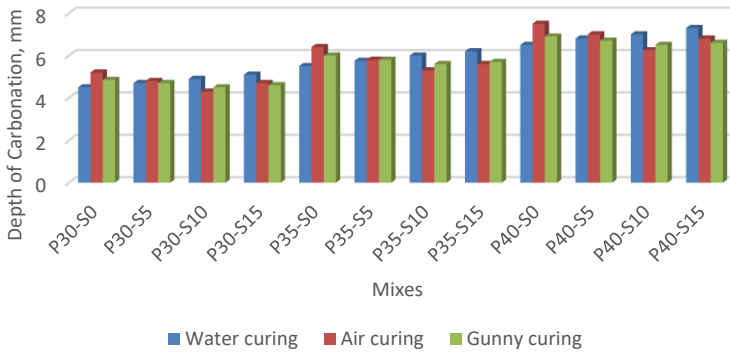


Fig. 13. Carbonation depth of PPC-based SCC mixes with and without super absorbent polymer in different curing regimes

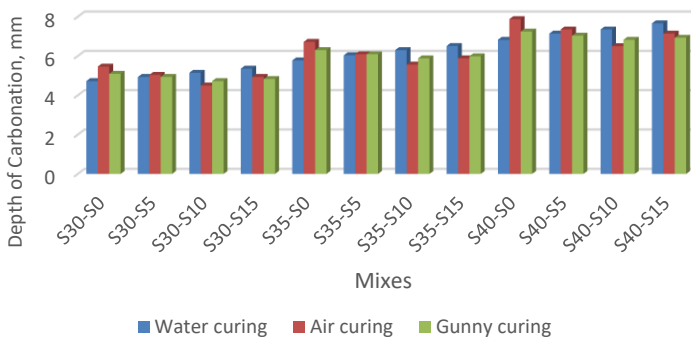


Fig. 14. Carbonation depth of PSC-based SCC mixes with and without super absorbent polymer in different curing regimes

### 3.5 Freezing-Thawing

Mass loss or gain of SCC specimens can be observed in Figures 15 and 16. In reference mixtures, for instance, P30-S0 and S30-S0, the mass has been lost by to 0.38% and 0.24%, respectively. It may be due to the weakening of ITZ. In the case of internal curing mixtures: water-curing mixtures showed a mass loss, but air-curing and gunny mixtures showed a mass gain. It may be due to water-curing mixtures of SAP hydrogel causing macro cracks. In the case of air and gunny bag mixtures, SAP hydrogel released the total water before the freeze-thaw experiment and thickened the ITZ. However, Nanosized SAP particles again absorb the water up to 1% of the mass. This mass is not high because denser ITZ will not allow an increment of the size of the hydrogel. Other studies (34)(35) also aligned with the same phenomenon. Mass loss has been observed in reference concrete and internally cured concrete with water curing. However, in air curing and gunny bag curing, it has been observed that mass has gained after 100 freezing-thawing cycles. The mass loss in water curing mixtures around 0.25% to 0.5%. However, in best SAP mixtures in air curing, the mass has gained 0.4 % to 0.9%.

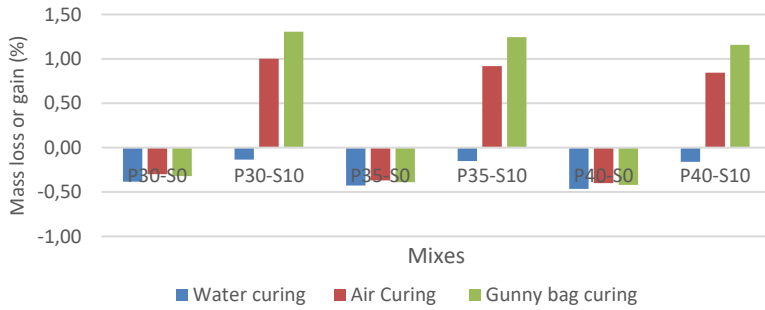


Fig. 15. Mass loss or gain of PPC-based SCC mixes with and without super absorbent polymer at different curing regimes

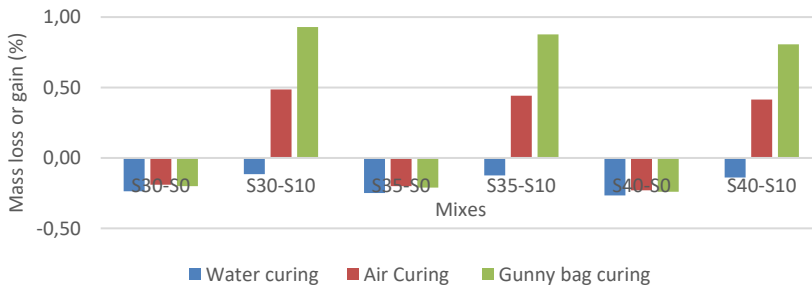


Fig. 16. Mass loss or gain of PSC-based SCC mixes with and without super absorbent polymer in different curing regimes

In Figures 17 and 18, the results of the compressive strength test without freeze-thaw and with freeze-thaw for PPC and PSC mixtures, respectively. In the legends of figures 17 and 18, of “w/o” stands for “without”. Compressive strength in the water curing regime with and without SAP was decreased.

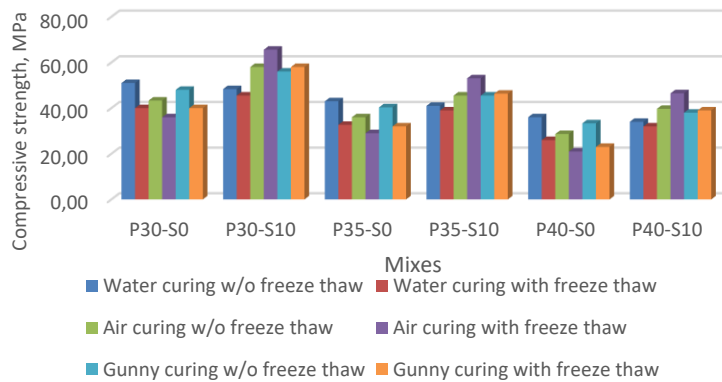


Fig. 17. Compressive strength of PPC-based SCC mixes with and without freeze-thaw effect in different curing regimes

However, in the air curing and gunny bag curing regimes with freeze and thaw cycles, specimens were shown to increase compressive strength results, which may be due to the full redemption of water from SAP particles and improved ITZ throughout the specimen. In the case of water curing, SAP particles have not released the water and become macro void and weaken the ITZ. In the case of reference, freeze-thaw cycles damaged the concrete microstructure and led to lower strength than those without freeze-thaw cycles. Previous research (36)(37) also concluded the same analogy for freeze-thaw cycle experiments on internally cured mixtures with SAP. Regarding Mass change previous studies (38) (35)(37)approve that SAP Mass has lost in water curing regime and mass has increased in the air curing and intermittent curing regimes. And increment of compressive strength after freezing and thawing was also observed in other studies with air curing due to lowest air voids and lesser water content present in those mixtures (39)(40)(41).

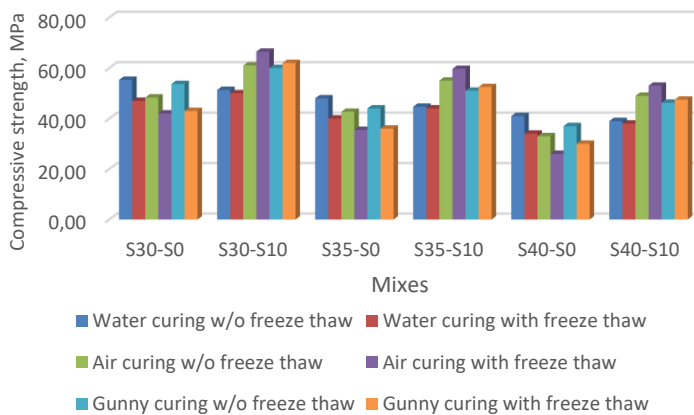


Fig. 18. Compressive strength of PSC-based SCC mixes with and without freeze-thaw effect in different curing regimes

### 3.6 Scanning Electron Microscopy

SEM photographs of a few chosen mixes were obtained to determine the impact of freeze-thaw cycles' impact on the concrete microstructure. Figures 19 and 21 show the cracks in the microstructure of reference concrete mixtures (P35-S0, S35-S0). These cracks were responsible for the reduction of compressive strength after freezing-thawing. However, the internal curing mixtures (P35-S10, S35-S10) with best SAP dosage of 0.1% showed denser ITZ in their microstructure. This can be observed in Figures 20 and 22 for PPC and PSC mixtures, respectively. Consequently, the freezing-thawing exposures specimens shown increased compressive strength values. These results aligned with the results freeze-thaw cycle test. Hence internal curing with SAP in air and gunny bag curing enhances durability, especially against freeze-thaw conditions. Other studies (42) also confirms that microstructure of concrete improved by hydration of cementitious materials to full extent.

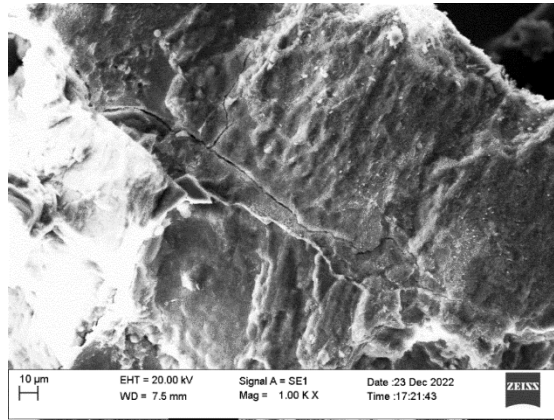


Fig. 19. SEM image of P35S0 mix in standard water curing after freeze and thaw

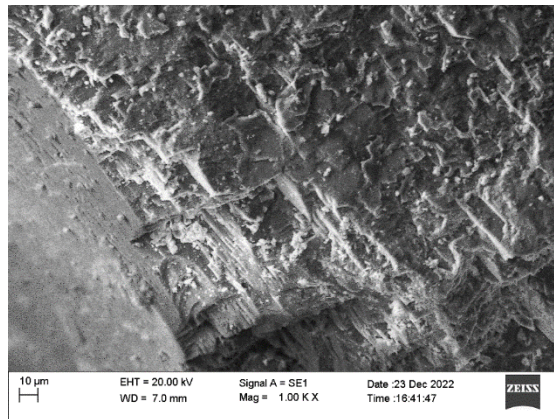


Fig. 20. SEM image of P35S10 mix in air curing regime after freeze and thaw

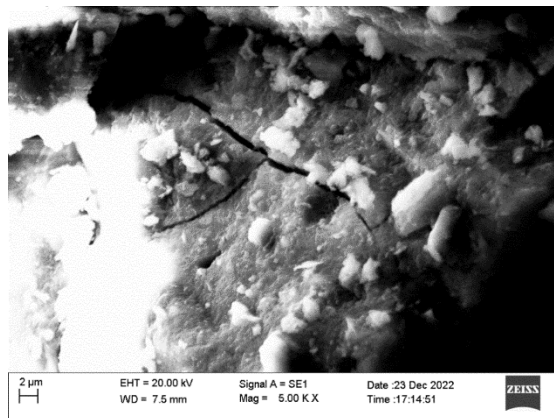


Fig. 21. SEM image of S35S0 mix in standard water curing regime after freeze and thaw

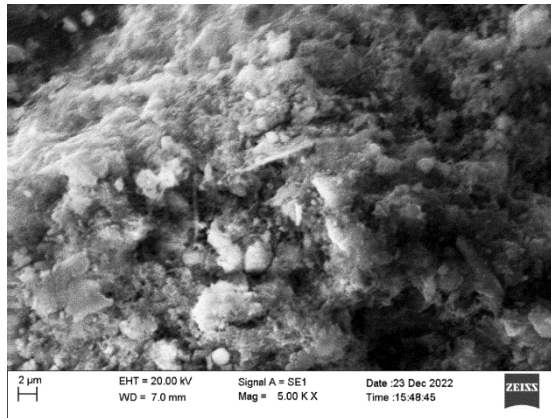


Fig.22. SEM image of S35S10 mix in air curing regime after freeze and thaw

#### 4. Conclusions

From the above experimental investigation following conclusions could be drawn.

- T500 values of optimum SAP mixes were increased by 7-8% compared to the reference mix. The slump flow diameter of SAP mixes was decreased by around 4.9-5.7% compared to the reference concrete mix.
- The v-funnel time of SAP mixes was increased by 12.5% to 15.5% compared to the reference concrete mix.
- Fresh concrete test results reveal that the workability has decreased with adding SAP into the mix. It is due to dry SAP absorbing the water from the mix initially. However, all the workability results are within the limits of standard specifications.
- Super absorbent polymer has shown enhanced strength results in air curing regime especially. The compressive strength in PPC and PSC mixtures increased with best SAP dosage in air curing in the range of 10% to 15% as compared to control mixes in water curing. Compressive strength and flexural strength increased with SAP dosage up to 0.1% in air curing and gunny bag curing.
- The flexural strength in PPC and PSC mixtures has been increased with best SAP dosage in air curing in the range of 14% to 20% as compared to control mixes in water curing.
- Carbonation depth has decreased in air curing and gunny bag curing in SAP mixes. Depth of carbonation decreased by 4-8% in best SAP mixes in air curing compared to control mix in water curing.
- Mass loss has been observed in reference concrete and internally cured concrete with water curing. However, in air curing and gunny bag curing, it has been observed that mass has gained after 100 freezing-thawing cycles. The mass loss in water curing mixtures around 0.25% to 0.5%. However, in best SAP mixtures in air curing, the mass has gained 0.4 % to 0.9%.
- Compressive strength has been decreased after freezing-thawing cycles in the water curing regime. On the other hand, for cubes with air curing compressive strength has been enhanced.
- Scanning electron microscope images also revealed that cracks had been developed in reference concrete in water curing. SAP mix with air curing regimes shows that denser microstructure.

## Acknowledgments

The authors acknowledge the BASF Company Raipur, India for providing a Super plasticizer throughout the research work.

## References

- [1] Dang J, Zhao J, Du Z. Effect of Superabsorbent Polymer on the Properties of Concrete. *Polymers (Basel)*. 2017;9(672):1-17. <https://doi.org/10.3390/polym9120672>
- [2] Ghasemi N, Fathi M, Mazhari M. A comparison between mechanical and physical properties of concretes containing superabsorbent polymer and polymers. *Asian J Civ Eng*. 2023 Sep 29;24:391-400. <https://doi.org/10.1007/s42107-022-00506-z>
- [3] Reinhardt H, Assmann A. Effect of Superabsorbent Polymers on Durability of Concrete. In: *RILEM State of the Art Reports 2*. 2012. p. 115-35. [https://doi.org/10.1007/978-94-007-2733-5\\_9](https://doi.org/10.1007/978-94-007-2733-5_9)
- [4] Olawuyi BJ, Boshoff WP. Influence of SAP content and curing age on air void distribution of high performance concrete using 3D volume analysis. *Constr Build Mater* [Internet]. 2017;135:580-9. <https://doi.org/10.1016/j.conbuildmat.2016.12.128>
- [5] Zhutovsky S, Kovler K. Effect of internal curing on durability-related properties of high performance concrete. *Cem Concr Res*. 2012;42(1):20-6. <https://doi.org/10.1016/j.cemconres.2011.07.012>
- [6] Song C, Cheol Y, Choi S. Effect of internal curing by superabsorbent polymers - Internal relative humidity and autogenous shrinkage of alkali-activated slag mortars. *Constr Build Mater* [Internet]. 2016;123:198-206. <https://doi.org/10.1016/j.conbuildmat.2016.07.007>
- [7] Wyrzykowski M, Gorges M, Lura P, Cusson D, Margeson J, Belie N De, et al. Effect of superabsorbent polymers ( SAP ) on the freeze - thaw resistance of concrete : results of a RILEM interlaboratory study. 2017.
- [8] Dang J, Zhao J, Miao W, Du Z. Effect of superabsorbent polymer on the shrinkage and crack resistance of concrete at early age. *Iran Polym J* [Internet]. 2018;1-10. <https://doi.org/10.1007/s13726-018-0615-8>
- [9] Geiker MR, D.P.Bentz, O.M.Jensen. SP-218-9: Mitigating Autogenous Shrinkage by Internal Curing. 2014.
- [10] Tange M, Mejlhede O, Kovler K, Zhutovsky S. Can superabsorbent polymers mitigate autogenous shrinkage of internally cured concrete without compromising the strength? *Constr Build Mater* [Internet]. 2012;31:226-30. <https://doi.org/10.1016/j.conbuildmat.2011.12.062>
- [11] Tan Y, Lu X, He R, Chen H, Wang Z. Influence of superabsorbent polymers ( SAPs ) type and particle size on the performance of surrounding cement-based materials. *Constr Build Mater* [Internet]. 2021;270:121442. <https://doi.org/10.1016/j.conbuildmat.2020.121442>
- [12] Wang F, Yang J, Hu S, Li X, Cheng H. Influence of superabsorbent polymers on the surrounding cement paste. *Cem Concr Res* [Internet]. 2016;81:112-21. <https://doi.org/10.1016/j.cemconres.2015.12.004>
- [13] Beushausen H, Gillmer M, Alexander M. The influence of superabsorbent polymers on strength and durability properties of blended cement mortars. *Cem Concr Compos* [Internet]. 2014;52:73-80. <https://doi.org/10.1016/j.cemconcomp.2014.03.008>
- [14] Baloch H, Usman M, Rizwan SA, Hanif A. Properties enhancement of super absorbent polymer ( SAP ) incorporated self-compacting cement pastes modified by nano silica ( NS ) addition. *Constr Build Mater* [Internet]. 2019;203:18-26. <https://doi.org/10.1016/j.conbuildmat.2019.01.096>



- [15] Hasholt MT, Jensen OM. Chloride migration in concrete with superabsorbent polymers. *Cem Concr Compos* [Internet]. 2015;55:290-7. <https://doi.org/10.1016/j.cemconcomp.2014.09.023>
- [16] Yang J, Wang F, He X, Su Y. Pore structure of affected zone around saturated and large superabsorbent polymers in cement paste. *Cem Concr Compos* [Internet]. 2019;97(June 2018):54-67. <https://doi.org/10.1016/j.cemconcomp.2018.12.020>
- [17] Ma X, Liu J, Wu Z, Shi C. Effects of SAP on the properties and pore structure of high performance cement-based materials. *Constr Build Mater* [Internet]. 2017;131:476-84. <https://doi.org/10.1016/j.conbuildmat.2016.11.090>
- [18] Schröfl C, Mechtcherine V, Gorges M. Relation between the molecular structure and the efficiency of superabsorbent polymers (SAP) as concrete admixture to mitigate autogenous shrinkage. *Cem Concr Res*. 2012;42:865-73. <https://doi.org/10.1016/j.cemconres.2012.03.011>
- [19] Kong X, Zhang Z, Lu Z. Effect of pre-soaked superabsorbent polymer on shrinkage of high-strength concrete. *Mater Struct* [Internet]. 2015;48:2741-58. <https://doi.org/10.1617/s11527-014-0351-2>
- [20] Laila R, Gnana B, Gurupatham A, Roy K, Lim JBP. Influence of super absorbent polymer on mechanical , rheological , durability , and microstructural properties of self-compacting concrete using non-biodegradable granite pulver. *Struct Concr*. 2020;1-24.
- [21] Laila R, Gnana B, Gurupatham A, Roy K, Lim JBP. Effect of super absorbent polymer on microstructural and mechanical properties of concrete blends using granite pulver. *Struct Concr*. 2019;1-18.
- [22] Venkateswarlu K, Deo SV, Murmu M. Effect of Super absorbent polymer on workability, strength and durability of self consolidating concrete. *IJE Trans B Appl*. 2021;34(5):1118-23. <https://doi.org/10.5829/ije.2021.34.05b.05>
- [23] IS-10262:2019. Concrete Mix Proportioning-Guidelines (Second Revision). *Bur Indian Stand*. 2019;1-40.
- [24] IS:516-1959. Method of Tests for Strength of Concrete. *Bur Indian Stand*. 2018;(1-24).
- [25] ASTM C666-08. Standard Test Method for Resistance of Concrete to Rapid Freezing and Thawing. *ASTM Int*. 2008;03:1-6.
- [26] Ma X, Yuan Q, Liu J, Shi C. Effect of water absorption of SAP on the rheological properties of cement-based materials with ultra-low w / b ratio. *Constr Build Mater* [Internet]. 2019;195:66-74. <https://doi.org/10.1016/j.conbuildmat.2018.11.050>
- [27] Shen D, Wang T, Chen Y, Wang M, Jiang G. Effect of internal curing with super absorbent polymers on the relative humidity of early-age concrete. *Constr Build Mater* [Internet]. 2015;99:246-53. <https://doi.org/10.1016/j.conbuildmat.2015.08.042>
- [28] Pourjavadi A, Mahmoud S, Khaloo A, Hosseini P. Improving the performance of cement-based composites containing superabsorbent polymers by utilization of nano-SiO<sub>2</sub> particles. *Mater Des* [Internet]. 2012;42:94-101. <https://doi.org/10.1016/j.matdes.2012.05.030>
- [29] Dang J, Zhao J, Du Z. Effect of superabsorbent polymer on the properties of concrete. *Polymers (Basel)*. 2017;9(12). <https://doi.org/10.3390/polym9120672>
- [30] Pourjavadi A, Fakoorpoor SM, Hosseini P, Khaloo A. Interactions between superabsorbent polymers and cement-based composites incorporating colloidal silica nanoparticles. *Cem Concr Compos*. 2013;37(1):196-204. <https://doi.org/10.1016/j.cemconcomp.2012.10.005>
- [31] Farzarian K, Pimenta Teixeira K, Perdigão Rocha I, De Sa Carneiro L, Ghahremaninezhad A. The mechanical strength, degree of hydration, and electrical resistivity of cement pastes modified with superabsorbent polymers. *Constr Build Mater*. 2016;109:156-65. <https://doi.org/10.1016/j.conbuildmat.2015.12.082>
- [32] Kellouche Y, Boukhatem B, Ghrici M, Rebouh R, Zidou A. Neural network model for predicting the carbonation depth of slag concrete. *Asian J Civ Eng* [Internet]. 2021;1-14. <https://doi.org/10.1007/s42107-021-00390-z>

- [33] Xu J, Qin X, Huang Z, Lin Y, Li B, Xie Z. Effect of Superabsorbent Polymer (SAP) Internal Curing Agent on Carbonation Resistance and Hydration Performance of Cement Concrete. 2022;2022. <https://doi.org/10.1155/2022/3485373>
- [34] Shang H, Yi T. Freeze-Thaw Durability of Air-Entrained Concrete. *Sci World J.* 2013;1-7. <https://doi.org/10.1155/2013/650791>
- [35] Jones WA, Weiss WJ. Freeze Thaw Durability of Internally Cured Concrete Made Using Superabsorbent Freezes. *Freeze Thaw Durability of Internally Cured Concrete Made Using Superabsorbent Polymers. 4th Int Conf Durab Concr Struct.* 2014;3-11. <https://doi.org/10.5703/1288284315376>
- [36] Taner S, Meyer C, Herfellner S. Effects of internal curing on the strength, drying shrinkage and freeze - thaw resistance of concrete containing recycled concrete aggregates. *Constr Build Mater.* 2015;91:288-96. <https://doi.org/10.1016/j.conbuildmat.2015.05.045>
- [37] Gołaszewski J, Gołaszewska M, Cygan G. Performance of Ordinary and Self-Compacting Concrete with Limestone after Freeze - Thaw Cycles. *Buildings.* 2022;12(1-18). <https://doi.org/10.3390/buildings12112003>
- [38] Mechtcherine V, Schröfl C, Wyrzykowski M, Gorges M, Lura P, Cusson D, et al. Effect of superabsorbent polymers (SAP) on the freeze-thaw resistance of concrete: results of a RILEM interlaboratory study. *Mater Struct Constr.* 2017;50(1). <https://doi.org/10.1617/s11527-016-0868-7>
- [39] Mönnig S, Lura P. Superabsorbent Polymers - An Additive to Increase the Freeze-Thaw Resistance of High Strength Concrete.
- [40] Riyazi S, Kevern JT, Mulheron M. Super absorbent polymers ( SAPs ) as physical air entrainment in cement mortars. *Constr Build Mater [Internet].* 2017;147:669-76. <https://doi.org/10.1016/j.conbuildmat.2017.05.001>
- [41] Saadi M, Al-Attar T, Hasan S. Freezing and thawing resistance of internally cured high performance concrete. *MATEC Web Conf.* 2018;162:1-4. <https://doi.org/10.1051/mateconf/201816202011>
- [42] Kanthe VN, Deo S V, Murmu M. Effect of fly ash and rice husk ash on strength and durability of binary and ternary blend cement mortar. *Asian J Civ Eng.* 2018;6:1-8. <https://doi.org/10.1007/s42107-018-0076-6>

Blank Page

## Advancements in base isolation for seismic mitigation: Perspectives on elastomeric and lead rubber bearings

Dhirendra Patel<sup>\*a</sup>, Vishal Kumar Mourya<sup>b</sup>, Gaurav Pandey<sup>c</sup>, Rajesh Kumar<sup>d</sup>

Department of Civil Engineering, Indian Institute of Technology-BHU, Varanasi, India

### Article Info

### Abstract

#### Article history:

Received 27 Sep 2023  
Accepted 22 Jan 2024

#### Keywords:

Dampers;  
Base isolation;  
Passive energy;  
Peak accelerations;  
Vibration period;  
Frequency

Base isolation represents an environmentally sustainable and highly effective technique for mitigating structural responses to strong seismic forces generated by plate boundary tectonic activities. Its primary benefits include preventing structural collapse, minimizing property damage, and safeguarding human lives during severe earthquakes. This passive, energy-efficient approach is often complemented by supplementary dampers to further reduce seismic impact. This study provides a comprehensive overview of elastomeric and lead rubber isolators, covering their theoretical, experimental, and numerical aspects. The paper examines the seismic response of structures equipped with elastomeric and lead rubber bearings, including a discussion of their pros and cons. This paper presents the comparison of fixed base and rubber isolated base in SAP 2000 to assess the effectiveness of base isolation. Additionally, it presents findings from shaking table tests, relevant building codes, and practical applications, considering the impact of events beyond initial design parameters. The review delves into the historical evolution of elastomeric and lead rubber-bearing systems, offering valuable insights into their contemporary understanding. Furthermore, the paper introduces three-dimensional isolators designed to attenuate ground motion responses in both horizontal and vertical directions. It investigates the effects of soil-structure interaction and evaluates isolator responses under blast and impact aircraft loading conditions. Notably, specific types of bearings exhibit exceptional energy dissipation capabilities during catastrophic seismic events, leading to reduced floor acceleration and inter-storey sway at critical levels. In conclusion, the study offers future recommendations and identifies potential constraints in this field.

© 2024 MIM Research Group. All rights reserved.

## 1. Introduction

Earthquakes, ancient and unpredictable natural hazards, shake the earth beneath us, impacting structures and systems with the potential for significant loss of life and property. In seismic engineering, two vital aspects are considered as seismic loading and building resistance. Traditional seismic design aims to prevent building collapse during strong earthquakes, but it often results in damage to non-structural elements and some structural components, rendering buildings non-functional. This can be problematic, especially for critical structures such as nuclear plants, hospitals, government buildings, and other critical structures. To address the challenges posed by strong earthquakes, the concept of seismic base isolation is introduced.

\*Corresponding author: [dhirendrapatel.rs.civ17@itbhu.ac.in](mailto:dhirendrapatel.rs.civ17@itbhu.ac.in)

<sup>a</sup> [orcid.org/0009-0004-1633-2437](https://orcid.org/0009-0004-1633-2437); <sup>b</sup> [orcid.org/0009-0009-4348-9911](https://orcid.org/0009-0009-4348-9911); <sup>c</sup> [orcid.org/0009-0008-3750-3097](https://orcid.org/0009-0008-3750-3097);

<sup>d</sup> [orcid.org/0000-0001-5145-588x](https://orcid.org/0000-0001-5145-588x)

DOI: <http://dx.doi.org/10.17515/resm2024.15ma0927rv>

Res. Eng. Struct. Mat. Vol. 10 Iss. 3 (2024) 1017-1049

The base isolation technique involves implementing specially designed devices inserted between the superstructure and its foundation, effectively decoupling the structure from intense seismic motion. The utilisation of the seismic Base Isolation (BI) system represents an innovative approach within the realm of earthquake-resistant structural design, currently implemented across various nations [1-4]. Laminated elastomeric bearings are presently the most extensively utilised devices among the various types available. The composition comprises successive layers of rubbers and steel, where the rubber layers are subjected to vulcanization to bond with the steel layers. Including steel shim layers effectively mitigates the likelihood of bulging in the rubber layer, resulting in a notable enhancement in vertical stiffness. The presence of these layers has a slight effect on the shear stiffness. Studies shown that excessive damping at smaller, more realistic displacements may stiffen the isolation system, impacting its effectiveness and affecting internal equipment [5]. The three most prevalent kinds of laminated rubber bearings are Lead Rubber Bearings, High Damping Rubber Bearings, and Natural Rubber Bearings.

Base isolation systems are a resilient, efficient, and practical approach to safeguard structures and non-structural components against seismic risks. Nevertheless, significant shifts due to intense seismic forces can potentially result in detrimental effects on both the bearing and the overall structural integrity. The concept of decoupling involves altering the inherent vibration period of a building to a longer duration, as depicted in Fig. 1. The shown picture illustrates a decrease in spectral acceleration when the natural period shifts. This suggests that when the fundamental natural frequency does not align with the frequency of the seismic excitation, it serves as a preventive measure against catastrophic consequences. The increase in the duration of the structural time-period results in greater relative displacements, as illustrated in Fig. 2. The mitigation in inter-storey drift and floor acceleration in the superstructure is observed across all risk categories. Various isolation techniques have efficiently diminished the dynamic behaviour during low to moderate earthquakes and restrained displacement during more severe seismic events.

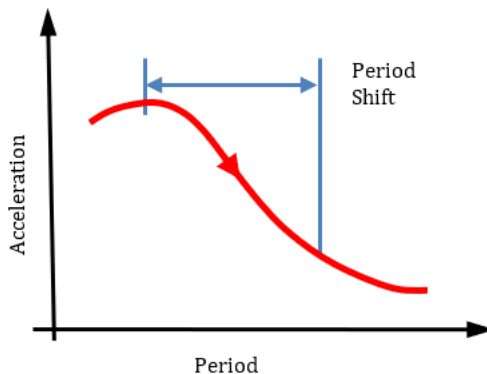


Fig. 1. Time Period shift

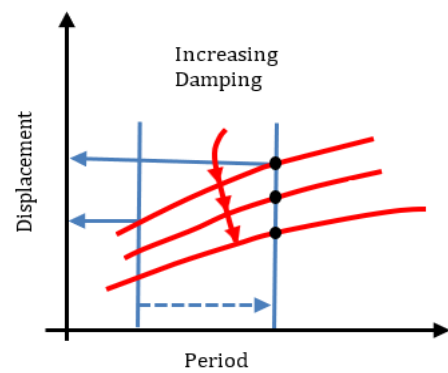


Fig. 2. Displacement design response spectra

Primarily, it is imperative to identify strategies for reducing the expenses associated with the implementation of base isolation systems to facilitate their widespread use in both retrofitting and new building endeavours [6]. Furthermore, it is imperative to conduct a comprehensive assessment to evaluate the potential ramifications of device malfunctions on the adjacent infrastructure in the event of seismic occurrences. The behaviour of structures that are equipped with foundation isolation can be divided into two different

components: the performance of the bearings and the behaviour of the superstructure. In the event of a failure in one of these components, there is a potential for the complete collapse of the entire system [7]. The countries prone to severe earthquakes have adopted the technique on a large scale. Japan, USA, China, European nations, New Zealand, etc., are pioneering in developing the technique and implementing suitable isolators as a convenience. The isolator is widely applied in retrofitting old historical buildings and new constructions. Fig.3 shows the insertion of isolators in the structure between foundation and superstructure.

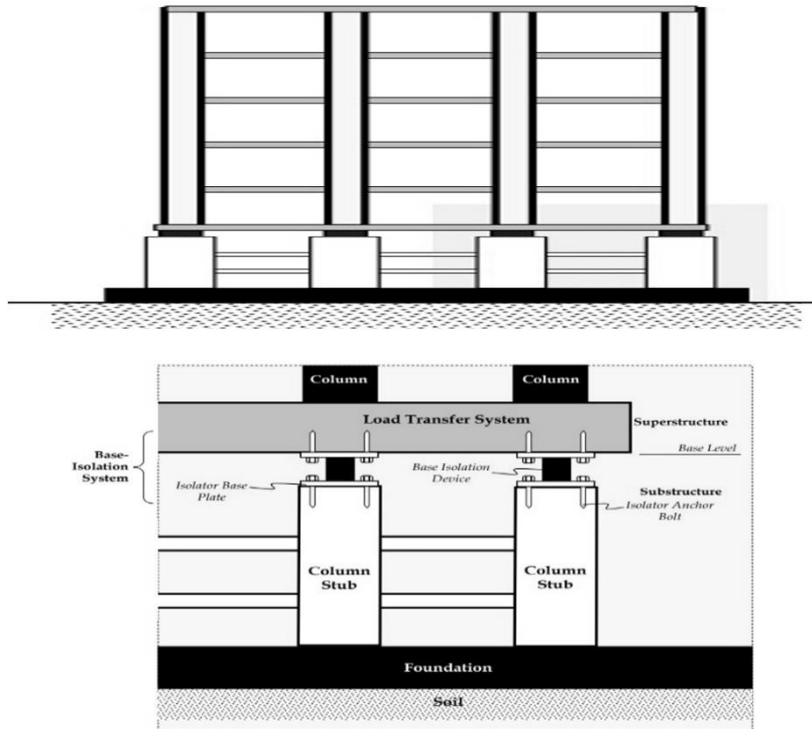


Fig. 3. Sectional representation of Base-Isolated Structure [IS 1893 Part 6]

The laminated rubber bearings are capable of sustaining high load in compression and also withstand more than one movement in shear. It is classified into three types: (i) Natural rubber bearings, which use natural rubber, which is less damping and has moderate flexibility. Therefore, it is used to withstand the effects of pre-stressing, creep, and shrinkage in bridges, and for base isolated buildings, it is combined with supplemental energy absorption devices like steel, viscous dampers, and lead [8]; (ii) High Damping Rubber Bearings (HDRB) has highly capable energy absorbing rubber material; (iii) Lead Rubber Bearings have high damping and extensively implemented in bridges and buildings to safeguard against strong ground motions. The seismic responses of fixed-base and various base isolation models for typical low- and mid-rise reinforced concrete buildings are compared [9]. This study analyses 352 cases with 11 ground motion pairs, it finds that LRB isolators are preferable for regular buildings without re-centering issues. The isolator must: (i) re-centre itself during strong earthquakes, depending on seismic intensity and duration; (ii) withstand wind forces with minimal horizontal restraint; (iii) tolerate vibrations, requiring damping to reduce relative superstructure-foundation movement; (iv) support superstructure weight for unrestricted horizontal movement; and (v) enable

back-and-forth movement to keep the superstructure at rest [10-12]. Ongoing efforts in advanced isolation bearings focus on adaptive system development. The flow chart mentioned in Fig. 4 shows the development of elastomeric and lead rubber bearings.

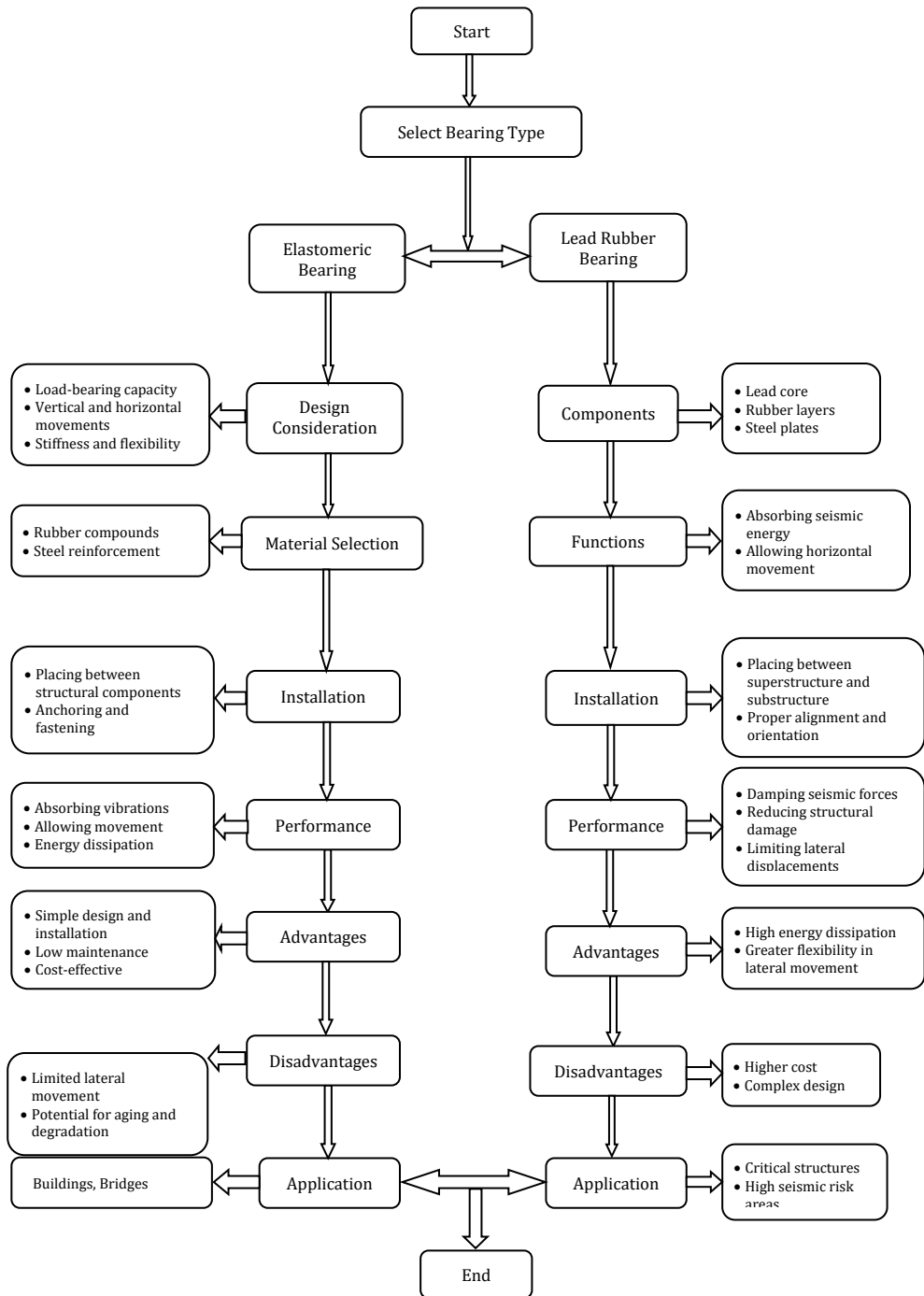


Fig. 4. Flow Chart representation of the Elastomeric Rubber Bearing and LRB

This paper presented a detailed analysis and application of lead and elastomeric rubber bearing. The elastomeric bearings are isolators comprised of a loading plate, fixing plate, alternate layers of rubber layer, and steel shim, while LRB consists of a loading plate, a fixing plate, an alternate layer of rubber layer, a steel layer, and a lead core inserted at the centre. The primary quality of laminated rubber bearings is their strong vertical rigidity, which maintains structural weight while retaining horizontal flexibility. The rubber layers increase the system's horizontal flexibility, shifting the building's natural period away from the region's projected earthquakes' peak time, which reduces seismic amplifications. Moreover, the structural inter-storey drift is significantly diminished during seismic activity because displacements are centred at the level of isolation systems. Consequently, the damage in structural and non-structural elements is diminished. The steel shim plates are provided to protect rubber layers experiencing large deformations when bearings are subjected to heavy loads. These bearings are rigid in vertical directions but ductile in horizontal directions. The vertical rigidity of the interior steel plates is hundreds of times greater than the horizontal stiffness [13]. The experimental investigations were done to examine compression modulus behaviour for the rubber block attached to the rigid end of the plates [14]. There are many devices to be used as base isolation systems in buildings, but lead rubber bearings and elastomeric bearings provide convenient, inexpensive, and suitable solutions against seismic excitation. The steel plates are inserted to reduce the response of rubber bulging, i.e., to increase the vertical stiffness of the isolator [3,15]. A new type of laminated bearings recognized as fibre-reinforced elastomeric bearings (FREI) is introduced where fibre fabric is used instead of steel shims plates [16]. This paper provides a numerical and experimental investigation of isolator bearings, including an exploration of their constants and equations employed in various numerical simulations. The shake table test is used to analyse the responses and simulate the experimental results in the laboratory. In recent times, a multitude of scholars has proposed novel methodologies to achieve flexible behaviour in isolators, regardless of whether they are based on lead rubber bearing or elastomeric rubber bearing mechanisms. Elastomeric and lead-rubber bearings are extensively employed bearings in practice. During seismic occurrences, the bearings within an isolation system experience significant axial compressive loads resulting from the combined effects of gravity and overturning forces. These loads are accompanied by substantial lateral displacements occurring simultaneously. Nevertheless, research has demonstrated that the capacity of elastomeric bearings to withstand critical loads decreases as lateral displacement increases. Therefore, it is imperative to demonstrate stability at the greatest displacement when designing isolation systems consisting of these types of bearings [4]. While bearings offer numerous advantages, they also come with certain drawbacks. This study explores the impact of temperature fluctuations on the lead core in LRB and delves into the issues related to cavitation and buckling in rubber layers.

This study offers a thorough examination of lead rubber and elastomeric bearings, encompassing their interaction with foundations and superstructures, soil effects, as well as responses to blasts and aircraft impact loading. Unlike previous literature, this review integrates various aspects, including soil-structure interaction, 3-D BI system and applications in diverse fields. Additionally, it evaluates the pros and cons of these bearings and provides insights into future research directions with limitations as closing remarks. Both bearing types offer unique advantages and applications in enhancing the earthquake resistance of buildings and infrastructure. This introduction provides a glimpse into the essential characteristics and functions of lead rubber and elastomeric bearings in seismic-resistant design.

The field of seismic BI technology has witnessed notable progress in the creation of advanced and sustainable base isolation devices, which possess the ability to modify their



properties in accordance with different intensities of seismic loading. The utilization of advance systems exhibits the potential to augment the overall efficacy of BI across various threat scenarios. In brief, BI techniques have made significant advancements since its inception, providing a robust approach to safeguard structures from seismic hazards. Through continuous study and invention, BI is undergoing constant development, resulting in enhanced safety and reliability of infrastructure in regions susceptible to earthquakes. The advancement in base isolation techniques has resulted in novel BI systems that showcase adaptable capabilities. The behaviour is considered adaptable when the Isolation characteristics exhibit substantial changes in response to varying loading levels. Recently, the perception of adaptive behaviour has garnered noteworthy consideration among scholars and researchers. This paper summarizes the historical developments and current understanding of adaptive BI devices in situations where active control mechanisms are not available. It was observed that adaptive devices possess a noteworthy capacity to disperse the input energy during intense seismic actions.

## 2. Historical Developments

The compilation of pertinent data about the numerical and practical evaluation of the chosen base isolators was sourced from credible international conferences, research papers, journal articles, and high-quality studies. The greatest emphasis was given to submissions that investigated isolation devices with adaptable characteristics. This review involves the utilisation of numerical investigations, modelling techniques, and experimental validations. In the present context, adaptive devices refer to mechanisms that exhibit distinct softening characteristics, followed by significant stiffening reactions and modifications in damping ratio as movement magnifies. Base Isolation is not a new tool; earlier in China and Italy, it was used in monasteries, bridges, etc. It was made of layered material, which allows relative movements over each other. Its history can be traced back to 1870 when Touaillon [17] proposed the idea of decoupling the superstructure and modelled seismic isolation system. The technique was implemented by Frank Wright in the Imperial Hotel, Tokyo, in 1921. His design was enormously controversial [18]. The rudimentary concept behind this method is to decouple the structure to reduce the detrimental response of the strong ground motion. In the late 1930s, the notion of a flexible first-storey was proposed [19,20]. It examined the response by reducing the lateral stiffness of columns at first-storey considering deformations concentrated at first-storey columns underground motion load. It concluded that columns at first-storey behave elastically, i.e., having low damping. Later on, in the late 1970s, the concept of a soft first-storey, which is a modified investigation of the flexible first-storey concept, was proposed. It considered that the first-storey columns yield during seismic excitation, thus controlling the displacement response and producing energy-absorption mechanisms. But these concepts failed to consider the three-dimensional effect of earthquakes and were implemented to the response of the higher storey, but potentially detrimental effects can occur at first-storey columns. Many roller bearings have been proposed, tested, and patented [21-26]. The stability of rubber bearings by theoretical approaches by considering linearity in rubber and small displacements was proposed [27-29]. The Haringx theory was applied to predict the reduction in horizontal stiffness on increasing axial loads [30]. The implementation of rubber bearings was first implemented in a school building in Skopje, Yugoslavia. It was a three-storey RC building completed in 1969 [31]. It was founded on Neoprene rubber. Since 1969, elastomers have been employed in seismic isolation, benefiting from their near incompressibility, capacity to endure substantial recoverable strains, and low shear modulus under comparatively low stress.

With the advent of new research, there has been a significant extent of improvement has been made in understanding the function and operation of rubber bearings. The application and principles of rubber bearing isolator were proposed by [32] and its design details and stability by [33,34]. The lead rubber bearing was applied first in Clayton building in 1981 [35]. The structural components consist of the superstructure, which encompasses elements above the base level, like columns, beams, walls, and roofs supported by the substructure. The substructure, located below the base level, includes foundation elements such as footings or piles that transfer loads to the ground. A base-isolation system involving isolators made of materials like rubber or steel, mitigates seismic effects by allowing independent movement between the superstructure and the substructure, absorbing, and dissipating seismic energy [11,36-37].

In the past few decades, the technique has grown significantly worldwide. Earlier, the investigations were performed based on mechanical characteristics of the bearings under large deformations in horizontal directions having constant vertical load [35,38-42]. Furthermore, many experiments were conducted to validate the results [40,41,43-45]. This analysis and experiment were limited to unidirectional only. Later, the analysis and experiment were conducted to validate the response of bearings in multi-directions. The seismic BI system in two horizontal directions is employed in buildings and bridges. Park 1986 [46] proved the significance of coupling effects under multi-axial loadings. The multi-axial response of steel dampers and HDRB was examined by Yasaka [41]. The response of Teflon bearings subjected to triaxial loadings was investigated by Mokha [47]. The multi-axial loading is applied on laminated rubber bearings to envisage the cyclic response of the bearings [48]. It studied the mechanical behaviour of laminated bearings under biaxial, triaxial, and small deformations. Fig.5 shows the optimal steps and design parameters for the advancement of a smart BI system [49]. There are various kinds of seismic BI systems developed to shield structures from intense ground quakes. However, the elastomeric bearings and LRB are commonly employed isolators. The numerical and experimental analysis of elastomeric bearings and LRB based on BI systems and their outstanding agreement with results gives imminence confidence to structural designers to implement confidently. The ongoing developments and research to protect structures from the detrimental effect of seismic excitation are important steps to ensure the seismic safety of buildings.

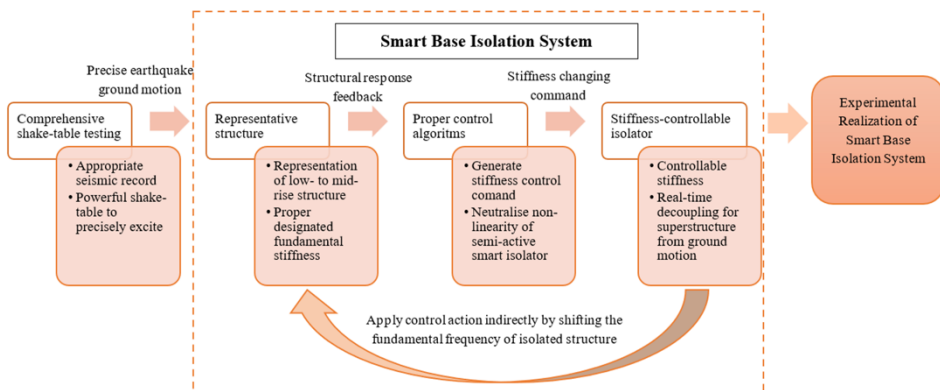


Fig. 5. Fundamental setup for the smart isolation system [49]

### 3. Guidelines and Development of Modern Isolators

Elastomeric materials are well-suited for use as BI systems due to their capability to endure significant retrievable strains. Rubber varieties like polychloroprene or polyisoprene, as well as rubber-like substances such as polyurethane, are potential options for rubber isolators. To augment both the bending and vertical characteristics of these isolators, a blend of rubber elastomer infused with fibres or steel is frequently employed. Tailored responsiveness to varying input levels can be attained by capitalizing on natural rubber's strain-induced crystallization feature or by utilizing elastomeric isolators with unbonded or partially bonded fibre reinforcement. Additionally, achieving desired adaptive qualities in elastomeric isolators often involves integrating supplemental dampers.

Currently, various building codes such as UBC 1997, AASHTO 1999, Euro Code 8 Section 10 Part 1, EN 15129, EN 1998-1 Section 4 & 8, NTC 2008, FEMA 273, FEMA 274, FEMA 356, FEMA 450, FEMA p695, ASCE 7-05, ASCE 41-06 Clause 9, ASCE 7-16 Chapter 17, ASCE 7-22, and IS 1893 (Part 6): 2022 are utilised to conduct linear and non-linear analyses in order to design most base isolation (BI) structures. The ISO 22762-1 standard is employed in the field of elastomeric bearing design and protection. There are multiple standards available that offer guidance regarding the material qualities of bridge and structural bearings. The document EN 15129 [50] provides a comprehensive overview of the material properties associated with Anti-Seismic devices, such as rubber elastomeric isolators. The standard EN 1337-3 [51] primarily addresses the topic of elastomeric bearings, including detailed specifications about the mechanical and physical characteristics of rubber elastomeric materials. ISO 6446 [52] delineates the stipulations for elastomeric rubber bearings materials employed in bridges, whilst ASTM 4014 [53] offers standardized criteria for elastomeric materials utilised in bridge bearings. Nevertheless, the existing criteria fail to consider the potential impact of the constituents present in elastomeric rubber compounds on the characteristics of rubber constituents. Table 1 shows the comparison of different codes for linear equivalent analysis. Therefore, it is evident that additional investigation is essential in this particular domain to investigate the effect of rubber elastomer constituents on the mechanical and dynamic characteristics of the isolator.

Table 1. Equivalent Linear Analysis codal comparison of different parameters [54]

Structure	Sign	Algeria	Taiwan	Japan	USA	China	Italy
Superstructure	$Q_s$	$\frac{Q_{ISO}}{R_i}$	$\frac{Q_{ISO}}{R_i}$	$Q_{ISO}$	$\frac{Q_{ISO}}{R_i}$	$Q_{ISO}$	$\frac{Q_{ISO}}{R_i}$
	$Q_j$	$\frac{Q_s M_i H_i}{\sum_{j=1}^n M_j H_j}$	$\frac{Q_s M_i H_i}{\sum_{j=1}^n M_j H_j}$	$\gamma(A_i Q_\xi + Q_e)$	$\frac{Q_s M_i H_i}{\sum_{j=1}^n M_j H_j}$	$\frac{Q_s M_i H_i}{\sum_{j=1}^n M_j H_j}$	$M_j S_a(T_e, \xi_e)$
Substructure	$Q_b$	$\frac{K_e D_D}{0.8 R_i}$	$\frac{K_e D_D}{0.8 R_i}$	$Q_{ISO}$	$K_{e,max} D_D$	$Q_{ISO}$	$Q_{ISO}$
Time period	$T_e$	$2\pi \sqrt{\frac{M}{K_e}}$	$2\pi \sqrt{\frac{M}{K_e}}$	$2\pi \sqrt{\frac{M}{K_e}}$	$2\pi \sqrt{\frac{M}{K_{e,min}}}$	$2\pi \sqrt{\frac{M}{K_e}}$	$2\pi \sqrt{\frac{M}{K_e}}$
Isolation System	$D_D$	$\frac{M \sqrt{\frac{7}{2+\xi}} S_a T_e}{K_e}$	$\frac{g}{4\pi^2} \frac{S_{ad} T_{el}^2}{B}$	$\frac{M F_h(\xi) Z G_S S_o(l)}{K_e}$	$\frac{g}{4\pi^2} \frac{S_{D1} T_D}{B_D}$	$\frac{Q_{ISO}}{K_e}$	$\frac{M S_a(T_e, \xi_e)}{K_{e,min}}$

$D_{TD}$	$y_i \frac{(1+\frac{12e}{b^2+d^2})}{b^2+d^2}$	$y_i \frac{(1+\frac{12e}{b^2+d^2})}{b^2+d^2}$	1.1	$y_i \frac{(1+\frac{12e}{b^2+d^2})}{b^2+d^2}$	$y_i \frac{(1+\frac{12e}{b^2+d^2})}{b^2+d^2}$	$y_i \frac{(1+\frac{12e}{b^2+d^2})}{b^2+d^2}$
$Q_{ISO}$	$K_e D_D$	$K_e D_D$	$K_e D_D$	$K_{e,max} D_D$	$S_a(T_e) \beta M$	$K_{e,max} D_D$
$D_M$	$1.5 D_{TD}$	$1.5 D_{TD}$	$\gamma D_{TD}$	$D_M$	$\lambda_S D_{TD}$	-

Notations

$D_D$ : Design Displacement

$Q_{ISO}$ : Shear force

$Q_j$ : Portion of  $Q_S$  that is assigned to Level  $i$

$M_i$ : Portion of  $M$  that is located at or assigned to Level  $i$

$M_j$ : Portion of  $M$  that is located at or assigned to Level  $j$

$H_i$ : Height above the base of Level  $i$

$H_j$ : Height above the base of Level  $j$

$Q_b$ : Minimum lateral force

$S_{D1}$ : Design 5 percent damped spectral acceleration parameter at 1-s period

$T_D$ : The effective period of the isolated structure at design displacement

$B_D$ : Numerical coefficient related to the effective damping of the isolation the system at the design displacement

$R_i$ : Reduction factor linked to the ductility of the superstructure

$Q_S$ : Shear force at the base of the superstructure

$A_i$ : Seismic shear force coefficient distribution

$\beta(\xi, T_e)$ : Response reduction factor

$S_a(T_e, \xi_e)$ : Spectral acceleration

$\xi$ : Equivalent damping factor

$\lambda_S$ : Property Modification Factor

$K_e$ : Effective stiffness

$K_{e,max}$ : Maximum effective stiffness

$K_{e,min}$ : Minimum effective stiffness

$D_M$ : Maximum design displacement

$D_{TD}$ : Total design displacement

$y_i$ : Distance between the centre of rigidity of the isolation system rigidity and the element of interest measured perpendicular to the direction of seismic loading under consideration

$e$ : Actual eccentricity

$b$ : Shortest plan dimension of the structure

$d$ : Longest plan dimension of the structure

$Z$ : Seismic hazard zone factor

$G_S$ : Soil amplification factor

Rubber substances, such as polychloroprene or polyisoprene, as well as materials with rubber-like characteristics, such as polyurethane [55], may be viable options for elastomeric isolators. The incorporation of a composite material comprising of rubber elastomers, which are reinforced with steel or fibres, is a prevalent approach to improving the bending and vertical characteristics of the bearing. The attainment of adaptable behaviour at various levels of input can be accomplished by the utilization of strain-induced crystallization, a characteristic inherent to natural rubber [56], or by employing partially bonded or unbonded fibre-reinforced elastomeric isolators [57-59]. In elastomeric rubber isolators, it is a prevalent practice to achieve the needed adaptability through the incorporation of additional dampers [60,61]. Numerous studies, both numerical [61-64] and experimental [65,66], have examined the incorporation of steel dampers into elastomeric isolators. Yuan [60] introduced an innovative polyurethane

elastomeric steel shim isolator attached through steel dampers designed to remain inactive during short displacements. Addressing the requirement for higher vertical capability bearings, particularly for heavyweight and larger span bridges, engineers introduced a polyurethane elastomer (PUE) material with enhanced shear performance [54]. PUE consists of both rigid and ductile sections, allowing for the adjustment of mechanical properties [67,68]. PUE bearings consist of notable vertical strength and shear deformability, capable of achieving an eventual shear strain of 300% and compressive stress exceeding 60 MPa in experiments. PUE demonstrates an energy dissipation capability of approximately 10%-14% at a shear strain of 150%. To mitigate extreme displacement during severe ground motion, the system was enhanced by integrating hysteretic dampers to reinforce the polyurethane bearing. This combination allows for the synergistic application of the bearing's high vertical strength and energy dissipation capability. The steel damper-reinforced polyurethane bearing is composed of a polyurethane bearing with four C-shaped hysteretic dampers. This configuration has been considered to attain a damping of 20% when subjected to a shear strain of around 150% [60]. The steel dampers and PUE are mounted to the upper and lower plates, correspondingly. An initial clearance is provided between the PUE and the steel ring in order to allow for unrestricted movement of the superstructure in response to mild load impacts. To mitigate the effects of frictional heating and maintain low stiffness during minor events, a circular sheet made of polytetrafluoroethylene (PTFE) is incorporated into the bottom plate of the system. This PTFE sheet serves the dual purpose of safeguarding the system from excessive heat generated by friction and ensuring its flexibility under minor disturbances. Therefore, in the case of small shifts, reactions are mostly governed directly by the PUE. However, for bigger displacements beyond the preliminary gap, the steel dampers come into play and contribute to the dissipation of the seismic energy.

An alternate methodology for the process of developing Isolators leverages a characteristic of natural rubber known as strain-induced crystallization [69]. The process of crystallization has the ability to take place in a broad range of natural rubber combinations, but the shear strain essential for crystallization (generally 100% or higher) depends on combining and filler content. The occurrence of Strain-Induced Crystallization (SIC) was readily apparent in guayule and dandelion natural rubbers following purification using acetone, crosslinking with Sulphur, and subsequent application of strain. The guayule natural rubber demonstrated a more notable strain-induced crystallization (SIC) phenomenon when exposed to substantial stretching in comparison to the Hevea natural rubber.

In contrast, dandelion natural rubber displayed a SIC behaviour similar to that of Hevea natural rubber [70]. Building upon this property, Yang [9] introduced a system called crystallizing rubber isolation (CRS). Yang [9] also conducted numerical assessments to compare the performance of CRS with that of the lead plug system, featuring bilinear hysteresis, concerning structural and equipment response. The study revealed that the structural floor acceleration results were larger for the lead plug system when considering shorter durations, which is consistent with the behaviour typically observed in bilinear systems. Nevertheless, this approach is less appropriate for safeguarding conventional machinery that possesses shorter natural durations. On the other hand, the CRS system demonstrated reduced floor acceleration responses that fell within the designated period range, so effectively safeguarding the devices. With the advent of modern research and new technology, there are many others 'Adaptive' seismic isolation system has been developed other than Elastomeric Rubber Bearing and LRB, which is being in practice.

## 4. Factors Affecting Bearing Performance

In the realm of seismic engineering, there are three critical factors that require consideration: the occurrence of cavitation and buckling in bearings, the influence of temperature on the performance of lead cores, and the interaction between soil and structure. These elements play a fundamental role in determining the efficiency of base isolation systems, and they are subjects of extensive research and enhancement in earthquake-resistant construction.

### 4.1. Cavitation and Buckling Phenomena in Bearings

Cavitation in rubber bearings, particularly elastomeric ones used for seismic isolation, arises from micro-cracks in the rubber volume and can result in irreparable damage [71]. It leads to material degradation, reduced bearing performance, loss of load-carrying capacity, increased vibrations and displacements, and poses a risk of failure in critical structures. To mitigate cavitation, engineers and researchers consider material selection, damping devices, optimized design, advanced analysis, and experimental testing. Cavitation damage increases with higher tensile strain amplitudes, and no additional damage occurs if the preceding maximum strain is not surpassed. Exceeding the prior maximum strain results in new cavity formation and additional damage, leading to a decrease in cavitation strength, which eventually stabilizes at a minimum value [72].

Furthermore, the study involved conducting investigations on a total of sixteen rubber bearings obtained from two different manufacturers. These bearings had comparable geometric characteristics but differed in terms of their shear moduli. The objective of the study was to gain insights into the cavitation behaviour exhibited by these bearings. The researchers conducted an investigation into the effects of cavitation on shear and axial properties. They performed post-cavitation tests to gather data and subsequently verified a tension model for elastomeric bearings using the experimental results. This model was then incorporated into software platforms such as OpenSees, ABAQUS, and LS-DYNA [73].

Low shear stiffness in bearings leads to a well-studied buckling phenomenon, with theory providing reasonably accurate design safety factors against buckling instability [74-76]. This theory, based on linear elastic analysis, is applied despite elastomers not being strictly linearly elastic. However, elastomers used in bearings typically exhibit significant linearity in shear over a wide strain range [77]. Studies by Kelly and other researchers [78-80] confirm that the linear theory, though an approximation, is generally accurate and sufficient for most design needs. The phenomenon of rubber-bearing buckling has been extensively investigated under compressive loads, yet there remains a research gap concerning buckling under tension. Experimental validation of the response of steel-reinforced bearings under high shear strain was performed [81]. They employed a non-linear analytical model depending upon the Koh-Kelly framework, corroborated by empirical findings, which encompassed elastomer non-linearity, substantial rotations, and displacements, as demonstrated by Nagarajaiah and Ferrell. The predictive behaviour of multi-layered elastomeric bearings was assessed through finite element numerical simulation using ABAQUS software [16]. Notably, the occurrence of buckling is induced by the low shear stiffness. Theoretically, buckling is rooted in linear elastic model analysis. However, the practicality deviates from this, given that elastomers exhibit non-linear behaviour, closely approximating the elastic range within a shear strain. Regarding design considerations, the linear theory proves relatively suitable and accurate. Through this analysis, it was deduced that the mechanism of an elastomeric isolator in tension, mirror its behaviour in compression. When subjected to tension, the rubber layers at the bearing's central region undergo rotations in opposing directions, engendering shear deformation due to the tensile force. Consequently, substantial displacements allow the isolator's upper portion to ascend. Owing to non-linear geometric effects inherent in the cylindrical rubber

model, the compressive load leading to buckling surpasses the corresponding load in tension. In compression, the vertical load remains nearly constant, and rubber bearings deflect horizontally. In contrast, tension entails a gradual reduction in vertical load accompanied by horizontal deflection.

#### 4.2. Impact of Temperature on Lead Core Performance

The Finite Element Analysis (FEM) was performed considering the steel, rubber, and LRB isolation, but it was limited to mechanical behaviour only [15,82]. The numerical and experimental examination was accomplished to appraise the effect of lead core heating on durability degradation. It extensively investigated the mechanical response of LRB and proposed a model based on Kalpakidis and Constantinou [83-85]. This model accounts for the effects of lead-core heating under cyclic shear loadings. The system has the ability to forecast the instantaneous temperature of the lead core and its immediate impact on the properties and strength of the bearings [86]. This model is expressed as the bi-linear hysteretic model, which is further executed and analysed in SAP2000 and 3D-BASIS computer software. Further, the results were validated by [83-85]. The bounding analysis theory is applied in the context of the lead-core rubber response of bearings to evaluate the importance of lead-core heating. In this analysis, the material characteristics variations are considered at the time of bearings fabrication. Additionally, it incorporates the changes in the mechanical behaviour of the isolators that occur during the life span of bearings due to loading history, environmental changes, and aging. It was accounted by analysis done through upper bound and lower bound properties. The scaling of lead rubber bearing was considered 3-4 times reduced-sized specimen for investigation [87]. They proposed a model that considered the rise in temperature in the lead core owing to the repeated cyclic motion of LRB, which is governed by the subsequent set of equations:

$$\frac{dT_L}{dt} = \frac{\sigma_{YL0} \exp(-E_2 T_L) \cdot v(t)}{\rho_L c_L h_L} - \frac{k_s T_L}{a \cdot \rho_L c_L h_L} \left( \frac{1}{F} + 1.274 \cdot \left( \frac{t_s}{a} \right) \cdot (\bar{t})^{-1/3} \right) \quad (1)$$

$$F = \begin{cases} 2 \cdot \left( \frac{\bar{t}}{\pi} \right)^{\frac{1}{2}} - \frac{\bar{t}}{\pi} \cdot \left[ 2 - \left( \frac{\bar{t}}{4} \right)^2 - \left( \frac{\bar{t}}{\pi} \right)^3 - \frac{15}{4} \left( \frac{\bar{t}}{\pi} \right)^3 \right], \bar{t} < 0.6 \\ \frac{8}{3\pi} - \frac{1}{2(\pi \cdot \bar{t})^{\frac{1}{2}}} \cdot \left[ 1 - \frac{1}{3 \cdot (4\bar{t})} + \frac{1}{6 \cdot (4\bar{t})^2} - \frac{1}{12 \cdot (4\bar{t})^3} \right], \bar{t} \geq 0.6 \end{cases} \quad (2)$$

$$\bar{t} = \frac{\alpha_s t}{a^2} \quad (3)$$

where,  $T_L$  lead core temperature rises at time  $t$ ,  $v(t) = |du/dt|$ , where  $u$  = motion of the lead-rubber bearing, Parameter  $\bar{t}$  is referred to as the 'dimensionless time'. In Eq. (1)–(3),  $\sigma_{YL0}$ , initial effective yield stress of lead,  $\rho_L$  is the density of lead,  $c_L$  is the specific heat of lead,  $a$  is the radius of the lead core,  $k_s$ , thermal conductivity of steel,  $\alpha_s$  is the thermal diffusivity of steel,  $t_s$  is the total thickness of the shim plates,  $h_L$  is the height of the lead core, and  $E_2$  related the effective yield stress of lead to its temperature. Here,  $E_2$  is experimentally determined from the testing of lead samples [84]. The effect of lead core heating with LRB in near-fault zone is studied deeply [88], finding minimal impact from geometric parameters. Bounding analyses tend to overestimate displacements, especially with higher earthquake magnitudes and larger lead core diameters. The rise in lead core temperature decreases with increasing lead core diameter due to reduced cyclic displacement amplitudes. The post-elastic period and rubber height have negligible effects on lead core heating. Additionally, the study explores the influence of low temperatures on LRB hysteretic properties [89]. Conditioning full-scale LRBs from -20 °C to 20°C, the study applies displacement-controlled cyclic motions at frequencies of 0.1 and 0.5 Hz. Results reveal that post-yield stiffness and characteristic strength increase with decreasing

temperature, with characteristic strength showing greater sensitivity to temperature variations than post-yield stiffness.

### 4.3. Influence of Soil-Structure Interaction

The concept of soil-structure interaction within a BI system pertains to the dynamic interplay and interaction between the foundation (structure) and the encompassing soil when exposed to external pressures, such as seismic quakes. The aforementioned interaction has the potential to exert a substantial influence on the performance of the BI system and the overall reaction of the building during seismic events. The impact of soil-structure interaction (SSI) is disregarded during isolator design, often assumed to involve a rigid base [90]. Yet, sacking SSI's influence leads to inaccurate assessments of structural response. SSI can be defined as a bidirectional interaction: the soil's behaviour influences the structure's motion, and vice versa. Evaluations of bridge seismic responses, considering elastomeric bearings and accounting for SSI, are presented [91]. In 1978, Bielak [92] employed the equivalent linearization method to scrutinize the harmonic response of a bilinear hysteretic structure resting on a viscoelastic half-space. When soil flexibility is neglected, and the BI system is assumed linear, results are deduced (78). Extending Bielak's model [93], SSI's effect on the non-linear seismic response of the BI system in simple elastic structures was explored. It was deduced that, minus SSI effects and in undamped scenarios, a harmonic motion emerges beyond the isolator's steady-state response, resulting in unbounded superstructures. Furthermore, it was found that assuming a rigid BI system aligns with the outcomes of [94] for elastic 1-DoF systems. If the superstructure's rigidity is assumed, [92] findings hold. Nevertheless, recent research proposes that under intense ground motion, non-linear effects (e.g., gapping, uplift, sliding) frequently occur near the soil-structure boundary [95]. SSI effects are categorized into two types: (a) Kinematic Interaction and (b) Inertial Interaction. While kinematic interaction remains under investigation, inertial interactions have been explored (3). Soft soil resonates more than rock, intensifying shaking and elevating the natural period at peak response to align with the range of isolated building vibration natural periods. Considering SSI's mutual influence, Han [96] adopted an iterative approach for numerically simulating base-isolated systems in nuclear power plants. The authors incorporated isolator material non-linearity. The SSI analysis outcome showcases a noteworthy reduction in horizontal displacement for isolated nuclear power plants. Linear equivalent SSI analysis [97] and non-linear SSI analysis of isolated nuclear structures with rigid basemats were conducted [98]. The reference study adhered to ASCE 4-16 for non-linear analysis, following a multi-step procedure integrating equivalent linear methods and time-domain techniques that account for both SSI effects and isolator non-linear behaviour. An array of literature explores numerical simulations concerning the interplay between SSI and BI systems, predominantly focusing on the horizontal component of seismic motion. However, addressing the effects of the transverse component is crucial for a comprehensive understanding of isolator behaviour and field response.

## 5. Experimental Modelling of Elastomeric and Lead Rubber Bearings

Over the course of more than three decades, a significant amount of shaking table testing has been conducted on buildings equipped with base isolation systems. This testing has occurred simultaneously with the advancement of isolation devices designed for use in large-scale structures and the global development and refinement of base isolation practices. The initial tests were primarily focused on validating various isolation devices and establishing the feasibility of the concept, but they lacked rigorous criteria for measuring the responses of buildings. The development of elastomeric bearings has outpaced the progress of friction-based sliding systems. Shake table experiments were performed on several of the original systems at the Earthquake Engineering Research



Centre (EERC) located at the University of California. The systems comprised elastomeric bearings with low damping, elastomeric rubber bearings with steel dampers [99], and elastomeric rubber bearings with improved damping through a friction fail-safe mechanism. The lead-rubber bearing (LRB), which originated in New Zealand [100], was subjected to shake table testing at EERC for evaluation purposes [101]. The evaluation of systems was conducted on a 5-storey frame assembly, which allowed for the examination of responses in higher modes and the assessment of the efficacy of different techniques to implement seismic isolation. Numerous studies have frequently shown that isolation systems characterised by elevated levels of damping, particularly nonlinear damping, have proven to be successful in managing isolator displacements. However, this approach has also been found to lead to amplified floor accelerations and heightened high-frequency responses. The effect of tension on rubber bearings was investigated by experimental analysis [102]. It considered sixteen rubber bearings to perform experiments, including lead-plug rubber bearings, natural rubber bearings, and high-damping rubber bearings. It evaluated the characteristics and factors involved in the performance of rubber bearings, including tensile properties, compression, and shear response. The shake table is used for experimental testing of the bearing.

A comprehensive shake table test was conducted in Japan to evaluate the extent of seismic damage in a realistic manner [103]. The experiment involved the evaluation of multi-storey building models using shake tables and sliding elastomeric bearings [104]. Astroza [105] conducted an experiment on a whole five-storey reinforced concrete (RC) building using the NEES-UCSD shaking table. The study focused on analysing the building's structural reactions, non-structural components, and dynamic interactions under different ground motions. The specimens used in this study were subjected to various conditions, such as forced vibration, impact-free vibration, and ambient vibration while being supported by fixed and isolated bases. These conditions were compared to the SEAONC Tentative Code of 1986 [104]. The investigation encompassed a total of eight distinct ground motion records. A three-storey reinforced concrete masonry building was employed in high seismicity zones, utilising a rubber elastomeric bearing isolator to mitigate lateral force responses. This structure was built at a one-quarter scale [106]. In their study, Wu and Samali (2002) [107] conducted a shake table analysis to verify the accuracy of their numerical findings pertaining to a 5-storey steel frame building that was outfitted with laminated rubber bearings. A 3m×3m shaking table was employed in the study, with a maximum acceleration of ±0.9g, a load capacity of up to 10 tonnes, and a maximum stroke of ±100mm. The frequency of the input waveform spanned from 0.1 to 50 Hz, while the time axis was scaled down to one-third of its original size. In 2007, a study was conducted in China to analyse a high-rise building model consisting of 30 storeys. The analysis was performed on a shake table of 4m4m, with a maximum payload capacity of 250 KN [108]. The frequencies observed in the study spanned from 0.1 Hz to 50 Hz, while the maximum accelerations recorded were 0.7g in the vertical direction, 1.2g in the longitudinal direction, and 0.8g in the transverse direction.

The adaptability of a base isolation system was investigated by Madden [109] and Patrick [110] through the implementation of laboratory experiments with scale-model building structures. Over the years, as time has advanced, researchers have consistently introduced fresh ideas and innovations in the field of base isolation. These concepts have been validated through successful shake table testing. The dynamic properties were assessed by means of the autoregressive with exogenous term (ARX) approach and the frequency response function (FRF) curve-fitting method [111], based on floor acceleration measurements. This research aimed to detect structural damage in high-rise steel buildings under realistic ground conditions using full-scale shaking table tests. In their study, Tagliaferro [112] performed a shaking table analysis on a steel pallet racking structure, which incorporated a seismic isolation device. The base isolation system

underwent 3-D shaking table testing at the E-defence facility, also known as the Hyogo Earthquake Engineering Research Centre, located in Japan. The testing was conducted on a 15m×20m platform with a load-bearing capacity of 12000 metric tonnes, specifically designed for tiny full-scale buildings. At maximum payloads, the system exhibited horizontal accelerations above 0.9 times the acceleration due to gravity (0.9g) and vertical accelerations of 1.5 times the acceleration due to gravity (1.5g). The experiment conducted at E-Defence [113] involved subjecting a steel frame building with five storeys to seismic shaking. The latest shake table experiment conducted at E-defence examined the performance of lead rubber bearings and the realistic reaction of a full-scale isolated structure. This experiment yielded valuable insights into various aspects, such as base shear, floor acceleration, and maximum storey drift. The comprehensive shaking table experiments conducted on BI structures unveiled significant impairment to non-structural elements. Nevertheless, unpredictable ground motions and significant horizontal displacements at the isolator level for extended durations and during extreme occurrences have generated apprehension inside base isolation (BI) systems. The design of isolators for extreme events may lead to stiffness that exhibits insufficient responsiveness to lower ground vibrations.

## 6. Numerical Modelling of Elastomeric and Lead Rubber Bearings

Implementing numerical modelling techniques performs a vital task in comprehending and enhancing the capability of elastomeric rubber bearings and LRB within structural solutions. The procedure encompasses several steps, including the definition of geometric and material properties, the selection of suitable constitutive models, the application of boundary conditions and loadings, the execution of finite element analysis (FEA), the incorporation of contact and friction modelling, the integration of damping mechanisms, the performance of non-linear analysis, the validation and calibration of the model, the execution of sensitivity analysis and optimisation, and the interpretation of the obtained results. Numerical simulations offer valuable insights into the functioning of isolation devices across diverse situations, facilitating design improvements and bolstering seismic resilience.

### 6.1. Material Properties used for Numerical Simulations and Analysis

The behaviour of rubber is like homogenous, isotropic, hyper elastic, and incompressible solids. The elastic characteristics of rubber in terms of potential strain energy function  $U$  in terms of Green's deviatoric strain invariants are as follows:

$$U = f(I_1, I_2, I_3) \quad (4)$$

$I_1, I_2, I_3$  are first, second and third deviatoric strain invariant of the green deformation tensor in terms of  $\lambda_1, \lambda_2, \lambda_3$ .

$$I_1 = \lambda_1^2 + \lambda_2^2 + \lambda_3^2 \quad (5)$$

$$I_2 = \lambda_1^2 \lambda_2^2 + \lambda_2^2 \lambda_3^2 + \lambda_3^2 \lambda_1^2 \quad (6)$$

$$I_3 = \lambda_1^2 \lambda_2^2 \lambda_3^2 \quad (7)$$

The design and modelling of hyper-elastic materials hinge on the careful selection of an appropriate strain-energy function  $W$ , as well as the precise determination of material constants. The choice of a particular model is contingent upon the inherent material properties. The equations presented herein illustrate various models, along with their respective material constants and model parameters utilized in numerical simulations. These values are crucial for numerical analysis of the rubber hyper elastic properties.

6.1.1. Aruda-Boyce strain energy potential model [114-117]

$$U = \mu \left\{ \frac{1}{2} (\bar{I}_1 - 3) + \frac{1}{20\lambda_m^2} (\bar{I}_1^2 - 9) + \frac{11}{1050\lambda_m^4} (\bar{I}_1^3 - 27) + \frac{19}{7000\lambda_m^6} (\bar{I}_1^4 - 81) + \frac{519}{673750\lambda_m^8} (\bar{I}_1^5 - 243) \right\} + \frac{1}{D} \left( \frac{J^{el}-1}{2} - \ln J^{el} \right) \tag{8}$$

Table 2. Coefficients for Model calculated by ABAQUS®

Mu	Mu_0	Lamda_M	D	R <sup>2</sup>
0.4283	0.4462	3.9142	1.712e <sup>-3</sup>	0.9902

6.1.2. Marlow Model

The strain energy function for the Marlow form are as follows [114]:

$$U = U_{dev}(\bar{I}_1) + U_{vol}(J^{el}) \tag{9}$$

$U_{dev}$  is a deviatoric part of strain energy per unit volume and  $U_{vol}$  is volumetric part

6.1.3. Ogden Model

The potential strain energy function for the Ogden model are as follows [114]:

$$U = \sum_{i=1}^N \frac{2\mu_i}{\alpha_i^2} (\bar{\lambda}_1^{\alpha_i} + \bar{\lambda}_2^{\alpha_i} + \bar{\lambda}_3^{\alpha_i} - 3) + \sum_{i=1}^N \frac{1}{D_i} (J^{el} - 1)^{2i} \tag{10}$$

Table 3. Coefficients for Model calculated by ABAQUS®

Mu_I	Alpha_I	D_I	R <sup>2</sup>
0.4451	-0.2241	1.824e <sup>-3</sup>	0.9896

6.1.4. Mooney-Rivlin Model

The potential strain energy Mooney-Rivlin model are as follows [114,118-119]:

$$U = C_{10}(\bar{I}_1 - 3) + C_{01}(\bar{I}_2 - 3) + \frac{1}{D_1} (J^{el} - 1)^2 \tag{11}$$

Table 4. Coefficients for Model calculated by ABAQUS®

C <sub>10</sub> (MPa)	C <sub>01</sub> (MPa)	D <sub>1</sub>	R <sup>2</sup>
0.3339	-3.37e <sup>-4</sup>	1.5828e <sup>-3</sup>	0.9881

6.1.5. Neo-Hookean Model

The potential strain energy function for Neo-Hookean Model are as follows [114]:

$$U = C_{10}(\bar{I}_1 - 3) + \frac{1}{D_1} (J^{el} - 1)^2 \tag{12}$$

Table 5. Coefficients for Model calculated by ABAQUS®

C <sub>10</sub> (MPa)	D <sub>1</sub>	R <sup>2</sup>
0.2587	1.5828e <sup>-3</sup>	0.9710

6.1.6. Yeoh Model

The potential strain energy function for Yeoh Model are as follows [114]:

$$U = C_{10}(\bar{I}_1 - 3) + C_{20}(\bar{I}_1 - 3)^2 + C_{30}(\bar{I}_1 - 3)^3 + \frac{1}{D_1}(J^{el} - 1)^2 + \frac{1}{D_2}(J^{el} - 1)^4 + \frac{1}{D_3}(J^{el} - 1)^6 \tag{13}$$

For N=3, the equation can be written as:

$$U = \sum_{i=1}^3 C_{10}(\bar{I}_1 - 3)^i + \sum_{i=1}^3 \frac{1}{D_i}(J^{el} - 1)^{2i} \tag{14}$$

Table 6. Coefficients for Model calculated by ABAQUS®

$C_{10}$ (MPa)	$C_{20}$ (MPa)	$C_{30}$ (MPa)	$D_1$	$D_2$	$D_3$	$R^2$
0.2019	$4.43e^{-5}$	$1.29e^{-4}$	$2.183e^{-3}$	$8.68e^{-5}$	$-1.794e^{-5}$	0.9962

6.1.7. Van der Waals model [114]

The potential strain energy equation for Van der Waals Model are as follows:

$$U = \mu \left\{ -(\lambda_m^2 - 3)[\ln(1 - \eta) + \eta] - \frac{2}{3}a \left( \frac{\bar{I} - 3}{2} \right)^{\frac{3}{2}} \right\} + \frac{1}{D} \left( \frac{J_{el}^2 - 1}{2} - \ln J_{el} \right) \tag{15}$$

Where,  $\bar{I} = (1 - \beta)\bar{I}_1 + \beta\bar{I}_2$  and  $\eta = \sqrt{\frac{\bar{I}-3}{\lambda_m^2-3}}$ ,  $\lambda_m$ = locking stretch, a= global interaction  $\beta$ = invariant mixture parameter,  $\mu$ = shear modulus.

6.1.8. Polynomial Model

The potential strain energy function of Polynomial model are as follows:

$$U = \sum_{i+j=1}^N C_{ij}(\bar{I}_1 - 3)^i(\bar{I}_2 - 3)^j + \sum_{i=1}^N \frac{1}{D_i}(J^{el} - 1)^{2i} \tag{16}$$

Where  $C_{ij}$  and  $D_i$  are temperature dependent parameter

6.1.9. Reduced Polynomial Model

The model is the same as the Polynomial Model by omitting the second deviatoric invariant of the Cauchy Green tensor. The potential strain energy functions are as follows:

$$U = \sum_{i=1}^N C_{i0}(\bar{I}_1 - 3)^i + \sum_{i=1}^N \frac{1}{D_i}(J^{el} - 1)^{2i} \tag{17}$$

$C_{i0}$ ,  $D_i$  are material constant, N= material constant (positive numbers N=1,2,3)

$\mu$ ,  $\lambda_m$  and D are temperature-dependent parameters  $D = \frac{2}{K}$ ; and  $\bar{I}_1 = \bar{\lambda}_1^2 + \bar{\lambda}_2^2 + \bar{\lambda}_3^2$  and  $\bar{I}_2 = \bar{\lambda}_1^{(-2)} + \bar{\lambda}_2^{(-2)} + \bar{\lambda}_3^{(-2)}$ , where  $\bar{\lambda}_i = J^{-\frac{1}{3}}\lambda_i$ ; J= Jacobean determinant where  $J = \lambda_1\lambda_2\lambda_3$ ,  $J^{el}$  is the elastic volume ratio, and K is the bulk modulus. The  $\mu_i$  and  $\alpha_i$  are constants that depend upon shear behaviour and  $D_i$  is compressibility.

6.1.10. Numerical Analysis of Bearings

Numerical modelling of rubber bearings and LRBs provides valuable insights into their behaviour under dynamic loading conditions and aids in the development of more effective and reliable seismic isolation systems. The finite element micro-modelling of lead rubber

bearings was performed in ADINA software [82]. The micromodels give more detailed and accurate results of stress, strain, and strength of LRBs. The modelling and analysis of low-damping rubber bearings and LRB inserted into BI structures presented for design basis earthquakes (DBE). Earlier, although numerous experiments were performed to evaluate the effectiveness of elastomeric bearings and LRB, but very few of them were evaluated numerically. However, with the recent developments in software, the results were verified experimentally and numerically to justify the effectiveness of bearings. The size and the dimensions of its different parts are shown in Table 7 for Elastomeric rubber bearings and in Table 8 for lead rubber bearings. The finite element model of passive control lead rubber and elastomeric bearings is presented [15]. The numerical modelling and analysis using the stiffness matrix of laminated rubber bearings were performed to evaluate the behaviour of columns by Haringx's theory, which considered two independent variables, i.e., rotation angle and lateral displacement [120].

Table 7. Comparison of elastomeric rubber bearing

Proposed by	Outer Diameter ( $d_o$ )mm	Lead Core Diameter	Thickness of single Rubber Pads ( $t_r$ )	Total Number of Rubber pads	Thickness of steel shims	Total number of steel pads	Horizontal Stiffness (KN/mm)	Displacement $\Delta_{max}$ (mm) at lateral Force (KN)
Basshofi et al. 2019 [121]	350	60	7	15	0.5	14	0.49	90mm at 50KN
Robinson and Tucker (1980) [35]	600	105	-	-	5	8	1.7±0.1 (without lead plug)	45mm at 160KN
Kalpakiadis and Constantinou [84]	1000	200	6.7	30	4.8	29	-	400mm at 1200KN
Weisman and Warn(2012) [4]	152	30	3	20	3	19	-	70mm at 18 KN

Table 8. Comparison of lead rubber bearing

Proposed by	Basshofi 2019[121]	Robinson and Tucker [35] (1980)	Kalpakiadis and Constantinou [87]	Weisman and Warn(2012)[4]	Doudoumis 2005	Kanbir [122]
Outer Diameter ( $d_o$ )mm	350	600	1000	152	601	520
Lead Core Diameter(mm)	60	105	200	30	116.8	75
Thickness of single Rubber Pads ( $t_r$ )(mm)	7	-	6.7	3	9.5	14.4
Total Number of Rubber pads(mm)	15	-	30	20	11	18
Thickness of steel shims (mm)	0.5	5	4.8	3	3.0	2.0
Total number of steel pads (mm)	14	8	29	19	10	17
Displacement $\Delta_{max}$ (mm) at lateral Force (KN)	90mm at 50KN	45mm at 160KN	400mm at 1200KN	70mm at 18 KN	152.4mm at 260KN	-

To assess the effectiveness of elastomeric bearings, a comparison between fixed base and rubber-isolated base structures has been conducted using SAP 2000. The analysis considered a linear elastic structure—a 10-story RC residential building located in Dhaka [95]. The center-to-center spacing is 7.62 meters in both directions. The given data includes the following: characteristic strength of 28 MPa, yield stress of 414 MPa, a live load of 2.4 KPa, a dead load (excluding self-weight) of 4.8 KPa, slab thickness of 150 mm, exterior corner dimensions of 750 mm × 750 mm, exterior middle column dimensions of 950 mm × 950 mm, interior column dimensions of 1000 mm × 1000 mm, and various beam sizes, including 525 mm × 825 mm, 600 mm × 900 mm, and 550 mm × 900 mm. Additionally, grade beams of 300 mm × 375 mm each are considered. There are two types of isolators used in this analysis: the first is LRB, and the second one is HDRB. The

dimensions and properties of different isolators are as mentioned. The plan dimension of the lead rubber bearing is 800 mm, the layer thickness is 10 mm, the number of layers is 16, the lead core size is 150 mm, and the total height of the bearing is 240 mm. The horizontal effective stiffness for LRB is 2306.5 kN/m. The plan dimension of HDRB is 950 mm, the layer thickness 10 mm, the number of layers is 16, the lead core size is 175 mm, and the total height of the bearing is 240 mm. The horizontal effective stiffness for HDRB is 5186.92 kN/m. The horizontal stiffness for the total isolation system is 83586.28 kN/m. The results are presented for both fixed base and isolated base structures. Fig. 6 illustrates the schematic representation of the building in Mode 1 for the fixed base, while Fig. 7 depicts the schematic representation of the isolated base structure in the same mode. Further details are provided in Table 9. The pushover analysis is conducted to generate the capacity curve of the building, both with isolator and without isolator as shown in Fig. 8.

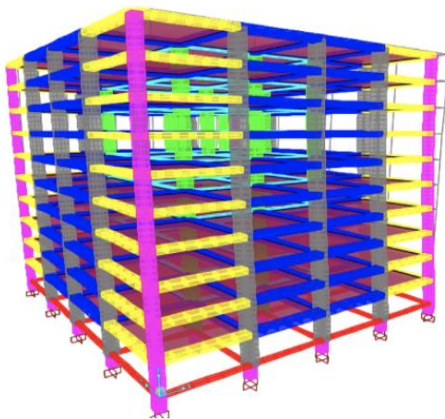


Fig. 6. Response of Fixed Base structure in Mode 1

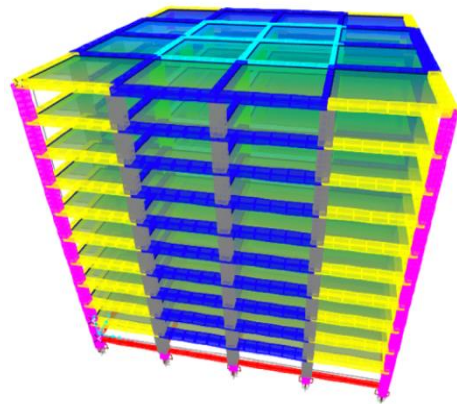


Fig. 7. Response of Isolated Base structure in Mode 1

Table 9. Modal Responses of fixed-base and isolated-base structures in SAP 2000

Mode	Fixed Base				Isolated Base			
	Time Period(s)	Cumulative Mass Participation Ratio			Time Period(s)	Cumulative Mass Participation Ratio		
		X	Y	RZ		X	Y	RZ
Mode 1	1.107558	0.24341	0.58255	0	2.702076	0.01856	0.95672	0
Mode 2	1.107558	0.82596	0.82596	0	2.702076	0.97528	0.97528	0
Mode 3	1.000222	0.82596	0.82596	0.82689	2.485254	0.97528	0.97528	0.99527
Mode 4	0.343231	0.83508	0.91326	0.82689	0.712116	0.9882	0.9882	0.99527
Mode 5	0.343231	0.92238	0.92238	0.82689	0.712116	0.99889	0.99889	0.99527

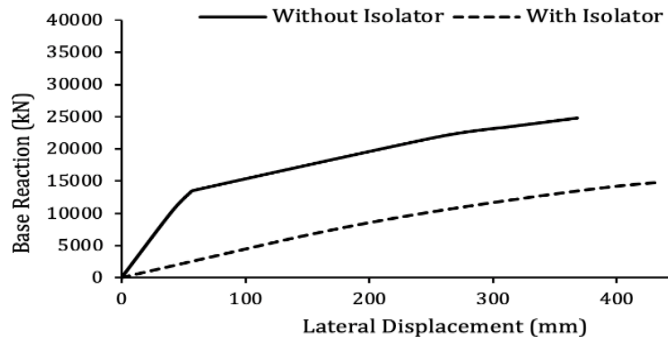


Fig. 8. Pushover curve for RC frame building

## 7. Enhancing Seismic Mitigation with 3-D Base Isolation Systems

While conventional base isolation effectively reduces the horizontal response of buildings to seismic forces, it falls short in addressing the transmission of vertical seismic components to the superstructure. This has led researchers to explore three-dimensional base isolation systems that account for both horizontal and vertical ground motion. In 1986, Kajima Corporation took the initiative to develop a three-dimensional laminated rubber-bearing seismic isolation system, showcasing its application in a two-storey RC structure in Japan [123]. The USA's nuclear industry also examined this approach later. Several novel 3D systems have emerged, going beyond mere design parameter adjustments. One such system is the GERB system, featuring helical springs that offer flexibility in both horizontal and vertical directions. Notably, the vertical frequency is three to five times that of the horizontal direction. This design aims to prevent excessive vertical movement caused by varying lateral loads, live loads, and wind loads. GERB has found applications in diverse industrial and residential buildings. Vertical base isolation systems provide adaptable support in the vertical direction through a grouping of metallic or air springs along with complementary damping mechanisms. Other 3D isolation systems include Rolling Seal-type air springs, Cable-reinforced air springs, Hydraulic 3D systems, and Coned Disk Spring systems.

A study was conducted involving the development and investigation of a three-dimensional (3-D) model for BI structures, employing a single degree of freedom (DOF) model [124]. Through time history analysis, the damping influence of the isolation layer on building response characteristics was examined. The thickness of the rubber layer played a significant role in notably decreasing the vertical frequency. An assessment of the advantages and challenges associated with 3-D isolation systems in nuclear facilities was performed in comparison to horizontal isolators [125]. Linear analysis was carried out to establish the merit of 3-D isolators in nuclear power plants, with a recommendation for future non-linear analysis and modelling of bearings to capture coupling behaviour. The notion of implementing periodic material foundations for nuclear plants located in high-intensity seismic zones was endorsed [126,127]. Periodic materials, originating from solid-state physics, have been artificially engineered by arranging contrasting materials in a periodic manner. These materials are categorized as 1-D, 2-D, and 3-D. Experimental verification has confirmed the efficacy of a 3-D periodic foundation in safeguarding superstructures from incoming hazardous seismic waves in both vertical and horizontal orientations, as well as torsional modes. The study further delved into the three-dimensional modelling and response of laminated rubber bearings and LRB [128]. This

analysis utilized a five-storey scaled steel frame structure subjected to Northridge, El Centro, and Kobe earthquakes. Employing the Opensees 3-D numerical simulation model, an examination was conducted into the combined influence of the BI and SSI effects on various building arrangements [129]. Three models were considered: fixed base, linear BI model, and non-linear BI model. The analysis encompassed 240 non-linear 3-D models for numerical assessment, aiming to establish the correlation and efficiency in predicting spectral accelerations. Notably, a relationship was established between the elongation ratio and damping enhancement concerning the stiffness ratio through the observation of distinct trends across different arrangements. While the numerical simulations and responses of the 3-D BI system with SSI effects have been derived considering the horizontal aspects of seismic excitation, further investigations are warranted to encompass the synchronised impact of both horizontal and vertical earthquake components for comprehensive field response simulations.

## 8. Seismic Base Isolation in the Nuclear Structures

The utility of this technique is not just confined solely to building structures; it extends to nuclear power plants as well. In 2000, Ebisawa et al. [130] introduced a program for applying base isolation systems to nuclear components, presenting a case study demonstrating its viability. This technique can be effectively harnessed within nuclear power plants to bolster safety measures and mitigate the potential for seismic vulnerabilities. The inaugural successful integration of a base isolator into a nuclear facility can be traced to Cruas, France, where four operational units were established in 1983. Furthermore, during the 1980s, an additional two-unit nuclear power plant in Koeberg, South Africa, was brought into operation [131]. To facilitate seismic analysis, including the incorporation of the Bouc-Wen model to assess the impact of second hardening on floor response spectra, the model was adapted into the OpenSees software platform [132]. This endeavour accounted for two distinct material characteristics and variations in robust earthquake motion.

In the past, limited technical guidance and knowledge existed regarding the implementation, examination, and design of BI systems for nuclear plants, coupled with associated financial risks. In response, the Department of Energy and the Nuclear Regulatory Commission (NRC) in the USA initiated research projects to advance tools and procedures for implementing BI systems in nuclear power plants. Through mutual consensus, ASCE 4-16 and ASCE/SEI 43-19 have now incorporated a base isolation chapter. The comprehensive guidelines and standards pertaining to seismic isolation of nuclear structures were published within ASCE 4-16 in 2017. This publication advocates a multi-step nonlinear soil-structure interaction (SSI) analysis based on the base isolation design response spectrum, encompassing both nonlinear behaviour and SSI effects. The multi-step approach integrates equivalent-linear methods and time domain analysis. The NRC has also issued three technical reports concerning the analysis, design, and response of seismic base isolation systems in nuclear power plants: (a) NUREG/CR-7253, "Technical Considerations for Seismic Isolation of Nuclear Facilities" [133], (b) NUREG/CR-7254, "Seismic Isolation of Nuclear Power Plants Using Sliding Bearings" [134], and (c) NUREG/CR-7255, "Seismic Isolation of Nuclear Power Plants Using Elastomeric Bearings" [135]. Ongoing applications of base isolation include nuclear reactors in France, such as the Jules Horowitz Reactor and the International Thermonuclear Experimental Reactor. The former is a fusion reactor. A wealth of research articles, conference papers, and technical reports substantiate the efficacy of seismic isolation standards for nuclear power plants. However, certain gaps necessitate thorough addressing: (a) Developing an enhanced base isolator that aligns with nuclear power plant standards and requirements, accompanied by specific guidelines and protocols. (b) Precisely characterizing advanced



isolated nuclear reactors, with a distinct focus on soil-structure interaction and fluid-structure interactions. (c) Conducting meticulous analysis and estimation of advanced isolated reactors, encompassing both vertical and horizontal seismic intensity inputs at the point of action. (d) Investigating the impact of radiation exposure from nuclear facilities on the mechanical properties of bearings.

## 9. Impact and Consequences of Beyond Design Events

It is essential to consider the performance of isolated structures not only during seismic events but also when subjected to non-seismic events and blast loads, which can exceed the design basis. Explosive incidents directed at buildings release substantial energy rapidly, resulting in waves and extreme heat reaching temperatures around 4000°C, along with a significant increase in pressure well beyond atmospheric levels. The impact of blast loads on structures unfolds in distinct phases: firstly, shock waves cause damage to the building's exterior, followed by penetration into the interior, exerting pressure on various building elements. The columns and internal slabs, along with occupants, were adversely affected by the pressure resulting from the detonations.

In the subsequent phase, the structure's framework encountered substantial loading, responding to the intense ground motion and short-duration impulses, as documented by the NRC [136]. Evaluations of both conventional nuclear plants and those equipped with a base isolation (BI) system were conducted in the context of blast loading, encompassing ground shock-induced blasts and air blasts [137]. The employment of LS-DYNA facilitated response history analyses for these scenarios, revealing a significant reduction in ground shock response when BI systems were integrated. A study investigated the performance and response of base-isolated buildings utilizing elastomeric isolators when subjected to blast loads while maintaining robust seismic protection [138]. This research involved numerical simulations of five-storey structures, considering fixed base, base-isolated, and isolated base configurations alongside supplementary passive control devices. These control mechanisms included tuned-mass dampers and non-linear bumpers.

A three-dimensional (3-D) model was developed to examine the dynamic features of the BI CPR1000 containment system exposed to several aircraft-induced loads [139]. The extent of structural damage was influenced by factors like impact velocity, aircraft angle, and aircraft type. Varied aircraft impacts produced distinct impact loads and energy. Notably, even under similar isolation conditions, the CPR1000 containment's displacement and acceleration responses differed due to the varying properties introduced by diverse aircraft loads. Structures with appropriately high stiffness experienced minimal damage under aircraft impact loads. The impact's brief duration meant that artificial intelligence (AI) directly affected the superstructure. Consequently, the BI system held limited effects over the plastic strain dispersal within the containment. The potential for extreme displacement and acceleration responses leading to internal equipment failure existed. It was concluded that introducing damping into isolation bearings could expedite the dissipation of aircraft impact energy. A post-blast scenario demonstrated that structures employing the BI system exhibited reduced absolute acceleration, peak-storey displacement, and storey drift [140,141].

## 10. Pros and Cons of Bearings

Elastomeric rubber bearings and LRB are types of base isolation (BI) devices that effectively mitigate the impact of seismic shaking on structures, providing notable benefits in terms of performance and structural safeguarding. These devices absorb and dissipate seismic energy, thereby isolating the structure from ground motion during earthquakes. As a result, the stresses and vibrations transmitted to the building are significantly

reduced. These cost-effective solutions are applicable to structures of varying sizes and can be easily implemented in both new and retrofit building projects, leading to reduced construction timelines. Due to their well-established reliability backed by comprehensive research and a demonstrated history of excellent seismic performance spanning several decades, these structures require less maintenance, ultimately resulting in reduced long-term construction expenses.

Elastomeric rubber bearings have certain limitations, including their ability to support vertical loads, susceptibility to potential creep and degradation over time, sensitivity to temperature fluctuations, and restricted displacement capacity. These limitations can pose challenges in structures subjected to significant vertical loads and during highly intense seismic events. Regular maintenance and replacement may also become necessary. On the other hand, the use of Lead Rubber Bearings raises environmental and health concerns due to the toxic nature of lead. Additionally, these bearings primarily rely on friction to dissipate energy, which can potentially limit their effectiveness when compared to alternative systems. The manufacturing and installation costs of these systems can be higher, and their performance in severe earthquake events may not be optimal. Careful design and installation are crucial, as improper implementation can compromise their effectiveness.

Over a century ago, the earliest known use of current seismic isolation methods was documented. However, comprehensive studies and significant applications of these techniques have only recently begun. Consequently, numerous investigations have been conducted by academicians, leading to the development of numerous methodologies. The review of elastomeric bearings has so far only been done in a very restricted way in multiple studies. The eccentricity in the isolated structure is the distance amid the centre of mass and the center of stiffness. If eccentricity exists in isolated structures, then chances of torsional coupling are possible [142]. It was concluded that if the isolator has an eccentricity of small or zero ( $e_b/L < 0.2$ ), then corner-displacements magnification  $\bar{U}_{cb}$  is small ( $\bar{U}_{cb} < 1.3$ ), despite the superstructure having a large eccentricity ( $e_b/L < 0.4$ ). Therefore, it is concluded that superstructure eccentricity has less effect. It has been concluded [143] that increasing  $e_b/L$  leads to an increase in Torque Amplifications. The non-linear behaviour of torsionally coupled BI buildings subjected to random earthquakes having different parameters was investigated [144]. He concluded that if isolator eccentricity increases, then the effectiveness of the base isolator decreases while reducing the torsional response of the superstructure [145]. The two horizontal components of earthquakes are investigated to evaluate the influence of torsion on the seismic response of the structures. To evaluate the response, the parameters are varied, e.g., the ratio of eccentricity to a radius of gyration, mass, and stiffness with height, number of storeys, etc. Torsional irregularities in base-isolated systems, stemming from architectural and functional changes, need careful consideration during design. While base isolators reduce seismic demands, the alignment of the isolator rigidity centre and superstructure mass centre is crucial to minimize torsional effects on seismic response. It was concluded from the study that LRB isolators display greater sensitivity to torsional effects when compared to other isolators [146]. Models of LRB isolators featuring 10% and 20% eccentricities indicate average displacements that are 11% and 14% higher, respectively, than those observed in models without eccentricity. In contrast, FPS isolators show a disparity of less than 5%. The influence of eccentricities on rubber-isolated structures is contingent upon the torsional frequency of the isolation system.

The selection of an appropriate isolation system to protect a structure involves consideration of various factors. These factors include the seismic risk magnitude of the area, the expected displacement capacity, concerns related to uplift, the long-term performance, durability, and maintenance requirements, as well as the cost implications.

The primary function of BI systems is to offer a mechanism capable of fulfilling various performance objectives during different seismic events, thereby ensuring the protection of both the structural and non-structural elements, even under highly intense seismic conditions. Several experimental studies and numerical simulations have been conducted on various kinds of BI systems that demonstrate seismic features. Additional investigation is required to (i) collect three-dimensional response data for buildings employing contemporary isolation systems, (ii) evaluate the precision of current analytical and numerical models in forecasting demands on primary, secondary, and non-structural systems, and (iii) advance our comprehension of the seismic susceptibility of secondary and non-structural systems across diverse scenarios. This study has the potential to uncover constraints in traditional isolation techniques employed to defend these systems, hence motivating the investigation of new strategies to attain total three-dimensional safety.

## 11. Conclusions

This study provides an overview of significant research on seismic elastomeric and lead rubber bearings, both in terms of numerical and experimental techniques, while conducting a historical evaluation of isolation approaches. Additionally, it categorizes useful strategies based on their underlying mechanisms and contrasts their benefits and drawbacks. While these bearings are effective in reducing ground-shaking forces, existing research has also identified limitations that must be addressed to ensure their optimal performance. The following highlights the closing remarks:

- It is essential to validate the assumptions made in the fabrication, manufacturing, and material properties of the LRBs. It gives a satisfactory understanding of mechanical behaviour, and allows the identification of critical areas, thus significantly contributing to the improvements in their designs.
- It is concluded from the literature that the bearing should provide adequate horizontal flexibility to extend the building's natural period and accommodate spectral demands. It must possess adequate energy dissipation capacity to restrict displacements within the prescribed limits, ensuring structural integrity. It should maintain an appropriate level of rigidity, allowing the BI building to behave comparably to a fixed-base structure under normal service loads.
- Elastomeric bearings, such as LRBs, are susceptible to deterioration over a period of time, which may impair functionality. The rubber material might degrade and lose its flexibility when exposed to weathering, UV radiation, and other adverse environmental conditions. Further, research is required to create more resilient rubber polymers that can endure exposure to these elements over an extended period of time.
- Extreme temperatures could have a detrimental effect on the efficiency of the bearings because they are temperature-sensitive. Consequently, their capability to mitigate seismic forces may be influenced by alterations in their stiffness, damping, and other mechanical characteristics. Therefore, further study is needed to create more robust bearings.
- Significant deformations might take place in bearings during severe tremors, which may impair their long-term functioning. To precisely forecast how bearings will perform amid substantial deformation, research is required to create more accurate analytical and numerical models and robust testing procedures and guidelines.
- As a consequence of their propensity for compression set, these bearings may begin to lose their elasticity and become less capable to withstand seismic stresses. This is especially problematic for structures that experience low-frequency vibrations.

Further study is required to create materials that are more durable and capable of withstanding compression sets.

- These bearings must be installed and maintained appropriately in order to function at their best. However, installation and maintenance can be difficult and call for specialized expertise and tools. Better maintenance and installation methods that are affordable and simple to use need to be developed through investigation.
- If the ratio of eccentricity to the radius of gyration increases, then modal energy and input energy are reduced. The reduced stiffness of the structure along the height does not influence the energy reduction.
- It is proved from triaxial loading analysis that the coupling effect cannot be neglected. Therefore, to manufacture an accurate base-isolated model with HDRB or natural rubber bearings with rational and economical design, proper material characteristics and coupling effects must be considered.
- It was observed from the literatures that an increase in the number of rubber layers enhances the horizontal flexibility of the isolator; thus, the vibration period of the structure increases, leading to a significant reduction in seismic amplification. During the period of seismic activity, the inter-storey drifts are reduced significantly as displacements are concentrated at the isolator level. Thus, it leads to minimizing damages in structural and non-structural components of the structure.
- An increase in the number of rubber layers improves the isolator's horizontal flexibility; as a result, the vibration period of the structure lengthens, resulting in a considerable decrease in seismic amplification. As displacements are localised at the isolator level during a seismic event, inter-storey drifts are greatly reduced. As a result, it helps to reduce impairment to both structural and non-structural elements of the structure.

There are several challenges associated with elastomeric and LRB that must be addressed to optimize their performance in mitigating seismic forces. Through the resolution of these challenges, researchers have the potential to enhance the overall efficacy and reliability of bearings, thereby leading to the creation of structures that are more resilient and less prone to risks in earthquake-prone areas. The field of base isolation systems has witnessed significant progress in the development and investigation of adaptive properties, specifically in relation to elastomeric and lead rubber bearings. Certain types of building infrastructure devices have demonstrated a significant capability to disperse the input energy in the event of dangerous seismic occurrences. These devices have proven to be beneficial for structures that house delicate equipment situated in regions prone to prolonged seismic activity. Nevertheless, it was observed from the review that certain categories of isolation devices may prove to be more advantageous when subjected to ground motions of low to moderate intensity.

There is a need for ongoing evaluation of the BI system to ensure that it fulfils all the requirements necessary for its application in these domains. Certain deliberated selections are presently limited to investigation only and potentially not deemed practical or economically viable for large-scale use at present. Hence, it is recommended that future research endeavours explore cost-effective and pragmatic approaches for implementing these solutions in real-world architectural structures and across a wide range of applications. It is suggested that a comprehensive investigation be undertaken, encompassing numerical simulations and experimental analyses, to explore a wider range of isolation systems that demonstrate seismic isolation properties. This investigation should also consider multifaceted ground motions with varying intensities and diverse properties.

## References

- [1] Calvi PM, Calvi GM. Historical development of friction-based seismic isolation systems. *Soil Dyn Earthq Eng*. 2018;106. <https://doi.org/10.1016/j.soildyn.2017.12.003>
- [2] Beirami Shahabi A, Ahari GZ, Barghian M. Base isolation systems-a state of the art review according to their mechanism. *J Rehabil Civ Eng*. 2020;8(2):37–61. <https://doi.org/10.22075/JRCE.2019.16186.1306>
- [3] Tubaldi E, Mitoulis SA, Ahmadi H. Comparison of different models for high damping rubber bearings in seismically isolated bridges. *Soil Dyn Earthq Eng*. 2018;104:329–45. <http://dx.doi.org/10.1016/j.soildyn.2017.09.017>
- [4] Weisman J, Warn GP, Asce AM. Stability of Elastomeric and Lead-Rubber Seismic Isolation Bearings. *J Struct Eng*. 2012;138(2):215–23. [https://doi.org/10.1061/\(ASCE\)ST.1943-541X.0000459](https://doi.org/10.1061/(ASCE)ST.1943-541X.0000459)
- [5] Ozer E, Inel M, Cayci BT. Seismic Performance Comparison of Fixed and Base-Isolated Models. *Iran J Sci Technol*. 2022;47(3):1–17. <http://dx.doi.org/10.1007/s40996-022-00936-4>
- [6] Michalis F, Vassiliou, Anastasios Tsiavos BS. Dynamics of inelastic base-isolated structures subjected to analytical pulse ground motions. *Earthq Eng Struct Dyn*. 2013. <https://doi.org/10.1002/eqe.2311>
- [7] Marasco S, Cimellaro GP. Introduction to Dynamics of Structures and Earthquake Engineering. 2018. <http://dx.doi.org/10.1007/978-3-319-72541-3>
- [8] Skinner, R. I., Robinson, W. H., and McVerry GH. An introduction to seismic isolation. Wiley, New York. 1993.
- [9] Yang TY, Konstantinidis D, Kelly JM. The influence of isolator hysteresis on equipment performance in seismic isolated buildings. *Earthq Spectra*. 2010;26(1):275–93. <https://doi.org/10.1193/1.3276901>
- [10] Skinner RI, Kelly TE, Robinson BWH. Structural Engineers.
- [11] Naeim F and K. Design of Seismic Isolated Structures: From Theory to Practice. 1999.
- [12] Alam MS, Bhuiyan MAR, Billah AHMM. Seismic fragility assessment of SMA-bar restrained multi-span continuous highway bridge isolated by different laminated rubber bearings in medium to strong seismic risk zones. *Bull Earthq Eng*. 2012;10(6):1885–909. <https://doi.org/10.1007/s10518-012-9381-8>
- [13] Gent AN, EA Meinecke. Compression, bending and shear of bonded rubber blocks. *Polym Eng Sci*. 1970;10(1):48–53.
- [14] Gent, A.N., Lindley P. The compression of bonded rubber blocks. *Proc Inst Mech Eng*. 1959; 173:111–7.
- [15] Ali H-EM, Abdel-Ghaffar AM. Modeling of Rubber and Lead Passive-Control Bearings for Seismic Analysis. *J Struct Eng*. 1995;121(7):1134–44. [https://doi.org/10.1061/\(asce\)0733-9445\(1995\)121:7\(1134\)](https://doi.org/10.1061/(asce)0733-9445(1995)121:7(1134))
- [16] Toopchi-Nezhad H, Drysdale RG, Tait MJ. Parametric study on the response of stable unbonded-fiber reinforced elastomeric isolators (SU-FREIs). *J Compos Mater*. 2009;43(15):1569–87. <https://doi.org/10.1177/0021998308106322>
- [17] Touaillon J. Improvement in buildings. US Pat No 99,973. 1870;
- [18] Kelly JM. Aseismic base isolation: review and bibliography. *Soil Dyn Earthq Eng*. 1986;5(4):202–16. [https://doi.org/10.1016/0267-7261\(86\)90006-0](https://doi.org/10.1016/0267-7261(86)90006-0)
- [19] Martel RR. The Effects of Earthquake on Buildings with a Flexible First Storey. *Bull Seismol Soc Am*. 1929;19(3):167–78.
- [20] Bednarski EJ. Flexible “First-Story” Construction for Earthquake Resistance. *Transactions ASCE*. 1935;657–60.
- [21] Ryuiti O. Experiment on Earthquake Construction using Roller Type Damper. *J Archit Inst Japan*. 1941;32.
- [22] Ryuiti O. A Note on the Seismofree Foundation. *J Archit Inst Japan*. 1951;42.
- [23] Ryuiti O. A Study of the Seismofree Building Structures. *J Archit Inst Japan*. 1952;43.

- [24] Ryuiti O. Practical Use of Seismofree Foundation. *J Archit Inst Japan*. 1956;47.
- [25] Caspe MS. Earthquake Isolation of Multi-Storey Concrete Structures. *J Am Concr Inst*. 1970; 11:923–33.
- [26] Caspe MS. Base Isolation from Earthquake Hazards, an Idea Whose Time Has Come! In: 8th World Conference on Earthquake Engineering, San Francisco. 1984. p. 1031–8.
- [27] Haringx JA. On highly compressible helical springs and rubber rods and their application for vibration-free mountings, Part-I. *Philips Res Rep*. 1948;3:401–49.
- [28] Haringx JA. On highly compressible helical springs and rubber rods and their application for vibration-free mountings, III. *Philips Res Rep*. 1949; 4:206–20.
- [29] Haringx JA. On highly compressible helical springs and rubber rods and their application for vibration-free mountings, II. *Philips Res Rep*. 1949; 4:49–80.
- [30] Gent AN. Elastic stability of rubber compression springs. *J Mech Eng Sci*. 1964;6(4):318–26.
- [31] Seigenthaler R. Earthquake-Proof Building Supporting Structure with Shock Absorbing Damping Elements. *Schweizerische Bauzeitung*, Nr. 1970;20.
- [32] Derham CJ. Basic Principles of Base Isolation. In: Proceedings of the International Conference on Natural Rubber for Earthquake Protection of Buildings and Vibration Isolation, Kuala Lumpur, Malaysia. 1982. p. 247–56.
- [33] Thomas AG. The Design of Laminated Bearings. In: Proceedings of the International Conference on Natural Rubber for Earthquake Protection of Buildings and Vibration Isolation, Kuala Lumpur, Malaysia. 1982. p. 229–43.
- [34] Derham CJ. Rubber Bearings for Base Isolation of Structures. In: Asian Regional Conference on Tall Buildings and Urban Habitat, Kuala Lumpur, Malaysia. 1982.
- [35] Robinson WH, Tucker AG. Test results for lead-rubber bearings for Wm. Clayton Building, Toe Toe Bridge and Waitotukupuna Bridge. *Bull New Zeal Soc Earthq Eng*. 1981;14(1):21–33. <https://doi.org/10.5459/bnzsee.14.1.21-33>
- [36] Malhotra PK. Dynamics of seismic impacts in base-isolated buildings. *Earthq Eng Struct D*. 1997;26(8):797–813.
- [37] Marsico MR. Seismic isolation and energy dissipation: theoretical basis and applications. University of Naples Federico II; 2008.
- [38] Fujita, T., Suzuki, S., and Fujita S. Hysteretic restoring force characteristics of high damping rubber bearings for seismic isolation. *ASME PVP Conf-JSME Co-sponsorsh*. 1989; 181:35–41.
- [39] Mazuda, T., Shiojiri, H., Oka, Y., Fujita, T., and Seki M. Experiment on large-scale seismic isolation elements. In: Trans of the 10th SMiRT-K. 1989. p. 691–6.
- [40] Aiken, I. D., Kelly, J. M., Clark, W. P., Tamura, K., Kikuchi, M., and Itoh T. Experimental studies of the mechanical characteristics of three types of seismic isolation bearings. In: Proc, 3rd World Conf on Earthquake Engineering, Madrid, Spain. 1992.
- [41] Yasaka A (1995). Dynamic behaviors of rubber bearings for base isolation. PhD dissertation, Dept of Architectural Engineering, the University of Tokyo, Japanese.
- [42] Mori, A., Moss, P. J., Cooke, M., and Carr AJ. The behavior of bearings used for seismic isolation under shear and axial load. *Earthq Spectra*. 1999;15(2):199–224.
- [43] Sano, T., and Pasquale GD. A constitutive model for high damping rubber bearings. *J Press Vessel Technol*. 1995; 117:53–8.
- [44] Hwang, J. S., and Ku SW. Analytical modeling of high damping rubber bearing. *J Struct Eng*. 1997;123(8):1029–36.
- [45] Hwang, J. S., Wu, J. D., Pan, T.-C., and Yang G. A mathematical hysteretic model for elastomeric isolation bearings. *Earthq Eng Struct Dyn*. 2002; 31:771–89.
- [46] Park YJ, Wen YK AA-S. Random vibration of hysteretic systems under bi-directional ground motions. *Earthq Eng Struct Dyn*. 1986; 14:543–57.
- [47] Mokha, A. S., Constantinou, M. C., and Reinhorn AM. Experimental study and analytical prediction of earthquake response of a sliding isolation system with a spherical system. Tech Rep NCEER-90-0020 State Univ New York, Buffalo, NY. 1990.

- [48] Abe M, Asce M, Yoshida J, Fujino Y, Asce M. Multiaxial Behaviors of Laminated Rubber Bearings and Their Modeling . I : Experimental Study. J Struct Eng. 2005;130(8):1119–32.
- [49] Li Y, Li J. Overview of the development of smart base isolation system featuring magnetorheological elastomer. Smart Struct Syst. 2019;24(1):37–52. <https://doi.org/10.12989/sss.2019.24.1.037>
- [50] Anti-Seismic Devices. EN 15129, 2009.
- [51] EN 1337 Part 3. European Standards Structural Bearings – Elastomeric Bearings. 2005.
- [52] ISO 6446. International Standard Rubber Products – Bridge Bearings – Specification for Rubber Materials. 1994.
- [53] ASTM D4014. American Society for Testing and Materials Standard Specification for Plain and Steel-Laminated Elastomeric Bearings for Bridges. 2012.
- [54] Ounis HM, Ounis A, Djedoui N. A new approach for base isolation design in building codes. Asian J Civ Eng. 2019;20(6):901–9. <https://doi.org/10.1007/s42107-019-00153-x>
- [55] Yuan Y, Wang S, Tan P, Zhu H. Mechanical performance and shear constitutive model study of a new high-capacity polyurethane elastomeric bearing. Constr Build Mater 2020;232:117227. <https://doi.org/10.1016/j.conbuildmat.2019.117227>
- [56] Toopchi-Nezhad H, MJ T, RG D. Lateral Response Evaluation of Fiber- Reinforced Neoprene Seismic Isolators Utilized in an Unbonded Application. J Struct Eng. 2008;134:1627–37. [https://doi.org/10.1061/\(ASCE\)0733-9445](https://doi.org/10.1061/(ASCE)0733-9445)
- [57] Toopchi-Nezhad H, Tait M, RG Drysdale. Shake table study on an ordinary low- rise building seismically isolated with SU-FREIs (stable unbonded-fiber reinforced elastomeric isolators). Earthq Eng Struct Dyn. 2009;38(11):1335–57. <https://doi.org/10.1002/eqe.923>
- [58] Engelen N Van, Osgooei P, Tait M, Konstantinidis D. Partially bonded fiber- reinforced elastomeric isolators (PB-FREIs). Struct Control Heal Monit. 2015;22(3):417–32.
- [59] Kelly JM, NC Van Engelen. Fiber-reinforced elastomeric bearings for vibration isolation. J Vib Acoust. 2016;138.
- [60] Yuan Y, Wei W, Ni Z. Analytical and experimental studies on an innovative steel damper reinforced polyurethane bearing for seismic isolation applications. Eng Struct . 2021; 239:112254. <https://doi.org/10.1016/j.engstruct.2021.112254>
- [61] Sheikhi J, Fathi M, R Rahnavard. Natural rubber bearing incorporated with high toughness steel ring dampers. Structures. 2020;24:107–23.
- [62] Rahnavard R, Thomas RJ. Numerical evaluation of steel-rubber isolator with single and multiple rubber cores. Eng Struct. 2019;198.
- [63] Sheikhi J, M Fathi, Rahnavard R, Napolitano R. Numerical analysis of natural rubber bearing equipped with steel and shape memory alloys dampers. Structures. 2021; 32:1839–55. <https://doi.org/10.1016/j.istruc.2021.03.115>
- [64] Nguyen XD, Guizani L. Analytical and numerical investigation of natural rubber bearings incorporating U-shaped dampers behaviour for seismic isolation. Eng Struct. 2021; 243:112647.
- [65] Xiang N, Alam MS, Li J. Shake table studies of a highway bridge model by allowing the sliding of laminated-rubber bearings with and without restraining devices. Eng Struct. 2018; 171:583–601. <https://doi.org/10.1016/j.engstruct.2018.05.121>
- [66] Kakolvand H, M Ghazi, B Mehrparvar, S Parvizi. Experimental and Numerical Study of a New Proposed Seismic Isolator Using Steel Rings (SISR). J Earthq Eng. 2020;1–30. <https://doi.org/10.1080/13632469.2020.1822227>
- [67] H Guo, Guo W, AV Amirkhizi. Constitutive modeling of the tensile and compressive deformation behavior of polyurea over a wide range of strain rates. Constr Build Mater 2017; 150:851–9. <https://doi.org/10.1016/j.conbuildmat.2017.06.055>

- [68] Oprea S. Effects of Fillers on Polyurethane Resin-based Polyurethane Elastomeric Bearing Materials for Passive Isolation. *J Compos Mater.* 2008;42(25):2673–85. <https://doi.org/10.1177/0021998308096329>
- [69] Loos K, AB Aydogdu, Lion A, Johlitz M, J Calipel. Strain-induced crystallisation in natural rubber: a thermodynamically consistent model of the material behaviour using a serial connection of phases. *Contin Mech Thermodyn.* 2021;33(4):1107–40. <https://doi.org/10.1007/s00161-020-00950-9>
- [70] Ikeda Y, Junkong P, Ohashi T, Phakkeeree T, Sakaki Y, Tohsan A, et al. Strain-induced crystallization behaviour of natural rubbers from guayule and rubber dandelion revealed by simultaneous time-resolved WAXD/tensile measurements: Indispensable function for sustainable resources. *RSC Adv.* 2016;6(98):95601–10. <https://doi.org/10.1039/c6ra22455e>
- [71] Lefèvre V, Ravi-Chandar K, Lopez-Pamies O. Cavitation in rubber: an elastic instability or a fracture phenomenon? *Int J Fract.* 2015;192(1):1–23. <https://doi.org/10.1007/s10704-014-9982-0>
- [72] Kumar M, Whittaker A, Constantinou M. An advanced numerical model of elastomeric seismic isolation bearings. *Earthq Eng Struct Dynam.* 2014;43(13):1955–74.
- [73] Kumar M, Whittaker AS, Constantinou MC. Experimental investigation of cavitation in elastomeric seismic isolation bearings. *Eng Struct.* 2015; 101:290–305. <http://dx.doi.org/10.1016/j.engstruct.2015.07.014>
- [74] M Imbimbo, JM Kelly. Stability aspects of elastomeric isolators. *J Earthq Spectra.* 1997;13(3):431–49.
- [75] KL Ryan, AK Chopra. Approximate analysis methods for asymmetric plan base-isolated buildings. *Earthq Eng Struct Dyn.* 2002; 31:33–54.
- [76] JM Kelly, MR Marsico. Stability and post-buckling behavior of non-bolted elastomeric isolators. *Seism Isol Prot Syst.* 2010;(1):41–54. <http://dx.doi.org/10.2140/siaps.2010.1.41>
- [77] Kelly JM. Analysis of fiber-reinforced elastomeric isolators. *J Seism Earthq Eng.* 1999;2(1):19–34.
- [78] J.M. Kelly, M. EERI. *Base Isolation: Linear Theory and Design.* 1990.
- [79] P Pan, D Zamfirescu, Nakashima M, Nakayasu N, Kashiwa H. Base-isolation design practice in Japan: introduction to the post-Kobe approach. *J Earthq Eng.* 2005;9(1):147–71.
- [80] JM Kelly, DA Konstantinidis. *Mechanics of rubber bearings for seismic and vibration isolation.* Wiley, New York. 2011.
- [81] I. G. Buckle and H. Liu. Experimental determination of critical loads of elastomeric isolators at high shear strain. *NCEER Bull.* 1994;8(3):1–5.
- [82] Doudoumis IN, Gravalas F. Analytical Modeling of Elastomeric Lead-Rubber Bearings with the use of Finite Element Micromodels. In: 5th GRACM International Congress on Computational Mechanics. 2005.
- [83] Kalpakidis IV Constantinou MC. Effects of heating and load history on the behavior of lead-rubber bearings. Technical Report MCEER-08-0027, Multidisciplinary Center for Earthquake Engineering Research, University at Buffalo, State University of New York, Buffalo, NY. 2008.
- [84] Kalpakidis I, Constantinou M. Effects of heating and load history on the behavior of lead-rubber bearings. *Tech RepNo MCEER-08-0027.* 2008;1–270.
- [85] Kalpakidis I V., Constantinou MC. Effects of Heating on the Behavior of Lead-Rubber Bearings. I: Theory. *J Struct Eng.* 2009;135(12):1440–9.
- [86] Kalpakidis I V., Constantinou MC, Whittaker AS. Modeling strength degradation in lead-rubber bearings under earthquake shaking. *Earthq Eng Struct Dyn.* 2010;39:1533–49. <https://doi.org/10.1002/eqe.1039>



- [87] Kalpakidis I. V., Constantinou M.C. Principles of scaling and similarity for testing of lead-rubber bearings. *Earthq Eng Struct Dyn.* 2010;(39):1551-68. <https://doi.org/10.1002/eqe.1041>
- [88] Ozdemir G, Dicleli M. Effect of lead core heating on the seismic performance of bridges isolated with LRB in near-fault zones. *Earthq Eng Struct Dyn.* 2012;41(14):1989-2007. <https://doi.org/10.1002/eqe.2170>
- [89] Yasar C, Volkan K, Cavdar E, Ozdemir G. Variation in Mechanical Properties of a Lead-Rubber Bearing Exposed to Low Temperature. *J Cold Reg Eng.* 2023;37(3). <http://dx.doi.org/10.1061/JCRGEI.CRENG-698>
- [90] Mahmoud S, Austrell PE, Jankowski R. Simulation of the response of base-isolated buildings under earthquake excitations considering soil flexibility. *Earthq Eng Eng Vib.* 2012;11(3):359-74. <https://doi.org/10.1007/s11803-012-0127-z>
- [91] Neethu B, Das D. Effect of dynamic soil-structure interaction on the seismic response of bridges with elastomeric bearings. *Asian J Civ Eng.* 2019;20(2):197-207. <https://doi.org/10.1007/s42107-018-0098-0>
- [92] Jacobo Bielak. Dynamic response of non-linear building-foundation systems. *Earthq Eng Struct Dyn.* 1978; 6:17-30.
- [93] Luco JE. Effects of soil-structure interaction on seismic base isolation. *Soil Dyn Earthq Eng.* 2014; 66:167-77. <http://dx.doi.org/10.1016/j.soildyn.2014.05.007>
- [94] Paul C. Jennings, Jacobo Bielak. Dynamics of Building-Soil Interaction. 1972.
- [95] Bolisetti C, Whittaker AS, Coleman JL. Linear and nonlinear soil-structure interaction analysis of buildings and safety-related nuclear structures. *Soil Dyn Earthq Eng.* 2018; 107:218-33. <https://doi.org/10.1016/j.soildyn.2018.01.026>
- [96] Han X, Marin-Artieda C. A case study on the seismic protection of equipment using lead-rubber bearings. *Struct Congr 2015 - Proc 2015 Struct Congr.* 2015;1962-74. <https://doi.org/10.1061/9780784479117.169>
- [97] Zhou Z, Wei X. Seismic Soil-Structure Interaction Analysis of Isolated Nuclear Power Plants in Frequency Domain. *Shock Vib.* 2016;2016. <https://doi.org/10.1155/2016/6127895>
- [98] Lee E haeng, Jung D ri, Rhee I, Kim J min. A nonlinear soil-structure interaction analysis technique based on seismic isolation design response spectrum for seismically isolated nuclear structures with rigid basemat. *Nucl Eng Des.* 2021; 381:111334. <https://doi.org/10.1016/j.nucengdes.2021.111334>
- [99] J.M. Kelly, Skinner, M.S., Beucke, K.E. Experimental Testing of an Energy Absorbing Seismic Isolation System. 1980.
- [100] Robinson WH. Lead-rubber hysteretic bearings suitable for protecting structures during earthquakes. *Earthq Eng Struct Dyn.* 1982; 10:593-604.
- [101] J.M. Kelly, Hodder S.B. Experimental Study of Lead and Elastomeric Dampers for Base Isolation Systems. 1981.
- [102] Iwabe N, Takayama M, Kani N, Wada A. Experimental Study on the Effect of Tension for Rubber Bearings. *12 World Conf Earthq Eng.* 2000;1-8.
- [103] Tsai CS, Chiang TC, Chen BJ. Shaking Table Tests of a Full-Scale Steel Structure Isolated with MFPS. *Am Soc Mech Eng Press Vessel Pip Div PVP.* 2003;466(3):41-7.
- [104] Michel S. Chalhoub, Member, ASCE JMK. Comparison of SEAONC Base Isolation Tentative Code to Shake Table Tests. *J Struct Eng.* 1990;116(4):925-38.
- [105] Astroza R., J.P. Conte, J.I. R, H. Ebrahimian, Hutchinson T.C. Shake table testing of a full-scale five-story building: system identification of the five-story test structure. *Struct Congr.* 2013;1472-84.
- [106] Paulson TJ, Abrams DP, Mayes RL. Shaking-Table Study of Base Isolation for Masonry Buildings. *J Struct Eng.* 1991;117(11):3315-36.
- [107] Wu YM, Samali B. Shake table testing of a base isolated model. *Eng Struct.* 2002;24(9):1203-15. [https://doi.org/10.1016/S0141-0296\(02\)00054-8](https://doi.org/10.1016/S0141-0296(02)00054-8)

- [108] Lu X, Zhou Y, Lu W. Shaking table model test and numerical analysis of a complex high-rise building. *Struct Des Tall Spec Build.* 2007;16(2):131–64. <https://doi.org/10.1002/tal.302>
- [109] Madden GJ, Symans MD, Wongprasert N. Experimental Verification of Seismic Response of Building Frame with Adaptive Sliding Base-Isolation System. *J Struct Eng.* 2002;128(8):1037–45. [https://doi.org/10.1061/\(asce\)0733-9445\(2002\)128:8\(1037\)](https://doi.org/10.1061/(asce)0733-9445(2002)128:8(1037))
- [110] Brewick Patrick, A Johnson Erik, Eiji Sato, Sasaki Tomohiro. Modeling the Dynamic Behavior of Isolation Devices in a Hybrid Base-Isolation Layer of a Full-Scale Building. *J Eng Mech.* 2021;146(11):1–17. [https://doi.org/10.1061/\(asce\)em.1943-7889.0001774](https://doi.org/10.1061/(asce)em.1943-7889.0001774)
- [111] Ji X, Fenves GL, Kajiwara K, Nakashima M. Seismic Damage Detection of a Full-Scale Shaking Table Test Structure. *J Struct Eng.* 2011;137(1):14–21. [https://doi.org/10.1061/\(asce\)st.1943-541x.0000278](https://doi.org/10.1061/(asce)st.1943-541x.0000278)
- [112] Tagliafierro B, Montuori R, Castellano MG. Shake table testing and numerical modelling of a steel pallet racking structure with a seismic isolation system. *Thin-Walled Struct.* 2021; 164:107924. <https://doi.org/10.1016/j.tws.2021.107924>
- [113] Dao ND, Okazaki T, Mahin SA, Zahgi AE, Kajiwara K, Matsumori T, et al. Experimental Evaluation of an Innovative Isolation System for a Lightweight Steel Moment Frame Building at E-Defense. 2011;41171. [https://doi.org/10.1061/41171\(401\)256](https://doi.org/10.1061/41171(401)256)
- [114] Ali. A Review of Constitutive Models for Rubber-Like Materials. *Am J Eng Appl Sci.* 2010;3(1):232–9. <https://doi.org/10.3844/ajeassp.2010.232.239>
- [115] Shahzad M, Kamran A, Siddiqui MZ, Farhan M. Mechanical characterization and FE modelling of a hyperelastic material. *Mater Res.* 2015;18(5):918–24. <https://doi.org/10.1590/1516-1439.320414>
- [116] Saedniya M, Behzad S. Numerical modeling of elastomeric seismic isolators for determining force – displacement curve from cyclic loading. *Int J Adv Struct Eng.* 2019;11(3):361–76. <https://doi.org/10.1007/s40091-019-00238-6>
- [117] Arruda EM, Boyce MC. A three-dimensional constitutive model for the large stretch behavior of rubber elastic materials. *J Mech Phys Solids.* 1993;41(2):389–412. [https://doi.org/10.1016/0022-5096\(93\)90013-6](https://doi.org/10.1016/0022-5096(93)90013-6)
- [118] Chagnon G, Marckmann G, Verron E. A comparison of the Hart-Smith model with Arruda-Boyce and Gent formulations for rubber elasticity. *Rubber Chem Technol.* 2004;77(4):724–35. <https://doi.org/10.5254/1.3547847>
- [119] Khajehsaeid H, Arghavani J, Naghdabadi R. A hyperelastic constitutive model for rubber-like materials. *Eur J Mech A/Solids.* 2013; 38:144–51. <http://dx.doi.org/10.1016/j.euromechsol.2012.09.010>
- [120] Chang CH. Modeling of laminated rubber bearings using an analytical stiffness matrix. *Int J Solids Struct.* 2002;39(24):6055–78. [https://doi.org/10.1016/S0020-7683\(02\)00471-7](https://doi.org/10.1016/S0020-7683(02)00471-7)
- [121] Basshofi Habieb A, Tavio T, Milani G, Wijaya U. 3D-Finite element modeling of lead rubber bearing using high damping material. *MATEC Web Conf.* 2019; 276:01013.
- [122] Kanbir Z, Özdemir G, Alhan C. Modeling of Lead Rubber Bearings via 3D- BASIS , SAP2000 , and OpenSees Considering Lead Core Heating Modeling Capabilities. *Int J Struct Civ Eng Res.* 2018;7(4):294–301. <https://doi.org/10.18178/ijscer.7.4.294-301>
- [123] J.M. Kelly. *Base Isolation in Japan.* Rep No UCB/EERC-88/ 20, Univ California, Berkeley, CA. 1988.
- [124] Wang T, Wang F. Three-dimensional base-isolation system using thick rubber bearings. 2012; 8341:1–8. <https://doi.org/10.1117/12.916965>
- [125] Zhou Z, Wong J, Mahin S. Potentiality of Using Vertical and Three- Dimensional Isolation Systems in Nuclear Structures. *Nucl Eng Technol.* 2016;48(5):1237–51. <http://dx.doi.org/10.1016/j.net.2016.03.005>

- [126] Mo YL, Witarto W, Chang K, Wang S, Tang Y, Kassawara RP. Periodic Material-Based Three-Dimensional ( 3D ) Seismic Base Isolators for Small Modular Reactors. 2019. <https://doi.org/10.1007/978-981-13-3278-4>
- [127] Witarto Witarto, Wang SJ, Yang CY, Wang J, Mo YL, Chang KC, et al. Three-dimensional periodic materials as seismic base isolator for nuclear infrastructure Three-dimensional periodic materials as seismic base isolator for nuclear infrastructure. AIP Adv. 2019;045014. <https://doi.org/10.1063/1.5088609>
- [128] Bagerzadeh Karimi MR, Aghabalaie Khordachi M. Assessing the three-dimensional seismic behavior of the multi-degree-of-freedom (MDOF) structure with LCRB and LRB control systems. Asian J Civ Eng. 2020;21(5):871–84. <https://doi.org/10.1007/s42107-020-00246-y>
- [129] Forcellini D. The assessment of the interaction between base isolation (BI) technique and soil structure interaction (SSI) effects with 3D numerical simulations. Structures. 2022; 45:1452–60. <https://doi.org/10.1016/j.istruc.2022.09.080>
- [130] Ebisawa K, Ando K, Shibata K. Progress of a research program on seismic base isolation of nuclear components. Nucl Eng Des. 2000;198(1):61–74. [https://doi.org/10.1016/S0029-5493\(99\)00279-4](https://doi.org/10.1016/S0029-5493(99)00279-4)
- [131] Lee HP, Cho MS, J. Y. Park. Developing Lead Rubber Bearing for Seismic Isolation of Nuclear Power Plants. In: 15 World Conference on Earthquake Engineering. 2011.
- [132] Jung J, Woon H, Han J, Hong J. Effect of second hardening on floor response spectrum of a base-isolated nuclear power plant. Nucl Eng Des. 2017; 322:138–47. <http://dx.doi.org/10.1016/j.nucengdes.2017.06.004>
- [133] Kammerer, A.M., Whittaker AS, Constantinou MC. Technical considerations for seismic isolation of nuclear facilities. NUREG/CR-7253. United States Nuclear Regulatory Commission, Washington, D.C. (ML19050A422). 2019.
- [134] Kumar M, Whittaker AS, Constantinou M. Seismic isolation of nuclear power plants using sliding bearings. NUREG/CR-7254. United States Nuclear Regulatory Commission, Washington, DC (ML19158A513). 2019; a.
- [135] Kumar M, Whittaker AS, Constantinou MC. Seismic isolation of nuclear power plants using elastomeric bearings NUREG/CR-7255. United States Nuclear Regulatory Commission, Washington, DC. ML19063A541). 2019; b.
- [136] NRC (National Research Council). ISC security design criteria, National Academies Press, Washington, DC. 2003.
- [137] Huang Y, Whittaker AS. Response of Conventional and Base-Isolated Nuclear Power Plants to Blast Loading. 2009;(SMiRT 20):1–10.
- [138] Zhang R, Phillips BM, Asce AM. Performance and Protection of Base-Isolated Structures under Blast Loading. J Eng Mech. 2015;1–12. [https://doi.org/10.1061/\(ASCE\)EM.1943-7889](https://doi.org/10.1061/(ASCE)EM.1943-7889)
- [139] Mei R, Li J, Lin G, Zhu X. Dynamic assessment of the seismic isolation influence for various aircraft impact loads on the CPR1000 containment. Nucl Eng Technol. 2018;50(8):1387–401. <https://doi.org/10.1016/j.net.2018.08.003>
- [140] Kangda MZ, Bakre S. The Effect of LRB Parameters on Structural Responses for Blast and Seismic Loads. Arab J Sci Eng. 2018;43(4):1761–76. <https://doi.org/10.1007/s13369-017-2732-7>
- [141] Kangda MZ, Bakre S. Positive-Phase Blast Effects on Base-Isolated Structures. Arab J Sci Eng. 2019;44(5):4971–92. <https://doi.org/10.1007/s13369-018-3667-3>
- [142] David M. Base Isolation for Torsion Reduction in Asymmetric Structures Under Earthquake Loading. 1980;8(October 1979):349–59.
- [143] Nagarajaiah, Satish, Andrei M. Reinhorn, Michalakis C. Constantinou, Torsion in Base-Isolated Structures with Elastomeric Isolation Systems. J Struct Eng. 1993;119(10):2932–51. <https://doi.org/10.1107/S0365110X55001746>
- [144] Jangid RS, Datta TK. Nonlinear Response of Torsionally Coupled Base Isolated Structure. J Struct Eng. 1994;120(1):1–22.

- [145] Fallahian M, Paytam F, Khoshnoudian F. Seismic behavior of torsionally coupled base-isolated structures. *Proc Inst Civ Eng Struct Build.* 2016;169(3):159–73. <https://doi.org/10.1680/jstbu.14.00056>
- [146] Ozer E, Inel M, Cayci BT. Seismic behavior of LRB and FPS type isolators considering torsional effects. *Structures.* 2022;37(December 2021):267–83. <https://doi.org/10.1016/j.istruc.2022.01.011>

Blank Page

## Spectral analysis of cross-hole sonic logging data for pile integrity assessment

Ilya Lozovsky\*<sup>1,a</sup>, Aleksei Churkin<sup>2,3,b</sup>

<sup>1</sup>Geoelectromagnetic Research Center, Branch of Schmidt Institute of Physics of the Earth, Russian Academy of Sciences, Moscow, Troitsk, Russia

<sup>2</sup>Gersevanov Research Institute of Bases and Underground Structures (NIIOSP), Research Center of Construction JSC, Moscow, Russia

<sup>3</sup>Schmidt Institute of Physics of the Earth, Russian Academy of Sciences, Moscow, Russia

### Article Info

#### Article history:

Received 15 Nov 2023

Accepted 11 Jan 2024

#### Keywords:

Pile testing;

Nondestructive testing;

Ultrasonic;

Cross-hole sonic

logging;

Deep foundations;

Bored piles

### Abstract

Ensuring the safety of foundations requires advanced non-destructive testing techniques. Cross-hole sonic logging (CSL) is a widely adopted method for evaluating the integrity of deep foundation elements, such as bored piles, barrettes, and diaphragm walls. This method involves analyzing the propagation time and relative energy of ultrasonic pulses transmitted and registered by probes inserted into pre-installed access tubes. However, in certain cases, standard analyses may not effectively distinguish anomalous signals arising from defects and other factors unrelated to concrete quality. Our study explores the potential of an alternative frequency-domain approach for CSL data analysis. We propose new attributes to quantify ultrasonic signal spectra, including spectrum area, normalized spectrum area, weighted mean frequency, and maximum frequency. These attributes are automatically calculated, eliminating the need for additional data processing time and minimizing the risk of human error. The proposed approach was applied to CSL data collected from two bored piles of 46 m length and successfully identified signals classified as anomalous through standard time-domain analysis. Further research is deemed necessary to fully explore the potential of the frequency-domain approach in enhancing the information content and reliability of CSL pile integrity testing.

© 2024 MIM Research Group. All rights reserved.

## 1. Introduction

The safety of a building begins with a strong and reliable foundation. Bored pile foundations are esteemed for their high bearing capacity, adaptable geometry, cost-effectiveness, and minimal environmental impact. However, deviations from construction standards can introduce defects, compromising the bearing capacity and durability of these foundations. Therefore, it is imperative to employ non-destructive testing techniques capable of thoroughly assessing the structural integrity of deep foundation elements [1–3]. These techniques rely on various physical phenomena, such as ultrasound propagation [4–7], low-frequency acoustic waves [8,9], heat transfer [10,11], and others. Fig. 1 offers a comparative diagram illustrating the various non-destructive testing methods employed [3, 12–14]. These methods exhibit significant variations in their prevalence, scope, and resolution. The choice of the testing method depends on the specific issues to be addressed, structural design, soil conditions, regulatory requirements, and testing costs. The necessity for further development of non-destructive testing methods for deep foundations arises

\*Corresponding author: [i.n.lozovsky@gmail.com](mailto:i.n.lozovsky@gmail.com)

<sup>a</sup> orcid.org/0000-0001-9298-6513; <sup>b</sup> orcid.org/0000-0002-4043-9590

DOI: <http://dx.doi.org/10.17515/resm2024.82me1115rs>

Res. Eng. Struct. Mat. Vol. 10 Iss. 3 (2024) 1051-1063

from the technical complexities, high costs, and limited applicability of direct quality control methods, alongside the increasing number of underground construction projects in urban settings.

Currently, cross-hole sonic logging (CSL) stands out as a widely adopted method for pile integrity testing, actively applied in practical scenarios. The testing procedure is subject to regulation by standards and technical codes in various countries [15]. However, despite its prevalence, significant variation exists in testing procedures and CSL data interpretation criteria [16]. In certain cases, current approaches to CSL data analysis may struggle to distinguish ultrasonic anomalies caused by defects and other factors unrelated to concrete quality [16]. These approaches also offer limited capabilities for evaluating the strength of concrete and identified defects [4]. Additionally, the effectiveness of current CSL data analysis techniques can be compromised by diverse sources of errors [15]. Consequently, there is a pressing need to explore novel data analysis techniques to enhance the reliability and informativeness of CSL.

In this paper, we present an approach to analyze CSL test data in the frequency domain and introduce new parameters (attributes) for quantifying recorded signal spectra. The Materials and Methods section delineates fundamental CSL testing principles, current data analysis methods, and a step-by-step procedure for attribute calculation. The Results section shares our initial experience in applying these attributes to ultrasonic signals and profiles. The Conclusions section addresses the potential and limitations of the proposed techniques.

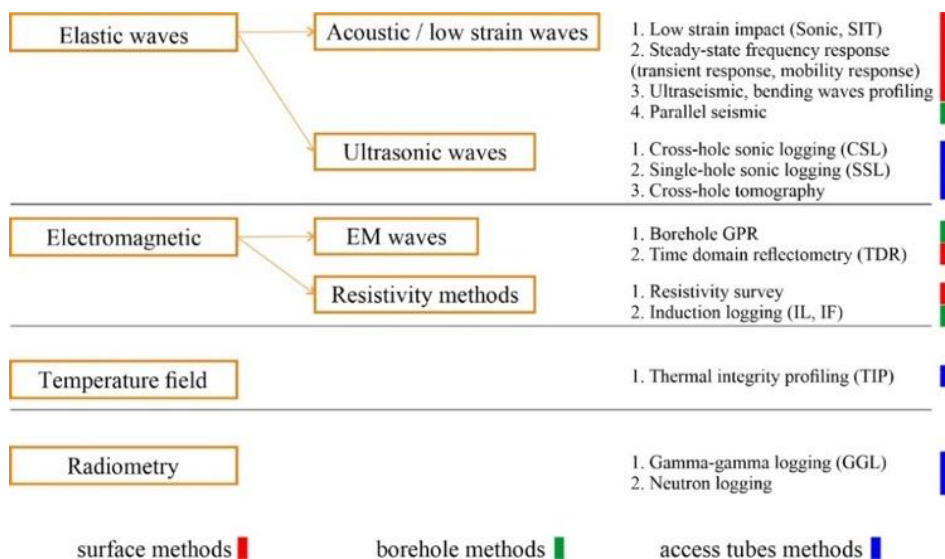


Fig. 1. Non-destructive methods for pile integrity testing. Modified from [13]

## 2. Materials and Methods

### 2.1. CSL of Deep Foundation Elements

Cross-hole sonic logging is the most common non-destructive integrity testing method for deep foundation elements with pre-installed access tubes [7]. This test relies on the analysis of ultrasonic wave propagation within the pile body. Ultrasonic waves are generated and received by ultrasonic probes, including a transmitter and at least one receiver, which are inserted into access tubes made of steel or plastic (PVC) with typical

diameters of 40 to 60 mm (Fig. 2). These access tubes are installed in the reinforcing cage during pile construction and require filling with water before testing.

The testing should be conducted no earlier than 3 to 7 days after casting. The standard testing procedure involves raising the probes synchronously from the bottom of the access tubes to the top of the structure while generating and receiving ultrasonic waves at fixed depth intervals. Subsequently, the recorded data is processed and presented graphically. The testing procedure is governed by technical codes and specifications in various countries, such as the US, UK, France, China, and others, with the ASTM D6760 code often serving as the de facto standard in many regions [7].

The method of data acquisition through access tubes determines the controlled volume of the drilled shaft body and the measurement techniques employed [4,8,17]. Cross-hole configurations are the predominant choice for the application of ultrasonic testing, whereas single-hole configurations are used less frequently [3]. Several techniques are utilized to enhance the understanding of defect properties and geometry, with cross-hole tomography representing the most advanced approach. In addition to the ray-based traveltime tomography [18], new methods are under development, including attenuation-based and full-wave inversion techniques [2,19,20].

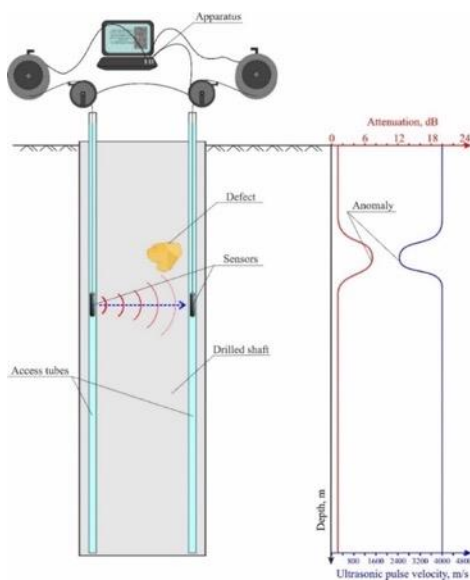


Fig. 2. CSL pile integrity testing arrangement. Modified from [4]

### 2.2. CSL Data Analysis

The results of ultrasonic measurements for each pile comprise sets of ultrasonic signals recorded in each pair of access tubes, forming ultrasonic profiles. The raw data for each ultrasonic profile is visualized as a waterfall diagram, or seismogram, where signal strength (voltage) is represented by color (Fig. 3a). Visual analysis of a waterfall diagram allows for the rapid identification of changes in signal amplitudes and first arrival times (FAT), enabling the assessment of data quality, such as signal-to-noise ratio and the choice of signal gain value.

The registered ultrasonic data is qualitatively characterized through the calculation of parameters for each recorded signal. In accordance with ASTM D6760 requirements, the set of estimated parameters should encompass the First Arrival Time (Fig. 3b) and the



Relative Energy (RE, Fig. 3c). Additionally, this list may be extended to include the Wave Speed of ultrasonic pulses.

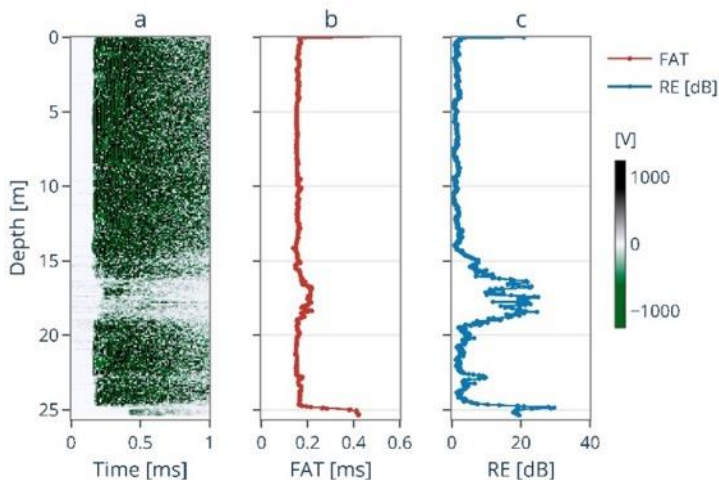


Fig. 3. An example of an ultrasonic profile for a pile with two defects: waterfall diagram (a); FAT (b) and RE (c) plots

The FAT value corresponds to the arrival time of the first waves, which travel in the fastest path between the transmitter and receiver and can be distinguished during signal analysis. To expedite the process, FAT is typically determined using automated picking algorithms [21]. However, for anomalous signals (those with low amplitude or noise), FAT estimates should be manually corrected. Following the picking procedure, the average FAT value and the deviations from the average value (%) should be calculated for each ultrasonic profile. Calculating the average FAT value should employ a robust average algorithm, as outlined in [22].

FAT values can be employed to calculate the wave speed. This calculation should consider the additional travel time in both the water and the access tube material:

$$V = L / (t_0 - 2(\frac{L_{tube}}{V_{tube}} + \frac{L_{water}}{V_{water}})) \tag{1}$$

where,  $V$  – wave speed,  $L$  – the distance between the probes,  $t_0$  – FAT value,  $L_{tube}$  – tube wall thickness,  $L_{water}$  – the distance between the access tube and the ultrasonic probe in it (travel path in water),  $V_{tube}$  – longitudinal wave speed in tube material (typically 5100 m/s in steel and 2300 m/s in PVC),  $V_{water}$  – longitudinal wave speed in water (typically 1500 m/s).

The Relative Energy characterizes the attenuation of ultrasonic waves transmitted through the pile. According to ASTM D6760 [7], Relative Energy is defined as:

$$RE = 20 \log \frac{E}{E_0} \tag{2}$$

where,  $E$  represents the energy of a given pulse, calculated by summing the absolute values of the pulse amplitudes, and  $E_0$  is the reference energy, set as a constant value equal to the maximum energy of an ultrasonic profile or a fixed high value [23]. Energy values can be calculated for two preset time intervals: either for at least five cycles starting from the FAT (approximately 0.1 ms), or for the full length of the signal.

While FAT characterizes the fastest wave path between the transmitter and receiver, RE for both time intervals describe a larger area [4,23]. Therefore, it is necessary to include both FAT and RE in the analysis. In some cases, RE can be helpful in distinguishing FAT anomalies caused by defects from those unrelated to concrete quality, as discussed in [4,24].

The processed ultrasonic data should be classified into one of the categories proposed by Sellountou et al. [16]: class A (acceptable), class B (conditionally acceptable), and class C (highly abnormal), according to the rating criteria presented in Fig. 4. However, it is worth noting that the RE criteria may need slight adjustments based on the dominant frequency of ultrasonic probes. Additionally, the FAT delay values can be substituted with wave speed deviations to account for the differences in the depths of transmitter and receiver probes and the additional travel time in the water and access tube, as described in Eq. (1).

It's important to emphasize that the rating criteria presented should not be the sole means for evaluating pile quality [16]. Highly abnormal CSL data necessitate additional measurements or analysis to distinguish defects from other sources of ultrasonic anomalies and prevent misinterpretation of test results.

In CSL tests, the receiver signal represents the superposition of different types of ultrasonic waves arriving at the probe. Standard time-domain analysis is not fully able to capture and describe the complex full-wave structure of the received signals. While comprehensive full-wave analysis of CSL data is currently constrained due to inherent ambiguity of inverse problems and computational limitations, simpler yet effective techniques can be employed to complement and enhance standard time-domain procedures.

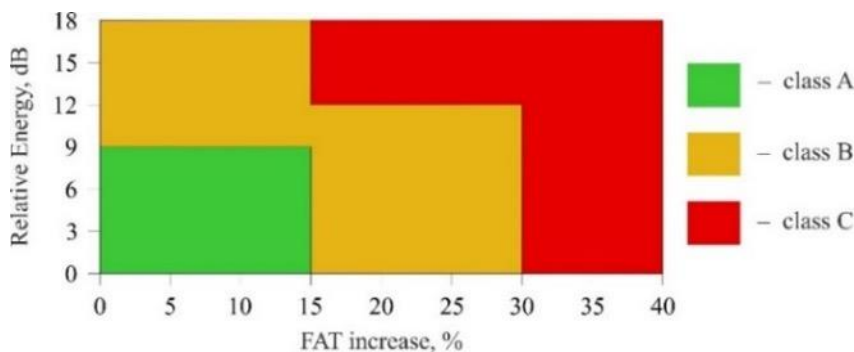


Fig. 4. Graphical representation of ultrasonic data rating criteria. Modified from [16]

### 2.3. Calculation of Spectral Attributes for CSL Data

In this section, we introduce a technique for analyzing CSL data in the frequency domain and offer a step-by-step procedure for calculating CSL data spectral attributes to complement the standard set of FAT and RE.

To begin, we convert an ultrasonic signal from the time domain to the frequency domain using the Fast Fourier Transform algorithm. This algorithm separates the input signal into components contributing at discrete frequencies:

$$A_k = \sum_{n=0}^{N-1} a_n e^{-i2\pi kn/N}, \quad k = 0, \dots, N - 1, \tag{3}$$

where  $\{a_k\} = a_0, \dots, a_{N-1}$  represents the input signal amplitudes,  $\{A_k\} = A_0, \dots, A_{N-1}$  represents the Discrete Fourier Transform (DFT) of the input signal amplitudes, and  $N$  is the number of samples.

Next, we normalize (rescale) the calculated sequence of DFT by its maximum value ( $A_{max}$ ) to emphasize the signal's frequency content rather than its amplitudes, taking advantage of the consistent source probe signals:

$$A_k^{norm} = \frac{A_k}{A_{max}}, k = 0, \dots, N - 1 \tag{4}$$

In non-destructive testing, there is a crucial requirement for regulatory control, prompting the development of formalized algorithms to analyze measurement results. To quantitatively characterize the calculated spectrum, we introduce a set of spectral attributes that have been previously proposed for the analysis of seismic microzonation data, ground-penetrating radar, slab impulse-response tests [25-26], low strain impact, and parallel seismic methods for pile integrity testing [27-28]. These attributes include spectrum area  $S_n$ , normalized spectrum area  $S_{n\_norm}$ , weighted mean frequency  $f_w$ , and maximum frequency  $f_{max}$ .

Spectrum area attributes  $S_n$  and  $S_{n\_norm}$  approximate the area under the spectrum graph using the trapezoidal rule:

$$S_n = \sum_{i=0}^{\frac{N}{2}} \frac{A_i + A_{i+1}}{2} df \tag{5}$$

$$S_{n\_norm} = \sum_{i=0}^{\frac{N}{2}} \frac{A_i^{norm} + A_{i+1}^{norm}}{2} df \tag{6}$$

Where  $df$  represents the frequency resolution. The weighted mean frequency  $f_w$  is calculated by the equation:

$$f_w = \frac{\sum_{i=0}^{\frac{N}{2}} f_i A_i}{\sum_{i=0}^{\frac{N}{2}} A_i} \tag{7}$$

Where  $f_i$  represents spectrum frequencies. The maximum frequency  $f_{max}$  is the frequency that corresponds to the maximum spectrum value.

### 3. Results

#### 3.1 Spectral Attribute Analysis for Selected Ultrasonic Signals

To illustrate the proposed approach for CSL data analysis, let's examine the ultrasonic signals associated with either a defect or good quality concrete. Fig. 5 shows signals classified into class A (Fig. 5a) and class C (Fig. 5b), along with their amplitude spectra and normalized amplitude spectra. These signals were acquired using the Cross Hole Analyzer (CHAMP; Pile Dynamics, Inc., USA) instrument equipped with ultrasonic transducers featuring a nominal frequency of 45 kHz.

In the time domain, a Class C signal exhibits an increased FAT and a significant decrease in amplitudes, quantified with a FAT delay of 74% and RE of -15.1 dB (with a Class A signal used as the reference data). The spectrum of the signal associated with good-quality

concrete displays multiple peaks, with the majority of its energy concentrated between 35 – 90 kHz. In contrast, the spectrum of the signal associated with the defect exhibits a prominent peak near 45 kHz, corresponding to the dominant frequency of the ultrasonic probes. Another important distinction between the two spectra is the substantial loss of both high (>90 kHz) and low (<35 kHz) frequencies in the spectrum of the Class C signal.

The spectral attributes calculated for the analyzed signals are presented in Table 1. The Class C signal is characterized by a significantly lower value of spectrum area  $S_n$ , primarily due to increased signal attenuation. Additionally, the Class C signal is characterized by lower values of the normalized spectrum area  $S_{n,norm}$  and the weighted mean frequency  $f_w$ , resulting from a concentration of coefficients of the frequency components around the dominant frequency of the ultrasonic probes. It's noteworthy that the maximum frequency  $f_{max}$  of both signals exhibits relatively close values.

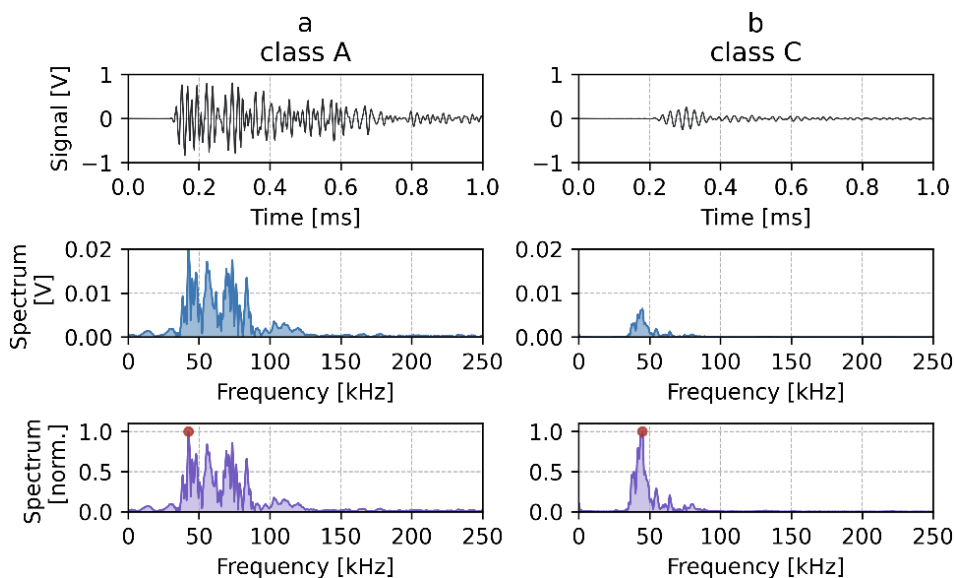


Fig. 5. Class A (a) and class C (b) ultrasonic signals, their spectra, and normalized spectra. The red dots on normalized spectra represent the maximum frequency ( $f_{max}$ )

Table 1. Spectral attributes of sample signals

Signal	$S_n$ [V·Hz]	$S_{n,norm}$ [Hz]	$f_w$ [Hz]	$f_{max}$ [Hz]
Class A	565	27750	72990	42560
Class C	72	11065	52230	44950

### 3.2 Spectral Attribute Analysis for Ultrasonic Profiles

We proceed by examining sets of CSL data collected from two bored piles measuring 1 m in diameter and 46 m in length. The CSL data was acquired using CHAMP equipment, with measurements taken at approximately 50 mm depth intervals, following the ASTM D6760 procedure (Fig. 6). Standard time-domain analysis of the waterfall diagram, FAT and RE values for Pile 1 (Fig. 7, a-c) reveals an ultrasonic anomaly within the depth range of 41.4-41.9 m, falling somewhere between Classes B and C. A similar analysis conducted for Pile 2 (Fig. 8, a-c), has identified multiple anomalies within the depth range of 10.5 – 14.7 m, classified as Class C.

Next, we converted each ultrasonic signal into the frequency domain and displayed the ultrasonic profile data as spectrum waterfall diagrams (Fig. 7d, 8d) and normalized spectrum waterfall diagrams (Fig. 7e, 8e). Similar to standard waterfall diagrams, these representations were generated by converting each spectrum into a narrow strip where its amplitudes were color-coded, and then stacking these strips together. This approach enables us to visually compare and analyze the variations in the frequency content of ultrasonic signals with depth.

The spectra of the ultrasonic signals that were identified as anomalous in the time-domain analysis exhibit a significant reduction in amplitudes for frequencies greater than 90 kHz and less than 30 kHz. To capitalize on this observation, let's proceed with further analysis of the frequency-domain data in three distinct ranges: 0-30, 30-100, and 100-250 kHz.

For a quantitative characterization of the frequency-domain data, we have computed spectral attributes. Weighted mean frequency  $f_w$  and maximum frequency  $f_{max}$  calculated for these three frequency ranges are presented in subplots (f, h, j) of Figures 7 and 8. Spectrum area  $S_n$  and normalized spectrum area  $S_{n,norm}$  calculated for the same frequency ranges are shown in subplots (g, i, k). Prior to plotting, the  $S_n$  and  $S_{n,norm}$  graphs were normalized by their respective maximum values.

In the frequency range of 0-30 kHz, a significant reduction in the values of the proposed attributes is observed at the depth ranges identified as anomalous by the time-domain analysis. Specifically,  $f_{max}$ , representing the maximum spectrum amplitude in the selected frequency range, decreases by up to the first hundred Hz.  $f_w$  experiences a reduction of more than 50% from its background value of 20 kHz. The significant drop in both  $S_n$  and  $S_{n,norm}$  for both piles clearly indicates anomalies as well.

In the frequency range of 30-100 kHz, there is a noticeable reduction in  $S_n$  for both piles, particularly influenced by the RE of the signals. However,  $f_{max}$  does not provide a clear indication of anomalies. On the other hand,  $f_w$  and  $S_{n,norm}$  only point to anomalies for Pile 2 (Fig. 8), associated with highly abnormal ultrasonic signals.

In the frequency range of 100-250 kHz, we observe significant local reductions in both  $S_n$  and  $S_{n,norm}$ , along with increases of  $f_w$  values for both piles. In the case of Pile 1,  $f_{max}$  does not reveal anomalies, whereas for Pile 2, it does indicate anomalies, although with a notable degree of scatter.



Fig. 6. Field photographs of the CSL testing procedure for bored piles

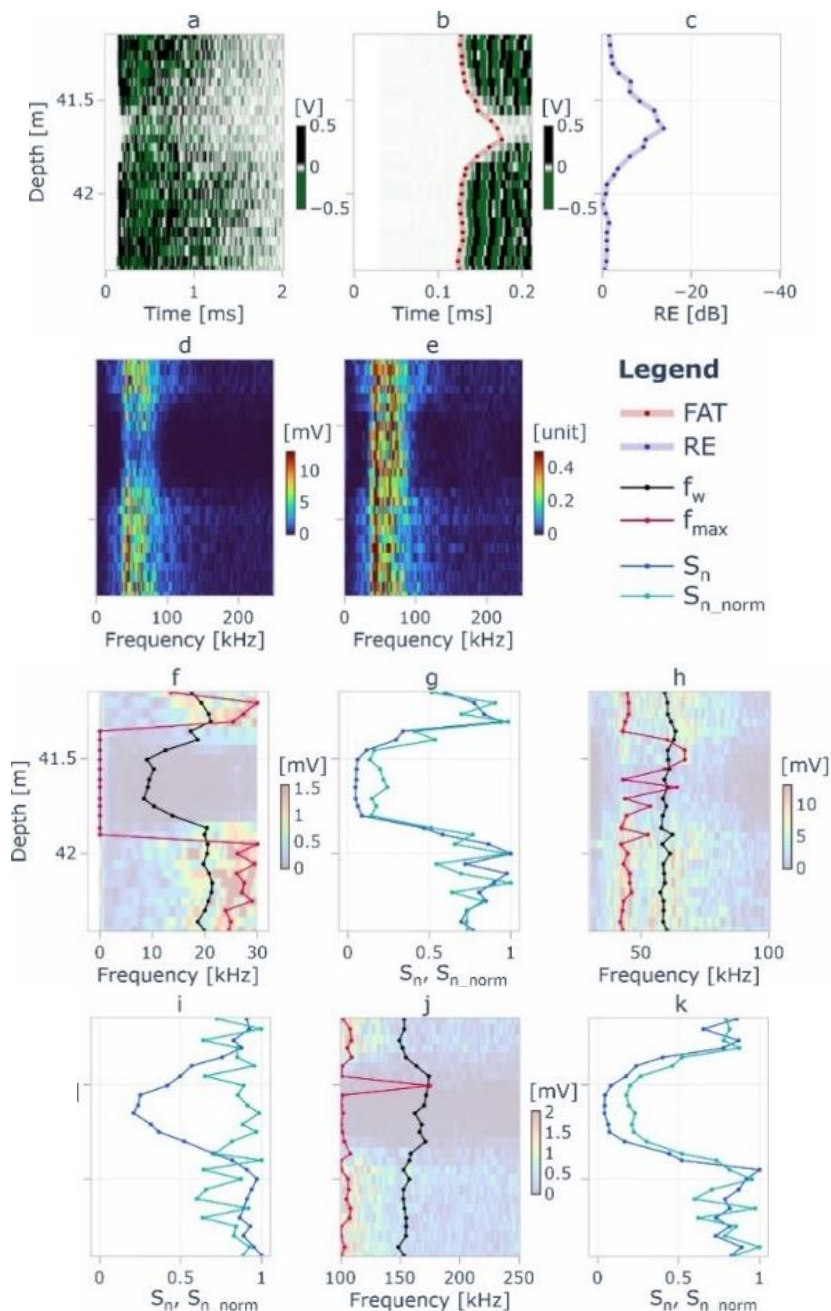


Fig. 7. CSL results from Pile 1 with an anomaly falling between Classes B and C. Subplots: (a) Waterfall diagram (full length, 2 ms), (b) FAT overlaying waterfall diagram, (c) Relative Energy, (d) Spectral waterfall diagram (full frequency range), (e) Normalized spectral waterfall diagram (full frequency range). Weighted mean frequency  $f_w$  and maximum frequency  $f_{max}$  (overlaid on the spectral waterfall diagram) are calculated for frequency ranges 0-30, 30-100, and 100-250 kHz and displayed in subplots (f, h, j). Spectrum area  $S_n$  and normalized spectrum area  $S_{n\_norm}$  calculated for the same frequency ranges are shown in subplots (g, i, k)

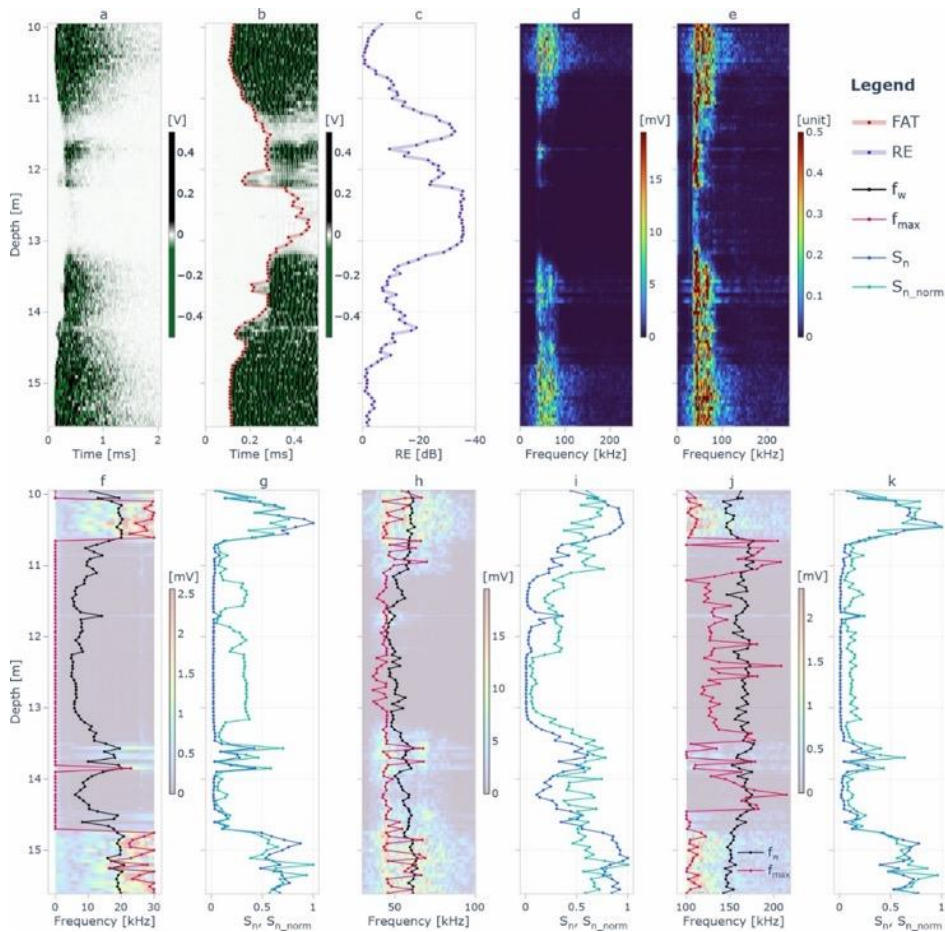


Fig. 8. CSL results from Pile 2 with several Class C anomalies. Subplot descriptions are provided in the Fig. 7 caption

#### 4. Conclusions

In this study, we introduced an alternative frequency-domain approach for analyzing CSL pile integrity testing results. We proposed new attributes to quantitatively characterize frequency-domain data, including spectrum area  $S_n$ , normalized spectrum area  $S_{n\_norm}$ , weighted mean frequency  $f_w$ , and maximum frequency  $f_{max}$ . Additionally, we introduced the use of spectrum waterfall diagrams to provide a visual means of comparing and analyzing variations in the frequency content of ultrasonic signals with depth.

The proposed approach was successfully applied to examine CSL data collected from two bored piles using CHAMP equipment. The frequency-domain analysis provided results consistent with standard time-domain interpretation. Specifically, we observed a notable reduction in signal spectra amplitudes for frequencies below 30 kHz and above 90 kHz at the depth intervals recognized as anomalous in the time-domain analysis. All the spectral attributes calculated for the 0-30 kHz frequency range exhibited significant decreases at these intervals. When computed for the frequency range of 100-250 kHz, attributes  $S_n$  and  $S_{n\_norm}$  showed substantial reductions, while attribute  $f_w$  displayed an increase at the same depth intervals.

The effectiveness of the proposed spectral attributes in identifying anomalous signals was demonstrated, offering a valuable complement to the basic set of FAT and RE. The automation of attribute calculation involves straightforward computations and eliminates the need for interactive operator involvement, thereby avoiding additional data processing time and reducing the risk of human error. Furthermore, these attributes can serve as valuable input data for tomographic inversions or signal classification using artificial neural networks.

Further research and validation efforts are essential to comprehensively assess the performance of the frequency-domain approach across diverse scenarios. This includes applying frequency-domain analysis to both numerical simulations and experimental data, involving testing piles with prefabricated defects of varying sizes, locations, and materials. Identified limitations are primarily associated with the CSL data collection process, emphasizing the need for properly selected gain and sampling rates during data acquisition. Avoiding data clipping and adhering to appropriate sampling rates, following established guidelines such as those outlined by ASTM D6760, is crucial. While there are no specific recommendations for equipment modifications, it is noted that CSL equipment used should have a broad dynamic range, a characteristic shared by most modern CSL equipment. It is important to acknowledge the potential influence of noise and artifacts on the calculated attributes, emphasizing the need for a preliminary analysis of frequency domain data, such as inspecting spectrum waterfall diagrams, to ensure the reliability of interpretation.

In summary, this study presents a promising approach to enhance CSL data analysis for detecting defects in bored piles, potentially opening the door to more advanced applications in the future.

### **Acknowledgement**

The research was carried out under the state task of Geoelectromagnetic Research Center, Branch of Schmidt Institute of Physics of the Earth, Russian Academy of Sciences. State task no. FMWU-2022-0023, State registration no. 122040600109-9.

### **References**

- [1] Amir JM. Pile Integrity Testing: History, Present Situation and Future Agenda. Proceedings of the 3rd Bolivian International Conference on Deep Foundations, Santa Cruz de La Sierra, Bolivia. 2017: 17-32.
- [2] Hussein MH, Goble GG. A Brief History of the Application of Stress-Wave Theory to Piles. Current Practices and Future Trends in Deep Foundations, ASCE, 2004:186-201. [https://doi.org/10.1061/40743\(142\)11](https://doi.org/10.1061/40743(142)11)
- [3] Amir JM. Pile integrity testing: All about the methods of pile NDT, 2nd edition, Piletest.com, 2020.
- [4] Lozovsky IN, Zhostkov RA, Churkin AA. Numerical Simulation of Ultrasonic Pile Integrity Testing. Russ J Nondestruct Test. 2020; 56: 1-11. <https://doi.org/10.1134/S1061830920010064>
- [5] Camp WM III, Holley DW, Canivan GJ. Crosshole Sonic Logging of South Carolina Drilled Shafts: A Five Year Summary, Contemporary Issues In Deep Foundations, ASCE, 2007.
- [6] Hajali M, Abishdid C. Cross-hole sonic logging and frequency tomography analysis of drilled shaft foundations to better evaluate anomalies locations. DFI Journal. 2014; 8: 27-38. <https://doi.org/10.1179/TBC14Z.0000000001>



- [7] D18 Committee. ASTM D6760 - 16. Test Method for Integrity Testing of Concrete Deep Foundations by Ultrasonic Crosshole Testing, 2016.
- [8] White B, Nagy M, Allin R. Comparing cross-hole sonic logging and low-strain integrity testing results. *The Application of Stress-Wave Theory to Piles: Science, Technology and Practice*, Lisbon, Portugal. 2018: 471-476.
- [9] D18 Committee. ASTM D5882 - 16. Test Method for Low Strain Impact Integrity Testing of Deep Foundations, 2016.
- [10] D18 Committee. ASTM D7949 - 14. Test Methods for Thermal Integrity Profiling of Concrete Deep Foundations, 2014.
- [11] Johnson KR. Analyzing thermal integrity profiling data for drilled shaft evaluation. *DFI Journal* 2016; 10: 25-33. <https://doi.org/10.1080/19375247.2016.1169361>
- [12] Coe JT, Mahvelati S, Asabere P. Application of non-destructive testing and geophysical methods to evaluate unknown foundation geometry. *Proceedings of 29th Central Pennsylvania Geotechnical Conference*, Hershey, Pennsylvania, USA, 2017.
- [13] Churkin A. Development of geophysical complex application technique for buried monolithic structures quality control, Ph.D. Thesis, Moscow State University, Moscow, 2020.
- [14] Gao T. A Critical Analysis of Existing Intelligent Analytical Techniques for Pile Integrity Test. *Proceedings of the 8th International Conference on Hydraulic and Civil Engineering: Deep Space Intelligent Development and Utilization Forum (ICHCE)*, Xi'an, China, 740-751, 2022. <https://doi.org/10.1109/ICHCE57331.2022.10042772>
- [15] Amir JM, Amir EI. *Critical Comparison of Ultrasonic Pile Testing Standards. The Application of Stress-Wave Theory to Piles: Science, Technology and Practice*, Lisbon, Portugal, 2008.
- [16] Sellountou AE, Amir JM, Chernauskas L, Hertlein B, Kandarlis P, Kovacs T, et al. Terminology and evaluation criteria of crosshole sonic logging (CSL) as applied to deep foundations. *DFI*, 2019. <http://www.dfi.org/viewpub.asp?tid=WP-CSL-2019> (accessed October 8, 2023).
- [17] Amir JM, Amir EI. Capabilities and Limitations of Cross Hole Ultrasonic Testing of Piles. *Contemporary Topics in Deep Foundations*, Orlando, USA, 536-543, 2009. [https://doi.org/10.1061/41021\(335\)67](https://doi.org/10.1061/41021(335)67)
- [18] Lozovsky IN, Churkin AA, Zhostkov RA. Localization of Defects in Bored Pile Physical Model Using Cross-Hole Ultrasonic Tomography. *Bull Russ Acad Sci Phys* 2020; 84: 215-9. <https://doi.org/10.3103/S1062873820020203>
- [19] Kordjazi A, Coe JT. An Experimental Design Approach for Structural Integrity Testing of Drilled Shafts Using Full Waveform Inversion. *IFCEE 2021*, Dallas, USA, 453-462, 2021. <https://doi.org/10.1061/9780784483404.041>
- [20] Kordjazi A, Coe JT, Afanasiev M. Nondestructive Evaluation of Drilled Shaft Construction Anomalies Using Full Waveform Tomography of Simulated Crosshole Measurements. *J Nondestruct Eval* 2020; 40: 3. <https://doi.org/10.1007/s10921-020-00728-8>
- [21] Amir EI. Determining First Arrival Time and Wave Speed in Cross-Hole Ultrasonic (CSL). *Piletest.com*, 2016. <https://www.piletest.com/show.asp?id=Engineer> (Access Date: October 1, 2023).
- [22] JGJ 106-2014. Technical code for testing of building foundation piles, 2014.
- [23] Amir EI. Relative Energy in Cross-Hole Ultrasonic (CSL). *Piletest.com*, 2016. <https://www.piletest.com/show.asp?id=Engineer> (Access Date: 1, 2023).
- [24] Amir JM, Amir EI, Felice CW. Acceptance criteria for bored piles by ultrasonic testing. *Proceedings of the 7th International Conference on the Application of Stress wave Theory to Piles*, Kuala Lumpur, Malaysia, 2004.
- [25] Churkin AA, Khmel'nitskii AY, Kapustin VV. Evaluation of soil-structure contact state by normalized acoustic response analysis. *Soil Mech Found Eng* 2022; 59: 453-458. <https://doi.org/10.1007/s11204-022-09836-1>

- [26] Lozovsky IN, Churkin AA. Multiscale entropy analysis for slab impulse response testing. Bull Russ Acad Sci Phys. 2023; 87(10): 1518-1522. <https://doi.org/10.3103/S1062873823703604>
- [27] Kapustin VV, Churkin AA. Assessment of the Contact between Piles and Soil via the Dynamic Attributes of Acoustic Signals. Moscow Univ Geol Bull. 2020; 75: 435-45. <https://doi.org/10.3103/S0145875220040092>
- [28] Shmurak DV, Churkin AA, Lozovsky IN, Zhostkov RA. Spectral Analysis of Parallel Seismic Method Data for Surveying Underground Structures. Bull Russ Acad Sci Phys. 2022; 86: 79-82. <https://doi.org/10.3103/S1062873822010221>

Blank Page



Research Article

## RSM based modelling and optimization of Marshall properties of steel-slag and lime-modified asphalt mixtures

Oguntayo Daniel<sup>1,a</sup>, Ogundipe Olumide<sup>2,b</sup>, Aluko Oluwasegun<sup>2,c</sup>, Babatunde Yusuf<sup>3,d</sup>

<sup>1</sup>Dept. of Civil and Mining Engineering, Confluence University of Science and Technology, Osara, Nigeria

<sup>2</sup>Civil Engineering Department, Ekiti State University, Ado-Ekiti, Nigeria

<sup>3</sup>Civil Engineering Department, University of Ilorin, Ilorin, Nigeria

### Article Info

### Abstract

#### Article history:

Received 17 Nov 2023

Accepted 22 Jan 2024

#### Keywords:

Response surface methodology;  
Box Behnken design;  
Modified asphalt mixtures;  
Steel slag;  
Lime;  
Marginal aggregates

Statistical and optimization techniques are useful tools in understanding the interactions and relationships between the asphalt mix variables and the contribution of each variable to the resulting asphalt mixture properties. This study explores the response surface methodology to study the influence of steel slag and lime on the Marshall properties of asphalt mixtures using Box Behnken Design tool. The independent variables considered are steel slag (0-100%), lime (0-4%) and bitumen (4-8%). The stability, flow, Marshall quotients, bulk density, Vb and VMA obtained were 1.98-6.35kN, 3.27-4.53 mm, 0.53-1.60kN/mm, 2.08-2.29 kg/m<sup>3</sup>, 7.67-14.7% and 14.02-24.63%, respectively; indicating that the steel-slag and lime-modified asphalt mixtures satisfy the specification limits recommended by the asphalt institute and Nigeria General Specification for Roads and Bridges. The models' analysis of variance revealed could well predict the Marshall properties of the mixtures, and the terms of steel-slag, lime and bitumen content are significant. Likewise, based on the optimization analysis, 24.93% of steel slag, 2.43% of lime and 5.51% of bitumen content were selected as the optimal values for the modified asphalt mixtures. Additionally, a mean error of less than 5% was attained for all the responses, demonstrating the effectiveness of RSM in designing asphalt mixtures.

© 2024 MIM Research Group. All rights reserved.

## 1. Introduction

The exceptional performance of asphalt mixture has made it a widely used paving material worldwide [1]. In service life, asphalt pavements are exposed to mechanical load from vehicle axles and negative environmental conditions such as thermal load [2]. Permanent deformation is created in the asphalt by the repeated vehicular loads arising from the traffic density [3-4]. These loads result in pavement degradation, thereby reducing the intended service life. To minimize the impacts, there is a need to modify the asphalt mixtures to improve the properties of the asphalt. Incorporating various materials in the asphalt mix has been found suitable for transforming the mechanical and binding properties of asphalt. Modifying the asphalt mixes enhances the performance and increases the service life of asphalt pavement [5-6]. Steel slags are industrial waste from the production of steel. They are non-metallically inert, containing silicates, aluminosilicates, and calcium aluminosilicates [7].

It constitutes about 15 – 20 % of steel/iron production. It has been estimated that 14, 21, 30, and 100 million tons of steel slags are annually generated as waste in Europe, Japan, India, and China, respectively [8]. Currently, there is no reliable data regarding the annual

\*Corresponding author: [dnloguntayo@gmail.com](mailto:dnloguntayo@gmail.com)

<sup>a</sup> [orcid.org/0000-0003-0400-6103](https://orcid.org/0000-0003-0400-6103); <sup>b</sup> [orcid.org/0000-0002-2783-1336](https://orcid.org/0000-0002-2783-1336); <sup>c</sup> [orcid.org/0000-0002-2292-4250](https://orcid.org/0000-0002-2292-4250);

<sup>d</sup> [orcid.org/0000-0002-5714-3673](https://orcid.org/0000-0002-5714-3673)

DOI: <http://dx.doi.org/10.17515/resm2024.83ma1117rs>

Res. Eng. Struct. Mat. Vol. 10 Iss. 3 (2024) 1065-1084

generation of slag in Nigeria. However, it has been reported that one tone of rolled steel would produce half tone of slag [9-10]. Nigeria has over 30 steel manufacturers with annual steel production of 2.2 million tons [11], which suggested that roughly 1 million tons of slag are produced during the year. Most of the waste is in landfills and occupies huge land areas. Also, it threatened the natural water and soil due to the proclamation of alkaline leachates [12]. As a result, researchers have made efforts to use steel slag as construction materials. Steel slag is reported to improve the strength properties of concrete and geopolymer concrete [13]. Using steel slag in an asphalt mixture would promote sustainable construction and reduce its environmental effect [14].

Lime is a natural, chemically active material with the ability to resist moisture, reduce the chemical ageing of bitumen, and improves the bonding strength between asphalt binder and aggregates [15-16]. It is commonly used as an anti-stripping agent and added to aggregates to improve the resistance of asphalt pavement to moisture damage. Moisture on asphalt pavement can damage the structure, such as rutting, raveling, cracking, bleeding, and localized failure [17]. There are three major forms of lime; dolomitic lime (CaO.MgO), hydrated lime (Ca (OH)<sub>2</sub>), and quick lime (CaO), but hydrated lime is usually used in asphalt mixtures [17].

Statistical and optimization techniques are useful tools for understanding the interactions and relationships between the asphalt mix variables and the contribution of each variable to the resulting properties of the asphalt [18-23]. One of the commonly adopted statistical tools in the design of experiments (DOE) is response surface methodology (RSM) [4]. The RSM approach considers the influence of several factors at different levels on the response simultaneously and gives a suitable predictive model to describe the relationship between the various factors [24-25]. This offers an opportunity to modify the mix proportions of the asphalt constituents to achieve desired properties, and it eliminates a situation whereby the target strength characteristic is not attained or the production of asphalt with excessive strength [2, 26]. Additionally, compared to traditional methods, utilizing RSM would significantly reduce the number of experiments needed to model the response functions [27]. Designing, conceiving, developing, and assessing new scientific studies and products depend on the RSM. It is also effective in enhancing current research and output. Hence, by incorporating RSM into pavement technologies, researchers can access more rapid, accurate, and reliable methods of analyzing changes in pavement performance and improved experimental matrices [28].

The mix proportioning of the constituent materials is crucial to achieve the desired targeted qualities. Hence, the design of the experiment (DOE) using software tools like RSM for mix proportioning is essential. The RSM was utilized in this study to investigate the influence of steel slag and lime on the Marshall properties of asphalt mixtures. The utilization of RSM in this study will identify the ideal substitution of steel-slag and lime in asphalt mixtures that are most effective to the performance of steel-slag and lime-modified asphalt mixtures.

## 2. Materials and Methods

### 2.1. Materials

- *Aggregate:* The granite used for the coarse aggregate was 12.5mm, and 10mm granite, was sourced from a local market in Omu-Aran, Kwara State. As the fine aggregate, quarry dust that passes through a 4.75 mm sieve was employed. The filler used in this study is stone dust that passes a 75-µm sieve. Table 1 displays the aggregates' characteristics and Fig. 1 shows the grading curve used for asphalt mixture.

- **Steel slag:** The steel slags from Prism Steel Mills Limited in *Ikirun*, Nigeria, were used in this study (see Figure 2). Because it was produced during the refinement of scrap steel in an electric-arc furnace, this slag is also known as an electric-arc furnace (EAF) slag. The 12.5mm coarse aggregate was replaced with steel slag.
- **Bitumen:** Penetration grade 60/70 of bitumen was used in this study. Table 2 displays the properties of bitumen.

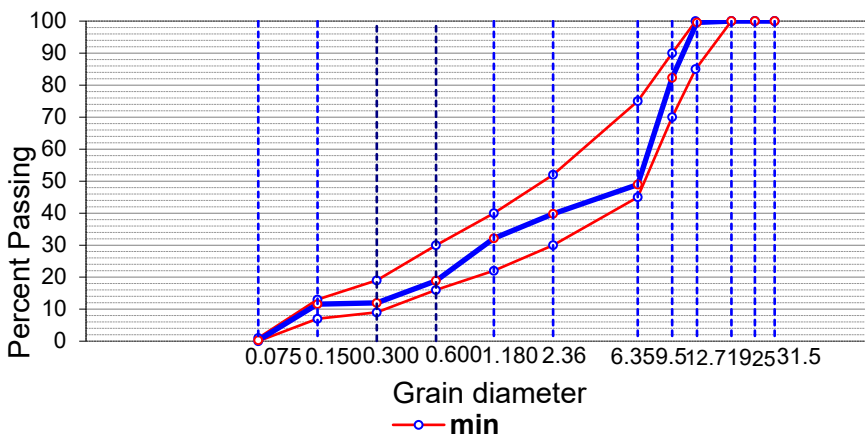


Fig. 1. Asphalt mixture grading curve



Fig. 2. Samples of steel-slag

Table 1. Aggregate properties

Parameters	Steel-slag	Granite	Specification	Standard
Aggregate Impact Value (%)	9.5	19.44	30% max	[29]
Aggregate crushing value (%)	13.6	17.2	30% max	
Specific gravity	2.44	2.71	2.5-3.0	
Flakiness index (%)	19.1	23.6	30% max	
Elongation (%)	18.7	13.3	30% max	
Aggregate abrasion value (%)	30.2	26.7	40% max	
Water absorption (%)	1.69	0.17	4% max	

Table 2. Bitumen Properties

Parameters	Specification	Value	Standard
Penetration @ 25°C	60-70	66	
Ductility @ 25°C	100 MIN	121	
Solubility	99.5 MIN	107.00	
Viscosity (secs)	2400 MIN	2753	
Flash Point (C)	≥ 250	287	
Softening Point	55-65	56	[29]
Specific gravity @ 25°C	1.01-1.06	1.02	
Minimum Loss on Heat for 5 hours at 163°C	Max. 0.2	0.08	
Drop in Penetration after heating	Max. 20	13.5	

### 2.2. Mix Design

The Design Expert software version 13 was used to create the experimental runs utilising the Box Behnken Design (BBD) approach. Table 3 displays the three factors (independent variables) that were taken into consideration: steel slag (A), lime (B) and bitumen (C). The generated experimental run used for steel-slag and lime-modified asphalt mixtures is shown in Table 4.

Table 3. Independent parameters, including coded levels

Parameters	Code	Unit	Coded parameter levels		
			-1	0	+1
Steel Slag	A	%	0	50	100
Lime content	B	%	0	2	4
Bitumen content	C	%	4	6	8

Table 4. Experimental design for steel-slag and lime modified asphalt mixtures

S/N	Steel Slag; A (%)	Lime Content; B (%)	Bitumen Content; C (%)
1	0	2	4
2	0	4	6
3	100	2	4
4	100	2	8
5	0	0	6
6	50	0	4
7	50	2	6
8	50	0	8
9	100	4	6
10	50	2	6
11	50	2	6
12	50	2	6
13	50	2	6
14	0	2	8
15	100	0	6
16	50	4	4
17	50	4	8

### 2.3. Mixture Preparation and Testing

Two design techniques that are commonly used in asphalt mixtures are the Marshall and Superpave techniques, in which the volumetric features are seen as responses to the creation of more dependable asphalt mixtures.

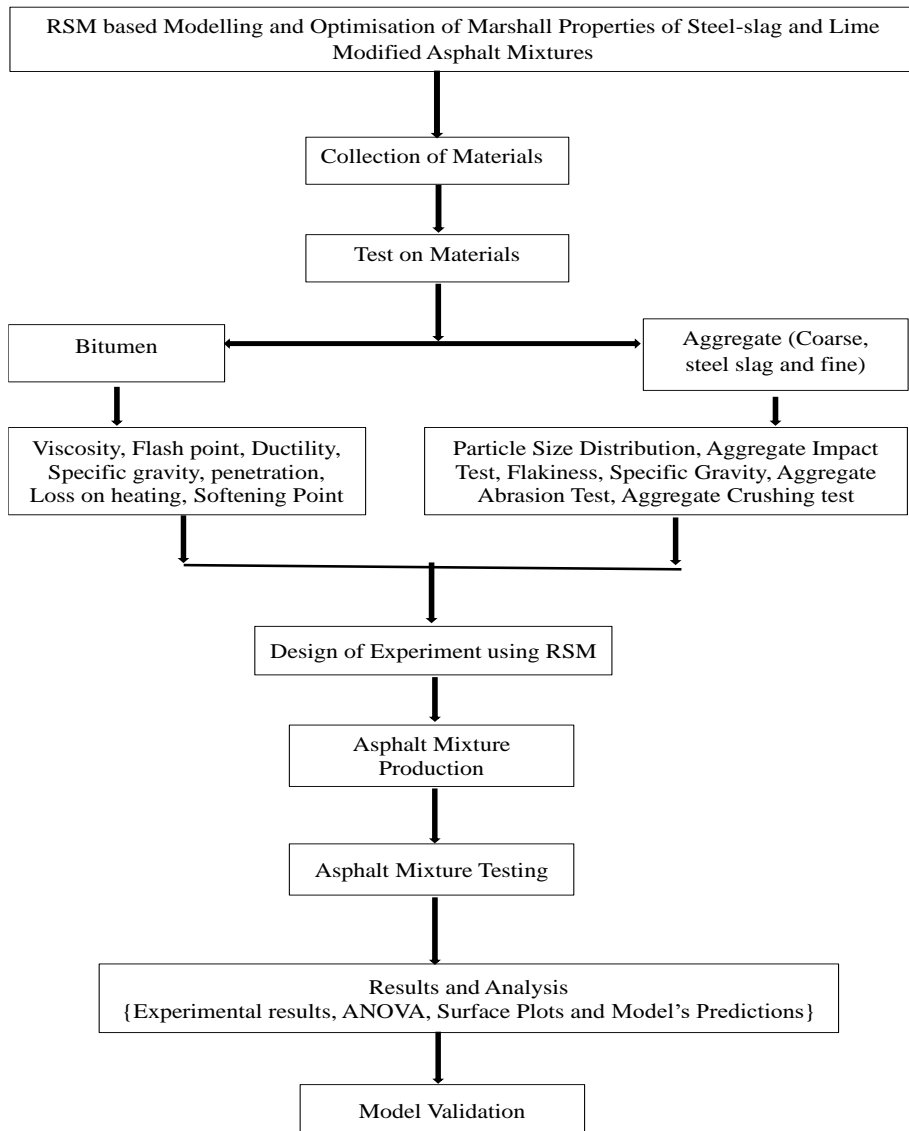


Fig. 3. Flow chart for the study

Nonetheless, the Marshall approach's relative simplicity, affordable equipment, and straightforward process make it a highly well-liked asphalt mixture design method [1, 30-31]. In this study, the asphalt mixtures were made using the Marshall method in compliance with ASTM D 1559-89 [32] standards using Table 4. The constituent materials were heated, mixed, then compacted using 75 blows (top and bottom) to create the mixes.



Following compaction, the mixtures, measuring roughly 101 mm in diameter and 63.5 mm in thickness, were suitably placed on a level, smooth surface and let to rest overnight at room temperature before being tested. Figure 3 displayed the flowchart of the research methodology used to achieve the study.

### 3. Results and Discussion

#### 3.1 Marshall Properties of the Steel-slag and Lime-Modified Asphalt Mixtures

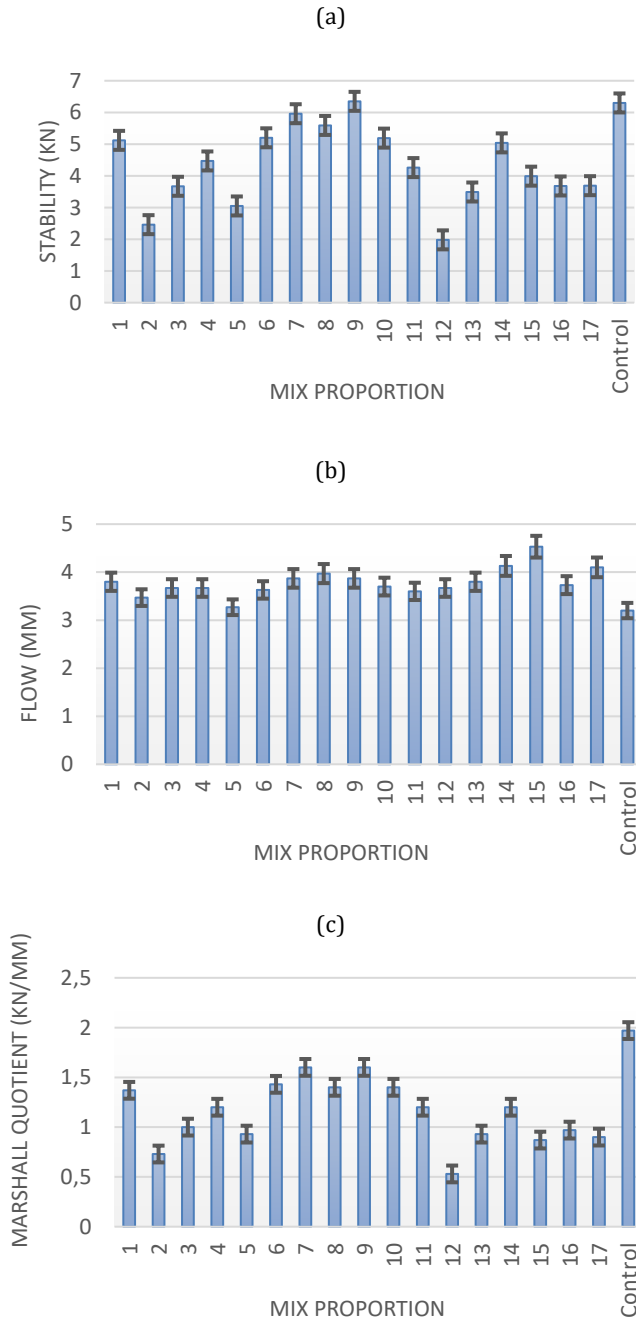
Figure 4 displays the Marshall properties of the steel-slag and lime-modified asphalt mixtures. While the Marshall stability values vary, mixture (Mix-9) with 100% steel slag and 4% lime has the highest Marshall Stability at 6.35kN and mixture (Mix-12) with 50% steel-slag and 2% lime has the lowest Marshall Stability at 1.98kN. In addition, whereas the mixture (Mix-15) with 100% steel slag and 0% lime produced the highest flow, the mixture (Mix-5) with 0% steel slag and 0% lime produced the lowest flow. This mixture's high flow value also implies strong flexibility, which improves the HMA pavement's capacity to deform without cracking. It can infer that the mixture's Marshall stability is increased by adding steel slag and lime, whilst the flow is the opposite. As a result, when modifying asphalt mixtures for strength (stability), steel slag and lime are preferred. However, the Marshall test necessitates both higher stability and lower flow [33]; while the Marshall flow of asphalt concrete refers to its resistance to slow settlements and movements in the sub-grade without cracking, the Marshall stability of asphalt concrete refers to its resistance to pushing and rutting under traffic [16]. In addition, except mixes 14, 15, and 17, all of the modified asphalt mixtures' obtained flows fall within the advised range of 2-4 mm for wearing course application. Additionally, only mixes 12, 5, and 2 falls below the suggested minimum of 3.5kN for the stability value.

The material's resistance to shear loads and permanent deformation is measured by the Marshall quotient (MQ). The ratio of the asphalt mixture's stability to flow is sometimes called the rigidity of the asphalt mix [34]. Mix-7 with 50% steel slag and 2% lime and Mix-9 with 100% steel slag and 4% lime had the highest MQ of 1.60 kN/mm, as shown in Figure 4c. The stability that is reached when the flow is still low is what is causing this increase in MQ; as the flow increases, the strength drops [35]. In addition, it has been found that the combinations with the highest MQ values contain both lime and steel slag. Consequently, lime and steel slag can be used to enhance asphalt mixtures.

Additionally, Figure 4d demonstrates that mixes 15 (100% steel slag and 0% lime), 11 (50% steel slag and 2% lime), and 6 (50% steel slag and 0% lime) all achieved the highest bulk density value of 2.29 kg/m<sup>3</sup>. The inclusion of micro-fine lime particles in the HMA, which raise the mix's density [36], causes the increase in bulk density.

The term "void in mineral aggregate" (VMA) refers to the empty space between the aggregate particles in a compacted mix. It indicates the available space for bitumen to coat each aggregate particle adequately. It can be seen from Figure 4f that the VMA values of the steel slag and lime-modified asphalt mixtures range from 14.82% to 24.63% for mixture 3 (100% steel slag and 2% lime) and mixture 8 (50% steel slag and 0% lime), respectively. This trend of VMA values is due to the difference in the aggregate gradings of the two materials (steel slag and granite)

Overall, the results shown in Figure 4 might not truly reflect the effect of steel slag and lime on Marshall's properties because of the variations in values obtained. However, in general, it can be seen that it is possible to produce steel-slag and lime-modified asphalt mixes that satisfy the specification limits recommended by the Asphalt institute [37] and Nigeria General Specification for Roads and Bridges [29].



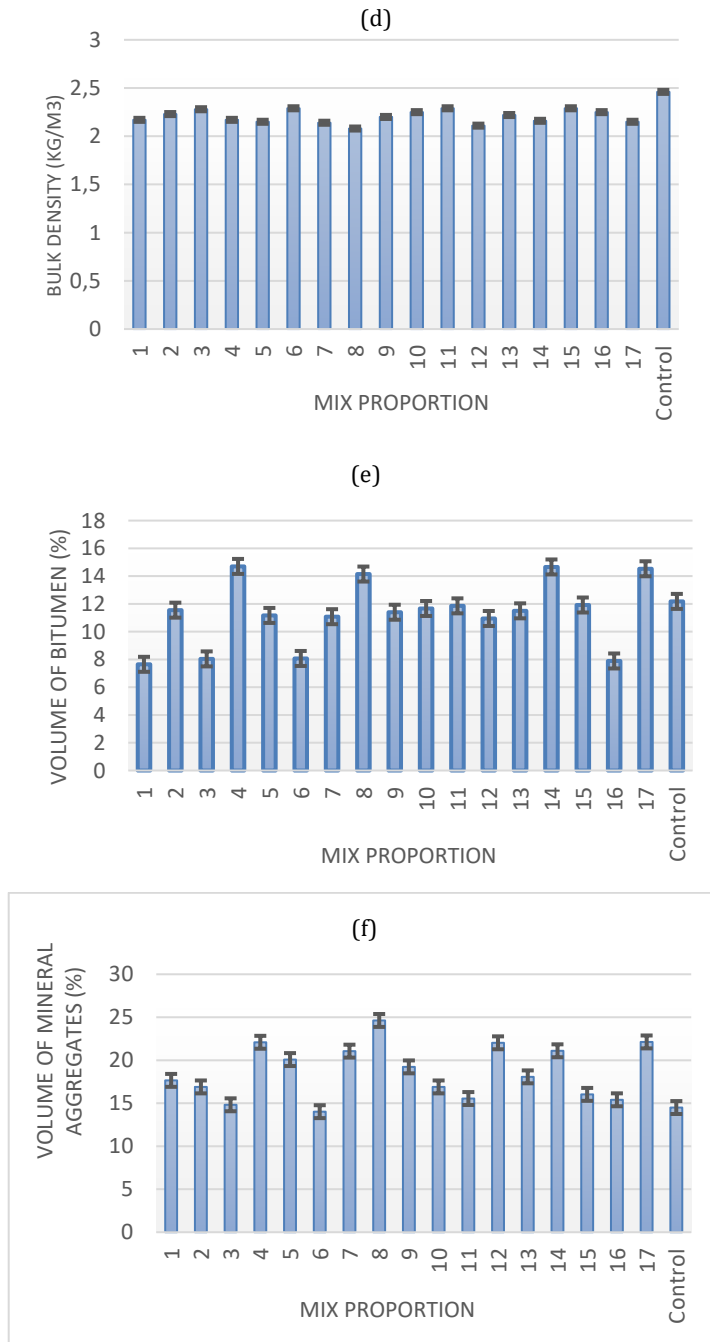


Fig. 4. Marshall Properties of Steel-slag and lime-modified asphalt mixtures (a) Stability (b) Flow (c) MQ (d) Bulk density (e) Vb and (f) VMA

### 3.2 Response Surface Analysis

#### 3.2.1 The Analysis of Variance (ANOVA) and Regression Models for the Modified Asphalt Mixtures

Table 5 shows the results of the ANOVA for the Marshall characteristics of steel slag and lime-modified asphalt. After demonstrating the highest F-values for flow, stability, Marshall quotient, bulk density, volume of bitumen, volume of mineral aggregates, and volume filled with bitumen, respectively, along with the necessary Prob>F0.05 in all of the models investigated for the volumetric properties, bitumen content was found to be the most influencing and significant factor among the independent variables. These values were 10.87, 33.92, 41.74, 13.44, 853.26 and 22.8. The model's F-values of 4.84, 14.59, 12.64, 4.50, 284.85, and 7.76 for all the responses, along with Prob>F values of 0.0001 for all responses, demonstrate the model's relevance. A P>F value of 0.05 typically denotes that the model's terms are significant (Bala et al., 2018). In all the models, the difference between the adjusted and predicted R<sup>2</sup> is less than 0.2, justifying that the models are significant and selected to fit the experimental data more. The range of expected values at design points against the average prediction error yields what is known as "adequate precision" (AP). According to the fundamental criteria, an AP ratio greater than 4 is acceptable [24]. For all responses, this study found AP ratios of 7.1081, 12.1590, 10.8185, 5.6483, 44.2315 and 7.8572. The selected models may satisfactorily travel the design space using BBD to supply the parameters for the ideal mix design, as indicated by these values, which also suggest an adequate signal. The coefficients of the polynomial model were calculated to fit the experimental data. The final regression model equations regarding significant factors are expressed in Equations [1]-[6]. Similar regression equations were reported by Lapian et al. [3] and Wang et al. [1].

Table 5. ANOVA results for properties of steel-slag and lime modified asphalt mixtures

Response	SoD	SoS	DoF	MS	F-value	P-value	Comment
<b>Flow</b>							
Model		0.7717	3	0.2572	4.84	0.0178	SD=0.2306
A		0.1326	1	0.1326	2.49	0.1383	Mean=3.12
B		0.0612	1	0.0612	1.15	0.3026	R <sup>2</sup> =0.6185
C		0.5778	1	0.5778	10.87	0.0058	Adj. R <sup>2</sup> =0.4581
Residual		0.6911	13	0.0532			AP=7.1081
Lack of Fit		0.4193	9	0.0466	0.6854	0.7078	
Pure Error		0.2719	4	0.0680			
<b>Stability</b>							
Model		45.91	9	5.10	14.59	0.0009	SD=0.5913
A		3.77	1	3.77	10.78	0.0134	Mean=5.82
B		1.44	1	1.44	4.11	0.0823	R <sup>2</sup> =0.9494
C		11.86	1	11.86	33.92	0.0006	Adj. R <sup>2</sup> =0.8843
AB		3.50	1	3.50	10.00	0.0159	AP=12.1590
AC		2.71	1	2.71	7.74	0.0272	
BC		0.0506	1	0.0506	0.1448	0.7148	
A <sup>2</sup>		1.15	1	1.15	3.29	0.1124	
B <sup>2</sup>		18.80	1	18.80	53.78	0.0002	
C <sup>2</sup>		3.04	1	3.04	8.69	0.0215	

Residual	2.45	7	0.3496				
Lack of Fit	0.8291	3	0.2764	0.6833	0.6072		
Pure Error	1.62	4	0.4045				
<b>Marshall Quotient (MQ)</b>							
Model	6.46	9	0.7175	12.64	0.0015	SD =0.2382	
A	0.6294	1	0.6294	11.09	0.0126	Mean=1.90	
B	0.2567	1	0.2567	4.52	0.0710	R <sup>2</sup> =0.98	
C	2.37	1	2.37	41.74	0.0003		
AB	0.2587	1	0.2587	4.56	0.0702	Adj. R <sup>2</sup> =0.8675 AP=10.8185	
AC	0.1339	1	0.1339	2.36	0.1685		
BC	0.0048	1	0.0048	0.0841	0.7803		
A <sup>2</sup>	0.2209	1	0.2209	3.89	0.0891		
B <sup>2</sup>	2.37	1	2.37	41.80	0.0003		
C <sup>2</sup>	0.2203	1	0.2203	3.88	0.0895		
Residual	0.3973	7	0.0568				
Lack of Fit	0.0775	3	0.0258	0.3229	0.8100		
Pure Error	0.3198	4	0.0800				
<b>Bulk Density</b>							
Model	0.0486	3	0.0162	4.50	0.0225	SD=0.06	
A	0.0002	1	0.0002	0.0433	0.8384	Mean=2.21	
B	0.0000	1	0.0000	0.0035	0.9539	R <sup>2</sup> =0.8509	
C	0.0485	1	0.0485	13.44	0.0028	Adj. R <sup>2</sup> =0.70396 AP= 5.6483	
Residual	0.0469	13	0.0036				
Lack of Fit	0.0247	9	0.0027	0.4965	0.8240		
Pure Error	0.0221	4	0.0055				
<b>Volume of bitumen (Vb)</b>							
Model	87.20	3	29.07	284.85	< 0.0001	SD=0.3194	
A	0.1307	1	0.1307	1.28	0.2781	Mean=11.34	
B	0.0006	1	0.0006	0.0054	0.9426	R <sup>2</sup> =0.9850	
C	87.07	1	87.07	853.26	< 0.0001	Adj. R <sup>2</sup> =0.8616 AP= 44.2315	
Residual	1.33	13	0.1020				
Lack of Fit	0.7304	9	0.0812	0.5446	0.7939		
Pure Error	0.5961	4	0.1490				
<b>Voids in the Mineral Aggregates (VMA)</b>							
Model	99.99	3	33.33	7.76	0.0032	SD=2.07	

A	1.59	1	1.59	0.3696	0.5537	Mean=18.69
B	0.1478	1	0.1478	0.0344	0.8557	
C	98.25	1	98.25	22.87	0.0004	Adj. R <sup>2</sup> =0.5589
Residual	55.85	13	4.30			AP= 7.8572
Lack of Fit	25.60	9	2.84	0.3760	0.8973	
Pure Error	30.25	4	7.56			

$$\begin{aligned}
 \text{Stability (kN)} = & 6.656 - 0.68625A + 0.42375B - 1.2175C - 0.935AB \\
 & - 0.8225AC + 0.1125BC - 0.523A^2 - 2.113B^2 \\
 & + 0.8495C^2
 \end{aligned} \tag{1}$$

$$\text{Flow (mm)} = 3.12412 + 0.12875A - 0.0875B + 0.26875C \tag{2}$$

$$\begin{aligned}
 MQ \left( \frac{kN}{mm} \right) = & 2.25419 - 0.280495A + 0.179147B - 0.544157C \\
 & - 0.254307AB - 0.182947AC - 0.0345347BC \\
 & - 0.229049A^2 - 0.750617B^2 + 0.228752C^2
 \end{aligned} \tag{3}$$

$$\text{Bulk Density} = 2.21339 + 0.00441667A + 0.00125B - 0.0778333C \tag{4}$$

$$V_b = 11.3401 + 0.127833A + 0.00829167B + 3.29896C \tag{5}$$

$$\text{VMA} = 18.6876 - 0.445542A - 0.135917B + 3.50445C \tag{6}$$

### 3.2.2 Normality Plot for the Marshall Properties of Steel-slag and Lime-Modified Asphalt Mixtures

To ensure that the actual vs anticipated plots and residuals for every property under investigation were normal, data were evaluated. The normal probability plots of the residuals and the actual vs anticipated data for the asphalt mixtures treated with lime and steel slag are shown in Figure 5(a-f).

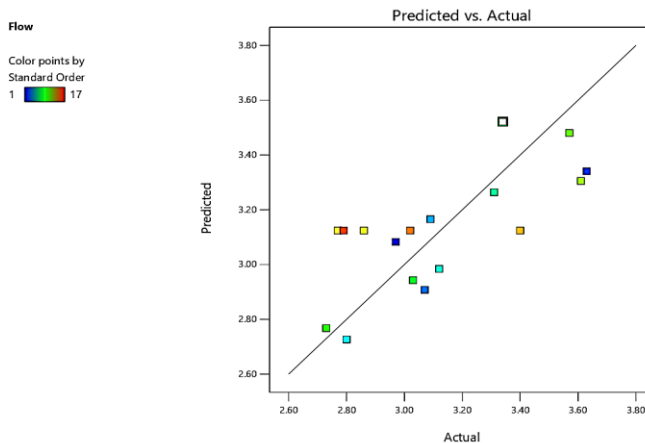


Fig. 5a. Normal probability distribution plot of flow for steel-slag and lime-modified asphalt mixtures

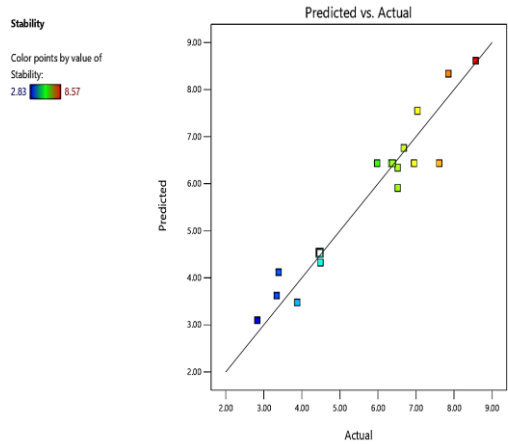


Fig. 5b. Normal probability distribution plot of stability for steel-slag and lime-modified asphalt mixtures

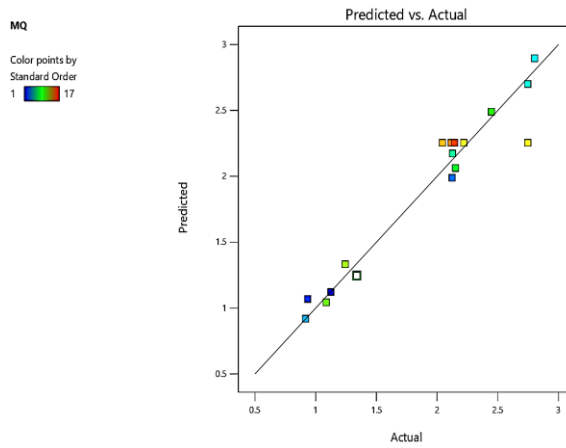


Fig. 5c. Normal probability distribution plot of MQ for steel-slag and lime-modified asphalt mixtures

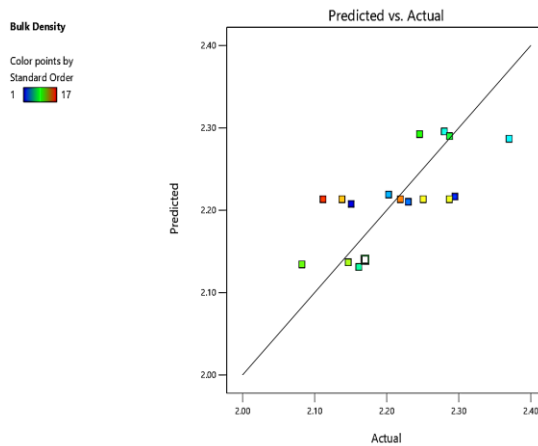


Fig. 5d. Normal probability distribution plot of Bulk Density for steel-slag and lime-modified asphalt mixtures

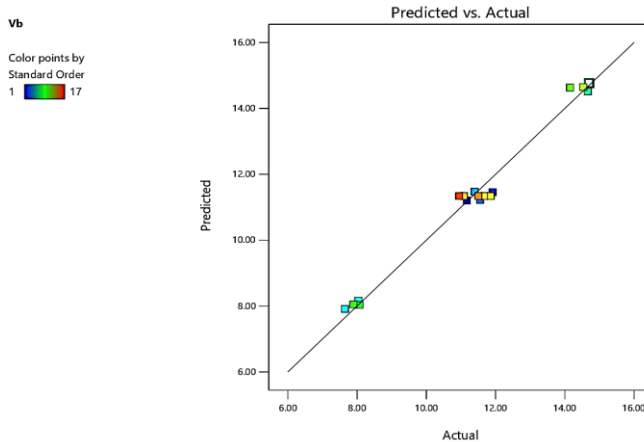


Fig. 5e. Normal probability distribution plot of Vb for steel-slag and lime-modified asphalt mixtures

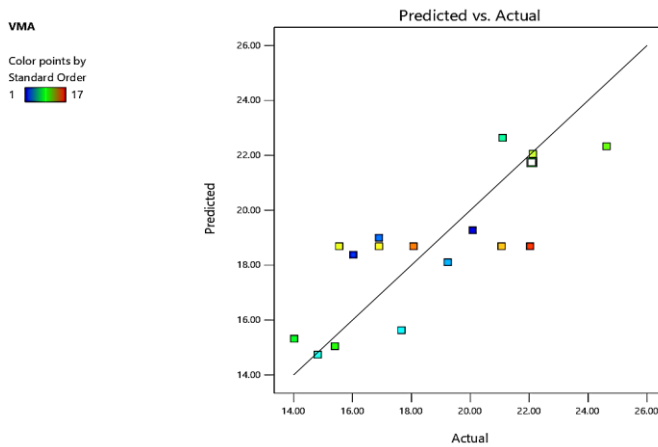


Fig. 5f. Normal probability distribution plot of VMA for steel-slag and lime-modified asphalt mixtures

From the Figures of the normal probability of students' residuals for all the properties, it can be seen that there is very less scattered along the straight line. This shows that the data is normally distributed, and almost all variations were credited to the variable factors studied. Plot predictions against actual values were used to check the model's suitability. The plot of predicted against actual indicates whether an acceptable agreement exists between the experimental results and those found from developed models. From the plots of predicted versus actual for all the properties, it can be seen that the observed points are relatively on a straight line. This justified that adequate agreement exists between the experimental results and those obtained from the model. Thus, it was evident that, in general, a normal distribution plot was a useful option for assessing the interested responses.

### 3.2.3 Surface Plots of the Marshall Properties of Steel-slag and lime-modified Asphalt mixtures

To examine the interactive relationship between the parameters and the properties of the asphalt mixtures modified with lime and steel slag under optimal conditions, response

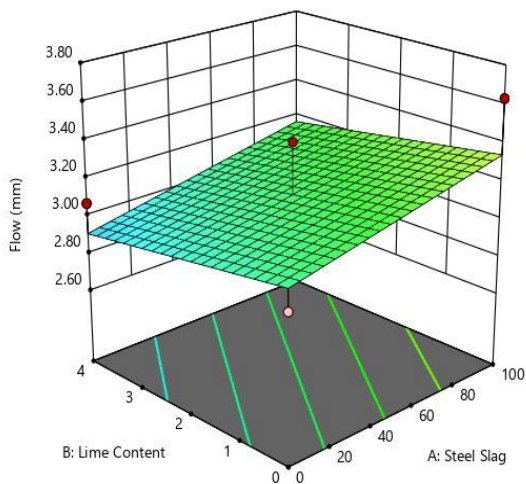


surface plots are utilized. The three-dimensional surface views (3D surface plots) show the detailed behavior of the independent variables within the experiment.

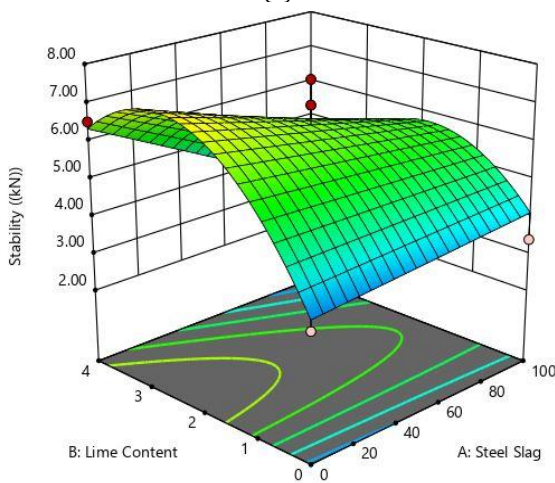
The 3D response surfaces plots for the Marshall responses based on the effects of the interactive variables, steel-slag, lime and bitumen content, as shown in Figures 6 (a-f).

The response surfaces for flow (Figure 6a) show that the factors have significant interaction effects on the flow. It can be observed that a decrease in the lime content increased the flow. Furthermore, with an increase in the steel slag by up to 73%, the flow increased slightly.

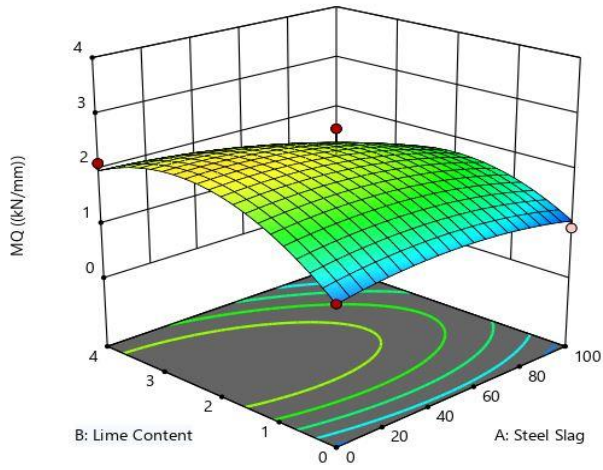
Figure 6b shows the response surfaces for the Marshall stability of the steel slag and lime-modified asphalt mixtures. The 3D plot curvature indicates that as the lime content increases up to 2%, there was an increase in the Marshall stability and a decrease afterwards. The addition of steel slag resulted in constant stability. Hence, stability is strongly influenced by lime content. It was also reported by Ogundipe [38] that the utilization of lime in asphalt mixtures resulted in an increment in stability. Furthermore, based on the plot, it is evident that all of the parameters interact well with one another.



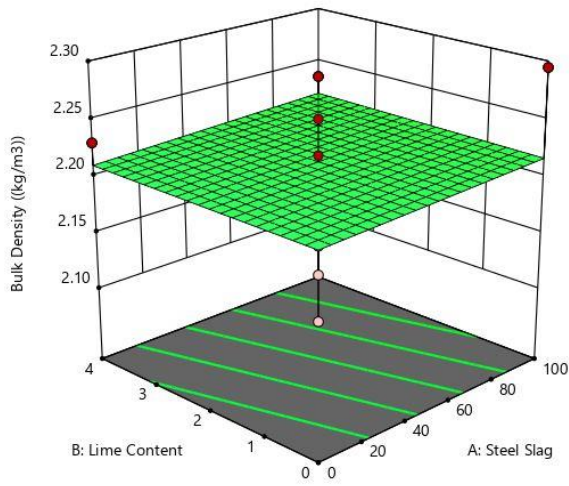
(a)



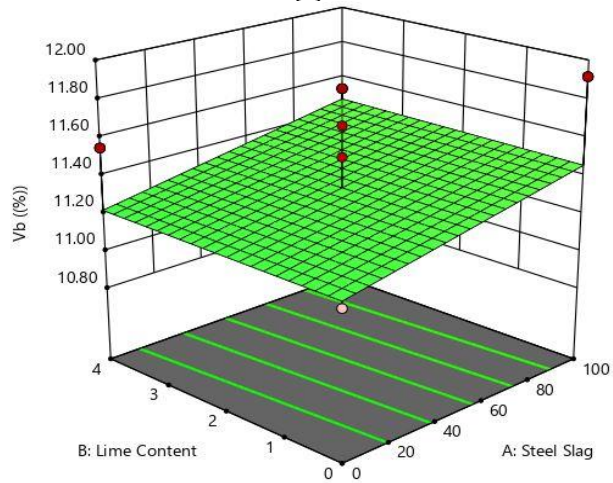
(b)



(c)



(d)



(e)

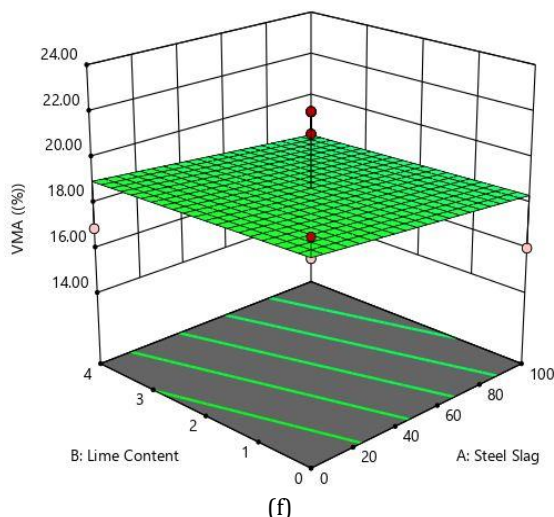


Fig. 6. Response surface plots for the Marshall properties of steel-slag and lime-modified asphalt mixtures

### 3.2.4 Mix Design Optimization

In this study, design variables were optimized, and the accuracy of the developed models was assessed using the RSM optimization tool, a numerical optimization method. The target aims for each mix design factor (A, B, and C) selected, as shown in Table 6 for steel-slag and lime modified, was set to achieve this. The intended stability, MQ, and bulk density, VMA, were defined as maximal to get the greatest results. To achieve great performance, the desired flow was defined in the range. According to the optimization results, the ideal values to meet the design requirements are 24.93% steel slag, 2.43% lime and 5.51% bitumen content. A second experiment was run to verify the model's predictions based on the ideal projected mix design elements.

Table 6. Design conditions for optimisation

Responses	Units	Lower limit	Upper limit
Flow	Mm	2	4
Stability	kN	Maximum range	
MQ	kN/mm	Maximize	
Bulk Specific gravity	kg/m <sup>3</sup>	Maximum	
VMA	%	17	
Vb	%	non	

Table 7. Optimum conditions achieved for steel-slag and lime-modified asphalt mixtures

Response	Unit	Predicted	Observed	Error (%)
Flow	mm	3.12	3.04	2.63
Stability	kN	6.67	6.58	2.13
MQ	kN/mm	2.25	2.16	4.17
Bulk density	kg/m <sup>3</sup>	2.21	2.19	0.91
Vb	%	11.34	11.22	1.07
VMA	%	18.69	19.25	2.91

Table 7 shows the percentage error difference; It showed that the expected values for the developed models agree with the experimental values, with less than 5% for all responses. In Liu et al. [39], the error between the predicted and actual values of the asphalt indexes was also found to falls within an acceptable range.

## 5. Conclusions

The mix proportioning of the constituent materials is crucial to achieve the desired targeted qualities. Hence, the design of the experiment (DOE) using software tools like RSM for asphalt mix proportioning is essential. Incorporating RSM into pavement technologies, researchers can access more rapid, accurate, and reliable methods of analyzing changes in pavement performance and improved experimental matrices. In this study, the Box Behnken Design (BBD) tool in Response Surface Methodology (RSM) was used to investigate the impact of steel slag and lime on the Marshall characteristics of asphalt mixtures. The following conclusions can be made in light of the analysis in this study:

- The experimental results show that the steel-slag and lime-modified asphalt mixtures satisfy the specification limits recommended by the Asphalt Institute and the Nigeria General Specification for Roads and Bridges.
- The results of the ANOVA analysis of the models are statistically significant for all the responses.
- Lime content significantly affects Marshall stability and quotient more than the steel-slag content.
- Steel slag and lime have significant interactive effects on the flow.
- A mathematical model was successfully developed to predict the Marshall properties of steel slag and lime-modified asphalt mixtures. In all the models, the difference between the adjusted and predicted  $R^2$  is less than 0.2, justifying that the models are significant and selected to fit the experimental data more.
- Based on the response surface plot, it is evident that all of the parameters interact well with one another
- According to the optimisation results, the ideal values to meet the design requirements are 24.93% steel slag, 2.43% lime and 5.51% bitumen content. Furthermore, a mean error of less than 5% was achieved for all the responses; this indicates that optimisation using RSM is very effective for asphalt mixture design with high-performance properties.
- In this study, steel slag of size 12.5mm was used as coarse aggregates; other sizes (for coarse and fine aggregates) should be experimented with for future works.

## Acknowledgement

The authors appreciate the contribution of all technical staff of Civil Engineering Department, Landmark University, Omu-Aran, Nigeria.

## References

- [1] Wang W, Cheng Y, Tan G. Design optimisation of SBS-modified asphalt mixture reinforced with eco-friendly basalt fiber based on response surface methodology, *Materials*, 2018; 11(8), 1311. <https://doi.org/10.3390/ma11081311>
- [2] Bala N, Napiyah M, Kamaruddin I. Application of Response Surface Methodology for mix design optimisation of nanocomposite modified asphalt mixtures, *GEOMATE Journal*, 2017; 13(39), 237-244. <https://doi.org/10.21660/2017.39.58554>
- [3] Lopian FE, Ramli MI, Pasra M, Arsyad A. The performance modeling of modified asbuton and polyethylene terephthalate (PET) mixture using response surface methodology (RSM), *Applied Sciences*, 2021; 11(13), 6144. <https://doi.org/10.3390/app11136144>

- [4] Moghaddam TB, Baaj H, Hossain S K. Adoption of statistical analysis to evaluate the permanent deformation of Polyethylene Terephthalate (PET) modified asphalt mixtures. In TAC 2016: Efficient Transportation-Managing the Demand-2016 Conference and Exhibition of the Transportation Association of Canada.
- [5] Aladegboye OJ, Oguntayo OD, Al-Ihekwa E, Daniel TE, Chiadighikaobi PC, Ng'andu P. Evaluation of Volumetric Properties of Cassava Peel Ash Modified Asphalt Mixtures, *Civil Engineering Journal*, 2022; 8(10), 2110-2124. <https://doi.org/10.28991/CEJ-2022-08-10-07>
- [6] Oguntayo D, Ogundipe O, Aladegboye O, Ogunkunbi G, Babatunde Y, Aransiola O. Performance Evaluation of Hospital Waste Ash-Modified Asphalt Mixtures, *Advances in Civil Engineering*, 2023; 6880766. <https://doi.org/10.1155/2023/6880766>
- [7] Kim S, Usman M, Park C, Hanif A. Durability of slag waste incorporated steel fiber-reinforced concrete in marine environment, *Journal of Building Engineering*, 2021; 33, 101641. <https://doi.org/10.1016/j.jobbe.2020.101641>
- [8] Ali AB, Sharif MB, Irfan-ul-Hassan M, Iqbal Y, Akmal U, Alabduljabbar H, Deifalla AF. Coupled Effect of Polypropylene Fibers and Slag on the Impact Resistance and Mechanical Properties of Concrete, *Materials*, 2022; 15(16), 5654. <https://doi.org/10.3390/ma15165654>
- [9] Zhang X, Chen J, Jiang J, Li J, Tyagi RD, Surampalli RY. The potential utilization of slag generated from iron-and steelmaking industries: a review, *Environmental geochemistry and health*, 2020; 42(5): 1321-1334. <https://doi.org/10.1007/s10653-019-00419-y>
- [10] Lobato NCC, Villegas EA, Mansur MB. Management of solid wastes from steelmaking and galvanizing processes: A brief review, *Resources, Conservation and Recycling*, 2015; 102: 49-57. <https://doi.org/10.1016/j.resconrec.2015.05.025>
- [11] Adegbite O. Minister for Mines and Steel development remarks at acquisition of Standard Metallurgical Company plants by KAM Steel Integrated Company Limited, 2020; available: <https://businesstraffic.com.ng/kam-steel-increases-capacity-with-acquisition-of-n60bn-steel-plant-in-ogun-state/>. Accessed on 10th June, 2022 by 9:22am.
- [12] Kumar MM, Sivakumar VL, Devi VS, Nagabhooshanam N, Thanappan S. Investigation on Durability Behavior of Fiber Reinforced Concrete with Steel Slag/Bacteria beneath Diverse Exposure Conditions, *Advances in Materials Science and Engineering*, 2022. <https://doi.org/10.1155/2022/4900241>
- [13] Yuan TF, Choi JS, Kim SK, Yoon YS. Assessment of steel slag and steel fiber to control electromagnetic shielding in high-strength concrete, *KSCE Journal of Civil Engineering*, 2021; 25: 920-930. <https://doi.org/10.1007/s12205-021-0629-1>
- [14] Oguntayo D, Ogundipe M, Aluko O, Oguntayo B, Rahmon R, Ogundipe O. Nigerian Steel-slag for Road Works: Physical, Mineralogy and Micro-structural Characterization. In 2023 International Conference on Science, Engineering and Business for Sustainable Development Goals (SEB-SDG), IEEE, 2023; Vol. 1: 1-4. <https://doi.org/10.1109/SEB-SDG57117.2023.10124590>
- [15] Błażejowski K, Przemysław O, Wiktorja B, Marta WW. The effect of hydrated lime on asphalt mixtures with highly polymer modified bituminous bitumen (HiMA). 7th E&E CONGRESS Eurasphalt & Eurobitume, 2021; <https://www.researchgate.net/publication/350603679>
- [16] Moghaddam TB, Soltani M, Karim MR. Stiffness modulus of Polyethylene Terephthalate modified asphalt mixture: A statistical analysis of the laboratory testing results, *Materials & Design*, 2015; 68: 88-96. <https://doi.org/10.1016/j.matdes.2014.11.044>
- [17] Ismael MQ, Ahmed AH. Effect of hydrated lime on moisture susceptibility of asphalt mixtures, *Journal of Engineering*, 2019; 25(3); 89-101. <https://doi.org/10.31026/j.eng.2019.03.08>

- [18] Dehnad MH, Damyar B, Farahani HZ. Rheological evaluation of modified bitumen by EVA and crumb rubber using RSM optimization, *Advances in Materials Science and Engineering*, 2021; 1-8. <https://doi.org/10.1155/2021/9825541>
- [19] Nassar AI, Thom N, Parry T. Optimising the mix design of cold bitumen emulsion mixtures using response surface methodology, *Construction and Building Materials*, 2016;104: 216-229. <https://doi.org/10.1016/j.conbuildmat.2015.12.073>
- [20] Haghshenas HF, Khodaii A, Khedmati M, Tapkin S. A mathematical model for predicting stripping potential of Hot Mix Asphalt, *Construction and Building Materials*, 2015; 75: 488-495. <https://doi.org/10.1016/j.conbuildmat.2014.11.041>
- [21] Hoseinpour-Lonbar M, Alavi MZ, Palassi M. Selection of asphalt mix with optimal fracture properties at intermediate temperature using Taguchi method for design of experiment, *Construction and Building Materials*, 2020; 262, 120601. <https://doi.org/10.1016/j.conbuildmat.2020.120601>
- [22] Awan HH, Hussain A, Javed MF, Qiu Y, Alrowais R, Mohamed AM, Fathi D, Alzahrani AM. Predicting marshall flow and marshall stability of asphalt pavements using multi expression programming, *Buildings*, 2022; 12(3), 314. <https://doi.org/10.3390/buildings12030314>
- [23] Yaro NSA, Sutanto MH, Habib NZ, Napiyah M, Usman A, Muhammad A. Comparison of Response Surface Methodology and Artificial Neural Network approach in predicting the performance and properties of palm oil clinker fine modified asphalt mixtures, *Construction and Building Materials*, 2022; 324, 126618. <https://doi.org/10.1016/j.conbuildmat.2022.126618>
- [24] Bala N, Kamaruddin I, Napiyah M, Danlami N. Polyethylene polymer modified bitumen: Process optimisation and modeling of linear viscoelastic rheological properties using response surface methodology, *Journal of Engineering and Applied Sciences*, 2018;13(9): 2818-2827.
- [25] Golchin B, Hamzah MO, Hasan MRM. Optimisation in producing warm mix asphalt with polymer modified binder and surfactant-wax additive, *Construction and Building Materials*, 2017;141: 578-588. <https://doi.org/10.1016/j.conbuildmat.2017.02.123>
- [26] Awolusi TF, Oke OL, Akinkulore OO, Sojobi AO. Application of response surface methodology: Predicting and optimising the properties of concrete containing steel fibre extracted from waste tires with limestone powder as filler, *Case studies in Construction materials*, 2019; 10, e00212. <https://doi.org/10.1016/j.cscm.2018.e00212>
- [27] Galan JJ, Silva LM, Pérez I, Pasandín AR. Mechanical behavior of hot-mix asphalt made with recycled concrete aggregates from construction and demolition waste: A design of experiments approach, *Sustainability*, 2019;11(13), 3730. <https://doi.org/10.3390/su11133730>
- [28] Omranian SR (2021). Application of Response Surface Method for Analysing Pavement Performance, *Response Surface Methodology in Engineering Science*, IntechOpen, 2019.
- [29] Federal Government of Nigeria. General Specification for road and bridges -Revised edition (volume ii), Federal Ministry of Works and Housing. Abuja, Nigeria, 2013.
- [30] Lv J, Zhancheng X, Yingmei Y, Jiantong Z, Xiaolong S, Chuanhai W. Comparison of asphalt mixtures designed using the Marshall and improved GTM methods, *Advances in Materials Science and Engineering*, 2018. <https://doi.org/10.1155/2018/7328791>
- [31] Radzi HM, Muniandy R, Hassim S, Law TH, Jakarni FM. An overview of asphalt mix designs using various compactors. In *IOP Conference Series: Materials Science and Engineering*, 2019; 512 (1): 012031). <https://doi.org/10.1088/1757-899X/512/1/012031>
- [32] ASTM D 1559 (1989). Standard test method for resistance to plastic flow of bituminous mixtures using Marshall apparatus.

- [33] Ahmedzade P, Sengoz B. Evaluation of steel slag coarse aggregate in hot mix asphalt concrete, *Journal of hazardous materials*, 2009; 165: 300-305. <https://doi.org/10.1016/j.jhazmat.2008.09.105>
- [34] Siswanto H, Supriyanto B, Pranoto, Chandra PR, Hakim AR. Marshall properties of asphalt concrete using crumb rubber modified of motorcycle tire waste. In *AIP Conference Proceedings*, 2017; 1887(1): 020039. <https://doi.org/10.1063/1.5003522>
- [35] Jaya RP, Hainin MR, Hassan NA, Yaacob H, Satar MKIM, Warid MNM, Ramli NI. Marshall stability properties of asphalt mixture incorporating black rice husk ash, *Materials Today: Proceedings*, 2018; 5(10): 22056-22062. <https://doi.org/10.1016/j.matpr.2018.07.068>
- [36] Al-Taher MG. (2018). *Finite Elements Performance Analysis of Asphalt Pavement Mixtures Modified Using Nano-Additives*, Ph.D. Dissertation, Institute of Engineering, EL-Shorouk Academy.
- [37] Asphalt Institute (2015). *Mix Design Methods for Asphalt Concrete and Other Hot-Mix Types*. Manual Series No. 2 (MS-2). Asphalt Institute. Lexington, KY
- [38] Ogundipe OM. Marshall stability and flow of lime-modified asphalt concrete, *Transportation Research Procedia*, 2016; 14: 685-693. <https://doi.org/10.1016/j.trpro.2016.05.333>
- [39] Liu H, Wang J, Lu W, Zhang N. Optimization Design and Mechanical Performances of Plant-Mix Hot Recycled Asphalt Using Response Surface Methodology, *Materials*, 2023; 16(17): 5863. <https://doi.org/10.3390/ma16175863>

## Observed failure modes in existing URM buildings after November 26, 2019 earthquake in Albania

Enio Deneko<sup>1,a</sup>, Hüseyin Bilgin<sup>\*2,b</sup>

<sup>1</sup>Faculty of Civil Engineering, Polytechnic University of Tirana, Tirana, Albania

<sup>2</sup>Department of Civil Engineering, EPOKA University, Tirana, Albania

### Article Info

### Abstract

#### Article history:

Received 02 Dec 2023

Accepted 22 Jan 2024

#### Keywords:

URM buildings;

Failure modes;

Structural weaknesses;

Retrofitting

This study explores the vulnerability of Unreinforced Masonry (URM) structures to seismic events, aiming to uncover the causes of failure and propose reconstruction strategies. Despite often being devastated in powerful earthquakes, URM buildings show damage even in mild to moderate seismic events. Field assessments after a magnitude 6.4 earthquake near Durres, Albania, in 2019, revealed severe damage in masonry buildings and adobe dwellings. Weak structural connections, insufficient roof support, and the absence of bond beams in load-bearing walls were identified as key contributors to the observed damage. The survival of masonry buildings post-earthquake does not guarantee seismic safety. The study recommends reinforcement techniques like shotcrete application, space reduction, and corner reinforcement, along with innovative methods such as Fiber Reinforced Polymer (FRP) use, for existing undamaged unreinforced buildings. These measures aim to prevent damage in the aftermath of destructive earthquakes, offering insights for the resilience of URM structures.

© 2024 MIM Research Group. All rights reserved.

## 1. Introduction

Albania, located in the southwestern Balkans as depicted in Fig. 1, is susceptible to a variety of moderate and significant earthquakes due to the presence of multiple active fault lines in the region, a characteristic that has been evident throughout its historical record [1]. On September 21 and November 26, 2019, two separate seismic activity occurred, causing a significant damage in Albania, a region characterized by a high seismic hazard [2]. These earthquakes had a profound impact on important cities of the country, including Durres and Tirana. Various types of structural systems experienced damage at different degrees, ranging from minor to severe, or complete collapse [3]. Numerous structures managed to withstand the initial earthquake. However, following the second tremor that occurred three months later, it imposed a greater degree of damage and worsened the extent of destruction [4]. The earthquake sequences in 2019 provided valuable lessons for both reinforced concrete (RC) and masonry structures in urban and rural areas [5].

In rural regions, particularly in poor villages, residents often construct their homes using readily available materials. This is a common practice across most of Albania's villages, where dwellings are frequently built using materials like brick, rubble stone, or adobe. Many of these buildings have been in existence for generations, passed down from one family member to the next. As a result, these structures have aged significantly, leading to a loss of strength and stability. Moreover, such structures were typically built without the involvement of essential engineering services. All these factors combine to increase the

\*Corresponding author: [hbilgin@epoka.edu.al](mailto:hbilgin@epoka.edu.al)

<sup>a</sup> orcid.org/0009-0000-7236-5242; <sup>b</sup> orcid.org/0000-0002-5261-3939

DOI: <http://dx.doi.org/10.17515/resm2024.106ea1202rs>

Res. Eng. Struct. Mat. Vol. 10 Iss. 3 (2024) 1085-1107



vulnerability of these structures, making them susceptible to damage and destruction even during moderately sized tremors [6-7].



Fig. 1. Active fault map of Albania [1]

The seismic event in Durres on November 26, 2019, registering a magnitude of  $M_w = 6.4$ , resulted in substantial damage, as illustrated in Fig. 2. To assess the failures in masonry buildings, field visits were conducted in both major cities and the surrounding villages affected by this earthquake. The Durres district, where these affected villages are situated, is approximately 35 kilometres from the capital centre of Tirana and is located along the Adriatic Sea coast.

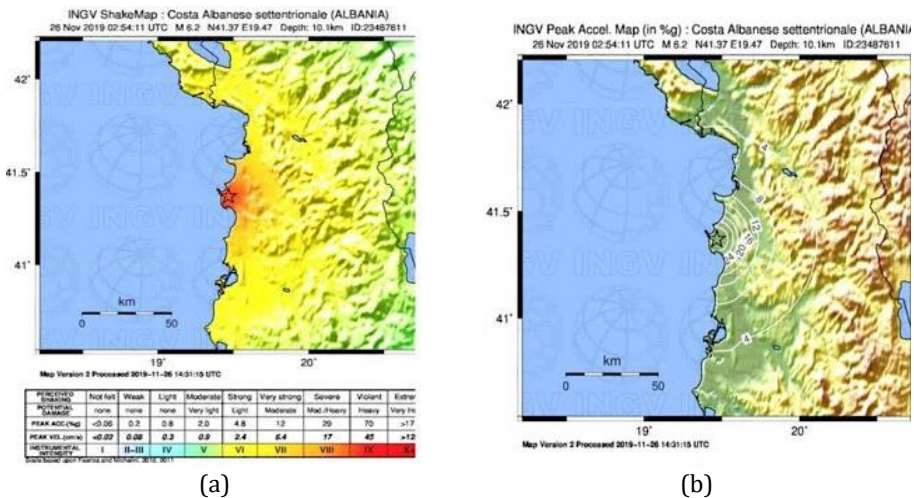


Fig. 2. Intensity map of November 26, 2019 Durres/Albania earthquake (INGV, 2019)

The Earth serves as an exceptional laboratory, enabling the examination of a building's response following seismic events. Identifying structural damage in the aftermath of an

earthquake is an essential step in post-disaster management. Consequently, numerous detailed studies have been conducted by researchers after earthquakes. These studies involve the observation of structural damage and the acquisition of valuable insights into the causes of failures.

Fig. 3 illustrates the accelerometric stations associated with the November 26, 2019 earthquake (M6.4), while Table 1 provides a tabulation of the measured acceleration values.

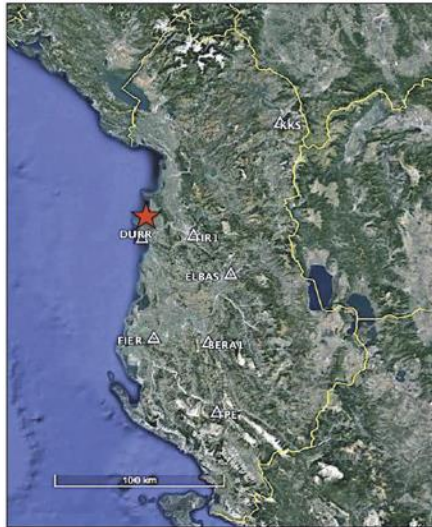


Fig. 3. Dispersion of the nearest accelerometer stations that captured the seismic activity, (red star: epicentre)

Structural behaviour of URM buildings was studied in the aftermath of 2010 Christchurch earthquake in New Zealand [8]. Kaplan and colleagues investigated the damage, both structural and non-structural, to different buildings in the aftermath of the 2009 L'Aquila earthquake in Italy [9]. Following the 2010 Chile earthquake, earthquake behaviour of masonry buildings was analysed by Astrosa and co-authors [10]. Basset and Guardiola investigated the damages inflicted by the 2011 earthquake, to masonry dwellings in Spain [11]. Saha et al. investigated seismic damage to buildings after the 2017 Tripura earthquake in Bangladesh [12]. Chen and collaborators evaluated structural damage in the aftermath of the 2014 Yunnan earthquake in China [13]. Sorrentino and colleagues investigated the behaviour of typical masonry buildings in response to seismic events in Italy in 2016 [14]. Gautam and Chaulagain explored structural performance during the Gorkha earthquake in Nepal on April 25, 2015, and shared the lessons learned [15]. Shakya and Kawan evaluated the building damage in Nepal - Kathmandu earthquake [16]. Aras and Düzci studied the earthquake response of commonly encountered traditional masonry houses in Çanakkale following seismic activities [17]. Vlachakis and co-authors assessed the damage and failure mechanisms of masonry houses in the aftermath of the 2017 Greece earthquake [18]. Bayraktar and colleagues conducted on-site observations to assess how masonry structures performed during the 2011 Earthquakes in eastern part of Turkey [19]. Atmaca et al. evaluated the performance of building structures in Turkey considering previous earthquake events [20]. Valente [21] explored the seismic response of two historic masonry palaces through 3-D structural analyses. The results of structural analyses shown a significant dependence of damage distributions and seismic response on the dynamic and geometric characteristics of the structures. Isik et al. [22] examined the masonry damages in Adıyaman province following the 2023 Kahramanmaraş earthquakes

in Türkiye. They asserted that the predominant cause of structural damage is attributed to weak structural features.

Table 1. Accelerometric stations and measured acceleration values of November 26, 2019 Earthquake (M6.4) (Fig. 3)

Station Code	Recording Station Location	Vs30 (m/s)	Site	Measured									Dist. to epicentre km
				PGA (cm/s <sup>2</sup> ) / PGV (cm/s) / PGD (cm)			E-W			V			
				N-S			E-W			V			
DURR	Durres	200	Free field	192.0	38.55	14.0	122.3	14.4	4.52	114.5	7.18	4.39	15.6
TIR 1	Tirana	310	Free field	110.0	6.65	1.77	113.9	7.57	1.80	43.49	2.16	0.73	33.7
BERA1	Berat	1.010	Free field	10.65	0.68	0.16	15.10	0.92	0.29	7.91	0.53	0.13	93.7
ELBAS	Elbasan	405	2-story building	19.75	1.70	0.44	13.69	0.87	0.22	11.88	0.96	0.23	65.8
FIER	Fier	375	2-story building	17.83	1.20	0.57	17.39	1.50	0.59	8.80	0.74	0.35	83.2
KKS	Kukes	750	1-story building	7.87	0.79	0.40	7.87	0.95	0.51	-	-	-	105
TPE	Tepelene	690	2-story building	6.28	0.79	0.22	5.36	0.72	0.26	3.88	0.37	0.11	128.2

The primary objective of this paper is to centre on the recognition of damage patterns and the proposal of seismic reinforcement strategies for pre-existing unreinforced masonry structures following the earthquake that occurred on November 26, 2019. This research involves an evaluation of the structural deficiencies and performance of masonry buildings. The observed damage patterns are categorized into four main types: entire collapse, damage on corners, in-plane, and out-of-plane failures.

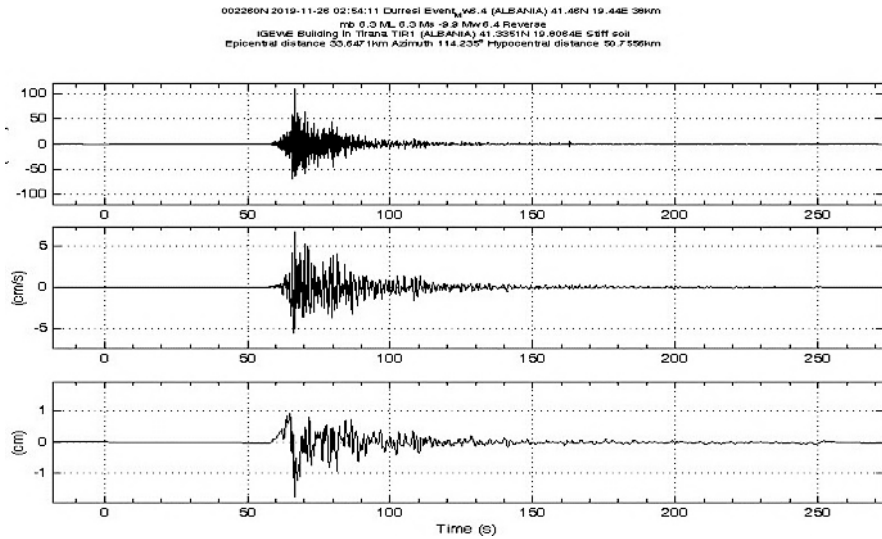
## 2. Features of November 26, 2019 Earthquake

On November 26, 2019, at 03:54 CET, Durres city experienced a notable seismic event. This earthquake was characterized as moderately strong, with a magnitude of  $M_w = 6.4$ . The intensity map, depicted in Fig. 2, illustrates the affected zones, with active faults indicated by red lines. Detailed acceleration values recorded at different locations can be found in Table 1.

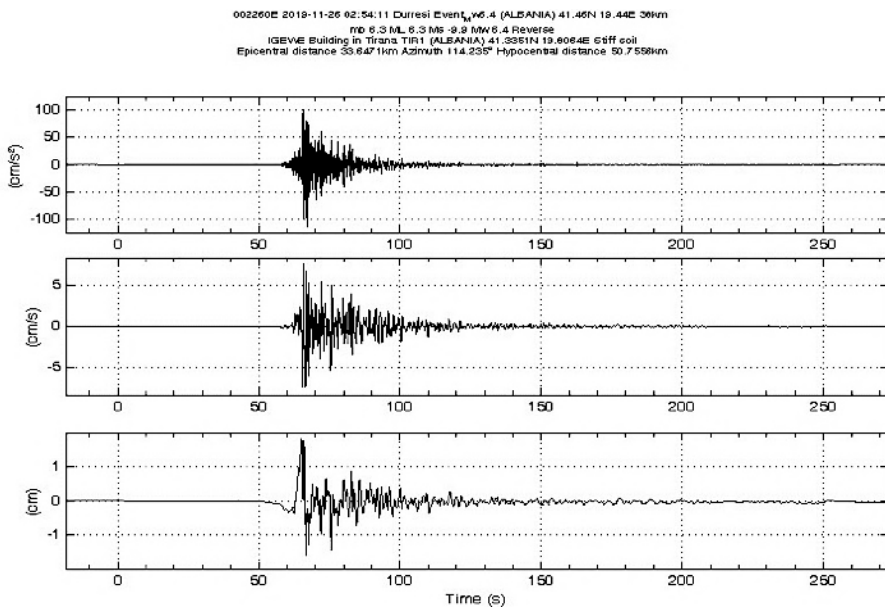
Durres station recorded the highest ground acceleration values, measuring  $192.0 \text{ cm/s}^2$  for the North–South (N–S) component,  $122.30 \text{ cm/s}^2$  for the East–West (E–W) component, and  $114.5 \text{ cm/s}^2$  for the vertical component. Acceleration recordings, encompassing three components and obtained from the provided site address, can be observed in Fig. 4.

Furthermore, Fig. 5 presents a comparative assessment of the response spectra in the East–West and North–South directions, contrasting them with the specifications outlined in Eurocode 8 [23].

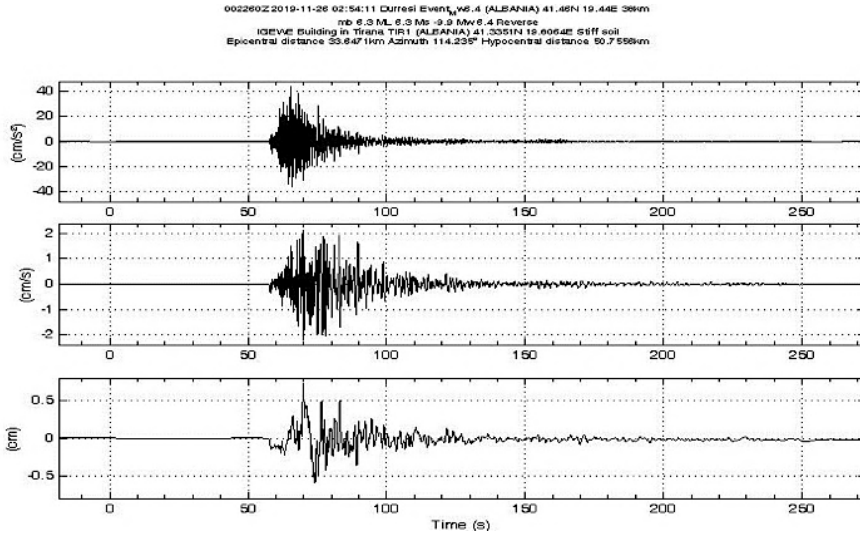
It's worth noting that, despite the earthquake's response spectra registering relatively lower values compared to the EC-8 design spectra, the observed villages still experienced significant structural failures and asset losses. Moreover, the spectral accelerations derived from the recorded data, as depicted in Fig. 5, consistently exhibit values 1.5 - 2.0 times greater than the spectral periods ranging from 0.2 - 0.8 seconds, as specified by the building code. This observation is noteworthy, given that the fundamental periods of many buildings in the affected areas typically fall within this range.



a) November 26, 2019 Earthquake North-South component



b) November 26, 2019 Earthquake East-West component



c) November 26, 2019 Earthquake Vertical component

Fig. 4. Time histories of acceleration in Tirana (TIR1 Station, [https://www.geo.edu.al/tirana\\_record/](https://www.geo.edu.al/tirana_record/))

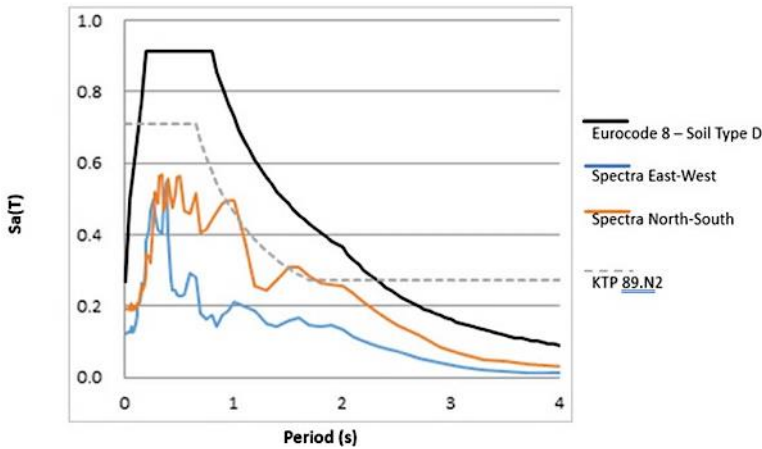












Fig. 5. Comparison of response spectrum with design spectra (EC-8) [23-24]

### 3. Identified Collapse Mechanisms in Pre-Modern URM Buildings and Solution Methods

In the significant urban regions of Albania [25], there were approximately 44,500 dwellings, including adobe, masonry, and RC structures. Many of the masonry buildings in the affected regions were of low to moderate height and were constructed in various time periods. These structures were primarily composed of adobe, stone, and brick-briquette masonry, with mortar in the walls containing cement. The documented failures in masonry structures can be classified into four primary types: entire failure, damage on corners, in-plane and out-of-plane failures. The following section provides a detailed account of these structural deficiencies and failures. The amounts of damage sustained by these dwellings

because of the earthquake on November 26, 2019, are presented in Table 2, adopted from EMS-98 [26]. Upon examining this table and figure, it becomes evident that the masonry buildings experienced severe damage due to the earthquake in 2019.

Table 2. Classification of damage in masonry structures in accordance with EMS-98 [26]

Classification of Damage to Masonry Buildings				
Grade	Damage Level	Schematic	Sample	Description
1	Slight			No structural damage, slight non-structural damage
2	Moderate			Slight structural damage, moderate non-structural damage
3	Heavy			Substantial to heavy damage, moderate structural damage, heavy non-structural damage
4	Very Heavy			Heavy structural damage, very heavy non-structural damage
5	Destruction			Very heavy structural damage, total or near total collapse

The criteria for categorizing post-earthquake building damage inventory and usability involve classifying buildings into five damage degrees. The initial two levels, DS1 (Grade 1) and DS2 (Grade 2), designate buildings that are immediately usable after the earthquake and do not require repair. These structures exhibit minor non-structural damage and extremely isolated and negligible structural damage. The subsequent levels, DS3 (Grade 3) and DS4 (Grade 4), categorize buildings as temporarily unusable. Such structures display extensive non-structural damage and significant structural damage yet have a repairable structural system. The final level, DS5 (Grade 5), classifies buildings as unusable. These structures are either destroyed or have experienced partial or complete collapse of the structural system. The regulations and recommendations regarding the investigation process also provide a detailed damage description for each damage degree, facilitating a thorough examination of the building.

A post-earthquake damage assessment was conducted over 44,000 buildings (Table 3) using a methodology outlined in reference [26]. This approach was designed to identify damage levels and collapse mechanisms in various architectural elements of the investigated structures, as outlined in Table 3. Approximately 90% of the examined buildings were deemed suitable for immediate occupancy, while the remaining portion was classified as unsuitable for occupancy [27].

**Table 3. Number of buildings investigated by Construction Institute and corresponding damage states [27]**

City	DS0	DS1	DS2	DS3	DS4	DS5	TOTAL
DURRES	22,605	2,761	2,384	1,735	1,855	626	31,966
Durres	13,737	1,801	1,210	804	582	205	18,339
Kruje	1,672	529	582	454	690	137	4,064
Shijak	7,196	431	592	477	583	284	9,563
LEZHE	494	364	421	326	402	43	2,050
Kurbin	343	244	294	196	215	28	1,320
Lezhe	150	110	112	126	166	9	673
Mirdite	1	10	15	4	21	6	57
TIRANE	5,651	1,560	1,258	737	974	386	10,566
Kamez	138	233	163	46	65	18	663
Kavaje	18	89	137	126	108	12	490
Tirane	207	528	481	348	458	60	2,082
Vore	5,288	710	477	217	343	296	7,331
TOTAL	28,750	4,685	4,063	2,798	3,231	1,055	44,582

**3.1 Entire or Partial Destruction**

This category of destruction occurs once the structural integrity of a building is compromised by the impact of out-of-plane mechanisms. In rural areas of Albania, especially in the countryside, dwellings frequently feature roofing systems constructed from locally sourced materials. Many of these masonry buildings employ timber logs for their roofing and flooring systems. Over time, these structures, which are typically old and have been exposed to various environmental conditions, experience a decline in the strength of their walls.

The collapse of these buildings can be attributed to several factors, one of which is the weight of the heavy earthen roofs. To keep the structure away from rain and snow, additional layers of soil are frequently added to the roof. Consequently, the thickness and mass of the earthen roofs gradually increase, resulting in a higher load borne by the building during an earthquake.





Fig. 6. Collapse of masonry buildings

The structural walls and timber logs are unable to withstand this heightened horizontal load, causing the walls to shift out-of-plane and leading to a complete collapse. Fig. 6 visually illustrates the observed damage of this particular type across different regions. To reduce the risk of total collapse, it is crucial to refrain from using adobe buildings and earthen roofs. Instead, consider implementing lighter roofing systems that incorporate horizontal and vertical bond beams during construction. This approach helps distribute the loads more effectively and enhances the building's seismic resilience.

### 3.2 Damages on Corners

Effective wall connections are essential for preventing both widespread and localized damage in masonry structures. Unfortunately, this aspect is often overlooked, with traditional connections persisting in wall construction. It is of paramount importance to give special consideration to these connections [28].

One common consequence of inadequate connections between structural walls is the occurrence of corner damages. These damages commonly occur at connections between walls, primarily due to the lack of strong links between them. Problems such as the utilization of low-quality materials, inferior workmanship, and insufficient provision of bond beams have contributed to the failure of adobe and stone masonry residences. Damage on corners was a prevalent issue observed in buildings within the earthquake affected areas.



Fig. 7. Observed corner damages



In numerous cases, inadequate wooden beams and improper ties were noted at the junctions of the affected buildings. The structural failures were significantly influenced by the weak bonds between the walls, compounded by the lack of horizontal or vertical bonding ties. Fig. 7 depicts a visual representation of the corner damage observed in masonry dwellings during the earthquake in Albania.

To mitigate corner failures, it is recommended to avoid the use of adobe or stone rubble in the construction of structural walls. Instead, hewn stone or brick materials should be employed, accompanied by the incorporation of reinforced concrete (RC) bond beams in both orthogonal directions. Adhering to modern seismic guidelines, it is crucial to maintain uniform thickness for these beams and walls, especially at the structure's edges. Fig. 8 illustrates the application of bond beams in masonry constructions as a preventive measure against corner damages.

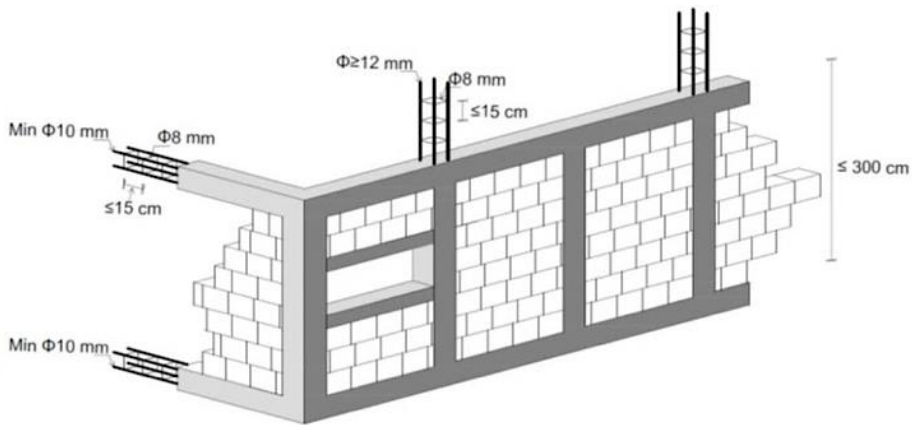


Fig. 8. Detailed design of horizontal and Vertical tie beams in load-bearing walls [modified from source 29]

For these beams, it is imperative that the concrete used possesses a minimum compressive strength of 20 MPa, along with the inclusion of  $\emptyset 8$  stirrups. The spacing between these stirrups should not exceed 15 cm, and a longitudinal bar must be included. Additionally, for the creation of a sturdy diaphragm, an RC flat plate with a minimum thickness of 10 cm should be constructed. In accordance with Eurocode-8 [23] standards, the linkage between slabs and walls should be established with steel connections or RC ring girders. Flat RC beams must be furnished with longitudinal rebars, with a cross-sectional area not less than  $2 \text{ cm}^2$ .

On the other hand, the utilization of the confined system is recommended for newly constructed masonry structures in Eurocode 8, ensuring the integrity of the building. However, applying this technique to existing buildings poses challenges and comes with high costs.

### 3.3 Out-of-Plane Damages

Masonry walls exhibit notably better structural performance within the structure's plane than in the perpendicular, out-of-plane behaviour, due to their inherent in-plane rigidity. These walls exhibit flexibility when subjected to forces perpendicular to the earthquake motion. Consequently, shear forces become influential within the plane of the wall, leading to in-plane mechanisms. Additionally, a flexural mechanism emerges in the weaker direction, giving rise to out-of-plane mechanisms.

This situation often results in out-of-plane mechanisms, which are considered undesirable due to their brittle behaviour when compared to in-plane mechanisms. Various factors, including insufficient connections between neighbouring walls, weak wall-to-floor connections, unsupported wall lengths, and inadequate vertical and horizontal bond beams, can contribute to the development of out-of-plane mechanisms. These mechanisms are characterized by their inability to resist tensile shear forces on the wall face.

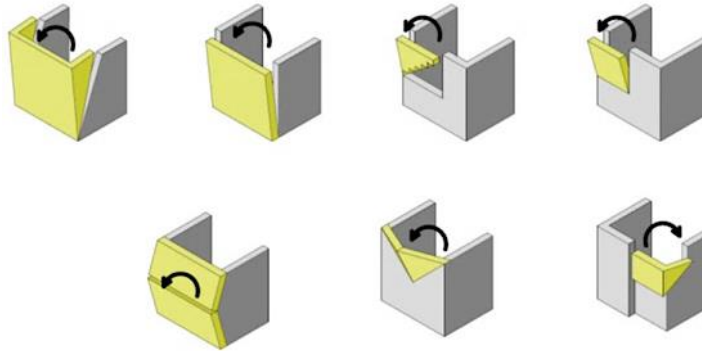


Fig. 9. Various out-of-plane mechanisms

A significant contributor to out-of-plane mechanisms is the positioning of timber logs that bear the load of the building's floors in a single direction. This arrangement results in the transfer of earthquake loads from perpendicular walls to the timber logs, making walls without support from these logs susceptible to out-of-plane overturning. Fig. 9 schematically outlines various out-of-plane mechanisms, while Fig. 10 illustrates observed out-of-plane mechanisms in unreinforced masonry (URM) buildings across different villages following the November 26, 2019, earthquake in Albania.

To prevent these mechanisms and ensure proper wall connection, it is crucial to establish a rigid diaphragm, particularly when structural walls lack reinforced concrete bond beams. Otherwise, partial or total failure mechanisms can occur.

To mitigate the occurrence of this out-of-plane mechanism, several measures can be taken. Firstly, it is crucial to limit the unsupported length of a load-bearing wall. Additionally, incorporate reinforced concrete horizontal and vertical bond beams into the construction, as illustrated in Fig. 11. Moreover, it is vital to ensure the presence of bearing walls in both the x- and y-directions, as recommended in reference [23].



Fig. 10. Observed out-of-plane collapses of walls

Specifically, vertical bonding girders should be positioned at the edges of the building, extending the full height of the storey. Moreover, these vertical beams should be spaced along the wall at intervals of approximately 4 meters [23, 30-31]. It's advisable to avoid the use of tall and lengthy unsupported walls.

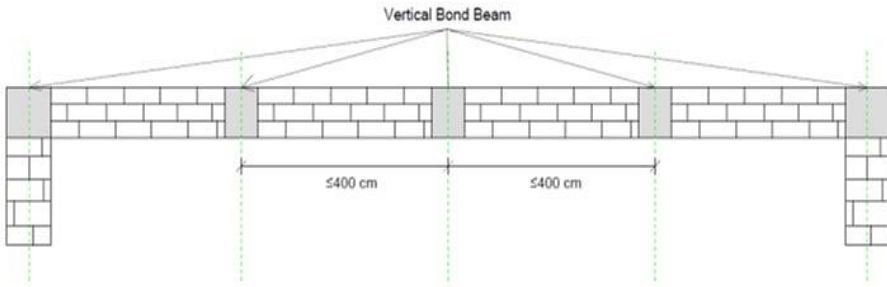


Fig. 11. Management of vertical bonding beams within the layout. Adapted from [30]

Fig. 12 provide visual examples illustrating the presentation of vertical bonding girders. Detailed designs for flat bonding girders at the intersection wall (a) and the angle wall (b) are also showcased. These measures are designed to improve the seismic resilience of the structure and decrease the risk of out-of-plane mechanisms.

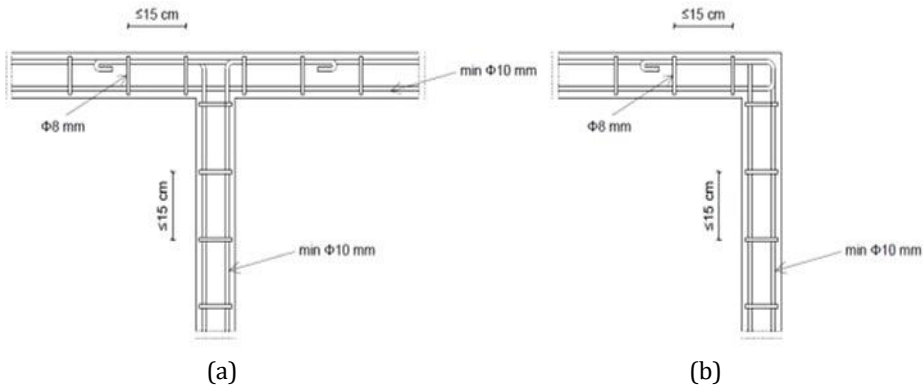


Fig. 12. The design details for horizontal bonding girders at a joint (a) and a junction (b) are outlined. Adapted from [30]

### 3.4 In-Plane Mechanisms

In-plane mechanisms can develop from various forms of structural failures, encompassing sliding, tensile, flexural-bending, crushing, and shear. It's important to note that these different failure modes can sometimes occur concurrently. Additionally, an increase in vertical load on the wall can lead to the development of cracks. In an in-plane mechanism, lateral seismic forces cause shear forces to act within the structure's plane. Fig. 13 schematically illustrates the distribution of in-plane loading, depicting a scenario where vertical loading is the sole influencing factor.

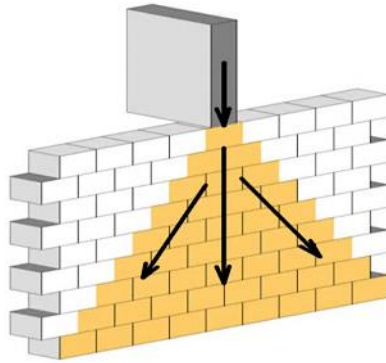


Fig. 13. Illustration of the distribution of in-plane loading. Adapted from [32]

In-plane loading can give rise to different types of damage, including flexural and shear cracks, or a combination of both. In Fig. 14a, sliding damage is portrayed, characterized by the gradual development of lateral cracks along the bed-joints of the masonry wall. This process divides the wall in two segments that move alongside the fracture plane. The formation of tensile cracks along an oblique of the bed-joints gives rise to diagonal shear cracks, ultimately dividing the wall in two segments. If shear cracks propagate by the in-plane direction of the wall, it becomes unstable, resulting in a loss of load-bearing capacity. Fig. 14b schematically illustrates this failure.

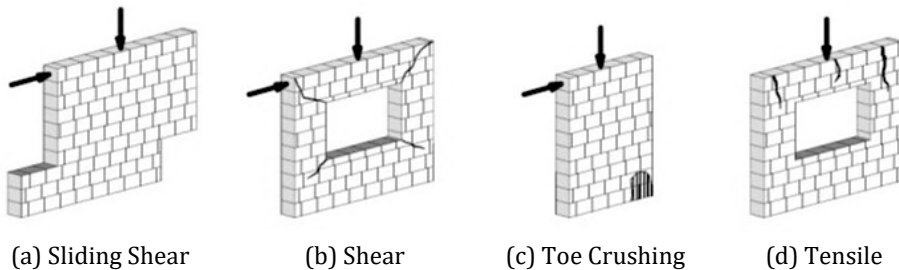


Fig. 14. Common in-plane failing modes observed on walls due to the combination of earthquake and imposed loading. Adapted from [33]

Fig. 14c showcases toe-crushing, a type of damage characterized by perpendicular compression and lateral tensile cracks concentrated at the base or "toe" of the wall segment. Lastly, Fig. 14d presents splitting damage, which results from in-plane vertical loading. When the tensile stress induced by earthquake forces is greater than the tensile strength of the wall, vertical cracks appear along the elevation of the wall.

The prevalence of the in-plane mechanism involving sliding shear in masonry buildings can be attributed to the inadequate shear strength of the masonry walls and the absence of appropriate reinforced concrete (RC) bond beams. Fig. 15 visually presents examples of in-plane failures observed in masonry dwellings across various villages. This type of failure underscores the importance of reinforcing masonry structures to enhance their resilience during seismic events.



Fig. 15. Shear failure

The existence of bond beams is essential for establishing structural integrity, but numerous masonry structures in the earthquake-affected villages lacked adequate and suitable bonding girders to enhance the complete horizontal shear capacity of their walls. Moreover, these structures featured sizable openings, which led to a reduction in wall stiffness and an amplification of shear effects. To mitigate this form of damage, it is advisable to incorporate reinforced concrete (RC) bond beams and decrease the size of openings in the load-bearing walls. Fig. 16 visually depicts this type of damage, emphasizing the significance of addressing these structural deficiencies to enhance the seismic resilience of masonry buildings.



Fig. 16. Shear effect in masonry buildings

Crushing failure represents another type of in-plane failure, manifesting when the vertical part of earthquake motion is greater than the compressive strength of the load-bearing wall. Initially, vertical cracks propagate across the vertical transverse segment of the wall, followed by splitting along the longitudinal partition. Fig. 17 visually demonstrates the total loss of internal structural integrity in a masonry wall caused by crushing damage resulting from the dividing crash of the masonry segment.



Fig. 17. Crushing failure of the walls

This kind of damage is frequently witnessed in adobe and multi-leaf debris stone wall segments, mainly because of the absence of appropriate flat bonding planks. In other words, insufficient interlocking between connecting bearing walls at corners leads to the occurrence of this type of damage. To prevent this type of failure, it is essential to incorporate proper horizontal bond beams, which can enhance the seismic resilience of these structures.

#### 4. Recommendations for Repairing and Retrofitting Masonry Structures

URM buildings that are susceptible to complete collapse or have been identified as having poor earthquake resistance ought to be dismantled. Instead, new structures should be constructed in adherence to contemporary engineering standards and prevailing seismic regulations.

Extensive research has been conducted to explore ways of enhancing the strength and durability of URM structures. The primary objective of all retrofitting methods is to improve their ability to resist loads or extend the time it takes for them to collapse when subjected to unexpectedly high external forces. Retrofitting masonry structures involves three key concepts: i) mitigating external forces; ii) upgrading existing buildings; and iii) enhancing integrity. The initial two concepts have been succinctly covered and demonstrated in a handful of research documents [34-35], while the third concept has received limited attention. This section will delve into a detailed presentation of some of the commonly encountered concepts and their practical applications.

##### 4.1 Retrofitting Masonry Buildings

The primary objective of all retrofitting methods is to bolster the horizontal load bearing capacity of the walls. On the other hand, an additional contribution can be achieved by reducing the weight of the roof through the installation of a lighter roofing material, instead of an earthen roof. One of the commonly employed methods for surface treatment is the application of shotcrete and ferrocement. It involves initially covering the structural wall with a steel mesh secured by cotters. Subsequently, high-strength cement mortar is sprayed onto the wall's surface, creating a uniform new layer. This method can be applied to one or both surfaces of the wall and provides increased performance to the wall.

Shotcrete is run by spraying it over a mesh of wire installed on the surface of the masonry wall, as depicted in Fig. 18. Typically, the overlay thickness falls within the range of 7 cm

to 15 cm [36-37]. Shear dowels are commonly required to facilitate shear transfer between the masonry-shotcrete interface. Prior to applying shotcrete, it is essential to remove wythes of bricks and fill the voids. Enhancements to the retrofitting of shotcrete can be achieved when the substrate surface becomes notably rough following the removal of loose or deteriorated portions [38].

While this approach is applicable to various masonry buildings to enhance the strength and stiffness, including those made of adobe, stone, and brick, it's worth noting that employing this method in older buildings may not always be cost-effective. On the other hand, this method has drawbacks, including time-consuming application and the alteration of original aesthetics. Consequently, it is deemed unsuitable for the retrofitting of masonry historical monumental structures. In such cases, demolishing the old structure and constructing a new one could be a more suitable approach.

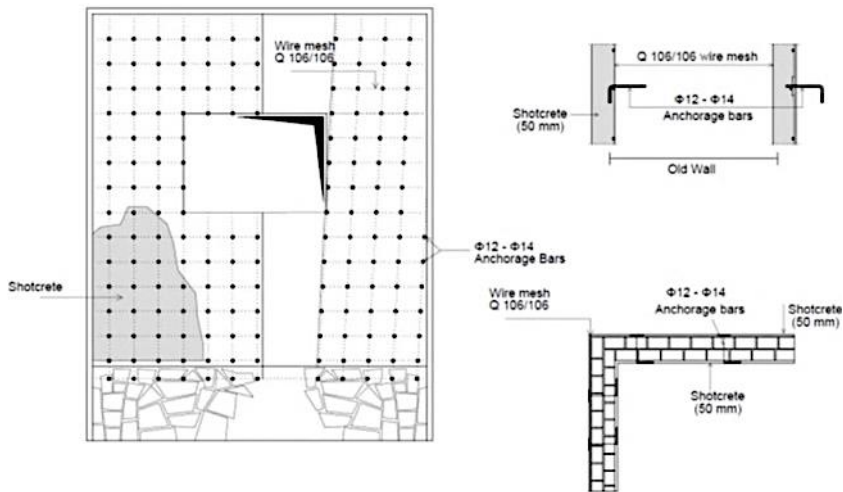


Fig. 18. Diagram depicting the application of shotcrete. Adapted from [39]

Fig. 19 illustrates another method called mesh reinforcement, which involves strengthening an URM wall segment by confining it with bonding struts and applying fibre-reinforced polymer (FRP) from one corner to the other. The initial application of FRP composite for retrofitting or reinforcing existing structures was in the realm of concrete. Subsequently, its usage has been expanded to include other types of structures such as masonry and timber. This extension has garnered important attention in research, with thorough studies deployed on its application across various structural materials [40].

FRP is a composite material that comprises high-strength fibres like carbon, glass, and aramid. When employed for reinforcing existing masonry structures, FRP demonstrates superior strength and ductility compared to traditional materials. This technique enhances the in-plane load-bearing capacity of the wall while preventing out-of-plane damage.

Retrofitting unreinforced masonry (URM) walls with FRP composites can result in a significant improvement in strength, typically ranging from 1.1 to 3 times [41, 42]. Research has shown that the resistance of masonry walls can be enhanced by 13-84% through an analysis of walls retrofitted with carbon fibre. The degree of improvement may vary depending on the specific structure undergoing retrofitting. In another study [43], FRP was observed to increase the shear resistance of masonry buildings by 3.3 times.

Although reinforcing masonry panels with FRP offers advantages such as minimal added mass, low disruption, and a relatively substantial enhancement in strength, this technique

has drawbacks, including its high cost, the need for advanced technical expertise, and alterations to the structure's appearance. The initial cost of FRP material is approximately 5 to 10 times higher than that of steel [44], posing a significant consideration in the selection of retrofitting approaches.

Nevertheless, it's important to acknowledge that attaining the smooth surface necessary for the use of FRP in masonry buildings constructed with rough stone can pose a challenge. As a result, strengthening with FRP may not be feasible for such structures. Additionally, due to the higher cost of FRP compared to concrete and steel, applying FRP to masonry buildings constructed using conventional techniques in rural areas may not be a cost-effective solution. In such cases, shotcrete application could be a more practical alternative.

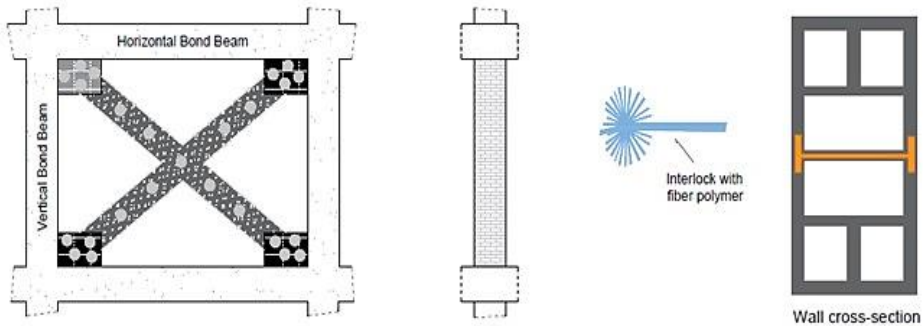


Fig. 19. Reinforcing URM segments using FRP polymer. Adapted from [39]

One effective method for enhancing structural integrity involves minimizing the size of openings or sealing off excess spaces, such as oversized spaces and entrances. Based on the modern guidelines (TEC-2018), it is recommended to restrict the width of openings within a wall plane to less than 3 meters. Furthermore, the proportion of the total length of open spaces to the length of unsupported wall within the wall plane should not surpass 40%. Additionally, in compliance with EC8, the ratio of wall length to the greater net height of adjacent spaces must adhere to specific minimum values (0.50 for stonemasonry and 0.40 for other brick categories).

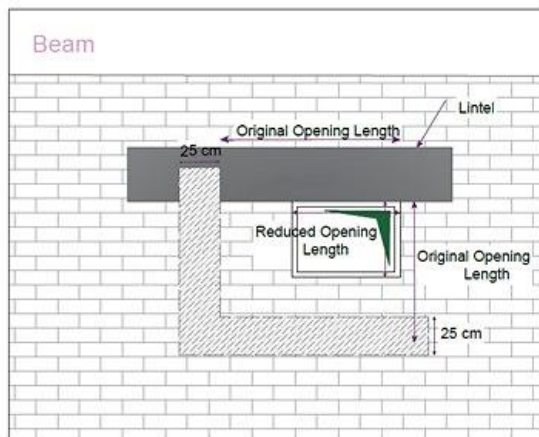
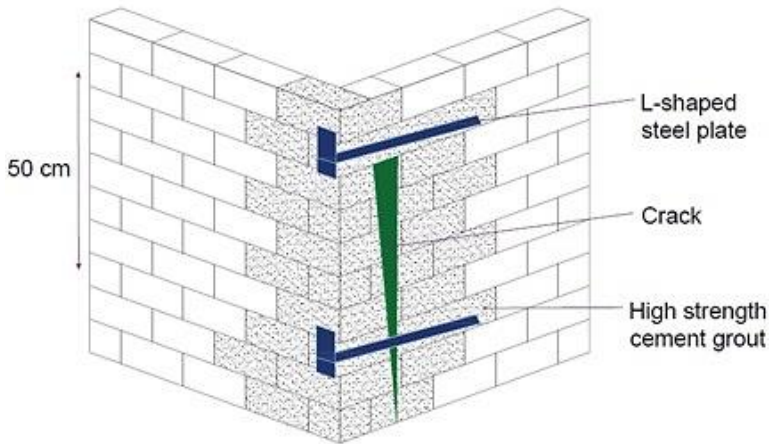


Fig. 20 Reduction of space in a wall segment. Adapted from [39, 45]

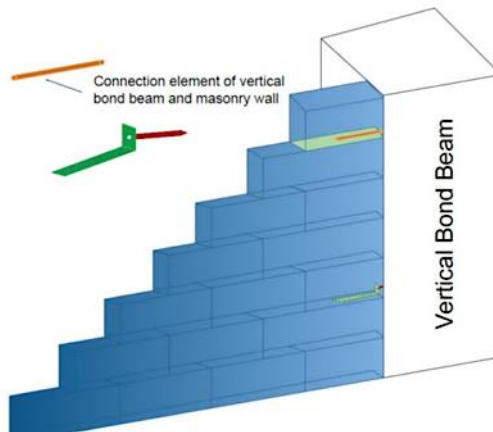


Among the various reinforcement techniques, this approach stands out as one of the most practical and applicable to whole masonry constructions. Its application improves the overall in-plane resistance of the load bearing wall, significantly contributing to structural performance during seismic events. Fig. 20 offers a schematic representation of this reinforcement approach.

Figs. 21a and 21b demonstrate strategies for strengthening the junctions of masonry blocks and establishing links between wall segments and vertical bonding joists, respectively. In the case of wall corners, connecting them with steel plates and anchoring them together is recommended. Subsequently, any pin holes in the walls should be sealed by prepared mortar shot. The method depicted in Fig. 21a is feasible and cost-effective, suitable for application in all masonry buildings to prevent corner damages. On the other hand, the approach shown in Fig. 21b necessitates the presence of a vertical bond beam for implementation.



(a)



(b)

Fig. 21. (a) Schematic depiction of reinforcing the corner link among walls, and (b) Strengthening the connection between a wall and a vertical bond beam [adopted from [39]]

A study on masonry structures confined with constructional columns and ring beams, as outlined in [46], suggests that such structures exhibit favourable performance during earthquakes. The study concludes that the mechanical performance, including ductility and strength, of the masonry panels is primarily upheld by the confining elements.

#### 4.2 Repairing Existing URM Buildings

Maintaining masonry buildings is of utmost importance to safeguard them against the impact of earthquakes. Consequently, even minor cracks should not be overlooked and must be promptly repaired. To tackle such maintenance, U-formed steel tools and mortar injections are utilized. Small cracks, typically those with a width smaller than 2 mm, are reinforced with the steel components and then filled with mortar.

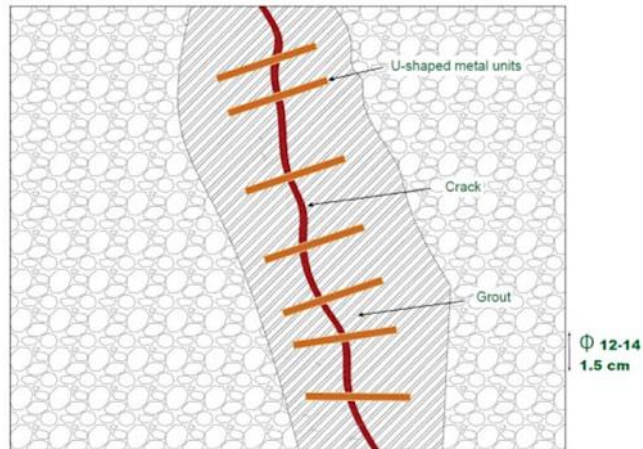


Fig. 22. Diagram depicting the repair of minor cracks. Adapted from [39, 45]

Fig. 22 provides both a schematic and a visual representation of the healing process. This repair method is applicable to all existing masonry buildings and can help prevent further deterioration, ensuring the longevity and stability of these structures.

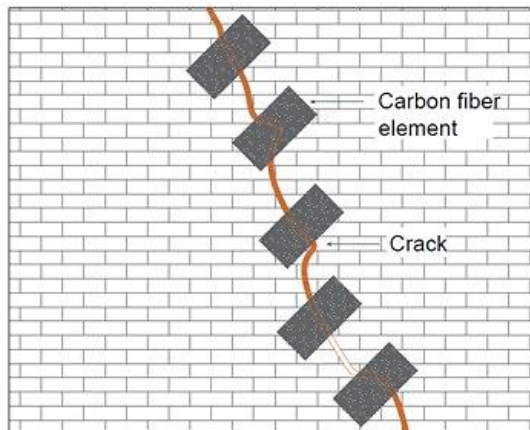


Fig. 23. Diagram depicting the repair of minor cracks. Adapted from [39, 45]

Another method for repairing masonry structures involves the use of Fiber Reinforced Polymer (FRP). FRP components are applied alongside the cracks, making this technique suitable for cracks with a width of less than 1 mm. As a result, this method effectively

prevents the further expansion of cracks. Fig. 23 offers a schematic representation of the application process. This repair technique is suitable for brick masonry structures. Nevertheless, this is crucial to highlight that the challenges of obtaining a smooth plane on rough stone may limit the applicability of this method to buildings constructed with such materials.

Apart from strengthening the superstructure, certain reinforcement methods can be applied to the soil and foundations. One approach involves lowering the groundwater level to a depth below the foundation by using drainage techniques. During the implementation of this approach, it is essential to take precautions to avoid differential settlements within the building.

Another way to reinforce the foundation system is by expanding the footing size and redirecting the structural loads to deeper, more stable layers using an appropriate system. Additionally, the load-bearing capability of the ground can be increased through techniques like jet grouting. However, it's important to note that this method of strengthening can be costly.

## **5. Conclusions and Recommendations**

The literature discusses the failure modes in URM structures during earthquakes, especially following destructive ones. This study highlights that URM structures, often built by unqualified individuals, exhibit poor earthquake response and are susceptible to destruction even in mid-size earthquakes. Therefore, this paper assesses the potential damage that could occur during a catastrophic earthquake and presents various strengthening options.

The Dures/Albania earthquake ( $M_w = 6.4$ ) resulted in significant damage patterns. To assess this damage, urban centers and their surrounding areas near the earthquake's epicenter were visited, and various building typologies were examined. Site visits revealed that the earthquake response of the affected structures fell below expectations, primarily because they were not built in accordance with engineering standards and modern seismic guidelines. Consequently, the anticipated structural behaviour was not accomplished, even when subjected to mid-sized tremors. The primary causes of these failures were identified, and recommendations to prevent life losses and mitigate assets losses are as follows:

The observed failures in the surveyed dwellings can be attributed to several factors. These include the inhesion of earthen roofs, which significantly contributed to the damage. Weak detailing of connections between walls, encompassing both wall-to-wall and wall-to-roof connections, further exacerbated the structural issues. Additionally, the absence or inadequacy of bonding struts within the load-bearing walls played a crucial role in the failures. Both out-of-plane and in-plane mechanisms were identified as failure modes, showcasing the structural vulnerabilities. Building on sloping land aggravated these issues, and foundation collapses were also observed as critical factors in the overall failures.

Here are some recommendations to avoid future damage:

- If replacing heavy roofs with lighter roofing systems is not possible, it is advisable to consider demolishing these structures. Subsequently, new houses should be constructed using advanced construction practices and adhering to seismic code specifications.
- In cases of localized corner damages, the recommended method involves fixing separations in the corner walls and reinforcing them. However, if the damage is extensive and compromises the structural integrity, it is advisable to reconstruct the walls.

- To mitigate the damage induced by out-of-plane actions to a masonry wall, several measures could be implemented. These include applying FRP polymer from one corner to another, reducing the size of large openings, and reinforcing corners with iron anchor coats. Moreover, an additional protective measure for the masonry wall involves enveloping it with a steel mesh and fastening it securely with cotters prior to the application of shotcrete.
- To prevent in-plane failures, it's vital to reinforce structural walls along the wall plane. The recommended strategies for addressing out-of-plane mechanisms are equally applicable to in-plane mechanisms.
- To prevent damages related to loose soil, it is imperative to construct buildings on level ground and establish robust footings. Effectively addressing these concerns involves lowering the groundwater level below the foundation and expanding the foundation width.
- To protect buildings from potential earthquakes, it is crucial to prevent the formation of microcracks, and any existing micro-cracks should be carefully fixed using U-formed steel apparatus and cement injections.
- A considerable portion of masonry buildings predates the 1990s, constructed in accordance with the building code requirements of that era. This has led to the development of diverse construction practices and significant technical deficiencies in these buildings. While masonry structures demonstrate robustness under vertical loads, they exhibit fragility and are vulnerable to severe damage when subjected to horizontal loads, such as those encountered during earthquakes.

This paper has revealed that URM structures situated in active earthquake regions in Albania exhibit notably poor seismic performance. Even a moderate earthquake resulted in considerable structural damage. To avert potential harm in rural areas, it is imperative to construct earthquake-resistant dwellings in accordance with contemporary seismic codes and construction practices, while also retrofitting existing undamaged structures.

## References

- [1] Bilgin H, Hysenlliu M. Comparison of near and far-fault ground motion effects on low and mid-rise masonry buildings. *Journal of Building Engineering*. 2020; 30: 101248. <https://doi.org/10.1016/j.jobe.2020.101248>
- [2] Bilgin H. Effects of near-fault and far-fault ground motions on nonlinear dynamic response and seismic damage of masonry structures. *Engineering Structures*. 2024;300:117200. ISSN 0141-0296. <https://doi.org/10.1016/j.engstruct.2023.117200>
- [3] Leti M, Bilgin H. Predicting the Seismic Performance of Typical R/C Residential Buildings. In: Ademović N, Mujčić E, Mulić M, Kevrić J, Akšamija Z (eds) *Advanced Technologies, Systems, and Applications VII*. IAT 2022. Lecture Notes in Networks and Systems. Springer, Cham. [https://doi.org/10.1007/978-3-031-17697-5\\_2](https://doi.org/10.1007/978-3-031-17697-5_2)
- [4] Leti M, Bilgin H. Damage potential of near and far-fault ground motions on seismic response of RC buildings designed according to old practices. *Research on Engineering Structures and Materials*. 2022;8(2). <http://dx.doi.org/10.17515/resm2022.392ea0123>
- [5] Bidaj A, Bilgin H, Hysenlliu M, Premti I, Ormeni R. Performance of URM structures under earthquake shakings: Validation using a template building structure by the 2019 Albanian earthquakes. *Engineering Structures and Materials*. 2022. <http://jresm.org/archive/resm2022.440ea0531>
- [6] Shkodrani N, Bilgin H, Hysenlliu M. Influence of interventions on the seismic performance of URM buildings designed according to pre-modern codes. *Journal of*

- Research on Engineering Structures and Materials. 2021;7(2):315-330.  
<https://doi.org/10.17515/resm2020.197ea0331>
- [7] Freddi F, Novelli V, Gentile R, et al. Observations from the 26th November 2019 Albania earthquake: the earthquake engineering field investigation team (EEFIT) mission. *Bulletin of Earthquake Engineering*. 2021; 19: 2013-2044.  
<https://doi.org/10.1007/s10518-021-01062-8>
- [8] Ingham J, Griffith M. Performance of unreinforced masonry buildings during the 2010 Darfield (Christchurch, NZ) earthquake. *Australian Journal of Structural Engineering*. 2010;11(3):207-224.
- [9] Kaplan H, Bilgin H, Yilmaz S, Binici H, Oztas A. Structural Damages of L'Aquila Earthquake. *Hazards Earth Syst Sci*. 2010; 10: 499-507.  
<https://doi.org/10.5194/nhess-10-499-2010>
- [10] Astroza M, Moroni O, Brzev S, Tanner J. Seismic performance of engineered masonry buildings in the 2010 Maule earthquake. *Earthquake Spectra*. 2012;28:385-406.
- [11] Basset-Salom L, Guardiola-Villora A. Seismic performance of masonry residential buildings in Lorca's city centre, after the 11<sup>th</sup> May 2011 earthquake. *Bulletin of Earthquake Engineering*. 2014;12(5):2027-2048.
- [12] Saha R, Debnath R, Dash S, Halder S. Engineering reconnaissance following the magnitude 5.7 Tripura earthquake on January 3, 2017. *Journal of Performance of Constructed Facilities*. 2020;34(4):04020052.
- [13] Chen H, Xie Q, Dai B, Zhang H. Seismic damage to structures in the Ms=6.5 Ludian earthquake. *Earthquake Engineering and Engineering Vibration*. 2016;15(1):173-186.
- [14] Sorrentino L, Cattari S, Porto F, Magenes G, Penna A. Seismic behaviour of ordinary masonry buildings during the 2016 central Italy earthquakes. *Bulletin of Earthquake Engineering*. 2019;17(10):5583-5607.
- [15] Gautam D, Chaulagain H. Structural performance and associated lessons to be learned from world earthquakes in Nepal after 25 April 2015 (MW 7.8) Gorkha earthquake. *Engineering Failure Analysis*. 2016; 68: 222-243.
- [16] Shakya M, Kawan CK. Reconnaissance based damage survey of buildings in Kathmandu valley: an aftermath of 7.8 Mw, 25 April 2015 Gorkha (Nepal) earthquake. *Engineering Failure Analysis*. 2016; 59: 161-184.
- [17] Aras F, Düzci E. Seismic performance of traditional stone masonry dwellings under Çanakkale seismic sequences. *Journal of Performance of Constructed Facilities*. 2018;32(4):04018029.
- [18] Vlachakis G, Vlachaki E, Lourenço PB. Learning from failure: damage and failure of masonry structures, after the 2017 Lesvos earthquake (Greece). *Engineering Failure Analysis*. 2020;104803.
- [19] Bayraktar A, Altunışık AC, Muvafık M. Field investigation of the performance of masonry buildings during the October 23 and November 9, 2011, van earthquakes in Turkey. *Journal of Performance of Constructed Facilities*. 2016;30(2):04014209.
- [20] Atmaca B, Demir S, Günaydın M, et al. Lessons learned from the past earthquakes on building performance in Turkey. *Journal of Structural Engineering & Applied Mechanics*. 2020;3(2):61-84.
- [21] Valente M. Seismic behavior and damage assessment of two historical fortified masonry palaces with corner towers. *Engineering Failure Analysis*. 2022; 134: 106003.
- [22] Isık E, Avcil F, Büyüksaraç A, et al. Structural damages in masonry buildings in Adıyaman during the Kahramanmaraş (Türkiye) earthquakes (Mw 7.7 and Mw 7.6) on 06 February 2023. *Engineering Failure Analysis*. 2023; 151: 107405.
- [23] Eurocode 8: design of structures for earthquake resistance - Part 1: general rules, seismic actions and rules for buildings.
- [24] KTP-N.2-89, Technical aseismic regulations. Publication of Academy of Sciences and Ministry of Constructions (in Albanian). Tirana, Albania (1989).

- [25] Bilgin H, Shkodrani N, Hysenlliu M, Ozmen HB, Işık E, Harirchain E. Damage and performance evaluation of masonry buildings constructed in 1970s during the 2019 Albania earthquakes. *Engineering Failure Analysis*. 2022; 131: 105824. <https://doi.org/10.1016/j.engfailanal.2021.105824>
- [26] Grünthal G (Ed.). European Macroseismic Scale 1998 (EMS-98), European Seismological Commission, subcommission on Engineering Seismology. Conseil de l'Europe, Cahiers du Centre Europeen de Geodynamique et de Seismologie. 15, Luxembourg, 1998-1999.
- [27] Hysenlliu M. Vulnerability Assessment of Current Masonry Building Stock in Albania, Ph.D. thesis, EPOKA University, Department of Civil Engineering.
- [28] Jasinski R, Galman I. Testing joints between walls made of AAC masonry units. *Buildings*. 2020;10(4):69.
- [29] Ural A, Doğangün A, Sezen H, Angın Z. Seismic performance of masonry buildings during the 2007 Bala, Turkey earthquakes. *Natural Hazards*. 2012;60(3):1013–1026.
- [30] Turkish Seismic Code, 2007, Ankara, Turkey (in Turkish).
- [31] Turkey Building Earthquake Code 2018, Ankara, Turkey (in Turkish).
- [32] McKenzie WM. *Design of Structural Masonry*, Palgrave, New York, 2001.
- [33] Tomazevic M. *Earthquake-resistant Design of Masonry Buildings*, vol. 1, World Scientific, 1999.
- [34] Chuang SW, Zhuge Y. Seismic retrofitting of unreinforced masonry buildings-a literature review. *Australian Journal of Structural Engineering*. 2005;6(1):25-36. <https://dx.doi.org/10.1080/13287982.2005.11464942>
- [35] Bhattacharya S, Nayak S, Dutta SC. A critical review of retrofitting methods for unreinforced masonry structures. *International Journal of Disaster Risk Reduction*. 2014; 7:51-67. <https://dx.doi.org/10.1016/j.ijdrr.2013.12.004>
- [36] Abrams DP. New perspectives on seismic rehabilitation. *Proceedings of the Asia-Pacific workshop on Seismic Design and Retrofit of Structures*, 1998 Taipei, Taiwan.
- [37] Karantoni F, Fardis M. Effectiveness of seismic strengthening techniques for masonry buildings.
- [38] Augenti N, Nanni A, Parisi F. Construction failures and innovative retrofitting. *Buildings*. 2013;3(1):100-121. <https://dx.doi.org/10.3390/buildings3010100>
- [39] Celep Z. *Introduction to Earthquake Engineering and Earthquake Resistivity Design*, Beta Press and Distribution Corporation, Istanbul, 2018 (in Turkish).
- [40] Teng JG, Chen JF, Smith ST, Lam L. Behaviour and strength of FRP-strengthened RC structures: A state of the art review. *Proc. Inst. Civ. Eng., Struct. Build*. 2003;156(1):51-62. <https://dx.doi.org/10.1680/stbu.2003.156.1.51>
- [41] Alcaino P, Santa-Maria H. Experimental response of externally retrofitted masonry walls subjected to shear loading. *Journal of Composites for Construction*. 2008;12(5):489-498. [https://dx.doi.org/10.1061/\(ASCE\)1090-0268\(2008\)12:5\(489\)](https://dx.doi.org/10.1061/(ASCE)1090-0268(2008)12:5(489))
- [42] ElGawady MA, Lestuzzi P, Badoux M. A review of retrofitting of unreinforced masonry walls using composites. *Proceedings of the 4th International Conference on Advanced Composite Materials in Bridges and Structures*, 2004 Calgary, Alberta.
- [43] Mahmood H, Ingham J. Diagonal compression testing of FRP-retrofitted unreinforced clay brick masonry wallettes. *Journal of Composites for Construction*. 2011;15(5):810-820. [https://dx.doi.org/10.1061/\(ASCE\)CC.1943-5614.0000209](https://dx.doi.org/10.1061/(ASCE)CC.1943-5614.0000209)
- [44] "Does FRP have an economic future?", *Proceedings of the 4th conference on advanced composite materials in bridges and structures*, 2004 Calgary, Alberta.
- [45] ACI (American Concrete Institute). *Specification for Masonry Structures*, vol. 530, ACI, Farmington Hills, MI, 1998; 1–98. ASCE 6-98/TMS 602-98.
- [46] Okail H, Abdelrahman A, Abdelkhalik A, Metwaly M. Experimental and analytical investigation of the lateral load response of confined masonry walls. *HBRC Journal*. 2016;12:33-46. <https://dx.doi.org/10.1016/j.hbrcej.2014.09.004>

Blank Page

## Effects of seawater and acidic environment on mechanical properties of iron powder-loaded glass-epoxy composite laminates: Experimental and analytical investigation

Youcef Gheid<sup>\*1,a</sup>, Abdennacer Chemami<sup>1,b</sup>, Djamel Gaagaia<sup>2,c</sup>, Hamza Aouaichia<sup>3,d</sup>

<sup>1</sup>Industrial Mechanics Laboratory, Dept. of Mechanical Eng., Badji Mokhtar-Annaba University, Algeria

<sup>2</sup>Dept. of Mechanical Eng., Badji Mokhtar-Annaba University, Algeria

<sup>3</sup>Research Center in Industrial Technologies CRTI, Algeria

### Article Info

### Abstract

#### Article history:

Received 07 Dec 2023

Accepted 24 Jan 2024

#### Keywords:

Composite laminate;

Iron powder;

Flexure strength;

Hydrochloric acid;

Seawater;

Immersion

This study assesses the impact of seawater and acidity on a glass epoxy composite filled with pure iron powder. Plates with varying iron content (15%, 20%, and 25%) were created using contact molding, with 30% glass fiber content. After dividing the plates into samples, a three-point bending examination was conducted following ISO14125 standards. The samples were immersed in saltwater (Group A), an acidic solution (Group B), or kept dry for comparison (Group C). Each subgroup had 15 specimens (5 for each iron %), immersed for over 60 days before undergoing bending tests. Results showed a significant decline in flexural strength, with a maximum reduction of 29.7% in Group A and 37.9% in Group B, while Young's modulus decreased up to 34.8% in Group A and 45.6% in Group B. The two-way ANOVA approach confirmed these findings, and microscopic examinations and FTIR analysis after immersion elucidated physical alterations and chemical reactions. Despite certain advantages, such as specific applications, the composite's limitations in corrosion resistance, durability, and production cost may restrict its relevance in various industrial and real-world applications. Consideration of these factors is essential before choosing this material for a specific project.

© 2024 MIM Research Group. All rights reserved.

## 1. Introduction

In recent years, the use of fiber-reinforced composite materials in engineering has grown significantly. This increase is due to advances in how these materials are made, making them more suitable for various technical uses [1]. Industries like aerospace and automotive are particularly interested in lightweight materials that are also strong, leading to a higher demand for composite materials [2].

One specific type of these materials, known as glass-epoxy composites, reinforced with various substances, including different metals, has become important in different industries because of its exceptional strength [3]. Researchers have studied how adding different metals, like iron powder, affects the strength of these materials [4-7].

Previous research has examined the impact of nanoparticles on the micro-mechanical and surface properties of poly (urea-formaldehyde) composite microcapsules [8]. Additionally, they have explored the thermo-mechanical behavior of epoxy composites, incorporating various fillers like E-glass fibers and iron oxide particles, as well as the mechanical

\*Corresponding author: [youcef.gheid@univ-annaba.dz](mailto:youcef.gheid@univ-annaba.dz)

<sup>a</sup> [orcid.org/0000-0002-8561-6757](https://orcid.org/0000-0002-8561-6757); <sup>b</sup> [orcid.org/0009-0005-5754-6324](https://orcid.org/0009-0005-5754-6324); <sup>c</sup> [orcid.org/0000-0002-4645-2884](https://orcid.org/0000-0002-4645-2884);

<sup>d</sup> [orcid.org/0000-0003-0272-5446](https://orcid.org/0000-0003-0272-5446)

DOI: <http://dx.doi.org/10.17515/resm2024.116me1207rs>

Res. Eng. Struct. Mat. Vol. 10 Iss. 3 (2024) 1109-1123



performance of glass/epoxy composites enriched with micro- and nano-sized aluminum particles [9, 10]. Other studies have delved into composite materials that include iron powder and mixed glass fiber-reinforced polymers, with the aim of comprehending their properties and performance. Besides, researchers have examined the use of waste iron filings to enhance glass fiber-reinforced epoxy (GFRE) composites, analyzing the influence of factors such as particle size, interface adhesion, and loading on particulate-polymer composites [11, 12].

Despite their strength, these composites face challenges when they are exposed to harsh conditions. Prolonged exposure to corrosive substances like acids or seawater can significantly weaken these materials, especially in terms of their flexural strength [13]. Epoxy resins are used to hold these materials together and protect them from harsh conditions like water and salt [14]. However, epoxy can absorb moisture over time, which can harm its physical properties and the components made with it [14]. Abdel-Magid et al. studied the effects of seawater and temperature on glass/epoxy and glass/polyurethane composites. After a year of immersion, glass/epoxy composites absorbed 2.5% of their weight in water at ambient temperature and 5% at 65°C. Tensile strength reduced by 0.8% at room temperature and 6% at 65°C, indicating accelerated water absorption and reduced strength at higher temperatures [15]. Silva et al. explored the degradation of GFRP laminates through 2500 hours of immersion in a saline solution. Tensile strength retention was 84% at 35°C, 70% at 50°C, and 61% at 65°C, revealing swelling and plasticization in the GFRP composites, leading to microcracking and fractures [16]. A study explores the enhanced mechanical resilience of SiO<sub>2</sub>-epoxy polymer nanocomposites in seawater, revealing minimal strength reduction compared to unmodified materials, with optimal performance achieved at a 3% SiO<sub>2</sub>-epoxy ratio over a six-month exposure period [17]. Other researchers evaluated the impact of corrosive conditions on epoxy nanocomposites with BN nanoplatelets, enhancing mechanical and tribological properties. And found that, despite the corrosive influence on mechanical performance, tribological behavior improves with exposure, acting as a lubricant and forming a protective layer [18].

Researchers have conducted numerous studies on the impact of water and seawater on GFRP composites, assessing factors like flexural strength, tensile strength, compressive strength, and elastic modulus [19, 20]. Bagherpour et al. examined the effects of concentrated HCl on aged fiber glass polyester composites. After 21 days of acid immersion at 35°C, a significant destructive impact was observed, as acid infiltrated the composite, forming cavities and cracks, and reducing mechanical properties [21]. Additionally, the flexure strength and modulus of elasticity in a glass fiber/epoxy composite decreased over time when exposed to hydrochloric acid (HCl) and sodium hydroxide (NaOH), resulting in mechanical degradation [22]. Similar degradation was observed in Kevlar/epoxy and carbon/epoxy laminates subjected to low-velocity impact tests following immersion in HCl and NaOH [23].

While previous research has contributed significantly to our understanding of how glass-epoxy composites behave in challenging conditions, there are still important questions that need to be investigated regarding the behavior of these laminates, specifically when they are loaded with iron powder in such conditions. This study aims to fill these knowledge gaps by examining how the amount of iron powder, along with environmental conditions, affects the flexural strength of glass-epoxy laminated composites. We will use statistical analysis (ANOVA) to evaluate their relative impacts and potential interactions. The inclusion of iron powder is of particular relevance, given its abundance in the Annaba region, situated in the eastern part of Algeria, due to the presence of the sedimentary iron complex. Beyond addressing material availability, this choice aligns with sustainable practices, emphasizing the repurposing of waste materials.

## 2. Materials and Methods

### 2.1. Specimen's Preparation

The laminated composite plates were prepared in the laboratory, using epoxy resin as matrix and reinforced with eight (08) plies of an E-glass fiber mat, which was kept constant at 30% of the total mass for each plate. Additionally, pure iron (99.998%) powder with grain sizes equal to or smaller than 32 $\mu$ m was incorporated as a filler material, with varying percentages of the filler (15%, 20%, and 25%). The laminates were produced by hand lay-up technique, with the resin of choice being a commercially available epoxy, selected based on its local market availability. Densities of the matrix and reinforcement are presented in Table 1. The iron powder was combined with resin and hardener and afterward introduced into a controlled environment equipped with a vacuum pump to facilitate the removal of entrapped air bubbles. According to the epoxy manufacturer's instructions, the polymerization process can take up to seven (07) days.

Table 1. Material's densities

Material	Density (g/cm <sup>3</sup> )
Mat fiberglass E	2.7
Epoxy resin	1.1

The bending specimens illustrated in Figure 1 were dimensioned in accordance with the standards stated in the ISO 14125 standard. An 1100 W CROWN cutting machine equipped with a 250mm diameter diamond disc and a lubrication system was utilized to cool the specimens and aid in the cutting process.

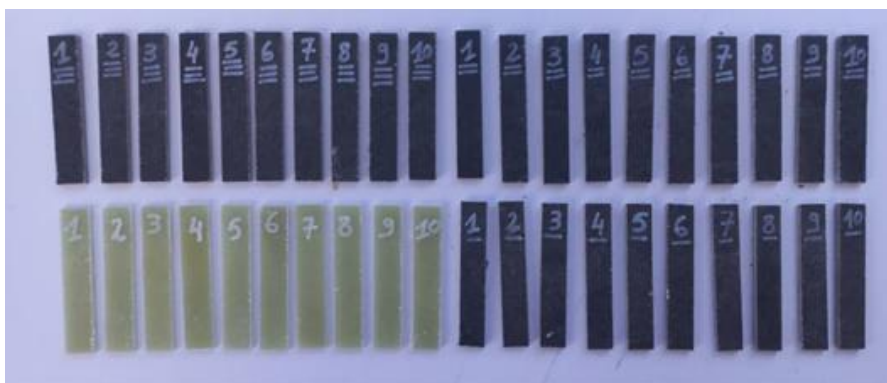


Fig. 1. Laminated specimens

### 2.2 Solution Preparation

Two discrete forms of media were generated for the purpose of conducting experiments. The initial medium was prepared by utilizing seawater obtained from a coastal area in the Annaba region. Following the collection process, the specimen underwent a rigorous sterilization procedure, subsequently undergoing meticulous drying within specialized ovens. The second medium was prepared as shown in Figure 2 by diluting pure hydrochloric acid (HCl) with distilled water until it reached a pH value of 2. Similar to the initial medium, this subsequent medium likewise underwent a process of sterilization and subsequent drying through the utilization of specialized ovens. These preparations will enable the submersion of the test specimens that have been prepared for our forthcoming tests.

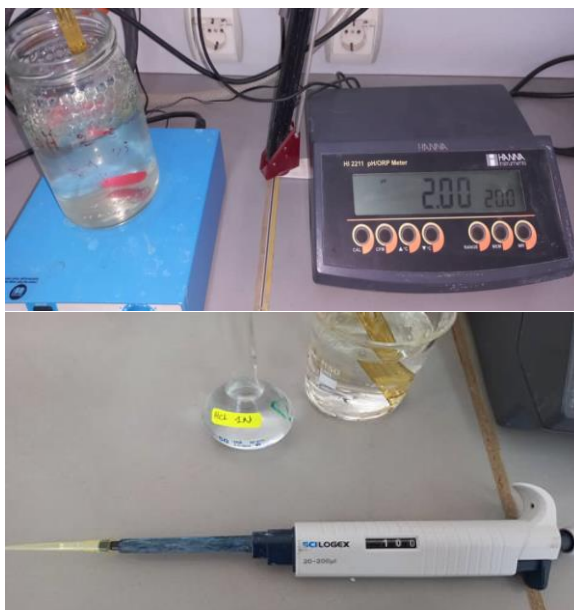


Fig. 2. Acidic solution preparation

### 3. Experimental Procedure

The specimens were partitioned into three distinct groups as demonstrated in Table 2, denoted Group A, Group B and Group C. Within Group A, three subgroups were exposed to seawater, whilst the three B subgroups were submitted to an acidic solution with a pH value of 2, while the remaining subgroups stay unsubmerged for comparison.

Table 2. Specimen’s grouping

Group	Subgroups	Iron content (W%)	Solution
A	A-1	15	Seawater
	A-2	20	Seawater
	A-3	25	Seawater
B	B-1	15	Acid
	B-2	20	Acid
	B-3	25	Acid
C	C-1	15	/
	C-2	20	/
	C-3	25	/

#### 3.1 Submersion’s Impact on Specimen Weight

The dry non immersed, and immersed specimens were weighed to measure  $W_0$ , submerged in the two different solutions for no less than 1440 hours, where the samples were removed to measure their individual weight as shown in Fig. 3,  $W_i$ , for each time interval, using an analytical balance with a resolution of 0.0001g resolution. The weight measurements are detailed in table 3, in which:

- **T0 (Time Zero):** Refers to the initial time when the specimens are submerged or subjected to the experimental conditions.
- **T1 to T6:** These time points represent specific intervals during the experiment, indicating when measurements or observations were taken. For instance, T1 might signify measurements taken after 10 days, T2 after 20 days, and so forth. Each subsequent time point (T3, T4, T5, and T6) would similarly denote additional intervals or milestones in the experiment, helping to track changes over time.



Fig. 3. Weight measurement operation

Table 3. Specimen’s weight measurement detailed

Group	Sub-group	T0	T1	T2	T3	T4	T5	T6
A	1	7.6049	7.6070	7.6085	7.6098	7.6123	7.6246	7.6655
	2	7.957	7.9608	7.9620	7.9636	7.9649	7.9755	7.9989
	3	8.4760	8.4807	8.4835	8.4837	8.4865	8.4964	8.5227
B	4	7.5305	7.5275	7.5244	7.5253	7.5175	7.513933	7.5152
	5	7.8348	7.8326	7.8303	7.8301	7.8231	7.8163	7.8026
	6	8.8055	8.8005	8.7974	8.7889	8.7817	8.7808	8.7616

### 3.2 Moisture Absorption

Measuring moisture absorption of the studied specimens has been done using the simple formula in Eq. (1) as follows:

$$\% = (W_i - W_0) \div W_0 \tag{1}$$

Where,  $W_0$  is the initial weight of samples,  $W_i$  is the weight of samples after up taking moisture.

### 3.3 Flexure testing

The 3-points flexure testing schematized in fig. 4, was conducted at the “Mining and Metallurgy Research Unit”, formerly known as “URMA”, which is a part of the “Research Centre in Industrial Technologies” (URMM/CRTI) located in Annaba (Algeria). The MTS 43, a universal machine, is outfitted with a force sensor and is under the control of a computer. A minimum of five (5) tests were applied for each subgroup, using specimens mean dimensions displayed in Table 4. In this case, speed and temperature were 10 mm/min and 25 °C, respectively. The load cell illustrated in Fig. 5, also known as a dynamometer, is

linked to an acquisition chain that enables the concurrent measurement of displacement time, load, and deformation. The data collection and result processing were conducted using computer technology, specifically the MTS TestSuite software. A total of 6 experiments and combinations of variables were conducted, in order to measure the flexural strength and Young's modulus.

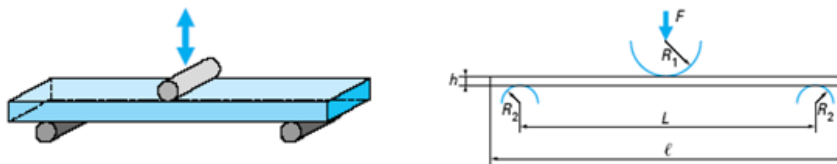


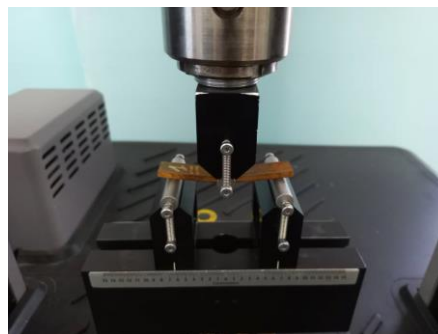
Fig. 4. Three points bending scheme

Table 4. Specimen mean dimensions

Length (l) mm	Outer span (L) mm	Width (b) mm	Thickness (h) mm
80	64	14	4



(a)



(b)

Fig. 5. Bending test procedure (a) and (b)

### 3.4 Microscopic and FTIR Equipment

Observations of microfibrils, surface topography, and the rupture area were conducted using a light microscope. The type of microscope equipment used for this research was the Leica ATC 2000 Microscope, Wetzlar.

Meanwhile, the FTIR spectra were recorded at the “Water and Environmental Science and Technology Laboratory” located in University Mohamed Cherif Messaidia, Souk Ahras, Algeria, using an IRAffinity-1S FTIR at a measuring range between 500 and 4000  $\text{cm}^{-1}$

## 4. Results and Discussion

### 4.1. Submersion’s Impact on Specimen Weight

This study employed a Two-Way ANOVA approach to examine the variations in the weight of the specimens when subjected to immersion in two distinct solutions for ne less than 60 days: a seawater environment and an acidic solution. The present investigation took into account the variables of immersion duration and the proportion of iron powder loading.

The outcomes exhibited noteworthy disparities in comparison to the specimens that were not subjected to immersion, which can be referred to as the control group (C).

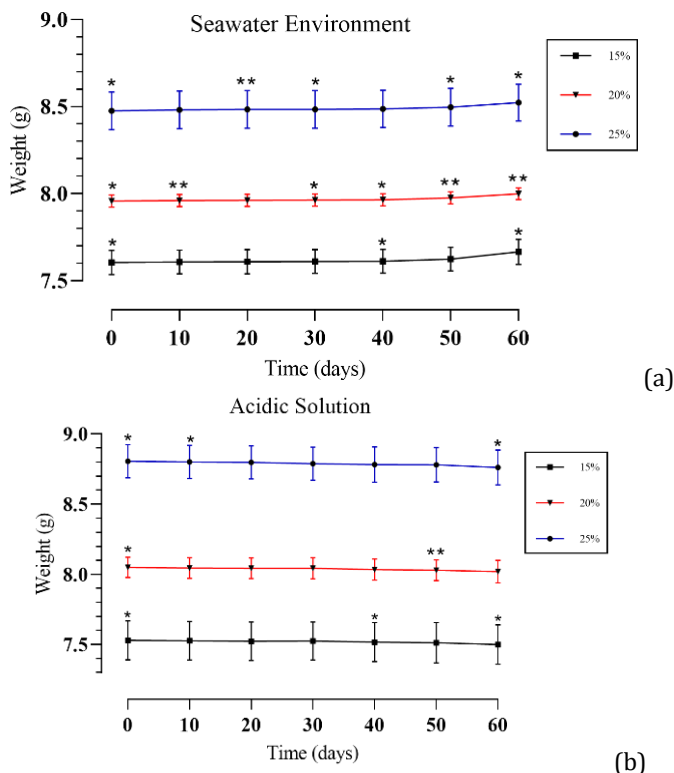


Fig. 6. Charts (a) and (b) display the evaluation of the masses of various test specimens over time

Compared with the control, the weight change illustrated in Fig. 6 was significant ( $p < 0.05$ ), proportional to the time of immersion. In such a way a noticeable increase in weight was observed over time in specimens immersed in seawater (Fig. 6-a), indicating significant water absorption. This aligns with findings from Abdel-Magid et al., who reported increased water absorption in glass/epoxy composites exposed to seawater over a year, supporting the impact of seawater on weight gain in composite materials [15]. On the other hand, specimens that were fully submerged in the acidic solution exhibited a weight reduction (Fig. 6-b) that was directly related to the duration of exposure. This echoes the findings of Bagherpour et al., who investigated the effects of concentrated HCl on aged fiber glass polyester composites [21]. This weight decrease phenomenon could be attributed to corrosion and material degradation. In corrosive environments like acidic solutions, the chemical reactions involving the iron powder within the composite may release iron ions, leading to material corrosion. This corrosion process contributes to the observed loss of material mass, aligning with Bagherpour et al.'s observations of significant destructive impacts in acid-immersed composites.

#### 4.2 Moisture absorption and Weight loss

The process of moisture absorption was quantified for specimens that were submerged in seawater (Table 5). It was shown that these specimens exhibited moisture absorption, leading to a subsequent increase in their overall weight. On the other hand, the specimens

that were submerged in the acidic solution exhibited a reduction in mass as shown in Table 6.

Table 5. Sub-groups moisture absorption

Sub-group	Absorption (%)
1	0.79
2	0.52
3	0.55

Table 6. Sub-groups weight loss

Sub-group	Weight loss (%)
1	0.20
2	0.41
3	0.50

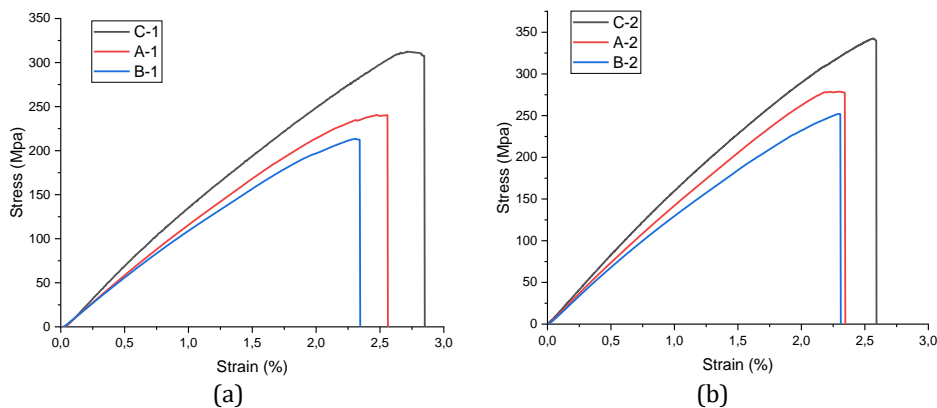
A direct correlation is noted between the quantity of iron powder present in the laminate and the corresponding reduction in moisture absorption. Stated otherwise, an increase in resin content corresponds to an increase in the moisture absorption capacity of the composite material. Furthermore, it was observed that the test specimens, when subjected to immersion in the acidic solution, exhibited a reduction in weight that was directly proportionate to the quantity of iron contained within them. The observed reduction in weight can be ascribed to the deterioration of the composite material caused by the influence of hydrochloric acid (HCl), as mentioned before.

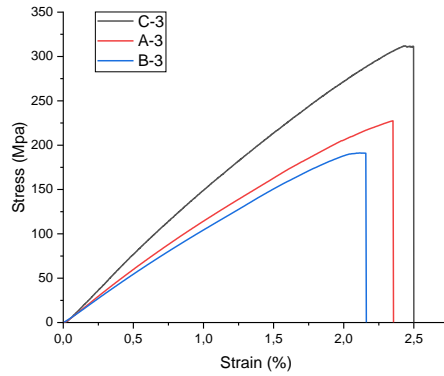
### 4.3. Flexure Strength and Young Modulus

#### 4.3.1 Experimental Result Detailed

The analysis focused on the results obtained from a three-point bending experiment carried out on specimens that underwent immersion for a minimum period of 60 days. Figure 7 illustrates the typical stress/strain curve for each group, with detailed results of Flexural Strength and Young’s Modulus for each subgroup presented in Table 7.

In such a case that, Fig. 7(a) depicts the stress/strain plot for the subgroup submerged in seawater. In Fig.7(b), the stress/strain plot illustrates the performance of the subgroup submerged in an acidic solution. Finally, Fig. 7(c) presents the stress/strain plot for the non-submerged subgroup, referred to as the control group.





(c)

Fig. 7. Typical plot of Flexure Stress (Mpa) against strain (%)

Table 7. Three points bending test results detailed

Group	Subgroups	Iron content (W%)	Solution	Flexure Strength (Mpa)	Young's Modulus (Mpa)
A	1	15	Seawater	240.5714	10211.82
	2	20	Seawater	263.7119	11162.67
	3	25	Seawater	219.1429	9830.429
B	1	15	Acid	201.5714	8961.479
	2	20	Acid	243.9256	9588.857
	3	25	Acid	193.5714	8200.84
C	1	15	/	310.822	15107.267
	2	20	/	341.198	16366.777
	3	25	/	311.998	15097.248

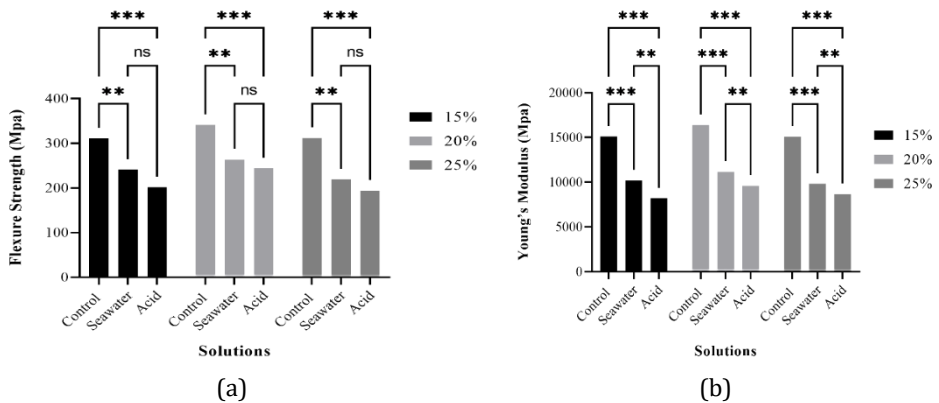


Fig. 8. ANOVA study charts for Flexural Strength (a) and Young's modulus (b).

The present investigation utilized a Two-Way ANOVA approach to investigate the changes in flexure strength and Young's modulus. The current study considered the factors of flexural strength and Young's modulus, as well as the solution type and iron powder loading %. The results (as shown in Fig. 8) displayed significant differences when



compared to the samples that were not exposed to immersion, which can be referred to as the control group (C). The observed reduction in both flexure strength and Young's modulus was found to be statistically significant when compared to the control group ( $p < 0.05$ ). After the results were evaluated using the ANOVA method, the findings of the study (Fig. 8) demonstrated a significant decrease in both flexural strength and Young's modulus in the immersed composites as compared to the composites that were not subjected to immersion.

The Flexure Strength of Composites 1, 2, and 3 (Fig. 8-a) in Group A decreased by 22.6%, 22.7%, and 29.7%, respectively. Likewise, within group B, laminates 1, 2, and 3 demonstrated a reduction in their flexural strength of 35.1%, 28.5%, and 37.9% correspondingly.

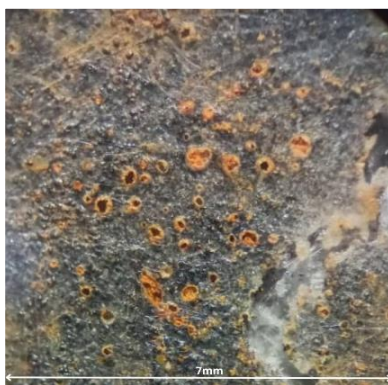
When examining Young's modulus (Fig. 8-b), it was observed that Group A, immersed in seawater, experienced reductions of 32.4%, 31.8%, and 34.8% in subgroups 1, 2, and 3, respectively, when compared to their non-immersed counterparts. In contrast, Group B, exposed to the acidic solution, demonstrated a more substantial decline, with decreases of 40.6%, 41.4%, and 45.6% in subgroups 1, 2, and 3, respectively, compared to their non-immersed counterparts. These findings underscore the significant impact of the acidic solution on Young's modulus in comparison to the specimens not subjected to immersion.

A notable observation was made while comparing the specimens that underwent immersion in an acidic solution with those that were exposed to seawater, as a more prominent reduction in both flexural strength and Young's modulus was observed. In line with the observations from the study conducted by A. M. Amaro et al. [22], the results obtained similarly highlight a notable reduction in flexural strength and Young's modulus for specimens immersed in an acidic solution compared to those exposed to seawater. This correspondence further underscores the higher reactivity of acidic solutions and the consequent mechanical degradation observed in laminates, as indicated in the mentioned study.

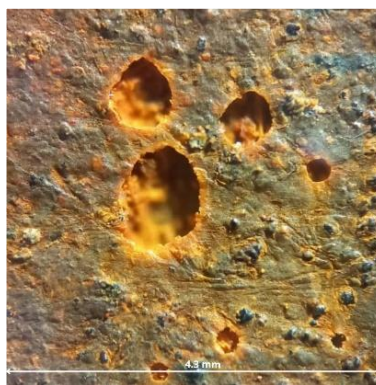
The results presented above emphasize the need to consider environmental factors when evaluating the durability and effectiveness of composite materials in real-world situations.

#### 4.4 Microscopic and FTIR analysis

The microscopic photos depict the specimen's immersion in an acidic solution, both before and after the immersion process. These images demonstrate the formation of pores on the epoxy layer (Fig. 9-a-b), which functions as the matrix for the specimen. The observed phenomena elucidate the notable decline in the mechanical strength of the specimens when subjected to immersion in the acidic solution.



(a)



(b)



(c)

Fig. 9. Microscopic images of the surfaces of the specimens immersed in the acid solution (a) (b) and seawater (c)



(a)



(b)

Fig. 10. Microscopic images of the fracture surface of a test specimen (a) (b)

The microscopic images in Fig. 10 reveal the oxidation of iron grains within the glass fibers, which led to a reduction in the mechanical properties of the various specimens. The diagram of the Fig.11 displays the FTIR spectra of distinct specimens while immersed in different solutions: seawater, a pH 2 acid medium, and specimens that were not immersed. The absorption peaks occur at a frequency of  $3865\text{ cm}^{-1}$ , which is specifically related to the stretching vibration of hydroxyl (-OH) bonds found in functional groups like water or other hydroxylated compounds. This frequency range also includes values between  $3800$  and  $3900\text{ cm}^{-1}$ . Seawater inherently contains hydroxyl groups.

The frequency at  $3734\text{ cm}^{-1}$  corresponds to the stretching vibration of a carbonyl (C=O) bond present in specific organic or inorganic compounds, including corrosion products prevalent in the maritime environment or due to the iron powder presence in our composite.

The peak observed at  $1743\text{ cm}^{-1}$  corresponds to the stretching vibration of the C=O bond in the -COO- functional group. Additionally, the peaks at  $1473\text{ cm}^{-1}$  and  $1373\text{ cm}^{-1}$  are associated with the bending vibration of the -CH<sub>3</sub> groups in the -CH (CH<sub>3</sub>)<sub>2</sub> moiety. The peak observed at  $1242\text{ cm}^{-1}$  corresponds to the stretching vibration of the C-O bond in the -COOH functional group, while the peak at  $1172\text{ cm}^{-1}$  is attributed to the stretching

vibration of a C-O bond. These could be found in functional groups such as esters, ethers, or the vibration of the C-O-C skeleton.

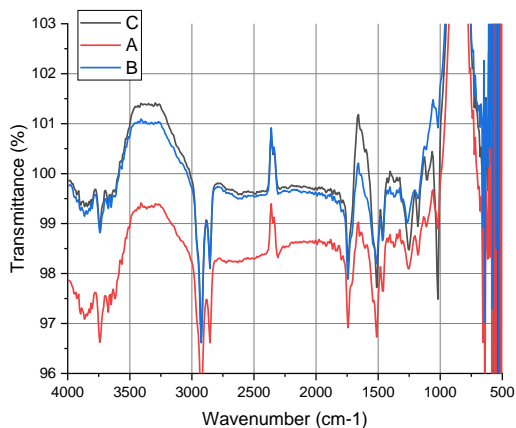


Fig. 11. Diagram of FTIR spectra for different specimens

The predominant peak belongs to the epoxy cycle within the region of 1270-1240  $\text{cm}^{-1}$ . The epoxy functions exhibit strong absorption at 1257  $\text{cm}^{-1}$ , which corresponds to the symmetrical vibrations of C-O-C. Additionally, there are two peaks at 1153  $\text{cm}^{-1}$  that correspond to the vibrations of CH<sub>2</sub> groups in the epoxy. The absorption at 3410 and 3382  $\text{cm}^{-1}$  in amines is attributed to the vibration of primary amine groups (-NH<sub>2</sub>) in the hardener structure [24].

The intense peak observed at 2931  $\text{cm}^{-1}$  and 2870  $\text{cm}^{-1}$  in other groups is associated with the CH groups of the alkane function, and its absorption limit occurs at 1567  $\text{cm}^{-1}$ . Ether groups exhibit two distinct absorption peaks at 1257 and 1233  $\text{cm}^{-1}$ . The first peak corresponds to C-O-C groups that are connected to aromatic cycles, while the second peak arises from the phatic stretching of carbon-oxygen (-O-CH<sub>2</sub>) bonds [25].

Epoxy contains functional groups known as epoxy groups (C-O-C) which have the ability to undergo a reaction with water. The three spectra exhibit a high degree of similarity. Nevertheless, alterations in the absorption bands linked to these functional groups, particularly in the range of 1018 to 1735  $\text{cm}^{-1}$ , may suggest chemical modifications associated with water absorption. This is evident in the changes observed in the bands at 1018  $\text{cm}^{-1}$ , 1118  $\text{cm}^{-1}$ , the 1249  $\text{cm}^{-1}$  vibration band, and the 1365  $\text{cm}^{-1}$  band, which affect the bonding bands.

Water absorption can cause the polymeric matrix to become softer, and acid can affect iron powder, leading to alterations in bonding vibration bands. The absorption bands related to C-C and C-O-C groups in the epoxy matrix may exhibit alterations that indicate modifications in the polymeric structure, as evidenced by the images showing cavities in the material matrix.

The absorption peak observed at 1404  $\text{cm}^{-1}$  corresponds to the presence of carbon-nitrogen bonds (CN). Additionally, the range between 1172 and 1200  $\text{cm}^{-1}$  is commonly linked to the stretching vibrations of C-N bonds in primary amines. Secondary and tertiary amines can also display bands in this region. However, the position of these bands may vary significantly depending on the characteristics of the group.

The presence of an absorption band at 1249  $\text{cm}^{-1}$  in an infrared spectrum can be indicative of many chemical bonds: CO (carbon-oxygen bonds): The stretching vibrations of CO bonds

can be linked to this particular location. It may also exist in functional groups like esters, ethers, or other molecules that have carbon-oxygen linkages. The presence of amines or nitriles can also result in stretching vibrations of CN bonds, which can contribute to this region.

Volenik's research demonstrates that a spectral peak at  $1100\text{ cm}^{-1}$ , accompanied by a smaller peak at  $1198\text{ cm}^{-1}$ , can be attributed to the vibrational motion of Si-O bonds in SiO<sub>2</sub> [26].

## **5. Conclusions**

The immersion of test samples containing varied proportions of iron powder (15%, 20%, 25%) in two distinct solutions (seawater and an acidic solution with a pH of 2) resulted in a notable decrease in mechanical characteristics, particularly in terms of flexural strength and Young's modulus. The drop confirmed using statistical ANOVA analysis, was 40% for specimens submerged in the acidic solution and 30% for those in seawater, highlighting the corrosive properties of the acidic environment. Furthermore, a clear link was observed between the proportions of iron powder loading.

The microscopic images offered a convincing elucidation for the decline in mechanical characteristics, as they unveiled the appearance of pores on the surfaces of specimens submerged in the acidic solution and severe corrosion in those exposed to saltwater. In addition, FTIR analysis provided a clear understanding of the chemical processes that took place in response to the various solutions.

This type of composite, composed of pure iron powder and epoxy fiberglass, has significant limitations for use in industrial or real-world applications. Firstly for its sensitivity to immersion, as the study has shown, immersion in seawater or an acidic solution has a significant impact on the mechanical properties of this composite. The reduction in flexural strength and Young's modulus can make this material unsuitable for applications that require high durability in humid or corrosive environments. Secondly its limited lifespan due to the rapid degradation of mechanical properties under immersion, this composite may have a limited lifespan in applications such as shipbuilding, marine structures, or chemical equipment requiring long-term corrosion resistance.

This composite, while unsuitable for corrosion-sensitive applications, finds relevance in non-corrosive environments, low-stress structural components, and cost-effective projects. Ideal for temporary structures and niche applications, its unique properties cater to demands beyond corrosion resistance. Acknowledging limitations, careful project consideration can unveil tailored applications for this composite, offering a balance of performance and cost-effectiveness. This composite can find application in non-corrosive environments, low-stress structural components, and cost-effective projects. Ideal for temporary structures and niche applications, its unique properties cater to demands beyond corrosion resistance. Acknowledging limitations, careful project consideration can unveil tailored applications for this composite, offering a balance of performance and cost-effectiveness.

## **References**

- [1] Rajak DK, Pagar DP, Menezes PL, Linul E. Fiber-Reinforced Polymer Composites: Manufacturing, Properties, and Applications. *Polymers*. 2019;11(10):1667. <https://doi.org/10.3390/polym11101667>
- [2] Mortas N, Er O, Reis PNB, Ferreira JAM. Effect of corrosive solutions on composites laminates subjected to low velocity impact loading. *Composite Structures*. 2014;108:205-211. <https://doi.org/10.1016/j.compstruct.2013.09.032>

- [3] Deng X, Zhang Z. Effects of Seawater Environment on the Degradation of GFRP Composites by Molecular Dynamics Method. *Polymers*. 2022;14(14):2804. <https://doi.org/10.3390/polym14142804>
- [4] Gülsoy, M., Taşdemir, M., & Ö., H. Mechanical Properties of Polymers Filled with Iron Powder. *International Journal of Polymeric Materials and Polymeric Biomaterials*. 2008;57(3):258-265. <https://doi.org/10.1080/00914030701473656>
- [5] Gungor, A. Mechanical properties of iron powder filled high-density polyethylene composites. *Materials & Design*. 2007;28(3):1027-1030. <https://doi.org/10.1016/j.matdes.2005.11.003>
- [6] Basavarajappa S, Arun KV, Davim J. Effect of Filler Materials on Dry Sliding Wear Behavior of Polymer Matrix Composites - A Taguchi Approach. *Journal of Minerals & Materials Characterization & Engineering*. 2009;8(5):379-391. <https://doi.org/10.4236/jmmce.2009.85034>
- [7] Salih SI, Nayyef S, Abd Alsalam AH, Hasan AM. Evaluation Mechanical Properties of Polymer Composites. *Eng. & Tech. Journal*. 2015;33(7):1348-1360. <https://doi.org/10.30684/etj.2015.116706>
- [8] Ghorbanzadeh Ahangari M, Fereidoon A, Jahanshahi M, Sharifi N. Effect of nanoparticles on the micromechanical and surface properties of poly(urea-formaldehyde) composite microcapsules. *Composites Part B: Engineering*. 2014;56:450-455. <https://doi.org/10.1016/j.compositesb.2013.08.071>
- [9] Vincent B, Natesan S, Anand G. Investigation on Thermo-Mechanical Behaviour of E Glass Fibre and Iron Oxide Filler Particles Reinforced Epoxy Composite. *International Journal for Research in Applied Science and Engineering Technology*. 2020;8:1522-1526. <https://doi.org/10.22214/ijraset.2020.4245>
- [10] Megahed M, Fathy A, Morsy D, Shehata F. Mechanical Performance of glass/epoxy composites enhanced by micro- and nanosized aluminum particles. *Journal of Industrial Textiles*. 2019;51(1). <https://doi.org/10.1177/1528083719874479>
- [11] Aravinth B, Vivek G, Gokulakrishanan S, Manikandan D. Synthesis and Mechanical Analysis of on iron powder of mixed glass fiber reinforced polymer composite Material. *International Research Journal on Advanced Science Hub*. 2020;2(11):26-29. <https://doi.org/10.47392/irjash.2020.216>
- [12] Mao H, Abushammala H, Waste Iron Filings to Improve the Mechanical and Electrical Properties of Glass Fiber-Reinforced Epoxy (GFRE) Composites. *Journal of Composites Science*. 2023;7(3):90. <https://doi.org/10.3390/jcs7030090>
- [13] Benmokrane B, Ali AH, Mohamed HM, ElSafty A, Manalo A. Laboratory assessment and durability performance of vinyl-ester, polyester, and epoxy glass-FRP bars for concrete structures. *Composites Part B: Engineering*. 2017;114:163-174. <https://doi.org/10.1016/j.compositesb.2017.02.002>
- [14] Soles CL, Chang FT, Gidley DW, Yee AF. Contributions of the nanovoid structure to the kinetics of moisture transport in epoxy resins. *Journal of Polymer Science Part B: Polymer Physics*. 2000;38(5). [https://doi.org/10.1002/\(SICI\)1099-0488\(20000301\)38:5<776::AID-POLB15>3.3.CO;2-1](https://doi.org/10.1002/(SICI)1099-0488(20000301)38:5<776::AID-POLB15>3.3.CO;2-1)
- [15] Mourad A-HI, Abdel-Magid BM, El-Maaddawy T, Grami ME. Effect of Seawater and Warm Environment on Glass/Epoxy and Glass/Polyurethane Composites. *Applied Composite Materials*. 2010;17(5):557-573. <https://doi.org/10.1007/s10443-010-9143-1>
- [16] Silva MAG, da Fonseca BS, Biscaia H. On estimates of durability of FRP based on accelerated tests. *Composite Structures*. 2014;116:377-387. <https://doi.org/10.1016/j.compstruct.2014.05.022>
- [17] Kaybal HB, Ulus H, Tatar AC, Demir O. Influence of seawater on mechanical properties of SiO<sub>2</sub>-epoxy polymer nanocomposites. *Res. Eng. Struct. Mat*. 2019;5(2):147-154. <https://doi.org/10.17515/resm2018.61is0802>

- [18] Sukur EF, Kaybal HB, Ulus H, Avc A. Tribological behavior of epoxy nanocomposites under corrosive environment: effect of high-performance boron nitride nanoplatelet. *Sigma Journal of Engineering and Natural Sciences*. 2023;41(6). <https://doi.org/10.14744/sigma.2022.00025>
- [19] Bian L, Xiao J, Zeng J, Xing S. Effects of seawater immersion on water absorption and mechanical properties of GFRP composites. *Journal of Composite Materials*. 2012;46(25):3151-3162. <https://doi.org/10.1177/0021998312436992>
- [20] Abrial H, Kadriadi D, Rodianus A, Mastariyanto P, Ilhamdi, Arief S, et al. Mechanical properties of water hyacinth fibers - polyester composites before and after immersion in water. *Materials & Design*. 2014;58:125-129. <https://doi.org/10.1016/j.matdes.2014.01.043>
- [21] Bagherpour S, Bagheri R, Saatchi A. Effects of concentrated HCl on the mechanical properties of storage-aged fiber glass polyester composite. *Materials & Design*. 2009;30(2):271-274. <https://doi.org/10.1016/j.matdes.2008.04.078>
- [22] Amaro AM, Reis PNB, Neto MA, Louro C. Effects of alkaline and acid solutions on glass/epoxy composites. *Polymer Degradation and Stability*. 2013;98(4):853-862. <https://doi.org/10.1016/j.polymdegradstab.2012.12.029>
- [23] Mortas N, Er O, Reis PNB, Ferreira JAM. Effect of corrosive solutions on composites laminates subjected to low velocity impact loading. *Composite Structures*. 2014;108:205-211. <https://doi.org/10.1016/j.compstruct.2013.09.032>
- [24] Lahlali D, Naffakh M, Dumon M. Cure kinetics and modeling of an epoxy resin cross-linked in the presence of two different diamine hardeners. *Polymer Engineering & Science*. 2005;45(12):1581-1589. <https://doi.org/10.1002/pen.20274>
- [25] George GA, Cash GA, Rintoul L. Cure monitoring of aerospace epoxy resins and prepregs by Fourier transform infrared emission spectroscopy. *Polymer International*. 1996;41(2):169-182. [https://doi.org/10.1002/\(SICI\)1097-0126\(199610\)41:2<169::AID-PI606>3.0.CO;2-2](https://doi.org/10.1002/(SICI)1097-0126(199610)41:2<169::AID-PI606>3.0.CO;2-2)
- [26] Voleník K, Lettner J, Hanousek F, et al. Oxides in plasma-sprayed chromium steel. *Journal of Thermal Spray Technology*. 1997;6:327-334. <https://doi.org/10.1007/s11666-997-0067-8>

Blank Page

## Determination of wear rate and coefficient of friction of Al6262 reinforced with different weight percentage of WC/MoS<sub>2</sub> under dry sliding condition

Kadapa Hemadri<sup>1,a</sup>, Ajith Arul Daniel S<sup>1,b</sup>, Vijayendra Kukanur<sup>2,c</sup>, Madeva Nagara<sup>3,d</sup>

<sup>1</sup>Dept. of Mechanical Eng., Vels Institute of Science, Technology & Advanced Studies, Tamil Nadu India

<sup>2</sup>Dept. of Mechanical Eng., H.K.E.Society's Sir.M.Visvesvaraya College of Engineering, Karnataka India

<sup>3</sup>Aircraft Research and Design Centre, HAL, Bengaluru, Karnataka, India

### Article Info

### Abstract

#### Article history:

Received 09 Oct 2023

Accepted 31 Jan 2024

#### Keywords:

Tungsten carbide;

Molybdenum di

Sulphide;

Wear;

Taguchi;

SEM analysis

A tribological investigation was undertaken on hybrid metal matrix composites based on Aluminum alloy 6262, incorporating varying weight percentages of Tungsten Carbide (WC) and Molybdenum disulfide (MoS<sub>2</sub>) under dry sliding conditions. Specifically, Tungsten Carbide was incorporated at 3%, 6%, and 9%, while Molybdenum disulphide was introduced at 2%, 4%, and 6%. The fabrication of these hybrid composites was accomplished using the stir casting technique. The experimental design followed an L27 orthogonal array, and Taguchi optimization was employed to identify the optimal combination of input parameters. The orthogonal array, signal-to-noise ratio and analysis of variance were employed to study the optimal testing parameters on developed composites. The optimal formulation, resulting in the minimum wear rate and coefficient of friction, was determined to be 9% WC, 6% MoS<sub>2</sub>, a load of 10N, a sliding velocity of 1 m/s, and a sliding distance of 400 m. Characterization was carried out for Al6262/WC/MoS<sub>2</sub> hybrid composite by using scanning electron microscopy (SEM).

© 2024 MIM Research Group. All rights reserved.

## 1. Introduction

In the field of composite materials, numerous investigations have been carried out. It exhibits higher material performance in comparison to traditional materials. A common composite, particularly in the automotive and aerospace industries, is aluminum-based material. This is due to its accessibility, affordable production costs, and simplicity of manufacturing [1-4]. The devices' everyday mechanical components are susceptible to wear and tear. Wear-resistant materials should be utilized in the machine in order to boost its reliability [5]. The automotive industry is placing greater focus on weight optimization since it lowers emissions and improves fuel economy. Aluminum alloys are being used more often because they help reduce weight and have other advantages including strong corrosion resistance, good formability, and recyclability [6]. A great deal of research has been done on the wear of aluminum composites. Stir casting is the most often used production technique for producing composites among many others [6]. Furthermore, the main issue with their usages includes deteriorated performance at high temperatures and poor friction coefficient and wear rate [7]. MMCs, which are hard ceramic elements reinforced in aluminum alloys, are used to solve these issues. Due to its increased

\*Corresponding author: [madev.nagaral@gmail.com](mailto:madev.nagaral@gmail.com)

<sup>a</sup> [orcid.org/0000-0003-6892-1020](https://orcid.org/0000-0003-6892-1020); <sup>b</sup> [orcid.org/0000-0002-7279-8491](https://orcid.org/0000-0002-7279-8491); <sup>c</sup> [orcid.org/0000-0002-6892-1020](https://orcid.org/0000-0002-6892-1020);

<sup>d</sup> [orcid.org/0000-0002-8248-7603](https://orcid.org/0000-0002-8248-7603)

DOI: <http://dx.doi.org/10.17515/resm2024.09me1009rs>

Res. Eng. Struct. Mat. Vol. 10 Iss. 3 (2024) 1125-1138



toughness, high stiffness, and excellent wear resistance, aluminum-based MMC is being employed more and more in these industries [8].

The addition of particles of hard ceramic is what has caused these increases in tribological properties. Wear is a major effect in the operation of many automotive components, including pistons, cylinder liners, connecting rods etc. [9]. These components are all made of aluminum-based MMC. The lowest wear rate was attained by experimenting Al/SiC nanocomposites with a 2-volume percent graphite addition the combined due to its self-lubricating properties [10]. Also, another research positive impact of soft MoS<sub>2</sub> particles improvements in Al/Al<sub>2</sub>O<sub>3</sub> composites' wear resistance and friction. Between touching surfaces, a protecting layer is created primary factor lowering the hybrid wear composites enhanced aluminum resistance to abrasion alloys through the creation of a hybrid composites. By adopting the stir casting technique [11], Al2219 combined with B<sub>4</sub>C & MoS<sub>2</sub> for composite materials. In the experiment, the morphology, density, micro hardness, tensile strength, and dry sliding wear test are all evaluated. The outcome shows that, as observed in the morphology of the matrix alloy, the reinforcement particles are spread arbitrarily and finely. In comparison to prepared composite material, Al2219 alloy has a comparatively low density and microhardness. Al2219 and MoS<sub>2</sub> have a minimum mechanical property and Al2219 alloy has a maximum tensile strength. Wear rate is reduced, and their wear resistance is increased by the addition of MoS<sub>2</sub> reinforcement [12]. Radhika and Jolith investigated the tribological properties of LM13/TiO<sub>2</sub>/MoS<sub>2</sub>. They take into account the applied force applied, sliding velocity, and sliding distance are their input parameters. In this work, the author used the Taguchi approach to determine sliding wear and came to the conclusion that TiO<sub>2</sub>/MoS<sub>2</sub> reinforced offers superior abrasion resistance [13]. Al6061/SiC/WC hybrid aluminum materials have been attempted under various weight percentages of reinforcement particulates [13]. The addition of stiffer and stronger reinforcement to the matrix material has boosted the hardness of AMMCs. The compression, tensile, and fatigue strength of the aluminum composite material can all be greatly improved by the addition of SiC and WC reinforcements to the matrix alloy [14].

## 2. Experimental Setup

As a matrix material, Al 6262 has been selected because of its good material qualities, high level of resistance to corrosion, and great weldability. Because of its inherent ability to lubricate itself, MoS<sub>2</sub> is used as reinforcement. Table 1 below illustrates the base material's chemical make-up. Before being cast, the reinforcements is heated for 25 minutes at 450°C. After warming the reinforcement, the Al6262 was melted in a graphite crucible at 550°C to 650°C. In order to prevent explosives, magnesium is added at 2% wrapped in aluminum foil and added to the aluminum matrix. After the reinforcement added all the materials is then stirred for 10 minutes at 800 rpm [15]. While the combination of Aluminum 6262, tungsten carbide, and molybdenum disulfide (MoS<sub>2</sub>) offers several limitations, combining these materials may pose challenges during the manufacturing process, especially in terms of fabrication, machining, or bonding. Specialized processes may be required, increasing production complexity. The Pin on Disc setup was used to find the wear rate of the developed composites. The EDAX analysis of the developed composites is shown in figure 1. The chemical combination of the base material is shown in Table 1.

Wear rate (  $W_i$  ) was then calculated by calculating using the following equation :

$$W_i = \frac{V}{LnS} \quad (1)$$

where V is volume rate and n are the applied load on ring and S is the sliding distance. The coefficient of friction can be calculated as follows.

$$F_f = \mu * N \tag{2}$$

$F_f$  is the frictional force,  $\mu$  is the coefficient of friction, and  $N$  is the applied normal load

Table 1. Typical chemical composition for aluminum alloy 6262

Si	Fe	Cu	Mn	Mg	Zn	Ti	Pb	Bi	Cr	Al
0.80	0.25	1.4	0.75	1.05	0.15	0.10	0.55	0.60	0.23	94.12

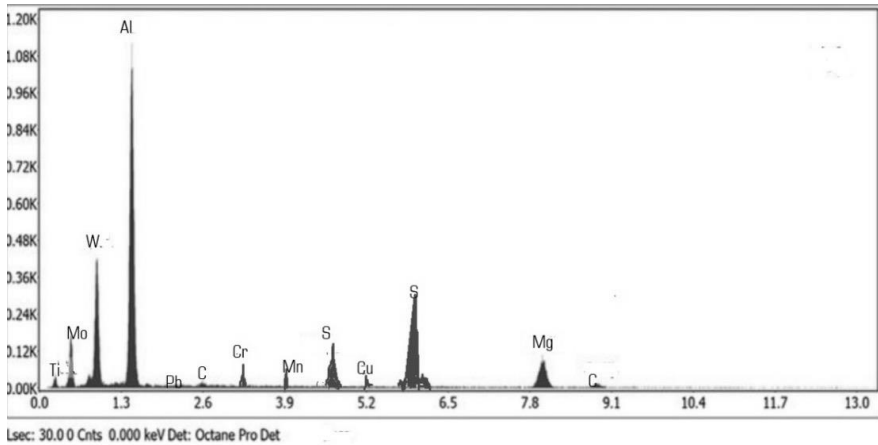


Fig. 1. EDAX analysis of the composites

### 3. Design of Experiments

The table 3 shows design of experiments used in this study is with five factor and three levels. The input parameters are wight percentage of tungsten carbide, weight percentage of molybdenum disulphide, load, sliding velocity and sliding distance. The Brinell hardness value of the composites is shown in table 2. When the weight percentage of the composites increases and the percentage of MoS<sub>2</sub> in intermediate level the hardness values is higher. When the volume fraction of the reinforcement in the composite is a critical factor. Increasing the volume fraction of reinforcement generally tends to enhance hardness up to a certain point. The uniform distribution of reinforcement particles within the Al 6262 matrix is essential. Agglomeration or uneven distribution can lead to localized variations in hardness. The output parameters are worn rate and coefficient of friction. Based upon these criteria L27 orthogonal array is chosen for performing the experiments as shown in Table 3.

Table 2. Hardness of the composites

WC	3	3	3	6	6	6	9	9	9
MoS <sub>2</sub>	2	4	6	2	4	6	2	4	6
BHN	76	80.2	75.6	81.5	84.3	80.2	87.6	92.2	86.7

Table 3. L27 Levels and factors

Factors	Unit	Level 1	Level 2	Level 3
WC	%	3	6	9
MoS2	%	2	4	6
Load	N	10	20	30
Sliding Speed	m/sec	1	1.5	2
Sliding Distance	m	400	800	1200

#### 4. Results and Discussion

##### 4.1 S/N Ratio and ANOVA

The figure 2 shows the Signal to noise ratio of wear rate. The decrease in wear rate trends to lower weight percentage of tungsten carbide. The results show that at 3 % of WC offers maximum wear rate. This is due to the hardness of the composite material. It is generally believed that contribution of hard particles to aluminum alloys results in an improvement of the wear resistance of the base alloy to a great extent [16]. At 3% of tungsten carbide the hardness of the composites is less. Owing to this tendency the density of the material is less which results increase in wear rate. In addition to 6% and 9% the hardness increases and the wear rate also reduces. In addition of MoS<sub>2</sub> the hardness starts increasing in addition of MoS<sub>2</sub> percentage. When MoS<sub>2</sub> is at 6% at WC at 9% the hardness of the material is higher. Due to increase in percentage of MoS<sub>2</sub> the self-lubricant properties of the materials increase which reduces the friction between the pin and the disc reduces which trends to loss of materials [17].

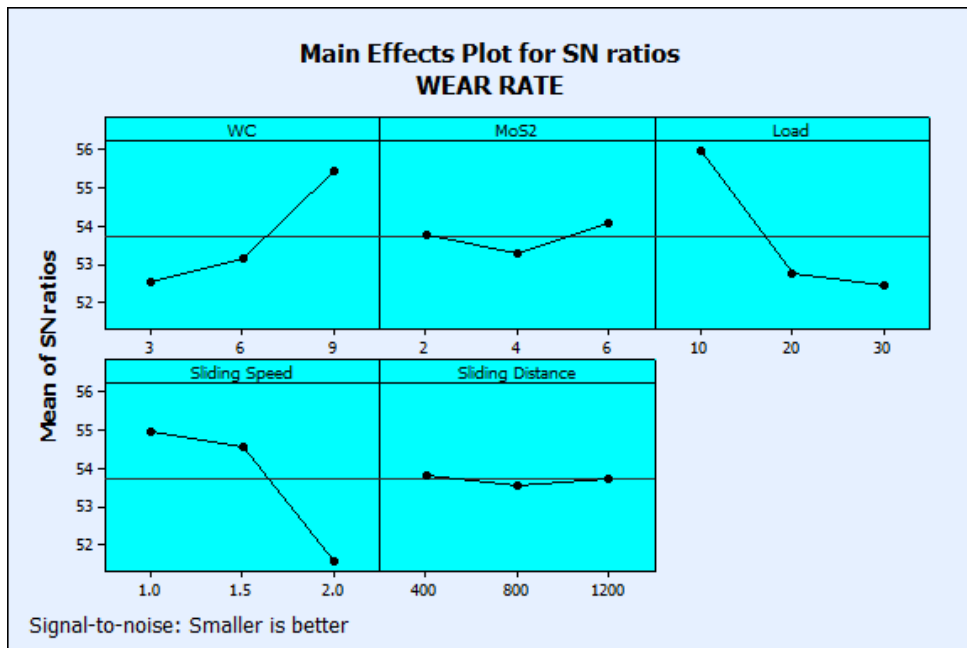


Fig. 2. S/N ratio graph for wear rate

Table 4. L27 orthogonal array and experimental results

	WC	MoS2	Load	Sliding Speed	Sliding Distance	Wear Rate	COF
1	3	2	10	1	400	0.00155	0.206
2	3	2	10	1	800	0.0015	0.236
3	3	2	10	1	1200	0.00165	0.255
4	3	4	20	1.5	400	0.002	0.308
5	3	4	20	1.5	800	0.0024	0.353
6	3	4	20	1.5	1200	0.00334	0.428
7	3	6	30	2	400	0.003	0.486
8	3	6	30	2	800	0.00345	0.453
9	3	6	30	2	1200	0.00365	0.476
10	6	2	20	2	400	0.00354	0.451
11	6	2	20	2	800	0.00342	0.472
12	6	2	20	2	1200	0.0025	0.334
13	6	4	30	1	400	0.00265	0.354
14	6	4	30	1	800	0.00205	0.297
15	6	4	30	1	1200	0.0023	0.311
16	6	6	10	1.5	400	0.00158	0.201
17	6	6	10	1.5	800	0.00155	0.189
18	6	6	10	1.5	1200	0.00131	0.177
19	9	2	30	1.5	400	0.00156	0.207
20	9	2	30	1.5	800	0.00182	0.245
21	9	2	30	1.5	1200	0.00192	0.287
22	9	4	10	2	400	0.00157	0.205
23	9	4	10	2	800	0.00193	0.216
24	9	4	10	2	1200	0.00176	0.201
25	9	6	20	1	400	0.00181	0.226
26	9	6	20	1	800	0.00165	0.248
27	9	6	20	1	1200	0.00127	0.165

The harder deformation of the counter surface penetrates the softer pin surface more as the applied stress increases. After each composite's critical load [18], with the application of load, the wear rate quickly starts to rise when the applied load increases to 20 N. The load at 30N the wear rate spikes to a very high level. In the event that the transitional load and the velocity of the composite increases in value by a large margin. Here is due to the noticeably greater frictional heating and as a result the pin material's localized adhesion to the counter surface as well as a rise in the surface structure's softening and more asperities can penetrate as a result larger deformation in wear surface are acquired [19]. The impacts graphic demonstrates that sliding speed is the parameter with the greatest relative impact. The plot clearly shows that wear rate of the composites reduces with sliding distance and reinforcement material but increases with sliding velocity [20]. It is common knowledge that the elastic modulus and temperature-related characteristics of composite materials can influence their tribological behavior. When two materials slide

against one another, heat is produced at the deformation, which raises the temperature at the interface and affects how viscoelastic the materials' reaction to tension. The temperature at the friction surface rises as sliding velocity increases, which may substantially impair the mechanical properties of the composites and cause significant loss in composite materials [21].

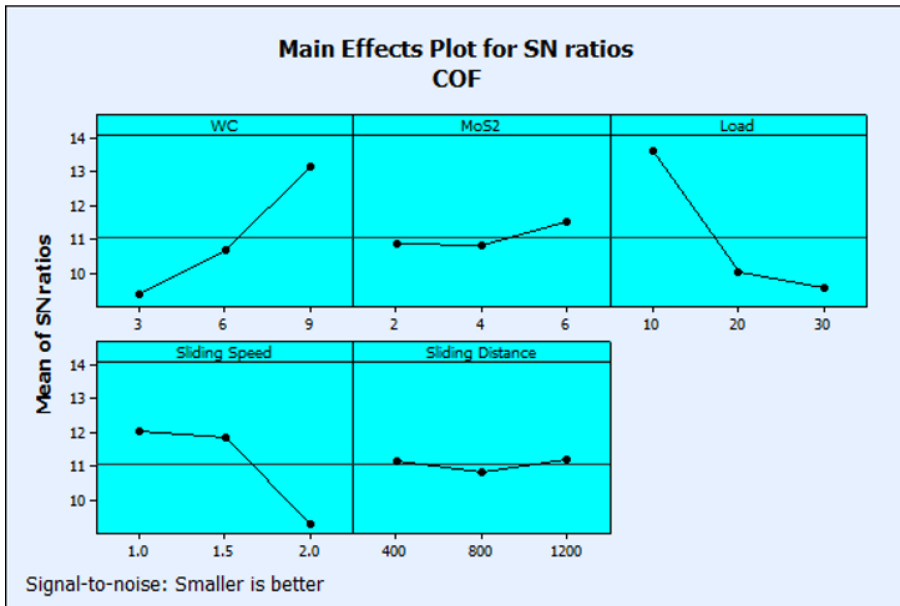


Fig. 3 S/N ratio graph for coefficient of friction

The Figure 3 shows the Signal to noise ratio of Coefficient of friction. The weight percentage of the tungsten carbide is the most significant parameters in friction coefficient. The initial finding in terms of the results is the drop in coefficient of friction as a result of an increase in the reinforcement's weight percentage. Comparing the reinforced AMMNCs to aluminum 6262 alloy indicated a lower coefficient of friction. It can be attributed to the composite's increased hardness, which results from the combination of abrasive particles and behaves as a tougher substance within the matrix [22]. Good surface adhesion occurs between the matrices and non-reinforcement whenever refractory bits are firmly bonded to the matrix. According to numerous studies, the COF of crystalline MoS<sub>2</sub> is typically low, at 6% in a dry sliding condition, this lubricating performance of MoS<sub>2</sub> is unique due to its self-lubrication properties. One explanation for this is that in a dry environment, MoS<sub>2</sub> particles good has adhesion and smaller particle sizes can easily fill the substrate's rough surface. Additionally, the reciprocating shear stress that occurs during the frictional process can disintegrate MoS<sub>2</sub> particles into lamella, resulting in a reduction in the sliding friction coefficient [23].

The COF are increased from 10N to 30N. When a force of 10N is applied, the WC percentages significantly increase the substrate's hardness of the composites and keep abrasive particles from becoming embedded in the contact area, effectively preventing cutting on friction. In the meantime, the interface's shear strength is outweighed by the cohesive force between the WC and the matrix materials. As a result, there is hardly any WC particle pull away first from contact area. As a result, compared to certain other loads, the COF at a 10N load is considerably less. When the load reaches 30N, the ultimate stress

begins to outweigh the binding effect between the WC and the substrates, leading to WC continuous extraction and cohesiveness occurs which leads higher friction coefficient.

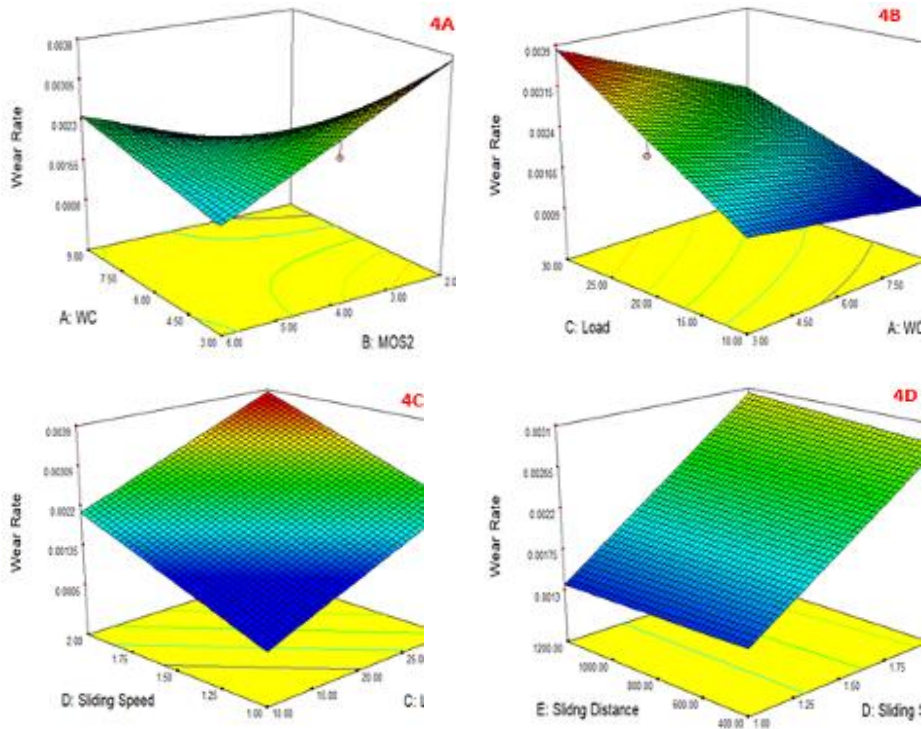


Fig. 4. Contour plot for input parameters Vs wear rate

The COF is shown in the graph is decreases up to 1 m/s before starting to rise as sliding speed increases rapidly [24]. The continuous development of a tribo layer at the contact surface is increased as sliding speed increases. Despite the fact that temperature increase increases as sliding velocity rises, the heat is in some ways beneficial for the development of a WC enrich interfacial layer, which in turn influences the development of compact layers at the contact area. However, when the sliding speed is increased beyond 1.5 m/s, a considerable quantity of heat is produced, which leads to the development of the composite pin softness results in increased in friction.

The figure 4A shows the contour plot for tungsten carbide and MoS<sub>2</sub> on wear rate. The graph indicates when the percentage of tungsten carbide increases from 3% to 6%. Wear rate is reduced from 0.0035 to 0.00275. When the weight percentage of tungsten carbide is 9 % the wear rate is less than 0.0015 grams this is mainly due to the density of the composite is higher so the loss of carbide particles which trends decrease in wear rate Also when the percentage of MoS<sub>2</sub> at 6% offers minimum wear rate due to its self-lubrication properties of MoS<sub>2</sub>[25]. The figure 4B shows the interaction graph of applied load and percentage of tungsten carbide on wear rate. Both the matrix alloys and the composites showed a direct relationship between weight loss and applied load. When the load is increased from 20N to 30 N the wear rate of material is high. However, when the weight percentage of reinforcement increases, the wear rate somewhat decreased. Both weight loss during the same applied load increased approximately continuously as sliding distance increased [25]. Figure 4C and 4D shows the interaction graph of applied load and sliding speed and sliding distance on wear rate. Additionally, it was found that as the

applied load increased up to its maximum, the effect of the sliding distance grew more severe. This might be connected to the heat created when the two abrasive connecting portions were engaged in the process of abrasive wear [26]. The test material softened as a result of the produced heat, which increased as the sliding distance.

The figure 5A shows the contour plot for tungsten carbide and MoS<sub>2</sub> on coefficient of friction. The friction between the pin and the disc is low when the weight Percentage of WC is increased. Initially the contact if friction at 3 % to 6% the friction between the plates is slightly decreased. Further when the percentage of WC is at 9% and at 6 % of MoS<sub>2</sub> the friction between the pin and disc is reduced. The figure 5B shows the interaction plot for wt. % of tungsten carbide and applied load on coefficient of friction. The impact of applied load on the resistance to wear reduced as the weight percentage of reinforcing particles increases. This may be explained by the addition of tungsten carbide particles mixed the matrix alloy, which increased hardness and decreased real area of contact, hence enhancing reducing of friction coefficient [27]. It is clear that the reinforcing particles can function as load-bearing components in composite made of aluminum composites, improving their friction. The figure 5C and figure 5D shows the interaction plot for sliding speed, Sliding distances and applied load on coefficient of friction. When the sliding velocity is increased from 1.5 m/sec to 2 m/sec the fiction between the pin and disc increases. The largest abrasion occurs at higher applied loads and highest sliding distances, producing excess heat in the two contacting surfaces and softening the interracial interactions between the matrix and reinforcement [28]. However, the effect of the applied load became more essential as the sliding distance increased.

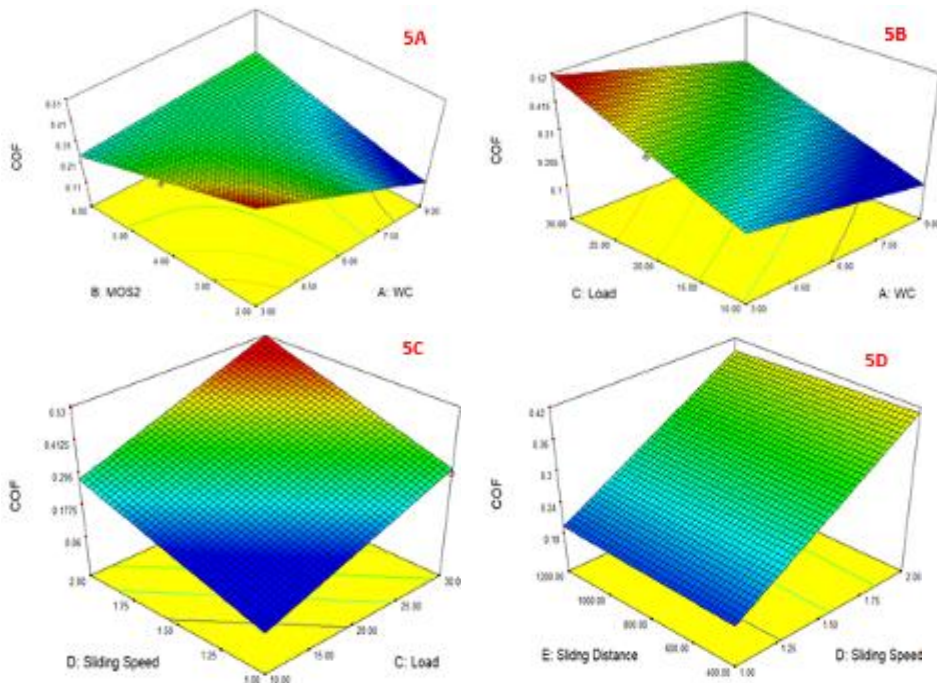


Fig. 5. Contour plot for input parameters vs coefficient of friction

Table 5. ANOVA for Wear Rate

Source	Sum of Square	df	Mean Square	F	p-value
Model	1.23E-05	9	1.37E-06	9.72	0.0001
A-WC	2.21E-06	1	2.21E-06	15.7	0.001
B-MoS2	8.25E-08	1	8.25E-08	0.59	0.0043
C-Load	3.93E-06	1	3.93E-06	27.95	0.0001
D-Sliding Speed	1.60E-06	1	1.60E-06	11.34	0.0037
E-Sliding Distance	1.08E-08	1	1.08E-08	0.076	0.0078
AB	1.35E-06	1	1.35E-06	9.59	0.0066
AC	9.65E-08	1	9.65E-08	0.69	0.0193
BC	2.26E-07	1	2.26E-07	1.6	0.0227
DE	2.90E-08	1	2.90E-08	0.21	0.0556
Residual	2.39E-06	17	1.41E-07		
Cor Total	1.47E-05	26			
R Square	91.20%				

ANOVA (Analysis of Variance) can be employed as a statistical method to analyze and compare the means of wear rates and coefficients of friction among multiple groups or experimental conditions. The ANOVA is employed for weight fraction of WC, MoS<sub>2</sub>, applied load, sliding speed and sliding distance. Table 5 and 6 shows the ANOVA value for wear rate and coefficient of friction. The results shows that weight percentage of WC and applied load are the most significant parameters which influences wear rate and coefficient of friction.

Table 6. ANOVA for coefficient of friction

Source	Sum of Square	df	Mean Square	F	p-value
Model	0.25	10	0.025	13.59	0.0001
A-WC	0.049	1	0.049	26.39	0.0001
B-MOS2	5.14E-04	1	5.14E-04	0.28	0.0605
C-Load	0.081	1	0.081	43.59	0.0001
D-Sliding Speed	0.03	1	0.03	16.03	0.001
E-Sliding Distance	5.56E-06	1	5.56E-06	3.01E-03	0.0957
AB	0.024	1	0.024	12.78	0.0025
AC	2.60E-04	1	2.60E-04	0.14	0.0712
BC	2.01E-03	1	2.01E-03	1.09	0.0312
CE	3.00E-06	1	3.00E-06	1.62E-03	0.0684
DE	4.81E-04	1	4.81E-04	0.26	0.0168
Residual	0.03	16	1.85E-03		
Cor Total	0.28	26			
R Square	92.29				



### 4.2 Regression Equation

Regression equations are mathematical models that help in understanding and predicting the relationship between two or more variables. The equation 3 and 4 shows the mathematical model for wear rate and coefficient of friction.

$$\begin{aligned} \text{Wear Rate} = & +2.175\text{E-}003 - 5.297\text{E-}004 * A - 1.279\text{E-}004 * B + 8.835\text{E-}004 * \\ & C + 7.878\text{E-}004 * D + 2.444\text{E-}005 * E + 8.781\text{E-}004 * A * B - 2.348\text{E-}004 * A * C - \\ & 2.538\text{E-}004 * B * C + 4.917\text{E-}005 * D * E \end{aligned} \quad (3)$$

$$\begin{aligned} \text{COF} = & +0.30 - 0.079 * A - 0.010 * B + 0.1 * C + 0.11 * D - 5.556\text{E-}004 * E + 0.12 * \\ & A * B - 0.012 * A * C - 0.024 * B * C + 5.000\text{E-}004 * C * E - 6.333\text{E-}003 * D * E \end{aligned} \quad (4)$$

### 4.3 Microstructure Analysis

The Figure 6a shows the worn-out surface which is identified through SEM images. Figure 6a shows the 9 % of WC and 4 % of MoS<sub>2</sub> and load of 10N. The figure 6b shows that 9 % of WC and 6 % of MoS<sub>2</sub> and load of 10N. When compared to figure 6a figure 6b has reduction in wear rate. Also, it can be found that the WC particles also have less worn-out area owing to its hardness value. It is commonly accepted that adding hard particles to aluminum alloys enhances the underlying alloy's wear resistance to a noticeable extent [29]. Good surface adhesion occurs between the matrices and non-reinforcement whenever refractory bits are firmly bonded to the matrix. According to numerous studies, the COF of crystalline MoS<sub>2</sub> is typically low, at 6% in a dry sliding condition, this lubricating performance of MoS<sub>2</sub> is unique due to its self-lubrication properties. Figure 6c shows the 6 % of WC and 6 % of MoS<sub>2</sub> and load of 20N. The figure 6c shows that 6 % of WC and 4 % of MoS<sub>2</sub> and load of 20N. When compared to figure 6d figure 6c exhibits better wear resistance. This is due to increased surface temperatures at the contact area encouraged the formation of low shear strength thermo on the rubbing surfaces [30]. The reduced resistive values were caused by a protecting tribo layer that accumulated on the surface of the materials at slower sliding speeds [31].

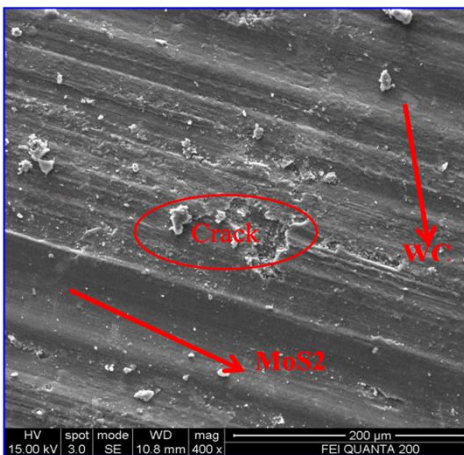


Fig. 6a. 9% WC & 4% MoS<sub>2</sub>, Load 10N

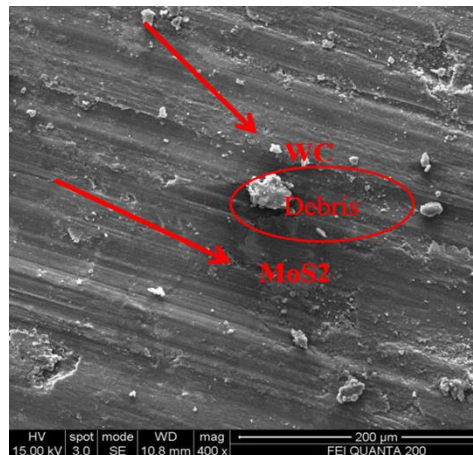


Fig. 6b. 9% WC & 6% MoS<sub>2</sub>, Load 10N

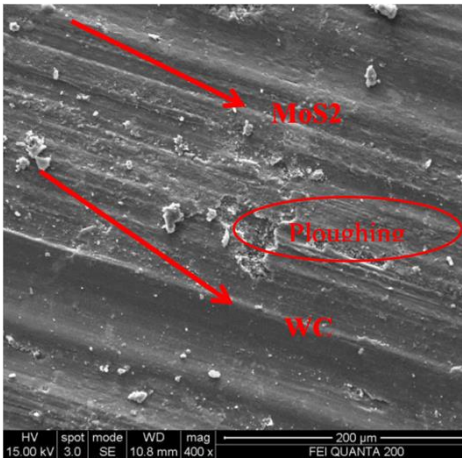


Fig. 6c. 6% WC & 6% of MoS<sub>2</sub>, Load 20N

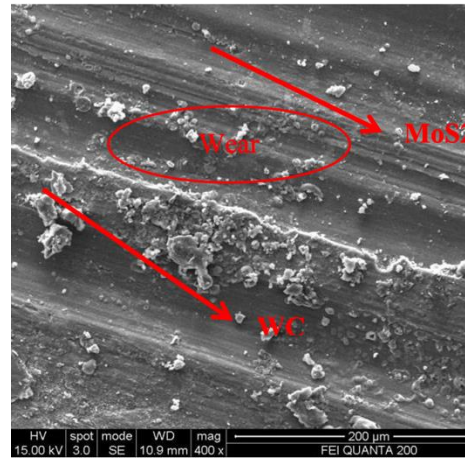


Fig. 6d. 6% of WC & 4% of MoS<sub>2</sub>, Load 20N

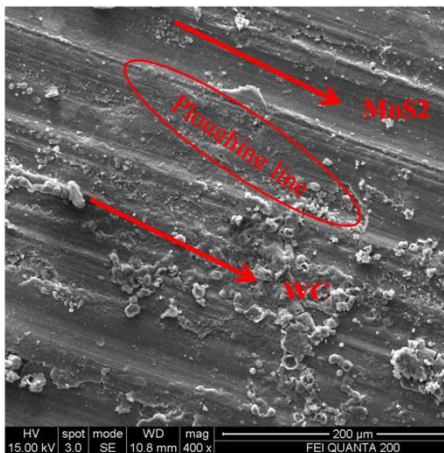


Fig 6e: 3% WC & 4% MoS<sub>2</sub>, Load 30N

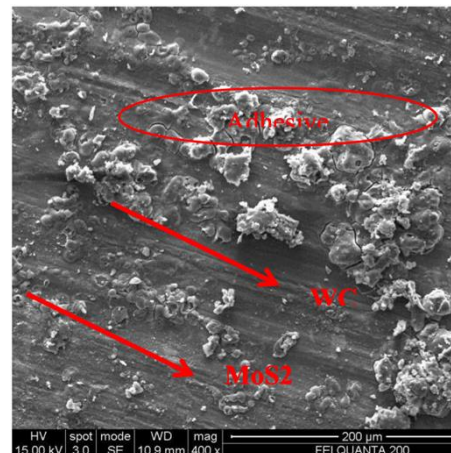


Fig. 6f. 3% WC & 2% MoS<sub>2</sub>, Load 30N

For a fixed sliding velocity, the rapid tribo layer covering formation at higher speeds tends to reduce the surface hardness of the composites. Figure 6e shows the 3 % of WC and 4 % of MoS<sub>2</sub> and load of 30N. The figure 6f shows that 3 % of WC and 2 % of MoS<sub>2</sub> and load of 30N. When compared to figure 6e figure 6f has significant loss of tungsten carbide particles due to low addition of MoS<sub>2</sub> particles. When the load reaches 30 N, the wear rate dramatically increases. In the event that the Composite's changeover load and velocity both significantly rise in higher load value. The rationalized adhesion of the pin substance to the counter surface, the increase in the softening of the surface structure, and the ability of more abrasive particles to penetrate the surface of the composites [32].

## 5. Conclusion

In this recent experiment, we successfully fabricated Al 6262/WC/MoS<sub>2</sub> hybrid composites using the stir casting technique, incorporating various weight percentages of Tungsten Carbide (WC) - specifically, 3%, 6%, and 9%. Taguchi optimization was applied to determine the optimal combination of input parameters for achieving improved wear rates and friction reduction. The experiment yielded important conclusions:

At a composition of 9% WC and 4% MoS<sub>2</sub>, the hardness reached 92.2 BHN. An increase in the weight percentages of both tungsten carbide and MoS<sub>2</sub> was found to enhance hardness, consequently leading to a reduction in wear rates. Taguchi optimization highlighted that the optimum combination for minimizing wear rates involved 9% WC, 6% MoS<sub>2</sub>, a 10N load, a sliding velocity of 1 m/sec, and a sliding distance of 400 m. The incorporation of hard particles significantly improved the wear resistance of the aluminum alloy base.

For achieving the lowest coefficient of friction, the optimal combination was identified as 9% WC, 6% MoS<sub>2</sub>, a 10N load, a sliding velocity of 1 m/sec, and a sliding distance of 400 m. Successful surface adhesion occurred between the matrices and non-reinforcement, particularly when refractory bits firmly bonded to the matrix. The addition of tungsten carbide particles to the matrix alloy increased hardness and reduced the real area of contact, thereby enhancing the reduction of the friction coefficient.

SEM analysis validated worn-out surfaces during dry sliding wear. The maximum occurrences of grooving, ploughing, micro-cutting, fracturing, and embrittlement were observed in the composite with 3% WC and 2% MoS<sub>2</sub> under a 30N load. This phenomenon was attributed to increased surface temperatures at the contact area, promoting the formation of a low shear strength thermo-affected layer on the rubbing surfaces. The reduced resistive values were linked to the presence of a protective tribo layer accumulating on the material surface, particularly under increased loads, resulting in a severe wear rate.

## References

- [1] Borenstein A, Hanna O, Attias R, Luski S, Brousse T, Aurbach D. Carbon-based composite materials for supercapacitor electrodes: a review. *Journal of Materials Chemistry A*, 2017; 5(25):12653-12672. <https://doi.org/10.1039/C7TA00863E>
- [2] Zhang Z, Xiao F, Qian L, Xiao J, Wang S, Liu Y. Facile synthesis of 3D MnO<sub>2</sub>-graphene and carbon nanotube-graphene composite networks for high-performance, flexible, all-solid-state asymmetric super capacitors. *Advanced Energy Materials*, 2014; 4(10): 1400064. <https://doi.org/10.1002/aenm.201400064>
- [3] Roy Atanu, Apurba Ray, Samik Saha, Monalisa Ghosh, Trisha Das, Biswarup Satpati, Mahasweta Nandi, Sachindranath Das. NiO-CNT composite for high performance supercapacitor electrode and oxygen evolution reaction. *Electrochimica Acta*, 2018; 283: 327-337. <https://doi.org/10.1016/j.electacta.2018.06.154>
- [4] Sahu SR, Rikka VR, Haridoss P, Chatterjee A, Gopalan R, Prakash R. A novel  $\alpha$ -MoO<sub>3</sub>/single-walled carbon nanohorns composite as high-performance anode material for fast-charging lithium-ion battery. *Advanced Energy Materials*, 2020;10(36): 2001627. <https://doi.org/10.1002/aenm.202001627>
- [5] Lou Zheng, Lili Wang, Kai Jiang, Zhongming Wei, Guozhen Shen. Reviews of wearable healthcare systems: Materials, devices and system integration. *Materials Science and Engineering Reports*, 2020; 140: 100523. <https://doi.org/10.1016/j.msere.2019.100523>
- [6] Anil Kumar R, Radhika N. Enhancement of mechanical and wear properties of tungsten carbide coated AA 6063 alloy using detonation gun technique. *Transactions of the IMF*, 2018; 96 (4):212-219. <https://doi.org/10.1080/00202967.2018.1477265>
- [7] Balaraj V, Nagaraj Kori, Madeva Nagaral, Auradi V. Microstructural evolution and mechanical characterization of micro Al<sub>2</sub>O<sub>3</sub> particles reinforced Al6061 alloy metal composites. *Materials Today: Proceedings*, 2021; 47: 5959-5965. <https://doi.org/10.1016/j.matpr.2021.04.500>
- [8] Raksha MS, Madeva Nagaral, Satish Babu Boppana, Chandrashekar Anjinappa, Mohammad Shahiq Khan, Mohammed Osman Abdul Wahab, Saiful Islam, Vivek Bhardwaj, Rohini Kumar Palavalasa, Mohammad Amir Khan, Abdul Razak, Impact of

- boron carbide particles and weight percentage on the mechanical and wear characterization of Al2011 alloy metal composites, ACS Omega, 2023; 8, 26:23763-23771. <https://doi.org/10.1021/acsomega.3c02065>
- [9] Madeva N, Shivananda BK, Virupaxi A, Kori SA. Development and mechanical-wear characterization of Al2024-nano B4C composites for aerospace applications. Strength, Fracture and Complexity, 2020; 13, 1:1-13. <https://doi.org/10.3233/SFC-190248>
- [10] Gupta JG, Avinash KA. Engine durability and lubricating oil tribology study of a biodiesel fuelled common rail direct injection medium-duty transportation diesel engine. Wear, 2021; 486: 204104. <https://doi.org/10.1016/j.wear.2021.204104>
- [11] Manivannan I, Ranganathan S, Gopalakannan S, Suresh S. Mechanical properties and tribological behavior of Al6061-SiC-Gr self-lubricating hybrid nanocomposites. Transactions of the Indian Institute of Metals, 2018; 71, 8: 1897-1911. <https://doi.org/10.1007/s12666-018-1321-0>
- [12] Saravanakumar A, Bhuvaneshwari V, Karthick Raja N, Karthi P. Tribological behaviour of AA2219/MoS2 metal matrix composites under lubrication. AIP Conference Proceedings, 2020; 2207.
- [13] Jojith, Radhika N. Mechanical and tribological properties of LM13/TiO2/MoS2 hybrid metal matrix composite synthesized by stir casting. Particulate Science and Technology, 2019; 37 (5): 570-582. <https://doi.org/10.1080/02726351.2017.1407381>
- [14] Madeva Nagaral, Auradi V, Bharath V. Mechanical characterization of 100 micron sized silicon carbide particles reinforced Al6061 alloy composites. Metallurgical and Materials Engineering, 2022; 28 (1): 17-32. <https://doi.org/10.30544/639>
- [15] Siddeshkumar NG, Suresh R, and Shiva Shankar GS. High temperature wear behavior of Al2219/n-B4C/MoS2 hybrid metal matrix composites. Composites Communications, 2020; 19: 61-73. <https://doi.org/10.1016/j.coco.2020.02.011>
- [16] Preethi K, Raju TN, Shivappa HA, Shashidhar S, Madeva Nagral. Processing, microstructure, hardness and wear behavior of carbon nanotube particulates reinforced Al6061 alloy composites. Materials Today: Proceedings, 2023; 81: 449-453. <https://doi.org/10.1016/j.matpr.2021.03.608>
- [17] Kumar C, Ramesh R, Malarvannan, Jaiganesh V. Role of SiC on mechanical, tribological and thermal expansion characteristics of B4C/Talc-reinforced Al-6061 hybrid composite. Silicon, 2020; 12 (6): 1491-1500. <https://doi.org/10.1007/s12633-019-00243-0>
- [18] Pankaj J, Sridhar , Madeva N, Vijay KM, Jayasheel H. A comparative study on microstructure and mechanical properties of A356-B4C and A356-Graphite composite. International Journal of Mechanical and Production Engineering Research and Development, 2018; 8 (2): 273-282. <https://doi.org/10.24247/ijmperdapr201830>
- [19] Zhai W, L B, Runhua Z, Xueling F, Guozheng K, Yong L, Kun Z. Recent progress on wear-resistant materials: designs, properties, and applications. Advanced Science, 2021; 8 (11): 2003739. <https://doi.org/10.1002/advs.202003739>
- [20] Moazami G, Mohammad, A Ne. Tribological behavior of self lubricating Cu/MoS2 composites fabricated by powder metallurgy. Transactions of Nonferrous Metals Society of China, 2018; 28 (5): 946-956. [https://doi.org/10.1016/S1003-6326\(18\)64729-6](https://doi.org/10.1016/S1003-6326(18)64729-6)
- [21] Kumar , Saravanan R, Madeva Nagaral. Dry sliding wear behavior of nano boron carbide particulates reinforced Al2214 alloy composites. Materials Today: Proceedings, 2023; 81: 191-195. <https://doi.org/10.1016/j.matpr.2021.03.065>
- [22] Alaneme KK, Adetomilola V F, Nthabiseng B M. Development of aluminium-based composites reinforced with steel and graphite particles: structural, mechanical and wear characterization. Journal of Materials Research and Technology, 2019; 8(1): 670-682. <https://doi.org/10.1016/j.jmrt.2018.04.019>

- [23] Zhang Y, Panpan L, Li Ji Xiaohong L, Hongqi W, Lei Ch, Hongxuan L Zhiliang J. Tribological properties of MoS<sub>2</sub> coating for ultra-long wear-life and low coefficient of friction combined with additive g-C<sub>3</sub>N<sub>4</sub> in air. *Friction*, 2021; 9(4): 789-801. <https://doi.org/10.1007/s40544-020-0374-3>
- [24] Öztürk B, Fazlı A, Sultan Ö. Hot wear properties of ceramic and basalt fiber reinforced hybrid friction materials. *Tribology International*, 2007; 40(1): 37-48. <https://doi.org/10.1016/j.triboint.2006.01.027>
- [25] Saravanakumar ABhuvaneswari V, Gokul G. Optimization of wear behaviour for AA2219-MoS<sub>2</sub> metal matrix composites in dry and lubricated condition. *Materials Today: Proceedings*, 2020; 27: 2645-2649. <https://doi.org/10.1016/j.matpr.2019.11.087>
- [26] Bharathi V, Ramachandra M, Srinivas S. Influence of fly ash content in aluminium matrix composite produced by stir-squeeze casting on the scratching abrasion resistance, hardness and density levels. *Materials Today: Proceedings*, 2017;4(8): 7397-7405. <https://doi.org/10.1016/j.matpr.2017.07.070>
- [27] Nemati N, Khosroshahi R, Emany M, Zolriasatein A. Investigation of microstructure, hardness and wear properties of Al-4.5 wt.% Cu-TiC nanocomposites produced by mechanical milling. *Materials and Design*, 2011; 32 (7): 3718-3729. <https://doi.org/10.1016/j.matdes.2011.03.056>
- [28] Jalilvand MM, Yousef ME. Effect of mono and hybrid ceramic reinforcement particles on the tribological behavior of the AZ31 matrix surface composites developed by friction stir processing. *Ceramics International*, 2020; 46(12): 20345-20356. <https://doi.org/10.1016/j.ceramint.2020.05.123>
- [29] Murali MR, Kempaiah UN, Manjunatha B, Madeva N, Auradi V. Processing and wear behavior optimization of B<sub>4</sub>C and rice husk ash dual particles reinforced ADC12 alloy composites using Taguchi method. *Materials Physics & Mechanics*, 2022; 50, 2:304-318.
- [30] Madeva Na, Deshapande RG, Auradi V, Satish BB, Samuel D, Anilkumar MR. Mechanical and wear characterization of ceramic boron carbide reinforced Al2024 alloy metal composites. *Journal of Bio-and Tribo-Corrosion*, 2021; 7: 1-12. <https://doi.org/10.1007/s40735-020-00454-8>
- [31] Cimenoglu H, Atar E, Motallebzadeh A. High temperature tribological behaviour of borided surfaces based on the phase structure of the boride layer. *Wear*, 2014; 309(1-2): 152-158. <https://doi.org/10.1016/j.wear.2013.10.012>
- [32] Daniel AA, Sakthivel M, Sudhagar S. Dry sliding wear behaviour of aluminium 5059/SiC/MoS<sub>2</sub> hybrid metal matrix composites. *Materials Research*, 2017; 20: 1697-1706. <https://doi.org/10.1590/1980-5373-mr-2017-0009>

## The effect of multi-walled carbon nanotubes on mechanical properties and water adsorption of lightweight foamed concrete

Rami J. Sldozian<sup>1,a, 2,b</sup>, Alexander E. Burakov<sup>2,c</sup>, Dhafer Z. M. Aljaboobi<sup>2,d</sup>, Ali Jihad Hamad<sup>3,e</sup>, Alexey G. Tkachev<sup>2,f</sup>

<sup>1</sup>Applied Sciences Department, University of Technology, Iraq

<sup>2</sup>Tambov State Technical University, Tambov, Russian Federation

<sup>3</sup>Department of Building and Construction Technology Engineering, Engineering Technical College of Mosul, Northern Technical University, Mosul, Iraq

### Article Info

#### Article history:

Received 19 Nov 2023

Accepted 02 Feb 2024

#### Keywords:

Lightweight concrete;  
Carbon nanotubes;  
Nanomodification;  
CVD synthesis;  
Compression and  
flexural strength tests;  
Water absorption

### Abstract

The paper investigates the impact of carbon nanotube-based modifiers on the performance characteristics of lightweight foamed concrete (LFC). The method involves saturating quartz sand with a solution containing a catalyst for carbon nanotube (CNT) growth, followed by the subsequent chemical vapor deposition (CVD) synthesis of CNTs. Evaluation of nanomodified sand samples was conducted using SEM and TEM, thermogravimetry, Raman spectroscopy, and XRD. Compression and flexural strength tests of (LFC) specimens indicated that the optimal proportion of nanomodified sand introduced is 1% by weight with a particle size of 0.16 mm. This resulted in a notable 35% increase in compressive strength and an approximately 32% improved in flexural strength. Furthermore, the modified sample with CNT-based sand exhibited a 27% reduction in water absorption. The paper also presents a potential mechanism to explain the impact of carbon nanotube-based modified sand on the evolving structure of (LFC).

© 2024 MIM Research Group. All rights reserved.

## 1. Introduction

Cementitious materials have emerged as the predominant choice for structural applications in civil engineering, primarily attributed to their economical pricing and consistent operational effectiveness. Globally, Portland cement has garnered substantial utilization as one of the most prevalent commodities. [1-4].

The key characteristics of a structural material encompass its strength, rigidity, resistance to fractures, energy absorption potential, and ductility. Nevertheless, enhancing all these attributes poses a challenge when it comes to traditional cement-based materials [5-8]. These materials are associated with certain established drawbacks, such as relatively limited tensile strength and suboptimal viscosity. Concrete is prone to the formation of cracks, providing pathways for the infiltration of water and corrosive substances like de-icing salts. This, in turn, initiates the deterioration of both the material and the commonly employed reinforcing steel, giving rise to various concerns regarding their long-term resilience and safety [9,10]. The addition of nanoscale particles can improve the properties of concrete mainly because of the effect of increased surface area on reactivity and because the cement paste fills the nanopores. Nano-silica and nano titanium dioxide are two of the most well-known additives in the field of nanomodified concrete [11]. Moreover,

\*Corresponding author: [100385@uotechnology.edu.iq](mailto:100385@uotechnology.edu.iq)

<sup>a</sup>[orcid.org/0000-0003-2056-9176](https://orcid.org/0000-0003-2056-9176); <sup>b</sup>[orcid.org/0000-0003-0850-9365](https://orcid.org/0000-0003-0850-9365); <sup>c</sup>[orcid.org/0000-0003-4871-3504](https://orcid.org/0000-0003-4871-3504);

<sup>d</sup>[orcid.org/0000-0002-8248-5050](https://orcid.org/0000-0002-8248-5050); <sup>e</sup>[orcid.org/0000-0001-5591-4983](https://orcid.org/0000-0001-5591-4983); <sup>f</sup>[orcid.org/0000-0001-5099-9682](https://orcid.org/0000-0001-5099-9682)

DOI: <http://dx.doi.org/10.17515/resm2024.86ma1119rs>

Res. Eng. Struct. Mat. Vol. 10 Iss. 3 (2024) 1139-1154

nanomaterials may improve the ductility and compressive strength of concrete. Concrete's strength and ductility can also be improved by using carbon nanotubes (CNTs) and nanofibers. Furthermore, the use of nanomodified cements or nano-sized paste additives can improve shrinkage characteristics and reduce permeability, both of which can increase the strength of concrete [12–15]. Concrete's long-term and early shrinkage could be effectively reduced with the addition of CNTs, that can be attributed to the filler, nucleation, and bridging properties of CNTs. One way that CNTs reduce capillary stresses is through their filler and nucleation effect, which reduces the amount of fine pores between hydration products because of their small diameters (20–40 nm) and high surface area [16,17].

The utilization of nanomaterials within cement, aimed at enhancing its mechanical properties, stands as a highly promising research frontier. Numerous investigations have delved into the integration of aluminum and clay in nano size [18-21]. When a small quantity of nanoparticles is uniformly distributed throughout a cement paste, hydrated cement compounds precipitate onto the nanoparticles due to their elevated surface energy. Consequently, these nanoparticles serve as nucleation sites, expediting the growth of the cement structure. C3S dissolution and the details of the C-S-H in cement paste have been observed to occur more quickly when colloidal nano silica is added a) Nanoparticle filling of the concrete pores and (b) the pozzolanic reaction of nano-SiO<sub>2</sub> with Ca(OH)<sub>2</sub> yielding additional C-S-H are two more mechanisms for improving performance. Particle size and the degree to which nanoparticles are effectively dispersed within the cement determine which method is best; colloidal dispersions work better than powdered versions [22,23].

In the research conducted by Sedaghatdoost et al. [24], it was documented that the incorporation of 0.1 wt. % the cement slurry that contain carbon nanotubes (CNT) maybe led to improve the flexural and compressive strength, with increases of up to 35%, 8%, and 11.2%, respectively, observed after a 28-day curing period. It is possible to explain this phenomenon by the nucleation effects of CNTs, which speed up hydration reactions. Hydrated products attach themselves to the carbon nanotubes (CNTs) and create a cohesive layer that covers the whole surface. Its filling qualities also enable CNTs to lower the average diameter and total volume of pores in cementing materials [25-27].

However, their limited dispersibility presents a challenge when using carbon nanotubes (CNTs) as nano-reinforcing agents in cementitious materials. When using nanofillers, such as carbon nanotubes (CNTs), in cement systems, the best reinforcement happens when the nanofillers are distributed uniformly and evenly. Isfahani et al.'s research indicates that a number of factors contribute to poor dispersion, including CNTs' large surface area and nano diameter as well as their propensity to form tightly bound bundles as a result of strong van der Waals forces. Furthermore, highly entangled agglomerates form within the liquid phase due to the high form factor and flexibility of CNTs [28-29]. Similarly, the existing literature underscores the recurrent issue of CNT agglomeration, which hampers their uniform distribution in the cement slurry. This lack of even distribution limits the CNTs' capacity to create an effective and continuous network within the substrate, one that can adequately support load transfer and mitigate crack formation [30-32].

In addition, the agglomeration of CNTs contributes to the creation of stress concentration points, resulting in the emergence of cracks [33]. Thus, achieving a consistent dispersion of CNTs is imperative, serving as a prerequisite for the effective utilization of CNTs in binding materials [34]. It can be confidently asserted that the enhancement of mechanical properties in the ultimate composite is closely linked to the uniform and effective dispersion of CNTs, allowing them to serve as connecting bridges between voids and cracks within porous cement-based structures.

To achieve this goal, the processes of introducing CNTs into cement-based materials (paste, mortar, and concrete) have to be complicated, in particular, by the obligatory use of additives or surfactants, as well as by preliminary chemical functionalization of CNTs [35-38].

In this paper, the authors investigated the properties of foamed concrete. Foamed concrete is a type of concrete that has a set of some useful properties (special porous structure, excellent anti-seismic, non-combustible and thermal insulation characteristics), making it more and more popular in construction. It is used as an effective structural and insulating material for roofing, non-bearing walls and thermal insulation of heat pipes [39, 40]. The use of foamed concrete in buildings provides a reduction in construction costs, makes the construction process simpler. In addition, foamed concrete is a relatively "environmentally friendly" building material [41].

This study proposes an innovative method for effectively integrating carbon nanotubes (CNTs) into cement matrices without the need for additives, surfactants, or intricate chemical procedures. The approach involves pre-growing CNTs on sand particles before introducing them into the solution. The synthesis of CNTs on sand grains utilizes the (CVD) method, involving impregnating the sand with a catalyst for nanotube growth and employing a propane-butane mixture as a carbon source. This method offers a significant advantage by enabling the industrial production of nanomodified cement materials with enhanced physical, mechanical, and operational characteristics. Importantly, it eliminates the need for labor-intensive and costly stages of chemical functionalization of CNTs, as well as the use of surfactants and other functional additives.

## **2. Materials and Methods**

### **2.1. Growing CNTs on the surface of sand particles**

To create a layer of (CNTs) on the sand, an aqueous catalyst solution was prepared using precursors such as  $(\text{NH}_4)_6\text{Mo}_7\text{O}_{24}\cdot 4\text{H}_2\text{O}$ ,  $\text{Al}(\text{NO}_3)_3\cdot 9\text{H}_2\text{O}$ ,  $\text{Co}(\text{NO}_3)_2\cdot 6\text{H}_2\text{O}$ , and  $\text{Mg}(\text{NO}_3)_2\cdot 6\text{H}_2\text{O}$ . Citric acid ( $\text{C}_6\text{H}_8\text{O}_7$ ) served as a complexing agent. The resulting solution was continuously agitated using a magnetic stirrer at  $60^\circ\text{C}$  until complete dissolution of the initial components. Subsequently, quartz sand was introduced into the catalyst, and the impregnation process was carried out at  $140^\circ\text{C}$  within a fume hood. This step resulted in the formation of a spatial fractal gel structure containing chelate complexes with active catalyst metals, including Mo, Co, Mg, and Al, on the surface of the sand particles [42].

The sand with catalyst was subsequently heat-treated in an inert argon atmosphere within a CNT synthesis reactor at a temp of  $500^\circ\text{C}$  for a duration of one hour (conducted by NanoTechCenter Ltd., Tambov, Russia). This thermal treatment resulted in the creation of active sites for the growth of carbon nanotubes (CNTs) on the sand, particularly involving metal oxides like Mo, Co, Mg, and Al. After this stage, a carbon-containing gas, specifically a mixture of propane and butane, was introduced into the reactor, and the temp was raised to  $600^\circ\text{C}$ . The synthesis process lasted approximately 30 minutes. Once the CNT synthesis was completed, the modified sand was subjected to crushing and subsequent sieving.

### **2.2 Foamed Concrete Materials**

The lightweight concrete was made with Portland cement type I (Bazyan, Iraq), ASTM C150, and gradient quartz sand (Dwekhla, Alanbar, Iraq) from zone II. The sand had a specific gravity of 2.7 (Table 1). The sieve analysis shown in table 1 conforms to Iraqi Standard 45/1984. The foaming agent under the trademark MAXPN (Russia) was added.



Table 1. Granulometric composition of sand.

Partial residues on sieves, %						Specific gravity
2.5	1.25	0.63	0.315	0.16	<0.16	
15	16	16	30	21	2	2.73

### 2.3. Preparing Samples of Lightweight Foamed Concrete

For mixing, tap water was utilized, with a (water/cement) ratio of 0.5. The modified sand was employed with a sand weight ratio of (0.1, 0.2, 0.5, and 1%). After sieving the sand, three different particle sizes (0.63, 0.315, and 0.16 mm) were chosen. Then the mortar was prepared by adding water. After that, the lightweight-foamed concrete was created by adding the foam to the mixture—1.6 kg per m<sup>3</sup>. A prism mold was cast in the concrete mixture (40 x 40 x 160 mm). Samples were removed after 24 hours from the mold and water immersion to cure at 23±2°C according to ASTM C31. The compressive and flexural strengths were calculated according to Russian Standards 310.4-76 after 28 days.

The testing machine was single axle with a capacity of 2000 kN and an applied load of 0.4 MPa/s. The density was (1600–1750 Kg/m<sup>3</sup>), and the combination was calculated by volume ratios. The mix ratios are shown in Table 2.

Table 2. Preparation of the concrete mixture

Mix Proportion	W/C	Cement, Kg/ m <sup>3</sup>	Sand, Kg/m <sup>3</sup>	Water, Kg/ m <sup>3</sup>	Voids %
(1:1)	0.5	650	650	280	25-30

### 2.4. Material Characterization

Using scanning electron microscopy (SEM) with an Inspect S50 FEI ranging from 1 mm to 500 µm, the morphological and structural properties of the nanomodified sand were investigated. Additionally, the surface of foamed concrete specimens was examined using SEM analysis. (Thermo Fisher Scientific, Czech Republic), and transmission electron microscopy (TEM) using an FEI Tecnai Spirit M3000 (Zurich, Switzerland). A Bruker D8 ADVANCE X-ray diffractometer (Bruker, Germany) was used to determine the qualitative and quantitative phase composition of the nanomodified sand. Raman spectra were obtained on a DXR™ Raman microscope (Thermo Scientific Instruments Group, Waltham, MA, USA).

## 3. Results and Discussion

### 3.1. Assessing the Effect of CNTs Synthesis Time on The Strength Characteristics of Lightweight Concrete

To assess the effect of CNTs synthesis time on the sand surface, an experiment was carried out in which 1% of nanomodified sand with a fraction of 0.16 mm was added to the composition of the foamed concrete mixture. During the experimental investigations, the duration of carbon nanotube (CNT) growth was altered, with durations of 5, 15, 30, and finally 60 minutes being tested. The outcomes of these experiments are illustrated in Figures 1 and 2.

As indicated by Figures 1 and 2, the optimum synthesis time appears to be 30 minutes, during which a consistent and uniform structure of carbon nanotubes (CNTs) is established on the surface of the sand particles. Prolonging the synthesis beyond this point is a waste of time and may lead to the catalyst used for CNT growth becoming deactivated. Consequently, an extended synthesis period can result in a reduction in the proportion of

well-ordered CNTs, an increase in structural defects, and the formation of a notable quantity of disordered carbon.

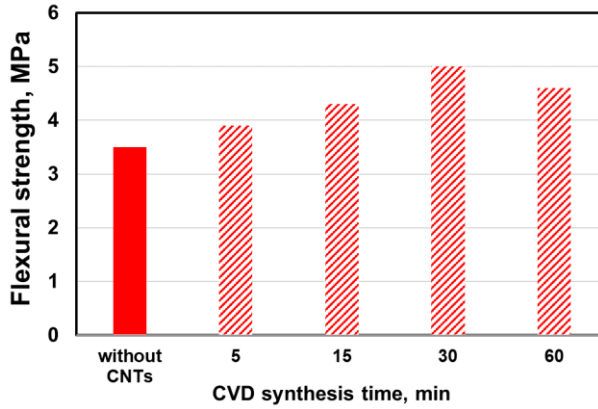


Fig. 1. Effect of CNTs synthesis time on sand surface on flexural strength

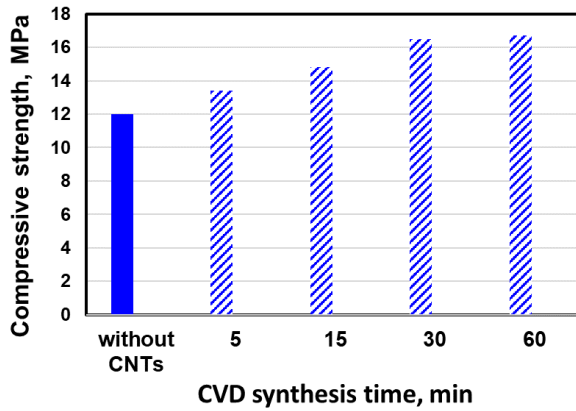


Fig. 2. Effect of CNTs synthesis time on sand surface on compressive strength

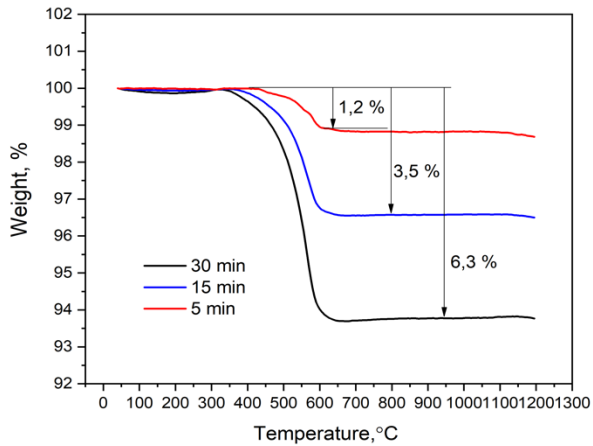


Fig. 3. TGA of nanomodified sand samples with different CNTs synthesis times

Additionally, it's worth noting the consistent progression in the strength details of foamed concrete containing modified sand. This can be attributed to the growing concentration of CNTs on the surface of sand over time, a phenomenon substantiated by thermogravimetric analysis, as depicted in Figure 3.

Considering to Figure 3, all the curves exhibit a notable decline in sample mass starting at 400°C. Specifically, at 600°C, it was observed that for a 5-minute synthesis, there was a weight loss of 1.2%, while for 15 minutes, the loss was 3.5%, and for 30 minutes, it increased to 6.3%. These weight loss percentages can be attributed to the CNTs grown on the surface of sand, as it is at 600°C that CNT destructurization occurs. Consequently, the 30-minute synthesis yielded the most substantial increase in CNT mass.

### 3.2 Characterization of Nanomodified Sand Samples

According to the SEM and TEM, the sand surface is covered with a layer of CNTs (Fig. 4, a). The nanotubes have an average diameter of approximately 30-50 nm, and the material also includes catalyst particles with diameters ranging from 30 to 70 nm. It can be seen in the TEM-image (Fig. 4, b) that the CNTs have an internal channel with a diameter of 10–20 nm.

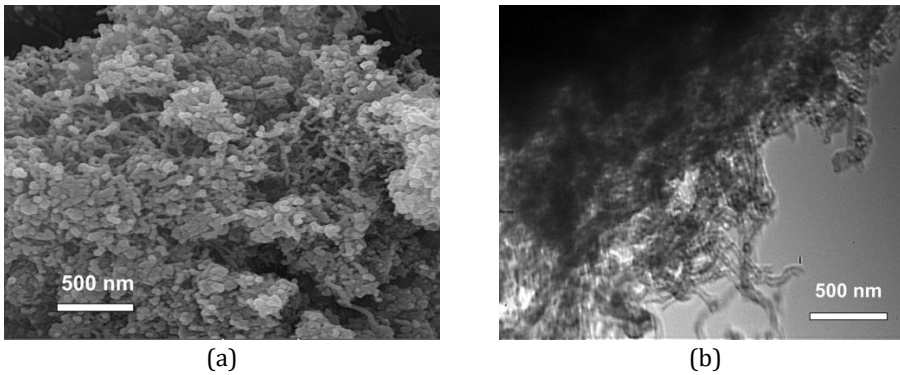


Fig. 4. SEM- (a) and TEM-image (b) of the nanomodified sand

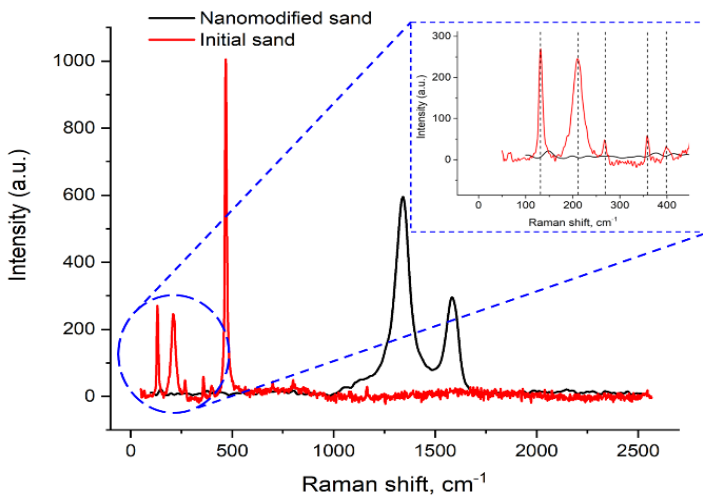


Fig. 5. Raman spectra of nanomodified sand filler and original sand

The Raman spectroscopy is considered to be an effective tool for the characterization of carbon nanomaterials because it provides information, in particular, on the degree of order

and on the purity of the material. The existence of carbon forms in the material can be tested from the characteristic bands in the spectrum (Fig. 5).

D-band (approximately 1340  $\text{cm}^{-1}$ ) indicates the presence of structural defects in the sample. G-band (approximately 1550–1600  $\text{cm}^{-1}$ ) informs about the degree of ordering of the graphene structure in the material. The third visible 2D signal (defined as the mode D overtone) is visible at about 2700  $\text{cm}^{-1}$  [43].

As can be seen from Fig. 5, the spectral pattern of the original and nanomodified sand is significantly different. The original sand has high intensity peaks at 130, 210, 467  $\text{cm}^{-1}$ , as well as weak peaks at 270, 360, 400  $\text{cm}^{-1}$ . The resulting spectrum is characteristic of the  $\beta\text{-SiO}_2$  crystal lattice [44]. The following characteristic lines were identified in the nanomodified sample: D  $\sim$  1345  $\text{cm}^{-1}$  band, G  $\sim$  1571  $\text{cm}^{-1}$  band, and 2D  $\sim$  2694  $\text{cm}^{-1}$  band. This observation verifies the existence of imperfect CNTs on the sand, since the D band is much more intense than the G band. The diffraction pattern of the original sand (Fig. 6) contains quartz ( $\beta\text{-SiO}_2$ ) as the main mineral [45, 46].

The XRD pattern (Fig. 3) shows several bands with peaks (0 0 2), (1 0 0), and (1 1 0), which correspond to carbon structures [43]. However, only the (0 0 2) reflection has a high intensity, while the other peaks are relatively small. The peak (0 0 2) is located at  $2\theta = 26^\circ$ . Reflection (1 0 0) at  $2\theta = 42^\circ$  corresponds to the CNT interlayer distance. The remaining peaks are attributed to quartz.

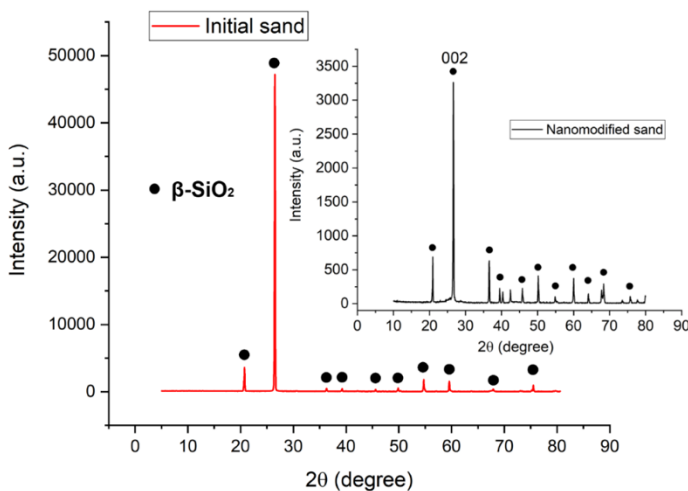


Fig. 6. X-ray diffraction pattern of nanomodified CNT sand

### 3.3. Assessing The Effect of The Percentage of Introduced Nanomodified Sand and Its Fraction on Strength Characteristics and Water Absorption

In this paper, the introduction of nanomodified sand additives of three fractions of 0.16, 0.315 and 0.63 mm was studied. The percentage of introduced nanomodified sand was: 0.2; 0.5; 1; 2 wt. %. The results are shown in Figs. 7, 8.

The maximum increase in compressive strength ( $\sim$  35%) is observed when adding 1% wt. nanomodified sand filler with a size of 0.16 mm, an increase in flexural strength of  $\sim$  32%.

It is assumed that the smaller the size of the sand particles, the greater the specific surface area they have, which will allow the synthesis of large quantities of CNTs. In addition, with the same weight of different fractions, the 0.16 mm fraction will contain a larger number of particles, therefore, the contact area of CNTs with cements will be increased.

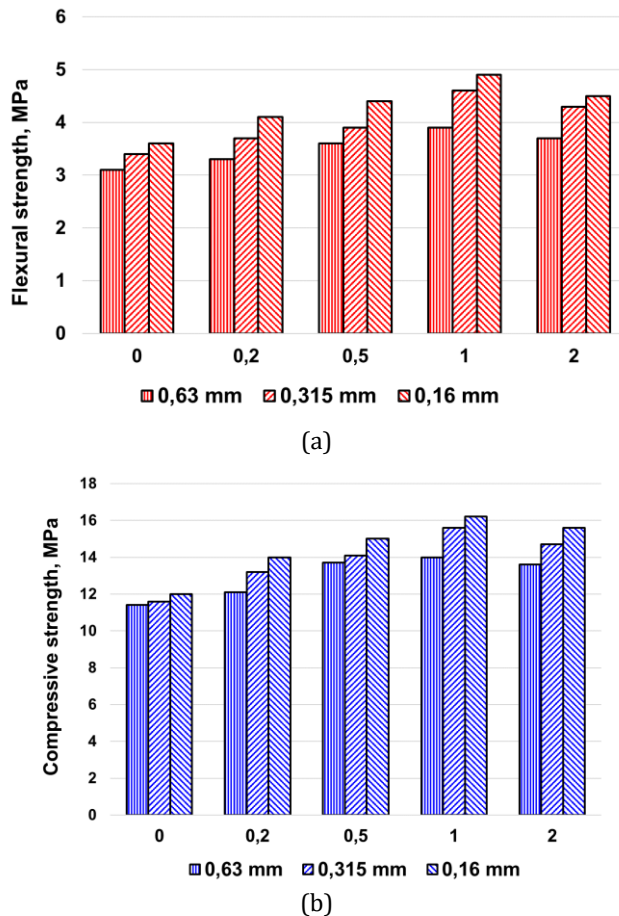
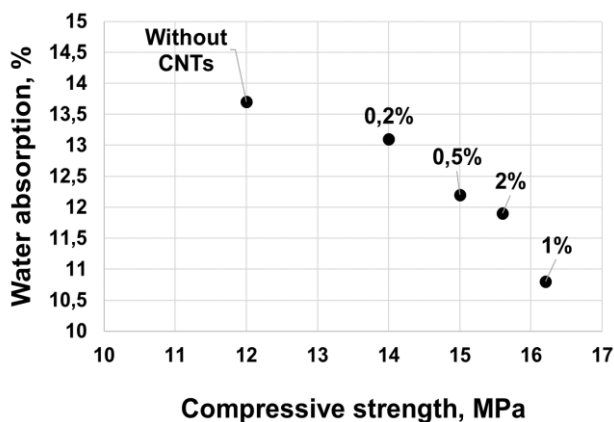
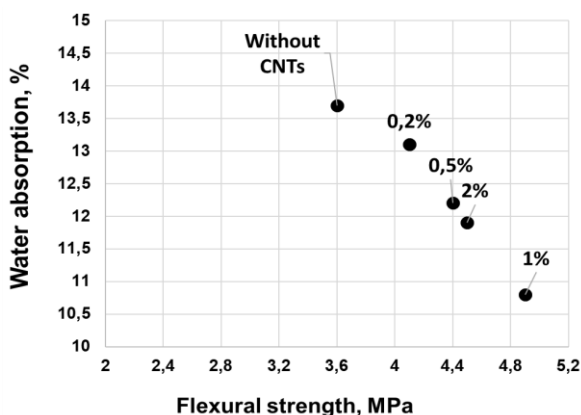


Fig. 7. The flexural (a) and compressive (b) strength test

Thus, it was found that when making 1% wt. nanomodified sand filler with a size of 0.16 mm, the minimum value of water absorption is achieved (27% less than the control sample without CNTs). The reduction in the percentage of water absorption may be due to the hydrophobic nature of the CNT surface. Thus, by adding CNTs to the cement mixture, the inter pore walls of the concrete are compacted and, as a consequence, the access of water to the volume of concrete is reduced. During the hydration of Portland cement, a number of chemical transformations occur, due to which needle-shaped crystals appear on the surface of cement grains when interacting with water. In a short time, the number of these neoplasms increases, and a so-called “reinforcing” gel is formed, which forms a developed spatial network. Then, after 8-10 hours, the gelation process continues and the entire volume is filled with calcium hydro silicates and their modifications, depending on the composition of the cement composition. The remaining voids are filled with clinker minerals. After the hydration process is completed, the cement stone hardens and becomes durable. Considering the above, in order to influence the chemical transformations during the hydration of cement, it is necessary to introduce additional chemically active reagents into the cement mixture. In this work, the authors suggest that CNTs synthesized on the surface of sand, in addition to accelerating the hydration process due to the active functional surface - the CNT shell creates an increased surface area of the sand. Therefore, nanomodified sand creates additional centers for crystal formation, thereby intensifying and qualitatively improving the cement hardening process.



(a)



(b)

Fig. 8. The effect of the percentage of introduced nanomodified sand on the water absorption of lightweight concrete

### 3.4. Substantiation of the Effect of Improving the Mechanical and Operational Characteristics of Concrete

Using carbon nanotubes to modify different types of concrete materials offers significant advantages over using unmodified concrete; they have a positive effect on the strength properties of samples, Improves the strength of concrete by reducing crack growth and propagation, thus improving the strength properties of concrete [47].

According to the literature review, carbon nanotubes act as crystallization centers for calcium silicate in hardened foam concrete and stimulate the structure formation of hardened calcium silicate binders with high crystallinity, observed in the pore walls compared to conventional control samples Compared to traditional control samples [48,49].

There are multiple interaction mechanisms between CNTs and cement mortar, the most important of which is the crack filling provided by carbon nanotubes [50]. The microstructure of concrete samples can change in the presence of carbon nanotubes for hydration products. The area adjacent to the surface of the CNTs (which affects the properties of the composite) is affected by the kind of the interaction of the CNTs with the cement (e.g., chemical bonds between surfaces, van der Waals forces), and interwoven).

These mechanisms also count on the chemical bonds between CNTs and hydrates [51]. The study also found that introducing carbon nanotubes into cementitious materials through nanoindentation will lead to the make of a large amount of high-hardness C-S-H in the composite. [52, 53]. The hydration products formed near the CNT surface fill the free space between the particles in the pore structure of the cement stone, while the pores in the sample without the nano modifier remain empty. As a result, the total porosity decreases and the concrete density increases, thus increasing the mechanical properties of the sample [53].

However, in order to improve the strength and technical properties of concretes, it is necessary to obtain a uniform dispersion of CNTs so that they act as effective structure formers and hydration accelerators, as well as connecting bridges between the boundaries of cracks and voids in a porous cement-based matrix. The development of new methods and equipment to control the problems of agglomeration and uneven distribution of CNTs in the structure of a concrete sample is very relevant. The synthesis of CNTs directly on the surface of the sand aggregate using the CVD method to create concrete compositions with improved properties contributes to the solution of the above problems when using CNTs in a concrete mixture. Figure 9 shows a possible mechanism of effect of the developed additive (nano-modified sand) on the structure of lightweight concrete.

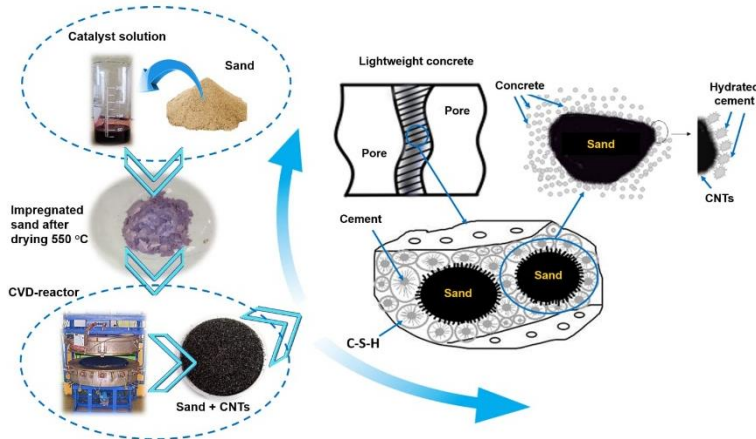


Fig. 9. Illustration of the effect of modified sand on the structure of a foamed concrete sample

The mechanism illustrated in Figure 9 provides insights into the enhancement of the physical and mechanical properties of the samples. This improvement is a consequence of the expedited hydration processes induced by the presence of carbon nanotubes (CNTs), leading to the formation of additional crystallization sites and an increased volume of new structures, such as C-S-H, tobermorite, and gel phases. These newly formed structures occupy the intergranular spaces between the larger calcium hydroxide (CH) and ettringite grains.

The overall increase in strength can be attributed to the creation of a pseudo-framework formed by nanomodified sand particles encased in a shell of hydrated cement grains. This pseudo-framework enhances the regularity and packing density at the 'cement stone-aggregate' interface, resulting in a reduction in the size of the newly formed structures in this area. Consequently, this leads to a decrease in the number of sized pores. Furthermore, a denser cement stone structure results in reduced water absorption, which, in turn, mitigates deformation caused by water crystallization at low temperatures. This

improvement augments the frost resistance of the final construction products made from modified foamed concrete.

### 3.5. Comparative Analysis Of Strength Tests of Carbon Nanotube Concrete Compositions

As a result of the literature review, no studies were found aimed at the synthesis and use of nanomodified sand to improve the properties of foamed concrete. However, the results of this study were compared with publications on the use of CNTs as foamed concrete Nano modifiers. The results are shown in Table. 3.

Table 3. Comparative results of mechanical testing of foamed concrete containing CNTs for compressive strength.

No.	Concrete composition	Compressive strength, MPa	CNTs concentration, %	Reference
1.	CNTs + with lightweight filler based on silica aerogel	5.4	0	[54]
		6.1	0.04	
		6.4	0.1	
		6.7	0.15	
		7.2	0.30	
		7.4	0.45	
2.	Foamed concrete + CNTs	19.77	0.08	[55]
		7.51	0	
3.	Foamed concrete + CNTs + nano silica (NS)	9.23	3% NS	[56]
		8.58	0.5% CNTs + 2.5% NS	
		8.64	1% CNTs + 2% NS	
		7.71	1.5% CNTs + 1.5% NS	
		10.42	2% CNTs +1% NS	
		9.22	2.5% CNTs + 0.5% NS	
4.	Foamed concrete + CNTs + recycled polystyrene	6.32	3% CNTs	[57]
		7	0	
		9	0.05	
5.	Foamed concrete + CNTs + superplasticizer	10	0.1	[58]
		5.4	0	
		5.91	0.02	
		5.53	0.04	
6.	Foamed concrete + nanomodified sand	5.52	0.06	This paper
		16.2	0.006	

Thus, it can be argued that, in comparison with the results of publications of international research teams in the field of modification of CNT foamed concrete, samples containing nanomodified sand in their composition have a significant advantage in mechanical characteristics. At the same time, the percentage of introduced CNTs is much less than in the compared works. All the above proves the relevance, a promising outlook of the study goal and objectives, and its undoubted scientific novelty.



#### 4. Conclusion

The study's experimental results pointed to the following:

- The using of CNTs are intentionally formed on the surface of quartz sand particles used as the filler in lightweight foamed concrete, to improve the qualities of the material. Complex diagnostics were performed on samples of nanomodified sand utilizing a variety of analytical techniques. It was established that a uniform CNT layer was created on the sand surface. Based on the sand filler's particle size and the mass % of the nano modifying additive, a thorough analysis of the performance characteristics of foamed concrete mixtures of various compositions was conducted.
- Adding 1% weight of nanomodified sand filler with a fraction of 0.16 mm has been found to yield the highest increases in sample strength, with 35% and 32% increases in compression and flexural strength, respectively.
- The water absorption in the modified sample is 27% lower than that of the control sample when sand modified with carbon nanotubes is added.
- A possible mechanism for how the developed additive (nanomodified sand) affects the foamed concrete's composition is suggested by the study. Accelerated hydration processes, the appearance of additional crystallization centers in the presence of CNTs, and an increase in the volume of neoplasms like C-S-H, tobermorite, and gel phases that fill the intergranular spaces are all described as improving the samples' mechanical, physical, and operational properties.

#### References

- [1] Ueda T. Material mechanical properties necessary for the structural intervention of concrete structures. *Engineering*. 2019;5(6):1131–1138. <https://doi.org/10.1016/j.eng.2019.02.012>
- [2] Sindu BS, Sasmal S. Properties of carbon nanotube reinforced cement composite synthesized using different types of surfactants. *Construct. Build. Mater*. 2017;155:389–399. <https://doi.org/10.1016/j.conbuildmat.2017.08.059>
- [3] Hamad AJ, Aghajan Sldozian RJ, Mikhaleva ZA. Effect of ceramic waste powder as partial fine aggregate replacement on properties of fiber-reinforced aerated concrete. *Engineering Reports*. 2020;2(3):e12134. <https://doi.org/10.1002/eng2.12134>
- [4] Hamad AJ, Sldozian Aghajan RJ. Flexural and flexural toughness of fiber reinforced concrete-American standard specifications review. *GRD Journals-Global Research and Development Journal for Engineering*. 2019;4(3):5-13.
- [5] Gdoutos EE, Konsta-Gdoutos MS, Danoglidis PA. Portland cement mortar nanocomposites at low carbon nanotube and carbon nanofiber content: A fracture mechanics experimental study. *Cem. Concr. Compos*. 2016;70:110–118. <https://doi.org/10.1016/j.cemconcomp.2016.03.010>
- [6] Hamad AJ. Size and shape effect of specimen on the compressive strength of HPLWFC reinforced with glass fibres. *Journal of King Saud University-Engineering Sciences*. 2017;29(4):373-380. <https://doi.org/10.1016/j.jksues.2015.09.003>
- [7] Dawood ET, Hamad AJ. Toughness behaviour of high-performance lightweight foamed concrete reinforced with hybrid fibres. *Structural concrete*. 2015;16(4):496-507. <https://doi.org/10.1002/suco.201400087>
- [8] Sa C, Bensalem Rb. Effect of Adding Recycled Sand and Fines Retained from Eggshell Waste on the Mechanical Properties and Durability of SCC and SFSCC. *Engineering and Technology Journal*. 2023;41(05):629-641. <http://doi.org/10.30684/etj.2023.137162.1340>
- [9] Hogancamp J, Grasley Z. The use of microfine cement to enhance the efficacy of carbon nanofibers with respect to drying shrinkage crack resistance of portland cement

- mortars. Cem. Concr. Compos. 2017;83:405–414. <https://doi.org/10.1016/j.cemconcomp.2017.08.006>
- [10] Geraldo RH, Pinheira SMM, Silva JS, Andrade HMC, Dweck J, Gonçalves JP, Camarini G. Gypsum plaster waste recycling: A potential environmental and industrial solution. *J. Clean. Prod.* 2017;164:288–300. <https://doi.org/10.1016/j.jclepro.2017.06.188>
- [11] Nasibulina LI, Anoshkin IV, Nasibulin AG, Cwirzen A, Penttala V, Kauppinen EI. Effect of carbon nanotube aqueous dispersion quality on mechanical properties of cement composite. *J. Nanomater.* 2012;2012. <https://doi.org/10.1155/2012/169262>
- [12] Tolchikov YN, Aljaboobi DZM. Research into the process of synthesis of carbon nanomaterials on the cement binder. *Adv. Mater. Technol.* 2022;7:290-298. <https://doi.org/10.17277/jamt.2022.04.pp.290-298>
- [13] Tyson BM, Abu Al-Rub RK, Yazdanbakhsh A, Grasley Z. Carbon nanotubes and carbon nanofibers for enhancing the mechanical properties of nanocomposite cementitious materials. *J. Mater. Civ. Eng.* 2011;23:1028–1035. [https://doi.org/10.1061/\(asce\)mt.1943-5533.0000266](https://doi.org/10.1061/(asce)mt.1943-5533.0000266)
- [14] Nwa-Davida CD, Onwukab DO, Njokub FC, Ibearugbulemb OM. Prediction of Fresh and Hardened Properties of Concrete Containing Nanostructured Cassava Peel Ash Using Ibearugbulemb's Approach. *Engineering and Technology Journal.* 2023;41(05):652-665.
- [15] Abdulmunem SS, Hasan SS. Effect of Glass Wastes on Basic Characteristics of Controlled Low-Strength Materials. *Engineering and Technology Journal.* 2022;40(11):1-10. <http://doi.org/10.30684/etj.2022.132930.1155>
- [16] Hawreen A, Bogas JA. Creep, shrinkage and mechanical properties of concrete reinforced with different types of carbon nanotubes. *Construction and Building Materials.* 2019;198:70-81. <https://doi.org/10.1016/j.conbuildmat.2018.11.253>
- [17] Tran NP, Gunasekara C, Law DW, Houshyar S, Setunge S, Cwirzen A. A critical review on drying shrinkage mitigation strategies in cement-based materials. *Journal of Building Engineering.* 2021;38:102210. <https://doi.org/10.1016/j.jobbe.2021.102210>
- [18] Shah SP, Hou P, Konsta-Gdoutos MS. Nano-modification of cementitious material: Toward a stronger and durable concrete. *Journal Sustainable Cement-Based Materials.* 2015;5:1–22. <https://doi.org/10.1080/21650373.2015.1086286>
- [19] Yeşilmen S, Al-Najjar Y, Balav MH, Şahmaran M, Yildirim G, Lachemi M. Nano-modification to improve the ductility of cementitious composites. *Cem. Concr. Res.* 2015;76:170–179. <https://doi.org/10.1016/j.cemconres.2015.05.026>
- [20] Slodzian RA, Hamad AJ, Al-Rawe HS. Mechanical properties of lightweight green concrete including nano calcium carbonate. *Journal of Building Pathology and Rehabilitation.* 2023;8(1):3. <https://doi.org/10.1007/s41024-022-00247-1>
- [21] Slodzian RJ, Hamad AJ, Zayza MJ, Zeidan SA. Thermal Treatment Influence of Metakaolin on the Concrete Properties. *Journal of Pharmaceutical Negative Results.* 2022:1847-1855. <https://doi.org/10.47750/pnr.2022.13.S01.220>
- [22] Du S, Wu J, Alshareedah O, Shi X. Nanotechnology in cement-based materials: A review of durability, modeling, and advanced characterization. *Nanomaterials.* 2019;9. <https://doi.org/10.3390/nano9091213>
- [23] Kawashima S, Hou P, Corr DJ, Shah SP. Modification of cement-based materials with nanoparticles. *Cem. Concr. Compos.* 2013;36:8–15. <https://doi.org/10.1016/j.cemconcomp.2012.06.012>
- [24] Sedaghatdoost A, Behfarnia K. Mechanical properties of Portland cement mortar containing multi-walled carbon nanotubes at elevated temperatures. *Construct. Build. Mater.* 2018;176:482–489. <https://doi.org/10.1016/j.conbuildmat.2018.05.095>
- [25] Mendoza Reales OA, Dias Toledo Filho R. A review on the chemical, mechanical and microstructural characterization of carbon nanotubes-cement based composites. *Construct. Build. Mater.* 2017;154:697–710. <https://doi.org/10.1016/j.conbuildmat.2017.07.232>

- [26] Xu S, Liu J, Li Q. Mechanical properties and microstructure of multi-walled carbon nanotube-reinforced cement paste. *Construct. Build. Mater.* 2015;76:16–23. <https://doi.org/10.1016/j.conbuildmat.2014.11.049>
- [27] MacLeod AJN, Collins FG, Duan W, Gates WP. Quantitative microstructural characterisation of Portland cement-carbon nanotube composites using electron and X-ray microscopy. *Cem. Concr. Res.* 2019;123. <https://doi.org/10.1016/j.cemconres.2019.05.012>
- [28] Alatawna A, Birenboim M, Nadiv R, Buzaglo M, Peretz-Damari S, Peled A, Sripada R. The effect of compatibility and dimensionality of carbon nanofillers on cement composites. *Construct. Build. Mater.* 2020;232:117141. <https://doi.org/10.1016/j.conbuildmat.2019.117141>
- [29] Torabian Isfahani F, Li W, Redaelli E. Dispersion of multi-walled carbon nanotubes and its effects on the properties of cement composites. *Cem. Concr. Compos.* 2016;74:154–163. <https://doi.org/10.1016/j.cemconcomp.2016.09.007>
- [30] Konsta-Gdoutos MS, Metaxa ZS, Shah SP. Highly dispersed carbon nanotube reinforced cement based materials. *Cem. Concr. Res.* 2010;40:1052–1059. <https://doi.org/10.1016/j.cemconres.2010.02.015>
- [31] Xie XL, Mai YW, Zhou XP. Dispersion and alignment of carbon nanotubes in polymer matrix: A review. *Mater. Sci. Eng., R.* 2005;49:89–112. <https://doi.org/10.1016/j.mser.2005.04.002>
- [32] Sobolkina A, Mechtcherine V, Khavrus V, Maier D, Mende M, Ritschel M, Leonhardt A. Dispersion of carbon nanotubes and its influence on the mechanical properties of the cement matrix. *Cem. Concr. Compos.* 2012;34(10):1104-1113. <https://doi.org/10.1016/j.cemconcomp.2012.07.008>
- [33] Krause B, Mende M, Pötschke P, Petzold G. Dispersability and particle size distribution of CNTs in an aqueous surfactant dispersion as a function of ultrasonic treatment time. *Carbon.* 2010;48:2746–2754. <https://doi.org/10.1016/j.carbon.2010.04.002>
- [34] Parveen S, Rana S, Figueiro R, Paiva MC. Microstructure and mechanical properties of carbon nanotube reinforced cementitious composites developed using a novel dispersion technique. *Cem. Concr. Res.* 2015;73:215–227. <https://doi.org/10.1016/j.cemconres.2015.03.006>
- [35] Vidivelli B, Ashwini B. A study on carbon nanotube (CNT) in concrete. *Int. J. Eng. Res. Technol.* 2018;5:481–489.
- [36] Jayakumari BY, Swaminathan EN, Partheeban P. A review on characteristics studies on carbon nanotubes-based cement concrete. *Construct. Build. Mater.* 2023;367:130344. <https://doi.org/10.1016/j.conbuildmat.2023.130344>
- [37] Shahpari M, Bamonte P, Mosallam SJ. An experimental study on mechanical and thermal properties of structural lightweight concrete using carbon nanotubes (CNTs) and LECA aggregates after exposure to elevated temperature. *Construct. Build. Mater.* 2022;346:128376. <https://doi.org/10.1016/j.conbuildmat.2022.128376>
- [38] Zhang P, Su J, Guo J, Hu S. Influence of carbon nanotube on properties of concrete: A review. *Construct. Build. Mater.* 2023;369:130388. <https://doi.org/10.1016/j.conbuildmat.2023.130388>
- [39] Shah SN, Mo KH, Yap SP, Yang J, Ling TC. Lightweight foamed concrete as a promising avenue for incorporating waste materials: A review. *Resour. Conserv. Recycl.* 2021;164:105103. <https://doi.org/10.1016/j.resconrec.2020.105103>
- [40] Raj A, Sathyan D, Mini KM. Physical and functional characteristics of foam concrete: A review. *Construct. Build. Mater.* 2019;221:787–799. <https://doi.org/10.1016/j.conbuildmat.2019.06.052>
- [41] Kozłowski M, Kadela M. Mechanical characterization of lightweight foamed concrete. *Adv. Mater. Sci. Eng.* 2018;6801258. <https://doi.org/10.1155/2018/6801258>
- [42] Melezhik AV, Romantsova IV, D'yachkova TP, Bychkov ON, Shlykova AA, Smykov MA, Golovin YI. Effect of the matrix composition on the activity of metal oxide catalysts in

- CVD synthesis of carbon nanotubes. *Russ. J. Appl. Chem.* 2012;85:782–787. <https://doi.org/10.1134/S1070427212050175>
- [43] Burakov AE, Tyagi I, Burakova IV, Milyutin VV, Nekrasova NA, Melezhik AV, et al. Efficient removal of europium radionuclides from natural and seawater using mesoporous carbon-based material. *J. Mol. Liq.* 2022;365:120092. <https://doi.org/10.1016/j.molliq.2022.120092>
- [44] Chen X, Feng W, Zhang G, Gao Y. Raman spectra of quartz and Pb<sup>4+</sup>-Doped SiO<sub>2</sub> crystals at different temperature and pressure. *Crystals.* 2019;9:569. <https://doi.org/10.3390/cryst9110569>
- [45] Chung KM, Chen R. Black coating of quartz sand towards low-cost solar-absorbing and thermal energy storage material for concentrating solar power. *Sol. Energy.* 2023;249:98-106. <https://doi.org/10.1016/j.solener.2022.11.028>
- [46] Qu F, Li W, Tang Z, Wang K. Property degradation of seawater sea sand cementitious mortar with GGBFS and glass fiber subjected to elevated temperatures. *J. Mater. Res. Technol.* 2021;13:366–384. <https://doi.org/10.1016/j.jmrt.2021.04.068>
- [47] Rashad AM. Effect of carbon nanotubes (CNTs) on the properties of traditional cementitious materials. *Construct. Build. Mater.* 2017;153:81–101. <https://doi.org/10.1016/j.conbuildmat.2017.07.089>
- [48] Laukaitis A, Kerienė J, Kligys M, Mikulskis D, Lekūnaitė L. Influence of mechanically treated carbon fibre additives on structure formation and properties of autoclaved aerated concrete. *Construct. Build. Mater.* 2012;26:362–371. <https://doi.org/10.1016/j.conbuildmat.2011.06.035>
- [49] Yakovlev GI, Skripkiunas G, Polianskich IS, Lahayne O, Eberhardsteiner J, Urkhanova LA, et al. Modification of cement matrix using carbon nanotube dispersions and nanosilica. *Procedia Engineering.* 2017;172:1261–1269. <https://doi.org/10.1016/j.proeng.2017.02.148>
- [50] Parveen S, Rana S, Fangueiro R, Paiva MC. Microstructure and mechanical properties of carbon nanotube reinforced cementitious composites developed using a novel dispersion technique. *Cem. Concr. Res.* 2015;73:215–227. <https://doi.org/10.1016/j.cemconres.2015.03.006>
- [51] Singh AP, Gupta BK, Mishra M, Govind, Chandra A, Mathur RB, Dhawan SK. Multiwalled carbon nanotube/cement composites with exceptional electromagnetic interference shielding properties. *Carbon.* 2013;56:86–96. <https://doi.org/10.1016/j.carbon.2012.12.081>
- [52] Shah SP, Konsta-Gdoutos MS, Metaxa ZS, Mondal P. Nanoscale modification of cementitious materials. *Nanotechnology in Construction.* 2009;3:125–130. [https://doi.org/10.1007/978-3-642-00980-8\\_16](https://doi.org/10.1007/978-3-642-00980-8_16)
- [53] Zhang J, Liu X. Dispersion performance of carbon nanotubes on ultra-light foamed concrete. *Processes.* 2018;6. <https://doi.org/10.3390/pr6100194>
- [54] Adhikary SK, Rudžionis Ž, Tučkutė S, Ashish DK. Effects of carbon nanotubes on expanded glass and silica aerogel based lightweight concrete. *Sci. Rep.* 2021;11. <https://doi.org/10.1038/s41598-021-81665-y>
- [55] Baloch WL, Khushnood RA, Memon SA, Ahmed W, Ahmad S. Effect of elevated temperatures on mechanical performance of normal and lightweight concretes reinforced with carbon nanotubes. *Fire Technol.* 2018;54:1331–1367. <https://doi.org/10.1007/s10694-018-0733-z>
- [56] Narasimman K, Jassam TM, Velayutham TS, Yaseer MMM, Ruzaimah R. The synergic influence of carbon nanotube and nanosilica on the compressive strength of lightweight concrete. *J. Build. Eng.* 2020;32. <https://doi.org/10.1016/j.jobe.2020.101719>
- [57] Thang NC, Duc HN, Cong TT. Effect of carbon nanotube on properties of lightweight concrete using recycled expanded polystyrene (EPS). *IOP Conference Series: Materials*

Science and Engineering. 2020;869. <https://doi.org/10.1088/1757-899X/869/3/032049>

- [58] Adhikary SK, Rudzionis Z, Ghosh R. Influence of CNT, graphene nanoplate and CNT-graphene nanoplate hybrid on the properties of lightweight concrete. *Materials Today: Proceedings*. 2021;44:1979–1982. <https://doi.org/10.1016/j.matpr.2020.12.115>

## Axial compressive behavior of recycled aggregate concrete steel composite columns

Daniel Cruze<sup>1,a,\*</sup>, Chandan Sah<sup>1,b</sup>, Nijampatnam Manikanta<sup>1,c</sup>, Dhirendra Kumar Mandal<sup>1,d</sup>, Abhinash Kumar Jha<sup>1,e</sup>, A. Arun Solomon<sup>2,f</sup>

<sup>1</sup>Department of Civil Engineering, Hindustan Institute of Technology and Science, Padur, Chennai, India

<sup>2</sup>Department of Civil Engineering, GMR Institute of Technology, Rajam, Andhra Pradesh, India

### Article Info

### Abstract

#### Article history:

Received 19 Oct 2023

Accepted 01 Feb 2024

#### Keywords:

Recycled aggregate concrete;

Concrete-filled steel tube;

Compressive behavior; Composite column

In this Study the axial load-carrying capacity and behavior of a “Axial Compressive behavior of Recycled Aggregate Concrete Steel Composite Columns” (RACSCC) is investigated experimentally and simulated numerically. The study emphasizes the utilization of materials contributing to the circular economy in construction, specifically integrating steel and recycled aggregate into concrete. The environmentally sustainable concrete columns are formed by filling square steel tube sections with recycled aggregate concrete (RAC). The study includes six SRACC specimens and one bare conventional steel column. The specimens are subjected to axial compressive loading using the displacement control method. The investigation explores the impact of different coarse aggregate sizes of 12 mm, 16 mm, 22.4 mm, 25 mm, and 30 mm, obtained through sieving of demolished buildings materials. The study aims to address the impact of varying aggregate sizes on parameters such as maximum load-carrying capacity, strain, stress, lateral displacement, and failure patterns. The experimental results are validated and compared with the maximum load-carrying capacity, Strain, Stress, Lateral displacement, and failure patterns using numerical simulations conducted with the Ansys Workbench tool. The SRACC column comprises a hollow tube with 20 mm to 22.4 mm and 22.4 mm to 25 mm recycled aggregate and has a maximum load carrying capacity of 610.28 kN at 10 mm displacement. The local buckling failure occurred near the area load applied. The numerical simulations result for the composite columns agreed well with the experimental results. The results show the recycled aggregate concrete (RAC) have a massive potential for construction support in circular economy. To create composite columns using the RAC as an alternative building material that will help to create an environmentally Sustainable construction.

© 2024 MIM Research Group. All rights reserved.

## 1. Introduction

As natural resources continue to be depleted, the mounting environmental issues highlight the necessity for sustainable growth in a variety of industries, including civil engineering. With its ability to reduce solid waste in landfills, protect the ecosystem, save precious resources, and create self-sustaining material cycles, recycling used concrete stands as a powerful tool to encourage sustainable practices. Additionally, considering to the growing intensity of environmental degradation and resource depletion, the need to recycle and repurpose destroyed concrete has acquired substantial worldwide traction in recent years. The piling of leftover concrete that results from natural catastrophes like earthquakes and hurricanes makes the need for repurposing even more urgent. This predicts a likely

\*Corresponding author: [danielckarunya@gmail.com](mailto:danielckarunya@gmail.com)

<sup>a</sup> [orcid.org/0000-0002-4024-4742](https://orcid.org/0000-0002-4024-4742); <sup>b</sup> [orcid.org/0009-0009-7478-8199](https://orcid.org/0009-0009-7478-8199); <sup>c</sup> [orcid.org/0009-0002-3072-036X](https://orcid.org/0009-0002-3072-036X);

<sup>d</sup> [orcid.org/0009-0004-2521-853X](https://orcid.org/0009-0004-2521-853X); <sup>e</sup> [orcid.org/0009-0003-7428-8641](https://orcid.org/0009-0003-7428-8641); <sup>f</sup> [orcid.org/0009-0003-7428-8641](https://orcid.org/0009-0003-7428-8641)

DOI: <http://dx.doi.org/10.17515/resm2024.04ma1019rs>

development whereby demolition firms everywhere will be encouraged to expand their use of waste concrete recycling techniques.

Recycled aggregates could potentially be involved into composite steel columns, which has considerable potential for reducing the environmental effect of building operations. This is accomplished through lowering garbage that goes to landfills and the use of natural resources. Additionally, the use of recycled materials to concrete is showing a remarkable potential for improving its mechanical properties, including compressive and flexural strengths [1-3]. While increasing the total strength of large constructions, the combination of steel and concrete in building structures has shown a demonstrable potential for enhancing resistance to seismic occurrences [4-6]. In the field of construction and high-rise design, where optimization of composite parts has developed into an essential precept, this concept becomes more and more significant.

The outcomes of the research indicate the viability of recycling additional concrete and highlight the importance of recycled aggregate concrete (RAC) because of its advantageous characteristics, such as reduced thermal conductivity, improved ductility, and decreased specific gravity. Additionally, most of the Recycled Aggregate Concretes' (RACs) present applications are concentrated in non-structural areas such pavements and road embellishments. The potential for integrating RACs into structural frameworks, however, is yet largely unreached [7].

The utilization of recycled aggregates in place of natural aggregates in the creation of fresh concrete is at the basis of the current rise in interest in recycling waste concrete [8]. Utilizing their built-in seismic reliability, RACs show considerable potential for a variety of structural applications, prompting more study [9]. This type of recycled concrete, also known as recycled aggregate concrete (RAC), has its roots in early building techniques meant to protect rare natural aggregate supplies while resolving issues with waste storage. Through a series of operations that include crushing, washing, grading, and mixing crushed concrete particles in certain ratios, recycled aggregate is created by partially or entirely replacing recycled aggregate for natural aggregate [10-11]. The effects of aggregate particle size on mechanical characteristics are significant since bigger particles tend to increase compressive strength but may degrade flexural strength [12]. Therefore, it is still important to research how different aggregate sizes affect the flexibility of composite steel columns.

Recycled Aggregate Concretes (RACs) are making themselves competitors in the field of environmentally friendly construction materials, seamlessly collaborating with initiatives to promote low-carbon and sustainable development practices. [13-15]. Since RACs replicate the energy absorption and ductility characteristics of Natural Aggregate Concretes (NACs), which are crucial for obtaining strong aseismic performance, this relevance is especially relevant to seismically active areas [16-20].

The spacing of glass fiber-reinforced polymer (GFRP) spirals was reduced, which improved ductility and lateral confinement. The highest load-carrying capability was demonstrated by GFRP-reinforced recycled aggregate geopolymer concrete columns with eight longitudinal GFRP bars. Because of the greater confinement effect of thicker FRP on the recycled aggregate concrete-filled steel tube column, the specimen contained by a thicker fiber-reinforced polymer (FRP) has a higher axial strength and a larger ultimate strain. Failure mode, ultimate state, axial load-lateral deflection curves, load-strain curves, and dilation behavior are all factors to consider. Using the experimental database, a new ANN model for the load-carrying capacity of concrete-filled steel tube circular elements was also proposed [21-24].

Ali Faghidian studies the residual stress for Thick-Walled Tubes. For reconstructing residual fields and eigenstrains from constrained strain measurements in axially symmetric tubes, the smoothed inverse eigenstrain approach is reexamined. The salient feature of the smoothed inverse eigenstrain method is its capacity to produce an inverse solution that satisfies the requirements of continuum mechanics, in addition to mitigating the disparity between measurements and model predictions. The fewer experimental measurements are required to reconstruct the residual fields in their entirety [25-27].

This research examines the axial compressive behavior of composite steel columns that use recycled aggregates of varying sizes, including 12 mm, 16 mm, 22.4 mm, 25 mm, and 30 mm. Composite steel column specimens will be subjected to various loading conditions to determine their ultimate compressive strength. This study's findings will be beneficial in understanding how well composite steel columns with recycled aggregates of various sizes perform. The results can be used to improve the design of composite steel columns made from recycled aggregates, resulting in more environmentally friendly and cost-effective building techniques. The study also contributes to the growing body of knowledge on the use of recycled aggregates in the construction industry, which is crucial for creating a more sustainable built environment.

The aim of this research is to investigate how the use of recycled aggregates of varying sizes affects the axial compressive behavior of composite steel columns. The results will inform the development of eco-friendly building techniques and provide valuable insights into the performance of composite steel columns.

The potential integration of Recycled Aggregate Concretes (RACs) into structural frameworks remains largely unexplored, creating a significant knowledge gap in the field. Furthermore, while previous studies have acknowledged the positive mechanical properties of recycled materials, there is a lack of comprehensive research on how different aggregate sizes, particularly in the context of composite steel columns, affect flexibility. This study aims to fill this critical knowledge gap by investigating the axial compressive behavior of composite steel columns utilizing recycled aggregates of varying sizes (12 mm, 16 mm, 22.4 mm, 25 mm, and 30 mm). The research seeks to advance our understanding of the performance of such columns, contributing valuable insights to the design and implementation of more sustainable and cost-effective building techniques. Ultimately, the study strives to bridge the gap between existing knowledge and the potential applications of recycled aggregates in structural frameworks, enhancing the eco-friendliness of construction practices.

## **2. Materials and Methods**

The careful and thorough development of a detailed approach, combined with the creative integration of resources accurately chosen for their applicability, serve as the fundamental foundation of this inquiry. This methodical methodology is used to enable a thorough investigation into the many complications that underlying.

Six RACSCC with a 100 x 100 mm cross section and 1000 mm length with different aggregate sizes were subjected to axial compressive loading and studied using the displacement control method. The parameters examined included the aggregate size range of 10 mm, 16 mm, 22.4 mm, 25 mm, and 30 mm, which was sieved from the demolished building. The investigation's primary objective was on the M20 grade of concrete that had been utilized in the Study. The results of the experimental study indicate that recycled aggregate concrete filling inner steel tubes results in an increase in the axial compressive strength and a slight decrease in the ultimate axial strain of concrete compared with conventional hollow steel tubes. It was observed that increasing the amount of recycled aggregate leads to a slight increase in the ultimate axial stress and strain of the RACSCC.



The 6 specimens are validated numerically using the Ansys Workbench simulation tool. The results are compared with the maximum load-carrying capacity and failure patterns.

### 3. Methodology

Six RACSCC specimens with a 100 x 100 mm cross section and 1000 mm length with different aggregate sizes were subjected to axial compressive loading and studied using the displacement control method. The parameters examined included the aggregate size range of 10mm, 16mm, 22.4mm, 25mm, and 30 mm, which was sieved from the demolished building. The grade of concrete was M20 was used for the study. The results of the experimental study indicate that recycled aggregate concrete filling inner steel tubes results in an increase in the axial compressive strength and a slight decrease in the ultimate axial strain of concrete compared with conventional hollow steel tubes. It was observed that increasing the amount of recycled aggregate leads to a slight increase in the ultimate axial stress and strain of the RACSCC. The 6 specimens are validated numerically using the Ansys Workbench simulation tool. The results are compared with the maximum load-carrying capacity and failure patterns. The flowchart of the methodology is shown in Figure 1.

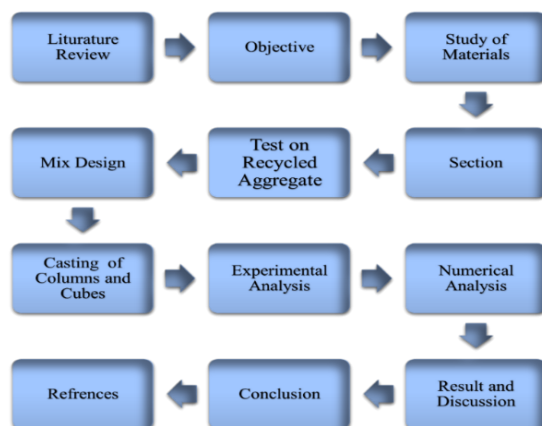


Fig. 1. Flowchart of methodology

#### 3.1. Experimental Analysis

In the experimental work, six composite columns were constructed using steel and concrete with varying sizes of recycled coarse aggregates. The dimensions of the columns were 100 x 100 mm for the cross section and 1000 mm for the length. The primary goal was to investigate how these columns behaved under compression loading until they experienced an axial displacement of 10 mm. The test included six composite column specimens (C1, C2, C3, C4, C5, and C6) along with the Hollow Steel Tube (H), and their descriptions were provided in table 1.

The reference column, C1, had a nominal aggregate size, while the other composite columns had different aggregate sizes. To ensure consistent material qualities, each column underwent a complete curing and drying process. Progressive loads were applied to the columns using a compression test setup, and axial displacement measuring devices (LVDT) were installed to precisely record deformations.

The loading continued until the desired displacement was reached for each column. During the tests, maximum load capacities and deformation characteristics were recorded, while closely monitoring any signs of distress or failure. The failure mode was analyzed, and the impact of recycled coarse aggregate size on the behavior of the composite columns under compression forces was studied.

This part serves as a gateway to the experimental component of the study, providing a broad overview of the experiments that were performed out together with an in-depth description of their results and implications.

### 3.1.1. Experimental Test Setup

The compression testing equipment that was used as the starting point of the test setup for the composite column included a load frame and hydraulic actuators. Throughout the testing procedure, this specialized equipment performed an important role of systematically and methodically applying incremental loads to the columns. The steel and recycled aggregate concrete composite columns, featuring dimensions of 100 x 100 mm for the cross section and 1000 mm for the length, were securely positioned within the compression testing machine. Each specimen underwent testing, including the hollow tube (H) and the specimens with various aggregate sizes (C1, C2, C3, C4, C5, and C6). Axial displacement measurement systems known as LVDTs (Linear Variable Differential Transformers) were installed to accurately measure the deformations during the test as shown in figure 2. These tools allowed for precise recording of how the columns deformed as the load was gradually applied. The specimens were subjected to compression loading until an axial displacement of 10 mm was obtained. During the loading process, the columns were carefully observed for any indications of distress or failure while their maximum load capacities and deformation characteristics were recorded. The comprehensive analysis of the column's performance and the influence of recycled coarse aggregate size on their structural behavior under compression forces was analyzed.

Table 1. Description of specimens

S. No.	Specimen No.	Description of Specimens
1	H	Hollow Steel Tube
2	C1	Steel tube filled with concrete, mixed with nominal size of recycled coarse aggregates ranges from 4.75 mm to 30 mm.
3	C2	Steel tube filled with concrete, mixed with recycled coarse aggregate size ranges from 30 mm to 25 mm.
4	C3	Steel tube filled with concrete, mixed with recycled coarse aggregate size ranges from 25 mm to 22.4 mm.
5	C4	Steel tube filled with concrete, mixed with recycled coarse aggregate size ranges from 22.4 mm to 20 mm.
6	C5	Steel tube filled with concrete, mixed with recycled coarse aggregate size ranges from 20 mm to 16 mm.
7	C6	Steel tube filled with concrete, mixed with recycled coarse aggregate size ranges from 16 mm to 10 mm.

This section illuminates the carefully regulated environmental circumstances to which... was subjected through a complex description of the specifics relevant to the experimental

analysis test setup. This diligent oversight ensures full research with the possibility for replication, acting as a cornerstone in achieving the goal of trustworthy and informative results.

Table 1 below methodically presents the whole information about the specimens, including numerous characteristics and features. This table explores the detailed differences in recycled coarse aggregate sizes that were specifically chosen for the wide range of specimens under study. This is in addition to providing a thorough summary of the specimen data.

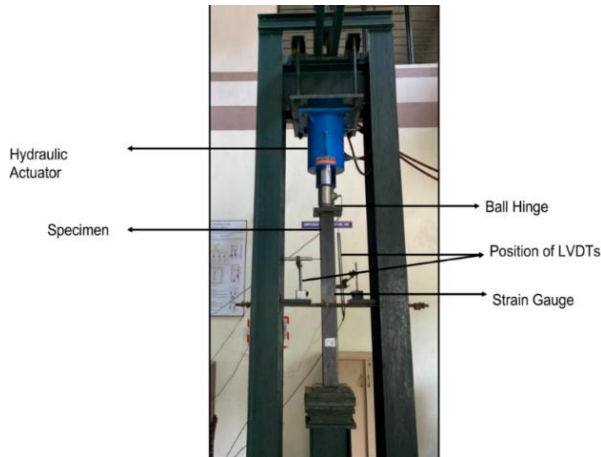


Fig. 2. Axial compression testing machine setup

### 3.2. Numerical Analysis

The numerical analysis of the composite columns was conducted using ANSYS software. The modeling of composite column is done in ANSYS space claim. The implementation of ANSYS for Numerical Analysis makes it possible for an immersive exploration of the simulated environment, where precise simulations are performed to investigate the complex behavioral characteristics displayed by steel recycled aggregate concrete composite columns under a range of different conditions. This computational effort explores the core of the column's reaction and offers an in-depth understanding of how it responds to various influences and elements in the simulated environment.

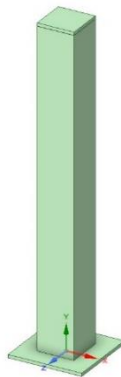


Fig. 3. Composite column modeling in ANSYS space claim

The specimens, labeled as C1, C2, C3, C4, C5, C6, and H (Hollow Steel Tube), were modeled and simulated to examine their response to axial compression. The dimensions of the columns, measuring 100 x 100 mm in cross-section and 1000 mm in length, were accurately represented in the numerical models shown in figure 3. The material properties, including steel and recycled aggregate concrete, were assigned based on their known characteristics and the results of concrete cube testing. In the numerical simulation, the columns were gradually subjected to increasing axial stresses until a displacement of 10 mm was achieved. The analysis yielded valuable findings, such as the distributions of strain and stress within the columns. By performing the numerical analysis in the ANSYS software, a comprehensive understanding of the mechanical response of the composite columns under axial compression was obtained, complementing the results of the experimental tests.

#### 4. Results and Discussion

##### 4.1. Test Observation and Failure Modes

This section presents a comprehensive narrative that intricately depicts the actual structural behavior exhibited by Steel Recycled Aggregate Concrete Composite Columns. The investigation delves deeply into the realm of test observations and failure mechanisms, offering a detailed tapestry of the columns' response to axial compressive behavior. The paper combines meticulous experimental exploration and advanced numerical analysis to provide insights into the ever-changing behavior of the columns. The understanding, derived from both experimental data and numerical insights, is extensive and multidimensional.

All six test specimens of the steel recycled aggregate concrete composite columns underwent failure analysis during axial compressive loading, as depicted in Figure 3. The resulting failure patterns reveal compressive failure at the uppermost part of the column due to the impact of compressive force. Unequal load distribution, stemming from eccentricity caused by factors like stress distribution variations, cross-sectional area differences, or initial misalignment, leads to non-uniform compressive force distribution along the column's length. This eccentricity, influenced by stress concentration, uneven cross-sectional areas, or structural imperfections, particularly the column's original out-of-straightness, results in greater compressive stress on the upper portion, leading to premature collapse.

Table 2. Comparative analysis of experimental and numerical results for SRACC columns

Column Specimen	Experimental simulation			Numerical simulation		
	Axial load, kN (max)	Axial displacement, mm (max)	Lateral displacement, mm (max)	Axial load, kN (max)	Axial displacement, mm (max)	Lateral displacement, mm (max)
H (hollow tube)	86.69372	10	2.68	100.744	10	2.773
C1	610.28	10	5.44	596.341	10	5.1589
C2	557.9329	10	5.73	597.924	10	5.829
C3	567.1965	10	5.17	598.995	10	5.271
C4	539.5923	10	5.08	598.552	10	5.203
C5	544.81	10	5.6	599.239	10	5.6987
C6	576.7239	10	5.2	610.285	10	5.663

The consistent failure pattern across all specimens, unaffected by the use of recycled coarse aggregate concrete in various size ranges, points to an initial flaw, such as a deviation in straightness, intensifying local stress concentration. This study not only sheds light on the behavior of steel recycled aggregate concrete composite columns under compressive loads but also underscores the critical significance of accurate design and detailing in averting premature failure. The findings emphasize the imperative role of meticulous design and additional information in preventing instances of early failure by gaining profound insights into the behavior of these composite columns under compressive pressures.



Fig. 4. Failure mode in experimental investigation

A detailed summary of the observed outcomes for each sample of SRACC columns, based on both experimental testing and numerical simulations, is shown in Table 2 below. The table is an invaluable resource that provides a concise, in-depth analysis that highlights the degree of agreement between numerical forecasts and experimental trial results. We compare these findings in order to verify that numerical simulations are a reliable means of forecasting the complex behavior of SRACC columns under different loading scenarios. Important parameters are included in this comparison study, which enables a thorough assessment of the model's dependability and correspondence with experimental data.

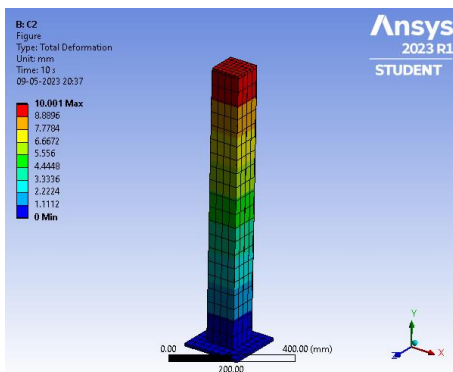


Fig. 5. Total deformation schematic view in numerical analysis

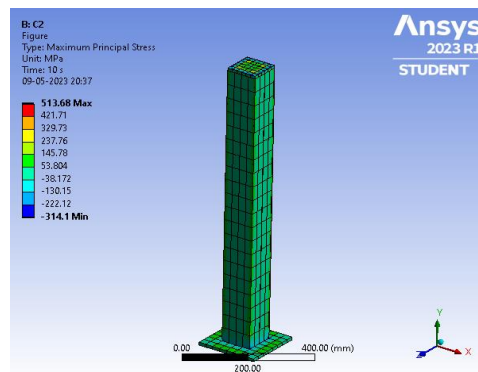


Fig. 6. Stress schematic view in numerical analysis

### 4.2. Axial Load–Axial Displacement Relationship

The relationship between axial load and axial displacement revealed significant information regarding the structural response to varying compressive pressures. The distinctive patterns in the axial load-axial displacement curves highlighted the column's deformation characteristics as the load increased. The curve in Figure 8 and Figure 9 illustrates the relationship between axial load and axial displacement for all specimens exposed to axial compressive stress for experimental analysis and numerical analysis, respectively. Each specimen was evaluated for a displacement of 10 mm, and both experimental analysis and numerical analysis were done on it.

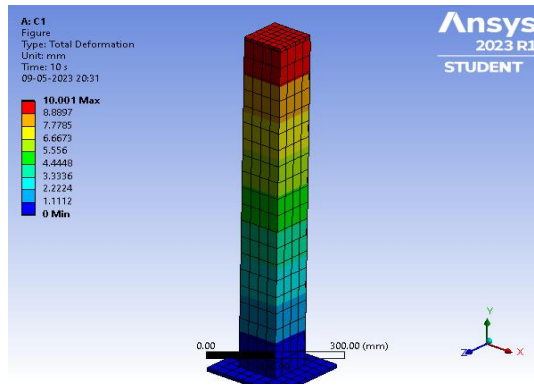


Fig. 7. Schematic view axial displacement in ANSYS

The axial displacement curves for the columns, indicated by the characters C1, C2, C3, C4, C5, C6, and H (Hollow Steel Tube), were observed. Among the columns, C1 exhibited the highest load at the displacement of 10 mm. In the experimental analysis, column C1 reached a maximum load of 610.28 kN, while in the numerical analysis, it achieved a maximum load of 596.72 kN. These values demonstrate the column's response to the applied axial stress. Three separate stages—elastic, yielding, and failure were seen on the curve. The graph shows linear displacement proportional to the increasing load during the elastic period. As soon as the yield point was reached, irreversible plastic deformation caused the yielding phase to behave nonlinearly. Additionally, it was found that the peak load rose as the size of the recycled coarse aggregate decreased, indicating changes in the compression behavior.

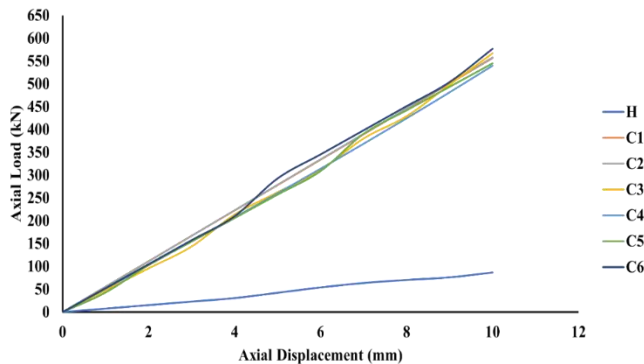


Fig. 8. Axial load vs axial displacement experimental analysis result curve

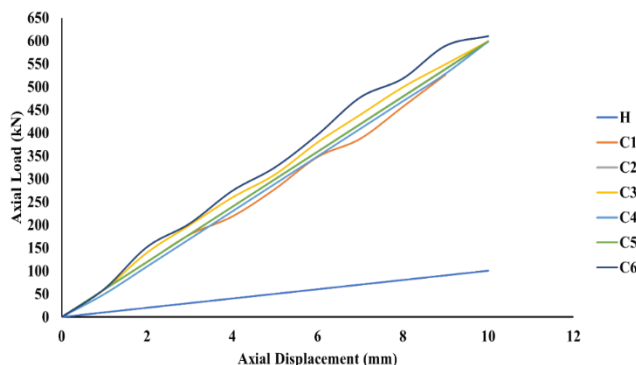


Fig. 9. Axial load vs axial displacement numerical analysis result curve

### 4.3. Axial Load–Lateral Displacement Relationship

The curve in Figure 11 and Figure 12. illustrates the relationship between Axial Load–lateral displacement relationship for all specimens exposed to axial compressive stress for experimental analysis and numerical analysis, respectively. The comparison between experimental and numerical data for the axial load-lateral displacement relationship allowed us to gain insight into the behavior of the composite columns. The numerical analysis yielded a slightly higher result of 5.829 mm compared to the experimental study, where a maximum lateral displacement value of 5.73 mm was observed.

The reliability and accuracy of the numerical simulation are certainly highlighted by the strong concordance between these two different approaches. The exact same patterns in the curves of the axial load-lateral displacement connection were clearly shown by both the thoroughly experimental investigation and the complex numerical analysis. These curves were initially defined by a linear response, but when lateral displacement increased gradually, they gracefully crossed over into the domain of nonlinear behavior.

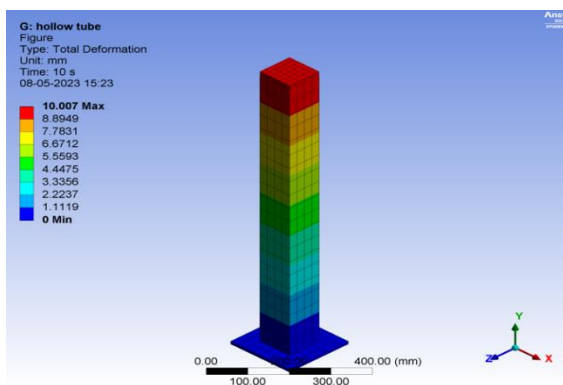


Fig. 10. Simulation Result in ANSYS

A more comprehensive understanding of the material's complex lateral response as it continuously interacts with increasing axial loads can be obtained through an in-depth investigation of the relationship between axial load and lateral displacement. This incisive analysis offers a lot of insightful information that is relevant to both theoretical and practical design and engineering considerations, as well as theoretical research.

Understanding how axial loading and lateral displacement interact allows for the development of effective and solid structural designs that take into consideration the behavior of the material under actual stress circumstances.

This perfect learning of findings from the experimental and numerical worlds adds a lot to our understanding. We obtain insights by examining the unique characteristics of these behaviors under axial loads that not only enhance our understanding but also enable observation and improving of composite column designs, leading the way for improved efficiency and analysis.

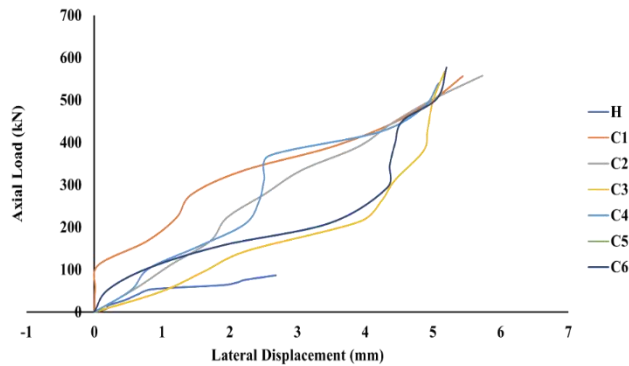


Fig. 11. Axial load vs lateral displacement experimental analysis result curve

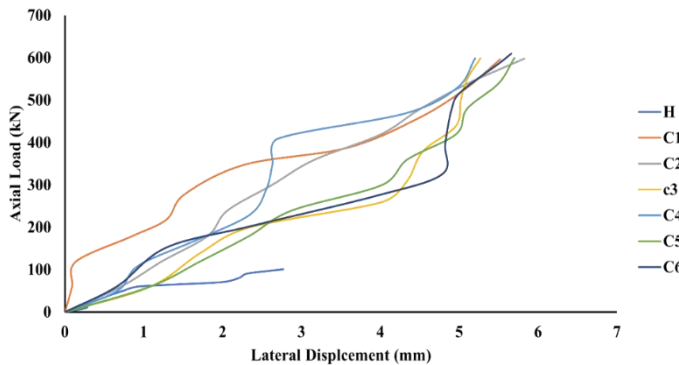


Fig. 12. Axial load vs lateral displacement numerical analysis result curve

#### 4.4. Axial Load–axial strain relationship

The relationship between axial load and axial strain for all specimens exposed to axial compressive stress for experimental analysis and numerical analysis, respectively, is shown by the curve in Figure 14 and Figure 15 respectively. The columns' stress-strain curves, named C1, C2, C3, C4, C5, C6, and H (Hollow Steel Tube), were observed. The experimental analysis provided the following relationship graphs between axial load and axial strain: After being Displaced by 10 mm, the analyzed column's axial load and axial strain relationship curve showed a typical reaction. As the load increased, the curve transitioned from an initial linear elastic area into a plastic zone. It is noted that column C1 showed a maximum strain in the numerical analysis of 0.004465 and an associated axial load value of 596.34 kN. According to the experimental study, column C3 experienced a maximum strain of 0.004442, on an axial load of 567.19 kN.



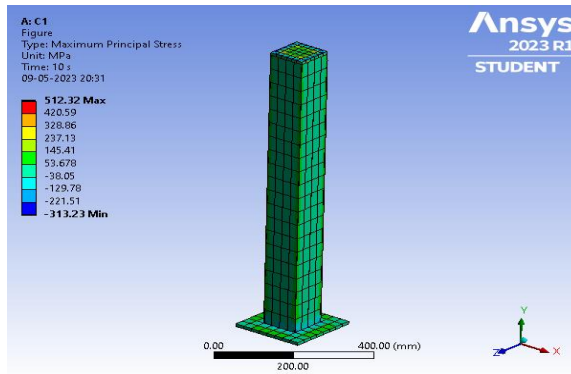


Fig. 13. Maximum principle stress simulation result

A full understanding of the material's unpredictable response as it interacts with gradually increasing axial loads is provided by the complex relationship that exists between axial load and axial strain.

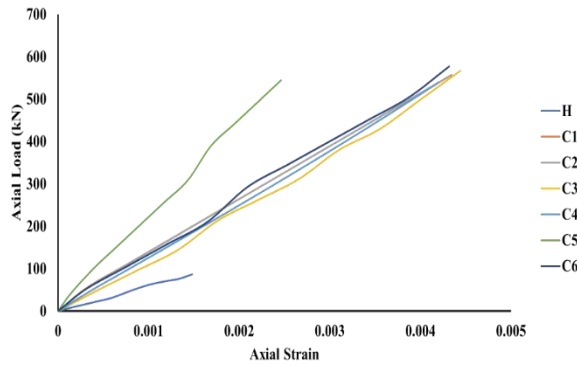


Fig. 14. Axial load vs axial strain experimental analysis result curve

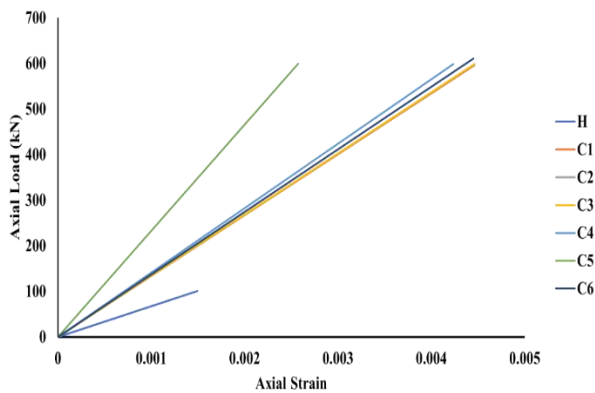


Fig. 15. Axial load vs axial strain numerical analysis result curve

This thorough research offers essential information that go beyond the surface, exploring the material's stiffness, yielding behavior, and ultimate strength when subjected to various axial loading levels. This in-depth knowledge of the material's mechanical behavior, which represents every stage from early elasticity to the point of yielding and final structural capacity, serves as essential for well-informed design and engineering considerations.

Considering the context of numerical analysis, the result of the numerical analysis, which described the relationship between axial load and axial strain in the column, showed a remarkable agreement with the experimental curve. This uniformity, a demonstration of the numerical model's accuracy, serves as a clear validation of its reliability. The simulation's capacity to accurately represent the structural integrity of the column in all of its details was demonstrated as its virtual environment consistently reflected the reality of the actual world.

#### 4.5. Axial Stress – Axial strain relationship

The axial stress and axial strain relationship curve for the analyzed column, subjected to a 10 mm displacement, was assessed through experimental and numerical analysis. The connection between stress and strain is shown in Figure 17 and Figure 18 providing insights into the column's behavior under load. The experimental curve displayed three phases: elastic, yielding, and failure.

During the elastic phase, the curve exhibited a linear stress-strain relationship, indicating elastic deformation. As the load increased, the curve transitioned into the yielding phase, characterized by significant plastic deformation and a nonlinear stress-strain relationship. The maximum strain in column C3 was 0.004442 (experimental) and 0.004465 (numerical), while in column C1, it was 0.004442 (experimental) and 0.004465 (numerical). Peak stress values varied among columns based on the size of the recycled coarse materials, highlighting the impact of aggregate size on the column's response to axial stress.

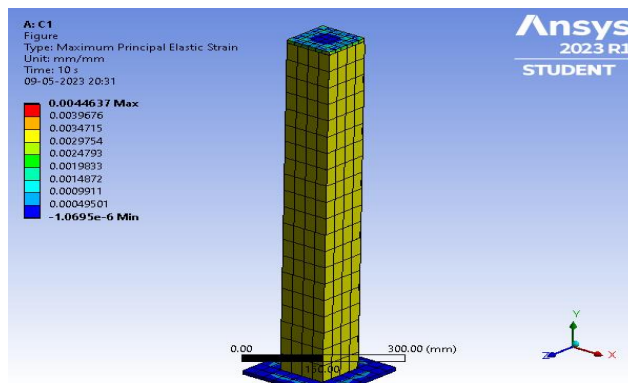


Fig. 16. Maximum principle strain simulation result

As the experimental curve effectively coincided with the results obtained from detailed numerical analysis, its accuracy was certainly confirmed. This complete agreement strengthened our confidence in the experimental results and enhanced our understanding of the complex details guiding the column's complex behavior to the continuous force of axial stress.

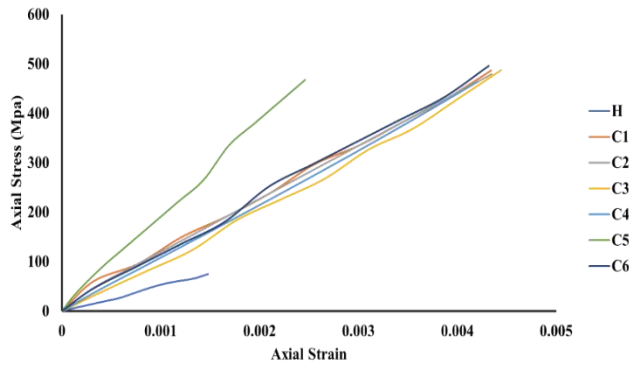


Fig. 17. Axial stress vs axial strain experimental analysis result curve

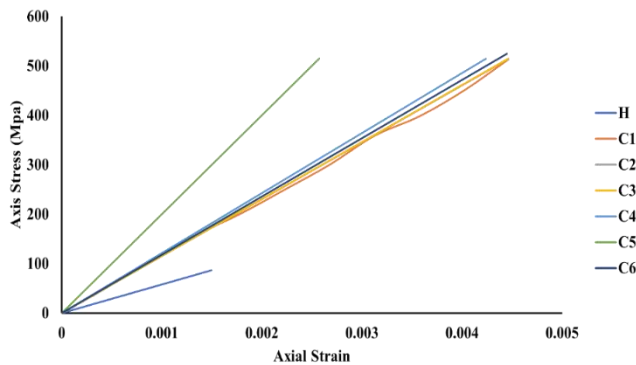


Fig. 18. Axial stress vs axial strain numerical analysis result curve

## 5. Critical Review and Discussions

The conclusions drawn from the experimental analysis and numerical simulations provide valuable insights into the performance of Steel Recycled Aggregate Concrete Composite (SRACC) columns. The axial compression tests on six specimens, featuring variations in the size of coarse aggregates, allowed for a comprehensive understanding of the effects of these modifications on stress, strain, ultimate strength, and load-bearing capacity.

The study highlighted a noteworthy finding concerning the strength of recycled aggregate concrete, indicating a 5% decrease compared to concrete with natural aggregates. This decline is attributed to the complete substitution of natural aggregates with recycled resources for both coarse and fine aggregates. However, the inclusion of recycled fine aggregate, containing fine cementitious substances, demonstrated an improvement in the strength properties of recycled fine aggregate concrete.

The experimental results showcased the superior compressive strength of the C6 column, while numerical analysis indicated a slightly lower strength. Discrepancies in strain values between experimental and numerical analyses for the C1 and C3 columns were observed, underscoring the need for precision in both methods.

The successful validation of experimental results by numerical analysis, with differences ranging from 2% to 5% across samples, substantiates the accuracy and dependability of the numerical simulation. However, the study identified a consistent compression failure in the uppermost portion of each specimen, suggesting irregular load distribution along their length. To address this, better load distribution methods are recommended for achieving a more uniform stress distribution.

the study emphasized the superior performance of composite columns C2 and C3 in terms of load, stress, strain, and displacement. Both experimental and numerical analyses supported the recommendation to implement these columns in practical applications. The concrete mixture with recycled aggregates ranging from 20 mm to 22.4 mm for C2 and 22.4 mm to 25 mm for C3 contributed to their enhanced performance characteristics. This practical recommendation aligns with the broader objective of promoting environmentally sustainable construction practices within the framework of a circular economy.

For the future studies that will forward the study of composite steel columns made using recycled aggregates. First off, more research into the long-term robustness and structural integrity of composite columns using recycled aggregates in different sizes might prove to be beneficial. A thorough grasp of the sustainability of these composite columns would also benefit from evaluation of their life cycle analysis and environmental effect. Enhancing the mix proportions of recycled aggregates to improve mechanical characteristics and reduce environmental impact might be the subject of future study. It would also be beneficial to look at how these columns might work in various structural arrangements and real-world building situations. Finally, working together with industry stakeholders might make it easier to translate research findings into real construction procedures, encouraging the broad use of environmentally friendly building methods.

## **6. Conclusions**

A detailed and in-depth investigation was carefully performed for the purpose of this deep research study. The primary objective of this study was to gain insight into the complex mechanics of axial load-carrying capacity and the complex behavior demonstrated by columns that represent the core characteristics of Axial Compressive behavior of Recycled Aggregate Concrete Steel Composite Columns (RACSCC). The results shown have emerged like a thoroughly made pattern, generated by the comprehensive evaluation of facts and information, and have been guided by the priceless knowledge gathered from real-world experiments and numerical simulation. The experimental investigation involved axial compression tests on six specimens of recycled aggregate concrete square steel columns, with designed variations in the size of coarse aggregates. The analysis of stress, strain, ultimate strength, and load-bearing capacity of the specimens revealed the effects of these modifications. The study demonstrated that the strength of recycled aggregate concrete was approximately 5% lower compared to concrete made with natural aggregates. This decrease can be attributed to the complete substitution of natural aggregates with recycled resources, both for coarse and fine aggregates. Additionally, it was observed that the inclusion of recycled fine aggregate, containing fine cementitious substances, in the concrete mixture improved the strength properties of recycled fine aggregate concrete.

The experimental study revealed that the C6 column exhibited a significantly higher compressive strength of 610.28 kN, while the numerical analysis indicated a slightly lower strength of 576.72 kN. Furthermore, the numerical analysis showed that the C1 column had a higher strain value of 0.004465, whereas the experimental analysis showed a slightly higher strain of 0.004424 for the C3 column. The numerical analysis using ANSYS software successfully validated the experimental analysis results, with a slight difference ranging from 2% to 5% across each of the samples. This confirms the accuracy and

dependability of the numerical simulation. The analysis of each specimen indicated that the uppermost portion consistently experienced compression failure, suggesting irregular load distribution along the length of the specimens. To achieve a more uniform stress distribution, better load distribution methods should be employed. In conclusion, the study found that composite columns C2 and C3 outperformed all other columns in terms of load, stress, strain, and displacement, as supported by both experimental and numerical analyses. The use of concrete mixed with recycled aggregates ranging from 20 mm to 22.4 mm for C2 and 22.4 mm to 25 mm for C3 resulted in these superior performances. Consequently, it is recommended to implement composite columns C2 and C3 as the preferred choice for practical applications, considering their enhanced performance characteristics.

## References

- [1] Choi WC, Yun HD. Compressive behaviour of reinforced concrete columns with recycled aggregate under uniaxial loading. *Eng Struct.* 2012;41:285-293. <https://doi.org/10.1016/j.engstruct.2012.03.037>
- [2] Xiao J, Li W, Fan Y, Huang X. An overview of study on Recycled Aggregate Concrete in China (1996-2011). *Constr Build Mater.* 2012;31:364-383. <https://doi.org/10.1016/j.conbuildmat.2011.12.074>
- [3] Dundu M. Compressive strength of circular concrete filled steel tube columns. *Thin-Walled Struct.* 2012;56:62-70. <https://doi.org/10.1016/j.tws.2012.03.008>
- [4] Xiao J, Huang Y, Yang J, Zhang Ch. Mechanical properties of confined recycled aggregate concrete under axial compression. *Constr Build Mater.* 2012;26:591-603. <https://doi.org/10.1016/j.conbuildmat.2011.06.062>
- [5] Cabral AE, Schalch V, Molin DC, Ribeiro JL. Mechanical properties modelling of Recycled Aggregate Concrete. *Constr Build Mater.* 2010;24:421-430. <https://doi.org/10.1016/j.conbuildmat.2009.10.011>
- [6] Yang YF, Han LH. Experimental behaviour of recycled aggregate concrete filled steel tubular columns. *J Constr Steel Res.* 2006;62:1310-1324. <https://doi.org/10.1016/j.jcsr.2006.02.010>
- [7] Etxeberria M, Marí AR, Vázquez E. Recycled aggregate concrete as structural material. *Mater Struct.* 2006;40:529-541. <https://doi.org/10.1617/s11527-006-9161-5>
- [8] Khatib JM. Properties of concrete incorporating fine recycled aggregate. *Cem Concr Res.* 2005;35:763-769. <https://doi.org/10.1016/j.cemconres.2004.06.017>
- [9] Varma AH, Ricles JM, Sause R, Lu LW. Seismic behaviour, and modelling of high-strength composite concrete-filled steel tube (CFT) beam-columns. *J Constr Steel Res.* 2002;58:725-758. [https://doi.org/10.1016/S0143-974X\(01\)00099-2](https://doi.org/10.1016/S0143-974X(01)00099-2)
- [10] Hajjar JF. Concrete-filled steel tube columns under earthquake loads. *Prog Struct Eng Mater.* 2000;2:72-81. [https://doi.org/10.1002/\(SICI\)1528-2716\(200001/03\)2:1<72::AID-PSE9>3.0.CO;2-E](https://doi.org/10.1002/(SICI)1528-2716(200001/03)2:1<72::AID-PSE9>3.0.CO;2-E)
- [11] Bairagi NK, Vidyadhara HS, Ravande K. Mix design procedure for recycled aggregate concrete. *Constr Build Mater.* 1990;4:188-193. [https://doi.org/10.1016/0950-0618\(90\)90039-4](https://doi.org/10.1016/0950-0618(90)90039-4)
- [12] Tam VWY, Wang K, Tam CM. Assessing relationships among properties of demolished concrete, recycled aggregate and recycled aggregate concrete using regression analysis. *J Hazard Mater.* 2008;152:703-714. <https://doi.org/10.1016/j.jhazmat.2007.07.061>
- [13] Andreu G, Miren E. Experimental analysis of properties of high performance recycled aggregate concrete. *Constr Build Mater.* 2014;52:227-235. <https://doi.org/10.1016/j.conbuildmat.2013.11.054>
- [14] Zhao H, Zhang WH, Wang R, Hou CC, Lam D. Axial compression behaviour of round-ended recycled aggregate concrete-filled steel tube stub columns (re-racfst):

- Experiment, Numerical Modelling and Design. Eng Struct. 2023;276:115376. <https://doi.org/10.1016/j.engstruct.2022.115376>
- [15] Li X, Wang R, Zhao H, Chen MT, Lam D. Bond behaviour of round-ended recycled aggregate concrete filled steel tube (re-racfst) columns. J Constr Steel Res. 2023;201:107700. <https://doi.org/10.1016/j.jcsr.2022.107700>
- [16] Yang D, Liu F, Wang Y. Axial compression behaviour of rectangular recycled aggregate concrete-filled steel tubular stub columns. J Constr Steel Res. 2023;201:107687. <https://doi.org/10.1016/j.jcsr.2022.107687>
- [17] Wu F, Wei Y, Lin Y, Zhao K, Huang L. Experimental study of bamboo scrimper-filled steel tube columns under axial compression. Eng Struct. 2023;280:115669. <https://doi.org/10.1016/j.engstruct.2023.115669>
- [18] Shweta A, Ma X, Zhuge Y, ElGawady M, Mills JE, Abd-Elaal E. Axial compressive behaviour of thin-walled composite columns comprise high-strength cold-formed steel and PE-ECC. Thin-Walled Struct. 2023;184:110471. <https://doi.org/10.1016/j.tws.2022.110471>
- [19] Zhong Y, Zhao O. Behaviour of eccentrically loaded circular recycled aggregate concrete-filled stainless steel tube stub columns. J Constr Steel Res. 2022;198:107568. <https://doi.org/10.1016/j.jcsr.2022.107568>
- [20] Wang B, Yan L, Fu Q, Kasal B. A comprehensive review on recycled aggregate and recycled aggregate concrete. Resour Conserv Recycl. 2021;171:105565. <https://doi.org/10.1016/j.resconrec.2021.105565>
- [21] Abdellatif S, Raza A, Alsulamy S, Khadimallah MA. Axial load-carrying capacity of concrete-filled steel tube columns: A comparative analysis of various modeling techniques. Mech Adv Mater Struct. 2023;1-23. <https://doi.org/10.1080/15376494.2023.2188325>
- [22] Liang J, Lin S, Li W, Liu D. Axial compressive behavior of recycled aggregate concrete-filled square steel tube stub columns strengthened by CFRP. Structures. 2021;29:1874-1881. <https://doi.org/10.1016/j.istruc.2020.12.084>
- [23] Raza A, Manalo AC, Rafique U, AlAjarmeh OS, Khan Q uz. Concentrically loaded recycled aggregate geopolymer concrete columns reinforced with GFRP bars and spirals. Compos Struct. 2021;268:113968. <https://doi.org/10.1016/j.compstruct.2021.113968>
- [24] Tang Y, Fang S, Chen J, Ma L, Li L, Wu X. Axial compression behavior of recycled-aggregate-concrete-filled GFRP-steel composite tube columns. Eng Struct. 2020;216:110676. <https://doi.org/10.1016/j.engstruct.2020.110676>
- [25] Faghidian SA. Analytical inverse solution of eigenstrains and residual fields in autofrettaged thick-walled tubes. J Pressure Vessel Technol. 2016;139(3) <https://doi.org/10.1115/1.4034675>
- [26] Faghidian SA. Analytical Approach for inverse reconstruction of eigenstrains and residual stresses in autofrettaged spherical pressure vessels. J Pressure Vessel Technol. 2017;139(4). <https://doi.org/10.1115/1.4035980>
- [27] Farrahi GH, Faghidian SA, Smith DJ. Reconstruction of residual stresses in autofrettaged thick-walled tubes from limited measurements. Int J Pressure Vessels Piping. 2009;86(11):777-784. <https://doi.org/10.1016/j.ijpvp.2009.03.010>

Blank Page

## Thin layer interface: An alternative modeling consideration in soil-structure interaction system

Gaurav D. Dhadse<sup>\*1,a</sup>, Gangadhar Ramtekkar<sup>2,b</sup>, Govardhan Bhatt<sup>2,c</sup>

<sup>1</sup>Dept. of Civil Engineering, G. H. Rasoni Institute of Engineering and Business Management, Jalgaon, India

<sup>2</sup>Dept. of Civil Engineering, National Institute of Technology, Raipur, India

### Article Info

#### Article history:

Received 26 Sep 2023

Accepted 15 Feb 2024

#### Keywords:

Finite element modeling;

Thin layer interface;

Soil-structure

interaction system;

Interface thickness;

Lateral load

### Abstract

The numerical modeling of a soil-structure interaction (SSI) system subjected to lateral loads depends mainly upon the interface behavior. The soil stiffness in relation to the structure is quite low, and the structure generally has a rough surface in contact with the soil. As a result of the slipping and rolling of soil grains caused by friction, a thin layer of shear zone forms in soil with the application of lateral loads. A thin layer interface is represented by the shear zone. As a result, the decision on the thickness requirement is critical for appropriate modeling of the thin layer interface, which is rarely documented by researchers. Furthermore, it has been reviewed in the literature that modeling the SSI system with a thin layer interface more accurately replicates the physical system than modeling it with a zero-thickness interface. The methodology for effective usage (in terms of proper interface thickness) of the thin-layer interface in SSI system using finite element (FE) modeling is proposed in this work. The thickness of the interface has also been determined via numerical modeling of a large direct shear test (DST).

© 2024 MIM Research Group. All rights reserved.

## 1. Introduction

The modeling of the SSI system with a thin layer interface has many advantages [1-3]. The performance and execution of numerical modeling considering thin layer interface mainly depends on the interface thickness [4]. This paper effectively deals with thin layer interface element as well as evaluation and execution of interface thickness for various normal stresses.

According to the reviewed literature, it has been reported that the thin layer interface is appropriately representing the physical state of the SSI problem than that of the zero-thickness interface [5-10]. Also, it has been noted that due to the bottom roughness of the footing, the soil particles slip as well as roll because of lateral loads as a result the thin layer interface has formed [11-13]. The interface acts differently than the rest of the soil [3, 14-16]. If both footing and underlying material act as solid such as footing-rock interaction, then the representation of interface has considered as zero thickness [17]. Such interface has been modeled with appropriate constant normal stiffness values and meshing aspect ratio, to avoid the numerical ill-conditioning [18-19]. It is worth to mention that many researchers showcased the computational difficulties that occur in zero thickness interfaces [2, 4, 18, 20-23]. In contrast, the recent software is using zero thickness interfaces for SSI problems by adopting only interface reduction factor with a high value of normal stiffness [24-29]. Such analysis is based on certain assumptions or approximations which have considered the interface performance by selecting only interface reduction factor, which may not be suitable for every soil and footing/structure condition. So,

\*Corresponding author: [gddhadse@yahoo.com](mailto:gddhadse@yahoo.com)

<sup>a</sup> orcid.org/0000-0002-8857-9509; <sup>b</sup> orcid.org/0000-0002-3063-4480; <sup>c</sup> orcid.org/0000-0002-8683-1918

DOI: <http://dx.doi.org/10.17515/resm2024.16me0926rs>

Res. Eng. Struct. Mat. Vol. 10 Iss. 3 (2024) 1173-1194



consideration of zero thickness interfaces in SSI problem is disadvantageous, whereas there are many advantages of using a thin layer interface.

The implementation of a thin layer interface necessitates the use of an appropriate evaluation interface thickness. According to Desai et al. [1], Dalili et al. [7] and Dhadse G.D. et al. [23], the interface thickness should be 0.1 to 0.01 of the adjacent element size. If the adjacent mesh size fluctuates, the thickness value is inconsistent and altering regardless of soil type or structure surface roughness. According to the literature, the interface thickness should be five times the average soil grain size [6, 11, 13, 30-33]. Whereas Fang H. and Wang W. [34], Saberi et al. [35] and Gennaro et al. [36] proposed the interface thickness should be 5 to 10 times the average particle size. The criteria given with respect to average particle size is realistic and varies according to grain size. But the formation of a thin layer interface is due to roughness of footing surface [11] in contact with soil and depends upon soil type, particle size, normal stress etc. [13, 30, 37-39]. As a result, the criterion based solely on particle size appears insufficient for determining optimal interface thickness for every SSI analysis situation.

The methodology for thickness evaluation and thin layer interface execution in FE modeling of the SSI system has been proposed in this study. The proposed methodology is inclusive of normal stress only, but the same methodology can be adopted by taking into consideration all interface thickness influencing parameters.

## **2. Proposed Problem Statement**

Many scholars have claimed that employing a thin layer over zero thickness interfaces has advantages. The research into the decision on interface thickness requirement is insufficient and requires further analysis. Few researchers had proposed the criteria based on grain size for the determination of interface thickness. This criterion may not be effective for every SSI system as the thickness predominantly relates to contact roughness and indirectly relates to soil type, grain size, normal stress etc.

The methodology for effective evaluation of interface thickness and execution of thin layer interface is proposed in the present study. The FE model of a large DST with a thin layer interface has been developed to validate the experimental results for various proposed thicknesses. The relation between normal stress and interface thickness has been established. The footing-soil interaction (FSI) problem considering zero thickness interfaces by Viladkar et al. [40] has been solved using the proposed thin layer thickness for the execution of the interface thickness. Non-linearity at the soil and interface has also been incorporated into FE formulations.

## **3. Finite Element Modeling**

The footing and soil mass is modeled with 8 noded isoparametric plane strain element. Each node in the element has two degrees of freedom (DoF) i.e. translations in  $\xi$  and  $\eta$  directions in a local coordinate system. The elements geometry is shown in Fig. 1. The mathematical formulation of the element is referred from J. N. Reddy [41], Chandrupatla and Belegundu [42], S.S. Rao [43] and O.C. Zienkiewicz et al. [44]. This element is very well compatible with 6 noded thin layer interface element as well as the various constitutive models of soil. Also, the element is useful in the proper evaluation of stresses near junction points [45].

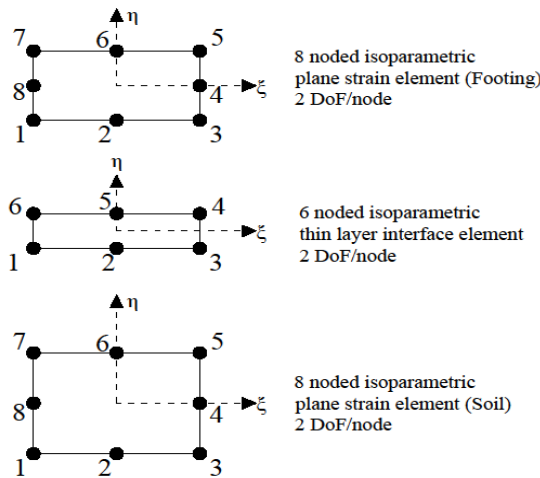


Fig. 1. Geometrical details of elements used for footing, interface and soil

### 3.1. Thin Layer Interface Element Formulation

The 6 noded thin layer isoparametric interface element depicted in Fig. 2 serves as a continuum interface between soil and footing. The element's constitutive performance is thought to differ from that of adjacent solid elements, and it is mostly determined by the interface's normal and shear stiffness (as determined by the shear test). The element is compatible with adjacent soil and footing element. Earlier, this element has been used by Sharma and Desai [3], Zaman et al. [14] and Noorzai et al. [9] to analyze various soil-structure interaction systems. In the present study, the same element is executed for analyzing the SSI problem with proper thickness. The detailed element stiffness matrix formulation is given below.

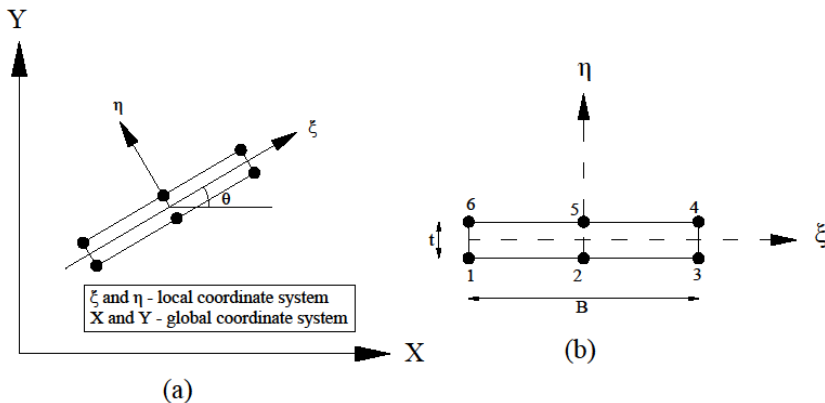


Fig. 2. Thin layer interface element representation in the global and local coordinate systems

The six-noded thin layer interface element is depicted in Fig. 2 in both global and local coordinate systems. In general, the interface details are evaluated in a local coordinate system, therefore the orientation of the interface is an important criterion. As a result, the formulation I generated in a local coordinate system and then transformed to the global system using the transformation matrix. It is also worth noting that as the interface

thickness approaches zero the in-plane stress and strain become minimal in compared to normal and shear stress and strain [3]. As a result, the contact response is approximate idealized by simply normal and shear stiffness.

In the global X and Y systems, U and V represent nodal displacement. In the local coordinate and system, u and v are the nodal displacements. Equation 1 gives the shape functions 'N' in the local coordinates system at each node,

$$\begin{aligned}
 N_1 &= \frac{1}{4}(-\xi)(1-\xi)(1-\eta) \\
 N_2 &= \frac{1}{2}(1-\xi^2)(1-\eta) \\
 N_3 &= \frac{1}{4}(\xi)(1+\xi)(1-\eta) \\
 N_4 &= \frac{1}{4}(\xi)(1+\xi)(1+\eta) \\
 N_5 &= \frac{1}{2}(1-\xi^2)(1+\eta) \\
 N_6 &= \frac{1}{4}(-\xi)(1-\xi)(1+\eta)
 \end{aligned} \tag{1}$$

The element displacement matrix in the global system is (Equation 2),

$$\delta_e = \{U_1 \quad V_1 \quad U_2 \quad V_2 \quad U_3 \quad V_3 \quad U_4 \quad V_4 \quad U_5 \quad V_5 \quad U_6 \quad V_6\}^T \tag{2}$$

1x12

Therefore, the displacement at any point within an element is given by Equation 3;

$$\begin{Bmatrix} U \\ V \end{Bmatrix} = \begin{bmatrix} N_1 & 0 & N_2 & 0 & N_3 & 0 & N_4 & 0 & N_5 & 0 & N_6 & 0 \\ 0 & N_1 & 0 & N_2 & 0 & N_3 & 0 & N_4 & 0 & N_5 & 0 & N_6 \end{bmatrix} \{\delta_e\} \tag{3}$$

$$U = N_i U_i$$

$$V = N_i V_i$$

The strain at any point within an element is given by strain displacement relationship as given in Equation 4,

$$\begin{Bmatrix} \epsilon_x \\ \epsilon_y \\ \gamma_{xy} \end{Bmatrix} = \begin{Bmatrix} \frac{\partial U}{\partial x} \\ \frac{\partial V}{\partial y} \\ \frac{\partial U}{\partial y} + \frac{\partial V}{\partial x} \end{Bmatrix} \tag{4}$$

$$\begin{matrix} \{\epsilon\} \\ 3 \times 1 \end{matrix} = \begin{matrix} [B] \\ 3 \times 12 \quad 12 \times 1 \end{matrix} \{\delta_e\}$$

where,  $\varepsilon_x, \varepsilon_y$  and  $\gamma_{xy}$  are axial strain, normal strain and shear strain respectively in the global system. Whereas 'B' is the strain displacement relation matrix and ' $\delta_e$ ' is the global element displacement matrix.

It is discussed earlier that, interface properties are in a local coordinate system, hence stress-strain relation is written as shown in Equation 5,

$$\begin{Bmatrix} \sigma_n \\ \tau \end{Bmatrix} = \begin{bmatrix} k_{nn} & k_{ns} \\ k_{sn} & k_{ss} \end{bmatrix} \begin{Bmatrix} v_r \\ u_r \end{Bmatrix} \tag{5}$$

where,  $\sigma_n$  and  $\tau$  are normal and shear stress (Local coordinate system).  $k_{nn}$  and  $k_{ss}$  are normal and shear stiffness whereas  $k_{sn}$  and  $k_{ns}$  are in-plane stiffness.  $v_r$  and  $u_r$  are relative displacements. As thickness is very small for the interface, the in-plane stresses are negligible, hence Equation 5 can be written as (Equation 6),

$$\begin{Bmatrix} \sigma_n \\ \tau \end{Bmatrix} = \begin{bmatrix} k_{nn} & 0 \\ 0 & k_{ss} \end{bmatrix} \begin{Bmatrix} v_r \\ u_r \end{Bmatrix} \tag{6}$$

As in-planes stresses are negligible, hence (Equation 7)

$$\begin{aligned} \varepsilon_x &= 0 \\ \sigma_x &= 0 \\ \varepsilon_y &= \varepsilon_n = \frac{v_r}{t} \because t = \text{thickness} \\ \sigma_y &= \sigma_n \\ \gamma_{xy} &= \gamma = \frac{u_r}{t} \end{aligned} \tag{7}$$

Thus equation 6 can be written as, (Equation 8)

$$\begin{Bmatrix} \sigma_n \\ \tau \end{Bmatrix} = \begin{bmatrix} tk_{nn} & 0 \\ 0 & tk_{ss} \end{bmatrix} \begin{Bmatrix} \varepsilon_n \\ \gamma \end{Bmatrix} \tag{8}$$

$$\{\partial\sigma\} = [D_e] \{\partial\varepsilon\}$$

Where, [De] is material matrix or relation matrix in the local coordinate system

To transform the local coordinate system into the global coordinate system, use the transformation matrix [T] in Equation 9,

$$[T] = \begin{bmatrix} s^2 & c^2 & -cs \\ -2cs & 2cs & (c^2 - s^2) \end{bmatrix} \tag{9}$$

where,  $s = \sin\theta$ ,  $c = \cos\theta$  and  $\theta$  is the angle made by interface with X-axis. Therefore, the global stress-strain relation matrix is expressed as (Equation 10)

$$\begin{Bmatrix} \sigma_x \\ \sigma_y \\ \tau_{xy} \end{Bmatrix}_{3 \times 1} = \begin{bmatrix} s^2 & -2cs \\ c^2 & 2cs \\ -cs & (c^2 - s^2) \end{bmatrix}_{3 \times 2} \begin{bmatrix} tk_{nn} & 0 \\ 0 & tk_{ss} \end{bmatrix}_{2 \times 2} \begin{bmatrix} s^2 & c^2 & -cs \\ -2cs & 2cs & (c^2 - s^2) \end{bmatrix}_{2 \times 3} \begin{Bmatrix} \varepsilon_x \\ \varepsilon_y \\ \gamma_{xy} \end{Bmatrix}_{3 \times 1} \quad (10)$$

$$\{\partial \sigma\} = [T]^T [D_e][T]\{\partial \varepsilon\}$$

Thus, the element stiffness matrix [K] in global form can be written as, (Equation 11)

$$[K] = \int [B]^T [T]^T [D_e][T][B] dv_e$$

$$[K] = \sum_{gp=1}^n [B]^T [T]^T [D_e][T][B] J |W_{gp} \quad (11)$$

$gp = gauss\ pt.$   
 $W_{gp} = weights$

where,  $v_e$  is the volume of the element. The MATLAB FE model for analyzing the SSI system with soil and interface non-linearity has been developed using the formulation of all the elements.

### 3.2. Soil and Interface Constitutive Modeling

Soil is a highly non-linear material. Many researchers have proposed various constitutive relations to predict the appropriate complex behavior of soil [46-47]. The choice of constitutive models amongst the available model depends on the type of soil as well as purpose and type of analysis [46]. Almost all the constitutive relations are compatible with FE formulation. Soil nonlinearity is typically integrated into FE formulation using an incremental iterative method. [48]. In the present analysis, the Hyperbolic Model proposed by Duncan-Chang [49-51] (based on associated flow rule [52]) is used to represent the response of the soil. In this model, the stiffness non-linearity and hardening are appropriately included whereas softening and dilatancy are not included [6]. It is amongst the commonly used model for SSI analysis due to its versatility. The tangent modulus 'ET' [45, 53] at every load step is evaluated using equation 12,

$$E_T = \left[ 1 - \frac{R_f(1 - \sin \phi)(\sigma_1 - \sigma_3)}{2(C \cos \phi + \sigma_3 \sin \phi)} \right]^2 K.P_a \left( \frac{\sigma_3}{P_a} \right)^n \quad (12)$$

where, 'R<sub>f</sub>' is failure ratio, 'φ' is the angle of friction, 'σ<sub>1</sub>' and 'σ<sub>3</sub>' are major and minor principal stresses, 'C' is cohesion, 'K' is Modulus number, 'P<sub>a</sub>' is atmospheric pressure and 'n' is the exponent.

In addition to soil non-linearity, interface non-linearity has also been considered in the present research. The interface hyperbolic model developed by Clough and Duncan 1971 [54] has been used in present investigation. The model is versatile as well as it solves the purpose of present study. The model is capable of dealing with cohesive soil-structure interface as well, because it is inclusive of interface adhesion. The hyperbolic relation is used to approximate the interface's stress-strain response [7, 40, 45] as given in equation 13. During lateral loading, the shear zone has been formed due to slipping and rolling of soil particles over the rough foundation surface. As the analysis has been performed with

the Finite Element Method, the slipping and rolling of the particles have been idealized by tangential stiffness value as express in equation 13 and the shear zone has been idealized with thin layer interface element (with appropriate thickness) as discussed in Section 3.1. The tangential stiffness ' $K_{ss}$ ' from equation 13 is evaluated at every load step whereas normal stiffness ' $K_{nn}$ ' is approximately evaluated as ' $E_t/t$ ' [3] (' $t$ ' is interface thickness). It is also reviewed from the literature that, due to a very thin interface, few problems may face computational difficulties as a result; arbitrary high value for normal stiffness is also considered [40, 45, 55].

$$\begin{aligned}
 K_{ss} &= (1 - \lambda_2)^2 K_i \\
 K_i &= k_j \gamma_w \left[ \frac{\sigma_n}{P_a} \right]^n \\
 \lambda_2 &= \frac{R_f \tau}{(C_a + \sigma_n \tan \phi)}
 \end{aligned} \tag{13}$$

From equation 13, ' $k_j$ ' is modulus number, ' $\gamma_w$ ' is the unit weight of water, ' $\sigma_n$ ' is normal stress, ' $P_a$ ' is atmospheric pressure, ' $R_f$ ' is failure ratio, ' $\tau$ ' is shear stress, ' $C_a$ ' is adhesion at the interface, ' $\phi$ ' angle of friction, ' $n$ ' is the exponent and ' $K_i$ ' is initial stiffness.

#### 4. Methodology

The non-linear plane strain SSI-FE model consisting of footing, soil and interface element has been developed in MATLAB. The mixed incremental iterative algorithm [48, 56] is used to apply non-linearity in soil mass and interface. The model is versatile and realistic with the availability of various elements and the inclusion of interface thickness. It is also able to solve variable degree of freedom system with ease.

In the current investigation, a 6 noded thin layer element has been selected for modeling the interface, together with an 8 noded plane strain isoparametric element for soil and footing. The developed FE model is validated using experimental findings from the large box shear test performed by Viladkar et al. [40] and also the same model has been checked for various interface thickness values. Further, the FSI problems with thin layer interface have been analyzed using the validated FE model.

##### 4.1. Proposed Procedure for Prediction and Execution of Interface Thickness

According to reviewed literature as per section 1, it is reported that the interface thickness for any SSI problem should lie between 5-10 times the average particle size. The said criterion is purely dependent on particle size without considering parameters such as surface roughness, soil type, normal stress etc. But for physical cases, the site conditions are completely different and interface thickness mostly depends on every parameter as mentioned. Hence thickness criteria may vary according to these parameters. As a result, the current study proposes a systematic technique for predicting interface thickness based on normal stresses.

In this study, for the large box shear test (details are given in section 5), only one type of sand and a single mild steel rough surface as a footing has been used. Thus particle size, sand type and surface roughness are kept constant whereas only normal stress keeps varying. It is decided to use four different interface thicknesses such as  $3D_{50}$ ,  $5D_{50}$ ,  $10D_{50}$  and  $12D_{50}$  ( $D_{50}$  is the mean diameter of sand particle) for every normal stress. These proposed thicknesses cover the criteria given in the literature as well as some values are beyond literatures.

The large box shear FE model has been analyzed for maximum shear stress for given normal stress. The result for tangential displacements (for every thickness) has been compared to get a value that approximately matches with experimental data. Thus for every normal stress, the interface thickness has found out. The plot between interface thickness and normal stress gives the best fit prediction about interface thickness based on a variation of normal stress. The predicted equation further used for the execution of thin layer interface in soil-structure interaction problem.

### 5. Validation of Large DST with Thin Layer Interface

The plane strain idealization with boundary conditions of large DST in FE modeling [57-58] is shown in Fig. 3. Each box is of dimension 300 x 300 x 75 mm. Shear stress acts on the side of the structure portion, whereas normal stress acts on the top of the upper box. The thin layer interface is located between two boxes as shown in Fig. 3. By maintaining normal stress constant, shear stress is applied with each load step, and tangential displacement is determined. Both boxes and interface has been discretized into 8 noded isoparametric and 6 noded thin layer isoparametric plane strain elements respectively. For the structure part, concrete or mild steel material is used (analyzed as linear elastic) with a rough bottom in contact with the soil whereas sand is used in the upper box.

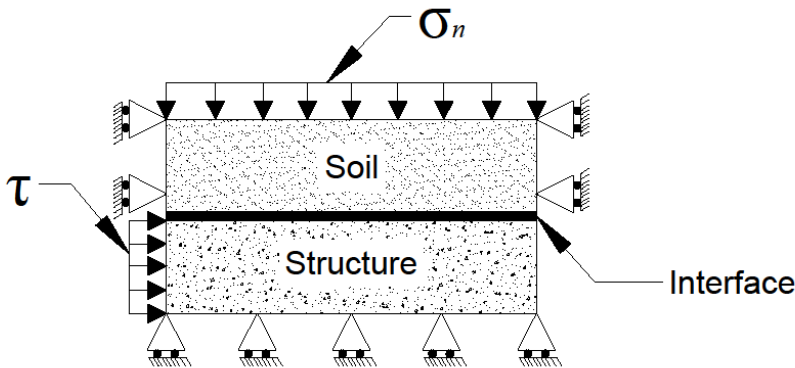
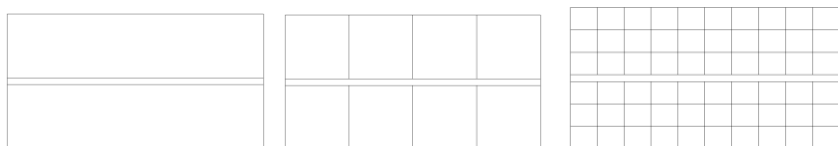
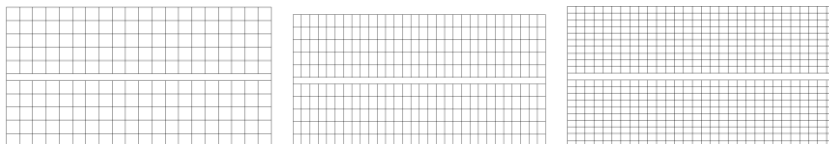


Fig. 3. Idealization of the large DST [57]



(a): No. of Elements = 02 (b): No. of Elements = 08 (c): No. of Elements = 60



(d): No. of Elements = 200 (e): No. of Elements = 300 (f): No. of Elements = 600

Fig. 4. Mesh configurations for large DST

Desai et al.'s example was used to conduct the mesh convergence study [1]. The linear elastic analysis is checked with various meshes as shown in Fig. 4 for the materials used by Desai et al. [1]. The result for tangential displacement (Table 1) is compared with the literature result.

The tangential displacement of large DST subjected to the normal stress of 0.955 N/mm<sup>2</sup> and shear stress of 0.5 N/mm<sup>2</sup> for all meshes is plotted in Fig. 5. The interface thickness is considered as 3mm for all mesh configurations. From Fig. 5, it is observed that the mesh configuration with 200 elements has been found optimum. Thus in further analysis, the same configuration of elements has been used. Also, the result for tangential displacement (mesh = 200 elements) from Table 1 is appropriately matching with literature results.

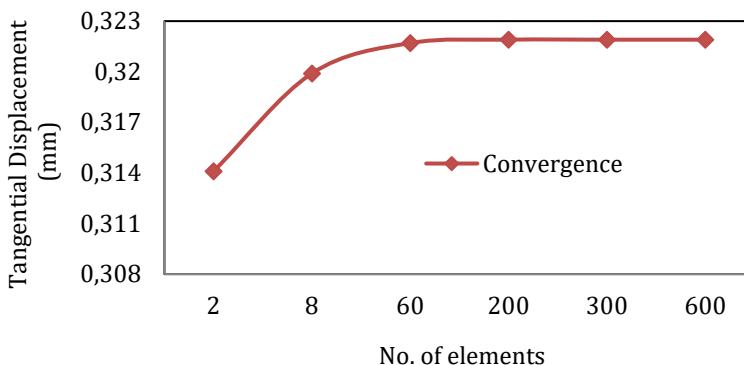


Fig. 5. Large box shear test mesh convergence analysis

Table 1. Validation with Desai et al. 1984[1]

Author	Tangential displacement (mm)
Desai et al.	0.34
Present Study	0.3219
% Variation	5.32 %

### 5.1. Prediction of interface thickness

The large box shear test performed on the soil-mild steel interface by Viladkar et al. [40] has been numerically modeled (section 5.0) in the present study to find out the interface thickness. The optimum mesh size as per Fig. 4(d) is used to discretize the soil, mild steel and interface. The experimental plot of tangential displacement against shear stresses for soil-mild steel interface shows non-linear nature. Thus, in addition to soil non-linearity; interface non-linearity has also been incorporated in the developed FE model. As the hyperbolic constitutive relation is used to represent soil and interface behavior as per section 3.2, the hardening and stiffness non-linearity can appropriately be included in the FE model. Hence, it is decided to analyze the system for maximum shear stress for given normal stress and the corresponding displacement is found out.

Table 2. Material properties for structure (Mild steel)

Sr. No.	Component	Elastic Modulus (N/mm <sup>2</sup> )	Poisson's Ratio
1	Structure (Mild steel)	2.1 x 10 <sup>5</sup>	0.3



The structure part is modeled as mild steel (considered as linear elastic) with a rough side in contact with sand. The test had been carried by Viladkar et al. [40] for four normal stress conditions such as 40.8 kPa, 61.24 kPa, 81.65 kPa and 102.07 kPa as shown in Fig. 6. The mild steel, sand, and interface material properties are provided in Table 2, Table 3 and Table 4 respectively.

Table 3. Material properties for sand

Sr. No.	Description	Value
1	Soil Type	SP
2	Unit weight	16.3 kN/m <sup>3</sup>
3	Relative Density	84%
4	Modulus Number 'K'	700
5	Exponent 'n'	0.50
6	Failure Ratio 'Rf'	0.90
7	Cohesion 'C'	0
8	The angle of Internal Friction 'ϕ'	41°
9	Poisson's Ratio of sand	0.3
10	Mean diameter of sand particle 'D <sub>50</sub> '	0.25 mm

Table 4. Material properties for interface

Sr. No.	Description	Value
1	Modulus Number 'k <sub>j</sub> '	8625
2	Exponent 'n'	0.662
3	Failure Ratio 'Rf'	0.82
4	Adhesion 'C <sub>a</sub> '	0
5	The angle of Internal Friction 'ϕ'	29.3°
6	Unit weight of water 'γ <sub>w</sub> '	0.00001 N/mm <sup>3</sup>
7	Atmospheric pressure 'P <sub>a</sub> '	0.10132 N/mm <sup>2</sup>

5.1.1 Result and Discussion

The graph of shear stress vs shear displacement by Viladkar et al. [40] is shown in Fig. 6 for the various normal stress conditions. To determine the thickness of the interface, the FE model for large DST has been subjected to normal stress and maximum shear stress. Normal stress is kept constant throughout loading, while shear stress is applied in stages.

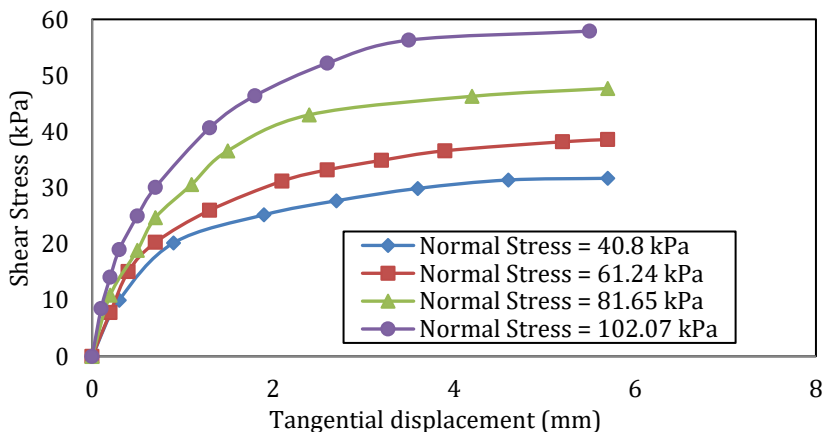


Fig. 6. Large box shear test result for sand-footing interface [40]

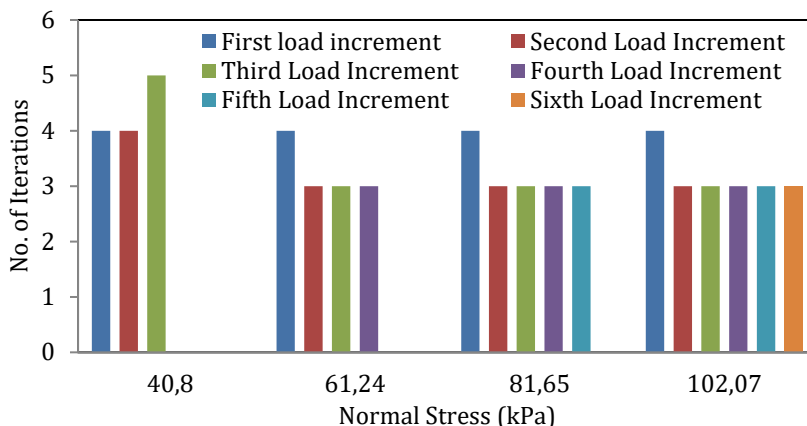


Fig. 7. No. of iterations performed for each normal stress during interface shear test

Fig. 8, Fig. 9, Fig. 10 and Fig. 11 show the results for tangential displacement (Experimental and FE model result) in interface shear test for each normal stress and maximum shear stress condition. (IT – Interface Thickness,  $\sigma_n$  – Normal stress and  $\tau$  – Shear stress)

The no. of iterations performed by the FE model for each load increment till convergence is shown in Fig. 7. For every normal stress, four different interface thicknesses (such as  $3D_{50}$ ,  $5D_{50}$ ,  $10D_{50}$  and  $12D_{50}$ ) have been considered. The tangential displacement for maximum shear stress of every interface thickness has been compared and a value having good agreement with the experimental result is considered in further analysis. Hence interface thickness is found out for every normal stress.

Results observed from Fig. 8, Fig. 9, Fig. 10 and Fig. 11 show consistent in nature i.e. as the interface thickness is increased, the corresponding tangential displacement is also increased. Because in the formulation of thin layer interface, the element stiffness is indirectly proportional to interface thickness, hence if the thickness is increased the corresponding tangential displacement also increased. For Fig. 8 and Fig. 9, interface thickness equal to  $5D_{50}$  show good results with 9 % and 1.53% difference with experimental results. Whereas, Fig. 10 with interface thickness of  $10D_{50}$  demonstrates good agreement with experimental results with a difference of 1.63%. In case of  $\sigma_n = 102.07$  kPa (Fig. 11),  $12D_{50}$  interface thickness gives appropriate result (difference = 0.9 %). Thus it can be said that considering common interface thickness for every normal stress is not suitable. The available criteria for interface thickness from literature seem insufficient, as for every normal stress the interface thickness is changing.

The maximum average change in tangential displacement from  $3D_{50}$  to  $12D_{50}$  is about 13% to 15% from Fig. 8 to Fig. 11. In the present study only variation of normal stress has been considered for determination of interface thickness (to achieve the objective of the paper) whereas there are various parameters such as particle size, moisture content, density, interface adhesion, etc. are responsible for change in interface thickness as per the literatures. Hence due to change in interface thickness, the system's response is very robust.

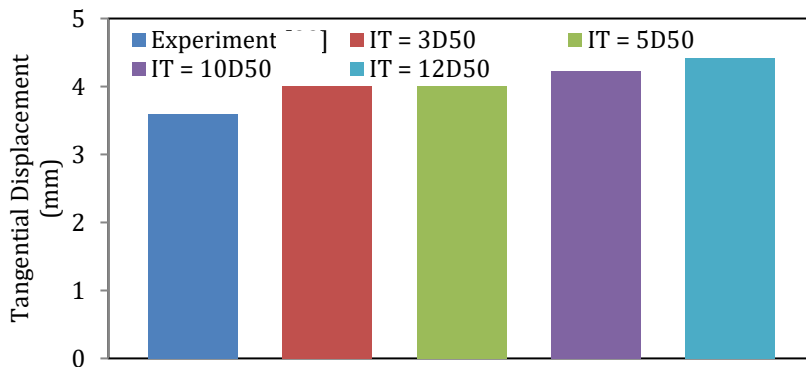


Fig. 8. Interface shear test - tangential displacement plot for  $\sigma_n = 40.8$  kPa and  $\tau = 30$  kPa

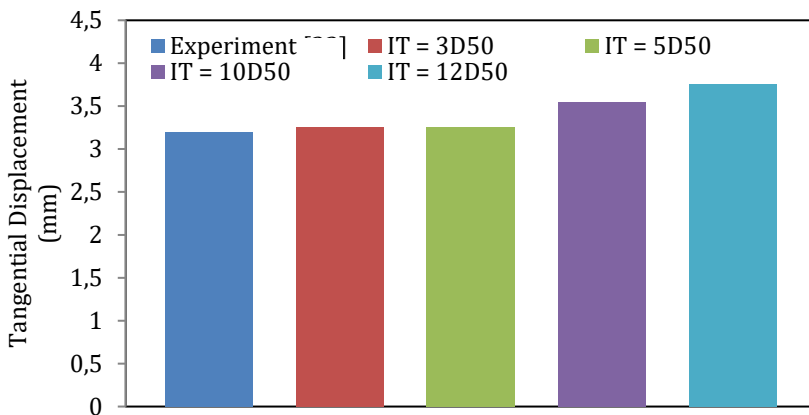


Fig. 9. Interface shear test - tangential displacement plot for  $\sigma_n = 61.24$  kPa and  $\tau = 35$  kPa

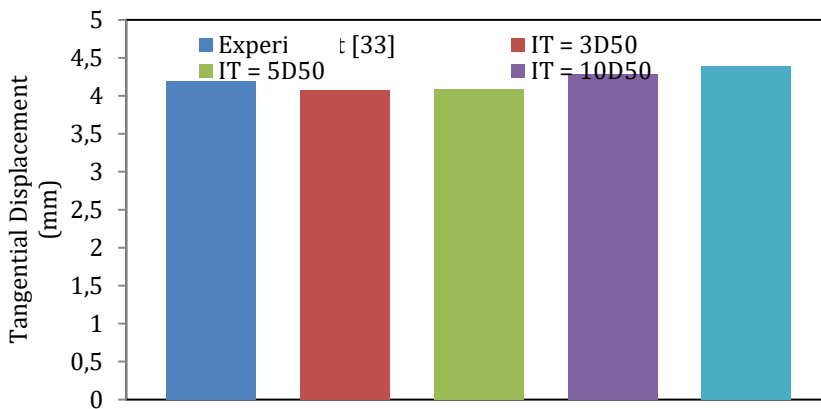


Fig. 10. Interface shear test - tangential displacement plot for  $\sigma_n = 81.65$  kPa and  $\tau = 46.3$  kPa

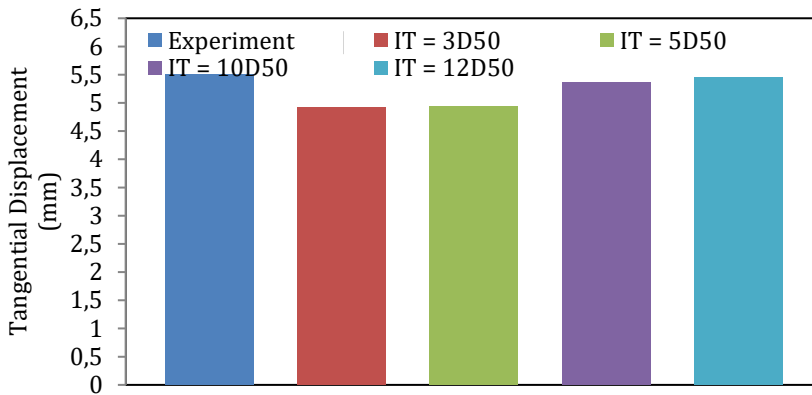


Fig. 11. Interface shear test - tangential displacement plot for  $\sigma_n = 102.07$  kPa and  $\tau = 57.9$  kPa

The interface thickness (thickness which validates with experimental values) observed from Fig. 8, Fig. 9, Fig. 10 and Fig. 11 have been plotted against corresponding normal stress values shown in Fig. 12. The graph is useful in predicting interface thickness for various normal stresses.

It is observed from Fig. 12 that, the interface thickness is increasing as normal stress goes on increasing. The formation of a thin layer interface is because of rolling and slipping of the sand particle due to contact roughness. In the present investigation, normal stress is increasing in addition to contact roughness, thus additional sand particles may take part in the shearing action. Therefore, such condition leads to increase in the interface thickness with respect to increase in normal stress.

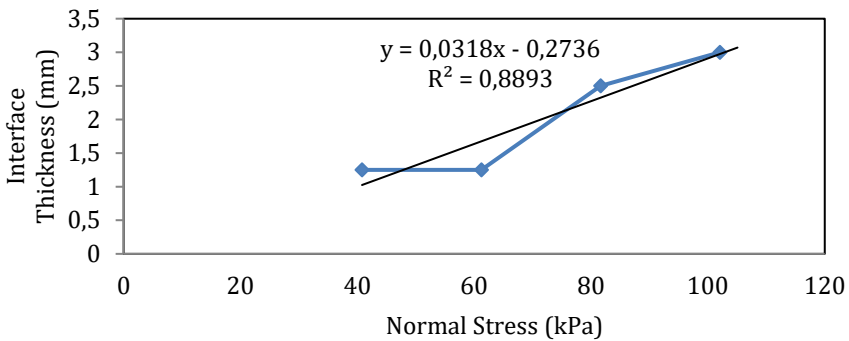


Fig. 12. Variation of interface thickness against normal stress

The graph shown in Fig. 12 has been fitted with a linear equation. The equation shows the prediction of interface thickness for various normal stress values. Present investigation is a proposed methodology for effective evaluation and execution of interface thickness hence the equation in Fig. 12 is limited for this particular study only. If the interface thickness (according to equation in Fig. 12) is less than  $5D_{50}$  then the minimum thickness of  $5D_{50}$  can be consider for analysis. To execute the predicted equation from Fig. 12, the FSI problem subjected to inclined-eccentric load has been solved with the developed FE model.

## 6. Implementation of Interface Thickness for SSI Analysis

The FSI problem experimented by Agrawal [59] and numerically modeled by Viladkar et al. [40] and Zedan [60] for zero thickness interface element has been considered in the present investigation for the execution of thin layer interface. The FE model has been developed as shown in Fig. 13. The settlement and horizontal displacement of the footing with a thin layer interface are compared and validated with an experimental and zero thickness FSI system. The thickness evaluation for the FSI problem has been carried out from the equation given in Fig. 12.

FSI system has consisted of strip footing resting on sand and subjected to eccentric inclined loads. The FE model is developed as a plane strain problem. Considering the thin layer interface, 3 different cases are analyzed (Fig. 14), such as,

Case I:  $D_f/B = 0$ ;  $e/B = 0.2$  and angle of inclination for inclined load with vertical =  $15^\circ$

Case II:  $D_f/B = 0$ ;  $e/B = 0.2$  and angle of inclination for inclined load with vertical =  $10^\circ$

Case III:  $D_f/B = 0$ ;  $e/B = 0.2$  and angle of inclination for inclined load with vertical =  $5^\circ$

where, ' $D_f$ ' is depth of the footing, ' $B$ ' is width of the footing and ' $e$ ' is eccentricity of load.

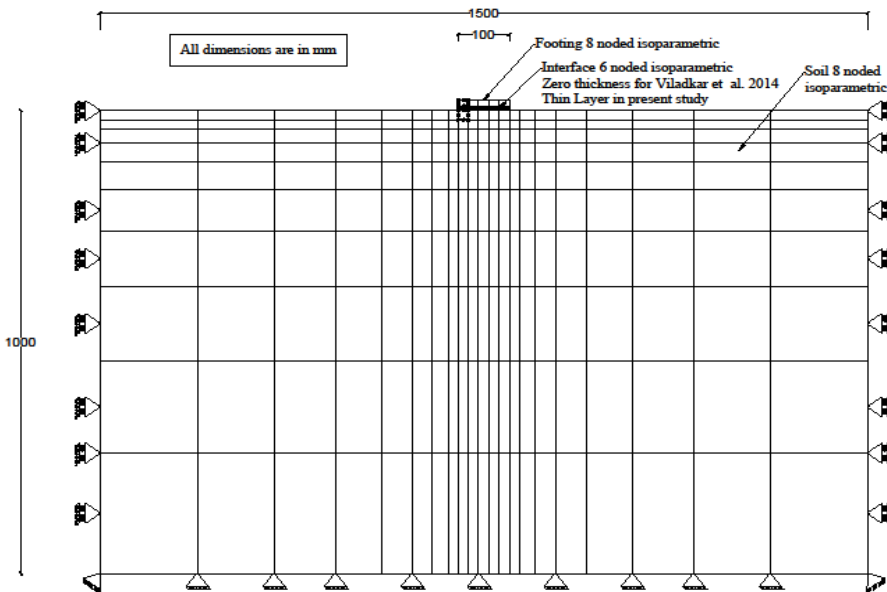


Fig. 13. FE model for FSI system

The soil and footing are discretized with 8-noded isoparametric elements, whereas the interface is discretized as a 6-noded thin layer interface element. The constitutive relations as discussed in section 3.2 are used for soil and interface. The footing is considered to be made up of mild steel (thickness = 12 mm) with the same roughness in contact with soil as that of large DST mild steel specimen. The materials used for carrying out FSI analysis are the same as those of large DST as discussed in section 5.1. Table 2, Table 3, and Table 4 show the properties for footing, soil, and interface.

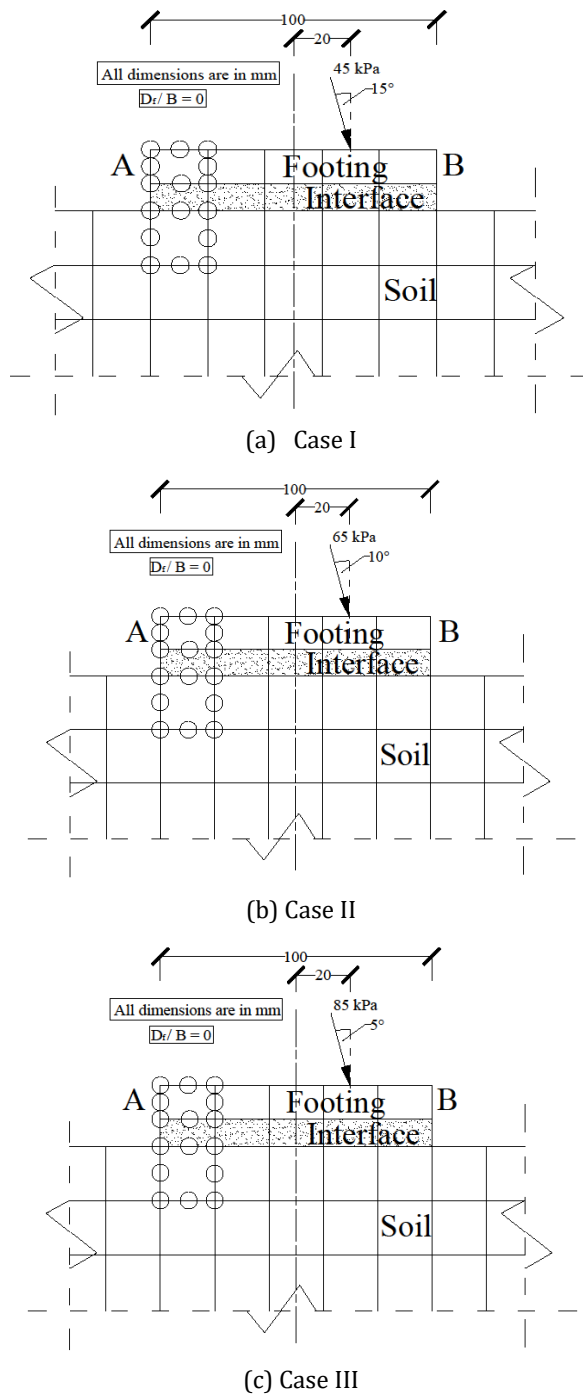


Fig. 14. Various cases considered for eccentric inclined loading in FSI problem

The interface thickness for the case I, case II and case III are 1.25 mm, 1.71 mm and 2.35 mm respectively. The thickness has been calculated based on the maximum normal stress acting on the footing from equation in Fig.12.

### 6.1. Result and Discussion

The FSI system with a thin layer interface's non-linear analysis (Fig. 13) for various cases (Fig. 14) has been carried out with a mixed incremental iterative procedure. The plot between pressure-settlement and pressure-horizontal displacement at end B (Fig. 14) of the footing for various cases are shown in Fig. 15 (a), Fig. 15 (b), Fig. 16 (a), Fig. 16 (b), Fig. 17 (a) and Fig. 17 (b).

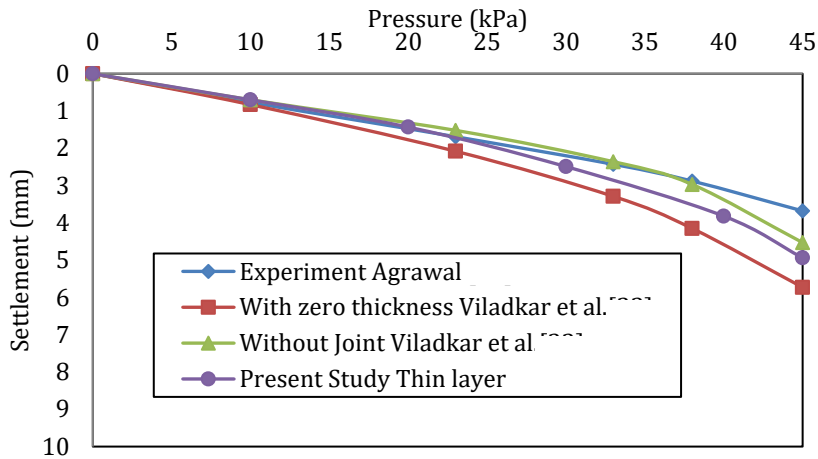


Fig. 15 (a). Pressure-Settlement plot for Case I

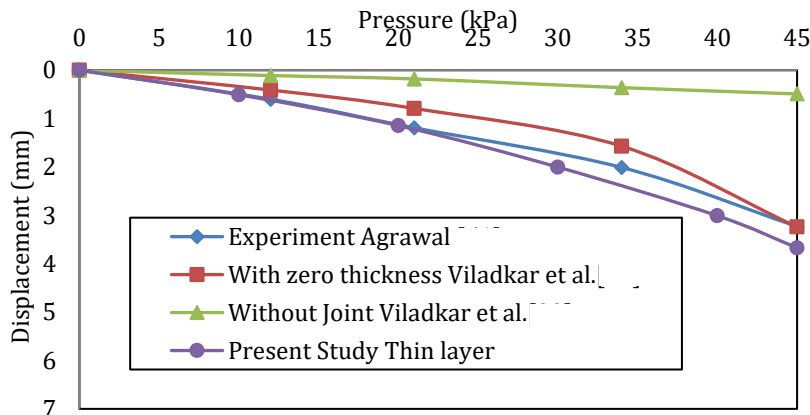


Fig. 15 (b). Pressure-Horizontal displacement plot for Case I

Fig. 15 (a) and Fig. 15 (b) shows the results for experimental analysis by Agrawal [59], numerical analysis (without interface and with zero thickness interface) by Viladkar et al. [40] and analysis considering thin layer interface as present investigation. For pressure-settlement, the effect of the interface is negligible because of the full bond between soil and footing. Wherein, pressure-horizontal displacement plot shows the necessity of interface. It is also reported that the results for settlement and horizontal displacement considering thin layer interface shows very good agreement with the experimental result.

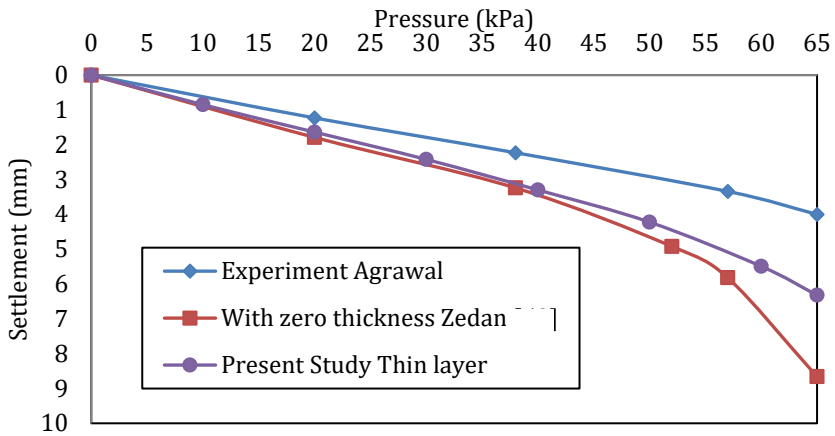


Fig. 16 (a). Pressure-Settlement plot for Case II

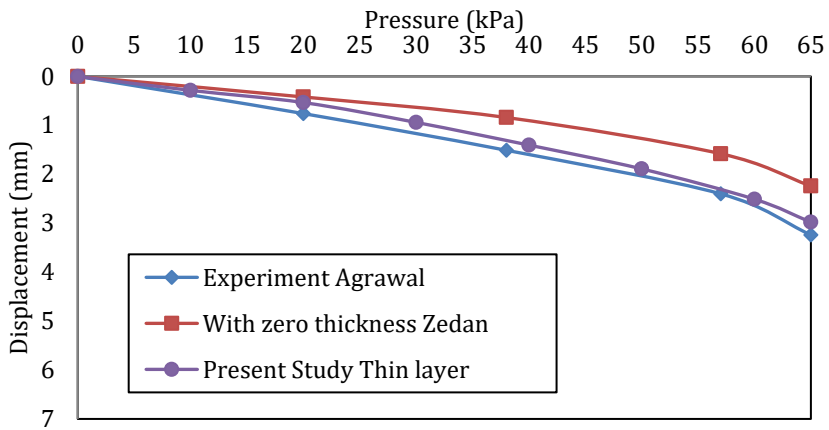


Fig. 16 (b). Pressure-Horizontal displacement plot for Case II

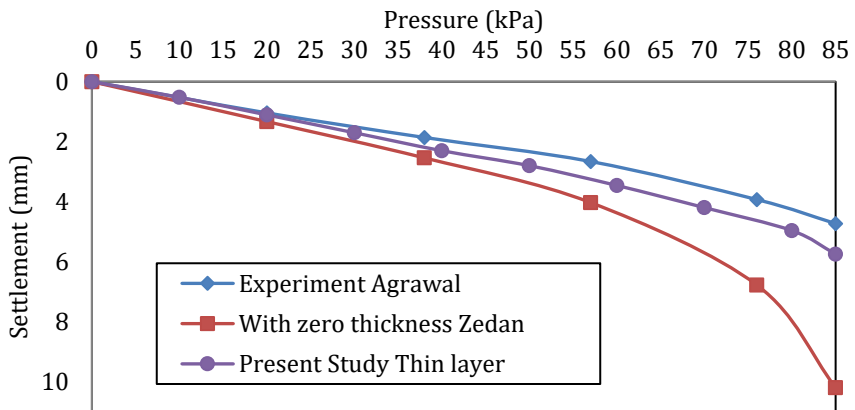


Fig. 17 (a). Pressure-Settlement plot for Case III



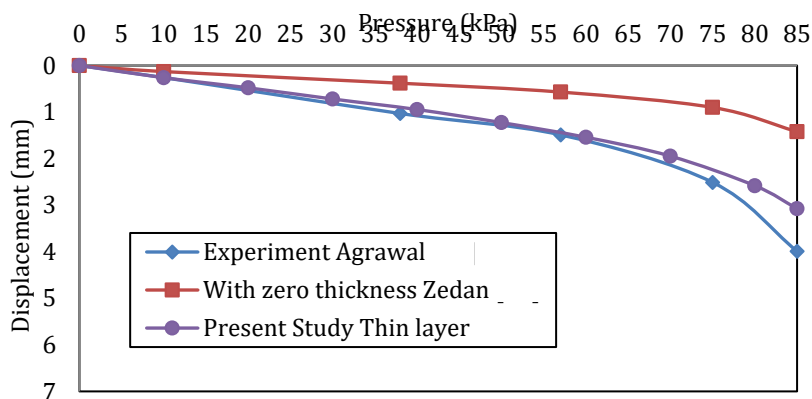


Fig. 17 (b). Pressure-Horizontal displacement plot for Case III

It is observed from Fig. 16 (a) to Fig. 17 (b) that the settlement and horizontal displacement considering thin layer interface shows appropriately matching results with experimental analysis. It is also noted that the results considering thin layer interface are superior to zero thickness interface. It may be because of consideration of normal stiffness for thin layer interface as ' $E_T/t$ ' and not a constant value. Thus, such value is giving more appropriate results than the constant value. Also by considering this normal stiffness, the interface nodes are not penetrating thus it satisfies the contact stiffness criteria.

In addition to the above, due to the roughness of footing in contact with the soil; the soil particles rotate and slip during the application of lateral loads thus it is obvious to form the thin shear zone just beneath the footing which is called as thin layer interface. Hence the SSI model with thin layer interface is giving realistic results as compared to the zero thickness interfaces.

There are some results such as Fig. 16 (a) and Fig. 17 (a), where the settlement by thin layer interface showing more than 10% difference with respect to experimental values. Such difference may be due to consideration of only normal stress for deciding the interface thickness. Whereas there may be a few other parameters responsible for interface thickness, such as surface roughness, particle size, and soil type, which need to be investigated further.

## 7. Conclusions

There are numerous advantages of using a thin layer interface over a zero-thickness interface. The selection of interface thickness is important and must be dealt with caution. The methodology for effective usage (in terms of interface thickness) of the thin-layer interface in FE modeling of the SSI system has been investigated in this work. The following findings are reached from the evaluation and execution of interface thickness,

- The parameters which are responsible for interface thickness such as, surface roughness, particle size, normal stress and soil type are varying for every soil condition. Thus, the criterion for interface thickness based only on  $D_{50}$  looks insufficient. Hence there is a need to propose a methodology consisting of these parameters for predicting appropriate interface thickness.
- The proposed methodology, which was used to evaluate interface thickness while taking normal stress into account, is also applicable to other contributing parameters.

- The non-linear hyperbolic model is suitable for modeling large DST. Thus it is useful in the evaluation of interface thickness.
- The relation between interface thickness and normal stress (derived from numerical validation of large DST) is useful in predicting interface thickness based on normal stress value. In general, such methodology can be adopted for various SSI systems for interface thickness prediction.
- The pressure-settlement response in the FSI system is independent of interface effect whereas under lateral and eccentric-inclined loading condition for appropriate horizontal displacement, interface consideration is necessary.
- The results for settlement and horizontal displacement in the FSI system considering thin layer interface have been improved in comparison to the zero-thickness interface.
- The proposed methodology for effectively utilizing thin layer interfaces in FE modeling of SSI problems has been successfully applied.

In order to obtain the more realistic results of SSI system, the consideration of proper thickness of thin layer interface (considering all variations in soil and structure) and advanced constitutive model is necessary.

## References

- [1] Desai CS, Jaman M, Lightner JG, Siriwardane HJ. Thin-Layer Elements for Interfaces and Joints. *Int J Numer Anal Methods Geomech.* 1984;8:19-43. <https://doi.org/10.1002/nag.1610080103>
- [2] Pande GN, Sharma KG. On joint/interface elements and associated problems of numerical ill-conditioning. *Int J Numer Anal Methods Geomech.* 1979;3(3):293-300. <https://doi.org/10.1002/nag.1610030308>
- [3] Sharma KG, Desai CS. Analysis and Implementation of Thin-Layer Element for Interfaces and Joints. *J Eng Mech.* 1992;118(12):2442-2462. [https://doi.org/10.1061/\(ASCE\)0733-9399\(1992\)118:12\(2442\)](https://doi.org/10.1061/(ASCE)0733-9399(1992)118:12(2442))
- [4] Potts DM, Zdravkovic L. Finite Element Analysis in Geotechnical Engineering. 1999.
- [5] Desai CS, Rigby DB. Modelling and Testing of Interfaces. In: Desai CS, Christian JT, editors. *Mechanics of Geomaterial interfaces.* CRC Press; 1995. pp. 107-125. [https://doi.org/10.1016/S0922-5382\(06\)80008-5](https://doi.org/10.1016/S0922-5382(06)80008-5)
- [6] Hu L, Pu J. Testing and Modeling of Soil-Structure Interface. *J Geotech Geoenviron Eng.* 2004;130(8):851-860. [https://doi.org/10.1061/\(ASCE\)1090-0241\(2004\)130:8\(851\)](https://doi.org/10.1061/(ASCE)1090-0241(2004)130:8(851))
- [7] Dalili Shoaie M, Huat BBK, Jaafar MS, Alkarni A. Soil-framed structure interaction analysis - A new interface element. *Latin Am J Solids Struct.* 2015;12(2):226-249. <https://doi.org/10.1590/1679-78251130>
- [8] Barros RC, Vasconcelos LAC de, Nogueira CL, Silveira RAM. Interface Elements In Geotechnical Engineering - Some Numerical Aspects and Applications. In: XXXVIII Iberian Latin-American Congress on Computational Methods in Engineering. Brazil; 2017. pp. 1-20. <https://doi.org/10.20906/CPS/CILAMCE2017-0174>
- [9] Noorzaei J, Thanoon WAM, Yeat WF, Pour PM, Jaafar MS. Numerical Modeling Of Railway Track Supporting System Using Finite-Infinite And Thin Layer Elements. *IJE Trans A Basic.* 2009;22(2):131-144.
- [10] Dhadse GD, Ramtekkar G, Bhatt G. Influence due to interface in finite element modeling of soil-structure interaction system: a study considering modified interface element. *Res Eng Struct Mater.* 2022;8(1):127-154. <https://doi.org/10.17515/resm2021.322st0702>
- [11] Uesugi M, Kishida H, Tsubakihara Y. Behaviour of sand particles in sand-steel friction. *Soils Found.* 1988;28(1):107-118. <https://doi.org/10.3208/sandf1972.28.107>

- [12] Hryciw RD, Irsyam M. Behavior of Sand Particles Around Rigid Ribbed Inclusions during Shear. *Soils Found.* 1993;33(3):1-13. [https://doi.org/10.3208/sandf1972.33.3\\_1](https://doi.org/10.3208/sandf1972.33.3_1)
- [13] Uesugi M, Kishida H. Frictional resistance at yield between dry sand and mild steel. *Soils Found.* 1986;26(4):139-149. [https://doi.org/10.3208/sandf1972.26.4\\_139](https://doi.org/10.3208/sandf1972.26.4_139)
- [14] Zaman MM, Desai CS, Drumm EC. Interface model for dynamic soil-structure interaction. *J Geotech Eng.* 1984;110(9):1257-1273. [https://doi.org/10.1061/\(ASCE\)0733-9410\(1984\)110:9\(1257\)](https://doi.org/10.1061/(ASCE)0733-9410(1984)110:9(1257))
- [15] Rezamand A, Afrazi M, Shahidikhah M. Study of Convex Corners' Effect on the Displacements Induced by Soil-Nailed Excavations Abbas. *J Adv Eng Comput.* 2021;5(4):277-290. <https://doi.org/10.55579/jaec.202154.344>
- [16] Riazi E, Yazdani M, Afrazi M. Numerical Study of Slip Distribution at Pre-existing Crack in Rock Mass using Extended Finite Element Method (XFEM). *Iran J Sci Technol Trans Civ Eng.* 2023;47:31-41. <https://doi.org/10.1007/s40996-023-01051-8>
- [17] Mayer MH, Gaul L. Segment-to-segment contact elements for modelling joint interfaces in finite element analysis. *Mech Syst Signal Process.* 2007;21(2):724-734. <https://doi.org/10.1016/j.ymsp.2005.10.006>
- [18] Day RA, Potts DM. Zero Thickness Interface Elements-Numerical Stability And Applications. *Int J Numer Anal Methods Geomech.* 1994;18:689-708. <https://doi.org/10.1002/nag.1610181003>
- [19] Afrazi M, Razavi M, Monjezi M, Bhatavdekar RM. Development and Evaluation of a Computer-Aided Educational Platform for Advancing Understanding of Slope Stability Analysis. 2023.
- [20] Beer G. An isoparametric joint/interface element for finite element analysis. *Int J Numer Methods Eng.* 1985;21:585-600. <https://doi.org/10.1002/nme.1620210402>
- [21] Kaliakin VN, Li J. Insight Into Deficiencies Associated With Commonly Used Zero-Thickness Interface Elements. *Comput Geotech.* 1995;17:225-252. [https://doi.org/10.1016/0266-352X\(95\)93870-0](https://doi.org/10.1016/0266-352X(95)93870-0)
- [22] Coutinho ALGA, Martins MAD, Sydenstricker RM, Alves JLD, Landau L. Simple zero thickness kinematically consistent interface elements. *Comput Geotech.* 2003;30(5):347-374. [https://doi.org/10.1016/S0266-352X\(03\)00013-2](https://doi.org/10.1016/S0266-352X(03)00013-2)
- [23] Dhadse GD, Ramtekkar G, Bhatt G. Finite Element Modeling of Soil Structure Interaction System with Interface: A Review. *Arch Comput Methods Eng.* 2021;28(5):3415-3432. <https://doi.org/10.1007/s11831-020-09505-2>
- [24] Arslan H. Finite Element Study of Soil Structure Interface Problem. *Electron J Geotech Eng.* 2005.
- [25] Skejic A. Interface formulation problem in geotechnical finite element software. *Electron J Geotech Eng.* 2012;17:2035-2041.
- [26] Yu Y, Damians IP, Bathurst RJ. Influence of choice of FLAC and PLAXIS interface models on reinforced soil - structure interactions. *Comput Geotech.* 2015;65:164-174. <https://doi.org/10.1016/j.compgeo.2014.12.009>
- [27] Damians IP, Yu Y, Lloret A, Bathurst RJ. Equivalent interface properties to model soil-facing interactions with zero-thickness and continuum element methodologies. *Fundam to Appl Geotech.* 2015:1065-1072.
- [28] Dhadse GD, Ramtekkar G, Bhatt G. Response of Single and Multilayered Flexible Base for Static and Earthquake Loading Under Framed RC Structure. In: Adhikari S, et al, editors. *Advances in Structural Technologies.* Springer Singapore; 2020. pp. 169-183. [https://doi.org/10.1007/978-981-15-5235-9\\_13](https://doi.org/10.1007/978-981-15-5235-9_13)
- [29] Dhadse GD, Ramtekkar G, Bhatt G. A Succinct Review on Soil Structure Interface Thickness. *Arch Comput Methods Eng.* 2023;30(6):3969-3976. <https://doi.org/10.1007/s11831-023-09926-9>
- [30] Uesugi M, Kishida H. Influential Factors of Friction Between Steel and Dry Sands. *Soils Found.* 1986;26(2):33-46. [https://doi.org/10.3208/sandf1972.26.2\\_33](https://doi.org/10.3208/sandf1972.26.2_33)

- [31] Hu L, Pu JL. Application of damage model for soil - structure interface. *Comput Geotech.* 2003;30:165-183. [https://doi.org/10.1016/S0266-352X\(02\)00059-9](https://doi.org/10.1016/S0266-352X(02)00059-9)
- [32] Zhang G, Zhang J-M. Unified Modeling of Monotonic and Cyclic Behavior of Interface Between Structure and Gravelly Soil. *Soils Found.* 2008;48(2):231-245. <https://doi.org/10.3208/sandf.48.231>
- [33] Dhadse GD, Ramtekkar G, Bhatt G. Effect of Particle Size , Moisture Content and Density on the Hyperbolic Model Parameters for Non-cohesive Soil. *Int J Eng.* 2022;35(09). <https://doi.org/10.5829/IJE.2022.35.09C.04>
- [34] Fang H, Wang W. A Three-Dimensional Multishear Bounding Surface Model of Granular Soil-Structure Interfaces under Monotonic and Cyclic Loading. *J Eng Mech.* 2020;146(7):1-18. [https://doi.org/10.1061/\(ASCE\)EM.1943-7889.0001796](https://doi.org/10.1061/(ASCE)EM.1943-7889.0001796)
- [35] Saberi M, Annan C, Konrad J. On the mechanics and modeling of interfaces between granular soils and structural materials. *Arch Civ Mech Eng.* 2018;18(4):1562-1579. <https://doi.org/10.1016/j.acme.2018.06.003>
- [36] Gennaro V De, Pande GN, Lerat P. Stability Problems in Soil-Structure Interfaces : Experimental Observations and Numerical Study. *Int J Geomech.* 2002;2(2):175-203. [https://doi.org/10.1061/\(ASCE\)1532-3641\(2002\)2:2\(175\)](https://doi.org/10.1061/(ASCE)1532-3641(2002)2:2(175))
- [37] Han F, Ganju E, Salgado R, Prezzi M. Effects of Interface Roughness , Particle Geometry , and Gradation on the Sand - Steel Interface Friction Angle. *J Geotech Geoenvironmental Eng.* 2018;144(12). [https://doi.org/10.1061/\(ASCE\)GT.1943-5606.0001990](https://doi.org/10.1061/(ASCE)GT.1943-5606.0001990)
- [38] Potyondy JG. Skin Friction between Various Soils and Construction Materials. *Géotechnique.* 1961;11(4):339-353. <https://doi.org/10.1680/geot.1961.11.4.339>
- [39] Fareghian M, Afrazi M, Fakhimi A. Soil Reinforcement by Waste Tire Textile Fibers: Small-Scale Experimental Tests. *J Mater Civ Eng.* 2023;35(2). [https://doi.org/10.1061/\(ASCE\)MT.1943-5533.0004574](https://doi.org/10.1061/(ASCE)MT.1943-5533.0004574)
- [40] Viladkar MN, Zedan AJ, Saran S. Nonlinear elastic analysis of shallow footings subjected to eccentric inclined loads. *Geomech Geoengin.* 2015;10(1):1-12. <https://doi.org/10.1080/17486025.2014.902117>
- [41] Reddy JN. *An Introduction to the Finite Element Method.* Vol 3. 1993.
- [42] Chandrupatla TR, Belegundu AD. *Introduction to finite elements in engineering.* Vol 4, no 01. 2012.
- [43] Rao SS. *The Finite Element Method in Engineering.* Fifth. Butterworth-Heinemann is an imprint of Elsevier; 2010.
- [44] Zienkiewicz OC , Taylor R , Zhu J , *The Finite Element Method: Its Basis and Fundamentals.* Vol 1. 2005.
- [45] Viladkar MN, Godbole PN, Noorzai J. Modelling of interface for soil-structure interaction studies. *Comput Struct.* 1994;52(4):765-779. [https://doi.org/10.1016/0045-7949\(94\)90358-1](https://doi.org/10.1016/0045-7949(94)90358-1)
- [46] Brinkgreve RBJ. Selection of Soil Models and Parameters for Geotechnical Engineering Application. In: *Soil Const. Model. Eval. Sel. Calibration* ASCE; 2005. pp. 69-98. [https://doi.org/10.1061/40771\(169\)4](https://doi.org/10.1061/40771(169)4)
- [47] Lade PV. Overview Of Constitutive Models For Soils. In: *Geo-Frontiers Congress 2005.* Austin, Texas, United States; 2005. pp. 1-34. [https://doi.org/10.1061/40771\(169\)1](https://doi.org/10.1061/40771(169)1)
- [48] Viladkar MN, Godbole PN, Noorzai J. Soil-structure interaction in plane frames using coupled finite-infinite elements. *Comput Struct.* 1991;39(5):535-546. [https://doi.org/10.1016/0045-7949\(91\)90062-Q](https://doi.org/10.1016/0045-7949(91)90062-Q)
- [49] Dong W, Hu L, Yu YZ, Lv H. Comparison between duncan and Chang's EB model and the generalized plasticity model in the analysis of a high earth-rockfill dam. *J Appl Math.* 2013;1-12. <https://doi.org/10.1155/2013/709430>
- [50] Pramthawee P, Jongpradist P, Kongkitkul W. Evaluation of hardening soil model on numerical simulation of behaviors of high rockfill dams. *Songklanakarin J Sci Technol.* 2011;33(3):325-334.

- [51] Rahnama H. A hyperbolic model for stress-strain behavior of unsaturated soils. In: 12th International Conference on Computer Methods and Advances in Geomechanics 2008; 2012-2021.
- [52] Pandey AK, Bisht RS. Numerical Modelling of Infilled Clay Brick Masonry Under Blast Loading. *Adv Instr Eng.* 2014;17(4):591-606. <https://doi.org/10.1260/1369-4332.17.4.591>
- [53] Noorzaei J, Viladkar MN, Godbole PN. Nonlinear soil-structure interaction in plane frames. *Eng Comput.* 1994;11(4):303-316. <https://doi.org/10.1108/02644409410799308>
- [54] Clough GW, Duncan JM. Finite element analyses of retaining wall behavior. *J Soil Mech Found Div.* 1971;97(12):1657-1673. <https://doi.org/10.1061/JSFEAQ.0001713>
- [55] Tancev L, Kokalanov G. Application of joint elements at finite element analysis of embankment dams. *Trans Eng Sci.* 1995;7:1-8.
- [56] Hora MS. Nonlinear interaction analysis of infilled frame-foundation beam-homogeneous soil system. *Coupled Syst Mech.* 2014;3(3):267-289. <https://doi.org/10.12989/csm.2014.3.3.267>
- [57] Stutz H, Mašin D, Sattari AS, Wuttke F. A general approach to model interfaces using existing soil constitutive models application to hypoplasticity. *Comput Geotech.* 2017;87:115-127. <https://doi.org/10.1016/j.compgeo.2017.02.010>
- [58] Moayed RZ, Tamassoki S, Izadi E. Numerical Modeling of Direct Shear Tests on Sandy Clay. *World Acad Sci Eng Technol.* 2012;61:1093-1097.
- [59] Agrawal R. Behaviour of shallow foundations subjected to eccentric - inclined loads. Thesis (PhD). University of Roorkee, India. 1986.
- [60] Zedan AJ. Finite Element Analysis of shallow foundations for Eccentric Inclined loads. Thesis (PhD). University of Roorkee, India, 2004.

## Predicting flexural-creep stiffness in bending beam rheometer (BBR) experiments using advanced super learner machine learning techniques

Alireza Roshan<sup>\*,1,a</sup>, Magdy Abdelrahman<sup>2,b</sup>

<sup>1</sup>Department of Civil, Architectural and Environmental Engineering, Missouri University of Science and Technology, Rolla, MO 65409, U.S.A

<sup>2</sup>Missouri Asphalt Pavement Association (MAPA) Endowed Professor, Department of Civil, Architectural and Environmental Engineering, Missouri University of Science and Technology, Rolla, MO 65409, U.S.A

### Article Info

### Abstract

#### Article history:

Received 27 Oct 2023  
Accepted 09 Feb 2024

#### Keywords:

*Flexural-creep stiffness;  
Bending beam  
rheometer;  
Long-term pavement  
performance;  
Machine learning super  
learner methods*

BBR test is commonly used to assess the low-temperature performance grade (PG) of asphalt binders, with the flexural-creep stiffness being a critical parameter calculated through this test. However, it has notable limitations that demand attention. The significant amount of asphalt binder needed for test specimens increases costs and resource consumption. Additionally, the complex and time-consuming specimen preparation process hinders testing efficiency and introduces result variability, affecting the accuracy and reliability of PG determinations. In recent years, machine learning (ML) has emerged as a promising substitute for predicting various engineering values. In this study, the primary focus was on harnessing super learner (SL) techniques to predict the creep stiffness of asphalt binders. The SL approach combines multiple ML algorithms to enhance predictive accuracy and reduce individual model biases. Bagging, boosting, and stacking algorithms were employed in the construction of these prediction models. To conduct the investigation, data from 1350 samples sourced from the Long-Term Pavement Performance (LTPP) website were utilized to explore the influence of six crucial variables on the creep stiffness of asphalt binders. The proposed method demonstrated high accuracy, nearing 90% in the coefficient of determination. The Stacking model achieved a low Mean Absolute Percentage Error of 2.86% and robust Prediction Accuracy of 97.14% for randomly selected data points. Furthermore, the sensitivity analysis highlighted the significance of distinct input variables in influencing the creep stiffness of asphalt binders. Notably, the test temperature emerged as the most influential factor affecting creep stiffness, according to the conducted study.

© 2024 MIM Research Group. All rights reserved.

## 1. Introduction

The asphalt pavements undergo significant impacts from climatic changes, which, in turn, profoundly impact the performance of asphalt mixtures and the characteristics of asphalt binder. As temperatures fluctuate, these materials experience significant transformations that directly influence their properties and response to external stresses. As temperatures decrease, the asphalt binder experiences a critical transition from a plastic state to a solid state. In colder conditions, the binder becomes much stiffer and exhibits a lower resistance to flow, resulting in increased viscosity. This change in viscosity affects the overall flexibility and resilience of the asphalt mixture, making it less capable of accommodating dynamic loads and stresses induced by traffic. The reduced flexibility and increased stiffness of the asphalt binder in colder climates can lead to several performance issues for

\*Corresponding author: [alireza.roshan@mst.edu](mailto:alireza.roshan@mst.edu)

<sup>a</sup>orcid.org/0000-0002-9399-3501; <sup>b</sup>orcid.org/0000-0002-8722-0203

DOI: <http://dx.doi.org/10.17515/resm2024.58me1027rs>

Res. Eng. Struct. Mat. Vol. 10 Iss. 3 (2024) 1195-1208

the asphalt pavement. It becomes more susceptible to cracking and fracture due to its limited ability to absorb the energy from vehicular loads. Additionally, the reduced flowability of the binder makes it challenging for the pavement to self-heal or recover from minor damages caused by traffic, further contributing to the overall deterioration of the pavement structure [1].

When asphalt pavements experience elevated tensile stress surpassing the movement resistance of the asphalt binder, it results in the formation of cracks within the binder, which eventually spread across the pavement surface. This phenomenon is known as low-temperature cracking, leading to significant functional and structural failures in the pavements [2]. To study and address these cracks that may occur during the asphalt pavement's design life, a specialized test is conducted on the asphalt binder material. This specific test is conducted to assess the creep stiffness value at low temperatures, serving as a crucial indicator of the asphalt binder's resistance to low-temperature cracking. The creep stiffness measurement provides valuable insights into how well the binder can withstand tensile stresses caused by low temperatures without undergoing excessive deformation or cracking. This property is crucial for ensuring the long-term performance and durability of asphalt pavements, especially in regions with colder climates or significant temperature variations [3]. To assess the asphalt binder's resistance to low-temperature cracking, a specialized test is conducted using an asphalt binder prismatic beam. The beam possesses specific dimensions, measuring 125 mm in length, 6.25 mm in height, and 12.5 mm in width. In the test, the prismatic beam is horizontally positioned in a cold fluid bath, and a constant load of 980 mN is applied at the midpoint of the beam. The deflection of the specimen is measured, and the creep stiffness is calculated using the actual load and specimen dimensions. The test is performed at various constant temperatures within the low-temperature range. At a loading time of 60 seconds, the creep stiffness and the corresponding m-value are derived. The m-value represents the absolute value of the slope of the stiffness versus time curve on a double logarithmic scale [4].

BBR has become the predominant testing method for assessing the low-temperature characteristics of asphalt binders, particularly those subjected to prolonged aging before undergoing BBR testing. Despite its widespread use, several authors have highlighted significant drawbacks associated with BBR testing, particularly concerning specimen preparation and testing conditions. One of the main drawbacks is the complexity and labour-intensive nature of preparing BBR test specimens. The process requires meticulous attention to detail and precise measurements to ensure accurate results. This can be time-consuming and may introduce variability in the test outcomes due to inconsistencies in specimen preparation. Additionally, the testing conditions in BBR may not always fully represent the real-world environmental conditions that the asphalt binders encounter in the field. For instance, the test temperatures in BBR may not accurately mimic the wide range of temperature fluctuations experienced by pavements in different geographic locations and climates. This limitation can impact the relevance and applicability of BBR results to actual pavement performance [5-7]. The direct grading process to determine the PG of asphalt pavements involves using devices like the Dynamic Shear Rheometer (DSR) and BBR to directly measure pavement performance. However, this approach requires a substantial budget, presenting challenges for researchers and pavement laboratories in certain countries. To address these limitations, researchers have explored alternative methods for indirectly assessing pavement performance, which are more accessible and cost-effective. One such indirect estimation method involves leveraging weather data, particularly the maximum and minimum air temperatures in construction regions, as a basis for assessing the PG grade. By utilizing weather data, researchers can infer the performance characteristics of the pavement under varying temperature conditions. Additionally, some researchers have proposed an indirect estimation of the PG grade based

on pavement characteristics under "real-world conditions" while adhering to the specifications of traditional grading systems used in developed countries. This approach aims to find a balance between cost-effectiveness and accuracy in assessing the PG grade [8]. During the Strategic Highway Research Program (SHRP), there was a consideration to use the DSR with parallel plate geometry for the low-temperature PG system. However, it was eventually not selected for this purpose due to a significant challenge. Researchers have acknowledged that DSR measurements at temperatures below approximately 5 °C led to compliance errors in dynamic responses, particularly evident when employing the standard thin film binder geometry. To overcome this limitation and accurately measure the low-temperature rheological properties of asphalt binder, SHRP developed the BBR. The BBR test was specifically designed to assess the stiffness and creep behaviour of asphalt binders under low-temperature conditions. By using the BBR, researchers were able to obtain more reliable and consistent data related to the performance of asphalt binders at lower temperatures [9]. Recognizing the challenges and limitations associated with the BBR for low-temperature binder evaluation, some researchers have sought an alternative approach. As a result, they have endeavored to shift from BBR-based testing to a method exclusively reliant on DSR. In this new approach, the DSR is utilized for these evaluations, three distinct geometries were employed: torsion bar, 8-mm Parallel Plate, and 4-mm Parallel Plate. However, it is important to highlight that testing asphalt binder at extremely low temperatures, such as -30°C, can only be accomplished using the 4-mm plate geometry. This limitation arises from the torque capacity constraints of motors in typical commercially available DSRs. The use of the 4-mm plate geometry allows researchers to accurately measure the rheological properties of asphalt binders under these extreme low-temperature conditions, enabling a more comprehensive assessment of their performance in challenging environments [10-12]. Recently, the approach to determining the BBR equivalent low performance grade has centered on converting the complex shear modulus ( $G^*(\omega)$ ) to creep compliance ( $D(t)$ ). This conversion involves transforming data acquired in the DSR frequency domain into the BBR time domain. Various interconversion methods have been employed in these studies, and they are grounded in linear viscoelastic theory. On the other hand, approximation-based methods offer simplified procedures to approximate the interconversion from DSR frequency domain to BBR time domain [13,14]. Indeed, while the approximation-based interconversion methods may not offer the same level of precision as rigorous methods in recent years, there has been a growing trend among researchers to explore the application of ML for evaluating the rheological parameters of asphalt binders.

ML techniques, such as regression, neural networks, and ensemble methods, have shown great promise in various engineering applications due to their ability to handle complex datasets and identify patterns that might not be easily discernible through traditional methods. In a research study, artificial neural network and self-validated ensemble modeling techniques were used to predict low-temperature fracture energy of asphalt mixtures and both methods showed high prediction accuracy [15]. In another study, new predictive models were developed to estimate the dynamic modulus and phase angle of asphalt concrete accurately. The models considered temperature and loading frequency as key factors, and statistical analysis revealed their effectiveness in providing precise estimations for these properties [16]. In other study, the Extreme Learning Machine (ELM) algorithm, optimized by Genetic Algorithm (GA), was employed to rapidly predict the low-temperature rheological properties of styrenic block copolymer modified asphalt based on the raw material properties. The GA-ELM model outperformed traditional models, reducing errors by 68.97-81.48% [17]. Another research introduced a data-driven Convolutional Neural Network (CNN) model to forecast the phase angle behavior of asphalt concrete mixtures. The proposed CNN model achieves an impressive  $R^2$  score of 0.90, indicating high accuracy in its predictions [18].



From the existing literature, it can be observed that ML methods have not been extensively used to predict the creep stiffness, considering various factors such as test temperature, penetration, kinematic viscosity, and absolute viscosity (dynamic) also the occurrence of physical hardening during the storage of BBR specimens at constant low temperatures has been observed in multiple studies [19-20]. Because physical hardening changes the rheological properties of asphalt binders the inclusion of the mentioned parameters contributes to the attainment of more precise predictions of creep stiffness prediction. Additionally, most of the mentioned algorithms in previous studies are individual learning algorithms, whereas new SL techniques, which are more accurate, powerful, and robust, are gaining popularity. The core concept of SL techniques involves training multiple weak learners with the training data and then combining them to create a strong learner. These weak learners are based on individual learning algorithms. As a result, group learning models (strong learners) significantly enhance prediction accuracy and model robustness. Three primary groups of algorithms for group learning are bagging, boosting, and stacking, and their distinctions can be found in a review article [21]. Great potential for improving the prediction accuracy and reliability of creep stiffness in asphalt binders is offered through the utilization of these advanced SL methods. This is attributed to the presence of non-linearities and interactions between various factors on asphalt binders. In high-dimensional feature spaces, a preference for nonlinear models such as bagging and boosting may arise for feature selection, regularization, and prediction, while simpler models like linear regression may suffice for fewer features [22].

The primary aim of this research is to develop a predictive model capable of forecasting creep stiffness in BBR Experiments using data collected from the LTPP dataset. The proposed model incorporates various factors that influence the rheological properties of the asphalt binder, primarily related to test conditions and binder properties. These influential factors include test temperature, penetration, kinematic viscosity, absolute viscosity (dynamic viscosity) and specific gravity. The model is constructed by training SL techniques with the collected data, resulting in a strong learner that can accurately predict the value of creep stiffness. Additionally, the research investigates the impact of key factors in the best model approach, such as the amount of training data, sensitivity, and the number of input variables. This comprehensive approach seeks to enhance the accuracy and reliability of predicting creep stiffness, contributing to a better understanding of asphalt binder behavior, and facilitating the design of more durable and resilient asphalt pavements.

## 2. Methods

ML techniques have proven highly advantageous in civil engineering, providing rapid and precise outcomes with minimal error rates. These ML methods can be categorized into three main groups: supervised learning, unsupervised learning (including clustering algorithms and Principal Component Analysis), and reinforcement learning. Supervised learning involves feeding the algorithm substantial volumes of labeled data containing input and output variables. By identifying patterns and learning from observations, the algorithm generates predictions until the error reaches an acceptable level. This type of learning can be further divided into two categories: classification and regression [23-24]. The diverse range of ML methods empowers civil engineering researchers to enhance efficiency and accuracy in their analyses and decision-making processes. In the context of predicting creep stiffness, a model is constructed using SL techniques trained with the collected data. This results in a robust learner capable of accurately forecasting creep stiffness values. Additionally, the research explores the impact of key factors in the best model approach, such as the amount of training data, sensitivity, and the number of input variables.

In contrast to the less powerful regression models previously used, this research focuses on harnessing the predictive capabilities of the SL approach to forecast creep stiffness in the BBR test. By combining and optimizing different base learners, the SL models aim to improve the accuracy and reliability of predictions for this important rheological property of asphalt binders. In this study, SL models were developed based on several ensemble methods, including Random Forest, Gradient Boosting Machine (GBM), Adaptive Boosting (AdaBoost), Extreme Gradient Boosting (XGBoost), Categorical gradient Boosting (CatBoost), and stacking, to estimate the Creep stiffness. Through a process of hyperparameter optimization, the optimal conditions for each ensemble algorithm were obtained using a grid search method to achieve the best performance. The effectiveness of the SL models was built using datasets collected from the LTPP database. A comparison was made regarding the performance of all models. Lower, Mean Squared Error (MSE), Root Mean Square Error (RMSE), Mean Absolute Error (MAE), and the higher R-squared ( $R^2$  score) indicated the superior performance of the SL models compared to other approaches, showcasing their robust predictive capabilities for estimating the Creep stiffness of asphalt binders.

### 2.1. Super Learner Machine Learning Techniques

The SL represents an ensemble machine learning algorithm that combines and utilizes various ensemble algorithms to achieve the best prediction model. Ensemble learning methods can be categorized into three distinct groups: bagging, boosting, and stacking, as depicted in Figure 1. All these methods were employed in our study. Initially, the bagging method, specifically the Random Forest algorithm, was employed. Subsequently, the boosting method, including GBM, AdaBoost, XGBoost, and Catboost, was incorporated. Ultimately, a stacking ensemble model was utilized to address any weaknesses and leverage the inherent strengths of each individual model. The objective was to combine predictions from the contributing methods through a meta-model. The implementation of these ensemble learning strategies aimed to bolster the precision and resilience of our predictive models.

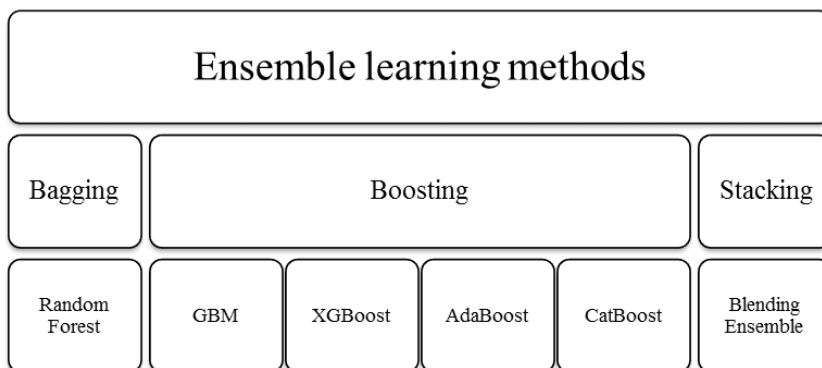


Fig. 1. Flowchart of ensemble methods

#### 2.1.1 Random Forest

Random Forest represents an ensemble learning technique based on bagging. It serves purposes in both regression and classification tasks. Random Forest entails the creation of multiple individual binary decision trees, each incorporating an element of randomness. This stochastic element encourages the trees to produce independent estimates, despite being constructed using a deterministic algorithm and a training dataset [25].

### 2.1.2 Gradient Boosting Machine (GBM)

GBM utilizes the gradient descent technique to construct models, taking into account the negative partial derivatives of the loss function. The initial model is adapted to fit the original data more effectively and is subsequently refined to address residuals and overcome limitations of the preceding model. This iterative process continues until a convergence criterion is satisfied [26].

### 2.1.3 Extreme Gradient Boosting (XGBoost)

XGBoost, a prominent boosting technique, expands on the principles of GBM. It involves the sequential development of regression trees, with each successive tree trained on the residuals of the preceding one. This approach effectively mitigates overfitting and enhances computational efficiency. Employing a level-wise learning strategy, XGBoost prioritizes splits that result in the most significant reduction in loss at each leaf [27].

### 2.1.4 Adaptive Boosting (AdaBoost)

AdaBoost employs multiple decision tree regressors as weak learners, extracting insights from diverse attributes within the dataset. The core idea behind AdaBoost revolves around iteratively updating parameters linked to a specific set of functions. This incremental incorporation of new trees fosters the creation of a resilient learner with improved predictive abilities [28].

### 2.1.5 Categorical Gradient Boosting (CatBoost)

CatBoost utilizes the entire dataset for training and introduces random permutations to each example. It introduces a novel method for computing leaf values during the selection of tree structures, effectively tackling the biased gradient challenges commonly faced by traditional boosting algorithms. Through these enhancements, CatBoost notably enhances model performance and the capacity to generalize [29].

### 2.1.5 Stacking

In contrast to bagging and boosting, stacking combines several classifiers or regressors produced by different machine learning algorithms, functioning across various levels or layers. Given the potential for the stacking ensemble model to generate various permutations via different ML algorithms, this research prioritized the application of this SL method. Here, linear regression was utilized as the meta-learner to amalgamate different algorithms, with the aim of achieving heightened accuracy [30].

## 3. Data Collection and Processing

The data utilized in this study were sourced from the LTPP website, a component of the Strategic Highway Research Program (SHRP). The chosen factors for investigation encompass test temperature, penetration, kinematic viscosity, absolute viscosity, and specific gravity. A comprehensive dataset consisting of 1350 data points was gathered, encompassing the specified input variables. To ensure the dataset's quality, missing data and outliers were filtered out, resulting in a final dataset of 1202 records of Creep stiffness values. The descriptive statistics of the influential parameters used for modelling are presented in Table 1.

Table 1. Statistical properties of dataset

ID	Data	Unit	mean	std	min	max
1	Flexural Creep Stiffness	MPa	265.92	148.56	36.00	775.00
2	M_Value	-	0.32	0.06	0.15	0.5
3	BBR Test Temperature	°C	-17.71	4.62	-30.00	-6.00
4	PENETRATION_77F	mm	34	19	1.00	114.00
5	PENETRATION_115F	mm	182	89.45	5.00	449.00
6	ABSOLUTE_VISC_140F	cP	5.28	1.42	5.50	1.24e+06
7	KINEMATIC_VISC_275F	cSt	1087.72	790.62	212.00	4553.00
8	SPECIFIC_GRAVITY	g/cm3	1.04	0.01	1.00	1.09

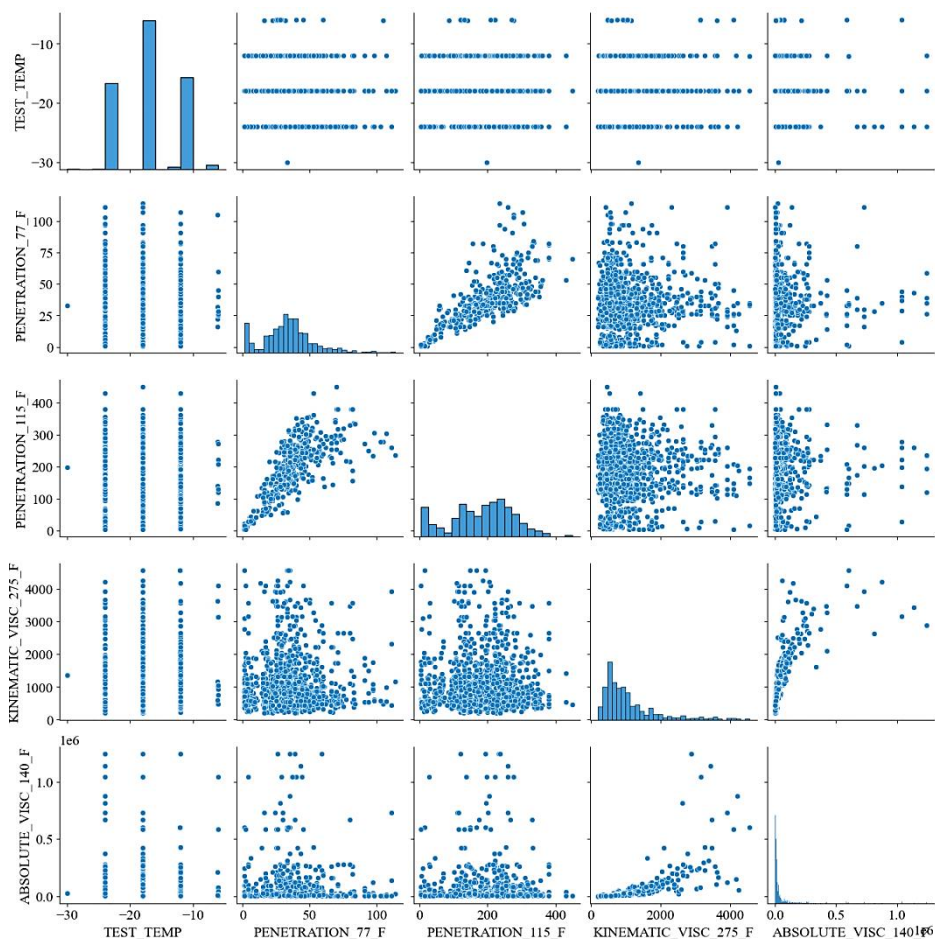


Fig. 2. Pair plot of some variable in dataset

Data visualization is a powerful and essential tool for gaining insights into qualitative data. By utilizing visualization techniques, we can effectively extract valuable information from datasets and detect patterns, outliers, and other irregularities. pair plots were utilized to visualize the data distribution of the dataset in this paper. The data distribution was

visualized through these pair plots, as depicted in Figure 2, providing intriguing insights into the relationships between different variables and contributing to a deeper understanding of the data's structure. Informed decisions could be made and potential trends or anomalies that might influence the analysis and modeling process were identified through data visualization. A data splitting strategy was adopted to develop and assess our ML model. The dataset was divided into two segments: a training sample comprising 75 percent of the data and a test sample containing the remaining 25 percent. The training sample was used to construct and train the ML model using various SL techniques. These methods were utilized to uncover the underlying patterns and relationships between the input features, such as test temperature, m-value, penetration, kinematic viscosity, absolute viscosity, specific gravity, and the Creep stiffness. Once the model was trained, its performance was evaluated using the test sample, which had been withheld during the training phase. By the trained model, the ability to accurately predict the Creep stiffness based on the provided input data was assessed. Valuable insights into the model's generalization and its performance on previously unseen data were provided by this evaluation. This rigorous testing ensured that new data could be effectively handled by our model, enabling accurate predictions in real-world scenarios.

#### 4. Results and Discussion

The main objective of this study was the development of accurate prediction models for estimating the Creep stiffness of BBR tests. To accomplish this, supervised ML algorithms were employed, with a specific emphasis on various ensemble models. Six ensemble models, including random forest, GBM, AdaBoost, XGBoost, CatBoost and a stacking method combining elements of boosting and bagging, were implemented using the scikit-learn library in Python. The use of these SL models aimed to predict the Creep stiffness based on the rheological properties of various asphalt binders. By training each model with the labeled dataset, intricate relationships between the input features and their corresponding Creep stiffness values were learned.

For the evaluation of the accuracy and effectiveness of these ML models, four widely used performance metrics, namely MSE, RMSE, MAE, and the  $R^2$  score, were employed. Valuable insights into the models' performance in accurately predicting the Creep stiffness values and capturing the underlying patterns in the data were provided by these metrics. The MSE quantifies the average squared difference between the actual and predicted values, providing an overall measure of prediction accuracy. The RMSE, derived from MSE, represents the square root of the average squared error, offering a measure of prediction deviation relative to the actual values. The MAE calculates the average absolute difference between the actual and predicted values, providing a straightforward measure of the model's predictive errors. Furthermore, the  $R^2$  score statistic serves as a crucial indicator of how well the influence of an independent variable explains the variance in a dependent variable. It assists in determining the extent to which the variability in the Creep stiffness values can be attributed to the variations in the input features.

In Figure 3, the visualization of the distribution of predicted results against actual results for all models presented and accompanied by the best fit line for the prediction distribution. Remarkably,  $R^2$  scores of 0.89, 0.886, and 0.885 were achieved by the Stacking, Random Forest, and GBM models, respectively, suggesting credible prediction outcomes. Deviation from the fit line was observed in some data points, notably in the calculations of AdaBoost and CatBoost. It is noteworthy that the dataset includes abrupt changes in specific values, negatively affecting the accuracy of sensitive algorithms such as AdaBoost and CatBoost. This resulted in lower  $R^2$  scores and higher MSE and RMSE for these models. In contrast, more accurate predictions on the test data were demonstrated by other algorithms, mainly due to their adeptness in capturing the nonlinear nature of the

dataset. Moreover, certain algorithms, especially those incorporating randomness (e.g., random forest), may yield slightly different results in each training iteration. This inherent variability can contribute to deviations. The reduced deviation observed in stacking can be attributed to its capacity to leverage the capabilities of a variety of well-performing models, resulting in predictions that surpass those of any single model in the ensemble. The non-linear connection between Creep stiffness and other variables is indicated by this finding, considering the characteristics of the dataset and the intricate interplay of various factors.

The metrics for all algorithms used in this study are presented in Table 2. The good performance of the stacking, Random Forest, and GBM models can be attributed to their adeptness in handling intricate and non-linear relationships between Creep stiffness and other variables. These models excel in addressing abrupt changes and nonlinearity within the dataset, resulting in more precise and accurate predictions. The lower MSE and RMSE values achieved by these two models further affirm their performance in capturing the intricate relationships between Creep stiffness and other variables.

Table 2. SL models metrics

Model	MAE	MSE	RMSE	R <sup>2</sup> score
Random forest	37.62	2795.42	52.87	0.886
GBM	37.56	2829.75	53.19	0.885
AdaBoost	47.07	3690.37	60.74	0.850
XGBoost	42.13	3402.20	58.32	0.862
CatBoost	39.10	2913.44	53.97	0.882
Stacking	36.36	2479.14	49.79	0.899

The accuracy results of all the models reinforce the notion that the transition from linear regression to ensemble models, specifically Boosting methods, enhances the capability to capture non-linear relationships present in the data. This, in turn, leads to significantly improved prediction accuracy for the targeted problem of estimating the Creep stiffness of asphalt binders.

The lower R<sup>2</sup> score of approximately 0.85 for the AdaBoost algorithm can be attributed to its sensitivity to outliers and noise in the data. AdaBoost, being an ensemble learning method, aims to sequentially fit weak learners to the data, with each subsequent model giving more weight to the misclassified points by the previous ones. This sensitivity to outliers and noise can lead to an overemphasis on capturing individual data points, causing the model to try fitting the noise in the data rather than generalizing the underlying patterns. As a result, the model may exhibit a lower R<sup>2</sup> score, indicating that it does not explain as much of the variance in the dependent variable as desired. Robust preprocessing techniques, such as outlier removal or data cleaning, could potentially improve the performance of AdaBoost in scenarios where outliers and noise have a significant impact on the model's fitting process.

A remarkable improvement is observed in all results obtained by the SL methods compared to the referencing work. The relationship between the predicted and actual values is closely aligned with the best fit line for the dataset in Figure 3. The radar plot depicted in Figure 4 provides a visual representation of the R<sup>2</sup> score values attributed to each method. The shape exhibited in the radar plot notably demonstrates the closely clustered values of R<sup>2</sup> score for each respective method, highlighting the similarity in their predictive performance.

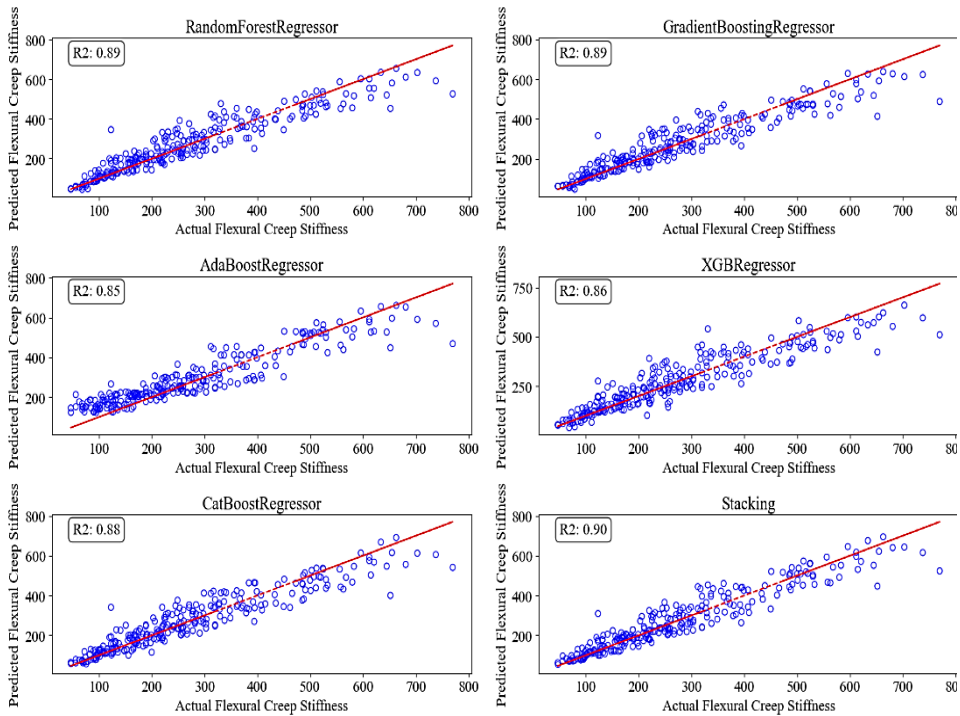


Fig. 3. Predicted vs actual values of the flexural-creep stiffness for the different methods

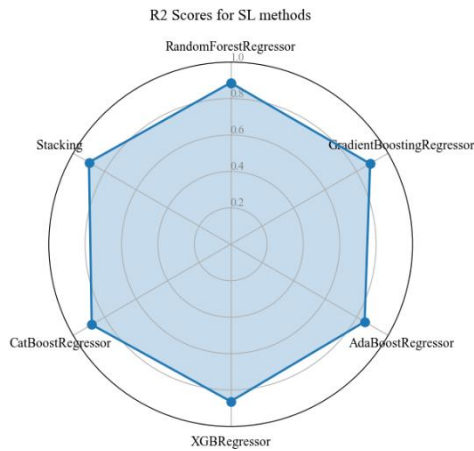


Fig. 4. Radar plot of  $R^2$  score different methods

In Figure 5, the feature importance of various factors selected for analysis was demonstrated. Given the best performance of GBM, it was selected to assess the feature importance of each factor. It is evident that the importance of the test temperature outweighs that of other factors, followed by penetration at 115°F, kinematic viscosity, and specific gravity, which exhibited higher significance in predicting the creep stiffness.

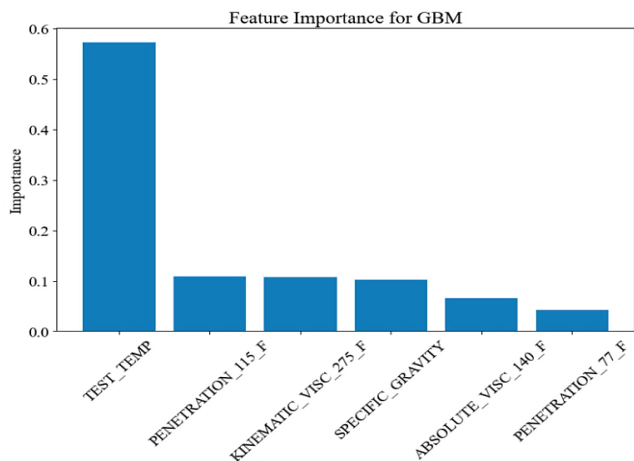


Fig. 5. Feature importance of GBM method

Table 3. Random selected actual vs prediction values of flexural-creep stiffness (MPa)

Actual Value	Random Forest	GBM	AdaBoost	XGBoost	CatBoost	Stacking
189	216	202	235	191	218	192
75.5	63	56	52	80	66	79
76	72	63	61	79	66	73
174	175	174	205	160	178	172
249	262	224	245	203	233	235
130	139	147	177	169	138	132
199	221	201	214	230	202	202

Table 3 presents the random display and comparison of the predicted values of the flexural-creep stiffness, obtained by various methods employed in this research, with the actual values from the test data. It is apparent that, in most cases, the prediction results are deemed acceptable; however, certain instances reveal that certain algorithms have generated values that are not considered satisfactory. This discrepancy could be attributed to the underfit of the algorithm for those specific values. The Stacking model achieved a low Mean Absolute Percentage Error (MAPE) of 2.86% and a high prediction accuracy of 97.14%. The GBM model, while slightly less accurate, still demonstrated a respectable MAPE of 10.56% and a prediction accuracy of 89.44% for the selected data points. This performance is attributed to the intrinsic nature and characteristics of these algorithms, allowing them to converge towards the accurate prediction value through the creation of multiple sub-branches and hidden layers.

**5. Conclusions**

In this study, the application of various SL machine learning models for predicting the Creep stiffness of asphalt binders in BBR experiments was explored. The aim was to develop accurate and robust prediction models that could provide a better understanding of the rheological behavior of asphalt binders under low-temperature conditions.



Through an extensive analysis using a diverse dataset and various ensemble learning methods, including Random Forest, GBM, CatBoost, XGBoost, Adaboost, and Stacking, prediction models were successfully constructed that achieved high accuracy in predicting the Creep stiffness. Along with the best fit line for the prediction distribution. Notably, the Stacking, Random Forest, and GBM models achieved  $R^2$  scores of 0.89, 0.886, and 0.885, respectively, indicated the strong ability of these methods to capture complex and non-linear relationships between the input variables and the target variable.

The comparison of randomly selected actual vs. predicted values of flexural-creep stiffness across different methods reveals compelling performance metrics. The Stacking model stands out with a notably low Mean Absolute Percentage Error (MAPE) of 2.86% and an impressive prediction accuracy of 97.14%. On the other hand, the GBM model, while slightly less accurate, maintains a respectable performance, showcasing a MAPE of 10.56% and a prediction accuracy of 89.44% for the specific data points under consideration.

The observed lower  $R^2$  score of approximately 0.85 in the AdaBoost algorithm can be ascribed to its susceptibility to outliers and noise within the dataset. This sensitivity to irregularities in the data poses a challenge, potentially leading to overemphasis on individual data points and thereby influencing the algorithm's overall performance.

Additionally, the importance of transitioning from conventional linear regression methods to ensemble learning techniques, particularly boosting methods, was emphasized in our research. These ensemble models were capable of handling non-linearity and abrupt changes within the dataset, resulting in improved prediction accuracy compared to traditional approaches like Linear Regression. The results of feature selection revealed that test temperature has an important effect on creep stiffness, leading to higher values.

In conclusion, this research successfully applied ML techniques to predict the low-temperature rheological properties of asphalt binders. The developed models showed promising results in accurately estimating the Creep stiffness, providing valuable insights for the design and engineering of more durable and resilient asphalt pavements. These findings contribute to the advancement of asphalt binder testing and characterization methods, paving the way for more efficient and sustainable infrastructure development in the field of civil engineering. Future studies can build upon this research by exploring additional factors and testing conditions to further enhance the predictive capabilities of ML models in asphalt binder evaluations.

## References

- [1] Basu A, Marasteanu MO, Hesp SA. Time-temperature superposition and physical hardening effects in low-temperature asphalt binder grading. *Transportation research record*. 2003;1829(1):1-7. <https://doi.org/10.3141/1829-01>
- [2] Roshan A, Ghasemi A. Laboratory Investigation of Micronized Lomashell Powder Effects on Asphalt Binder and Mix Performance. *Journal of Engineering & Technological Sciences*. 2023 May 1;55(3). <https://doi.org/10.5614/j.eng.technol.sci.2023.55.3.9>
- [3] Cannone Falchetto A, Moon KH, Wang D, Riccardi C. Investigation on the cooling medium effect in the characterization of asphalt binder with the bending beam rheometer (BBR). *Canadian Journal of Civil Engineering*. 2018;45(7):594-604. <https://doi.org/10.1139/cjce-2017-0586>
- [4] AASHTO T. 125; Standard Method of Test for Determining the Creep stiffness of Asphalt Mixtures Using the Bending Beam Rheometer (BBR). American Association of State Highway and Transportation Officials: Washington, DC, USA. 2016.

- [5] Wang D, Cannone Falchetto A, Riccardi C, Westerhoff J, Wistuba MP. Investigation on the effect of physical hardening and aging temperature on low-temperature rheological properties of asphalt binder. *Road Materials and Pavement Design*. 2021 May 4;22(5):1117-39. <https://doi.org/10.1080/14680629.2019.1665089>
- [6] Wang D, Falchetto AC, Riccardi C, Poulikakos L, Hofko B, Porot L, Wistuba MP, Baaj H, Mikhailenko P, Moon KH. Investigation on the combined effect of aging temperatures and cooling medium on rheological properties of asphalt binder based on DSR and BBR. *Road Materials and Pavement Design*. 2019 Apr 30;20(sup1):S409-33. <https://doi.org/10.1080/14680629.2019.1589559>
- [7] Lu X, Uhlback P, Soenen H. Investigation of bitumen low temperature properties using a dynamic shear rheometer with 4 mm parallel plates. *International Journal of Pavement Research and Technology*. 2017 Jan 1;10(1):15-22. <https://doi.org/10.1016/j.ijprt.2016.08.010>
- [8] Komaragiri S, Filonzi A, Masad A, Hazlett D, Mahmoud E, Bhasin A. Using the dynamic shear rheometer for low-temperature grading of asphalt binders. *Journal of Testing and Evaluation*. 2022 May 1;50(3):1622-33. <https://doi.org/10.1520/jte20210277>
- [9] Bahia HU, Anderson DA, Christensen DW. The bending beam rheometer; a simple device for measuring low-temperature rheology of asphalt binders (with discussion). *Journal of the Association of Asphalt Paving Technologists*. 1992;61. <https://doi.org/10.1520/stp18187s>
- [10] Carret JC, Falchetto AC, Marasteanu MO, Di Benedetto H, Wistuba MP, Sauzeat C. Comparison of rheological parameters of asphalt binders obtained from bending beam rheometer and dynamic shear rheometer at low temperatures. *Road Materials and Pavement Design*. 2015 May 25;16(sup1):211-27. <https://doi.org/10.1080/14680629.2015.1029696>
- [11] Zeng ZA, Underwood BS, Castorena C. Low-temperature performance grade characterisation of asphalt binder using the dynamic shear rheometer. *International Journal of Pavement Engineering*. 2022 Feb 23;23(3):811-23. <https://doi.org/10.1080/10298436.2020.1774766>
- [12] Sui C, Farrar MJ, Tuminello WH, Turner TF. New technique for measuring low-temperature properties of asphalt binders with small amounts of material. *Transportation research record*. 2010 Jan;2179(1):23-8. <https://doi.org/10.3141/2179-03>
- [13] Lu X, Uhlback P, Soenen H. Investigation of bitumen low temperature properties using a dynamic shear rheometer with 4 mm parallel plates. *International Journal of Pavement Research and Technology*. 2017 Jan 1;10(1):15-22. <https://doi.org/10.1016/j.ijprt.2016.08.010>
- [14] Yin H, Chehab GR, Stoffels SM, Kumar T, Premkumar L. Use of creep compliance interconverted from complex modulus for thermal cracking prediction using the M-E pavement design guide. *International Journal of Pavement Engineering*. 2010 Apr 1;11(2):95-105. <https://doi.org/10.1080/10298430802621531>
- [15] Mirzaiyanraheh D, Dave EV, Sias JE, Ramsey P. Developing a prediction model for low-temperature fracture energy of asphalt mixtures using machine learning approach. *International Journal of Pavement Engineering*. 2022 Jan 13:1-2. <https://doi.org/10.1080/10298436.2021.2024185>
- [16] Rahman AS, Mannan UA, Tarefder A. Binder rheology based dynamic modulus and phase angle predictive models for asphalt concrete. *Airfield and Highway Pavements*. 2017 Aug 27. <https://doi.org/10.1061/9780784480939.019>
- [17] Chen Q, Wang C, Song L. Prediction of low-temperature rheological properties of SBS modified asphalt. *Advances in Civil Engineering*. 2020 Dec 2;2020:1-8. <https://doi.org/10.1155/2020/8864766>
- [18] Hussain F, Ali Y, Irfan M, Ashraf M, Ahmed S. A data-driven model for phase angle behaviour of asphalt concrete mixtures based on convolutional neural network.

- Construction and Building Materials. 2021 Feb 1;269:121235. <https://doi.org/10.1016/j.conbuildmat.2020.121235>
- [19] Xu J, Fan Z, Lin J, Liu P, Wang D, Oeser M. Study on the effects of reversible aging on the low temperature performance of asphalt binders. Construction and Building Materials. 2021 Aug 9;295:123604. <https://doi.org/10.1016/j.conbuildmat.2021.123604>
- [20] Tan X, Huang G, Li X, Zhang M, Ma X, Zhang J. Research on the response of bitumen binder and bitumen mastic to physical hardening effect based on rheological properties. Construction and Building Materials. 2024 Jan 19;412:134875. <https://doi.org/10.1016/j.conbuildmat.2024.134875>
- [21] Sapkota SC, Saha P, Das S, Meesaraganda LP. Prediction of the compressive strength of normal concrete using ensemble machine learning approach. Asian Journal of Civil Engineering. 2023 Jul 8:1-4. <https://doi.org/10.1007/s42107-023-00796-x>
- [22] Malashin, I.P.; Tynchenko, V.S.; Nelyub, V.A.; Borodulin, A.S.; Gantimurov, A.P. Estimation and Prediction of the Polymers' Physical Characteristics Using the Machine Learning Models. *Polymers* 2024 Jan, 16, 115. <https://doi.org/10.3390/polym16010115>
- [23] Ahmadi M, Lonbar AG, Sharifi A, Beris AT, Nouri M, Javidi AS. Application of segment anything model for civil infrastructure defect assessment. arXiv preprint arXiv:2304.12600. 2023 Apr 25. <https://doi.org/10.48550/arXiv.2304.12600>
- [24] Upadhya A, Thakur MS, Sharma N, Sihag P. Assessment of soft computing-based techniques for the prediction of marshall stability of asphalt concrete reinforced with glass fiber. International Journal of Pavement Research and Technology. 2022 Nov;15(6):1366-85. <https://doi.org/10.1007/s42947-021-00094-2>
- [25] Singh B, Sihag P, Singh K. Modelling of impact of water quality on infiltration rate of soil by random forest regression. Modeling Earth Systems and Environment. 2017 Sep;3:999-1004. <https://doi.org/10.1007/s40808-017-0347-3>
- [26] Friedman JH. Greedy function approximation: a gradient boosting machine. Annals of statistics. 2001 Oct 1:1189-232. <https://doi.org/10.1007/s40808-017-0347-3>
- [27] Chen T, Guestrin C. Xgboost: A scalable tree boosting system. In Proceedings of the 22nd acm sigkdd international conference on knowledge discovery and data mining 2016 Aug 13 (pp. 785-794). <https://doi.org/10.1145/2939672.2939785>
- [28] Freund Y, Schapire RE. Experiments with a new boosting algorithm. In icml 1996 Jul 3 (Vol. 96, pp. 148-156). <https://doi.org/10.1145/238061.238163>
- [29] Zhang F, Fleyeh H. Short term electricity spot price forecasting using catboost and bidirectional long short term memory neural network. In 2019 16th International Conference on the European Energy Market (EEM) 2019 Sep 18 (pp. 1-6). IEEE. <https://doi.org/10.1109/eem.2019.8916412>
- [30] Wolpert DH. Stacked generalization. Neural networks. 1992 Jan 1;5(2):241-59. [https://doi.org/10.1016/s0893-6080\(05\)80023-1](https://doi.org/10.1016/s0893-6080(05)80023-1)

## Influence of seawater exposure at the splash zone on the reliability of the rebound hammer test in estimating concrete compressive strength

Philip Jun S. Celerinos<sup>\*a</sup>, Sarah Jayne C. Frigillana<sup>b</sup>, Joshua Jonielle D. Grande<sup>c</sup>, Norfatima G. H. Ali<sup>d</sup>, Jamie Angel C. Navarro<sup>e</sup>

*Civil Eng. Dept., School of Engineering and Architecture, Ateneo de Davao University, Davao City, Philippines*

### Article Info

### Abstract

#### Article history:

Received 11 Dec 2023

Accepted 23 Feb 2023

#### Keywords:

*Compressive strength;*

*Direct compression;*

*Rebound hammer;*

*Reliability;*

*Splash zone;*

*Seawater*

In the face of challenging environmental conditions encompassing seawater exposure and dynamic wave forces, the evaluation of concrete's durability and structural integrity in coastal structures becomes imperative. The non-destructive test using a rebound hammer device is still commonly used up to this day to assess concrete coastal structures. However, the reliability of this test is still in question since the rebound hammer still depends on the tested environment. Thus, this study aimed to appraise the reliability of the rebound hammer test in estimating the compressive strength of concrete under specific environmental conditions, namely seawater exposure and normal room conditions—utilizing a digital version of the rebound hammer. The exposure durations included one month, two months, and three months. Results showed that the average estimated strength derived from the rebound hammer test tended to overstate the actual compressive strength obtained through the direct compression test, attaining a maximum percent error of 72.7%. This suggests a notable influence of seawater exposure on rebound readings. Additionally, it was also found that concrete samples in the first, second, and third months of exposure to seawater environment had soluble chloride content values in ppm of 250, 220, and 235, and a capillary water absorption in  $\text{g}/(\text{mm}^2 \cdot \text{s}^{0.5})$  of 0.0196, 0.0151, and 0.0149, respectively. This showed that the properties of concrete used in this study could not influence the rebound reading results. Furthermore, the overestimation raises concern about the reliability of the rebound hammer test in accurately determining the actual compressive strength of concrete.

© 2024 MIM Research Group. All rights reserved.

## 1. Introduction

Concrete structures erected in marine conditions are always directly or indirectly exposed to seawater. Direct exposure occurs on offshore and coastal structures such as seawater contact, while indirect exposure is due to winds carrying seawater sprays that may affect nearby structures. Seawater chemically reacts with concrete which results in concrete deterioration. Exposure to saltwater may also cause abrasions due to the silt and sand in shallow parts of the sea, as well the effects of wave actions [1]. Many concrete structures are being continuously built in marine environments, despite the effects on the chemical and physical properties of concrete. When seawater and concrete interact, the concrete deteriorates due to the salinity content of seawater [2]. Sulfate attack, crystallization, and mechanical action of waves are some of the phenomena that can potentially deteriorate the concrete strength over a period of time [3].

\*Corresponding author: [pjscelerinos@addu.edu.ph](mailto:pjscelerinos@addu.edu.ph)

<sup>a</sup> [orcid.org/0009-0009-3919-2357](https://orcid.org/0009-0009-3919-2357); <sup>b</sup> [orcid.org/0009-0006-1810-1290](https://orcid.org/0009-0006-1810-1290); <sup>c</sup> [orcid.org/0009-0009-1430-659X](https://orcid.org/0009-0009-1430-659X);

<sup>d</sup> [orcid.org/0009-0003-2366-2808](https://orcid.org/0009-0003-2366-2808); <sup>e</sup> [orcid.org/0009-0000-3922-1263](https://orcid.org/0009-0000-3922-1263)

DOI: <http://dx.doi.org/10.17515/resm2024.120me1211rs>

Res. Eng. Struct. Mat. Vol. 10 Iss. 3 (2024) 1209-1229

Geographically, the Philippines being an archipelago, makes the rise of concrete infrastructure built near marine environments unavoidable. For instance, the highly anticipated proposed project in the Samal Island-Davao City Connector (SIDC) bridge had its groundbreaking ceremony in late 2022 [4], and the Davao City Coastal Road, a 17-kilometer road project, had the opening ceremony of its first section in Bago Aplaya in early 2022 [5]; hence, these two major projects built in Davao City emphasized the importance of structural integrity, particularly in these environmental conditions. Thus, its most affected area is between the atmospheric zone and the submerged zone due to the wetting and drying cycles of seawater that continuously occur in this spot. Apart from the presence of seawater itself, the waves that contact the area cause saltwater particles to infiltrate the concrete pores. As the area dries, the water will crystallize into salt particles. This repeated cycle will result in the deterioration of the concrete structure [1]. Thus, one of the tests that can be done to assess the integrity of concrete is the compressive strength test. The determination of compressive strength is a primary criterion used to assess whether the concrete mix is suitable and able to fulfill the requirements of its specific application [6].

When determining the compressive strength for destructive testing, the process involves producing a concrete cube, curing it under ideal conditions, and then destroying the cube while measuring the force required to break it. Such a procedure is commonly done using a direct compression test machine [7]. This method has the highest accuracy but takes time and effort, which can be relieved using non-destructive testing (NDT) techniques that are considered portable, less expensive, and easy to use [8]. Recent studies showed that measuring some concrete qualities and linking the measured properties to the mechanical properties of concrete is one technique that could approximately assess the compressive strength of the existing concrete structures [9]. Hence, non-destructive testing methods are used to assess the strength of concrete properties without having to break the structure or sample into pieces. Some examples of NDTs include the wireless maturity sensors, ultrasonic pulse velocity, and the rebound hammer tests. However, the most used NDT is the rebound hammer test [10]. The device used in this test can quickly determine the hardness value on the device scale without requiring the measurement of the concrete surface [11].

The rebound hammer test is an indirect method that does not measure concrete strength directly. It is frequently employed as a non-destructive technique for the evaluation of the durability and strength of concrete, specifically on historic structures, to assess their structural soundness due to the susceptibility of the country to natural disasters. It measures other properties, particularly surface hardness, where the strength is correlated and derived using conversion models provided alongside the acquired device from the manufacturer. The surface hardness of concrete must consider factors including age of concrete, calibration of the rebound hammer, carbonation, moisture content, presence of aggregates, presence of air voids and steel reinforcement, and temperature [8]. The rebound hammer uses a spring release mechanism to activate a hammer that impacts a plunger to drive into the concrete surface. The device will give a value from 10 to 100, which is called a rebound number (RN). This measurement will be correlated to estimate the compressive strength of concrete [12]. However, it has limitations that lead to a research field that studies its reliability in estimating the concrete compressive strength. Most studies proved its reliability, while some concluded that it is not dependable. Thus, a unique model cannot be all represented as a condition of concrete [10].

In the past twenty years, several research have been conducted to evaluate the performance of the rebound hammer test [13]. In the study of Li et al. [14], the impact of seawater on the development and effects of concrete were investigated. They emphasized the need to recognize that the environmental conditions during tidal seawater curing were significantly more pronounced than those of the concrete itself. Moreover, Bjegović et al.

[15] assessed the level of damage the concrete was exposed to the seawater environment and determined different mechanisms and intensities that influence the concrete during its service life. They stated that erosion and cavitation due to wave action can cause a progressive mass loss on a concrete surface, and the splash zone, which was the most exposed zone of concrete, had a higher chloride content, which allowed the deterioration of the steel reinforcement in concrete. Furthermore, Cheng et al. [16] have stated that typical physical degradations of concrete, such as leaching, wave erosion, repeated drying, and wetting, usually lead to the dissolution of hydration, increased porosity, and surface cracks. On the other hand, the experimental results by Panedpojaman & Tonnayopas [17] stated that despite a robust dataset correlating rebound numbers with compressive strength, the test was considered unreliable for accurate strength determination. Results have shown that environmental exposure impacts the concrete compressive strength, and the manufactured rebound curve often overestimates the actual compressive strength [18]. An experimental study by Sanchez & Tarranza [8] determined the reliability of the rebound hammer test in concrete cubes exposed to brackish water. They concluded that the rebound hammer test was not accurate in predicting the actual compressive strength but was still reliable in predicting the increase in compressive strength as time varied due to its rebound curve underestimating the actual compressive strength. Lastly, in more recent research conducted by Celerinos et al. [9], they assessed the use of rebound hammer in estimating concrete compressive strength when cured in three (3) specific environmental conditions: seawater, seawater in a controlled area, and potable water in a normal room condition. Their tests revealed that the rebound hammer had repeatedly underestimated the actual concrete compressive strength for the samples cured in all three (3) environments.

The abovementioned literature reviews have highlighted the importance of conducting more research and seeking further knowledge towards the specific environment on the compressive strength of concrete when using the rebound hammer test. Several researchers asserted the variables, including carbonation, concrete temperatures, maturity, surface texture, and water content may have possibly impacted the findings of performances, leading to a large data deviation [19]. Hence, a variety of rebound hammer devices are offered for sale in markets; however, their reliability is still in question. However, the studies of Li et al. [14], Bjegović et al. [15], and Cheng et al. [16] agreed that exposing concrete to fluctuating dry and wet conditions in seawater had severe effects on its properties, including heightened porosity, higher chloride content, and surface cracking. Hence, concrete structures exposed to the splash zone were the most susceptible to the effects of seawater on the characteristics and surface hardness of concrete. On top of that, Panedpojaman & Tonnayopas [17] revealed that rebound hammer test results relied on the age, carbonation, moisture content, surface smoothness, and temperature to measure the surface hardness of concrete. Yet, the device was still considered unreliable in estimating the actual compressive strength because of environmental factors and the overestimation of the manufactured rebound curves. This conclusion was consistent with the findings of Sanchez & Tarranza [8], such that the rebound hammer was not accurate in predicting the actual compressive strength, but it was reliable enough to predict the increase in compressive strength. Thus, the results obtained from using the rebound hammer test may have been affected by the conditions and factors to which the concrete was exposed to the splash zone of seawater.

This study prompted the expansion of knowledge on the rebound hammer test, since only a few studies [8-9, 14-16] had explored exposure to seawater in splash zone. Therefore, the present study aimed to determine the reliability of the rebound hammer test in estimating the compressive strength of concrete by comparing it to the direct compressive strength test after exposure to a seawater environment and normal room condition. The

study also determined if the change in climate in the Philippines setting, from dry season to wet season, had any significant difference in the compressive strength of the concrete samples since the duration of experimentation was divided into three months. The three batches of concrete samples subjected to compressive strengths were done in the month of July, August, and September, respectively. Moreover, the study provided observations of any possible carbonation development that might have affected the rebound reading of the concrete samples. It also investigated the impact of prolonged exposure in seawater environment on the durability of concrete through capillary absorption and chloride content. Lastly, the study correlated the compressive strengths from the rebound hammer test and direct compression test results and compared the rebound number reading and actual compressive strength of the samples exposed to the splash zone of seawater and stored in normal room conditions. Hence, linear regression analysis was used to generate a model from acquired data and to correlate rebound number and actual compressive strength.

**2. Materials and Methods**

**2.1. Concrete Cube Materials and Design Mixture**

In the context of this study, thirty (30) samples were produced for the experimentation. A 150-mm cubic shape was used for the concrete samples [8], along with a 150-mm diameter and 305-mm height cylindrical shape samples. The cylinder concrete samples were used to derive a 150-mm diameter and 50-mm depth samples for the capillary absorption test under RILEM TC 116-PCD standard [20]. These samples were then divided into two (2) groups for seawater exposure and the normal room condition with three (3) cubes used for testing each month per group, respectively. This study prepared the requisite materials for the concrete mix, including Ordinary Portland Cement Type II, 3/4-inch (19 mm) diameter crushed coarse aggregates, washed fine aggregates, and concrete cube molds, all of which were locally outsourced. Notably, the experiment involved subjecting the concrete to seawater exposure, necessitating Type II cement under ASTM C150 standards. The properties of fine aggregates and coarse aggregates were gathered through a series of tests, shown in Table 1. These series of tests were conducted in the laboratory of the Civil Engineering Department at Ateneo de Davao University, Davao City, Philippines. Furthermore, strict adherence to a water-cement ratio of 0.6 was maintained [21]. Coarse and fine aggregates were thoroughly sieved, conforming to ASTM C33 standards [22].

Table 1. Properties of materials

Materials	Parameter	Properties
Fine Aggregates	Specific Gravity	2.7
	Moisture Content (%)	15.72
	Absorption Values	8.26
Coarse Aggregates	Specific Gravity	2.39
	Moisture Content (%)	3.21
	Absorption Values (%)	1.4

The same table exhibits the properties of the fine aggregates and coarse aggregates used in the mixture for making the concrete samples. For fine aggregates, washed sand was utilized, and was sourced from KEAN Solid Blocks & Aggregates Industries Corp. in Davao City, Philippines. The results of the laboratory tests revealed a specific gravity of 2.7, moisture content of 15.72, and absorption value of 8.26. On the other hand, coarse aggregates used in the samples were composed of 3/4-inch (19 mm) diameter gravel, and was also sourced from KEAN Solid Blocks & Aggregates Industries Corp. The results of the laboratory tests revealed a specific gravity of 2.39, moisture content of 3.21%, and an

absorption value of 1.4. In addition, Figure 1 illustrates the particle size distribution of fine and coarse aggregates used in the concrete samples. These aggregates were sieved following the ASTM C33 standards [22].

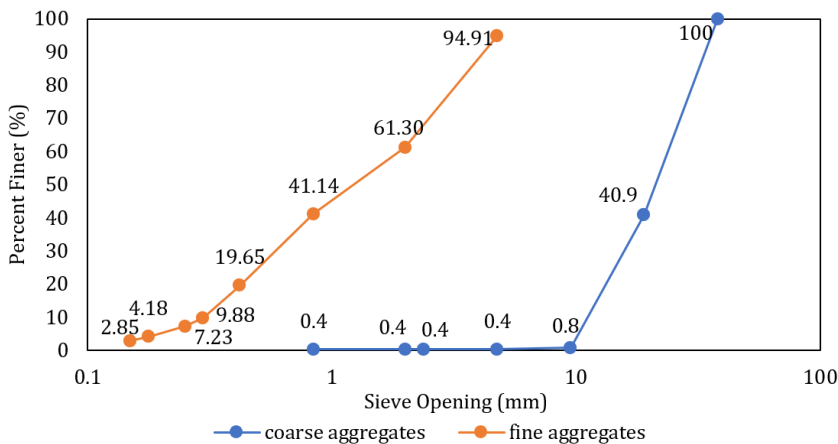


Fig. 1. Particle size analysis of fine and coarse aggregates

### 2.2. Concrete Mixing, Sample Making, and Curing

The concrete samples were prepared by employing the manual mixing method in accordance with the BS 1881-125:2013 standard [23]. Subsequently, the concrete mixture was integrated using clean water and was casted in a cubic mold using 3/4-inch-thick phenolic board to achieve a smooth finish concrete surface, adhering to the BS 1881-108:1983 standard [24]. All concrete samples underwent a standardized 28<sup>th</sup>-day curing process in a controlled environmental condition, following the guidelines of the BS 1881-111:1983 standard [25]. Regardless of the chosen method for maintaining moist air storage, a consistent temperature of  $20.0 \pm 5.0^\circ\text{C}$  was meticulously upheld. Table 2 shows the quantities of the raw materials used for the making of concrete samples.



Fig. 2. Concrete samples before curing stage

This study prepared the materials for concrete mixing, including Ordinary Portland Cement Type II, crushed coarse aggregates, and washed fine aggregates. Given that the concrete was exposed to seawater, the required cement type for mixing was Type II in accordance with ASTM C150 [21]. In the same mentioned table, the volume is  $0.118 \text{ m}^3$  and



the water-cement ratio is 0.6, where 25.47 kg is water, and 42.46 kg is cement. The coarse aggregate is 0.118 m<sup>3</sup>, and the fine aggregate is 0.059 m<sup>3</sup>. This proportion was consistently used for casting concrete mixtures. Also, Figure 2 shows the concrete cube and cylinder samples for this study. All samples were cured for 28<sup>th</sup> days in the laboratory of the Civil Engineering Department at Ateneo de Davao University.

Table 2. Quantities of ingredients

Volume (m <sup>3</sup> )	W/C Ratio	Water (kg)	Cement (kg)	Coarse Agg. (m <sup>3</sup> )	Fine Agg. (m <sup>3</sup> )
0.118	0.6	25.47	42.46	0.118	0.059

### 2.3. Exposure to Different Conditions

#### 2.3.1. Seawater Condition

The concrete cube and cylinder samples were divided into two (2) groups and were exposed to the following different environmental conditions: 1) seawater condition, and 2) normal room condition. The samples were exposed in the months of July, August, and September in the year 2023. The authors of this study had chosen those specific months since they were under the rainy seasons of the Philippines [26]; therefore, concrete samples under this condition underwent alternate cycles of drying and wetting. First, the exposure to seawater was located at Barangay San Jose, Samal, Davao del Norte, Philippines, specifically 7° 02' 36" N 125° 43' 16" E, as shown in Figure 3a. It is situated in a private beach property, with a small dock just a few meters from the seashore. The samples were structured to be exposed and undisturbed in the small dock. Second, the experimental setup involved exposing concrete cubes in a splash zone of seawater using a platform and fish net as a stabilizing medium, as shown in Figure 3b.

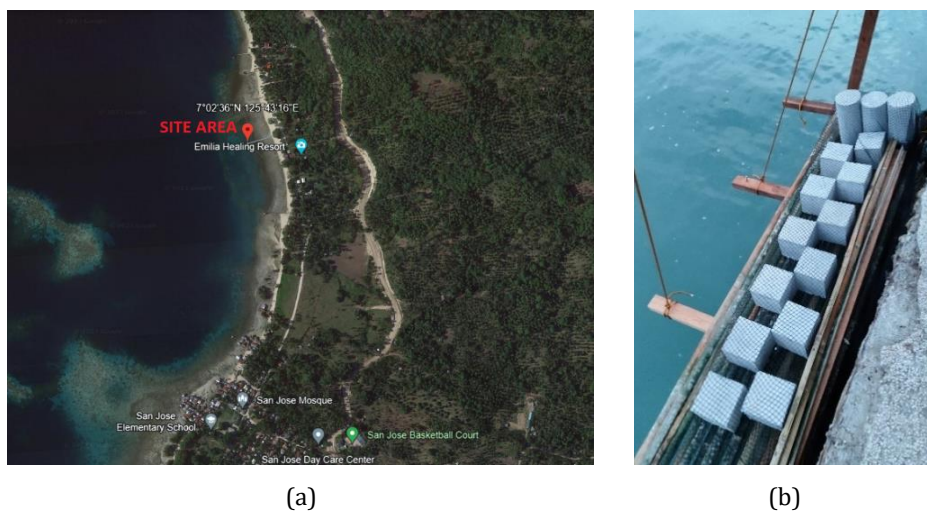


Fig. 3. Seawater environment in: (a) topographic view [28] and (b) concrete samples in the splash zone condition

Fifteen (15) concrete cubes and three (3) concrete cylinders were simultaneously exposed to the seawater for a specified duration. At monthly intervals, three (3) concrete cubes and one (1) concrete cylinder were taken for laboratory testing, continuing until the end of the third month. The authors conducted periodic visits to the site location to monitor and document any observable changes throughout the experiment. The specific location of the

seawater exposure in this experiment is the splash zone. It was identified as the region between air and sea, where tidal changes occurred; thus, waves hit the structure. This zone was considered an optimal environment for corrosion due to the intermittent wetting and drying of this area [27]. Conforming with the studies mentioned in the earlier section, this zone allowed the exposed concrete to be more susceptible to the influences of seawater, affecting its characteristics and surface hardness [14-16]. This current study emphasized the importance of concrete exposure to the splash zone, such that the effects of seawater on the compressive strength of concrete could be measured and analyzed.

### 2.3.2. Normal Room Condition

The concrete samples were stored under standard room conditions after a 28<sup>th</sup>-day curing period for a predetermined duration in the laboratory storage room of the Civil Engineering Department at Ateneo de Davao University, as shown in Figure 4. They were exposed in the months similar to those samples exposed to seawater. These samples served as the control group of the study. Having this group provided a baseline reference of comparison against the samples exposed in seawater. Initially, fifteen (15) concrete cubes were placed in the designated room and were left undisturbed under normal room temperature at  $20.0 \pm 5.0^\circ\text{C}$ . At monthly intervals, three (3) concrete cubes were systematically retrieved for testing, continuing until the third month. The authors regularly assessed the samples under this condition to monitor and note any potential alterations that might transpire during the study.



Fig. 4. Concrete samples in normal room condition after exposure

### 2.4. Series of Tests

After the concrete cubes were extracted from each environment during the first, second, and third months, the samples were then air-dried for forty-eight (48) hours before being weighed for its mass change, moisture content, and density. The concrete cube samples were then prepared to be subjected to the rebound hammer test adhering to the ASTM C805 standard [29]. Thereafter, the samples were systematically marked for ten (10) shots to obtain rebound readings, shown in Figure 5a. This study used a Digital Rebound Hammer Model TBT-TH225D from Nanjing T-Bota Sciotech Instruments & Equipment Co., Ltd., shown in Figure 5b. To maintain the integrity of the results, precautions were taken to avoid striking areas of the concrete surface exhibiting voids and cracks. Furthermore, a minimum spacing of 50 mm between points hit by the hammer was maintained throughout the testing process. In the experimental setup, the hammer was carefully positioned at a downward angle of 90 degrees, ensuring a level ground surface supported the specimen [29-31].

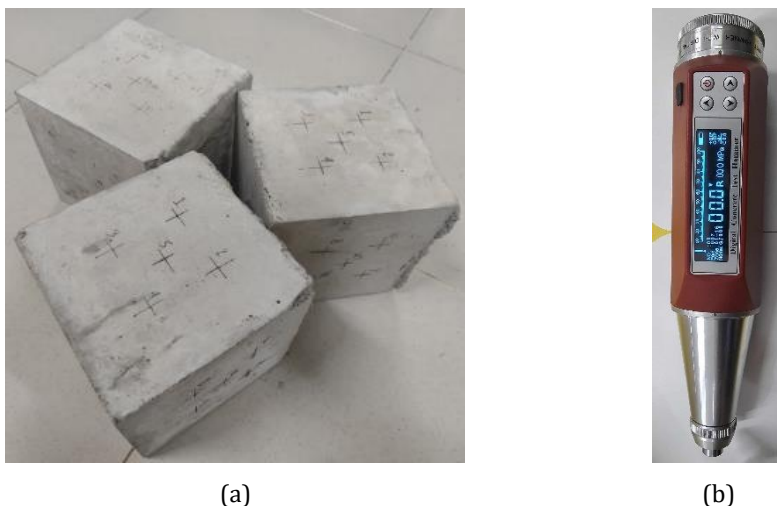


Fig. 5. Rebound hammer testing: (a) samples with marked zones, and (b) digital rebound hammer

Following the completion of the rebound hammer test, the concrete samples underwent loading until failure using a direct compression machine, shown in Figure 6, which was executed at TERMS Concrete and Materials Testing Laboratory Inc. in Davao City, Philippines. This process was undertaken to ascertain the true compressive strength of concrete samples.



Fig. 6. Direct compression machine

Subsequently, each sample went through a surface carbonation testing using the phenolphthalein method [32]. This step aimed to confirm the presence and degree of carbonation, a factor that significantly impacts rebound readings. The procedure involved applying liquid drops of phenolphthalein immediately after breaking the samples. A visual inspection was conducted on a cracked portion of concrete samples and sprayed with the phenolphthalein pH indicator. This indicator turned pink color on the cracked area with a pore solution higher than approximately pH 9, while the cracked with a pH lower than 9 retained a gray color [33]. The phenolphthalein used in this experiment has the following properties, as shown in Table 3. This chemical solution was purchased in Davao Mineral Laboratories, Inc. in Km. 6 Lanang, Barangay Buhangin, Davao City.

**Table 3. Properties of phenolphthalein solution**

Molecular mass (g/mol)	Purity (%)	Solution in ethanol (%)	Denatured (%)	ph balance	Density at 20°C (g/mL)	Color
318.328	98	1	90	8-10	0.059	Clear

In addition to the carbonation test in the concrete samples, further tests to determine the influence of the internal properties of concrete to the rebound readings were conducted. First, concrete samples of 5-mm depth from the surface was taken from the concrete cubes after carbonation for chemical analysis of chloride testing and was sent to the WVN Research and Laboratory at Elpidio Quirino Avenue, Talomo, Davao City, Philippines. The samples were turned into concrete powder to determine the soluble chloride content of the concrete (ppm). Second, the durability properties using capillary absorption test in the splash zone area of the exposed concrete cylinders in seawater were also taken using the following procedures. Three (3) samples were extracted during the first, second, and third months for the capillary absorption test as per the RILEM TC 116-PCD standard [20]. The standard test sample, with 150-mm diameter and 50-mm thick, was taken from concrete cylinders. The absorption was calculated by dividing the change in mass by the product of the cross-sectional area of the test specimen and the density of water. In this test, the temperature dependence of the water density was disregarded, and a value of 0.001 g/mm<sup>3</sup> was utilized. Figure 7 shows the taken samples for the capillary absorption test. The capillary absorption test was conducted in the Civil Engineering Department Laboratory at Ateneo de Davao University, Davao City, Philippines.



**Fig. 7. Samples underwent in capillary absorption test**

**2.5. Statistical Analysis**

The study utilized two statistical tools to comprehensively analyze and assess the gathered data. Specifically, the study employed Linear Regression Analysis and Two-tailed T-tests at a 95% confidence level ( $p < 0.05$ ). For the T-test, the average rebound numbers between the samples exposed to seawater and samples stored in normal room condition were compared, as well as their actual compressive strength. This analysis aimed to ascertain whether significant differences existed between samples subjected to these varying environments. Moreover, a paired sample T-test was also employed for the comparison between the actual concrete compressive strength versus average compressive strength derived from the rebound hammer test. Before conducting the T-test, a Shapiro-Wilk test was used to assess the normality of each group. This was done to ensure adherence to the assumption required for the T-test analysis. The regression analysis utilized a linear model

to examine the relationship between the rebound number and the actual compressive strength, which described the linear relationship between the response variable of actual compressive strength and the explanatory variable of the rebound number. The statistical analysis used the IBM® SPSS® statistics software version 22.0 [36] at the University Information Technology Office in Ateneo de Davao University, Davao City, Philippines.

A total of four (4) null hypotheses were formulated in this study for T-test, and four (4) complementary alternative hypotheses were formulated in opposition to these null hypotheses. The null hypotheses were listed as:

- $H_0$ : There is no significant difference in the actual compressive strength between the samples exposed to seawater and samples stored in normal room condition.
- $H_0$ : There is no significant difference in the rebound number acquired from digital rebound hammer between the samples exposed to seawater and samples stored in normal room condition.
- $H_0$ : There is no significant difference between the compressive strength of samples exposed to seawater acquired from direct compression test and digital rebound hammer test.
- $H_0$ : There is no significant difference between the compressive strength of samples stored in normal room condition acquired from direct compression test and digital rebound hammer test.

The alternative hypotheses were listed as:

- $H_1$ : There is a significant difference in the actual compressive strength between the samples exposed to seawater and samples stored in normal room condition.
- $H_1$ : There is a significant difference in the rebound number acquired from digital rebound hammer between the samples exposed to seawater and samples stored in normal room condition.
- $H_1$ : There is a significant difference between the compressive strength of samples exposed to seawater acquired from direct compression test and digital rebound hammer test.
- $H_1$ : There is a significant difference between the compressive strength of samples stored in normal room condition acquired from direct compression test and digital rebound hammer test.

To ascertain the appropriate hypothesis based on the data, the  $p$ -value was compared against the significance level of 0.05. The null hypothesis is accepted if the  $p$ -value is greater than 0.05, while the alternative hypothesis is accepted if the  $p$ -value is less than 0.05. The dataset encompassed samples of varying ages, specifically samples aged one, two, and three months.

### 3. Results and Discussion

#### 3.1. Direct Compression Test versus Rebound Hammer Test

The compressive strength values of the two sample variations, which were exposed in seawater environment and stored in normal room conditions, were obtained using rebound hammer and direct compression tests. Table 4 shows the results of the estimated average compressive strength from the rebound hammer test and the compressive strength from the direct compression test of concrete samples stored in a normal room condition. The compressive strength values from the rebound hammer test were in the range between 18 MPa to 19 MPa for the 1<sup>st</sup> month exposure, 19 MPa to 20 MPa for the 2<sup>nd</sup> month exposure, and 18 MPa to 21 MPa for the 3<sup>rd</sup> month exposure. On the other hand, the actual compressive strength values of the concrete samples were in the range between 14

MPa to 17 MPa for the 1<sup>st</sup> month exposure, 15 MPa to 19 MPa for the 2<sup>nd</sup> month exposure, and 15 MPa to 21 MPa for the 3<sup>rd</sup> month exposure.

Table 4. Compressive strength results for the rebound hammer versus direct compression at 1<sup>st</sup>, 2<sup>nd</sup>, 3<sup>rd</sup> months stored in normal room condition

Months Exposure	Sample No.	Estimated Average Compressive Strength from Rebound Hammer Test (MPa)	Actual Compressive Strength from Direct Compression Test (MPa)	%Error
1 <sup>st</sup>	1	18	14	28.57%
	2	19	17	11.76%
	3	19	15	26.67%
2 <sup>nd</sup>	4	19	19	0.00%
	5	20	18	11.11%
	6	19	15	26.67%
3 <sup>rd</sup>	7	20	21	4.76%
	8	21	22	4.55%
	9	18	15	20.00%

It can be observed that there were errors in the compressive strength results of the rebound hammer test for concrete samples for all months stored in normal room condition. The estimated average compressive strength from the rebound hammer test overestimated the compressive strength results of concrete samples stored in the normal room condition, as illustrated in Figure 8a. Conversely, the percentage error of compressive strength obtained by the rebound hammer test against the direct compressive test is plotted in Figure 8b. The minimum error has 0% on the 2<sup>nd</sup> month and the maximum error has 28.57% on the 3<sup>rd</sup> month.

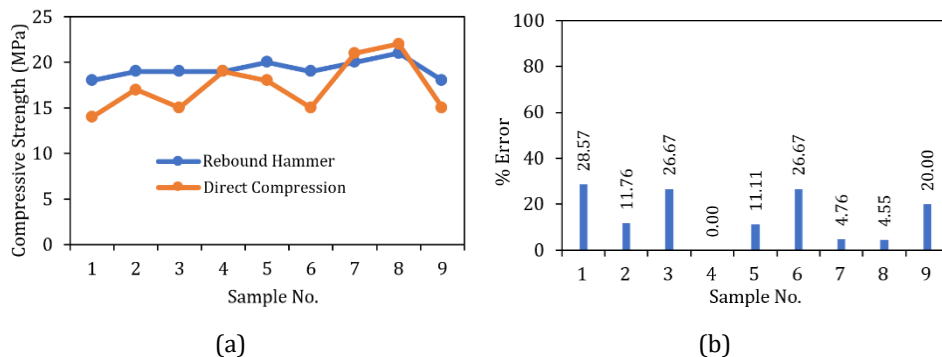


Fig. 8. Variations of concrete samples per storage period at normal room condition versus: (a) compressive strengths from the digital rebound hammer and direct compression, and (b) obtained %Error

Likewise, Table 5 shows the results of comparison of the rebound hammer test and the compressive strength obtained from the direct compression test of concrete samples exposed to seawater environment. The compressive strength values were in the range between 21 MPa to 25 MPa for the 1<sup>st</sup> month exposure, 19 MPa to 29 MPa for the 2<sup>nd</sup> month exposure, and 26 MPa to 32 MPa for the 3<sup>rd</sup> month exposure. However, the actual compressive strength values of the concrete samples were in the range between 13 MPa to 24 MPa for the 1<sup>st</sup> month exposure, 11 MPa to 24 MPa for the 2<sup>nd</sup> month exposure, and 18 MPa to 33 MPa for the 3<sup>rd</sup> month exposure.

Table 5. Compressive strength results for rebound hammer versus direct compression at 1<sup>st</sup>, 2<sup>nd</sup>, 3<sup>rd</sup> months exposed in seawater environment

Months Exposure	Sample No.	Estimated Average Compressive Strength from Rebound Hammer Test (MPa)	Actual Compressive Strength from Direct Compression Test (MPa)	%Error
1 <sup>st</sup>	1	22	13	69.23%
	2	25	24	4.17%
	3	21	16	31.25%
2 <sup>nd</sup>	4	19	11	72.73%
	5	29	24	20.83%
	6	19	12	58.33%
3 <sup>rd</sup>	7	32	32	0.00%
	8	27	33	18.18%
	9	26	18	44.44%

Similar to the previous comparison, the rebound hammer test still overestimated the compressive strength results of the direct compression test for the samples exposed in seawater environment. Figure 9a and Figure 9b show the overestimated results and the obtained percentage error for each month of exposure. Hence, the minimum error recorded 0% on the 3<sup>rd</sup> month and the maximum error recorded 72.73% on the 2<sup>nd</sup> month. In comparison with the results from the study of Celerinos et al [9], they have recorded a minimum percent error of 15.22% for all their sample variations and a maximum error of 59% that usually occurs in the latest curing period regardless of environmental condition. In this study, the minimum error obtained was 0% for both seawater environment and normal room condition. On the contrary, a maximum error of 72.73% occurred in concrete cubes exposed in the splash zone area of the seawater. The discrepancy might stem from the fact that, unlike the samples subjected to seawater exposure, the concrete samples kept in a standard room environment remained relatively stable and experienced fewer disturbances, potentially leading to a lower percentage of error. This could also be attributed to the dry-wetting cycles of the seawater waves during the duration of exposure that could led to an influence in the surface smoothness of the concrete cubes.

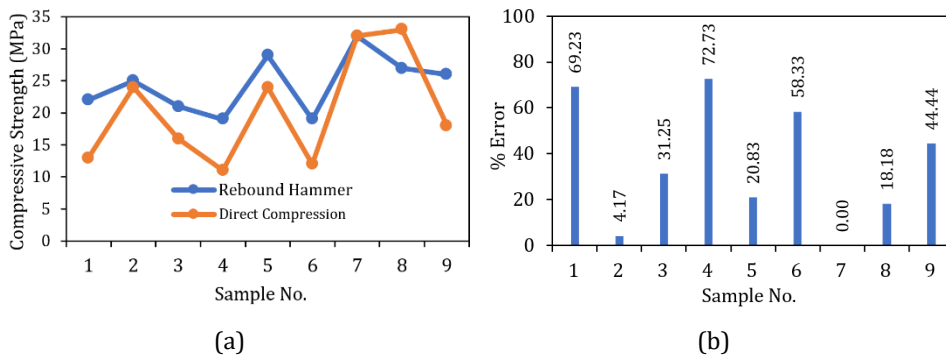


Fig. 9. Variations of concrete samples at normal room condition versus: (a) average compressive strength from the digital rebound hammer test and compressive strength from the direct compression test, and (b) obtained %Error

In addition, the average temperature in the site location was 31°C for the whole duration of the experiment with a weather described as mainly cloudy with precipitation. Therefore, the months wherein the samples were exposed was during a rainy season which may have further affected the surface properties of the concrete. The findings depicted in Figure 8a

and Figure 9a which show that the estimated average compressive strength through the digital rebound hammer device tended to overestimate nearly all results obtained from the direct compression test. This stands in contrast to the study of Celerinos et al [9], where a manual rebound hammer device consistently underestimated the values from the direct compression test. However, when compared to Co's study [40], their results didn't demonstrate a consistent trend of overestimation or underestimation. This inconsistency suggested varying degrees of accuracy in the rebound hammer test's predictions when compared to direct compression test results.

Moreover, Table 6 shows the comparison between the actual concrete compressive strength versus the estimated average compressive strength derived from the rebound hammer test. For both comparisons, it obtained a  $p$ -value of 0.036273 and 0.0007921 for samples exposed to seawater and samples stored in normal room condition, respectively. The T-test results revealed that there was a significant difference between the average compressive strength from rebound the hammer test and the actual compressive strength from the direct compression test, for the two sample variations. The results consistently presented an overestimation of the estimated average compressive strength of rebound hammer. The T-test results consistently rejected the null hypothesis, which indicated that the estimated compressive strength values significantly varied from the actual compressive strength. This discrepancy was quantified in the percentage errors as shown in Figure 8b and Figure 9b, wherein a maximum error of 72.73% was attained. This observation suggests a limitation for the rebound hammer test using a digital rebound hammer device when attempting to directly estimate the concrete's compressive strength.

Table 6. T-test results for comparison between rebound hammer and direct compression test

Variations	$p$ -value versus level of significance, $\alpha$	Remarks
Samples exposed to seawater	$p$ -value=0.036273 and $\alpha=0.05$ $p$ -value < $\alpha$ Reject the null hypothesis in favor of the alternative hypothesis	There is a significant difference between the compressive strength of samples exposed to seawater acquired from direct compression test and digital rebound hammer test.
Samples stored in normal room condition	$p$ -value=0.0007921 and $\alpha=0.05$ $p$ -value < $\alpha$ Reject the null hypothesis in favor of the alternative hypothesis	There is a significant difference between the compressive strength of samples stored in normal room condition acquired from direct compression test and digital rebound hammer test.

In addition, Figure 10 shows the rebound models generated for the concrete cubes exposed to seawater and normal room condition using the rebound number obtained from the digital version. The Multiple  $R$  for samples exposed to seawater and normal room condition were 0.80228 and 0.84028, which indicated a strong linear relationship between the estimated average rebound number and actual compressive strength. The acquired  $R^2$  values are 0.6436 and 0.7061 for samples exposed to seawater and samples stored in normal room condition, also the mentioned figure showed a moderate level of goodness of fit for the generated model.



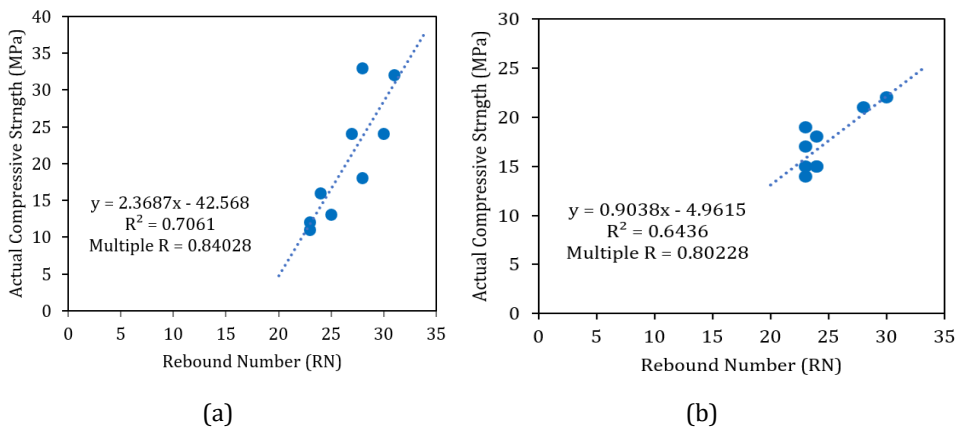


Fig. 10. Actual compressive strength versus rebound number: (a) stored in normal room condition, and (b) exposed to seawater environment

Furthermore, an observation of a consistent pattern emerged wherein there was a tendency to overestimate the actual compressive strength consistently. This discrepancy stems from potential inaccuracies caused by insufficient device calibration and reliance on the manufacturer’s standardized graph. These outcomes underscore the critical necessity for developing a customized curve tailored to the specific characteristics of the sample being tested. This observation highlighted the significance of addressing calibration issues within the rebound hammer devices based on concrete exposed in specific environmental condition to enhance their accuracy in assessing compressive strength. Thus, this study emphasized the importance of creating individualized calibration curves that consider the unique properties of the concrete or material under examination. Developing such tailored approaches could significantly improve the precision and reliability of rebound hammer assessments in determining compressive strength, ensuring more accurate results in structural evaluations and construction quality control.

### 3.2. Comparison of Results from Rebound Hammer Test and Actual Compressive Strength between Two Sample Exposed to Different Conditions

Table 7 shows the comparison of estimated average compressive strength acquired from the rebound hammer test versus the actual compressive strength from the direct compression test for each pair of sample variations stored in normal room condition and exposed to seawater environment. The purpose of the comparison was to determine whether the rebound reading was affected by the type of environment where the samples were exposed to. The *p*-value of 0.3322 was attained for the first comparison, which indicated a greater value than the set confidence level considering the two-tailed T-test. Hence, this variation failed to reject the null hypothesis, indicating that there was no significant difference between the two groups of samples when compared to their actual compressive strength. This implies that the length of duration of exposure to seawater did not significantly affect the concrete, where its actual compressive strength remained relatively unchanged.

The second comparison shows the results of average compressive strength acquired from the digital rebound hammer test for each pair of sample variations exposed to different conditions. The *p*-value of 0.16644 was obtained using the two-tailed T-test, which indicated that it was greater than the significance level. Thus, there was no significant difference between the estimated average rebound number obtained from a digital rebound hammer of concrete samples exposed to seawater and stored in normal room

condition. This meant that concrete cubes exposed to seawater rebound readings were partially similar compared to samples in normal room conditions.

Table 7. T-test results for comparison of rebound number and actual compressive strength between seawater exposure and normal room condition

Variations	<i>p</i> -value versus level of significance, $\alpha$	Remarks
Actual compressive strength of samples exposed to seawater versus stored in normal room condition	<i>p</i> -value=0.3322 and $\alpha$ =0.05	Actual compressive strength of samples exposed to seawater versus stored in normal room condition
Digital Rebound Number of samples exposed to seawater versus stored in normal room condition	<i>p</i> -value=0.1664 and $\alpha$ =0.05	Digital Rebound Number of samples exposed to seawater versus stored in normal room condition

The comparison of findings in the first comparison concerning the actual compressive strength of two different sample variations revealed no substantial differences in their values. The outcomes presented for the second comparison corroborated that observation. Despite the digital hammer lacked precision in predicting the actual strength, its consistency in detecting variations in strength after exposure still underscores its reliability as an indicator of change. This was similarly apparent in study of Sanchez & Tarranza [8], where their findings indicated that the rebound hammer successfully anticipated the changes of concrete’s strength over time.

The varied outcome of the digital iterations of the rebound hammer may be linked to the necessity for precise calibration according to its tested environment, given that the digital rebound hammer was newly purchased and underwent recent calibration. Additionally, the alignment of the digital hammer’s plunger might have disrupted the concrete surface, potentially influencing the disparity in results. In the study of Celerinos et al. [9], the distributed nature of the applied plunger force was observed as the rebound hammer struck a larger zone area. Consequently, the recorded rebound readings indicated lower strength in the adjacent edges and higher strength in the central zone.

### 3.3. Results for Carbonation Test in Two (2) Environmental Conditions

Upon commencement of the direct compression test, visible cracks appeared in the concrete cube samples. Subsequently, a carbonation test was conducted using a phenolphthalein liquid solution. The cracked areas of the concrete cube were promptly treated with the liquid solution to assess the presence of carbonation during exposure to seawater and normal room conditions. As depicted in Figure 11, the interior of the tested cracked section turned pink in less than a second, signifying the absence of carbonation. In this study, a phenolphthalein test was employed to confirm the presence of carbonation in concrete cube samples. The results revealed the absence of carbon development in all concrete cube samples exposed to two (2) environmental conditions throughout their specified exposure duration.

One of the factors that could affect the rebound readings is the existence of carbonation if the concrete surface [29]. In the investigation conducted by Celerinos et al. [9], consistent findings were observed as the cracked segments across all sample variations exhibited a pink coloration, suggesting the lack of carbonation in proximity to the concrete surface. This parallel outcome is also evident in the experimental study conducted by Sanchez &

Tarranza [8]. The tested sections of the samples, both within the cracked areas and on the surface, rapidly transitioned to a pink hue, signifying the absence of carbonation.



Fig. 11. Concrete samples after phenolphthalein test

### 3.4. Chloride Content Results

Table 8 shows the results of the soluble chloride content for the concrete cube samples that were exposed in the seawater during the first, second, and third months, respectively. As per Bjegović [15], the zone with the highest exposure, the splashing zone, where waves and wind carry seawater, had an acceptable chloride content for unreinforced concrete of less than 0.15% by weight of concrete (1500 ppm). Generally, the greatest concentration of chloride ions was present in the splash zone, where wave and wind actions contributed to a significant accumulation of chloride ions in surface layers [37]. From the observation, samples from the first, second, and third month had values of 250 ppm, 220 ppm, and 235 ppm, respectively.

Table 8. Soluble chloride content results

Month	Soluble Chloride (ppm)
1 <sup>st</sup>	250
2 <sup>nd</sup>	220
3 <sup>rd</sup>	235

Generally, according to Arya et al. [37], at the initiation of each wetting phase, the pores near the surface were initially empty, while those farther from the surface contained varying amounts of liquid. The outcomes for all concrete samples typically indicated that the greatest depth of penetration occurred during the initial wetting cycle, and this value diminished in subsequent cycles. This trend was logical and expected until the absorbed liquid's volume equaled the volume lost during drying [15]. The results from Table 8 indicated that these values of soluble chloride were within the acceptable limit before any form of corrosion could occur on the concrete structure due to exposure to seawater for three months. As a result, the influence of the chloride content within the concrete cubes can be disregarded as one of the reasons for the accuracy of the rebound hammer test that was conducted.

### 3.5. Capillary Absorption Results

Furthermore, Figure 12 visualizes the capillary water absorption of the concrete cylinders exposed in the seawater splash zone. It illustrates a graph depicting the relationship

between the water absorption rate and the time of absorption. The correlation between water absorption and the square root of time can be delineated into two distinct stages. Initially, during the first stage, there was a rapid linear increase in water absorption in tandem with the square root of time. Subsequently, as the concrete disc gradually reaches saturation, capillary water absorption diminishes, marking the onset of the second stage. In this stage, the water absorption curve exhibits a descending trajectory, reflecting a decrease in the water absorption rate. Therefore, it can be observed in Figures 12a, 12b, and 12c that the trendline between the three months were the same, indicating the same rate of change of absorption in the concrete cylinders during the entire duration of the experiment. It also showed the capillary water absorption coefficient of the concrete cylinders exposed in seawater in the first, second, and third month. The slope of the fitted equation during the initial stage was identified as the capillary absorption coefficient [39]. In this study, the linear fit of water absorption against the square root of time yielded a fitting correlation coefficient ( $R^2$ ) exceeding 0.9.

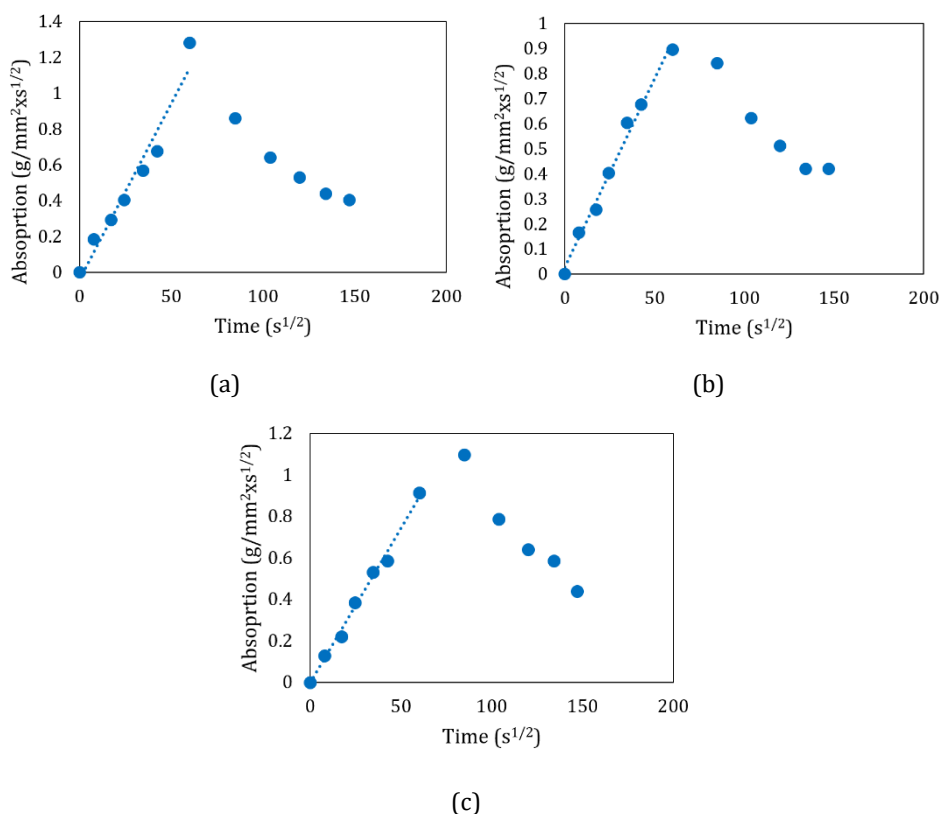


Fig. 12. Capillary water absorption results: (a) 1<sup>st</sup> month, (b) 2<sup>nd</sup> month, and (c) 3<sup>rd</sup> month

Table 9 shows the calculated capillary water absorption coefficient of the concrete cylinder for each month. The concrete cylinder in the first month had the highest coefficient of 0.0196 as the concrete was still not saturated due to its exposure to the seawater. Conversely, the second month, with a coefficient of 0.0151, and third month, with a coefficient of 0.0149, experienced lower capillary water absorption due to more prolonged exposure to the seawater. According to Balakrishna et al. [38], the absorptivity coefficient increases at initial time period due to an unsaturated pore structure, however as time goes

on the pore structure may reach a fully saturated condition that led to the decrease of the rate of absorption [38]. The close values, especially in the second and third months, indicate a stable rate of capillary water absorption within the concrete samples, which shows a weak influence of the seawater in the microstructure of the concrete specimens.

Table 9. Capillary water absorption results

Month	Capillary water absorption coefficient [g/(mm <sup>2</sup> *s <sup>0.5</sup> )]
1 <sup>st</sup>	0.0196
2 <sup>nd</sup>	0.0151
3 <sup>rd</sup>	0.0149

Also, as evident in Figures 12 that the absorption rate was consistently higher during the initial duration due to a differential gradient between the higher and lower concentration gradient sections. In this interval, there was a variation in the absorption rate until a specific time duration, followed by an increasing to decreasing pattern, indicating a smooth flow of the absorption rate. Upon reaching this pattern, the pore structure, cement paste, and concrete matrix became fully saturated, ultimately leading to the equilibrium state of the absorptivity coefficient [38]. In addition, according to Arya et al. [37], in all instances, with an increase in wetting-drying cycles, the net weight change decreased until it reached a constant level. At that point, the weight absorptivity value became constant. The distance absorptivity values were expected to stabilize when the value of effective porosity also reached a stable state. Therefore, from the results, the capillary water absorption has no influence in the accuracy of the rebound hammer test being conducted due to seawater exposure.

#### 4. Conclusion and Recommendations

The compressive strength for the concrete cubes exposed to normal room showed a maximum error of 28.57% compared to the concrete cubes exposed to seawater with a maximum error of 72.73%. The results consistently overestimated the average compressive strength results using digital rebound hammer device from the actual compressive strength. The low accuracy of the percentage error between all months showed the inability of the rebound hammer to determine the actual compressive strength of the concrete samples.

The study also revealed that the carbonation, capillary absorption, and total chloride content of the concrete cube samples showed little apparent changes after being exposed to the seawater condition. This implies that the properties of concrete were not able to significantly change within the whole duration of the experimentation and did not indicate any signs of deterioration. This was also reflected on the T-test results that there is no significant difference on the actual compressive strength of samples between those exposed to seawater and those under normal room condition. Thus, there was a significant difference in relation to the estimated average rebound numbers of the concrete cubes between the sample variations.

The T-test results further showed that the estimated average compressive strength from the rebound hammer test significantly exceeded the actual compressive strength for all variations in sample groups. Hence, across both environmental exposures of the samples, the average compressive strength consistently indicated an overestimation compared to the actual compressive strength, implying potential inaccuracies in the rebound readings. However, the rebound hammer was able to show a similar trend with that of the actual compressive strength which means that the device can be relied upon in knowing the decrease or increase in compressive strength of the concrete due to the environment. Nonetheless, the digital rebound hammer was less sensitive to surface properties of

concrete leading to its capability to estimate the changes in the actual compressive strength of the concrete.

Lastly, a strong linear relationship between the rebound number and actual compressive strength was evident for both sample variations as reflected on the correlation coefficient values acquired using the regression analysis. However, the coefficient of determination implies that the data has a high dispersion in both sample variations. This observation may be linked to the study's restricted availability of cube samples for analysis, potentially impacting the observed trend in the data due to the small sample size. Nevertheless, it is possible to generate a rebound hammer curve, provided a sufficient number of concrete samples are tested in order to predict a closer value to the actual compressive strength.

### Acknowledgement

The authors would like to acknowledge the School of Engineering and Architecture and the Civil Engineering Department at Ateneo de Davao University for their support and guidance throughout this research work.

### References

- [1] The Constructor. Concrete exposed to seawater-effects and preventions. August 4, 2018.
- [2] Pratiwi WD, Putra FD, Tajunnisa Y, Husin NA, Wulandari KD. A review of concrete durability in marine environment. InIOP Conference Series: Materials Science and Engineering 2021 Aug 1 (Vol. 1175, No. 1, p. 012018). IOP Publishing. <https://doi.org/10.1088/1757-899X/1175/1/012018>
- [3] Santhanam M, Otieno M. Deterioration of concrete in the marine environment. Marine concrete structures. 2016 Jan 1:137-49. <https://doi.org/10.1016/B978-0-08-100081-6.00005-2>
- [4] Parrocha A. PBBM to lead Samal-Davao bridge groundbreaking rites Thursday. Philippines News Agency. October 26, 2022.
- [5] A. L. C. IV. Coastal Road in Davao not an ordinary highway - DPWH. MindaNews. March 24, 2022.
- [6] Lysett T. Everything you need to know about concrete strength: Cor-TUF. Cor. January 1, 2022.
- [7] Destructive testing. Destructive Testing - an overview. ScienceDirect Topics.
- [8] Sanchez K, Tarranza N. Reliability of rebound hammer test in concrete compressive strength estimation. Int. J. Adv. Agric. Environ. Eng. 2014;1(2):198-202. <https://doi.org/10.15242/IJAEE.C1114040>
- [9] Celerinos PJ, Dedel PM, Fernandez NV, Muñoz KI, Suelan A. An assessment of rebound hammer test in estimating the concrete compressive strength in seawater. Research on Engineering Structures and Materials. 2023; 9(3): 947-967. <https://doi.org/10.17515/resm2023.712me0321>
- [10] Mishra AK, Dhungana A, Aithal PS. Analysis of the variation in different nondestructive testing and standards. Journal of Advanced Research in Civil and Environmental Engineering. 2022; 9: 1-11. <https://doi.org/10.24321/2393.8307.202201>
- [11] Kumavat HR, Chandak NR, Patil IT. Factors influencing the performance of rebound hammer used for non-destructive testing of concrete members: A review. Case Studies in Construction Materials. 2021 Jun 1;14:e00491. <https://doi.org/10.1016/j.cscm.2021.e00491>
- [12] Hearn A. 7 methods for testing concrete strength | for construction pros. June 11, 2019.

- [13] Kim JK, Kim CY, Yi ST, Lee Y. Effect of carbonation on the rebound number and compressive strength of concrete. *Cement and Concrete Composites*. 2009 Feb 1;31(2):139-44. <https://doi.org/10.1016/j.cemconcomp.2008.10.001>
- [14] Li P, Li W, Sun Z, Shen L, Sheng D. Development of sustainable concrete incorporating seawater: A critical review on cement hydration, microstructure and mechanical strength. *Cement and Concrete Composites*. 2021 Aug 1;121:104100. <https://doi.org/10.1016/j.cemconcomp.2021.104100>
- [15] Bjegović D, Serdar M, Baričević A, Jelčić Rukavina M. Assessing condition of concrete pier after three decades of exposure to sea water. *Građevinar*. 2015;67(12.):1155-64. <https://doi.org/10.1155/2015/145918>
- [16] Cheng S, Shui Z, Gao X, Yu R, Sun T, Guo C, Huang Y. Degradation mechanisms of Portland cement mortar under seawater attack and drying-wetting cycles. *Construction and Building Materials*. 2020 Jan 10;230:116934. <https://doi.org/10.1016/j.conbuildmat.2019.116934>
- [17] Panedpojaman P, Tonnyayopas D. Rebound hammer test to estimate compressive strength of heat exposed concrete. *Construction and Building Materials*. 2018 May 30;172:387-95. <https://doi.org/10.1016/j.conbuildmat.2018.03.179>
- [18] Karakul H. Investigation of saturation effect on the relationship between compressive strength and Schmidt hammer rebound. *Bulletin of Engineering Geology and the Environment*. 2017 Aug;76:1143-52. <https://doi.org/10.1007/s10064-016-0883-5>
- [19] Zemajtis JZ. Role of Concrete Curing. Portland Cement Association. 2023.
- [20] TC R. Permeability of concrete as a criterion of its durability Final report: Concrete durability-An approach towards performance testing. *Materials and Structures*. 1999;32:163-73. <https://doi.org/10.1007/BF02481509>
- [21] Ahmadi Moghadam H, Neshaei SA, Mirhosseini SM, Hassani Joshaghani A. Durability characteristics and mechanical properties of multi-walled carbon nanotubes reinforced concrete, a case study: Caspian seawater curing condition. *European Journal of Environmental and Civil Engineering*. 2023 Jan 2;27(1):140-58. <https://doi.org/10.1080/19648189.2022.2031303>
- [22] Mahr L. Aggregate testing standards. EnviroMINE, Inc. May 2, 2022.
- [23] British Standard Testing Concrete. Part 125: Methods for mixing and sampling fresh concrete in the laboratory.
- [24] British Standard Testing Concrete. Part 108. Method for making test cubes from fresh concrete.
- [25] British Standard Testing Concrete. Part 111. Method of Normal Curing of test specimens (20°C method).
- [26] Cabildo AV. 10 Tips for Travelling to the Philippines During Rainy Season. TripZilla, November 17, 2023.
- [27] Splash Zone - an overview | ScienceDirect Topics.
- [28] Google. Barangay San Jose, Samal, Davao del Norte satellite image. 2023.
- [29] Proper use of the Rebound Hammer Updated to reflect the changes to ASTM C805. Cemex.
- [30] Mulik, Deo, Dhupal, and Ghaywat, "Concrete Quality Assessment by Using Non-Destructive Test. Mar. 03, 2019.
- [31] Kolek J. Using the Schmidt Rebound Hammer. *Concrete Construction*.
- [32] WSDOT FOP for C 805 1 Rebound Hammer Determination of Compressive Strength of Hardened Concrete. WSDOT Materials Manual M 46-01.27. April 2017.
- [33] Herrera R, Kinrade SD, Catalan LJJ. A Comparison of Methods for Determining Carbonation Depth in Fly Ash-Blended Cement Mortars. *ACI Materials Journal*. April 2015; 112: 2. <https://doi.org/10.14359/51687452>
- [34] British Standard Testing Concrete. Part 114: Methods for Determination of Density of Hardened Concrete.
- [35] GB/T 50082-2009 English PDF (GBT 50082-2009).

- [36] IBM, "SPSS statistics for Windows." Version 22.0. Armonk, NY: IBM; 2013.
- [37] Arya C, Bioubakhsh S, Vassie P. Chloride penetration in concrete subject to wet/dry cycling: influence of moisture content. Proceedings of the Institution of civil engineers-Structures and Buildings. 2014 Feb;167(2):94-107. <https://doi.org/10.1680/stbu.12.00027>
- [38] Balakrishna M, Mohamad F, Evans R, Rahman M. Water absorption capacity of concrete cubes with absorptivity coefficient. Journal of Civil Engineering (IEB). 2020; 48(1): 17-27.
- [39] Yuan Y, Niu K, Tian B, Li L, Ji J, Feng Y. Effect of Metakaolin on the Microstructural and Chloride Ion Transport Properties of Concrete in Ocean Wave Splashing Zones. Materials. 2022 Dec 20;16(1):7. <https://doi.org/10.3390/ma16010007>
- [40] Co JRM. Assessment of the Reliability of Rebound Hammer Testing on the Estimation of Concrete Compressive Strength. BSCE thesis, Department of Civil Engineering, De La Salle University, Philippines. 2019.



Blank Page

## A state of art of review on strengthening of concrete structures using fabric reinforced cementitious matrix

Suyash Surendra Sagare<sup>a</sup>, Kirthiga R<sup>b</sup>, Elavenil S<sup>c\*</sup>

School of Civil engineering, Vellore Institute of Technology, Chennai Campus, Chennai 127, India

### Article Info

### Abstract

#### Article history:

Received 26 Dec 2023

Accepted 25 Feb 2024

#### Keywords:

*Fabric reinforced cementitious matrix;*  
*Fiber reinforced polymer;*  
*Cementitious matrix;*  
*Concrete members*

Renovation, refurbishment, restoration, and retrofitting of existing structures have grown more challenging issues for the construction profession. Construction buildings are susceptible to damage at the time of the earthquake and need strengthening to enhance their strength, stiffness, and ductility. Fabric-reinforced cementitious matrix (FRCM) techniques have been recently introduced to the construction sector as a feasible solution for fiber-reinforced polymers (FRP) in strengthening application. FRCM composed of high strength fabric grids with cement-based material serve as a binder for FRCM matrices. The binder employed for FRCM composed of cement-based mortar along with polymers are added to improve the bond strength properties. The cementitious matrix utilized in FRCM has superior thermal resistance and better compatibility with the concrete surface. The utilization of FRCM matrix for upgrading and restoring the concrete members is gaining more prominence as a replacement to FRP. This work conducts a thorough analysis of the application of FRCM techniques to concrete structural members like beams, columns, slabs, and beam-column joints. This paper primarily aims to present the FRCM process on structural members and to discuss the flexural, shear, and load carrying FRCM materials that are used in the field.

© 2024 MIM Research Group. All rights reserved.

## 1. Introduction

In recent decades, the imperative to upgrade existing structures has gained significant prominence due to factors such as aging, deterioration, environmental degradation, inadequate maintenance, and the need to align with contemporary design standards [1][2][3]. To address these challenges, Fiber Reinforced Polymers (FRP) have emerged as a popular solution for externally reinforcing structurally compromised buildings [4][2][5]. Their remarkable attributes, including a high strength-to-weight ratio, resilience to corrosion, quick and straightforward application, and less impact on geometry, have made them a preferred choice [6][7]. However, the utilization of FRP strengthening comes with certain limitations, particularly linked to the use of epoxy resins [8]. Notable issues encompass elevated costs, inadequate performance in high-temperature environments, incapability to be applied on damp surfaces, and interference with underlying materials like concrete or masonry [9].

Various retrofitting techniques include section modification, external post-tensioning, bonded steel plates, NSM steel, and externally bonded FRP laminates [10][11]. Each method offers distinct pros and cons, reflecting considerations of labor, durability, corrosion, fire performance, and cost-effectiveness [4]. Section modification results in an increase in the cross section as a whole by adding more steel reinforcement with stirrups. This raises the additional load since more concrete and steel are added, exposing them to

\*Corresponding author: [elavenil.s@vit.ac.in](mailto:elavenil.s@vit.ac.in)

<sup>a</sup>orcid.org/0009-0005-2907-7356; <sup>b</sup>orcid.org/0000-0003-3781-2355; <sup>c</sup>orcid.org/0000-0003-4964-829X

DOI: <http://dx.doi.org/10.17515/resm2024.133ma1226rv>

Res. Eng. Struct. Mat. Vol. 10 Iss. 3 (2024) 1231-1260

higher levels of corrosion [10]. The steel plate bonded to the damaged member's surface in the steel plate bonding method serves as an addition to the existing reinforcement. The exterior steel plate reduces the possibility of cracks and deflection and increases load-bearing capacity. Unfortunately, this method uses heavy-weight steel plates that are prone to corrosion, and installation costs are higher [4]. In the external post-tensioning procedure, tendons are drawn and attached to anchor points using pre-stressing rods or high-strength steel strands. Hence, this approach is ideal for retrofitting bridges [7]. In Near Surface Mounted (NSM) techniques, the FRP bar is glued to the existing concrete element by carving a groove in it and applying a suitable bonding agent. FRP is made of polymer that has been reinforced with fiber which provides it stiffness and strength and carries the load along the length of the fiber [5]. Despite the advantages of FRP, there are drawbacks related to resin properties and application challenges [12]. In response to these epoxy-related concerns, researchers have explored alternatives by advocating for the replacement of organic matrices (epoxy resins) with inorganic ones (mortar) [13]. This shift aims to overcome the challenges posed by epoxies and enhance the overall reinforcement technique [12][14]. However, the integration of fiber sheets into an inorganic matrix, such as mortar, has presented difficulties, primarily attributed to the granule size of the mortar [15]. Even finely textured mortar struggles to impregnate fiber bundles in the same manner as resins [16]. To surmount this hurdle, a breakthrough was achieved by substituting continuous fiber sheets with textiles, leading to improved bonding between fibers and the mortar-based matrix [8]. These novel composite materials were named as Fabric Reinforced Cementitious Matrix (FRCM) or Textile Reinforced Mortar (TRM) [17][18]. The utilization of mortar rather than epoxy elevates heat and fire resistance while improving concrete substrate compatibility [19][20]. Fig. 1 represents the types of retrofitting techniques.

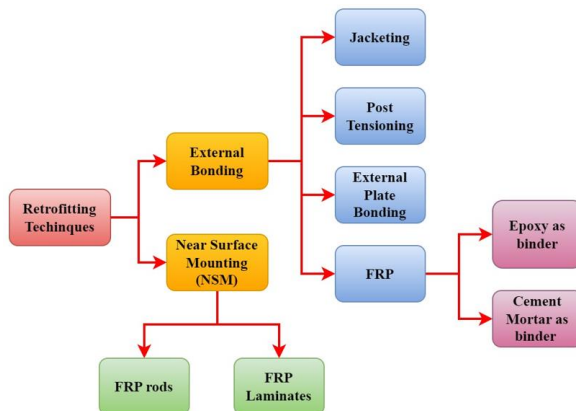


Fig. 1. Types of retrofitting techniques

FRCM combines with durable high-strength fibers in mesh configurations with inorganic matrices like cement or lime-based mortars [21]. This approach offers affordability, ease of use, fire resistance, and compatibility with concrete and masonry [22]. FRCM reinforcement comprises textile/Fabric mesh with oriented fiber roving for mechanical interlocking [23]. Externally bonded fabric-reinforced cementitious matrices exhibit a notable capability to augment the fatigue life of reinforced concrete members (RC) by redistributing stresses from internal steel reinforcement to the external composite fabric material [4]. Furthermore, the efficacy of fabric-reinforced cementitious matrices hinges upon the quality of the bond formed between the reinforced fabric and the concrete structural members [24]. Notably, these matrices demonstrate exceptional performance,

particularly at elevated temperatures, surpassing the conventional epoxy-treated (organic) retrofitting methods [25]. Moreover, fabric-reinforced cementitious matrices contribute minimally to the environmental impact of construction materials [26]. The application of polymer coatings into the nonmetallic textiles serves to enhance both the stability of the textile material and the mechanical connection between the textile and its matrix [1]. Nonetheless, this treatment renders the textiles less pliable, making their use on intricate shapes like U-shaped or fully wrapped structures challenging, much like steel fabrics [27]. The formulation of the mortar employed as the matrix within FRCM (Fabric Reinforced Cementitious Matrix)/ TRM (Textile-Reinforced Mortar) systems significantly influences its composite behavior [28]. Impregnating fibers with mortar holds paramount importance for establishing a robust bond between the fibers and the matrix [8]. An ideal mortar should encompass fine particles, possess plastic consistency, favorable workability, low viscosity, and ample shear strength (to prevent detachment from the substrate) [29]. As such, cement-based mortars are extensively utilized as the matrix in FRCM due to their suitability [30]. The mechanical attributes of the mortar, such as flexural strength and the bond with fiber roving, can be markedly enhanced through the incorporation of polymers [31].

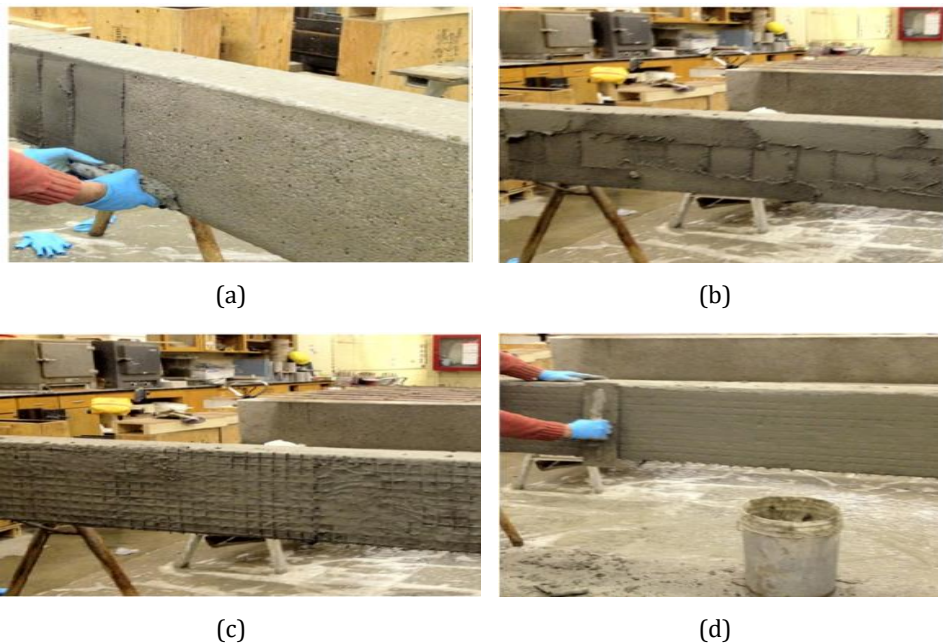


Fig. 2. FRCM strengthening steps: (a) Mortar application; (b) applying first layer of cement mortar; (c) FRP sheet embedded with first layer (d) finished with second layer of cement mortar [36]

Different types of fabric reinforcement material possess different types of physical properties such as Carbon-FRCM employs carbon fibers as reinforcement, renowned for their impressive strength-to-weight ratio, making them ideal for applications requiring both lightweight construction and high strength, such as the reinforcement and retrofitting of concrete structures [32]. Glass FRCM, on the other hand, incorporates glass fibers as reinforcement, providing corrosion resistance that makes it a preferred choice for environments exposed to harsh conditions, notably marine structures [24][33]. Basalt FRCM offers a balanced solution, blending the robust strength characteristics of carbon FRCM with the corrosion resistance of glass FRCM, and it finds applications across a

spectrum of structural needs [34]. Additionally, polyparaphenylene benzobisoxazole (PBO) FRM, utilizing PBO fibers like Zylon, offers exceptional strength and modulus within a cementitious matrix, catering to specialized high-performance requirements [35]. Fig. 2 shows the strengthening steps involved in FRM techniques.

The strengthening process through FRM/TRM jacketing encompasses several steps. Step 1 involves surface preparation to prepare the surface for bonding, it must be scrubbed, sandblasted, and cleaned. Step 2 entails mortar application on the concrete surface- A bonding primer is often applied to the prepared surface to improve the adhesion between the existing substrate and the FRM/TRM system. Step 3 followed the placing of fabric sheet and step 4 involves applying a final layer of mortar on top of the fabric stratum. A specially formulated mortar mix, which often includes cement, aggregates, and additives, is applied over the reinforcement layer. This mortar encapsulates and bonds with the fibers, creating a composite material that enhances the strength and durability of the structure. The mortar layer is typically applied in multiple coats, with each coat allowed to cure before the next one is added [36]. Fig. 2 shows the strengthening steps involved in FRM techniques.

This review paper provides a thorough analysis on the applications of FRM to strengthen the structural RC members. The insights presented herein are synthesized from a thorough examination of past studies and research endeavors. This paper aims to shed light on the remarkable potential and implications of FRM in advancing the field of structural engineering.

### 1.1. Significance of Research

FRM is extensively employed for strengthening and renovating the existing the concrete structures, such as buildings, dams, bridges, and other infrastructure. It is a useful technique for prolonging the lifespan and enhancing the performance of structures because it gives higher stiffness and load-bearing capability. Fig. 3 displays the research methodology adopted to review the paper.

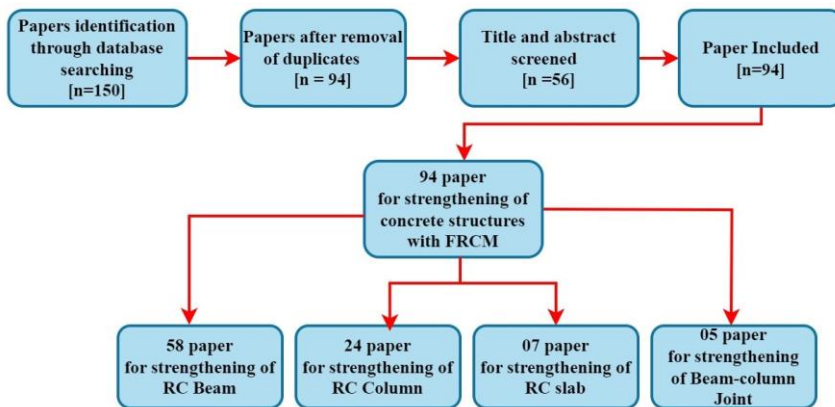


Fig. 3. Research methodology

## 2. Mechanical Properties

### 2.1. Properties of Fabric

The Fiber Reinforced Cementitious Matrix (FRM) approach utilizes composite materials in the form of grids, meshes [18], and fabrics reinforced with fibers, including basalt,

carbon, glass, steel and Polyparaphenylene Benzobisoxazole (PBO) [37][38][4][39]. These fibers exhibit varying densities, among these CFRP has high tensile strengths and also more stronger than steel [40]. The unit densities of CFRP vary between 1.5 to 1.6 g/cm<sup>3</sup>, whereas AFRP has 1.3 to 1.5 g/cm<sup>3</sup> and GFRP has 1.2 to 2.1 g/cm<sup>3</sup> [41]. Effective bonding in FRCM relies on a substantial contact area between the matrix and the surface, with the line of debonding determined by mortar properties, especially tensile strength, and the bond between reinforcement and mortar [42]. Fig. 4 represents the different types of fabric available in market.

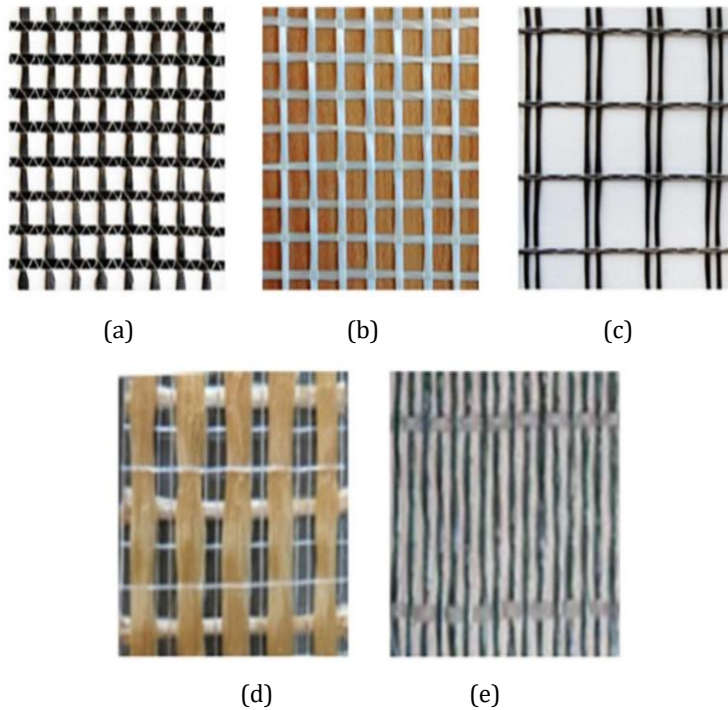


Fig. 4. Fabric reinforcement (a) Carbon (b) Glass (c) Basalt (d) Polyphenylene benzobisoxazole and (e) Steel fiber [1]

The strength of the composite mainly depends on the fibers. Table 1. represents the properties of fabric. FRCM are normally composed of one or multiple fabric with varying properties and its strength were mainly depends on the bond between the fabric and concrete substrate. When the bond has an adequate bonding strength, the capacity of the strengthened beam is examined by the quantity of fabric utilized. Trapko et al. reported that small scale concrete cylinder confined with PBO-FRCM increases while increasing the fabric layers [43]. The strengthening of concrete structures discussed in detail in section 3.

Table 1. Properties of fibers

Properties	Basalt	Carbon	Glass	PBO	Steel
Ultimate Tensile Strength [MPa]	3080	4320	2610	5800	3200
Young's Modulus [GPa]	95	240	90	270	206
Ultimate Strain [%]	3.15	1.8	2.9	2.15	1.55
Weight [g/m <sup>2</sup> ]	200	168	225	88	600
Width of tows/cords [mm]	5	4	3	5	0.9
Equivalent Thickness [mm]	15	10	25	10	5.5

### 2.1.1. Properties of Inorganic (Cement) Binders

The properties of FRCM mortar, particularly its tensile strength influence the performance of FRCM by reducing the cracking in the composite matrix. Gopinath et al. showed that an organic (Epoxy) binder used as an adhesive for concrete cylinders and strengthened with AR-glass fiber grid was found to be similarly bound by inorganic binders which include cement, silica fume, and fly ash has a compressive strength of 56 MPa [44]. When basalt-FRCM was used to strengthen RC beams against shear, it was shown that the polymer-modified mortar matrix performed better than cement mortar, with an improvement of almost 10%. Salloum et al. found that the hardness and strength of polymer-modified mortar were superior to those of cement mortar. Garcia et al. found that cement mortar provides an increased strength than pozzolanic mortar. Using cement mortar and polymer-modified mortar as binder, to strengthen RC beams with two layers of basalt fabric showed a maximum capacity of about 46% and 36%, respectively [45]. The beam strengthened with carbon and glass fabric showed an increases in flexural strength and also observed that use of an inorganic binder having a compressive strength of 20Mpa resulted in debonding failure during loading [46]. Enhancing cement mortar performance involves adding silica fume and polymers as binders [47]. Wu et al. observed that using cement mortar with PVA fibers, the strength of the RC beam improved [48]. The mechanical properties of inorganic binders retrofitted with concrete elements using fabric was collected and found that investigation is required to develop a new inorganic binder. Ameer Baiee et al. examined the influence of cement mortar with densified silica fume, undensified silica fume, Ground Granulated Blast Furnace Slag, and Fly ash. The test result shows that binary replacement consisting of 15% ground granulated blast furnace slag and 15% undefined Silica fume provides the optimum results [49].

## 3. Strengthening of Concrete Members with FRCM

### 3.1. Strengthening of RC Beams with FRCM

The performance of FRCM strengthened reinforced concrete (RC) beams is influenced by numbers of factors [21]. These factors include internal shear reinforcement quantity, fabric orientation, geometric configuration, bond scheme, end anchorage presence, application method (externally bonded, near surface embedded, or hybrid), strength of the substrate concrete, and composite stiffness [21][50][51]. Understanding these factors and their interplay is crucial in determining the shear capacity and failure modes of FRCM-strengthened beams [21]. Rizwan Azama et al. investigated on shear strengthening of RC deep beams with cement-based composites and these authors revealed that cement-based composites significantly improved the load-carrying capacity, with a 23% increase in ultimate load for CFRCM-strengthened beams [52]. Cement-based systems outperformed epoxy-based ones, attributed to bi-directional fabric providing better control of diagonal

shear cracking and improved bond performance. CFRP grids embedded in mortar exhibited the highest shear strengthening efficiency due to enhanced bond [52]. Tadesse et al. examined the three different types of failure modes for RC beams strengthened in shear. These authors observed the failure mode of strengthened beam as detachment of the FRCM laminates from the concrete substrate, particularly in the case of side bonded and U-jacketing. For fully wrapped FRCM system, observed the fabric rupture failure in the strengthened beams [21]. Maaddawy et al. investigated on strengthened corroded T-beams using FRCM. These authors found that corrosion caused significant strength reduction with a 22% loss in tensile steel which leads to 28% decrease in load carrying capacity of un-strengthened beams. The combination of externally bonded and internally embedded carbon FRCM layers proved more effective in increasing the flexural response [25]. Wang et al. investigates the residual bond behavior of different CFRP reinforcements in notched concrete beams exposed to elevated temperatures. Their findings show that the failure modes and load-displacement curves of the strengthened beams vary with temperature. The strength of cement-bonded CFRP grids outperforms epoxy-bonded CFRP sheets under high-temperature conditions, making the former system more fire-resistant [26]. Christian Escrig et al. done an experimental comparison of reinforced concrete beams strengthened against bending using various types of cementitious-matrix composite materials and found that there is a clear relationship between the strengthening materials and the development of crack patterns in the tested beams. While, examining the load-bearing capacity, it's observed that all the strengthening materials contribute to an increase in flexural displacement at the onset of the first crack and the yielding flexural displacement compared to an unmodified beam. This enhancement ranges from approximately 35% to 27%, depending on the specific material used. And also, when considering FRCM as reinforcement, it's noted that they have the effect of reducing the ductility of reinforced concrete beams while increasing their capacity by about 135% compared to beams without strengthening [32]. Fig. 5 shows the failure modes of strengthened RC beams.

Imran Rafiq et al. show that cementitious interfaces can control the debonding of FRCM to reduce the failure mode of strengthened beams. In addition, it concludes that the use of FRCM in the strengthening of RC beams increases ultimate load and cracking [53]. The TRM-based strengthening technique's lifetime and endurance were reported by Baiee et al. The findings showed that a corrosion degree of more over 10% can cause the cover to separate, losing its strengthening efficiency. For this reason, it is important to remove the cover before reinforcing RC beams [54].

The factors that control the failure mode of the strengthened beam are fabric type, matrix composition, arrangement and orientation of fabric layers, surface preparation, and environmental conditions. Different fabrics exhibit different behaviors due to their varying tensile strength, elastic modulus, and interaction with the cementitious matrix. The properties of matrix which includes cement types and additives affect the bond between the fabric and matrix. The fabric arrangement and orientation play an essential role to determine the failure mode. Poor surface preparation may lead to debonding failure. The durability of the FRCM system may be affected by variation in temperature and moisture conditions. The use of FRCM for strengthening the beam in flexural changed the failure mode from debonding to flexural failure and increased the ultimate load to 93% [55].

Mandor et al. explored the flexural performance of RC continuous beams enhanced with PBO-FRCM systems. The beams strengthened with one or two FRCM layers often failed due to fabric slippage or delamination. End anchors played a significant role in preventing fabric delamination [56]. FRCM strengthening improved the flexural stiffness in sagging, with increased layer count enhancing yielding and ultimate capacities [56][57]. Several factors have an impact on the fatigue performance of RC beams strengthened with FRCM,



including parameters such as reinforcement ratio, strengthening method, degree of damage, and the presence of sustained load-induced corrosion [58]. Their investigation involves the analysis of various aspects, including failure modes, crack progression, fatigue lifespan, mid-span deflection, and behavior at the interface between materials. They assess the efficacy of both U-shaped and single-sided strengthening techniques and highlights the influence of textile and reinforcement ratios on fatigue endurance. The combined influence of corrosion and sustained loading on fatigue life is explored, including the identification of different stages in mid-span deflection evolution. Additionally, the study underscores the impact of corrosion on the bonding of the FRCM layer and provides a formula for evaluating fatigue stiffness to assess the safety of strengthened beams subjected to fatigue loads [58]. Wang et al. investigated the beam strengthened with CFRP grid using polymer cement mortar at the varying temperature up to 600°C. They found that bi-directional fabric utilized in cement-based strengthening techniques has a better bond to the concrete substrate than unidirectional sheets deployed in epoxy-based strengthening techniques. And also, they identify that load carrying capacity increase of about 23%. Ombres et al. studied the flexural analysis of reinforced concrete beams strengthened with a PBO-FRCM. The strengthened beam significantly increases the flexural capacity about 44% than the un-strengthened beams [31].

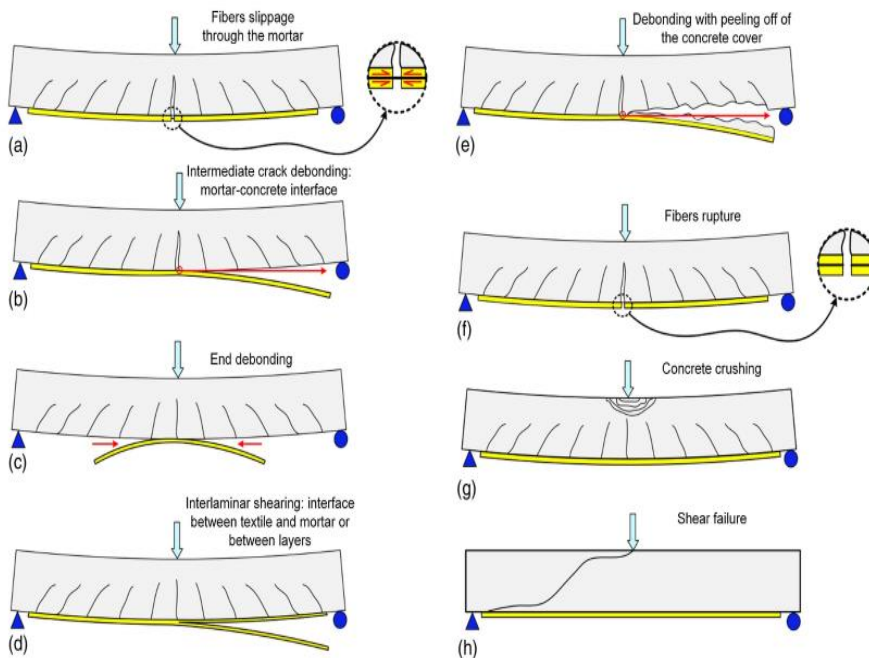


Fig. 5. Failure mode of Strengthened RC beam [1]

### 3.1.1. Theoretical study of RC beam strengthened with FRCM

The modeling of FRCM in finite element analysis (FEA) software involves defining materials, selecting suitable elements, and implementing interface modeling into practice to simulate the interaction among the various components. Define the parameters of the concrete material using appropriate model to response under loading conditions. The fabric reinforcement is modeled using shell element to define the behaviour of fabric and assigned the non-linear elastic material properties to define the fabric performance. By

utilizing the solid element to model the cementitious matrix and define the three-dimensional performance of the matrix. Fig. 6 represent the modeling of fabric, matrix, polypropylene and composite matrix. Fig. 7 shows the failure mode of hemp, sisal and glass fabric.

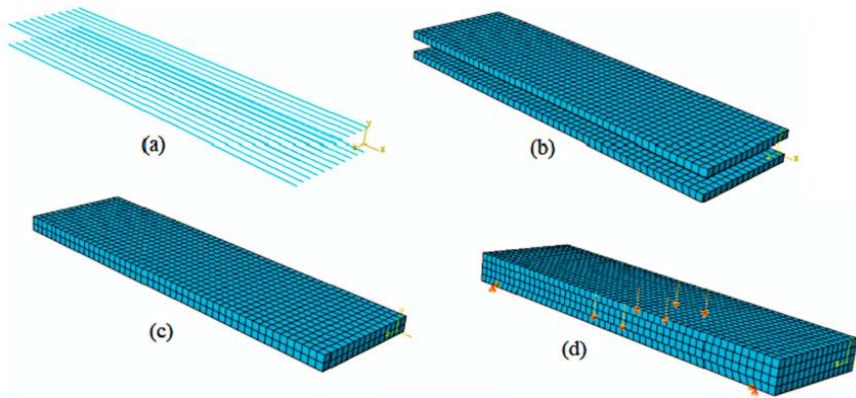


Fig. 6. Modeling (a) Fabric (b) Fabric (c) Polypropylene (d) Composite matrix [59]

Mercedes et al. studied the bending response of composite panels using different fabric. These authors compared the experimental results with the numerical simulation. The displacement for panels with hemp fabric attained the variation between 10 to 41% and for sisal and glass fabric attained the variation of about 1 to 14% [59]. A numerical study was conducted by Kalyani et al. to examine the flexural strengthened RC beams made of glass, Aramid, and hybrid FRP sheets. The study's findings demonstrate that utilizing hybrid FRP increases loading capacity of about 202.63% [60]. Ombres et al. studied that the beam strengthened with PBO-FRCM significantly increases the flexural capacity of about 44% than the un-strengthened beams [61]. Table 2. shows the summary of literature review of strengthened concrete beams.

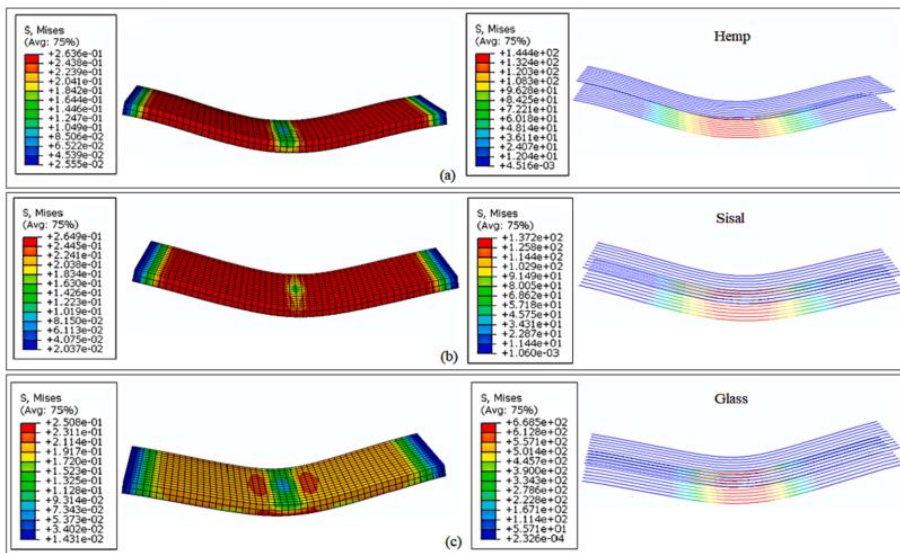


Fig. 7. Failure modes (a) Hemp fibers (b) Sisal Fibers (c) Glass Fiber [59]

Table 2. Summary of literature review of strengthened concrete beams

Ref.	Beam ID	Bonding Agent	Compressive strength of bonding agent (MPa)	Fabric Type	Tensile strength of Fabric (MPa)	No. of layers	$\sigma_c$ (MPa)	$\sigma_y$ (MPa)	Strengt. Method	Cont. Beam, Pc (kN)	Yield Load, Py (kN)	Ult. Load, Pu (kN)	(Pu/Pc )	Failure modes
(23)	M1-B3	Cement-based with polymers	25.37	Basalt	1540	3	33.1	662	Strip	56.7	59	66.8	1.18	IS
	M1-B6				6	60.2					73.7	1.3	IS	
	M1-G3			Glass	1375	3					58.9	68.2	1.2	FR
	M1-G6				6	62.3					77.9	1.37	IS	
	M2-B3	Cement Mortar	20.09	Basalt	1540	3					58.1	61.6	1.09	D
	M2-B6				6	29.5					60.9	1.07	D	
	M2-G3			Glass	1375	3					57.2	68.4	1.21	FR
	M2-G6				6	61.6					66.2	1.17	D	
(50)	S0-CGM	Cement Mortar	58	Carbon	0.325	1	61	494	U-wrap	1173.6 1310.1	-	1407.5	1.07	FR
	S250-CGM											1412.7	1.08	FR
	S0-CM											1446.6	1.1	FR
	S250-CM											1522.7	1.16	FR
	S0-CP											1322.3	1.01	FR
	S250-CP											1429.2	1.09	FR
(56)	S1-T1-P1-1	Cement Mortar	29	PBO	5800	1	22.7 7	515.44 521.89	Strip	74.85	80.1	87.42	1.17	CC

	S1-T1-P1-2									2					80.04	87.6	1.17	CC & D
	S2-T1-P1														45.03	54.24	1.09	CC
	S2-T1-P2-1									1					50.4	64.06	1.29	D
	S2-T1-P2-2									2	23.0	525.9		49.65	50.01	66	1.33	D
	S2-T1-P3-1									1	2	535.6			52.74	71.39	1.44	D
	S2-T1-P3-2									2					46.1	61.44	1.24	D
	S2-T2-P2									2	22.3	525.9		43.02	44.94	52.86	1.23	D
	S2-T2-P3									3	9	535.6			49.77	55.71	1.29	D
	BS2									2					-	82.66	1.36	SF
	BS3	Cement Mortar	23.9							4					-	83.51	1.37	SF
	BS4									4					-	88.74	1.46	SF
(44)	BS5			Basalt	623		20	684	U-wrap	60.8					-	92.53	1.52	SF
	BS6									2					-	83.38	1.37	SF
	BS7	PMM	56.4							4					-	83.38	1.37	SF
	BS8									4					--	96.26	1.58	SF
	BS9									4					-	114.1	1.876	SF
	S0-FRCM1									1					-	169.1	2.1	IS
	S0-FRCM2									2				80.4	-	196.7	2.45	IS
	S0-FRP-1									1						184.1	2.29	IS
(57)	S1-FRCM1	Cement mortar	74	Carbon	3800		45	520	U-wrap	143.5					-	234.7	1.64	IS
	S1-FRCM2									2					-	239.6	1.67	IS
	S1-FRP-1									1						239.8	1.67	IS
	S2-FRCM1									1				177.7	-	267.9	1.51	IS

	S2-FRCM2					2					275.8	1.55	IS		
	S2-FRP-1					1					281.4	1.58	IS		
(35)	SB-GT	Cement mortar	58	Glass	100	1	35	480	123.5	side-bonded	-	146.3	1.18	DT	
	UW-GT									U-wrap	-	180.2	1.46	DT	
	SB-CT1									side-bonded	-	155.5	1.26	DT	
	UW-CT1			U-wrap	-	151.8				1.23	DT				
	SB-CT2			Carbon	135	2				side-bonded	-	254.4	2.06	SF-D	
	UW-CT2									U-wrap	-	253.4	2.05	SF-D	
(51)	SH1	Cement mortar	43.9	PBO	5800	1	49.7	U-Wrap	272		261	279	1.03	FS	
	SH2										266	289	1.06	D & FS	
	SH4										263	306	1.13	CC	
	SS1										176	226	1.09	FS	
	SS2										184	249	1.21	FS	
	SS4										213	267	1.29	FS	
(52)	HP2	Cement mortar	43.9	PBO	5800	2	43.9	890	U-Wrap	272		266	285	1.05	FS-D
	HP4											263	302	1.11	FS
	HC2										Carbon	4300	2		257
	SP2			PBO	5800	2						184	249	0.92	FS-D
	SP4											213	267	0.98	FS
	SC2										Carbon	4300	2		264
(58)	B-A-S-Ao	Alkali-Activated Slag (AAS)	53.5	carbon	2300	-	42.5	1800	Strip	65.5		61.7	72.1	1.1	FS-FR
	B-A-L-Ao											63.4	75.9	1.16	FS-FR
	B-A-L-1.5Ao										carbon		67.8	82.8	1.26

	B-A-L-2Ao		carbon		-						66.8	74.4	1.14	FS-FR-D
(20)	BL-C	Cement Mortar	20	Carbon	4800	2	39.5	595	U-wrap	39.9	-	83.3	2.09	FS
	BL-P		30	PBO	5800						-	82.7	2.07	FS
	BL-G		40	Glass	2600						-	58.2	1.46	D
	BH-C		20	Carbon	4800						-	144	3.61	FR
	BH-P		30	PBO	5800						-	136	3.41	FS
	BH-C		40	Glass	2600						-	124	3.11	D
	BS1-01		Cement Mortar		Carbon						834	1	50	834
BS2-01	-	Glass		460	212	132	0.55	D & SF						
BS2-01		Carbon		834	-	113	0.47	D & SF						
BS2-02		Glass		460	-	166	0.69	D & SF						

where, SF- Shear failure; IS- Interlaminar shearing; D- Debonding; SS-Splitting of strut; CC-concrete crushing, FS- Fabric slippage, FR- Fabric rupture.

### 3.1.2. Summary

The efficiency of the strengthening system can vary greatly based on a variety of factors, including the number of layers, the material's characteristics, and the specifics of the reinforcement of the RC member. The flexural and shear capacity increase with the increases of externally applied fabric reinforcement and also the failure mode changes, while increasing the fabric layers. The use of fabric with multiple layers prevents the fibers from slippage failures. The mode of failure was shifted to interlaminar shearing, debonding at the matrix/concrete interface, and debonding with slippage of the concrete cover. The uses of polymer modified mortar shows better performance for FRCM.

### 3.2. Strengthening of RC Column using FRCM

Strengthening of reinforced concrete (RC) columns with FRCM is an effective technique to improve the structural performance and load-carrying capacity of existing columns. Strengthening of RC columns with FRCM offers a many advantages like improved the load-carrying capacity, increases the durability, and enhanced the fire resistance capabilities [62][63]. The resistance to axial loads and serviceability of columns can be considerably improved by the subsequent application of a TRC layer [62]. FRCM allows to increase the strength of eccentrically loaded reinforced concrete columns; with respect to the unconfined specimen [64]. This technique is a versatile and cost-effective solution for enhancing the structural performance of existing columns and also minimizing the disruption to the building or structure [65]. However, the effectiveness of FRCM strengthening depends on proper design, material selection, and installation, and it should be carried out by experienced professionals following industry guidelines and standards. Fig. 8 shows the schematic diagram for RC column strengthened with FRCM. Jinlin et al. reported that by adding three textile layers, the ultimate load was increased to 44%. They also noticed that transverse cracks that originate on the tension side of the structure extend towards the compression side and are accompanied by significant concrete crushing [66]. Liu et al. investigated the axial behavior of fire-damaged reinforced concrete (RC) columns strengthened with a textile reinforced externally bonded reinforcement system. This study reveals that TRE-strengthened specimens exhibited a failure mode characterized by tensile rupture of fiber rovings and increased the load carrying capacity and ultimate displacement by 18% to 107% and 36% to 146% [26].

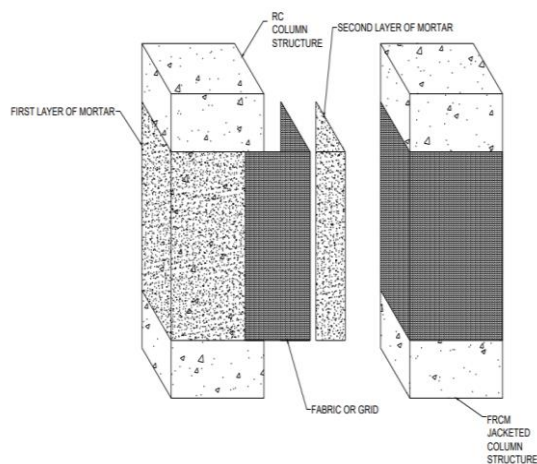


Fig. 8 Schematic diagram for RC Column strengthened with FRCM

Guo et al. investigated the seismic behavior of RC columns retrofitted with textile-reinforced mortar. These researchers revealed that the TRM jacket substantially enhanced shear capacity of about 54.3% to 55.2% and also noticed that displacement increases from 40.34% to 78.62%. By increasing the reinforcement ratio of carbon textiles, capacity of energy-dissipation increases with deformation. And also, it was observed that with an increase in axial load ratios, shear resistance exhibited a slight uptick, and also accompanied by a decrease in ductility as well as the energy-dissipation ability [29]. Alhoubi et al. studied the performance of reinforced concrete columns strengthened with PBO-FRCM systems was rigorously examined under pre-damage conditions. Their findings highlight the number of FRCM layers played a pivotal role in the failure mechanisms. The columns strengthened with two layers experienced internal delamination, while those with four layers suffered fabric rupture. [67]. Fig. 9 represents the mode of failure of FRCM-confined concrete members.

Zhang et al. investigates the effectiveness of Carbon Textile-Reinforced Concrete confinement (CTRC) in improving the performance of square concrete columns using uniaxial compression tests [17]. These scientists reported that substantial increases in load-carrying capacity and ductility, especially when utilizing four layers of textile. And also, they observed that adding short glass fibers with mortar mixer improved the performance of the strengthened beam [68]. The compressive strength of FRCM-confined concrete elements is significantly influenced by cross-sectional size, corner radius, scale effect, type of fiber mesh, and the number of FRCM layers [69] while, the fabric has less of an impact on the mortar stiffness. [70]. Alhoubi et al. assess the performance of RC columns strengthened with PBO-FRCM systems under two pre-damage conditions and they found that columns strengthened with two layers failed due to internal delamination, while those with four layers failed due to fabric rupture [71].

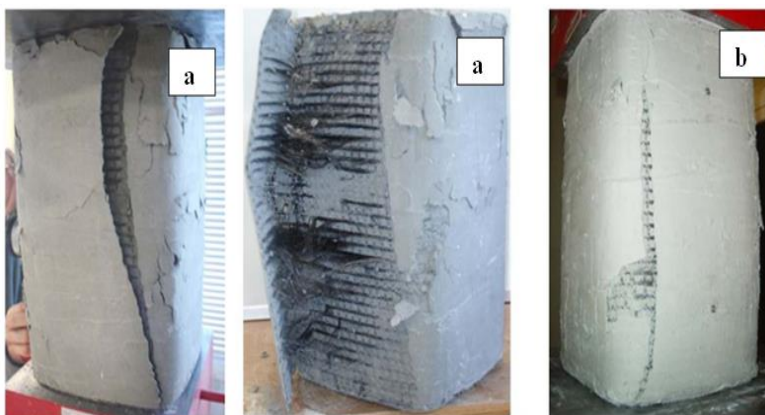


Fig. 9. Failure modes of FRCM-confined concrete members (a) Debonding (b) Rupture of the fabric [1]

Tello et al. studied the concentrically loaded columns strengthened with varying numbers of PBO-FRCM layers and reported that circular columns with two and four PBO-FRCM layers have higher capacity than the square columns [67]. Faleschini et al. examined the RC columns strengthened with CFRCM and observed the wide crack pattern in the specimens. As increasing the fabric layers the compressive strength of confined column increases as well as increases the ductility [72]. Napoli et al. examined the compressive strength of concrete externally confined with FRCM systems and they reveals that glass and carbon fabric systems exhibit the lowest strength than PBO as well as Steel [73]. Fig. 10 shows the crack pattern for strengthened RC column. Toska et al. studied the



effectiveness of RC column strengthened with FRCM through confinement and observed that the strengthened specimen enhanced the concrete strength ranging from 1.4 to 2.18 than the control specimen [74]. Chen et al. examined that textile-reinforced ECC-confined columns performed better in terms of strength and ductility than TRM-confined columns.[75].

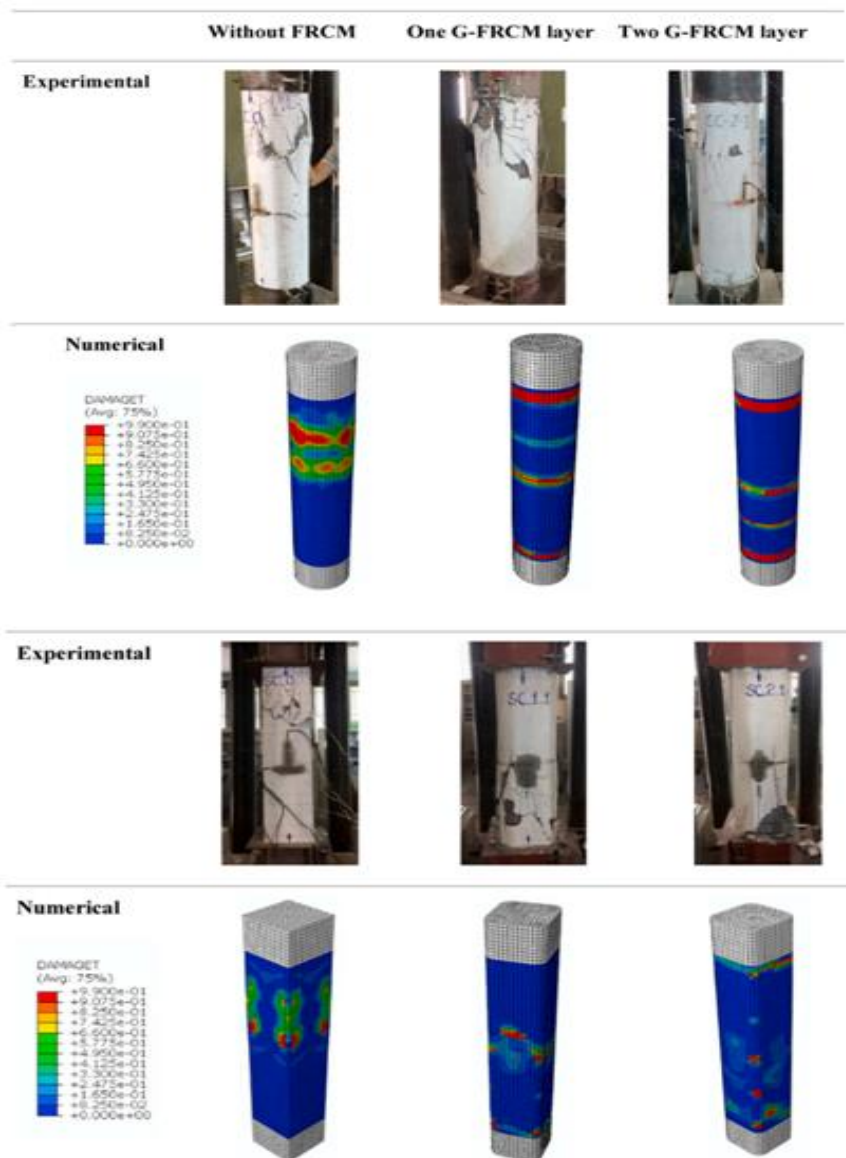


Fig. 10. Crack pattern for Strengthened RC Column [77]

According to Mohammad et al. study of FRCM-reinforced concrete columns using a probabilistic approach increased the axial load carrying capability of the strengthened beams. These authors also investigated the load-carrying capacity of FRCM-strengthened with FEM, Artificial neural network, and Monte Carlo simulation. The failure of concrete columns was simulated in the FEM using Concrete Damage Plasticity Modeling. The results

indicated failure on the column's tensile face, particularly tensile cracking. As a result, the experimental test and damage pattern were appropriately changed, increasing the CDPM stability in numerical calculations. It was found that column performance can be affected by changing the configurations instead of increasing the fabric layers [76].

Table 3. displays the summary of literature review of strengthened concrete columns. Glass fabric reinforced cementitious matrix was examined by Quyen et al. as a confinement material for RC column which meet the slenderness ratio. The authors report that for both single and double layers of FRCM, the Strengthening column increased by 22.1% and 55.5%, respectively. [77]. Reducing the fabric spacing, decreasing the core strength of concrete, and thickening the Engineered Cementitious Composites helps to improve the compressive response of pre-damaged columns [78]. Nguyen et al. reported that the non-linear computation of G-FRCM predicted more results than experimental results [69]. Ludovico et al. noticed that confinement made of basalt fibers that were bonded using cement mortar performed better than epoxy-based laminates [79][80]. The confined concrete column strengthened with FRCM shows good ductility property and increased the strength up to 20% [81], whereas using basalt as strengthening fabric, the load carrying capacity increased to 34% [82]. The column confined with CFRCM exhibited a considerable increase in compression strength, energy absorption, and deformability [83][84][85].

Table 3. Summary of literature review of strengthened concrete columns

Ref.	Column ID	Bonding Type	Compressive strength of Bonding agent (MPa)	Fabric Type	Tensile strength of fabric (MPa)	No. of Fabric Layers	Compressive Strength of FRCM Confined Concrete, $f_{cc}$ (MPa)	Peak strength on unconfined specimens, $f_{co}$ (MPa)	Average of ( $f_{cc} / f_{co}$ )	Average of ( $E_{ccu} / E_{cu}$ )	Failure Mode			
(77)	S3	Cement Mortar	30	Glass	1814	2	22.35	15.52	1.12	1.34	RF			
	S10					1	18.01	17.83	1.37	1.58				
	S11					1	20.15	17.83	1.37	1.58				
	S12					1	21.93	17.83	1.37	1.58				
	S13					2	23	17.83	1.12	1.34				
(78)	C-S2-D0	Cement Mortar	22.9	Carbon	1487	2	19.2	36.8	1.09	0.83	D			
	C-S3-D0						22.4	36.8	1.33	3.33				
	C-S4-D0						20	36.8	1.18	2.53				
	C-S5-D0						21.9	36.8	1.25	1.9				
	C-S6-D0						23.5	36.8	1.31	1.55				
	G-S3-D0			Glass	586	2	19.3	36.8	1.15	2.25				
	G-S4-D0						18.6	36.8	1.1	1.34				
	G-S5-D0						18.9	36.8	1.08	1.77				
	G-S6-D0						18.6	36.8	1.04	1.29				
(79)	G1-GRO3-Y-A,B	Grout		Glass		1	36.81	34.62	1.06	-	D			
	G1-GRO3-Y-A,B						42.31	34.62	1.22	-				
	G2-GRO3-Y-A,B						2	50.12	34.62	1.44		-		
	C1-GRO2-Y-A,B						Carbon		1	43.82		34.62	1.26	-
	C1-GRO3-Y-A,B									43.04		34.62	1.24	-

	C2-GRO3-Y-A,B			2	57.6		1.66	-	
	M1-1				25.51		1.17	1.24	
	M1-2				25.94		1.19	1.35	
	M1-3			1	27.47		1.26	1.28	
	M1-4				27.03		1.24	1.34	
	M1-5				24.42		1.12	1.33	
	M1-6	Pozzolanic Mortar	22.4		26.81		1.23	1.49	
	M2-1				29.21		1.34	1.44	
	M2-2				27.9		1.28	1.38	
	M2-3			2	26.38		1.21	1.52	
	M2-4				24.85		1.14	1.21	
	M2-5				27.25		1.25	1.38	
(80)	M2-6		Basalt	894	27.69	21.8	1.27	1.39	DF
	C1-1				29.21		1.34	-	
	C1-2				27.69		1.27	-	
	C1-3			1	29.87		1.37	-	
	C1-4				28.56		1.31	-	
	C1-5				28.99		1.33	-	
	C1-6	Cement Mortar	31.5		27.69		1.27	-	
	C2-1				28.34		1.3	-	
	C2-2				27.47		1.26	-	
	C2-3			2	27.25		1.25	-	
	C2-4				30.08		1.38	-	
	C2-5				28.78		1.32	-	

	C2-6					30.74		1.41	-				
(81)	CF2M-A	Pozzolanic Mortar	Carbon	2		20.83	16.8	1.24	3.81	RF			
	CF2M-B					20.58	16.08	1.28	4.4				
	CF3M-A					23.69	16.8	1.41	3.41				
	CF3M-B					23.96	16.08	1.49	2.79				
(84)	LDG-A-1	Cement Mortar	Glass	31.1	3240	29.4		1.44	3.88	RF			
	LDG-A-2					24.3		1.19	3.5				
	LDG-H-1					30		1.47	3.4				
	LDG-H-2					30		1.47	3.07				
	HDG-A-1					25.1		1.23	2.71				
	HDG-A-2					23.9	20.4	1.17	8.38				
	HDG-H-1					31.9		1.56	1.69				
	HDG-H-2					28.1		1.38	4.51				
	BGP-A-1					28.5		1.4	-				
	BGP-A-2					29.1		1.43	1.12				
(83)	BGP-H-1	Portland Cement Mortar	Glass, Basalt	2.49	4840	32.9		1.61	3.13	DF			
	BGP-H-2					30.7		1.5	2.47				
	M15_CF_1					Carbon	240	1	13.32			1.2	1.63
	M15_CF_2						270	2	13.98			1.23	1.53
	M45_PBO_1					PBO		1	18.14		11.4	1.64	3.23
	M45_PBO_2							2	17.27			1.51	2.96
(70)	M45_CF_1	Cement Mortar	Carbon	17	240	13.85		1.25	1.41				
	M45_CF_2					13.46		1.18	1.34				
(70)	C20-1		Carbon	31.9	1487	23	21.2	1.08	1.82	RF			

	C20-2				2	26.2		1.23	1.68	
	S20-1				1	20.3		0.95	1.97	
	S20-2				2	21.2		1	1.88	
	C33-1	Cement Mortar			1	19.8		0.93	1.49	
	C33-2				2	21.9		1.03	1.67	
	S33-1				1	17.1		0.8	2.43	
	S33-2				2	20.9		0.98	1.31	
	C20_D0_C2				1	17.63	13.15	1.34	1.276	
	S20_D0_C2				2	14.34	14.2	1.01	1.222	
(72)	S33_D0_C2	Cement Mortar	28.2	PBO	1487	3	21.09	16.58	1.27	1.2
	C20_D1_C2						17.62	13.15	1.34	0.655
	S20_D1_C2						14.67	14.2	1.03	0.777
	S33_D0_C2						14.98	16.58	0.9	1.1

where, D- Debonding, RF- Rupture Failure, DF – Ductile failure, CC- Concrete Crushing, SY-Steel Yielding.

The compressive strength and strain of the confined concrete improved with an increase in the number of applied FRCM layers. As the number of layers increases, the effectiveness generally decreases and the increase is typically non-proportional to the number of reinforcement. The efficiency of TRM jackets in enhancing the axial load-carrying capacity of confined concrete is largely dependent on the strength of the unconfined concrete; the jackets are more effective for lower unconfined concrete strength values.

### 3.3. Strengthening of RC Slab using FRCM

The RC slabs are stressed bi-axially and have a larger bottom surface area than RC beam, therefore adopting bi-directional fabric is more appropriate for strengthening the slabs. A study on the flexural behavior of two-way RC slabs reinforced with FRCM was carried out by Koutas et al. Their findings revealed that the stiffness and cracking stress of the slab were significantly enhanced by adding more layers [86]. Utilizing polymer-modified cement mortar as the binder, Bing L et al. investigated the strengthened slab's performance under fire exposure and found that the strengthening layer could withstand the fire for about 30 minutes [87]. Fig. 11 illustrate the strengthening method of RC slabs.

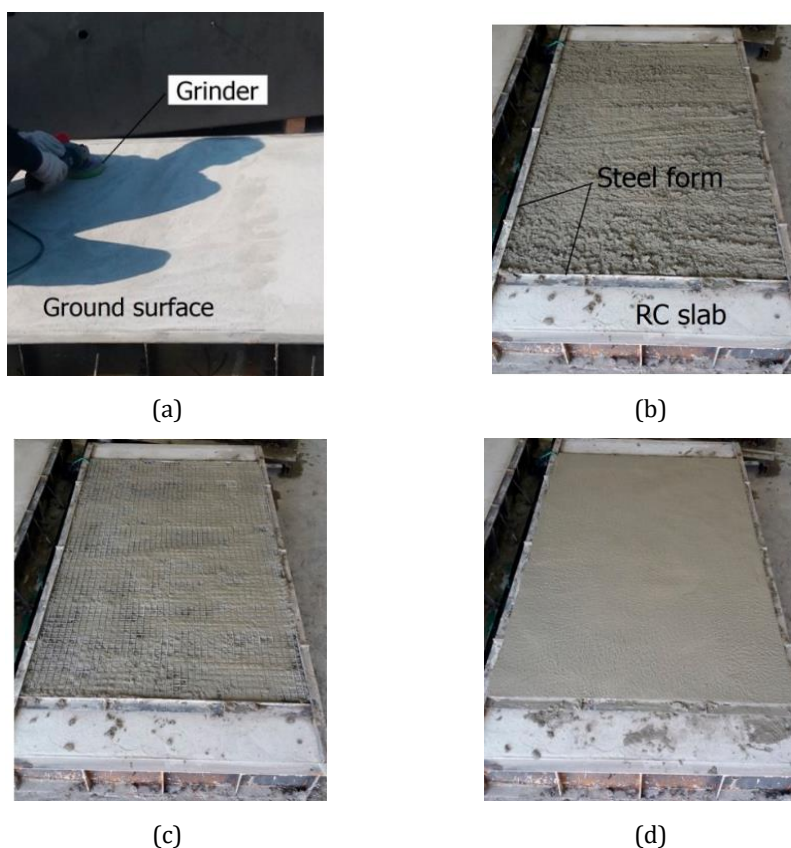


Fig. 11. Strengthening of RC slabs (a) surface preparation (b) Placing 1<sup>st</sup> mortar (c) Placing Fabric reinforcement (d) Finishing with 2<sup>nd</sup> layer of mortar [88]

Zhang et al. studied the flexural behaviour of RC slab using Geopolymer mortar as binder and found that strengthened slab delays the development of cracks, improves the post-cracking stiffness, and flexural capacity [89]. A study conducted by Kadhim et al. employed Carbon-FRCM to analyze two-way slabs strengthened in flexure. They observed that raising the FRCM reinforcement's width from 0 to 0.25 enhanced the final strength by 84%. Moreover, significant gains in strength of about 19% were observed when the width-to-span ratio increased from 0.25% to 1% [90]. Yoel et al. investigated the flexural strengthening of concrete slab with textile reinforced concrete and found that ultimate flexural capacity and stiffness of the strengthened slabs were increased to 165% and 112%, respectively than unstrengthened slab [88]. The researchers Sabbaghian et al. studied the flexural behavior of reinforced concrete (RC) slabs strengthened with thin laminates of High-Performance Fiber-Reinforced Cementitious Composite (HPFRCC). The laminates contain varying percentages of steel fibers (1% and 2%) and are applied with different binding methods (epoxy or mechanical anchorage), with or without internal bars (steel or GFRP). Experimental results show the enhancements in the load-bearing capacity and reduced the development of cracks and increased the ductility [91].

### 3.3.1. Summary

The RC slab capacity increases with FRCM techniques. By adding a greater number of layers to an RC slab greatly increased the slab's stiffness and cracking stress. And, also the strengthened slab delays the cracks development post-cracking stiffness, and increases the ductility.

### 3.4. Strengthening of Beam-Column Joint using FRCM

When a structure experiences a lateral cyclic load caused by an earthquake, the bending of adjacent members results in large magnitude stresses that can be directed in various directions, which leads to the failure of a beam-column connection. The beam-column joint is one of the most important structural parts. Its failure is viewed as undesirable since it can drastically reduce stiffness and strength, eventually causing the building to collapse as a whole. Exterior beam-column joints are restricted by surrounding beams in four directions, are more susceptible to failure during an earthquake than interior joints. The majority of the joints that failed in the most recent earthquake all over the world, to strengthen the beam-column joint of older and newly constructed building is required to prevent the gradual collapse of structures.

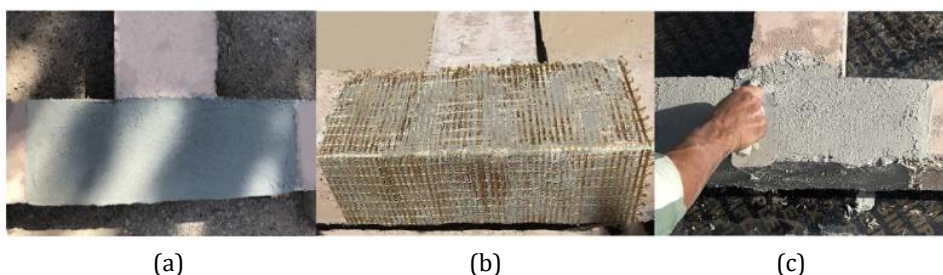


Fig. 12. Strengthening of beam-column joint (a) Applying the first layer of binder (b) Applying the fabric (c) Applying the second layer of binder [93]

An experimental study was carried out by Faleschin et al. to study the cyclic behavior RC exterior joints that were strengthened with FRP and FRCM composites. It was found that while FRP and FRCM composites were not able to restore the joint specimens capacity, FRCM composites were better than FRP at increasing the load capacity [92]. Yang et al. increased the shear strength of RC beams by employing basalt-FRCM and carbon-FRCM



with polymer-modified mortar and ECC [42]. Fig. 12 represents the strengthening of beam-column joint using FRCM

FRCM composites were applied by El-Maaddawy et al. to strengthen the corroded RC T-beams with basalt and carbon FRCM. They observed that the flexural capacity of the beam was found to be totally restored by the embedded carbon FRCM system, but not by the basalt FRCM [25]. Lim et al. study the beam-column joint strengthened by CFRP grid with ECC using high strength mortar. Their findings indicate that failure mechanism of the specimens may be changed by transferring the load joint to beam and the specimen's strength performance increases. Furthermore, the specimen exhibits enhanced ductility, enabling them to delay the failure [94]. Zuhair Murad et al. carried out an experimental study of the cyclic behaviour of retrofitted beam-column joints using FRCM by adopting U-shaped and X-shaped configuration. The specimens drift ratio, ductility, and stiffness were all greatly increased by the strengthened specimen up to 166%, 66%, and 11%, respectively. And, also U-shaped techniques performed better than X-shaped configuration [93].

#### 3.4.1. Summary

The load capacity of the beam-column joint was greatly increased by the FRCM strengthening approach. The failure modes modify from changing the load from joint to beam and increase the strength of the specimens. Additionally, the strengthened beam-column joint enhances its ductility, drift ratio, and stiffness of the strengthened specimen.

## 4. Conclusion

The application of FRCM presents unprecedented prospects for structural renovation and repair. The ensuing conclusions are distilled from a thorough analysis of the previously conducted studies. This summary covers the RC beam, column, slab, and beam-column joint strengthened with FRCM are briefly discussed.

The strengthening of RC beams with FRCM is found to be effective method for increasing the ultimate flexural and shear strength of the strengthened members. The strength gain increases non-proportionally as the number of FRCM layers increases.

The failure modes of flexural and shear strengthened concrete members are fabric roving, fabric rupture, debonding at the fabric-matrix interface, and concrete cover separation. Flexural strengthened beam elements exhibit more debonding at the fabric-matrix interface than shear strengthened beam.

The main effects of concrete confinement increased the compressive strength with greater axial deformation capacity. The strength gain in concrete columns strengthened by FRCM is reduced by eccentric loading.

The mode of failure for column is usually ductile failure due to rupture failure develops in the fabric. The mode of failure tends to be ductile because the rupture failure gradually spread towards the other fabric inside the reinforcement through the limited number of fibers. Debonding failures occurs at the end of the FRCM systems. Additionally, observed the fabric slippages, concrete crushing without causing damage to the fabric. Therefore, FRCM provide a versatile and cost-effective solution for upgrading the existing structures.

The fabric used for strengthening the structural members plays a vital role. The selection of fabric type varies on the application of FRCM. The carbon and PBO have high tensile strength, therefore for heavy damaged structural members' carbon and PBO fabric can be adopted to improve their performance.

The FRCM mortar that is used as a binder needs to be selected with carefully. The silica fume and fly ash used with cement mortar showed a higher compressive strength. As a result, cement containing silica fume and fly ash can be employed as binder for FRCM.

It is possible to prevent debonding failure modes by properly preparing the surface, selecting the right fabric and mortar, and proper implementation of FRCM techniques.

The RC slab capacity increases with FRCM techniques. By adding a greater number of layers to an RC slab greatly increased the slab's stiffness and cracking stress. And, also the strengthened slab delays the cracks development post-cracking stiffness, and increases the ductility.

The load capacity of the beam-column joint was greatly increased by the FRCM strengthening approach. The failure modes modify from changing the load from joint to beam and increase the strength of the specimens. Additionally, the strengthened beam-column joint enhances its ductility, drift ratio, and stiffness of the strengthened specimen.

According to the authors, using fabric-reinforced cementitious matrix composites to strengthen the concrete structures is a very promising method that is gaining interest from the worldwide scientific society. Future studies in this area should focus on the enhancing the fabric strengthening, studying the durability of the strengthening techniques with elevated temperature and developing design guidelines within the framework of existing design formulations. It is essential to investigate the behaviour of FRCM in different conditions, such as fire, gas blasting, extreme loading conditions, etc. It is necessary to conduct extensive research on the impact of FRCM under fire by experimentally with slow and quick heating rates which causes damages in strengthened members.

## Abbreviations

FRCM-Fabric Reinforced Cementitious Matrix; TRM – Textile Reinforced Mortar; FRP – Fiber Reinforced Polymer; FEM-Finite Element Modeling; RC –Reinforced concrete; NSM – Near Surface Mounted; GFRP-Glass Fabric Reinforced Polymer; CFRP-Carbon Fabric Reinforced Polymer; AFRP – Aramid Fabric Reinforced Polymer.

## References

- [1] Koutas LN, Tetta Z, Bournas DA, Triantafillou TC. Strengthening of Concrete Structures with Textile Reinforced Mortars State-of-the-Art Review. *J Compos Constr.* 2019;23(1):1–20.
- [2] Hoseynzadeh H, Mortezaei A. Seismic Vulnerability and Rehabilitation of One of the World's Oldest Masonry Minaret under the Different Earthquake Frequency Content. *J Rehabil Civ Eng.* 2021;9(4):12–36.
- [3] Tehrani P, Eini A. Seismic Performance Assessment of Steel Moment Frames with Non-parallel System Irregularity. *J Rehabil Civ Eng.* 2022;10(4):109–28.
- [4] Kirthiga R, Elavenil S. A review on using inorganic binders in fiber reinforced polymer at different conditions to strengthen reinforced concrete beams. *Constr Build Mater.* 2022;352(July).
- [5] P B, K RMS, R K. Strain Behaviour of Concrete Elements Retrofitted Using Organic and Inorganic Binders. *Asian J Appl Sci.* 2014;7(4):215–23.
- [6] Awani O, El-Maaddawy T, Ismail N. Fabric-reinforced cementitious matrix: A promising strengthening technique for concrete structures. *Constr Build Mater.* 2017;132:94–111. <http://dx.doi.org/10.1016/j.conbuildmat.2016.11.125>
- [7] Kirthiga R, Elavenil S. Potential utilization of sugarcane bagasse ash in cementitious composites for developing inorganic binder. *Ain Shams Eng J.* 2023;14(October).

- [8] Elsanadedy HM, Abbas H, Almusallam TH, Al-Salloum YA. Organic versus inorganic matrix composites for bond-critical strengthening applications of RC structures – State-of-the-art review. *Compos Part B Eng.* 2019;174(January).
- [9] Wang Z, Dai JG, Wang M, Chen L, Zhang F, Xu Q. Residual bond strengths of epoxy and cement-bonded CFRP reinforcements to concrete interfaces after elevated temperature exposure. *Fire Saf J.* 2021;124(75):103393. <https://doi.org/10.1016/j.firesaf.2021.103393>
- [10] Natraj K, Kirthiga R, Elavenil S. Structural performance of RCC building and strengthening the structural members with CFRP. *Mater Today Proc.* 202. <https://doi.org/10.1016/j.matpr.2023.04.304>
- [11] Mollaei S, Babaei M, Jalilkhani M. Assessment of damage and residual load capacity of the normal and retrofitted RC columns against the impact loading. *J Rehabil Civ Eng.* 2021;9(1):29–51.
- [12] Ebead U, Shrestha KC, Afzal MS, El Refai A, Nanni A. Effectiveness of Fabric-Reinforced Cementitious Matrix in Strengthening Reinforced Concrete Beams. *J Compos Constr.* 2017;21(2):04016084.
- [13] Hadi MNS, Algburi AHM, Sheikh MN, Carrigan AT. Axial and flexural behaviour of circular reinforced concrete columns strengthened with reactive powder concrete jacket and fibre reinforced polymer wrapping. *Constr Build Mater.* 2018;172:717–27. <https://doi.org/10.1016/j.conbuildmat.2018.03.196>
- [14] Abdulla AI, Razak HA, Salih YA, Ali MI. Mechanical properties of sand modified resins used for bonding CFRP to concrete substrates. *Int J Sustain Built Environ.* 2016;5(2):517–25. <http://dx.doi.org/10.1016/j.ijbsbe.2016.06.001>
- [15] Aljazeerai ZR, Myers JJ. Fatigue and flexural behaviour of reinforced concrete beams strengthened with a fibre reinforced cementitious matrix. *J Compos Constr.* 2016;21(3):128–34. [https://doi.org/10.1061/\(ASCE\)CC.1943-5614.0000726](https://doi.org/10.1061/(ASCE)CC.1943-5614.0000726)
- [16] ACI Committee 549.4R-13. Guide to Design and Construction of Externally Bonded Fabric-Reinforced Cementitious Matrix (FRCM) Systems for Repair and Strengthening Concrete Structures. ACI. 2013.
- [17] Raoof SM, Bournas DA. Bond between TRM versus FRP composites and concrete at high temperatures. *Compos Part B Eng.* 2017;127:150–65.
- [18] De Santis S, Carozzi FG, de Felice G, Poggi C. Test methods for Textile Reinforced Mortar systems. *Compos Part B Eng.* 2017;127:121–32. <http://dx.doi.org/10.1016/j.compositesb.2017.03.016>
- [19] Promis G, Gabor A, Maddaluno G, Hamelin P. Behaviour of beams made in textile reinforced mineral matrix composites, an experimental study. *Compos Struct.* 2010;92(10):2565–72. <http://dx.doi.org/10.1016/j.compstruct.2010.02.003>
- [20] Hashemi S, Al-Mahaidi R. Experimental and finite element analysis of flexural behavior of FRP-strengthened RC beams using cement-based adhesives. *Constr Build Mater.* 2012;26(1):268–73. <http://dx.doi.org/10.1016/j.conbuildmat.2011.06.021>
- [21] El-Sherif HE, Wakjira TG, Ebead U. Flexural strengthening of reinforced concrete beams using hybrid near-surface embedded/externally bonded fabric-reinforced cementitious matrix. *Constr Build Mater.* 2020;238:117748. <https://doi.org/10.1016/j.conbuildmat.2019.117748>
- [22] Song S, Deng M, Zhang M, Guo L, Dong Z, Li P. Flexural strengthening of reinforced concrete beams using textile-reinforced mortar improved with short PVA fibers. *Structures.* 2023;56(April):104824. <https://doi.org/10.1016/j.istruc.2023.07.014>
- [23] Toska K, Hofer L, Faleschini F, Zanini MA, Pellegrino C. Seismic behavior of damaged RC columns repaired with FRCM composites. *Eng Struct.* 2022;262(April).
- [24] Koutas LN, Papakonstantinou CG. Flexural strengthening of RC beams with textile-reinforced mortar composites focusing on the influence of the mortar type. *Eng Struct.* 2021;246(July).

- [25] El-Maaddawy T, El Refai A. Innovative Repair of Severely Corroded T-Beams Using Fabric-Reinforced Cementitious Matrix. *J Compos Constr.* 2016;20(3):04015073.
- [26] Liu WW, Ouyang LJ, Gao WY, Liang J, Wang TC, Song J, et al. Repair of fire-damaged RC square columns with CFRP textile-reinforced ECC matrix. *Eng Struct.* 2023;292:116530. <https://doi.org/10.1016/j.engstruct.2023.116530>
- [27] Elsanadedy HM, Almusallam TH, Alsayed SH, Al-Salloum YA. Flexural strengthening of RC beams using textile reinforced mortar - Experimental and numerical study. *Compos Struct.* 2013;97:40–55. <http://dx.doi.org/10.1016/j.compstruct.2012.09.053>
- [28] Alhoubi Y, El A, Abed F, El-maaddawy T, Tello N. Strengthening pre-damaged RC square columns with fabric-reinforced cementitious matrix ( FRCM ): Experimental investigation. *Compos Struct.* 2022;294:115784.
- [29] Guo L, Deng M, Li T. Seismic behaviour of RC columns retrofitted with textile-reinforced mortar (TRM) optimized by short PVA fibres. *Structures.* 2023;50(January):244–54. <https://doi.org/10.1016/j.istruc.2023.02.041>
- [30] Roof MS, Bournas AD. TRM versus FRP in flexural strengthening of RC beams\_ Behaviour at high temperatures. *Constr Build Mater.* 2017;154:424–37. <https://doi.org/10.1016/j.conbuildmat.2017.07.195>
- [31] Meriggi P, Santis S De, Fares S, Felice G De. Design of the shear strengthening of masonry walls with fabric reinforced cementitious matrix. *Constr Build Mater.* 2021;279:122452.
- [32] Escrig C, Gil L, Bernat-Maso E. Experimental comparison of reinforced concrete beams strengthened against bending with different types of cementitious-matrix composite materials. *Constr Build Mater.* 2017;137:317–29. <http://dx.doi.org/10.1016/j.conbuildmat.2017.01.106>
- [33] Al-Lami K, D’Antino T, Colombi P. Study of the Bond Capacity of FRCM- and SRG-Masonry Joints. *CivilEng.* 2021;2(1):68–86.
- [34] D’Antino T, Papanicolaou C (Corina). Comparison between different tensile test setups for the mechanical characterization of inorganic-matrix composites. *Constr Build Mater.* 2018;171:140–51. <https://doi.org/10.1016/j.conbuildmat.2018.03.041>
- [35] Ombres L, Iorfida A, Mazzuca S, Verre S. Bond analysis of thermally conditioned FRCM-masonry joints. *Meas J Int Meas Confed.* 2018;125(May):509–15. <https://doi.org/10.1016/j.measurement.2018.05.021>
- [36] Azam R, Soudki K. FRCM Strengthening of Shear-Critical RC Beams. *J Compos Constr.* 2014;18(5):04014012.
- [37] Marcari G, Basili M, Vestroni F. Experimental investigation of tuff masonry panels reinforced with surface bonded basalt textile-reinforced mortar. *Compos Part B Eng.* 2017;108:131–42. <http://dx.doi.org/10.1016/j.compositesb.2016.09.094>
- [38] D’Ambrisi A, Focacci F, Luciano R, Alecci V, De Stefano M. Carbon-FRCM materials for structural upgrade of masonry arch road bridges. *Compos Part B Eng.* 2015;75:355–66. <http://dx.doi.org/10.1016/j.compositesb.2015.01.024>
- [39] Aravind N, Nagajothi S, Elavenil S. Machine learning model for predicting the crack detection and pattern recognition of geopolymer concrete beams. *Constr Build Mater.* 2021;297:123785. <https://doi.org/10.1016/j.conbuildmat.2021.123785>
- [40] Garcez M, Meneghetti L, da Silva Filho LC. Structural Performance of RC Beams Poststrengthened with Carbon, Aramid, and Glass FRP Systems. *J Compos Constr.* 2008;12(5):522–30.
- [41] Soudki K, Alkhrdaji T. Guide for the Design and Construction of Externally Bonded FRP Systems for Strengthening Concrete Structures (ACI 440.2R-02). *Proceedings of the Structures Congress and Exposition.* 2005. 1627–1633.
- [42] Yang X, Gao WY, Dai JG, Lu ZD. Shear strengthening of RC beams with FRP grid-reinforced ECC matrix. *Compos Struct.* 2020;241:112120. <https://doi.org/10.1016/j.compstruct.2020.112120>

- [43] Trapko T. Behaviour of fibre reinforced cementitious matrix strengthened concrete columns under eccentric compression loading. *Mater Des.* 2014;54:947–54.
- [44] Gopinath S, Iyer NR, Gettu R, Palani GS, Murthy AR. Confinement effect of glass fabrics bonded with cementitious and organic binders. *Procedia Eng.* 2011;14:535–42.
- [45] Al-Salloum YA, Elsanadedy HM, Alsayed SH, Iqbal RA. Experimental and Numerical Study for the Shear Strengthening of Reinforced Concrete Beams Using Textile-Reinforced Mortar. *J Compos Constr.* 2012;16(1):74–90.
- [46] Jabr A, El-Ragaby A, Ghrib F. Effect of the fiber type and axial stiffness of FRCM on the flexural strengthening of RC beams. *Fibers.* 2017;5(1).
- [47] Tsesarsky M, Katz A, Peled A, Sadot O. Textile reinforced concrete (TRC) shells for strengthening and retrofitting of concrete elements: influence of admixtures. *Mater Struct.* 2015;48(1–2):471–84.
- [48] Wu C, Li VC. CFRP-ECC hybrid for strengthening of the concrete structures. *Compos Struct.* 2017;178:372–82.
- [49] Baiee A. Development Ultra-High Strength Cementitious Characteristics Using Supplementary Cementitious Materials. *J Eng Sci.* 2021;28(3):111–5.
- [50] Wakjira TG, Ebead U. A shear design model for RC beams strengthened with fabric reinforced cementitious matrix. *Eng Struct.* 2019;200(August):109698. <https://doi.org/10.1016/j.engstruct.2019.109698>
- [51] Hamzenezhadi A, Sharbatdar MK. Flexural strengthening of deficient reinforced concrete beams with post-tensioned carbon composites using finite element modelling. *J Rehabil Civ Eng.* 2020;8(4):28–46.
- [52] Azam R, Soudki K, West JS, Noël M. Shear strengthening of RC deep beams with cement-based composites. *Eng Struct.* 2018;172(March 2017):929–37.
- [53] Rafiq MI, Baiee A. Textile reinforced mortar based flexural strengthening of reinforced concrete beams. *Proc Int Struct Eng Constr.* 2020;7(1):1–6.
- [54] Ameer TB. Flexural Strength and Durability of Reinforced Concrete Beams Strengthened with High Performance Textile Reinforced Mortar. 2018.
- [55] Baiee A, Rafiq M, Lampropoulos A. Innovative technique of textile reinforced mortar (TRM) for flexural strengthening of reinforced concrete (RC) beams. *2nd Int Conf Struct Saf Under Fire Blast Load.* 2017;
- [56] Mandor A, El Refai A. Flexural response of reinforced concrete continuous beams strengthened with fiber-reinforced cementitious matrix (FRCM). *Eng Struct.* 2022;251(September 2021).
- [57] Mandor A, El Refai A. Strengthening the hogging and sagging regions in continuous beams with fiber-reinforced cementitious matrix (FRCM): Experimental and analytical investigations. *Constr Build Mater.* 2022;321(August 2021):126341. <https://doi.org/10.1016/j.conbuildmat.2022.126341>
- [58] Yin SP, Sheng J, Wang XX, Li SG. Experimental Investigations of the Bending Fatigue Performance of TRC-Strengthened RC Beams in Conventional and Aggressive Chlorate Environments. *J Compos Constr.* 2016;20(2):04015051. [https://doi.org/10.1061/\(ASCE\)CC.1943-5614.0000617](https://doi.org/10.1061/(ASCE)CC.1943-5614.0000617)
- [59] Mercedes L, Bernat-Maso E, Martínez B. Bending behaviour of sandwich panels of vegetal fabric reinforced cementitious matrix: Experimental test and numerical simulation. *Constr Build Mater.* 2022;340(November 2021):1–12.
- [60] Kalyani G, Pannirselvam N. Experimental and numerical investigations on RC beams flexurally strengthened utilizing hybrid FRP sheets. *Results Eng.* 2023;19(March).
- [61] Ombres L. Flexural analysis of reinforced concrete beams strengthened with a cement based high strength composite material. *Compos Struct.* 2011;94(1):143–55. <http://dx.doi.org/10.1016/j.compstruct.2011.07.008>
- [62] Ortlepp R, Ortlepp S. Textile reinforced concrete for strengthening of RC columns: A contribution to resource conservation through the preservation of structures. *Constr Build Mater.* 2017;132:150–60.

- [63] Mercimek Ö, Ghoroubi R, Özdemir A, Anil Ö, Erbaş Y. Investigation of strengthened low slenderness RC column by using textile reinforced mortar strip under axial load. *Eng Struct.* 2022;259(April 2021).
- [64] Ombres L, Verre S. Structural behaviour of fabric reinforced cementitious matrix (FRCM) strengthened concrete columns under eccentric loading. *Compos Part B Eng.* 2015;75:235–49. <http://dx.doi.org/10.1016/j.compositesb.2015.01.042>
- [65] Park SH, Dinh NH, Um JW, Choi KK. Experimental study on the seismic performance of RC columns retrofitted by lap-spliced textile-reinforced mortar jackets after high-temperature exposure. *Compos Struct.* 2021;256(April 2020).
- [66] Ran J, Li T, Wang H, Zhu Q, Zhang H, Du Y, et al. Behavior and design of circular concrete columns strengthened with textile-reinforced mortar subjected to eccentric compression. *Structures.* 2023;51(March):242–57. <https://doi.org/10.1016/j.istruc.2023.03.065>
- [67] Alhoubi Y, El Refai A, Abed F, El-Maaddawy T, Tello N. Strengthening pre-damaged RC square columns with fabric-reinforced cementitious matrix (FRCM): Experimental investigation. *Compos Struct.* 2022;294(May):115784. <https://doi.org/10.1016/j.compstruct.2022.115784>
- [68] Zhang Q, Wei ZY, Gu XL, Yang QC, Li SY, Zhao YS. Confinement behavior and stress-strain response of square concrete columns strengthened with carbon textile reinforced concrete (CTRC) composites. *Eng Struct.* 2022;266(January):114592. <https://doi.org/10.1016/j.engstruct.2022.114592>
- [69] Le K, Quyen M, Nguyen X huy, Banihashemi S. Experimental and numerical investigation for confined concrete elements with fabric reinforced cementitious matrix (FRCM). *Constr Build Mater.* 2023;382:131280.
- [70] Mercedes L, Castellazzi G, Bernat-Maso E, Gil L. Matrix and fabric contribution on the tensile behaviour of fabric reinforced cementitious matrix composites. *Constr Build Mater.* 2023; 363 (July 2022): 129693. <https://doi.org/10.1016/j.conbuildmat.2022.129693>
- [71] Tello N, Alhoubi Y, Abed F, El Refai A, El-Maaddawy T. Circular and square columns strengthened with FRCM under concentric load. *Compos Struct.* 2021;255(September 2020):113000. <https://doi.org/10.1016/j.compstruct.2020.113000>
- [72] Faleschini F, Zanini MA, Hofer L, Pellegrino C. Experimental behavior of reinforced concrete columns confined with carbon-FRCM composites. *Constr Build Mater.* 2020;243:118296. <https://doi.org/10.1016/j.conbuildmat.2020.118296>
- [73] Napoli A, Realfonzo R. Compressive strength of concrete confined with fabric reinforced cementitious matrix (FRCM): Analytical models. *Compos Part C Open Access.* 2020;2(August):100032. <https://doi.org/10.1016/j.jcomc.2020.100032>
- [74] Toska K, Faleschini F, Zanini MA, Hofer L, Pellegrino C. Repair of severely damaged RC columns through FRCM composites. *Constr Build Mater.* 2021;273:121739. <https://doi.org/10.1016/j.conbuildmat.2020.121739>
- [75] Al-Gemeel AN, Zhuge Y. Using textile reinforced engineered cementitious composite for concrete columns confinement. *Compos Struct.* 2019;210(October 2018):695–706. <https://doi.org/10.1016/j.compstruct.2018.11.093>
- [76] Irlandegani MA, Zhang D, Shadabfar M. Probabilistic assessment of axial load-carrying capacity of FRCM-strengthened concrete columns using artificial neural network and Monte Carlo simulation. *Case Stud Constr Mater.* 2022;17(June):e01248. <https://doi.org/10.1016/j.cscm.2022.e01248>
- [77] Cao MQ, Le Nguyen K, Nguyen XH, Banihashemi S, Si-Larbi A. Enhancing slender reinforced concrete columns with G-FRCM jackets: Experimental and numerical analysis of confinement effects and cross-sectional shape impact. *J Build Eng.* 2023;79(September).

- [78] Chen X, Xiong Z, Zhuge Y, Liu Y, Cheng K, Fan W. Numerical analysis of compressive behavior of pre-damaged concrete columns strengthened with textile-reinforced ECC. *Case Stud Constr Mater*. 2023;18(June).
- [79] Di Ludovico M, Prota A, Manfredi G. Structural Upgrade Using Basalt Fibers for Concrete Confinement. *J Compos Constr*. 2010;14(5):541-52.
- [80] Gonzalez-Libreros J, Zanini MA, Faleschini F, Pellegrino C. Confinement of low-strength concrete with fiber reinforced cementitious matrix (FRCM) composites. *Compos Part B Eng*. 2019;177(August):107407. <https://doi.org/10.1016/j.compositesb.2019.107407>
- [81] Zeng L, Li LJ, Liu F. Experimental study on fibre-reinforced cementitious matrix confined concrete columns under axial compression. *Kem u Ind Chem Chem Eng*. 2017;66(3-4):165-72.
- [82] García D, Alonso P, San-José JT, Garmendia L, Perlot C. Confinement of medium strength concrete cylinders with basalt Textile Reinforced Mortar. 13th Int Congr Polym Concr [ICPIC 2010] .2010;0-7.
- [83] Colajanni P, Fossetti M, MacAluso G. Effects of confinement level, cross-section shape and corner radius on the cyclic behavior of CFRCM confined concrete columns. *Constr Build Mater*. 2014;55:379-89. <http://dx.doi.org/10.1016/j.conbuildmat.2014.01.035>
- [84] Ombres L. Concrete confinement with a cement based high strength composite material. *Compos Struct*. 2014;109(1):294-304. <http://dx.doi.org/10.1016/j.compstruct.2013.10.037>
- [85] Donnini J, Spagnuolo S, Corinaldesi V. A comparison between the use of FRP, FRCM and HPM for concrete confinement. *Compos Part B Eng* . 2019;160(December 2018):586-94. <https://doi.org/10.1016/j.compositesb.2018.12.111>
- [86] Koutas LN, Bournas.A D. Flexural Strengthening of Two-Way RC Slabs with Textile-Reinforced Mortar: Experimental Investigation and Design Equations. *J Compos cons*. 2016;21(204):1-34. [https://doi.org/10.1061/\(ASCE\)CC.1943-5614.0000713](https://doi.org/10.1061/(ASCE)CC.1943-5614.0000713)
- [87] Li B, Li Z, Chen Z, Yang Z, Zhang Y. Experimental Study on the Structural Performance of Reinforced Truss Concrete Composite Slabs during and after Fire. *Buildings*. 2023;13(7).
- [88] Kim H yeol, You Y jun, Ryu G sung, Koh K taek, Ahn G hong. Flexural Strengthening of Concrete Slab-Type Elements with Textile Reinforced Concrete. *Materials (Basel)*. 2020;13.
- [89] Yan H, Yu H, Kodur V, Yuan M, Zhou Y. Flexural behavior of concrete slabs strengthened with textile reinforced geopolymer mortar. *Compos Struct*. 2022;284:115220.
- [90] Kadhim MMA, Jawdhari A, Adheem AH, Fam A. Analysis and design of two-way slabs strengthened in flexure with FRCM. *Eng Struct*. 2022;256(October 2021).
- [91] Sabbaghian M, Kheyroddin A. Flexural strengthening of RC one way slabs with high-performance fiber-reinforced cementitious composite laminates using steel and GFRP bar. *Eng Struct*. 2020;221(December 2019).
- [92] Faleschini F, Gonzalez-libreros J, Zanini MA, Sneed L, Pellegrino C. Repair of severely-damaged RC exterior beam-Column joints with FRP and FRCM. *Compos Struct*. 2018;
- [93] Murad YZ. Retrofitting heat-damaged non-ductile RC beam-to-column joints subjected to cyclic and axial loading with FRCM composites. *J Build Eng*. 2022;48(December 2021).
- [94] Lim C, Jeong Y, Kwon M. Experimental Study of Rc Beam-Column Joint Retrofitted By CFRP Grid With High Strength Mortar. *Constr Build Mater*. 2022;9(2).



Research Article

## Impact of treatment temperature of metakaolin on strength and sulfate resistance of concrete

Mutiu Adelodun Akinpelu<sup>1,a</sup>, Ash-Shu'ara Marafa Salman<sup>1,b</sup>, Yusuf Ayoola Jimoh<sup>2,c</sup>, Ibrahim Tunde Yahaya<sup>1,d</sup>, Hakeem Mayowa Salami<sup>1,e</sup>

<sup>1</sup>Department of Civil Engineering, Kwara State University, Malete, Kwara State, Nigeria

<sup>2</sup>Department of Geology and Mineral Science, Kwara State University, Malete, Nigeria

### Article Info

### Abstract

#### Article history:

Received 12 Oct 2023

Accepted 05 Feb 2024

#### Keywords:

Metakaolin;  
Calcined clay;  
Calcination temperature;  
Characterization;  
Concrete

Calcined clay, a widely studied supplementary cementitious material, has shown positive impacts on concrete's microstructural properties, strength development, and durability. The variation in raw clay mineral concentration across different locations influences the optimal calcination temperature needed to activate its pozzolanic reactivity. This investigation focuses on studying the effects of calcination temperature on the characterization and pozzolanic reactivity of Nigerian Kaolinite clay. The clay was calcined at temperatures ranging from 600°C to 900°C for 2 hours. Characterization involved X-ray Diffraction (XRD), X-ray Fluorescence (XRF), and Scanning Electron Microscope (SEM) analyses. Blended mixtures, incorporating 10%, 20%, 30%, and 40% metakaolin as cement replacement, were assessed for workability, strength, and durability properties at 7, 14, 28, and 56 days to determine the clay's pozzolanic reactivity. XRF categorized the metakaolin as a class N pozzolan, while XRD indicated that 800°C for 2 hours was necessary for complete dihydroxylation. Compressive, tensile, and sulfate resistance tests confirmed that treating the clay at 800°C for 2 hours optimized its performance. The mix with 10% metakaolin outperformed the control by 6.4%, 14.7%, and 14.1% in compressive strength at 14th, 28th, and 56th days, respectively. While the best performance was at 10% replacement, levels up to 30% also demonstrated satisfactory results compared to the control, showing potential for achieving desired strengths. Linear regression models were also developed to establish the relationship between compressive and split tensile strengths across curing periods. The resulting equations demonstrate excellent predictive performance with correlation coefficients ranging from 0.928 to 0.991.

© 2024 MIM Research Group. All rights reserved

## 1. Introduction

All over the world, concrete is the most widely used construction material and its demand is expected to increase because of the rapid urbanization and infrastructural developments across the globe [1], [2]. Cement remains the most important composition in concrete as it is used as the binder but its production causes proliferation of CO<sub>2</sub> due to disintegration of limestone [3]. Cement accounts for up to 5% of the global anthropogenic CO<sub>2</sub> emission [4], [5]. CO<sub>2</sub> has been identified as one of the greenhouse gases and its reduction is required to reduce the impact of global warming. Besides, it requires large amount of heat energy (1450°C) to produce cement from its clinker [5]. Therefore, the main concern of the industry is to reduce the carbon footprint, achieve cost efficient construction materials for a sustainable environment.

\*Corresponding author: [mutiu.akinpelu@kwasu.edu.ng](mailto:mutiu.akinpelu@kwasu.edu.ng)

<sup>a</sup>orcid.org/0000-0003-4681-9874; <sup>b</sup>orcid.org/0000-0001-8067-183X; <sup>c</sup>orcid.org/0000-0002-7013-996X;

<sup>d</sup>orcid.org/0000-0002-0878-2516, <sup>e</sup>orcid.org/0000-0002-0626-8855

DOI: <http://dx.doi.org/10.17515/resm2024.06ma1012rs>

Res. Eng. Struct. Mat. Vol. 10 Iss. 3 (2024) 1261-1279



Partial replacement of cement with supplementary cementitious materials (SCMs) from industrial by-products is another means of reducing consumption of ordinary Portland cement. Some of these SCMs are fly ash, silica fume, coffee silver skin, ground granulated blast furnace slag and agricultural wastes such as rice husk ash (RHA), and palm oil fuel ash. Utilization of SCMs enhanced strength and durability of concrete materials and this also serves as an indirect method of reducing CO<sub>2</sub> emissions into the atmosphere [6]. The limited availability of most of the aforementioned SCMs in Nigeria due to the low level of industrialization hinders their application in concrete production in the country.

Materials such as calcined clays are also pozzolanic and requires lower energy input compared to cement [7]. Its availability in commercial quantities in most parts of the world also makes it preferred to other industrial by-product pozzolan. Internationally, many studies have investigated the use of calcined clay in concrete in the form of kaolinite, smectite, muscovite, illite and montmorillonite as a partial replacement for cement. They are reported to impact positively on the microstructure development, workability and strength properties, resistance to carbonation and chloride penetration, as well as reduced heat of hydration [6], [8], [9]. The kaolinite content of the calcined clay is the most important factor influencing the mechanical performance of calcined clay of the blended cement [8].

Kaolinite is one of the clay minerals that is found in claystone. Other clay minerals include illite, smectite, chlorite, vermiculite and montmorillonite. Kaolinite is a sheet silicate mineral formed by the alteration (chemical weathering) of rocks rich in feldspar through the process of hydrolysis [10]. A claystone with high percentage of kaolinite as the clay mineral is commonly termed kaolinite clay [11]. Kaolinite clay is found in large quantities in various parts of the country including Adamawa, Borno, Abia, Delta, Ekiti, Kaduna, Katsina, Kogi, Ogun, Ondo, Oyo, Plateau and Kwara State. The estimated kaolin mineral deposit reserve in the country is about 2 billion metric tons [12].

Metakaolin (MK) is a product of calcination (thermal treatment) of Kaolinite clay at a temperature range of 600 to 900°C [5], [13]. It is the amorphous aluminosilicate (Al<sub>2</sub>O<sub>3</sub>.2SiO<sub>2</sub>) obtained when water is expelled from kaolinite clay (Al<sub>2</sub>Si<sub>2</sub>O<sub>5</sub>(OH)<sub>2</sub>) at high temperature [7], [14]. The process is known as dihydroxylation. The dihydroxylation process significantly influences the pozzolanic reactivity of the MK [7]. Various investigations have shown that the calcination temperature, heating duration and rate, cooling rate, and ambient conditions affect the composition and the reactivity of the resulting MK [13]. Studies such as those by Boakye et al. and others [15] have highlighted that the calcination temperature significantly impacts the pozzolanic activity index (PAI) of metakaolin. Calcination temperatures greater than 900°C often lead to increased crystallinity and reduced amorphous content, affecting the reactivity of metakaolin when blended with cementitious systems. Furthermore, investigations by Khaled et al. [16] emphasized that different calcination temperatures yield metakaolin with varying particle sizes and surface areas, influencing the pozzolanic reactivity and the microstructure of the resulting concrete. Research by Abiodun et al. [17] also indicated that metakaolin obtained at temperatures from 500°C to 800°C for 1hr duration exhibited enhanced mechanical properties in concrete, attributed to its amorphous phase content. In another study, Moodi et al. [14] investigated the effect of degree and duration of heating on the pozzolanic properties and reactivity of metakaolin obtained from Iranian kaolinite clay. The outcome of their study revealed that thermal treatment of 750°C to 850°C for 1hr was sufficient for the activation of the kaolin. It is worthy to emphasize that the concentration of the clay minerals as well as other impurities in a particular clay source varies for different locations as it depends on the parent rock and the degree of weathering. Therefore, the ideal temperature for calcination necessary to stimulate the pozzolanic reactivity within a specific clay source differs, contingent upon the mineralogical composition of the clay [13].

## 2. Research Significance

Despite the growing interest in supplementary cementitious materials (SCMs) for sustainable concrete production, a comprehensive exploration of the influence of treatment temperature on the performance of locally available kaolinite, especially in the context of Nigeria's construction industry, is not well addressed.

Nigeria, characterized by its rich reservoirs of kaolinite, presents a unique opportunity to investigate the practical viability of utilizing indigenous resources in concrete production. Despite this, the lack of comprehensive studies assessing the metamorphic effects of different calcination temperatures on Nigerian kaolinite and the subsequent performance of derived metakaolin in concrete production represents a gap in the current research landscape.

Addressing this gap is pivotal for several reasons. Firstly, it allows for a more profound understanding of the influence of indigenous metakaolin on concrete properties, encompassing its impact on workability, mechanical strength, durability, and resistance to environmental factors. Secondly, such investigation holds promise for developing tailored concrete mixtures that align with the specific climatic and environmental conditions prevalent in Nigeria, ensuring sustainable construction practices that resonate with the local context. Furthermore, a detailed exploration of locally sourced metakaolin offers a strategic pathway toward reducing dependency on imported SCMs, fostering economic sustainability within the construction sector. By providing empirical evidence on the feasibility and efficacy of utilizing Nigerian kaolinite-derived metakaolin, this research strives to offer pragmatic insights that could revolutionize concrete production practices in regions constrained by limited access to conventional SCMs.

Therefore, an in-depth investigation into the influence of treatment temperatures on Nigerian kaolinite, and subsequently, the performance of derived metakaolin in concrete formulations, stands as an indispensable step toward unlocking the full potential of indigenous materials in sustainable construction.

## 3. Materials and Methods

### 3.1 Materials

*Cement:* Portland limestone cement of grade 42.5 (Dangote 42.5R brand) obtained from a local supplier in Ilorin, Kwara state, Nigeria with its oxides composition and physical properties as presented in Table 1.

*Aggregates:* Naturally occurring river sand passing through BS sieve with aperture 2.36 mm was used as fine aggregates while coarse aggregates were angular-shaped granite chippings with maximum size of 12.5 mm. The granite chippings was purchased from a local vender while the sharp sand was sourced from Oyun River in Ilorin, Kwara State, Nigeria.

*Kaolin:* The kaolinite clay deposit was sourced from Lakiri village (Ogun State, Nigeria) located at latitude 7°19'25" N and longitude 3°28'44" E. The clay was first dried under natural atmospheric condition for some days and then grinded into powder and then sieved before being calcined at different temperature to produce metakaolin. Since there is no universally agreed optimal calcination temperature for metakaolin, the grinded clay samples were converted to metakaolin by applying heat treatment: Calcination at 600, 700, 800 and 900° C for 2 hrs. The resulting metakaolin samples passing through sieve BS 212-micron were characterized using X-Ray Fluorescence (XRF) spectrometer, X-ray Diffraction (XRD) and Scanning Electron Microscope (SEM) analysis. This is necessary to

determine the compounds, bond characteristics and morphology of the metakaolin, respectively.

### 3.2 Experimental Design and Mix Proportioning

In other to assess the impact of calcination temperature on the pozzolanic performance of metakaolin, a total of eight mixes, containing metakaolin prepared at different temperatures (600-900°C for 2 hrs), were investigated in this research as given in Table 1. The control mix was designed following the guideline given in COREN Concrete Mix design manual [18]. The percentage metakaolin varied as 10, 20, 30 and 40% in partial replacement of Portland Limestone Cement (PLC). Several tests were conducted on the fresh and hardened samples, and these include, setting time, workability, compressive strength, tensile strength, and sulfate resistance.

Table 1. Concrete Mix Design (kg/m<sup>3</sup>)

S/N	Mix Code	Percent	CEM I	MK	F. A	C.A	SP (liter/100kg of cement)	w/c
1	0MK000	0	470	0	595	1100	--	0.5
2	10MK600	10	423	47	595	1100	--	0.5
3	10MK700	10	423	47	595	1100	--	0.5
4	10MK800	10	423	47	595	1100	--	0.5
5	10MK900	10	423	47	595	1100	--	0.5
6	20MK800	20	376	94	595	1100	--	0.5
7	30MK800	30	329	141	595	1100	1.5	0.5
8	40MK800	40	282	188	595	1100	1.5	0.5

### 3.3 Test Methods

#### 3.3.1 Characterization Tests

The elemental composition in oxide form, phase transition and morphological characteristics of the calcined clay samples were determined using XRF, XRD and SEM analyses. The chemical compositions of the representative samples of the calcined clay were obtained using thermo Scientific ARL QUANT'X EDXRF Spectrometer at Umaru Musa Yar'adua University, Katsina. The output of XRF along with the provision of ASTM C618-17a [19], was used to determine either particles of Metakaolin are pozzolanic or not. X-Ray diffraction (XRD) measurements were carried out on randomly selected powdered samples of calcined clay using an Empyrean diffractometer with a copper anode material at the laboratory of the Nigeria Geological Survey Agency in Zaria, Kaduna state, Nigeria. The goniometer which forms the central part of the Empyrean diffraction system has a radius of 240 mm. The sample was analyzed using a 2-theta angle range of 5-80 deg C with a step of 0.026261 at 30 seconds per step. The morphology of the calcined clay samples was analyzed by SEM using a JOEL-JSM 7600F analyzer at the Rolab research and diagnostic laboratory, Ibadan, Nigeria.

#### 3.3.2 Fresh Property Tests

The normal consistency test was measured on a vicat apparatus in line with ASTM C187-98 [20]. The initial and final setting times of the blended cement paste samples were also measured according to ASTM C403/C403M-16 [21]. The workability properties of the

concrete mixes adopted in the study as reported in Table 1 were also determined through slump test as per BS 12350-2 [22].

### 3.3.3 Hardened Properties Tests

The compressive strength of each of the concrete mix codes were tested on 100 mm cube specimens after 7, 14, 28 and 56 days using a compression testing machine with load rate of 0.9 kN/s capacity. The cube preparation and compressive strength testing followed the procedure given in BS EN 12390-3 [23]. The freshly prepared concrete samples were filled up in three layers and each layer received 25 equally distributed strokes in the moulds. The concrete samples were demolded after 24 hours of casting and cured in water for 7, 14, 28 and 56 days before crushing. The reported compressive strengths were the average of three tested specimens at various curing days.

The tensile strength was tested on a cylindrical specimen of 100 mm diameter by 200 mm height as per the provision of BS EN 12390-6 [24]. The cylindrical moulds were filled with freshly prepared concrete samples in three layers with each layer receiving 25 equally distributed strokes. The samples were demolded after 24hrs and cured for 7, 14, 28 and 56-days prior to determination of the split tensile strength. The reported tensile strengths also represent the average of three tested specimens at various curing days.

### 3.3.4 Sulfate Resistance

Some concrete structures, such as storage tanks and wastewater sewers for industrial effluents, are exposed to aggressive environments including sulfuric acid solution. Degradation of concrete material occurs as it is exposed to such severe condition. The sulfate ions in the sulfuric acid solution react with portlandite to produce gypsum. The produced gypsum reacts with calcium aluminate hydrate to produce ettringite. The by-product, ettringite causes expansion of the concrete which eventually affects its strength. In this study, the resistance of the concrete mix to sulfate attack was determined in term of strength loss when the sample was cured in 5mol/dm<sup>3</sup> of sulfuric acid solution for 7, 14, 28 and 56 days respectively.

## 4. Results and Discussion

### 4.1 Effect of Treatment Temperature on The Characterization of Metakaolin

#### 4.1.1 Effect of Treatment Temperature on Chemical Composition of Metakaolin

The effect of calcination temperature on the chemical composition of the calcined clay samples, as determined by X-ray Fluorescence (XRF) analysis, is presented in Table 2. Metakaolin (MK), an aluminosilicate material, undergoes dehydroxylation during calcination, resulting in an increased Si/Al ratio and Al/OH ratios in the samples compared to those present in the kaolinite group  $[\text{Si}_4]\text{Al}_4\text{O}_{10}(\text{OH})_8 \cdot 4\text{H}_2\text{O}$ . Additionally, the thermally treated clay, as depicted in Table 2, contains traces of ferric oxide ( $\text{Fe}_2\text{O}_3$ ) and magnesia ( $\text{MgO}$ ), suggesting the presence of illite and smectite, albeit in minimal quantities.

Table 3 shows oxide compositions in the MK such that the  $\text{SiO}_2 + \text{Al}_2\text{O}_3 + \text{Fe}_2\text{O}_3$  should not be < 70% while Sulfur trioxide ( $\text{SO}_3$ ) is limited to 4% maximum, such that it can be classified as a class N pozzolan according to ASTM C618 [19]. The moisture content (mc) percentage is also limited to 3%. The results in Table 3 show that all the calcined clay samples meet the requirements for the oxides compositions of class N pozzolan. Based on these criteria, only MK700, MK800 and MK900 samples satisfied the requirements of class N pozzolan according to ASTM C618 [19] specification.

Table 2. Oxides composition and physical properties of the materials

	CEM I*	MK600	MK700	MK800	MK900	FA	CA
Al <sub>2</sub> O <sub>3</sub>	5.35	41.26	41.14	45.00	46.23		
SiO <sub>2</sub>	20.62	35.41	35.86	37.14	38.32		
Fe <sub>2</sub> O <sub>3</sub>	3.07	0.56	0.57	0.55	0.57		
CaO	61.79	0.03	0.03	0.02	0.02		
MgO	1.93	3.00	3.01	3.35	4.12		
K <sub>2</sub> O		0.12	0.13	0.1	0.1		
TiO <sub>2</sub>	0.12	1.62	1.64	1.74	1.78		
MnO	0.06	0.01	0.01	0.01	0.01		
SO <sub>3</sub>		0.13	0.09	0.11	0.08		
P <sub>2</sub> O <sub>5</sub>		0.16	0.13	0.15	0.14		
Specific gravity	2.83	2.29	2.14	2.11	2.04	2.44	2.03
Water absorption (%)	-	-	-	-	-	2.92%	0.40%
Fineness Modulus	-	-	-	-	-	2.2	2.65
Moisture Content %	-	6.5	2.36	2.56	1.42		
Fineness (%)	0.79%	-	-	-	-	-	

Salman et al. [1]\*

Table 3. Comparison of oxides to composition

Sample	SiO <sub>2</sub> +Al <sub>2</sub> O <sub>3</sub> + Fe <sub>2</sub> O <sub>3</sub> (%)	SO <sub>3</sub> (%)	MC (%)
MK600	77.23	0.13	6.5
MK700	77.57	0.09	2.56
MK800	82.69	0.11	2.36
MK900	85.12	0.08	1.42
ASTM C618	≥ 70	≤ 4	≤ 3

#### 4.1.2 Effect of Heat Treatment on Phases of Metakaolin

The calcination temperature (600°C, 700°C, 800°C, and 900°C) influences the phase transition of the calcined clay samples, as can be seen in Fig. 1. At 600°C calcination temperature, noticeable peaks include that of Kaolinite (K) and Quartz (Q). Calcining kaolinite before or at temperature of 600°C, the kaolin clay present in clay has not undergone complete transformation. Quartz is a crystal mineral of silica oxides abundantly available in the earth’s surface. At 700°C, the noticeable peaks include that of Kaolinite (K) and Anatase (A). Incomplete transformation of kaolin clay could only be the reason where kaolinite minerals could still be present in the calcined clay. The anatase is a crystalline mineral of titanium oxides and one of the major impurities found in kaolin clay [1]. Majority of the kaolinite and other materials present in the clay calcined at 600°C and 700°C calcination temperatures had been transformed to amorphous materials at the 800°C as indicated by the presence of fewer anatase peaks and presence of humps at points between when 2theta is 20° and 30°. At 900°C, the only noticeable peaks here are that of

anatase which are known for its titanium oxides origin. Several peaks of Kaolinite (K), Anatase (S) and Quartz (Q) shown in clay calcined at 600 and 700°C show that calcined clay at 600 and 700°C are majorly in crystal forms. Little broad humps noticed at 600 and 700°C may demonstrate presence of fewer amorphous materials. Presence of broad humps at between when 2theta is at between 20° and 30° in the diffractograms at calcination temperature of 800 and 900°C indicated the amorphousness of the materials. Peaks represented anatase shown presence of crystal materials at both phases. As shown in Fig. 1, clay calcined at 800°C has fewer anatase peaks in comparison to calcined clay at 900°C. The broad areas in calcined clay at 800°C is slightly bigger compared to that of 900°C, all of these indicated the degree of amorphousness in 800°C as compared to that 900°C. Presence of many anatase peaks in clay calcined at 900°C could be a sign indicating beginning of transformation from amorphous materials to crystal materials [25], [26].

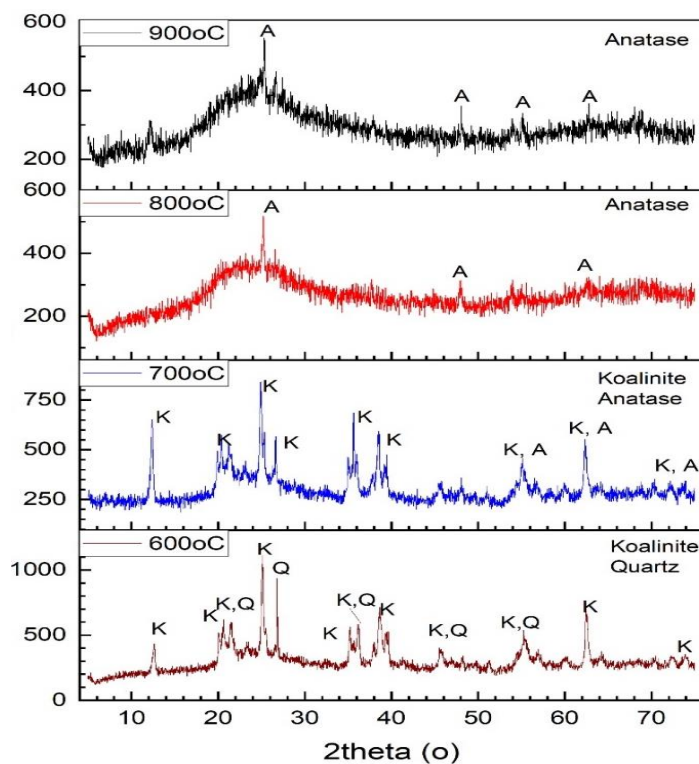


Fig. 1. XRD of the metakaolin at different calcination temperature

#### 4.1.3 Effect of Heat Treatment on the Microstructural Properties of Metakaolin

Kaolinite consists of alternating plate of silica and alumina connected by a strong bond. The micrographs of the calcined clay samples are presented in Fig. 2. At calcination temperature of 600°C, the calcined clay materials that are produced are closely packed together with some forms of voids indicating presence of microspores. They are arranged in regular pattern and their shape are majorly spherical. Also noticeable in calcined clay formed at 600°C are particles of different sizes indicating incomplete calcination of kaolin particles. At 700°C, the calcined clay formed are of different shapes; while some are irregular cuboid, others are flaky, and long cylindrical shapes. There are also noticeable micropores in the SEM micrographs of calcined clay formed at 700°C. Calcined clay formed

at 800°C have regular shapes with regularly arranged and packed particles. The noticeable micropores are smaller as compared to micropores found in calcined clay produced at the calcination temperature of 600 and 700°C. The arrangement of calcined clay formed at 900°C shows that the particles are not arranged in regular pattern, sizes and shape seems to be different greatly. The particles appeared at point as if they are cob wires and are in layers. The presence of micropores all around calcined clay particles. This may be a sign of transformation to crystalline particles.

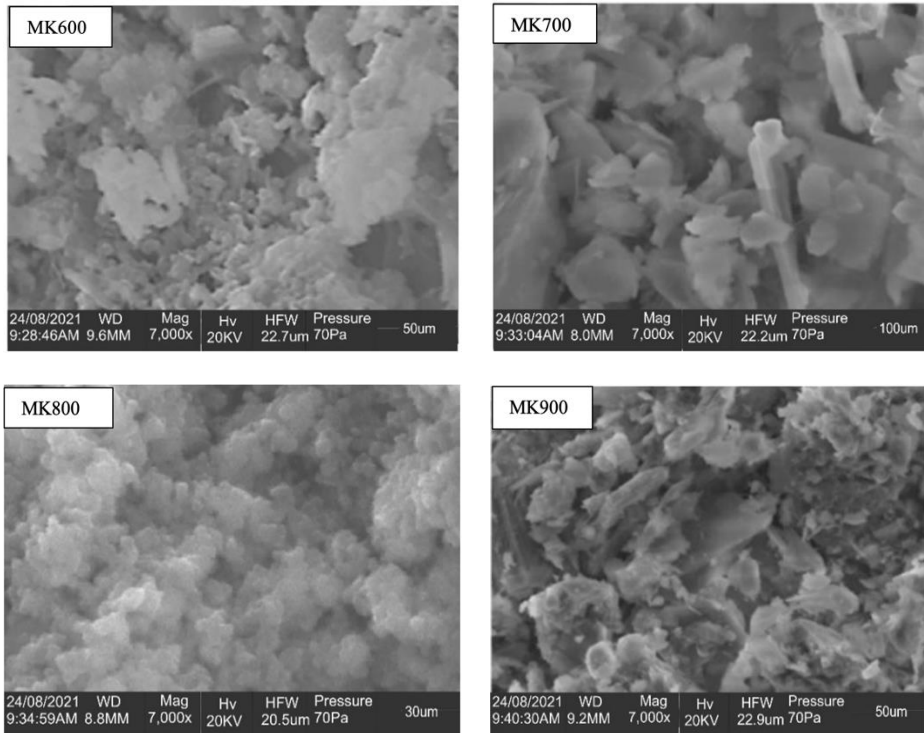


Fig. 2. SEM image of the metakaolin produced at different calcination

## 4.2 Effect of Metakaolin on Fresh Properties of Concrete

### 4.2.1 Initial and Final Setting Time

Table 4 presents the findings regarding the initial and final setting time of the cement paste blended with MK. The results revealed that replacement of cement with 10% metakaolin reduced both the final and initial setting time compared to the control group irrespective of the treatment temperature. Although, it was also observed that the setting time increased with increment in the treatment temperatures. This can be attributed to MK's ability to decrease the fluidity of cement, resulting in a reduction in free water content. As the setting time of cement primarily depends on the water-to-cement ratio, the addition of MK to the cement paste could effectively reduce the setting time. Similar observations have been reported by Khamchin et al. [27].

Contrarily, a study by Li et al. [28] reported that incorporating 5% to 20% metakaolin in cement increased both the final and initial setting time. It is important to mention that Li et al. (2022) used varying dosages of superplasticizer in their mix designs, which were

proportional to the quantities of MK. It is widely known that superplasticizers can influence the setting time of cement paste and concrete [29].

Moreover, as the percentage of MK replacement increased, the final and initial setting times of the cement paste also increased. This can be attributed to the fact that higher amounts of MK required more water to achieve the standard consistency of the cement paste. Consequently, the increased water-to-cement ratio delayed the rate of cement setting, resulting in a longer setting time. Thus, beyond a 20% replacement (specifically at 30% and 40%), the setting time of the cement paste exceeded that of the control, as indicated in Table 4.

Table 4. Initial and final setting time results

Setting time (mins)	CEM I	10MK600	10MK700	10Mk800	10MK900	20MK800	30MK800	40MK800
Initial	103	77	83	88	94	97	103	109
Final	349	309	316	323	332	348	351	358

#### 4.2.2 Workability of Concrete

The impact of metakaolin on the slump values of mixtures is illustrated in Fig. 3. The findings demonstrate that the workability of concrete mixtures is adversely affected by the inclusion of metakaolin. Fig. 3a reveals that as the treatment temperature of metakaolin increased from 600°C to 900°C, the slump values of the concrete mixtures decreased. The flow characteristics of concrete are significantly influenced by the morphological features of metakaolin, including its size, shape, and surface area. The SEM image of MK600 in Fig. 2 reveals particles that could hinder the flow of the concrete mixture, potentially impacting its flowability. Moreover, the presence of flaky and elongated cylindrical particles in the sample treated at 700°C (Fig. 2) might further restrict flow and adversely affect the concrete’s workability. The SEM micrographs also highlight the substantial surface area of well-arranged and densely packed MK800 particles, influencing water demand and the pace of pozzolanic reactions in the concrete mix. These increased surface areas offer more reactive sites for chemical interactions with calcium hydroxide, enhancing strength and durability. Nonetheless, it is important to note that excessively high surface areas can increase water demand and reduce workability due to heightened water absorption by the metakaolin particles.

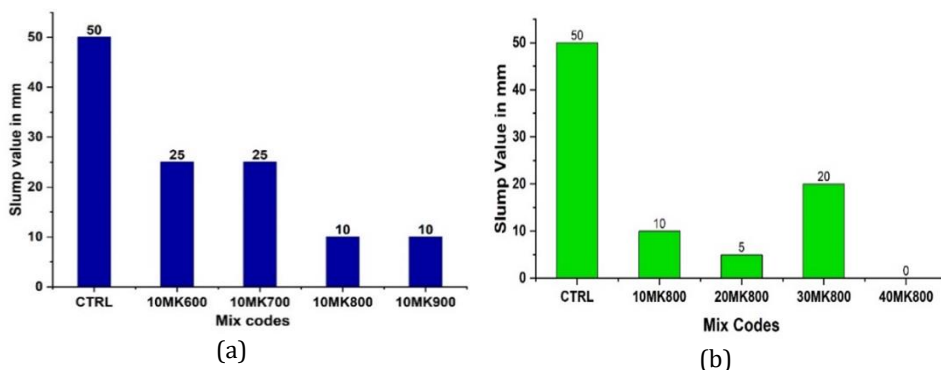


Fig. 3. Effect metakaolin on slump values

The effect of high-volume replacements is depicted in Fig. 3b. The results indicate that increasing the percentage replacement from 10% to 40% at 10% intervals significantly



decreases the slump flow and, consequently, the workability of the concrete. Among the mixes, the one containing 30% metakaolin treated at 800°C achieved a slump value of 20 mm, which is slightly higher than the other mixtures. It is important to note that this particular mix included superplasticizer, thus the improved workability can be attributed to the addition of superplasticizer. On the other hand, the mix incorporating 40% metakaolin as a cement replacement recorded zero slump. This further confirms that calcined clay has an adverse effect on concrete workability. Similar observations have been reported by Salau and Osemeke [30] and Salman et al. [1].

### 4.3 Effect of Metakaolin on the Strength Properties of Concrete

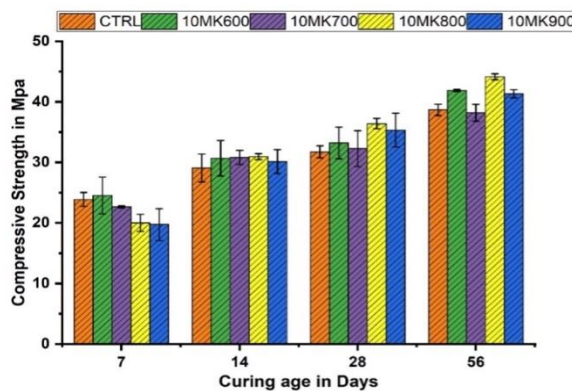
#### 4.3.1 Compressive Strength

The effect of partial replacement of cement with metakaolin (MK) obtained at different treatment temperatures on the compressive strength of concrete is depicted in Fig. 4. The results presented in Fig. 4a indicate that the inclusion of 10% MK by weight of cement reduced the 7-day strength of the concrete, except for samples containing MK obtained at 600°C, which exhibited a strength greater than that of the control by 2.7%. The reduction in early-age strength could be linked to several factors. As a pozzolanic material, its slower reaction compared to cement during early hydration stages delays strength development. Moreover, the particles of metakaolin fill spaces between cement grains, potentially altering the water-to-cementitious material ratio and causing a dilution effect that impacts early strength. Additionally, while metakaolin reacts with calcium hydroxide to form C-S-H gel, crucial for long-term strength, this process might not sufficiently compensate for reduced early strength due to its slower activation during the initial stages of concrete setting and curing. These combined effects contribute to the observed reduction in early strength when metakaolin is used as a replacement for cement.

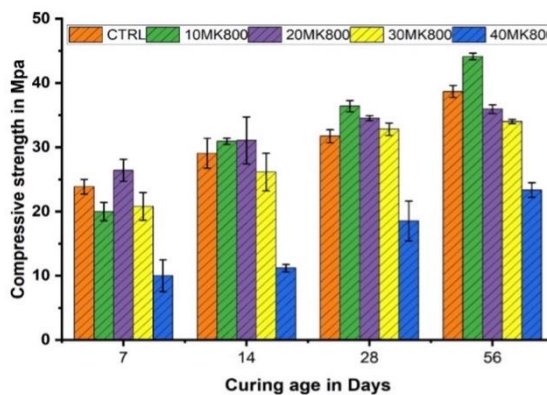
At the 14th day, all samples containing 10% MK exhibited compressive strength slightly exceeding that of the control, regardless of the calcination temperature. This suggests a faster rate of strength development in samples containing 10% MK between 7 and 14 days. The strength gain continued beyond the 28-day of curing, signifying the significant influence of the later-age pozzolanic effect of MK. The best performance in terms of 28-day and 56-day compressive strength was recorded in concrete samples containing 10% MK obtained at 800°C for 2 hours. The compressive strength of the mix (10MK800) was higher than that of the control by 14.72% and 14.12% at 28 days and 56 days, respectively. The observed increase in strength at 28 days and 56 days, resulting from the partial replacement of cement with metakaolin, could be attributed to several factors. The results of XRF presented in Table 3 and XRD depicted in Fig. 1 confirm the pozzolanic nature of metakaolin, hence its gradual reaction extending beyond the initial stages of concrete formation. This prolonged pozzolanic activity continually forms additional calcium silicate hydrate (C-S-H) gel, a key factor enhancing concrete strength over time. Furthermore, this pozzolanic activity enhances the formation of finer, more reactive particles, contributing to a denser and more homogeneous concrete microstructure, ultimately bolstering long-term strength. Additionally, the interaction between metakaolin and the cementitious matrix, notably in the presence of calcium hydroxide from cement hydration, generates a synergistic effect. This interaction further amplifies the formation of C-S-H gel, strengthening the concrete during the extended curing period. These intricate interactions, derived from metakaolin's pozzolanic properties and its significant influence on the concrete's microstructure and prolonged curing, collectively explain the observed increase in strength observed at 28 days and 56 days when metakaolin replaces cement in concrete formulations.

To examine the impact of higher volume replacement of cement with MK on concrete strength properties, samples containing 20%, 30%, and 40% of MK calcined at 800°C

(MK800) were tested at 7, 14, 28, and 56 days of curing, as reported in Fig. 4b. The mixes containing 10%, 30%, and 40% of MK800 exhibited lower strengths compared to the control at the 7-day curing period. Although the samples containing 20% MK800 showed strength higher than that of the control at 7 days, this result does not align with the other findings and is therefore considered an outlier. At the 14-day of curing, samples containing 10% and 20% MK800 exhibited compressive strength higher than the control by 6.4% and 6.9%, respectively, while mixes incorporating 30% and 40% MK800 exhibited lower strength than the control, with 40MK800 recording the lowest strength. At the 28-day of curing, only samples from the 40MK800 mix exhibited strength lower than the control by 41.6%, whereas the specimens from 10MK800, 20MK800, and 30MK800 mixes achieved strengths greater than the control by 14.71%, 8.82%, and 3.3%, respectively. At the 56-day mark, however, only the 10MK800 mixes showed an improvement in strength of 14.11% compared to the control. Consequently, it can be concluded that a 10% replacement of cement with MK demonstrated optimal performance in terms of 14-day, 28-day, and 56-day compressive strength. This aligns with the conclusions of Busari et al. [11] and Tawfiq et al. [31]. However, mixes containing up to 20% and 30% MK800 could still achieve 108.80% and 103.4% of the designed strength at 28 days and, 93% and 88% of the control strength at 56 days, respectively. Therefore, a replacement level of up to 30% may still be adopted to achieve the desired design strength but with adequate quality control checks.



(a)

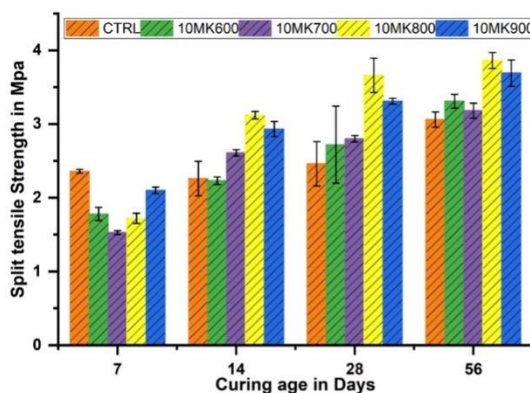


(b)

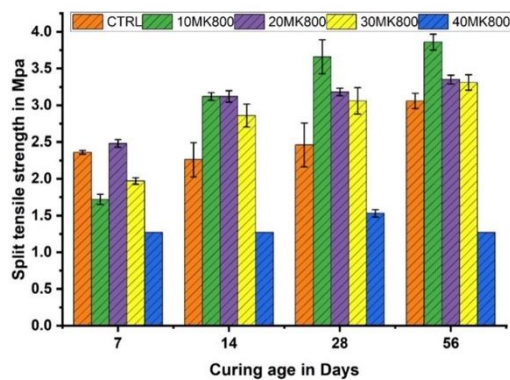
Fig. 4. Compressive strength of concrete containing metakaolin

### 4.3.2 Split Tensile Strength

Split tensile test is an indirect method of measuring tensile strength of concrete. The split tensile strength of the samples measured at 7, 14, 28 and 56-days is shown in Fig. 5. As expected, the result followed similar trend with that of compressive strength since the tensile strength is dependent on the compressive strength [32]. As shown in Fig. 5a, blending of cement with 10% MK negatively influenced the 7th day split tensile strength. The reduction in strength also increased with increase in calcination temperature. At 14th, 28th and 56th day, the tensile strengths of specimens incorporating 10% MK generally exceed that of the control irrespective of the calcination temperature with the calcined clay obtained at 800°C for 2hrs giving the best performance. The impact of higher volume replacements is indicated in Fig. 5b. Replacement of cement with 10%, 20% and 30% metakaolin led to increment in split tensile strength by 38.05%, 38.05% and 26.54% respectively at 14th day; 48.78%, 29.27%, and 24.34% respectively at 28th day; 26.14%, 9.45% and 8.17% respectively at 56-day. Just as in the case of compressive strength, the samples containing 20% MK800 showed strength higher than that of the control at 7 days, this result does not align with the other findings and is therefore considered an outlier. Although replacement of cement with 10% metakaolin gave the best performance as per split tensile strength for all the curing days, replacement level of up 30 % still outperformed the control after 56 days of curing.



(a)



(b)

Fig. 5. Split tensile strength of concrete containing metakaolin

### 4.4 Correlation Matrix

The correlation coefficient, a statistical indicator measuring the linear relationship between variables, was utilized in this study. Specifically, the relationship between the strength attributes of blended mixes integrating metakaolin treated at varied temperatures (ranging from 600 to 900°C for 2 hours) and control samples were evaluated. Tables 5A and 5B show results indicating strong positive correlations between the control samples and blended mixes. Notably, within the blended concrete mixtures, samples containing metakaolin calcined at 800°C exhibited the highest correlation values, reaching approximately 95% for compressive strength and 60% for split tensile strength, respectively. This is in line with Guilford’s rule of thumb with the following statistical ranges  $r < 20\%$ ,  $20\% < r < 40\%$ ,  $40\% < r < 70\%$ ,  $70\% < r < 90\%$ , and  $r > 90\%$ , corresponding to an almost negligible correlation, low correlation, moderate correlation, high correlation, and very high correlation, respectively [33], [34].

Table 5a. Correlations matrix for compressive strength

		CTRL	10MK600	10MK700	10MK800	10MK900
CTRL	r	1				
	p-value					
10MK600	r	0.853**	1			
	p-value	0.000				
10MK700	r	0.907**	0.896**	1		
	p-value	0.000	0.000			
10MK800	r	<b>0.949**</b>	0.855**	0.887**	1	
	p-value	<b>0.000</b>	0.000	0.000		
100MK900	r	0.904**	0.779**	0.873**	0.891**	1
	p-value	0.000	0.003	0.000	0.000	

\*\* . Correlation is significant at the 0.05 level.

Table 5b. Correlations matrix for tensile strength

		CTRL	10MK600	10MK700	10MK800	10MK900
CTRL	r	1				
	p-value					
10MK600	r	0.504	1			
	p-value	0.094				
10MK700	r	0.525	0.813**	1		
	p-value	0.080	0.001			
10MK800	r	<b>0.593</b>	0.759**	0.978**	1	
	p-value	<b>0.006</b>	0.004	0.000		
10MK900	r	0.562	0.865**	0.969**	0.954**	1
	p-value	0.057	0.000	0.000	0.000	

\*\* . Correlation is significant at the 0.05 level (2-tailed)

Thus, further investigation was conducted using the linear regression model (LRM) to establish the correlation between the compressive strength of concrete samples—incorporating varied percentages (0, 10, 20, 30, and 40%) of metakaolin obtained at an optimum temperature of 800°C—and their corresponding split tensile strength for each of the curing periods: 7 days, 14 days, 28 days, and 56 days. This follows that using this set of equations, either of the two parameters can be predicted if the other parameter is available. Four different linear equations were modeled; one per curing period. There were fifteen (15) samples per curing period, and these were divided into two parts. Part A consists of ten (10) data while Part B consists of the remaining five (5) data. Parts A and B

were used for model development and model validation respectively. The results of the model development and validation are shown in Tables 6-8.

As shown in Table 2, the R<sup>2</sup> values at the different curing periods range from 53% to 77%. This R<sup>2</sup> value shows how the independent variables were able to explain the dependent variables.

Table 6. Regression statistics

Parameter/Curing Periods	7days	14days	28days	56days
Multiple R	0.88	0.73	0.87	0.87
R <sup>2</sup>	0.77	0.53	0.75	0.76
Adj. R <sup>2</sup>	0.74	0.47	0.72	0.73
S.E. (n=10)	2.84	4.84	3.27	3.13

The p-values in all four cases, as seen in table 7, show that the independent variable (split tensile strength) is a good predictor of the dependent variable (compressive strength) as these values are less than 0.05 at a confidence interval of 95%. The null hypothesis is, therefore, rejected. Thus, the resulting linear simple regression equations are expressed in Equations 1-4.

Table 7. Linear regression model parameters

Variables	Coefficients	SE	P-value
$f_{cu4}$	$c_4$	13.52	4.64
	$f_{t4}$	7.18	1.41
$f_{cu3}$	$c_3$	9.85	4.65
	$f_{t3}$	7.67	1.56
$f_{cu2}$	$c_2$	7.16	6.82
	$f_{t2}$	7.42	2.47
$f_{cu1}$	$c_1$	-0.85	4.14
	$f_{t1}$	10.84	2.08

Model validation was done by using Equations 1-4 to predict the compressive strengths ( $f_{cu}$ ) at 7 days, 14 days, 28 days, and 56 days curing periods respectively using their corresponding split tensile strength ( $f_t$ ) values. The performances of these equations were evaluated by computing the Mean Errors (MEs) [33], [34], Correlation coefficient (r), Coefficient of Determination (r<sup>2</sup>) [35], and Nash Sutcliff Efficiency (NSE) [34] using Equations 5-8, respectively. The results are presented in Table 8.

$$f_{cu1} = -0.85 + 10.84f_{t1} \tag{1}$$

$$f_{cu2} = 7.16 + 7.42f_{t2} \tag{2}$$

$$f_{cu3} = 9.85 + 7.67f_{t3} \tag{3}$$

$$f_{cu4} = 13.52 + 7.18f_{t4} \tag{4}$$

$$ME = \frac{Exp. Value - Modeled Value}{Exp. Value} * 100 \tag{5}$$

$$r^2 = \left( \frac{\sum_{i=1}^n (\text{Exp. Value} - \overline{\text{Modeled Value}}) * (\text{Modeled Value} - \overline{\text{Modeled Value}})}{\sqrt{\sum_{i=1}^n (\text{Exp. Value} - \overline{\text{Exp. Value}})^2 * (\text{Modeled Value} - \overline{\text{Modeled Value}})^2}} \right)^2 \tag{6}$$

$$r = \left( \frac{\sum_{i=1}^n (\text{Exp. Value} - \overline{\text{Modeled Value}}) * (\text{Modeled Value} - \overline{\text{Modeled Value}})}{\sqrt{\sum_{i=1}^n (\text{Exp. Value} - \overline{\text{Exp. Value}})^2 * (\text{Modeled Value} - \overline{\text{Modeled Value}})^2}} \right) \tag{7}$$

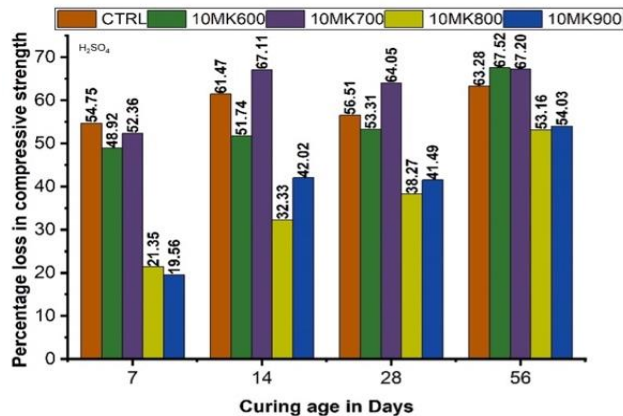
$$NSE = 1 - \left( \frac{[\sum_{i=1}^n (\text{Exp. Value} - \text{Modeled Value})^2]}{[\sum_{i=1}^n (\text{Exp. Value} - \overline{\text{Exp. Value}})^2]} \right) \tag{8}$$

Table 8. Model Performance Evaluation Results

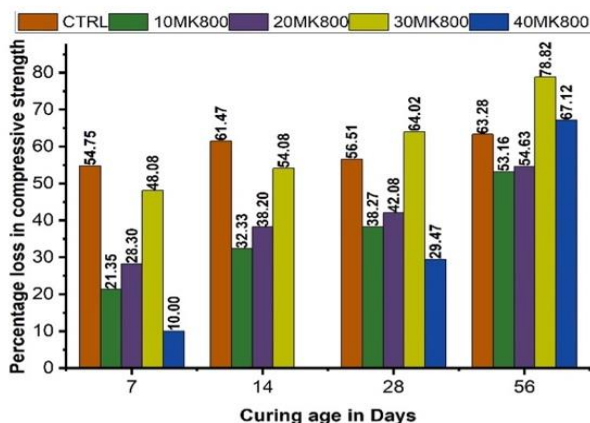
<i>f<sub>cu</sub></i>	Equations	A.M.E.	Corr. (r)	r <sup>2</sup>	N.S.E.	Remark
<i>f<sub>cu1</sub></i>	-0.85 + 10.84 <i>f<sub>t1</sub></i>	0.07	0.991	0.981	0.912	Excellent
<i>f<sub>cu2</sub></i>	7.16 + 7.42 <i>f<sub>t2</sub></i>	0.15	0.967	0.935	0.798	Excellent
<i>f<sub>cu3</sub></i>	9.85 + 7.67 <i>f<sub>t3</sub></i>	0.04	0.928	0.861	0.851	Excellent
<i>f<sub>cu4</sub></i>	13.52 + 7.18 <i>f<sub>t4</sub></i>	-0.03	0.961	0.923	0.903	Excellent

#### 4.5 Effect of Metakaolin on Resistance to Sulfuric Acid Attack

Fig. 6 shows the result of strength loss in the samples at various curing days. From Fig. 6a, it is clear that 10MK800 and 10MK900 mixes exhibited better resistance to strength loss across all the curing ages when compared to the control although 10MK800 performs better at 14, 28 and 56-days. This agrees with the report of Khatib et al. [7]. The percentage loss in strength was also observed to increase with the curing days. Fig. 6b shows that increasing the MK800 beyond 20% reduces the effectiveness of the concrete mix against acid attack after 56-days of curing. This further validates the previously presented XRD result, which showed that best pozzolanic property is obtained when the kaolinite clay is exposed to heat treatment for 2 hours. Other studies including the work of [3, 5, 36] have also reported that inclusion of MK in concrete mix alters the acid resistance property. Masood et al. [37] linked the improved durability performance to reduction in the portlandite produced in the blended mix since it contains lower quantity of cement.



(a)



(b)

Fig. 6. Percentage strength loss in concrete containing MK when cured in  $H_2SO_4$ 

It was also opined that MK particles could react with free portlandite in pozzolanic reaction to produce more C-S-H. Furthermore, Metakaolin's pozzolanic reaction leads to a denser concrete microstructure by filling voids and refining the pore structure. This densification reduces the pathways for sulfuric acid penetration, thereby minimizing the concrete's susceptibility to acid attack.

## 5. Conclusions

From the results of the experimental analysis on the impact of calcination temperature on pozzolanic reactivity of metakaolin conducted in this research, the followings are concluded:

- Blending of cement with 10 to 20 % of metakaolin reduced both the initial and final setting time of cement paste when compared to the control. Beyond 20% replacement, however, the setting time of the cement paste was higher than that of the control.
- The inclusion of metakaolin in the concrete mix negatively impacted its workability, regardless of the treatment temperature. This decline in workability could be attributed to the fine particle size and large surface area of the metakaolin particles leading to an increased water demand.
- This decline in workability could be attributed to the improved pozzolanic reaction within the concrete mix, resulting from the large surface area of metakaolin particles and subsequently leading to an increased water demand.
- The partial replacement of cement with metakaolin negatively impacted the 7th-day strength of concrete due to a delayed pozzolanic reaction of metakaolin, as a result of the dilution effect of metakaolin on cement.
- The mix incorporating 10% metakaolin as replacement for cement outperformed the control mix by 6.4%, 14.7% and 14.11% as per 14th, 28th and 56th day compressive strength respectively. However, mixes containing 20% and 30% metakaolin are still favorable, achieving 108.80% and 103.4% of the control strength at 28days, and 93% and 88% of the control strength at 56days respectively. Metakaolin reacts with calcium hydroxide formed in cement hydration, producing extra cementitious compounds such as calcium silicate hydrate (C-S-H) gel, which later enhances the overall strength of the concrete.

- Also, the optimum performance as per 14, 28 and 56 days split tensile strength was recorded in samples incorporating 10 % metakaolin thermal treated at 800 °C for 2 hrs. The tensile strength was improved by 38.0 %, 48.7 % and 26.1 % at 14th, 28th and 56th day respectively. However, it is worthy to note that mix containing 20% and 30% are still desirable as per tensile strength since they achieve strength higher than the control at after 14, 28 and 56 days of curing.
- With regards to resistance to acid attack, blending of cement with up to 20% metakaolin obtained at 800° C for 2 hrs showed better resistance to acid attack across all the curing ages when compared to the control and other mixes. This is due to the fact that metakaolin's pozzolanic reaction leads to a denser concrete microstructure by filling voids thereby reduces the pathways for sulfuric acid penetration.
- The correlation analysis also indicated strong positive associations between the compressive and tensile strength properties of concrete incorporating metakaolin. Specifically, the mix containing metakaolin treated at 800°C demonstrated the highest correlation, reaching 95% for compressive strength and 60% for split tensile strength.
- Based on these results, the optimum calcination temperature for the clay source considered in this study is 800°C for 2 hrs. The optimum performance in term of compressive strength, tensile strength and durability properties was recorded at 10% replacement, although replacement level of up to 30% could still be utilized to achieve the desired strength.

### Acknowledgement

The authors acknowledge that this study is supported by the Federal Government of Nigeria through the TETFUND Institution-Based Research (IBR) allocation: KWASUIBR/CSP/090320/VOL7/TETF2019/0092.

### References

- [1] Salman AM, Akinpelu MA, Yahaya IT, Salami HM. Workability and strengths of ternary cementitious concrete incorporating calcined clay and limestone powder. In: *Materials Today: Proceedings*. Elsevier Ltd; 2023. <https://doi.org/10.1016/j.matpr.2023.02.249>
- [2] Kumar P, Pasla D, Saravanan TJ. Self-compacting lightweight aggregate concrete and its properties : A review. *Constr Build Mater.* 2023;375:1-40. <https://doi.org/10.1016/j.conbuildmat.2023.130861>
- [3] Trümer A, Ludwig H, Schellhorn M, Diedel R. Effect of a calcined Westerwald bentonite as supplementary cementitious material on the long-term performance of concrete. *Appl Clay Sci.* 2019;168:36-42. D <https://doi.org/10.1016/j.clay.2018.10.015>
- [4] Ismail AH, Kusbiantoro A, Chin SC, Muthusamy K, Islam M, Tee KF. Pozzolanic reactivity and strength activity index of mortar containing palm oil clinker pretreated with hydrochloric acid. *J Clean Prod.* 2020;242:1-10. <https://doi.org/10.1016/j.jclepro.2019.118565>
- [5] Shi Z, Ferreiro S, Lothenbach B, Geiker MR, Kunther W. Sulfate resistance of calcined clay - Limestone - Portland cements. *Cem Concr Res.* 2019;116:238-251. <https://doi.org/10.1016/j.cemconres.2018.11.003>
- [6] Laidani ZE, Benabed B, Abousnina R, Gueddouda MK, Kadri E. Experimental investigation on effects of calcined bentonite on fresh , strength and durability properties of sustainable self-compacting concrete. *Constr Build Mater.* 2020;230:117062. <https://doi.org/10.1016/j.conbuildmat.2019.117062>



- [7] Khatib JM, Baalbaki O, Elkordi AA. Metakaolin. In: Waste and Supplementary Cementitious Materials in Concrete. Elsevier Ltd; 2018:493-511. <https://doi.org/10.1016/B978-0-08-102156-9.00015-8>
- [8] Dhandapani Y, Sakthivel T, Santhanam M, Gettu R, Pillai RG. Mechanical properties and durability performance of concretes with Limestone Calcined Clay Cement ( LC 3 ). Cem Concr Res. 2018;107(July 2017):136-151. <https://doi.org/10.1016/j.cemconres.2018.02.005>
- [9] Sabir BB, Wild S, Bai J. Metakaolin and calcined clays as pozzolans for concrete : a review. 2001;23. [https://doi.org/10.1016/S0958-9465\(00\)00092-5](https://doi.org/10.1016/S0958-9465(00)00092-5)
- [10] Haruna A, Kasham VA. X-Ray Florescence Analysis ( XRF ) of Kaolin in the South Eastern Nigeria. J Basic Appl Res. 2016;2(2):160-165.
- [11] Busari A, Dahunsi B, Akinmusuru J. Sustainable concrete for rigid pavement construction using de-hydroxylated Kaolinitic clay : Mechanical and microstructural properties. Constr Build Mater. 2019;211:408-415. <https://doi.org/10.1016/j.conbuildmat.2019.03.170>
- [12] Teme SC. Geotechnical characteristics of some clays from south-western Nigeria : implications for industrial utilization. Eng Geol. 1991;30:305-324. [https://doi.org/10.1016/0013-7952\(91\)90065-S](https://doi.org/10.1016/0013-7952(91)90065-S)
- [13] Bernal SA, Juenger MCG, Ke X, et al. Characterization of supplementary cementitious materials by thermal analysis. Mater Struct. 2017;50(1):1-13. <https://doi.org/10.1617/s11527-016-0909-2>
- [14] Moodi F, Ramezani-pour AA, Safavizadeh AS. Evaluation of the optimal process of thermal activation of kaolins. Sci Iran. 2011;18(4):906-912. <https://doi.org/10.1016/j.scient.2011.07.011>
- [15] Boakye K, Khorami M, Ganjian E, Saidani M. A review of the Effect of Calcination Temperature on the Properties of Calcined Clay Concrete A review of the Effect of Calcination Temperature on the Properties of Calcined Clay Concrete. Int J Eng Tech Inf. 2021;2(3):72-74. <https://doi.org/10.51626/ijeti.2021.02.00016>
- [16] Khaled Z, Mohsen A, Soltan A, Kohail M. Optimization of kaolin into Metakaolin : Calcination Conditions , mix design and curing temperature to develop alkali activated binder. Ain Shams Eng J. 2023;14(6):1-14. <https://doi.org/10.1016/j.asej.2023.102142>
- [17] Abiodun YO, Orisaleye JI, Adeosun SO. Effect of Calcination Temperatures of Kaolin on Compressive and Flexural Strengths of Metakaolin- Concrete. Niger J Technol Dev. 2023;20(1):33-43. <https://doi.org/10.4314/njtd.v20i1.1390>
- [18] Council for the Regulation of Engineering in Nigeria (COREN). Concrete Mix Design Manual, SPECIAL PUBLICATION NO. COREN/2017/016/RC. 1st ed.; 2017.
- [19] ASTM C618-17a. Standard Specification for Coal Fly Ash and Raw or Calcined Natural Pozzolan for Use in Concrete.; 2017.
- [20] 20. ASTM C187-98. Standard Test Method for Normal Consistency of Hydraulic Cement. ASTM Int 100 Barr Harb Drive, PO Box C700, West Conshohocken, PA 19428-2959 United States. Published online 2017.
- [21] ASTM C403/C403M-16. Standard Test Method for Time of Setting of Concrete Mixtures by Penetration Resistance. ASTM Int 100 Barr Harb Drive, PO Box C700, West Conshohocken, PA 19428-2959 United States. Published online 2016. doi:10.1520/C0403\_C0403M-16 [https://doi.org/10.1520/C0403\\_C0403M-16](https://doi.org/10.1520/C0403_C0403M-16)
- [22] BS EN 12350-2. Testing Fresh Concrete : Slump Test.; 2010.
- [23] BS EN 12390-3. Testing Hardened Concrete : Compressive Strength of Test.; 2019.
- [24] BS EN 12390-6. Testing Hardened Concrete : Split Tensile Strength.; 2010.
- [25] Kouamo HT, Elimbi A, Mbey JA, Sabouang CJN, Njopwouo D. The effect of adding alumina-oxide to metakaolin and volcanic ash on geopolymer products : A comparative study. Constr Build Mater. 2012;35:960-969. <https://doi.org/10.1016/j.conbuildmat.2012.04.023>

- [26] Wang Y, Shui Z, Sun T, Huang Y, Wang G. Effect of Fly Ash, Sinking Beads and Metakaolin on the Workability, Strength, Free Shrinkage and Chloride Resistance of Concretes: A Comparative Study. Arab J Sci Eng. 2018;43(10):5243-5254. <https://doi.org/10.1007/s13369-018-3068-7>
- [27] Khamchin F, Rasiah S, Sirivivatnanon V. Properties of Metakaolin Concrete - A Review. 2015;(October).
- [28] Li W, Hua L, Shi Y, et al. Influence of metakaolin on the hydration and microstructure evolution of cement paste during the early stage. Appl Clay Sci. 2022;229:1-11. <https://doi.org/10.1016/j.clay.2022.106674>
- [29] Yan R, Yin S, Zhang H, Wang L, Chen D. Effect of superplasticizer on the setting behaviors and mechanical properties of tailings-waste rock cemented paste backfills. Case Stud Constr Mater. 2023;18(November 2022):1-13. <https://doi.org/10.1016/j.cscm.2022.e01714>
- [30] Salau MA, Osemeke OJ. Effects of Temperature on the Pozzolanic Characteristics of Metakaolin-Concrete. 2015;6(3):131-143. <https://doi.org/10.9734/PSIJ/2015/13146>
- [31] Tawfiq AT, Metwally AK, Zaki W, Faried AS. Hybrid effect of nanosilica and metakaolin on mechanical properties of cement mortar. Int J Eng Res Technol. 2019;8(3):211e215.
- [32] Akinpelu MA, Odeyemi SO, Olafusi OS, Muhammed FZ. Evaluation of splitting tensile and compressive strength relationship of self-compacting concrete. J King Saud Univ - Eng Sci. Published online 2017.
- [33] Solihu H, Olakunle S. Availability , coverage , and access to the potable water supply in Oyo State Nigeria. Environ Challenges. 2021;5(October):100335. <https://doi.org/10.1016/j.envc.2021.100335>
- [34] Adegoke HA, Solihu H, Bilewu SO. Analysis of sanitation and waterborne disease occurrence in Ondo State, Nigeria. Env Dev Sustain. 2023;25:11885-11903. <https://doi.org/10.1007/s10668-022-02558-2>
- [35] Solihu H, Kidanewold BB, Abdulkadir A. Flood risk and flow variability assessment at the railway drainage structures: A case of the Ethio-Djibouti Railway Line, Ethiopia. Ghana J Geogr. 2022;14(2):175-208.
- [36] Siddique R, Klaus J. Applied Clay Science Influence of metakaolin on the properties of mortar and concrete: A review. Appl Clay Sci. 2009;43(3-4):392-400. <https://doi.org/10.1016/j.clay.2008.11.007>
- [37] Masood B, Elahi A, Barbhuiya S, Ali B. Mechanical and durability performance of recycled aggregate concrete incorporating low calcium bentonite. Constr Build Mater. 2020;237:1-8. <https://doi.org/10.1016/j.conbuildmat.2019.117760>

Blank Page

## Wind-induced torsional loads and responses of tall buildings

Ashish Singh<sup>1,a</sup>, Denise-Penelope N. Kontoni<sup>\*2,3,b</sup>, Sasankasekhar Mandal<sup>1,c</sup>

<sup>1</sup>Dept. of Civil Eng., Indian Institute of Technology (BHU), Varanasi, India

<sup>2</sup>Dept. of Civil Eng., School of Engineering, University of the Peloponnese, GR-26334 Patras, Greece

<sup>3</sup>School of Science and Technology, Hellenic Open University, GR-26335 Patras, Greece

### Article Info

#### Article history:

Received 11 Oct 2023

Accepted 04 Mar 2024

#### Keywords:

Tall building;

Wind load;

Wind-induced torsional load;

Wind tunnel

experiments

### Abstract

High-rise structures are prone to wind-induced forces. Wind load can be resolved into three parts: along-wind load, across-wind load, and torsional wind load. There are well-developed and reliable methods for calculating wind-induced loads in the along-wind direction for tall buildings. Numerous methods are also available to estimate the across-wind load, but this is not the case for the torsional behavior of tall buildings using wind tunnel experiments and full-scale investigations. This paper attempts to compile the current understanding of the wind-induced torsional response of tall buildings. The present study contributes to realizing the effects of wind-induced torsional loads on tall buildings and gives an in-depth understanding through a comparison of past studies.

© 2024 MIM Research Group. All rights reserved.

## 1. Introduction

Wind forces that fluctuate can cause significant dynamic motion in high-rise buildings. Tall buildings are bound to oscillate in three ways, *viz.*, two translational (along-wind and across-wind directions) and one rotational (torsional mode). The wind-induced loads and their components are represented in Fig. 1. Estimation approaches for along-wind loads are well stabilized and dependable for the purpose of the design of tall structures. Numerous methods are also available to evaluate across-wind loads. However, the estimation procedure is still not standardized for the torsional load caused by wind. The torsional loads are predominantly dynamic in nature. Torsional motions are particularly problematic since, unlike the other components of wind loads, they offer occupants an additional motion due to an apparent rotating horizon. Inhabitants of tall buildings are more likely to get disturbed due to torsional motion than due to translational motion [1]. Tamura *et al.* [2] conducted vibration perception tests to assess the habitability of buildings to vibration and pointed out that individuals can detect vibrations lower than their own "perception threshold" through visual or auditory cues. Kwok *et al.* [3] emphasized the importance of education in habitability. According to Kwok *et al.* [4], prolonged exposure to large-amplitude vibrations can cause dizziness, migraines, and nausea in tall building occupants. Wind-induced torsional vibration can increase displacement and acceleration at the edges of tall buildings. In addition to elevating the wind-induced loads on the primary wind-resistant structure, torsion can also trigger the swaying of outer walls. This, in turn, can impact the integrity of the curtain wall system and lead to increased wind-induced movements [5]. In buildings having longer torsional

\*Corresponding author: [kontoni@uop.gr](mailto:kontoni@uop.gr)

<sup>a</sup>orcid.org/0000-0001-7907-6179; <sup>b</sup>orcid.org/0000-0003-4844-1094; <sup>c</sup>orcid.org/0000-0002-5495-3793

DOI: <http://dx.doi.org/10.17515/resm2024.08st1011rv>

Res. Eng. Struct. Mat. Vol. 10 Iss. 3 (2024) 1281-1300

periods of vibration due to the existence of high eccentricities among the centers of rigidity, the center of mass, and aerodynamic forces, the wind-induced torque tends to be accentuated. The key reason for the development of torsional response is the non-coincidence of the mass center and elastic center of tall buildings.

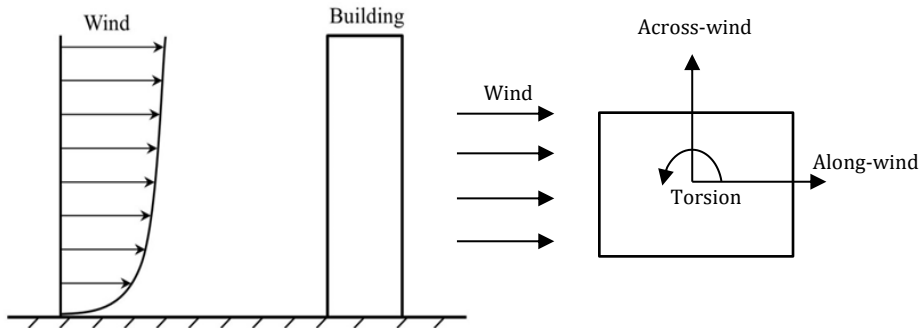


Fig. 1. Direction of wind loading and its components

A tall building can be subjected to wind-induced torsional load in three ways: (i) Due to its structural and architectural characteristics (non-symmetric cross-section, non-symmetrical mass and stiffness distribution), assuming wind load on a building is uniformly distributed across its faces, (ii) Due to the flow characteristics of the wind (uneven pressure distribution across the face, flow approaching at an oblique angle to the face) regardless of plan and shape of the building, and (iii) Due to Dynamic responses resulting into torsion of building. A schematic diagram (Fig. 2) illustrates the causes of wind-induced torsional loads. The most prominent source of wind-generated torsional moments about the vertical axis of the building is the uneven wind pressure distribution on the surrounding surfaces of the building. Torsional motions are particularly problematic since, unlike sway, they subject the occupants to a motion due to an apparent rotating horizon.

The cross-sectional shapes of a building predominantly influence the torsional loading. Cheung *et al.* [6] and Beneke & Kwok [7] concluded that the triangular-shaped model yielded a substantially stronger dynamic torsional response than any other shape. Bandi *et al.* [8] tested five modified triangular shapes in a boundary layer wind tunnel under urban flow conditions. They concluded that the helical models had a greater effect on aerodynamic characteristics. According to Boggs *et al.* [9], among the quadrilateral shapes, the parallelogram experiences unusually high torsion. The increase in torsion is of the order of 33% compared to rectangular shapes. The contribution of higher modes to the response of a wind-excited high-rise building other than the fundamental mode is trivial [10].

The vibration of the primary mode in each direction generally dominates a high-rise building's response to winds. It is crucial to evaluate the response at the top of the structure, particularly the corners, because the corners of a building encounter significant torsional response, *i.e.*, excessive strains and human discomfort. According to Kim and Kanda [11], adjusting the sectional shape by varying its cross-section with height could alter the flow pattern around the models, consequently decreasing wind-induced excitation. Notably, buildings having varying cross-sections with height (tapered and set-back) experienced a more significant torsional moment in urban terrain than in open terrain. Kareem [12] ascertained that the torsional response of symmetric building adds significantly to the overall dynamic response. Also, the combined lateral and torsional

kinematics further enhances the building response. Fig. 3 represents the normalized reduced modal spectra of torsional, across-wind, and along-wind forces in an urban environment for a square-section building developed by Kareem [13] in order to estimate the dynamic response of symmetrical and unsymmetrical buildings exposed to wind loads. As shown in Fig. 3, there is a sudden peak in torsional normalized reduced modal spectra at a reduced frequency of 0.10 which emphasizes the importance of torsional wind loading. A high-frequency base balance was used in a wind tunnel by Kijewski and Kareem [14] to compare the different international codes and standards. Moreover, they included cross-wind and torsional responses in their comparison. Liang *et al.* [15] found that torsional vibration contributes significantly to the dynamic response of buildings whose torsional stiffness was close to the lateral stiffness. According to Kim *et al.* [16], tapered and setback buildings (square cross-section), that had offsets in the windward diagonal direction, exhibited an increased torsional response, even if the total RMS accelerations were small.

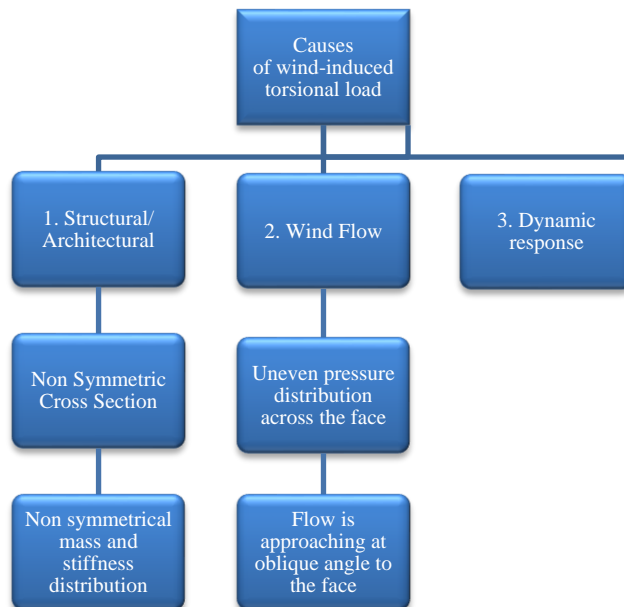


Fig. 2. Causes of wind-induced torsion in tall buildings

Because of the errors associated with modeling, the results of aeroelastic model studies for a structure with a specific geometry and dynamic qualities are difficult to apply to other buildings with identical geometries but distinct dynamic properties [17,18]. Hui *et al.* [19] stated that the mean and fluctuating torsion coefficients were significantly (1.5 times) higher in square buildings (than in rectangular buildings). Several studies of the wind response of tall buildings have been discussed by Hou and Jafari [20]. They also discussed various methodologies to measure the wind-induced response. The design for torsion resistance can be complex and depends on the structural frame's torsional properties. Wind load combinations including torsion were proposed by Stathopoulos *et al.* [21] for rectangular medium-rise buildings. Hu *et al.* [22] studied a high-rise building's translational and torsional responses during Typhoon Khanun. Their findings provide crucial empirical data for improving torsional wind-resistant design in tall buildings.

This paper is an attempt to compile the existing understanding of torsional wind load and responses. Codal provisions concerning torsional wind loading are discussed in section 2. Section 3 deals with wind tunnel tests in which torsional wind load on tall buildings is

analyzed. In section 4, various available analytical formulations are reviewed and presented in tabular form. A comparison of the various formulations is also made. Section 5 looks into different available measures for the mitigation of torsional responses. Finally, conclusions from the present study are drawn.

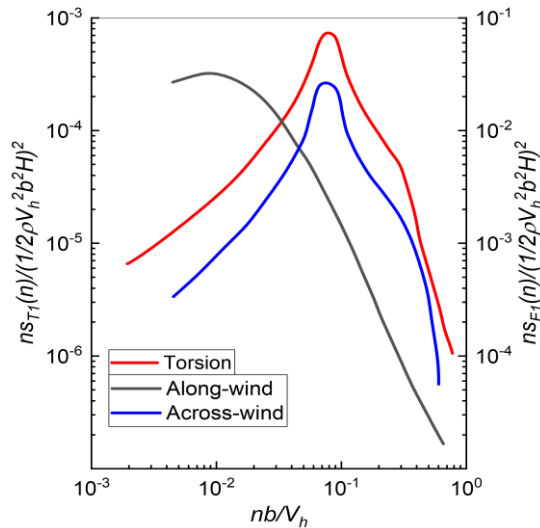


Fig. 3. Normalized reduced modal spectra of torsional, across-wind, and along-wind forces in urban environment for a square building [13]

## 2. Codal Guidelines on Torsional Wind Loading

Even though various wind tunnel tests have been performed for the estimation of torsional wind loads, very few international codes provide guidelines for incorporating torsional wind loading. A summary of the guidelines for torsional wind loading in some of the existing international wind loading codes is included in this section.

### 2.1. Japanese Code Guidelines

AIJ 1993 [23] first proposed the torsional wind load provision for tall buildings in the world building codes/standards. The same torsional wind load formula is kept in AIJ 2004 [24]. In addition, ISO 4354 [25] adopted the same formula following [23]. AIJ 2004 [24] dictated the calculation procedure to evaluate the torsional wind load in the design of slender and flexible buildings with  $H/\sqrt{BD}$  to be greater than three and  $U_H/f_1\sqrt{BD}$  greater than five.

### 2.2. Indian Code Guidelines

IS 875 (Part 3): 2015 [26] suggests that for tall buildings having unsymmetrical geometry the designs must incorporate torsional effects due to wind pressure. IS 16700:2017 [27] advised that if wind tunnel studies reveal torsional motions, the building's structural system should be modified to minimize these effects, The torsional velocity should be below 0.003 rad/s over the 10-year return period.

### 2.3. American Code Guidelines

ASCE 7-22 [28] introduces two load scenarios, namely maximum torsion with associated shear and maximum shear with corresponding torsion. According to ASCE 7-22 guidelines, for low-rise buildings, the maximum torsion can be assessed by utilizing 75% of the highest wind loads, along with an equivalent eccentricity of 15% of the building's dimensions.

ASCE 7-22 exempted torsional wind load calculation requirement for buildings with flexible diaphragms. It also stipulated that a building with torsional eccentricity larger than 5% of its width should be avoided in case the buildings have rigid diaphragms. By doing so, the occurrence of large shear forces from torsion effects and the resulting torsional story drift will be prevented, avoiding damage to interior walls and cladding.

#### 2.4. Canadian Code Guidelines

The National Research Council of Canada [29] provides guidelines for the evaluation of the maximum torsion by taking 56% of the maximum wind load with an eccentricity of (15%) of building dimensions.

#### 2.5. European Code Guidelines

The European code [30] considers the maximum torsion as 0.70 of maximum wind load with an additional equivalent eccentricity of 7% of building dimensions.

#### 2.6. Chinese Code Guidelines

GB 50009-2012 [31] introduced provisions for cross-wind and torsional dynamic response into wind load code in 2012. GB 50009-2012 [31] provides the formulation to estimate equivalent wind load induced by torsional dynamic response for rectangular high-rise buildings with  $H/\sqrt{BD}$  not more than 6 and the  $D/B$  ratio ranging from 1.5 to 5.

#### 2.7. Codal Comparison Study

Elsharawy *et al.* [32] estimated wind-induced torsional load on three tall buildings located in suburban terrain with an aspect ratio of 1 to 3 using the provisions of three international codes. The three codes referred to are the American [33], Canadian [34], and European [30]. A comparison of wind-induced torsional load evaluated from the three codes revealed that there exists wide variability.

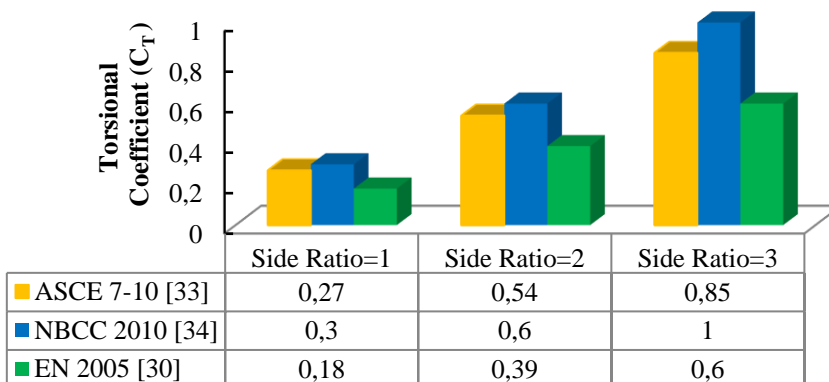


Fig. 4. Torsional coefficients for buildings ( $B=30$  m,  $H=60$ m,  $L/B=1, 2$  and  $3$ )

The evaluated equivalent eccentricity varied from 4.6% [34] to 17.8% [33] and the shear coefficient varied from 1.14 [33] to 1.8. Fig. 4 represents the torsional coefficients for three tall buildings having side ratios 1, 2, and 3. As the side ratio increases, the torsional coefficients also increase. Within the framework of the three standards, the Canadian standard [34] estimates the highest torsional coefficient of all the buildings, while the European standard [30] estimates the lowest torsional coefficient.



### 3. Wind Tunnel Studies

When assessing the wind load on tall buildings, wind tunnel tests have proven reliable and effective over the past few decades primarily because they can recreate the wind conditions in which tall buildings are immersed.

Initial work in determining the generalized torsional load is attempted by Tallin and Ellingwood [17] based on the wind tunnel data of Reinhold [35]. Applying a linear mode shape, their findings indicated that the RMS value of the real modal torque was 57% of the torque derived from a force balance, and 51% of the torque calculated using a cantilever mode shape. Zou *et al.* [36] carried out a series of wind tunnel tests to study the torsion-induced aeroelastic effect on tall buildings. Nine building models having varying ratios of sides and structural eccentricities are examined. A method has been proposed to calculate the aerodynamic stiffness against torsion and corresponding damping from extensive experimental data. In the absence of structural eccentricity, it is safe to neglect the torsional aerodynamic stiffness ratio. Their study concludes that it is advantageous to align the building face having the longer side normal to the dominant wind. It also observed that the wind-ward eccentricity enhances the torsional dynamic performance, in contrast to leeward eccentricity, which has the opposite effect.

Guzmán-Solís *et al.* [37] tested five rigid scale models in an atmospheric boundary layer wind tunnel to study wind-induced torsional loads on rectangular tall buildings. Each model had the same plan dimensions as the others, but different height aspect ratios. In the wind tunnel, two terrain categories were experimentally generated to evaluate each model under various wind directions. A new parametric equation was proposed based on experimental results to calculate torque coefficients at the base. Their equation includes both the aspect ratio and the wind direction as its variables. Zhang *et al.* [38] studied the stability of wind-excited eccentric tall buildings using an aero-elastic test rig designed for pure torsional vibration. Both the mean and dynamic torsional responses were experimentally studied to assess the predominant effect of the angle of wind incidence. They concluded that at a geometric eccentricity ratio of 10% tall buildings were most susceptible to torsional vibration. It also exhibited a significantly increased maximum mean response. Zhang *et al.* [39] investigated the impact of interference on torsional wind loads. They discovered that in the presence of nearby buildings, the torsional response of a structure can be amplified significantly, reaching up to 2.2 times the response of an isolated tall building model. This phenomenon occurs when the alternating vortex frequency aligns with the fundamental frequency of the building. Using a three-degree-of-freedom aeroelastic tall building model, Tang and Kwok [40] studied the interference mechanisms on both sway and torsional responses. Under an operating reduced wind velocity of 6, for an open terrain wind model, the experimental results concluded that both dynamic torsional and translational responses generally increased under interference effects due to the wakes of upstream buildings. Zou *et al.* [41] estimated wind loads on tall buildings through the study of torsional motion-induced vibrations. They concluded that wind loads in the torsional direction are correlated to the wind loads along and across wind directions. The study emphasized that torsional vibration augments the aerodynamic forces in all three directions, thus resulting in higher wind forces than that measured model. Furthermore, the study revealed that the impact of torsional vibration on aerodynamic forces is more significant at lower reduced wind speeds than at higher reduced wind speeds. Kim *et al.* [42] conducted wind tunnel tests on 13 super-tall building models with atypical building shapes under an urban area flow condition and concluded that the contribution of the torsional moment is almost negligible in super-tall buildings. Tamura *et al.* [43] conducted a study on six different polygon cross-section buildings and concluded that torsional moment coefficients decrease with the increasing number of sides, and the degree of decrease becomes small when the number of sides is larger than

5. Tanaka *et al.* [44] concluded that the torsional moment coefficient decreased for 4-side tapered and set-back building models whose projected area decreased with height.

Most of the wind tunnel studies in the context of torsional loading of tall buildings over the past few decades are summarized in Table 1.

Table 1. Summary of wind tunnel experiments for tall building torsional wind loads

Reference	Geometric Scale	Cross-section	Shape, Full-scale building height	Terrain ( $\alpha$ )	Turbulence Intensity at the top of the model (IH)	Measurements	Conclusion
Zhou et al. [45]	1:394	SQ, RC, TR, RM	ST, 200m	0.16, 0.35	-	RMS coefficient of across, along, and torsional wind loads.	Developed an interactive database to calculate the wind-induced response of tall building.
Liang et al. [46]	1:400	SQ, RC	ST, 320m	0.20	7%, 5.5%	Instantaneous fluctuating pressure.	Based on experimental results, proposed empirical formula for torque spectra, RMS torque coefficients, Strouhal number and coherence function of torque.
Thepmonkorn et al. [47]	1:300	RC	ST, 180m	0.15	10%	Perpendicular to the wind, parallel to the wind, and twisting response.	Interference effects from neighboring buildings on the wind response.
Li et al. [48]	1:500	RC	ST, 300m	0.22	12.8%	Instantaneous fluctuating pressure.	Empirical formulae of torque spectra, RMS torque coefficients, and vertical correlation functions.
Yoshie et al. [49]	1:500	RC	ST, 400m	0.14, (1/7)	-	Perpendicular to the wind, parallel to the wind, and twisting response.	Study the vibrational behaviors of different buildings under boundary layer wind.
Hou and Sarkar [50]	1:175	RC	ST, 182.9m	0.34 & tornado	17.7%	Acceleration in X, Y, and torsional direction (Axis is defined on the model).	Measure the wind-induced reactions of tall structures exposed to boundary layer winds versus tornadoes.
Zou et al. [36]	1:400	SQ, RC	ST, 360m	Urban terrain, (Cat C, China)	8%	Wind pressure and displacement response.	Investigate the effect of structural eccentricities on aeroelastic stiffness and damping ratios.
Guzmán-Solís et al. [37]	1:400	RC	ST, 200m	0.15, 0.29	10%, 15%	Shear force, bending moment, and torsion moment at the base of the model.	A new parametric equation is proposed to estimate torque coefficients.
Venanzi et al. [51]	1:500	RC	ST, 182.88 m	-, (open terrain)	-	Across wind base bending moment and Peak base torque.	AIJ provisions overestimate both peak torque and peak across-wind

						bending moments in some cases, resulting in a safe, but economically unfavorable design.
Zou et al. [41]	1:400	SQ, RC	ST, 360m	Open terrain (Cat C, China)	10%	Displacements of rims, wind pressure, and angular displacement
						Reduced wind speeds and torsional vibration amplitudes represent two significant parameters for aerodynamic forces.
<p>Note: <math>\alpha</math> is the exponent of the power-law, and corresponds to the terrain category; SQ: Square; RC: Rectangular; TR: Triangle; RM: Rhombus; ST: Straight; RD: Rounded Corners; RMS: Root Mean Square.</p>						

#### 4. Analytical and Empirical Formulations

Attempts towards an analytical evaluation of the torsional response date back to the 70s, when Patrickson & Friedmann [52] and Fouch & Safak [53] proposed simplified models of the torsional excitation mechanism that did not consider the contributions of the lateral turbulence and the vortex wake. Reinhold and Sparks [54] first conducted wind tunnel as well as full-scale experimental studies on torsional effects on a square section tall building having an H/B ratio of 8.33 and subjected to an urban wind environment. Kareem [10] criticized those procedures that ignore unsteady wake excitation and recommended the use of wind tunnel data for the first time. Isyumov and Poole [55] calculated the mean and dynamic torque components of the circumference of the building using weighted pneumatic averaging. They observed that pressure fluctuations on the back face due to vortex shedding significantly contribute to the dynamic torque and pressure fluctuations on the side face induced by vortex shedding were not significantly contributing to the overall torque. Katagiri *et al.* [56] introduced an analytical approach to assess the lateral-torsional response of tall structures caused by wind forces.

$$T_{max}[U(h)] = \psi\{\bar{T}[U(h)] + g_T T_{rms}[U(h)]\} \tag{1}$$

$$\bar{T}[U(h)] \approx 0.038\rho L^4 h n_T^2 U_r^2 \tag{2}$$

$$T_{rms}[U(h)] \approx 0.00167 \frac{1}{\sqrt{\zeta_T}} \rho L^4 h n_T^2 U_r^{2.68} \tag{3}$$

$$U_r = \frac{U(h)}{n_T L} \tag{4}$$

$$L = \frac{\int |r| ds}{A^{1/2}} \tag{5}$$

Greig [57] proposed an empirical model based on ten aero-elastic model tests, which predicts both the mean and the dynamic torsional response. Equation 1 shows the formula of peak base torque ( $T_{max}$ ). Expressions of linear base torque ( $\bar{T}$ ) and RMS base torque ( $T_{rms}$ ) are shown in Equations 2 and 3. In Equations 1 to 5,  $\psi$  is a reduction coefficient,  $\rho$  is the air density ( $\rho \approx 1.25 \text{ kg/m}^3$ ),  $h$  is the height of the building,  $g_T \approx 3.8$  is the torsional peak factor. In Equation 4,  $U_r$  is reduced velocity,  $U(h)$  is the wind speed at the tip of the building,  $n_T$  is the natural frequency and  $\zeta_T$  is the damping ratio in the fundamental torsional mode of vibration. In Equation 5,  $L$  is a shape parameter,  $ds$  is the elemental length of the building parameter, and  $|r|$  is the torque lever arm of the element  $ds$ .

Lythe and Slurry [58] used an experimentally derived database to establish an empirical estimation model for mean torsional loads. Also, they suggested that the large variety of torsion coefficients can be decreased by selecting appropriate normalizing factors and by

grouping coefficients as per the reasonable classification of the plan geometry of the building. Liang *et al.* [46] developed empirical formulae for torque spectra, RMS torque coefficients and coherence functions of torque for rectangular tall buildings. These formulae served as the basis for a frequency domain calculation method to estimate wind-induced torsional responses in such buildings. To analyze the torque spectra in rectangular tall buildings with different side ratios, Choi and Kanda [59] introduced a three-term empirical formula. Marukawa & Ohkuma [60] proposed an empirical formula for fluctuating across-wind and torsional forces for prismatic high-rise buildings.

Bazeos & Beskos [61] developed a numerical method to estimate torsional moments due to wind on isolated or a group of rigid buildings of varied cross-sections. While most of the research focused on isolated buildings only, Bazeos & Beskos [61] developed their method for a cluster of buildings as well. Their method uses the boundary elements to take care of the potential flow. Whereas it employs the discrete vortex method to take care of the viscous flow characteristics of the wind. To note, that method works iteratively in the time domain. That method has inherent difficulty in selecting flow separation points in case there is more than one building, especially when the building shapes are complicated.

Based on wind tunnel tests, Li *et al.* [62] proposed empirical formulas for estimating wind-induced torques on L-shaped tall buildings. It takes the side ratio of the building and the terrain category as key variables. Marukawa *et al.* [63] introduced an empirical formula for estimating across-wind and torsional acceleration in high-rise buildings with a rectangular cross-section.

#### 4.1 RMS Torque Coefficients ( $C_T$ )

Dynamic wind loads causing torsional motion in tall rectangular buildings can be determined by analyzing torque spectra, RMS torque coefficients, Strouhal number, and the coherence functions of torque. Various researchers have proposed a set of empirical relations for the RMS torque coefficient as shown in Table 2.

Table 2. Various Formulas for RMS Torque Coefficients

Author	RMS Torque Coefficients	RMS Torque Coefficient is dependent on (Variable)	Empirical formula suggested based on experimental investigations
Liang et al. [46]	$\check{C}_T = 0.054(D/B)^2 + 0.023$	Side ratio ( $\frac{D}{B}$ ) B= width of windward side, D= depth.	Torque Spectra, RMS torque coefficient, Strouhal Number, and Coherence functions of torque.
Li et al. [48]	$C'_{FT}(z) = a_1 + (a_2 - a_1)\left(\frac{z}{H}\right) + (a_3 - a_2)\left(\frac{z}{H}\right)^2$	Side ratio ( $\frac{D}{B}$ )	RMS force coefficients, power spectrum densities, and Vertical correlation functions of torsional wind loads.
Guzmán-Solís et al. [37]	$C_T = \frac{c_1 + c_2\left(\frac{H}{B}\right) + c_3\left(\frac{H}{B}\right)^2 + c_4\theta + c_5\theta^2 + c_6\theta^3}{1 + c_7\left(\frac{H}{B}\right) + c_8\theta}$	Wind direction ( $\theta$ ) & height aspect ratio ( $\frac{H}{B}$ )	Parametric equation for estimating torque coefficients at the base of rectangular buildings as a function of wind direction and aspect ratio.

Gui et al. [64]	$C'_T(z) = t'_1 + t'_2 \left(\frac{z}{H}\right) + t'_3 \left(\frac{z}{H}\right)^2$	Side ratio $\left(\frac{D}{B}\right)$	The Base root torque coefficient formula is given which is the function of the aspect ratio.
Marukawa & Ohkuma [60]	$C_T = f_{CT1} \left(\frac{D}{B}\right) + f_{CT2} \left(\frac{D}{B}\right) \cdot I_{UH}$	Side ratio $\left(\frac{D}{B}\right)$ and turbulence intensity (IUH).	RMS torque coefficient and overturning moment coefficient.

These empirical relations are dependent on structural parameters like side ratio, and height aspect ratio. Also, they are primarily dependent on wind field parameters such as turbulence intensity and angle of incidence.

#### 4.1.1 Variation of $C_T$ with the Side Ratio

Using the empirical relations given in Table 2 and AIJ 2004 [24], the present study plotted the RMS torque coefficients for various side ratios (D/B) from 0.5 to 2. It is observed from Fig. 5 that Liang *et al.* [46] proposed a formula that gives the maximum values of RMS torque coefficients and Li *et al.* [48] give the lowest values of RMS torque coefficients among the other empirical relations. The results from the proposed empirical relations of Marukawa and Ohkuma [60] & Gui *et al.* [64] are close to AIJ 2004 [24] and these three formulations yield values in between the extremes of Li *et al.* [48] and Liang *et al.* [46].

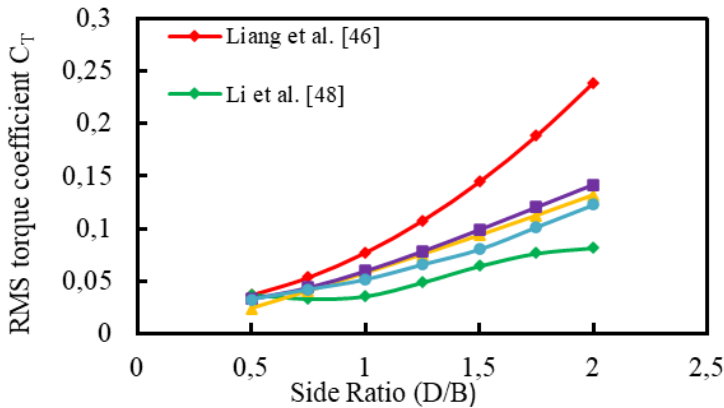


Fig. 5. Comparing the RMS torque coefficients of base torque using different formulations, considering side ratios ranging from 0.5 to 2

#### 4.1.2 Variation of $C_T$ Along the Height

Empirical relations for the variation of RMS torque coefficient along the height proposed by Li *et al.* [48] and Gui *et al.* [64] are compared in Fig. 6. It can be observed from Fig. 6 that  $C_T$  is increasing as the D/B ratio increases.  $C_T$  is maximum for D/B=2 indicating that oblong buildings having higher depth (dimension of the building along the flow direction) experience maximum torque. For a D/B ratio of one and greater than one, the Gui *et al.* [64] formulation provides higher  $C_T$  values than Li *et al.* [48]. However, for a D/B ratio of less than one, the formulation Li *et al.* [48] provides higher  $C_T$  values than Gui *et al.* [64]. The Height ratio in the Gui *et al.* [64] study varies from 4.61 to 5.05, whereas, in the study of Li *et al.* [48] height ratio varies from 3 to 4.61.

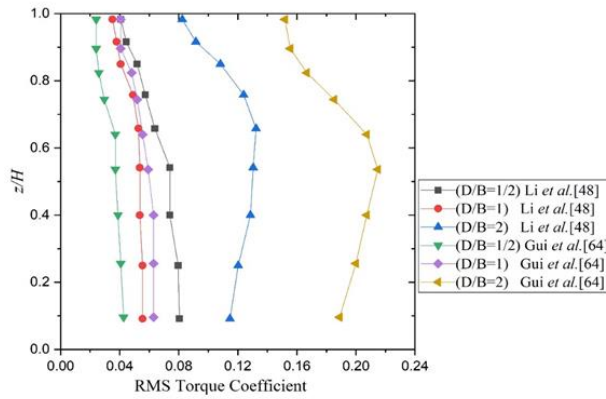


Fig. 6. Comparing the RMS torque coefficients of base torque using different formulations, considering height ratio

#### 4.1.3 Variation of $C_T$ with the Incident Wind Direction

The magnitude and direction of wind force are influenced by topographic features surrounding the building. The Mean and RMS base torsion coefficient are functions of incident wind direction. Guzmán-Solís *et al.* [37] proposed a new parametric equation based on extensive experimental wind tunnel data as shown in Table 2.

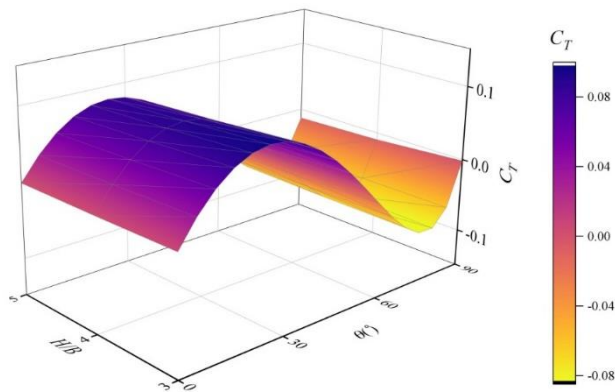


Fig. 7. The 3D plot depicts the variation of the mean torsion coefficient with respect to aspect ratio and wind direction, presenting outcomes derived from the proposed equation by Guzmán-Solís *et al.* [37]

The variation of  $C_T$  has been plotted in Fig. 7 with respect to wind direction as well as height aspect ratio. A similar trend is observed in Fig. 7 for all height aspect ratios. The maximum mean base torque coefficient of 0.1 occurs at  $25^\circ$ , whereas the minimum of -0.1 occurs at  $80^\circ$ . Bazeos and Beskos [61] reported variation of torsional moment coefficients with varying angles of wind incidence for an isolated square building. Beneke and Kwok [7] investigated the effect of incidence wind angle on mean and dynamic torque for rectangular, diamond, triangular, and D-shaped buildings models. The triangular model at  $\theta=100^\circ$  yields the largest dynamic response among all the models.

### 4.2 Power Spectra Density of Torque

The power spectra density of the torque is dependent on both the side ratio and slenderness ratio however Tang *et al.* [65] emphasized that the power spectra density of torque is more sensitive to the side ratio than the slenderness ratio.

Table 3. Various power spectra of the torque

Author	The Power spectra of torque	Range of Side Ratio (D/B) & Aspect Ratio ( $H/\sqrt{A}$ )
Choi and Kanda [59]	$\frac{f \cdot S_m(f)}{\sigma_M^2} = B_2 F_1(\psi_1) \left\{ \frac{f \cdot S_{ST}(f)}{\sigma_{ST}^2} + B_3 F_2(\psi_2) \frac{f \cdot S_{VS}(f)}{\sigma_{VS}^2} + B_4 \frac{f S_{FP}(f)}{\sigma_{FP}^2} \right\}$	$1/3 \leq D/B \leq 3,$ $4.0 \leq (H/\sqrt{A}) \leq 7.0$
	$\frac{nS(n)}{\sigma^2} = A \cdot \frac{1}{d\sqrt{\pi}} \exp \left[ - \left( \frac{\ln(\bar{n}) - 0.5d^2}{d} \right)^2 \right] + (1-A) \frac{C^{0.56} \left( \frac{\bar{n}}{k} \right)^{2.5}}{1.29 \left[ \left( 1 - \left( \frac{\bar{n}}{k} \right)^2 \right)^2 + C \cdot \left( \frac{\bar{n}}{k} \right)^2 \right]}$	$1 \leq D/B \leq 4,$ $4.0 \leq (H/\sqrt{A}) \leq 8.0$
Liang <i>et al.</i> [46]	$\frac{nS(n)}{\sigma^2} = A_1 \frac{C^{0.50} \left( \frac{\bar{n}}{k} \right)^3}{1.56 \left[ \left( 1 - \left( \frac{\bar{n}}{k} \right)^2 \right)^2 + C \cdot \left( \frac{\bar{n}}{k} \right)^2 \right]} + A_2 \cdot \frac{1}{d\sqrt{\pi}} \exp \left[ \left( \frac{\ln(\bar{n}) - 0.5d^2}{d} \right)^2 \right] + (1 - A_1 - A_2) \cdot \frac{\bar{n}^2}{8 \cdot \left( 1 + \left( \frac{\bar{n}}{k} \right)^2 \right)^2}$	$1/4 \leq D/B \leq 1,$ $4.0 \leq (H/\sqrt{A}) \leq 8.0$
Li <i>et al.</i> [48]	$\frac{fS(f)}{\sigma^2} = \frac{af}{(1+bf^c)^d} + \sum_{j=1}^N \frac{K_j (f/F_j)^2}{[1 - (f/F_j)^2]^2 + 4P_j^2 (f/F_j)^2}$	$1/2 \leq D/B \leq 2,$ $3.0 \leq (H/\sqrt{A}) \leq 5$
Gui <i>et al.</i> [64]	$\frac{f S_{M_T}(f)}{\sigma_{M_T}^2} = \sum_{i=1}^2 A_i \frac{S_{pi} \beta_i (f_r / f_{spi})^{\alpha_i}}{[1 - (f_r / f_{spi})^2]^2 + \beta_i (f_r / f_{spi})^2} + A_0 \frac{1}{1 + (\ln(f_r / f_{spi}))^2}$	$1/3 \leq D/B \leq 3,$ $4.0 \leq (H/\sqrt{A}) \leq 6.0$

Note:  $F_1$  is an overall shape control function;  $F_2$  has the role of considering negative chordwise correlation characteristics;  $S_{FP}(f)$  indicates the second spectral peak;  $S_{ST}$  and  $S_{VS}$  regular vortex shedding terms;  $B_1$  and  $B_2$  are contribution ratio;  $A, C, d,$  and  $k$  are coefficients depend on turbulence intensity ( $I_H$ ) and/or side ratio ( $D/B$ ) and/or aspect ratio ( $H/\sqrt{A}$ );  $\bar{n} = n/n_s, n_s = St \cdot \bar{U}(z)/B$  is the dominant frequency corresponding to the first peak;  $St$  is the Strouhal number and  $\bar{U}(z)$  is the mean wind speed;  $a, b, c, d, F_i, P_i, K_i, S_p, \beta, f_{sp}$  are parameters that depend on side ratio ( $D/B$ );  $\alpha_1=1, \alpha_2=2$

In Table 3, Choi and Kanda [59] provided an empirical formulation to describe the overall characteristics features of torque spectra for a square and rectangular tall building. They suggested that the results from the empirical relations should be compared with experimental data and emphasized the need for parameter sensitivity analysis.

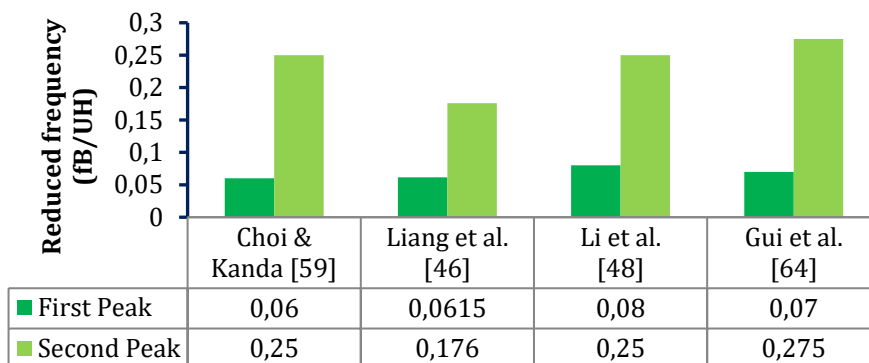


Fig. 8. Reduced frequencies at which first peak and second peaks are obtained

Various formulations have been provided by different researchers on Torque spectra. As it is observed from the plot of various torque spectra it is found that mostly there are two peaks in the curve at two different reduced frequencies. These frequencies are an important parameter for defining the wind environment characteristics. Liang *et al.* [46] stated that among the two peaks, the first is due to asymmetric pressure caused by vortex shedding on the two sides, and the second is due to the reattaching of separated flows. In Fig. 8, reduced frequencies relative to two peaks obtained by various authors are shown. Understanding the first and second peaks of reduced frequencies will be easier with this information.

## 5. Approaches for Mitigation of Torsional Wind Loads and Responses

A building's response to the wind is mostly determined by its aerodynamic characteristics (design wind speed, turbulence) and its mechanical properties (stiffness, mass, and damping) [66]. Xu *et al.* [67] showed that if the parameters of the tuned mass damper (TMD) were appropriately selected, TMDs were successful in reducing the building's torsional vibration. Kareem *et al.* [68] also mentioned the use of dampers in reducing torsional vibration in their detailed review. Kontoni and Farghaly [69] employed Tuned Mass Dampers (TMDs) to alleviate the impact of wind-induced loads on a steel high-rise structure. Using a smart tuned mass damper, Tse *et al.* [70] evaluated the system's performance and cost efficiency in suppressing wind-induced lateral-torsional movement of tall structures. During full-scale testing, Tamura *et al.* [71] concluded that the tuned liquid damper (TLD) not only showed efficiency but also performed well during strong winds. Ross *et al.* [72] demonstrate that TLD systems can reduce the twisting motions of high-rise buildings significantly. It was concluded by Pozos-Estrada & Hong [73] that peak responses caused by wind-induced torsional load could be reduced by employing TMDs with linear and nonlinear damping mechanisms and also considering correlated wind load effects influences the selection of dampers. Wang *et al.* [74] suggested installing a tuned mass damper-inerter (TMDI)/tuned mass damper (TMD) on a lower floor than the topmost floor to mitigate wind-induced vibration. The new integrated control system (ICS) approach proposed by Akyürek *et al.* [75] is designed with the intent of improving both the safety and performance of buildings with torsional irregularities. The conclusion is drawn that ICS is more robust than TMDs when it comes to limiting inter-story drift. Karami *et al.* [76] proposed a robust method for detecting damage in 3-D shear model structures based on identified Markov parameters and concluded that the controller used could effectively reduce the increase in the torsional response of the structure. In the study conducted by Lei *et al.* [77], the influence of a substantial side-ratio on the wind-induced torsional effects of super high-rise buildings was examined. The investigation yielded significant insights,



notably highlighting the efficacy of employing an active tuned mass damper (ATMD) as a viable solution. The ATMD exhibited a dual capability, proficiently mitigating both translational and torsional vibration responses induced by wind forces. That integrated approach holds promising prospects for substantially enhancing structural comfort in the presence of wind-induced vibrations.

Li *et al.* [78] examined the effect of corner chamfers on the aerodynamic performance of tall buildings. Fig. 9 represents the effect of the corner chamfer rate on the RMS torque coefficient. It is evident from Fig. 9, that wind-induced torsional loads decrease as corner chamfer rates increase. However, chamfering is more effective in lessening cross-wind load than torsional load. Pozas-Estrada *et al.* [79] compared torsionally sensitive structures with and without linear/nonlinear TMDs subjected to partially correlated wind forces with the probability of not exceeding specified wind-induced motion levels. Their study concluded that a slightly unconservative design is attained in most cases if the correlation between the along-wind force and the torsional moment is ignored in serviceability limit state design checking. Meena *et al.* [80] conducted a comparison between two regular and two irregular-shaped models. The study concluded that among the four models, the Y-shape model with a rounded corner exhibited the minimum base moment and the lowest coefficient of drag.

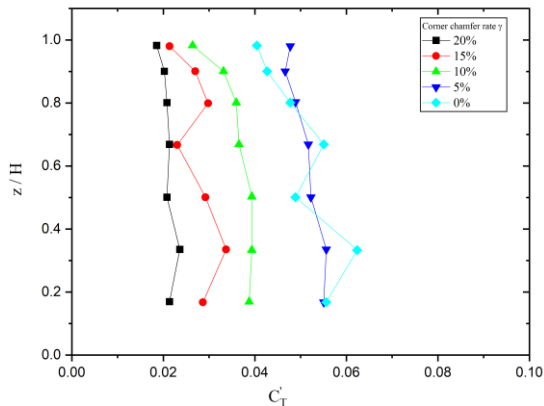


Fig. 9. Comparing the RMS torque coefficients using various chamfer rates ranging from 0-20% [78].

## 6. Conclusions

This paper summarizes important aspects of torsional wind loads on tall buildings available in the existing literature. There exist numerous studies which deal with the subject matter. It also reviews various methods to evaluate torsional wind load on tall buildings and their development so far.

- Various codal provisions on the torsional wind loads and responses have been emulated as available currently. Provisions of ASCE 07-22, NBCC 2020, and EN-2004 are similar; however, the results calculated differ considerably. The NBCC predicted values of the torsional coefficient are the maximum among the three. Therefore, it is concluded that these codal provisions are not sufficient enough, to evaluate the torsional wind loading. Wind tunnel studies as well as statistical and numerical methods must also be considered.
- Numerous wind tunnel experiments have been conducted to accurately assess torsional wind loads. These studies have mainly considered conventional cross-sections (square, rectangular, *etc.*). Based on the derived data, certain conclusive

theories have been provided, however, further detailed full-scale experimental studies are needed. There is still a need for extensive wind tunnel studies on tall buildings with irregular plans and varying cross-sections along the height.

- Various researchers have derived empirical formulations for the RMS torque coefficient, and torque spectra based on the data obtained from wind tunnel studies. The RMS torque coefficient is expressed in terms of side ratio, height aspect ratio, incident wind direction, and turbulence intensity. All the formulations unanimously found that the RMS torque coefficient increases with the depth dimension of the building. The RMS torque coefficient values attain a maximum at about 0.6 to 0.7 times the height of the building. It is observed from the formulations, that the angle of wind attack is an important parameter to determine the torsion wind loads. The maximum mean base torque coefficient is obtained at an angle of 25 degrees. The paper also lists empirical formulations for the power spectra density of torque.
- Various researchers have suggested the use of Tuned Mass dampers, Tuned liquid dampers, integrated control systems, and different passive measures to reduce the torsional responses. Some authors have also attempted shape optimization approaches to narrow down the torsional wind loads. However, the latter is not as effective as the former one.

This detailed literature study reveals that the simplified methods used to evaluate the torsional wind loads incorporate effective base wind shear and overturning moment. Nonetheless, additional work is needed to deal with wind-induced torsion adequately. The design of buildings may not always consider wind-induced torsional loads, but failing to represent these loads accurately may result in unrealistic spatial variations for design wind loads. In certain circumstances, such exaggerated loads may prove helpful. Proper estimates of wind-induced torsional loads affect the serviceability and long-term functional performance of buildings. Thus, this study concludes that torsional wind load and responses of tall buildings are essential and should not be overlooked during design. Further, the same should be looked into in greater detail through experimental wind tunnel studies and full-scale experiments. It is to be noted that torsional wind loads should be considered for the serviceability of tall buildings.

## References

- [1] Tallin A, Ellingwood B. Serviceability limit states: wind induced vibrations. *Journal of Structural Engineering*. 1984;110(10):2424-2437. [https://doi.org/10.1061/\(ASCE\)0733-9445\(1984\)110:10\(2424\)](https://doi.org/10.1061/(ASCE)0733-9445(1984)110:10(2424)).
- [2] Tamura Y, Kawana S, Nakamura O, Kanda J, Nakata S. Evaluation perception of wind-induced vibration in buildings. *Proceedings of the Institution of Civil Engineers-Structures and Buildings*. 2006;159(5): 283-293. <https://doi.org/10.1680/stbu.2006.159.5.283>.
- [3] Kwok K C S, Burton M D, Hitchcock P A. Human perception of tall building motions in strong wind environments. *The Sixth Asia-Pacific Conference on Wind Engineering (APCWE-IV)*, Seoul(Korea), pp. 248-262, 2005.
- [4] Kwok K C S, Hitchcock P A, Burton M D. Perception of vibration and occupant comfort in wind-excited tall buildings. *Journal of Wind Engineering and Industrial Aerodynamics*. 2009;97(7-8):368-380. <https://doi.org/10.1016/j.jweia.2009.05.006>.
- [5] Isyumov N, Case P C. Wind-induced torsional loads and responses of buildings. *Advanced Technology in Structural Engineering*. 2000, pp. 1-8. [https://doi.org/10.1061/40492\(2000\)83](https://doi.org/10.1061/40492(2000)83).
- [6] Cheung J C K, Melbourne W H. Torsional moments of tall buildings. *Journal of Wind Engineering and Industrial Aerodynamics*. 1992; 42(1-3): 1125-1126. [https://doi.org/10.1016/0167-6105\(92\)90119-U](https://doi.org/10.1016/0167-6105(92)90119-U).

- [7] Beneke D L, Kwok K C S. Aerodynamic effect of wind induced torsion on tall buildings. *Journal of Wind Engineering and Industrial Aerodynamics*. 1993;50:271-280. [https://doi.org/10.1016/0167-6105\(93\)90082-Y](https://doi.org/10.1016/0167-6105(93)90082-Y).
- [8] Bandi E K, Tamura Y, Yoshida A, Kim Y C, Yang Q. Experimental investigation on aerodynamic characteristics of various triangular-section high-rise buildings. *Journal of Wind Engineering and Industrial Aerodynamics*. 2013; 122: 60-68. <https://doi.org/10.1016/j.jweia.2013.07.002>.
- [9] Boggs D W, Hosoya N, Cochran L. Sources of torsional wind loading on tall buildings: Lessons from the wind tunnel. In *Advanced Technology in Structural Engineering*. 2000: pp. 1-8. <https://doi.org/10.1061/9780784404928>.
- [10] Kareem A, Wind-excited response of buildings in higher modes. *Journal of the Structural Division*. 1981; 107(4): 701-706. <https://doi.org/10.1061/JSDEAG.0005682>.
- [11] Kim Y, Kanda J. Effects of taper and set-back on wind force and wind-induced response of tall buildings. *Wind and Structures*. 2010; 13(6): 499-517. <https://doi.org/10.12989/was.2010.13.6.499>.
- [12] Kareem A. Wind induced torsional loads on structures. *Engineering Structures*. 1981; 3(2): 85-86.
- [13] Kareem A. Lateral-torsional motion of tall buildings to wind loads. *Journal of Structural Engineering*. 1985; 111(11): 2479-2496. [https://doi.org/10.1061/\(ASCE\)0733-9445\(1985\)111:11\(2479\)](https://doi.org/10.1061/(ASCE)0733-9445(1985)111:11(2479)).
- [14] Kijewski T, Kareem A. Dynamic wind effects: a comparative study of provisions in codes and standards with wind tunnel data. *Wind and structures*. 1998; 1(1): 77-109. <https://doi.org/10.12989/was.1998.1.1.077>.
- [15] Liang B, Tamura Y, Sukanuma S. Simulation of wind-induced lateral-torsional motion of tall buildings. *Computers & Structures*. 1997; 63(3): 601-606. [https://doi.org/10.1016/S0045-7949\(96\)00356-2](https://doi.org/10.1016/S0045-7949(96)00356-2).
- [16] Kim Y C, Kanda J, Tamura Y. Wind-induced coupled motion of tall buildings with varying square plan with height. *Journal of Wind Engineering and Industrial Aerodynamics*. 2011; 99(5): 638-650. <https://doi.org/10.1016/j.jweia.2011.03.004>.
- [17] Tallin A, Ellingwood B. Analysis of torsional moments on tall buildings. *Journal of wind engineering and industrial aerodynamics*. 1985; 18(2): 191-195. [https://doi.org/10.1016/0167-6105\(85\)90097-2](https://doi.org/10.1016/0167-6105(85)90097-2).
- [18] Shimada K, Tamura Y, Fujii K, Wakahara T. Wind induced torsional motion of tall building. In *Proc., 11th National Symposium Wind Engineering*. Tokyo (in Japanese), pp. 221-226, 1990.
- [19] Hui Y, Tamura Y, Yang Q. Analysis of interference effects on torsional moment between two high-rise buildings based on pressure and flow field measurement. *Journal of Wind Engineering and Industrial Aerodynamics*. 2017; 164: 54-68. <https://doi.org/10.1016/j.jweia.2017.02.008>.
- [20] Hou F, Jafari M. Investigation approaches to quantify wind-induced load and response of tall buildings: A review. *Sustainable Cities and Society*. 2020; 62: 102376. <https://doi.org/10.1016/j.scs.2020.102376>.
- [21] Stathopoulos T, Elsharawy M, Galal K. Wind load combinations including torsion for rectangular medium-rise buildings. *International Journal of high-rise buildings*. 2013; 2(3): 1-11. <https://doi.org/10.21022/IJHRB.2013.2.3.245>.
- [22] Hu J, Li Z, Zhao Z. Field Measurement on Translational and Torsional Wind-Induced Response of a High-Rise Building during Typhoon Khanun. *Buildings*. 2022;12(10):1698. <https://doi.org/10.3390/buildings12101698>.
- [23] Architecture Institute of Japan (AIJ), Recommendations for loads on buildings, Architectural Institute of Japan. Tokyo. Japan. 1993. (English version: 1996)
- [24] Architecture Institute of Japan (AIJ). Recommendations for loads on buildings. Architectural Institute of Japan. Tokyo. Japan. 2004. (In Japanese).

- [25] ISO 4354:2009, Second Edition: Wind Actions on Structures; International Organization for Standardization: Geneva, Switzerland. 2009.
- [26] IS 875 (Part 3): 2015. Bureau of Indian Standards. Indian Standard Code of Practice for design loads (other than earthquake) for buildings and structures. Part 3 – Wind loads. New Delhi, India 2015.
- [27] IS: 16700-2017. Bureau of Indian Standards. Criteria for structural safety of tall concrete buildings. New Delhi, India. 2017.
- [28] ASCE/SEI, Minimum design loads for buildings and other structures. ASCE/SEI 7-22, Structural Engineering Institute, Reston, VA, 2022.
- [29] NBCC, National Building Code of Canada (NBC). National Research Council of Canada (NRC), Ottawa, Canada, 2020, <https://doi.org/10.4224/w324-hv93>.
- [30] European Committee for Standardization (CEN), Eurocode 1: Actions on structures - Part 1-4: General actions - Wind actions, EN 1991-1-4, Brussels, 2005.
- [31] Ministry of Housing and Urban-Rural Development of the People's Republic of China. GB 50009-2012 Load Code for the Design of Building Structures. 2012.
- [32] Elsharawy M, Stathopoulos T, Galal K. Evaluation of wind-induced torsional loads on buildings by North American and European codes and standards. In Structures Congress. 2011; pp. 337-348. [https://doi.org/10.1061/41171\(401\)30](https://doi.org/10.1061/41171(401)30).
- [33] ASCE/SEI. Minimum design loads for buildings and other structures. ASCE/SEI 7-10. Structural Engineering Institute, Reston, VA, 2010.
- [34] NBCC, National Building Code of Canada (NBC), User's Guide - NBC 2010 Structural Commentaries (Part 4 of Division B), Canadian Commission on Buildings and Fire Codes (CCBFC), National Research Council of Canada (NRC), Ottawa, 2010.
- [35] Reinhold T A. Distribution and correlation of dynamic wind loads. Journal of Engineering Mechanics. 1983; 109(6): 1419-1436. [https://doi.org/10.1061/\(ASCE\)0733-9399\(1983\)109:6\(1419\)](https://doi.org/10.1061/(ASCE)0733-9399(1983)109:6(1419)).
- [36] Zou L, Li F, Song J, Shi T, Liang S, Mercan O. Investigation of torsional aeroelastic effects on high-rise buildings using forced vibration wind tunnel tests. Journal of Wind Engineering and Industrial Aerodynamics. 2020; 200: 104158. <https://doi.org/10.1016/j.jweia.2020.104158>.
- [37] Guzmán-Solís V, Pozos-Estrada A, Gómez R. Experimental study of wind-induced shear, bending, and torsional loads on rectangular tall buildings. Advances in Structural Engineering. 2020; 23(14): 2982-2995. <https://doi.org/10.1177/1369433220927280>.
- [38] Zhang W J, Xu Y L, Kwok K C S, Torsional vibration and stability of wind-excited tall buildings with eccentricity. Journal of Wind Engineering and Industrial Aerodynamics. 1993; 50: 299-308. [https://doi.org/10.1016/0167-6105\(93\)90085-3](https://doi.org/10.1016/0167-6105(93)90085-3).
- [39] Zhang WJ, Kwok K C S, Xu Y L, Aeroelastic torsional behavior of tall buildings in wakes. Journal of Wind Engineering and Industrial Aerodynamics. 1994; 51(2): 229-248. [https://doi.org/10.1016/0167-6105\(94\)90006-X](https://doi.org/10.1016/0167-6105(94)90006-X).
- [40] Tang U F, Kwok K C S. Interference excitation mechanisms on a 3DOF aeroelastic CAARC building model. Journal of Wind Engineering and Industrial Aerodynamics. 2004; 92(14-15): 1299-1314. <https://doi.org/10.1016/j.jweia.2004.08.004>.
- [41] Zou L, Xu G, Cai C S, Liang S. Wind tunnel tests of 3D wind loads on tall buildings based on torsional motion-induced vibrations. Wind and Structures. 2016; 23(3): 231-251. <https://doi.org/10.12989/was.2016.23.3.231>.
- [42] Kim Y C, Tamura Y, Tanaka H, Ohtake K, Bandi E K, Yoshida A. Wind-induced responses of super-tall buildings with various atypical building shapes. Journal of Wind Engineering and Industrial Aerodynamics. 2014; 133: 191-199. <https://doi.org/10.1016/j.jweia.2014.06.004>.
- [43] Tamura Y, Xu X, Tanaka H, Ohtake K, Kim Y C, Yoshida A, Yang Q. Effects of configurations of super-tall buildings on aerodynamic and wind-environmental

- characteristics. The 2018 World Congress on Advances in Civil, Environmental, & Materials Research (ACEM18, Incheon (Korea), 2018.
- [44] Tanaka H, Tamura Y, Ohtake K, Nakai M, Kim Y C. Experimental investigation of aerodynamic forces and wind pressures acting on tall buildings with various unconventional configurations. *Journal of Wind Engineering and Industrial Aerodynamics*. 2012; 107: 179-191. <https://doi.org/10.1016/j.jweia.2012.04.014>.
- [45] Zhou Y, Kijewski T, Kareem A. Aerodynamic loads on tall buildings: interactive database. *Journal of structural engineering*. 2003; 129(3): 394-404. [https://doi.org/10.1061/\(ASCE\)0733-9445\(2003\)129:3\(394\)](https://doi.org/10.1061/(ASCE)0733-9445(2003)129:3(394)).
- [46] Liang S, Li Q S, Liu S, Zhang L, Gu M. Torsional dynamic wind loads on rectangular tall buildings. *Engineering Structures*. 2004; 26(1): 129-137. <https://doi.org/10.1016/j.engstruct.2003.09.004>.
- [47] Thepmongkorn S, Wood G S, Kwok, K C S. Interference effects on wind-induced coupled motion of a tall building. *Journal of Wind Engineering and Industrial Aerodynamics*. 2002; 90(12-15): 1807-1815. [https://doi.org/10.1016/S0167-6105\(02\)00289-1](https://doi.org/10.1016/S0167-6105(02)00289-1).
- [48] Li Y, Zhang J W, Li Q S. Experimental investigation of characteristics of torsional wind loads on rectangular tall buildings. *Structural Engineering and Mechanics*. 2014; 49(1): 129-145. <https://doi.org/10.12989/sem.2014.49.1.129>.
- [49] Yoshie R, Kawai H, Shimura M, Wei R. A study on wind-induced vibration of super high rise building by multi-degree-of freedom model. *Journal of wind engineering and industrial aerodynamics*. 1997; 69: 745-755. [https://doi.org/10.1016/S0167-6105\(97\)00202-X](https://doi.org/10.1016/S0167-6105(97)00202-X).
- [50] Hou F, Sarkar P P. Aeroelastic model tests to study tall building vibration in boundary-layer and tornado winds. *Engineering Structures*. 2020; 207: 110259. <https://doi.org/10.1016/j.engstruct.2020.110259>.
- [51] Venanzi I, Cluni F, Gusella V, Materazzi A L. Torsional and across-wind response of high-rise buildings. In *Proceedings of the 12th International Conference on Wind Engineering AWES*, Cairns, Australia, 2007.
- [52] Patrickson C P, Friedmann P P. Deterministic torsional building response to winds. *Journal of the Structural Division*. 1979; 105(12): 2621-2637. <https://doi.org/10.1061/JSDEAG.0005314>.
- [53] Foutch D A, Safak E. Torsional Vibration of Along-Wind Excited Structures. *Journal of the Engineering Mechanics Division*. 1981; 107(2): 323-337. <https://doi.org/10.1061/JMCEA3.0002708>.
- [54] Reinhold T A, Sparks P R. The influence of wind direction on the response of a square-section tall building. *Proceedings Fifth International Conference on Wind Engineering*. New York, pp. 685-698, 1980.
- [55] Isyumov N, Poole M. Wind induced torque on square and rectangular building shapes. *Journal of Wind Engineering and Industrial Aerodynamics*. 1983; 13(1-3): 183-196. [https://doi.org/10.1016/0167-6105\(83\)90140-X](https://doi.org/10.1016/0167-6105(83)90140-X).
- [56] Katagiri J, Nakamura O, Ohkuma T, Marukawa H, Tsujimoto T, Kondo K. Wind-induced lateral-torsional motion of a tall building. *Journal of Wind Engineering and Industrial Aerodynamics*. 1992; 42(1-3): 1127-1137. [https://doi.org/10.1016/0167-6105\(92\)90120-Y](https://doi.org/10.1016/0167-6105(92)90120-Y).
- [57] Greig G L. Towards an estimate of wind-induced dynamic torque on tall buildings. PhD Thesis. University of Western Ontario. London. Canada, 20-40, 1980.
- [58] Lythe G R, Surry D. Wind-induced torsional loads on tall buildings, *Journal of Wind Engineering and Industrial Aerodynamics*. 1990; 36: 225-234. [https://doi.org/10.1016/0167-6105\(90\)90307-X](https://doi.org/10.1016/0167-6105(90)90307-X).
- [59] Choi H, Kanda J. Proposed formulae for the power spectral densities of fluctuating lift and torque on rectangular 3-D cylinders. *Journal of Wind Engineering and Industrial Aerodynamics*. 1993; 46: 507-516. [https://doi.org/10.1016/0167-6105\(93\)90318-I](https://doi.org/10.1016/0167-6105(93)90318-I).

- [60] Marukawa H, Ohkuma T. Formula of fluctuating wind forces for estimation of across-wind and torsional responses of prismatic high-rise buildings. *Journal of Structural and Construction Engineering*. 1996; 61: 33-42. [https://doi.org/10.3130/aijs.61.33\\_1](https://doi.org/10.3130/aijs.61.33_1)
- [61] Bazeos N, Beskos D E. Torsional moments on buildings subjected to wind loads. *Engineering analysis with boundary elements*. 1996; 18(4): 305-310. [https://doi.org/10.1016/S0955-7997\(96\)00040-9](https://doi.org/10.1016/S0955-7997(96)00040-9).
- [62] Li Y, Li Q S, Chen F. Wind tunnel study of wind-induced torques on L-shaped tall buildings. *Journal of Wind Engineering and Industrial Aerodynamics*. 2017; 167: 41-50. <https://doi.org/10.1016/j.jweia.2017.04.013>.
- [63] Marukawa H, Ohkuma T, Momomura Y. Across-wind and torsional acceleration of prismatic high rise buildings. *Journal of Wind Engineering and Industrial Aerodynamics*. 1992; 42(1-3): 1139-1150. [https://doi.org/10.1016/0167-6105\(92\)90121-P](https://doi.org/10.1016/0167-6105(92)90121-P).
- [64] Gui Y L I, Qiu-sheng L I, Yi-min D A I. Mathematical models for torsional fluctuating wind loads on rectangular tall buildings. *Engineering Mechanics*. 2015; 32(6): 177-182. (in Chinese) <https://doi.org/10.6052/j.issn.1000-4750.2013.11.1105>.
- [65] Tang Y, Gu M, Quan Y. Mathematical model of torsional fluctuating wind force on rectangular super-tall buildings. *Journal of Building Structures*. 2009; 30(5):198-2.4. (In Chinese).
- [66] Davenport A G. The response of six building shapes to turbulent wind. *Philosophical Transactions of the Royal Society of London. Series A. Mathematical and Physical Sciences*. 1971; 269(1199): 385-394. <https://doi.org/10.1098/rsta.1971.0039>.
- [67] Xu Y L, Kwok K C S, Samali B. Torsion response and vibration suppression of wind-excited buildings. *Journal of Wind Engineering and Industrial Aerodynamics*. 1992; 43(1-3): 1997-2008. [https://doi.org/10.1016/0167-6105\(92\)90623-I](https://doi.org/10.1016/0167-6105(92)90623-I).
- [68] Kareem A, Kijewski T, Tamura Y. Mitigation of motions of tall buildings with specific examples of recent applications. *Wind and structures*. 1999; 2(3): 201-251. <https://doi.org/10.12989/was.1999.2.3.201>.
- [69] Kontoni D-P N, Farghaly A A. TMD effectiveness for steel high-rise building subjected to wind or earthquake including soil-structure interaction. *Wind and Structures*. 2020; 30(4): 423-432. <https://doi.org/10.12989/WAS.2020.30.4.423>.
- [70] Tse K T, Kwok K C S, Tamura Y. Performance and cost evaluation of a smart tuned mass damper for suppressing wind-induced lateral-torsional motion of tall structures. *Journal of Structural Engineering*. 2012; 138(4): 514-525. [https://doi.org/10.1061/\(ASCE\)ST.1943-541X.0000486](https://doi.org/10.1061/(ASCE)ST.1943-541X.0000486).
- [71] Tamura Y, Fujii K, Ohtsuki T, Wakahara T, Kohsaka R. Effectiveness of tuned liquid dampers under wind excitation. *Engineering Structures*. 1995; 17(9): 609-621. [https://doi.org/10.1016/0141-0296\(95\)00031-2](https://doi.org/10.1016/0141-0296(95)00031-2).
- [72] Ross A S, El Damatty A A, El Ansary A M. Application of tuned liquid dampers in controlling the torsional vibration of high-rise buildings. *Wind and Structures*. 2015; 21(5): 537-564. <https://doi.org/10.12989/was.2015.21.5.537>.
- [73] Pozos-Estrada A, Hong H P. Sensitivity analysis of the effectiveness of tuned mass dampers to reduce the wind-induced torsional responses. *Latin American Journal of Solids and Structures*. 2015; 12: 2520-2538. <http://dx.doi.org/10.1590/1679-78251856>.
- [74] Wang Q, Qiao H, De Domenico D, Zhu Z, Xie Z. Wind-induced response control of high-rise buildings using inerter-based vibration absorbers. *Applied Sciences*. 2019; 9(23): 5045. <https://doi.org/10.3390/app9235045>.
- [75] Akyürek O, Suksawang N, Go T H. Vibration control for torsionally irregular buildings by integrated control system. *Engineering Structures*. 2019; 201: 109775. <https://doi.org/10.1016/j.engstruct.2019.109775>.

- [76] Karami K, Ahmadi H. Torsional control of asymmetric buildings using online 3-D damage detection and adaptive stiffness devices. *Structural Control and Health Monitoring*. 2021; 28(10): e2804. <https://doi.org/10.1002/stc.2804>.
- [77] Lei Z H, Bo L I, Wei Z H, Huaibing X U, Ping S H, Xiaohui X U. Research on wind-induced torsional vibration response and vibration control of super-tall building with a large side ratio. *Journal of Building Structures*. 2023; 4: 87-97. <https://doi.org/10.14006/j.jzjgxb.2022.0431>.
- [78] Li Y, Li C, Li Q S, Song Q, Huang X, Li Y G. Aerodynamic performance of CAARC standard tall building model by various corner chamfers. *Journal of Wind Engineering and Industrial Aerodynamics*. 2020; 202: 104197. <https://doi.org/10.1016/j.jweia.2020.104197>.
- [79] Pozos-Estrada A, Hong H P, Galsworthy J K. Reliability of structures with tuned mass dampers under wind-induced motion: a serviceability consideration. *Wind and Structures*. 2011; 14(2): 113-131. <https://doi.org/10.12989/was.2011.14.2.113>.
- [80] Meena RK, Raj R, Anbukumar S. Effect of wind load on irregular shape tall buildings having different corner configuration. *Sādhanā*. 2022;47(3):126. <https://doi.org/10.1007/s12046-022-01895-2>.

## Effect of GGBFS and fly ash proportions on fresh, tensile and cracking features of alkali activated concrete with low NaOH concentrations

Mangalapuri Venkateswarlu<sup>a</sup>, T.D Gunneswara Rao<sup>b</sup>

Department of Civil Engineering, National Institute of Technology, Warangal, India

### Article Info

#### Article history:

Received 02 Nov 2023  
Accepted 12 Mar 2024

#### Keywords:

Fly Ash;  
GGBFS;  
Alkali activated concrete;  
Tensile stress;  
Tension stiffening effect;  
Cracking characteristics

### Abstract

This study mainly investigated the tensile and cracking features of ash alkali activated concrete with different slag-fly ash proportions and low NaOH concentrations cured at ambient temperature. High-molarity NaOH leads to risk and is costly, whereas, in field conditions, heat curing is difficult. Therefore, in this study three mixes (mix-A, B and C) were developed using 0/100, 20/80, 40/60, 60/40, 80/20, and 100/0 slag-fly ash proportions in this study. Sodium hydroxide (SH) and sodium silicate (SS) were used as activators and concentrations of sodium hydroxide were used as 1M, 2M and 4M in mixes A, B and C respectively, but alkaline ratio (SS/SH) was fixed as 1.5 in all the mixes. Slump, and strength aspects (compressive, split tensile, and flexural) were evaluated. The tensile (tensile strength, tension stiffening) and cracking characteristics (crack spacing, crack width) were evaluated under uniaxial tensile loading on reinforced prismatic members. From test outcomes, workability in terms of slump of the composites decreased with increased percentage of slag or granulated blast furnace slag (GGBFS) in the total binder, but the tensile (tensile stress and tension stiffening effect) and compressive strengths increased with increasing percentage of GGBFS. Better cracking properties (i.e., minimum crack widths and reduced crack spacings) were observed when the mixes contained higher percentages of GGBFS. The obtained crack spacings were correlated with CEB-FIP model code, and existing research studies. The crack spacings obtained in this study are consistent with CEB-FIP model code. Finally, this study demonstrated that when slag-fly ash alkali activated concretes were prepared with solutions containing low NaOH concentrations and cured at room temperature (ambient), there was an increase in the strength and cracking properties with higher percentages GGBFS.

© 2024 MIM Research Group. All rights reserved.

## 1. Introduction

Sustainability and environmental issues are currently the need-of-the-hour in every aspect of development. In this context, utilization of industrial byproducts like fly ash, GGBFS, rice husk ash, Meta kaolinite, etc., play an important role in geopolymer concrete (GPC) and alkali activated concretes (AAC). GGBFS exhibits pozzolanic behaviour and good binding properties in base media with low heat of hydration, and it gives better mechanical and excellent durability characteristics [1]. But there were setting time and workability problems with this slag-based alkali activated concrete (SAAC) [2,3]. However, SAAC is a high brittle material due to the higher volume of GGBFS. This leads to development of shrinkage cracks and microcracks. The inclusion of low-calcium fly ash as a binder result in less strength under ambient curing conditions [4]. Curing condition plays very

<sup>\*</sup>Corresponding author: [mv718113@student.nitw.ac.in](mailto:mv718113@student.nitw.ac.in)

<sup>a</sup> orcid.org/0009-0008-7305-6845; <sup>b</sup> orcid.org/0000-0002-9145-044X

DOI: <http://dx.doi.org/10.17515/resm2024.67me1102rs>

Res. Eng. Struct. Mat. Vol. 10 Iss. 3 (2024) 1301-1320



prominent role in development of hydration and strength properties in fly ash-GGBFS alkali activated concretes [5]. Using low concentrations of NaOH instead of high levels of sodium hydroxide for concrete production can reduce the risk and cost associated with it. The NaOH solution molarity plays the prominent role in dissolution of compounds present in source materials such as alumina and silica [5,6]. Alkaline ratio (AR) plays an important role in strength development. High alkaline ratios lead to an uneconomical mix, and a low alkaline ratio leads to poor mechanical strength [6-8]. In the context of sustainability and environmental issues, industrial byproduct like fly ash, and GGBFS play an important role in the preparation of alkali activated geopolymer concrete [9]. As the increase of GGBFS and NaOH concentration, the workability of alkali activated concrete (AAC) decreases and setting times of AAC increased [3, 10-12]. The strength properties of alkali-activated fly ash-slag concretes (AAFSC) increase effectively with increasing slag (GGBFS) and sodium hydroxide molar concentrations, as well as decreasing the solution to binder ratio [10-12].

Knowledge of the tensile behaviour of reinforced concrete (RC) is required for a thorough knowledge of a structure's behaviour under normal and severe situations. In predicting the tensile behaviour of RC prisms, the tension stiffening effect has been extensively utilised [13-18]. All tension at a cracked part of a RC member is sustained by reinforcement. Bond action, however, effectively stiffens the member response and lowers deflections by allowing the concrete to continue to transmit tensile loads between the cracks. This phenomenon, referred to as "tension stiffening," and is essentially to account for the presence of average tensile stresses over zero in cracked concrete [19]. Gribniak et al. [20] developed a stochastic technique for tension stiffening assessment. The behaviour of components made of reinforced concrete under flexure does not necessarily match the tension-stiffening relationship shown in the uniaxial tension test [21-23]. Tension stiffening is crucial for controlling beam deflection [24]. It can be used to estimate multiple crack spacings and crack widths [21,24]. The tensile stress of concrete is reduced marginally by raising the reinforcement ratio. Transverse tensile cracking formed under higher steel stress in specimens having large cross sections [25]. Abdulrahman et al. found that geopolymer concrete has comparable tension-stiffening member behaviour as OPC concrete [26]. Cracks have a prominent effect on serviceability, good looking, and load transfer. A concrete member can easily crack due to its low tensile strength. The experiments gave a wide variety of data utilised to assess cracking characteristics in order to construct empirical equations used in the CEB-FIP Model Code, Eurocode-2, and Marti et al. [17,27,28]. Cracking aspects of reinforced concrete affected by the tension stiffening behaviour between the cracks. The increased tensile stiffness also helps reduce the crack width [29,30]. Tension stiffening significantly affected by the shrinkage [30]. But shrinkage did not influence the measured crack widths when crack spacing and strain between steel and concrete are related [30,31]. Compared to OPC concrete, geopolymer concrete exhibited higher first cracking loads and had less effect on the shrinkage of geopolymer concrete and also shrinkage effects do not need to be considered in GPC [32]. Even though several investigations were carried out on research on alkali-activated binders, in most studies, high molarity NaOH concentrations and heat curing conditions were preferred to study the structural behaviour of the concrete member. But high-molarity NaOH leads to risk and is costly, whereas in field conditions, heat curing is difficult.

## 2. Research Significance

From the existing literature, it is evident that most of the research studies are focused on fresh, mechanical, and durability characteristics GPC and AAC. Even though many studies have also reported on tensile and cracking characteristics of conventional concrete (OPC) but very few investigations are available on tensile and cracking characteristics of alkali activated and/ or geopolymer concretes. Even though several investigations were carried

out on research on alkali-activated binders, in most studies, high molarity NaOH concentrations and heat curing conditions were preferred to study the structural behaviour of the concrete member. But using a solution with such a high NaOH concentration and high alkaline ratio is risky as well as costly. To overcome these problems, there is a need to develop alkali activated concretes that can be cured in the field using low molarity solutions. Hence, this study mainly emphasizes the tensile (strength) and cracking characteristics of FSAAC with different replacement levels of GGBFS-fly ash, prepared with low concentrations of NaOH in an alkaline solution under ambient curing conditions.

### 3. Experimental Investigation

#### 3.1. Materials

In this investigation GGBFS and fly ash were used as binders. JSW Cement, Warangal provided the GGBFS, and a Ramagundam thermal power station in Telangana provided the class-F fly ash. The quantity and type of GGBFS were confirmed in accordance with IS 12089-1987 [33], while the fly ash was confirmed with IS 3812-1981 [34]. Fine and coarse aggregates were used in this study and confirmed with IS 383-1970 [35]. Physical characteristics of GGBFS, fly ash, fine aggregate, and coarse aggregate are mentioned in Table 1, whereas the chemical composition of GGBFS and fly ash is reported in Table 1. The ideal fine-to-coarse aggregate proportion for mixes B and C has been chosen as 45%:55% of overall aggregate volume and 30%:70% for mix A. Conplast SP430 superplasticizer (SP) (Fosroc Chemicals) was employed in this study, and this SP conformed with IS 9103-1999 [36] and dosage of SP used reported in Table 3. The alkali activator was a mixture of sodium hydroxide (NaOH) and sodium silicate ( $\text{Na}_2\text{SiO}_3$ ) solutions. In mixes A, B, and C, sodium hydroxide pellet concentrations of 1M, 2M, and 4M were employed, respectively. A constant Alkaline Ratio of 1.5 was adopted in wholly mixtures, as determined in earlier investigations [2,6,37].

Table 1. Physical and chemical features of GGBFS, fly ash, and aggregates

Physical and Chemical features	GGBFS	Fly ash	Fine aggregate	Coarse aggregate
CaO (%)	34.21	1.82	-	-
SiO <sub>2</sub> + Al <sub>2</sub> O <sub>3</sub> (%)	53.86	88.85	-	-
Fe <sub>2</sub> O <sub>3</sub> (%)	0.80	4.22	-	-
SO <sub>3</sub> (%)	0.90	0.37	-	-
MgO (%)	7.77	1.03	-	-
Other (Na <sub>2</sub> O + LOI) (%)	0.51	1.07	-	-
Density (kg/m <sup>3</sup> )	1300	1200	1650	1700
Specific gravity	2.90	2.11	2.63	2.73
Specific surface area (m <sup>2</sup> /kg)	355	450	-	-

#### 3.1. Materials

The current study took three mixtures into account, they are known as Mix A, B, and C. Mix-A, Mix-B and Mix-C have been developed using 0/100, 20/80, 40/60, 60/40, 80/20, and 100/0 slag-fly ash proportions as binders. The reason for using three different mixes, different fly ash and GGBFS, and three different molarity NaOH solutions is to achieve at least three standard grades of concrete (20 MPa, 40 MPa, and 60 MPa). Similarly, different proportions of fly ash and GGBFS are used to evaluate strength and cracking properties.

These mix compositions are easier for designers in concrete mix design when low-molarity NaOH solutions are added. The blending and proportioning were done in two phases. In the first phase, each mixture (A, B, and C) was incorporated with 0/100% GGBFS-fly ash proportion. In second phase, in all mixes (A, B, and C), GGBFS was replaced in place of fly ash at an interval of 20%, 40%, 60%, 80%, and 100%. There was an overall total of eighteen mixtures made. For this mix proportioning, the unit weight of AAC was taken as 2400 kg/m<sup>3</sup>. The mixture proportioning was calculated using that unit weight, which was derived from earlier research [2,37]. The mixing process of AAC is the same as conventional concrete [11,12]. Mix proportioning particulars are reported in Table 2. Following blending, mixes were employed to test the workability. After being removed from the moulds, the specimens were kept to remain at room temperature for curing.

Table 2. Mix proportioning details

Mix	Binder (B)		Alkaline solution (S)		Aggregates		SP (%)	Molarity (M)	S/B ratio
	GGBFS (kg)	Fly ash (kg)	NaOH solution (kg)	Na <sub>2</sub> SiO <sub>3</sub> solution (kg)	Fine aggregate (kg)	Coarse aggregate (kg)			
A	-	300	66	99	581	1354	6	1	0.55
	60	240	66	99	581	1354	6	1	0.55
	120	180	66	99	581	1354	6	1	0.55
	180	120	66	99	581	1354	6	1	0.55
	240	60	66	99	581	1354	6	1	0.55
	300	-	66	99	581	1354	6	1	0.55
B	-	400	72	108	819	1001	6	2	0.45
	80	320	72	108	819	1001	6	2	0.45
	160	240	72	108	819	1001	6	2	0.45
	240	160	72	108	819	1001	6	2	0.45
	320	80	72	108	819	1001	6	2	0.45
	400	-	72	108	819	1001	6	2	0.45
C	-	400	80	120	810	990	6	4	0.50
	80	320	80	120	810	990	6	4	0.50
	160	240	80	120	810	990	6	4	0.50
	240	160	80	120	810	990	6	4	0.50
	320	80	80	120	810	990	6	4	0.50
	400	-	80	120	810	990	6	4	0.50

### 3.4 Tests Performed

To measure the workability of freshly mixed concrete, a slump test was conducted. This slump test was performed as per the Indian standard IS: 7320 [38]. The compressive strengths of concrete cubes (100 x 100 x100 mm) were evaluated using the Tinius-Olsen Testing Machine (TOTM) at 7 and 28 days of curing as per the Indian standard: 516-1959 [39], and its capacity is 2000kN. For the split tensile strength, a test on a cylinder (100 mm dia. And 200 mm height) was also performed on the same equipment. A three-point loading test on prisms (500 x100 x 100 mm) was done for flexural strength according to ASTM C 293-02 [40]. Corresponding test diagrams were presented in Fig.1(a). Reinforced concrete prismatic specimens of size 600 x 60 x 60 mm were used in this study to explore the tensile and fracture properties. The specimens were subjected to uniform tension loading in a UTM with a capacity of 200kN. Two linear variable differential transducers (LVDT) were mounted on opposite faces of the concrete prism. The entire test setup is shown in Figs.1(b) and 1(c). The change in axial length (deformation) was measured using these LVDTs. The signals received by the LVDTs were recorded using a DAQ device. Cracks and their formations were observed during the test, and crack spacing was measured for every

1 kN increment of load. The test was continued until the steel bar yielded. During the test, crack widths were observed and measured at every 10 kN load. Maximum crack width values were measured on all surfaces. To establish realistic bar response, the study also tested a bare steel bar under similar loading conditions.

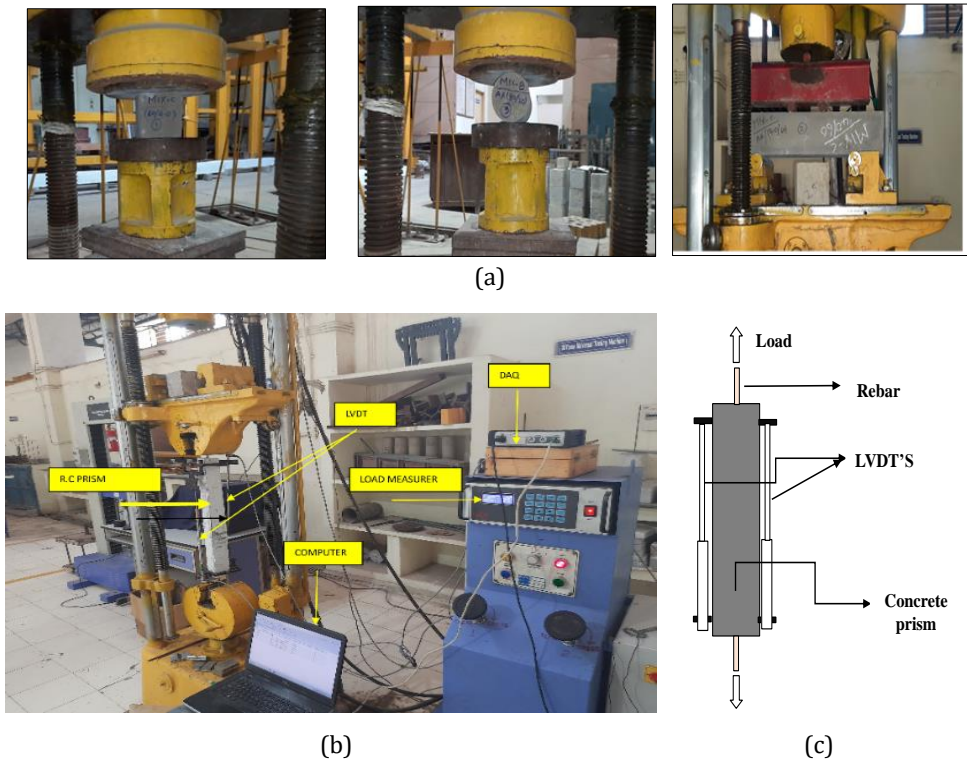


Fig. 1. (a) cube, cylinder and prism testing (b) Uni-axial tension set up (c) Reinforced concrete prism with steel bar under uni-axial tension

## 4. Results and Discussion

### 4.1 Workability

Figures 2(a) and 2(b) illustrated the workability of mixtures in terms of slump values and reduction in slump in percentages. From Figs. 2(a) and (b), in all mix combinations, Slump values increased when fly ash was substituted with GGBFS from 0% to 100%. This indicates increasing workability. Earlier investigations also revealed that as the increase of GGBFS and NaOH concentration, the workability of AAC decreased [3,9,12]. This may be due to the GGBFS particles having irregularly shaped and edged surfaces, while fly ash particles typically have round and smooth silt-sized particles. Hence, these small glass balls improve the flow and efficiency of fresh concrete as fly ash content increased. The highest decrement rate in mix-C was observed compared to mix-B and mix-A composites. From fig. 2(b), when the GGBFS percentage was increased from 0% to 100%, slump values decreased by 54.17% in mix A, 60.17% and 63.54% in mix B, C respectively.

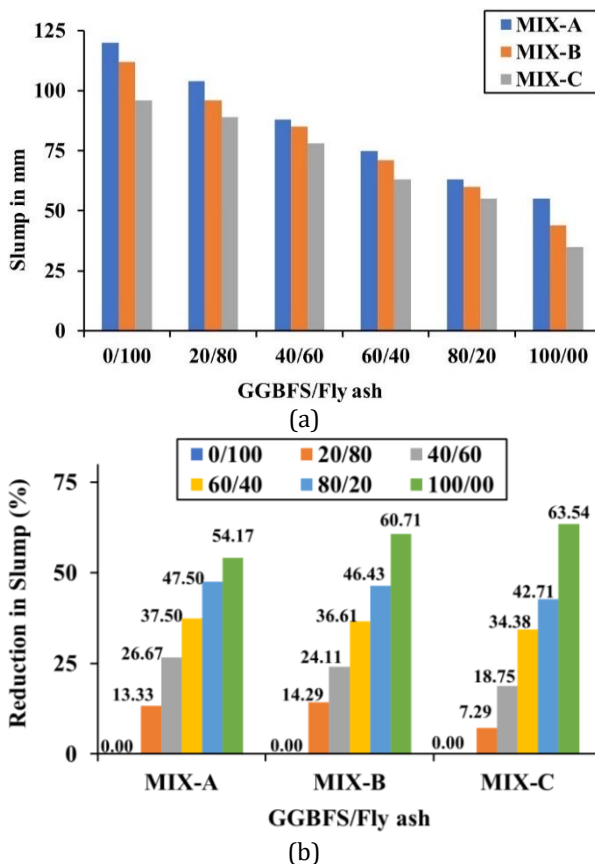


Fig. 2. (a) Workability of mixtures in terms of Slump values, 2(b) Reduction in slump in percentages with 100% fly ash (0/100 – GGBFS/Fly ash combination)

#### 4.2.1 Compressive Strength

In Figs. 3(a), and (b) the 7-day and 28-day compressive strength results of all mixes are shown. The compressive strength values increased when the GGBFS content was increased from 0% to 100% in all mixes. In this study, maximum compressive strengths were achieved after 28 days curing in mix-A, mix-B, and mix-C at 100% GGBFS and 0% fly ash content, which are 27.03 MPa, 49.51 MPa, and 65.81 MPa in mix-A, B, and C respectively. Previous research has also indicated that GGFBS increases compressive strength, which may be attributed to the high calcium levels present in GGBFS [3,9-12]. But the obtained compressive strengths decreased as the fly ash content increased. This may due to the inclusion of fly ash reduces the Si/Al ratio in the mixture, indicating that determining the relative quantities of  $AlO_4^-$  and  $SiO_4^{2-}$  generated in the geopolymer gel and determining the quantity of Si contained in the combination results in a low silicon/aluminum ratio that is associated with mixing with a high fly ash content. The compressive strength generally decreases as the Si/Al ratio decreases. The decrease in compressive strengths may due to the lower NaOH concentrations and provided curing conditions (i.e., ambient curing) in this study. The NaOH solution molarity plays the prominent role in dissolution of compounds present in source materials such as alumina and silica [5,6]. To obtain better geopolymerization, heat or high temperature curings are required when high fly ash levels are present in the mixes. But in this study all samples were cured at room temperature

only. The method of curing is also playing an important role in the geopolymerization process [3,5].

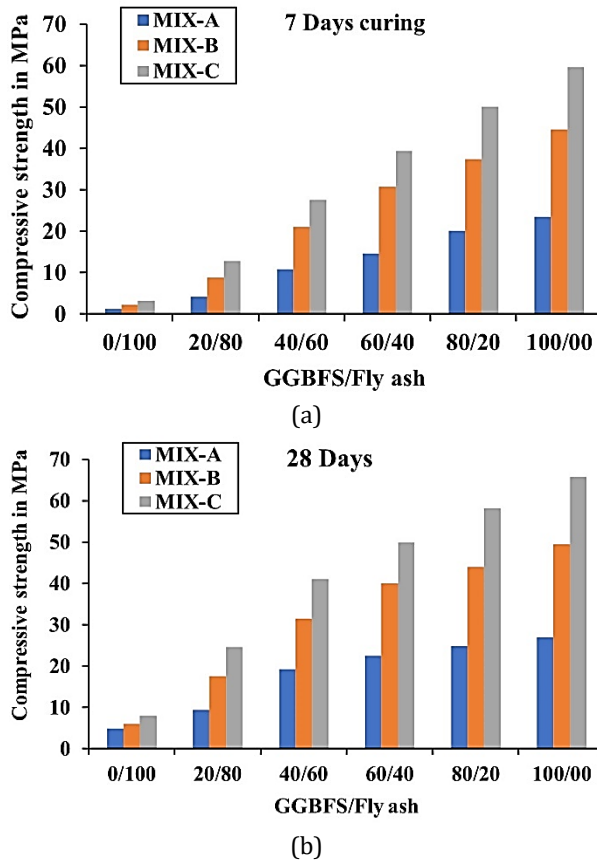


Fig. 3. Compressive strength values at various GGBFS and Fly ash proportions in mixes at: (a) 7 Days curing, (b) 28 Days curing

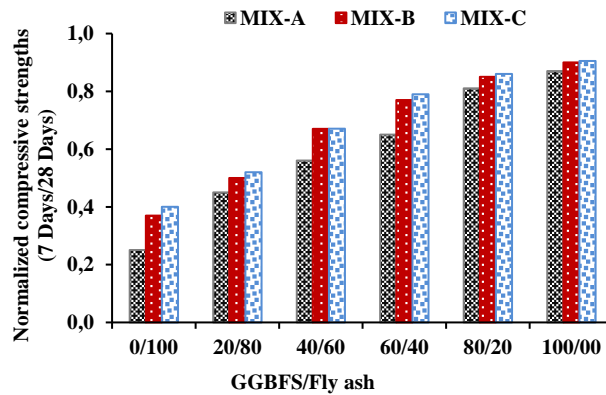


Fig. 4. Normalized compressive strengths (7 Days compressive strengths w.r.t 28 Days compressive strengths)

#### 4.2.2 Early and Later Gain Strengths

The 7-day compressive strengths of all mixes are comparable to 28-day compressive strengths as depicted in Fig.4. When 100% GGBFS was used as a binder (reference mixes), most mixes gained 80%–90% of their total strength at an early age (at 7 days). Among all the mixes, the initial strength reduction percentage is the lowest in mix-C. Compared to mix-B and mix-C, the initial gain strength reduction percentage in mix-A was observed to be higher. Up to 2/3 of the initial strength was observed when GGBFS content of 60% was used in B and C mixtures, but not in the case of mix-A. This is because the reactivity of the alkaline solution with GGBFS content is higher at an early age than the reactivity of the alkaline solution with fly content, and huge amount of fly ash content slows down the hydration process, whereas GGBFS enhances the hydration process and reactivity.

#### 4.2.3 Split Tensile and Flexural Strength

In Fig. 5, split tensile strength results for all mixes are shown. In all the mixes, as GGBFS increased, split tensile strengths increased. Split tensile strengths increased greatly as GGBFS in all mixes increased from 0% to 100% and the increment rate was very high at specimens having 60%, 80%, and 100% of GGBFS. However, these split tensile strengths decreased as fly ash in all mixes increased from 0% to 100% and the decrement rate was very high at 60%, 80%, and 100% fly ash containing specimens.

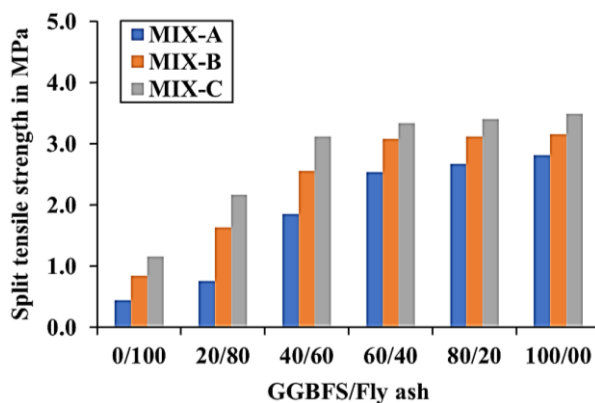


Fig. 5. Split Tensile strength values

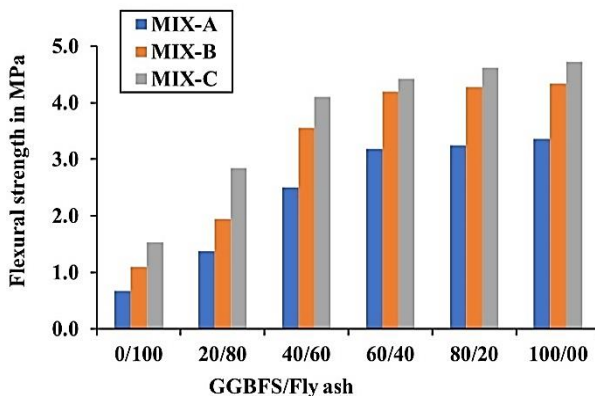


Fig. 6. Flexural strength values

In Fig. 6, the flexural strength results of all mixes are shown. As GGBFS content in all mixes increased from 0% to 100%, the flexural strength values increased. Diaz Loya et al. [41] also found that flexural strength values are higher for GGBFS content. But with the addition of 0%-40% GGBFS, flexural strength values decreased drastically, and the decrement rate was higher. Similar kind behaviour was reported by Sofi, M., et al. [42].

### 4.3 Tensile Behavior (Load-Member Strain Response)

To know the tensile behavior of specimens, first record the load displacement response. From this, the load-member strain response was obtained. The yield load and the first crack load were recorded and tabulated. The measured values first crack load, yield load and crack spacing are presented in Table 3. Similarly, average crack spacings, obtained from the present experimental study and various codes and previous studies, are given in Table 3. The first crack loads are increased as the GGBFS increased. From Table 3, in the mixes A, B and C yield loads in steel are slightly closer at 80% and 60% of GGBFS. This implies that fly ash and GGBFS combination increases the member's yield load carrying ability of steel bar when the member is in crack stabilization stage and after the first crack formation in the member.

Table 3. First Crack Loads, Yield loads and Crack Spacing details

Specimen designation (Mix-GGBFS/Fly Ash)	First crack load (kN)	Yield load in steel (kN)	Average crack spacing (mm)				No. of transverse cracks
			Marti et al. [23] (OPC)	CEB - FIB Model [32] (OPC)	G. Kaklauskas et al. [34] (OPC)	Experimental (FSAAC)	
A-00/100	5.70	41.50	112.11	83.33	90.51	85.44	5
A-20/80	4.74	42.60	112.11	83.33	90.51	81.07	6
A-40/60	6.10	43.11	112.11	83.33	90.51	78.21	7
A-60/40	8.76	45.50	112.11	83.33	90.51	74.61	7
A-80/20	8.85	46.50	112.11	83.33	90.51	74.07	7
A-100/00	9.80	47.00	112.11	83.33	90.51	72.25	6
B-00/100	5.26	40.50	112.11	83.33	90.51	83.10	6
B-20/80	6.11	43.86	112.11	83.33	90.51	80.76	6
B-40/60	9.40	44.50	112.11	83.33	90.51	78.35	7
B-60/40	12.30	45.96	112.11	83.33	90.51	75.99	7
B-80/20	13.20	45.50	112.11	83.33	90.51	75.21	7
B-100/00	13.40	48.00	112.11	83.33	90.51	73.32	7
C-00/100	5.56	40.70	112.11	83.33	90.51	83.43	7
C-20/80	8.30	43.98	112.11	83.33	90.51	80.67	6
C-40/60	10.50	45.00	112.11	83.33	90.51	77.50	6
C-60/40	12.50	46.50	112.11	83.33	90.51	72.40	6
C-80/20	13.20	46.65	112.11	83.33	90.51	71.51	7
C-100/00	15.13	49.13	112.11	83.33	90.51	70.12	7

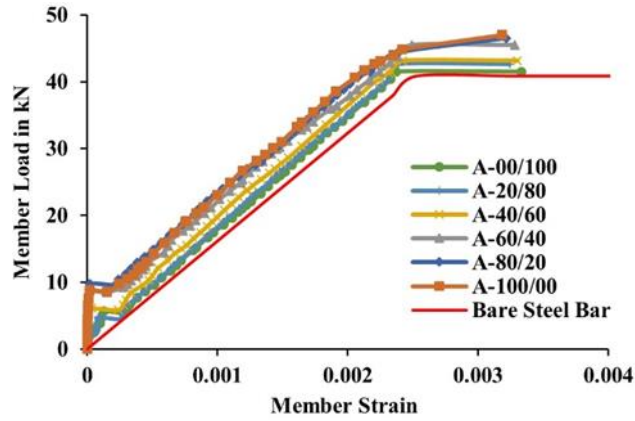
Figs. 7 (a), (b), and (c) illustrate the deformation response of the axis load member and a bare steel bar of mix-A, B, and C. The behaviour of the members is in starting linear as well as elastic until cracks appear in the concrete. After member develops cracks, the concrete contribution (average stress) decreased with increasing strain as more cracks form till cracking process stabilizes. Tension stiffening effect is slowly decreases after the crack is stabilized. Once the crack has stabilized, stiffness of members gradually decreased. The behaviour between cracks has the greatest influence on the tension stiffening of conventional concrete [19]. After cracking, it can be observed that mixes having 100%-0%



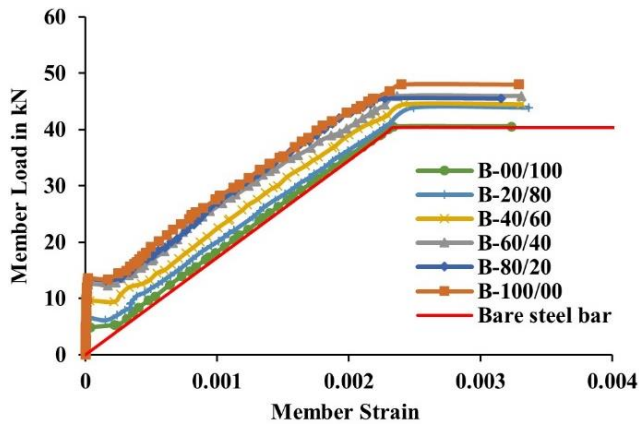
and 80%-20% GGBFS-fly ash exhibit more tension stiffening effect behavior than remaining mixtures. Similarly, all mixes also exhibited some desirable tension stiffening behavior when up to 60% of GGBFS was replaced. But when more than 60% of GGBFS was replaced, this tension-carrying capacity between the cracks was severely reduced. The reason for this is that as the fly ash increases, bonding between aggregates and the binder in the mixture decreases due to the better geopolymerization not achieved in the presence of small NaOH concentration and room temperature. Due to this, the bonding between concrete and steel can also decrease. Previous studies indicated that tension carrying capacity between cracks of concrete based on bond that occurred among concrete and steel; in relative to crack spacing, it established as per member cracks [29-31]. Tensile load carrying capacities at first crack load at different fly ash to GGBFS ratios, i.e., 0/100, 20/80, 40/60, 60/40, 80/20, and 100/0, while in Mix-A were 5.70 kN, 4.74 kN, 6.10 kN, 8.76 kN, 8.85 kN, and 9.80 kN, while in Mix-B were 5.26 kN, 6.11 kN, 9.40 kN, 12.30 kN, 13.20 kN, and 13.40 kN, and in Mix-C 5.56 kN, 8.30 kN, 10.50 kN, 12.50 kN, 13.20 kN, and 15.10 kN were observed, respectively. Similar results were observed in this study when compared with the studies of Albitar [32] and Ganesan et al. [45, 46]. In the Albitar [32] study, the first crack load was observed at 11.56 kN in fly ash-based GPC with a compressive strength of 35 MPa. Ganesan et al. [45] observed at 10 kN in plain fly ash-based GPC (FGPC) of M40-grade concrete. Ganesan et al. [46] study observed first crack load at 12.7 kN in plain fly ash and GGBFS-based GPC containing M40-grade concrete. In the present study, specimens that achieved 40 MPa compressive strength had a first crack load of 12.30 kN, 13.20 kN, and 13.40 kN in 60/40, 80/20, and 100/0 fly ash and GGBFS proportions of Mix-B mixes, respectively, and 12.50 kN in 60/40 fly ash and GGBFS proportions of Mix-C mixes. From this, it can be understood that fly ash and GGBFS combinations give better results than 100% fly ash specimens cured at room temperature. Similar behavior was observed in yield load as well.

In all mixes, whenever the GGBFS was rose to 80%, the load transfer of concrete among cracks was slightly similar compared to reference mixes (mixes having 100% GGBFS). When 0% GGBFS was used, all the mixes showed very low tensile strength, this may be due to the use of low concentrations of alkaline activated solution in the mixes and the lack of heat curing. Indeed, heat curing of concrete activated with fly-ash-based alkalis is essential for good polymerization [6]. But in our study, all the samples have been cured by ambient curing. As a result of the low concentration of the alkaline solution and the absence of heat curing, better hydration is not achieved at higher levels of fly ash contents. Tension stiffening effect was not effectively visible in A-mix compared to other two B and C mixes, since mix-A having low grade of strength of mixes. The tension stiffening capacity is more visible in members with a lower reinforcement ratio and higher concrete strength [43]. Mixes A, B, and C having 100%-0% and 20%-80% GGBFS-fly ash combinations showed slightly better tension stiffening effect compared to other mixtures.

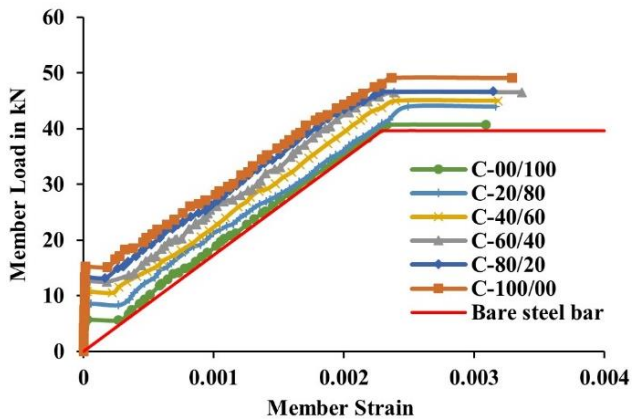
Figures 8 (a), (b), and (c) demonstration the tensile stress in concrete over member strain of all specimens. It is evident that among all mixes, the specimens with high GGBFS gave better tensile stress values compared to those with lower GGBFS. In the mixes A, B and C, specimens having 100% GGBFS showed highest tensile stress values. Similarly, specimens with 80% GGBFS also gave better values; this is due to better bonding between concrete and steel. Bond effects were primarily responsible for the tension stiffening effect in cracked R.C. members [29-31].



(a)



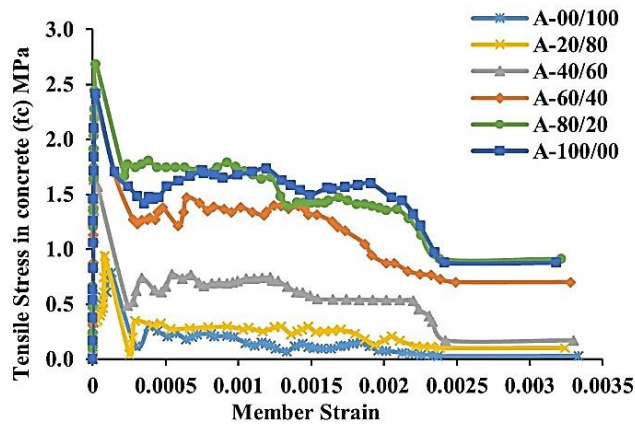
(b)



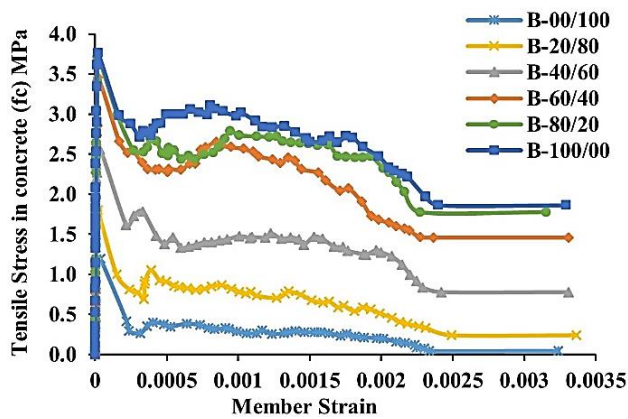
(c)

Fig. 7. Member Load vs Member Strain at various GGBFS and Fly ash ratios (a) Mix-A, (b) Mix-B, and (c) Mix-C

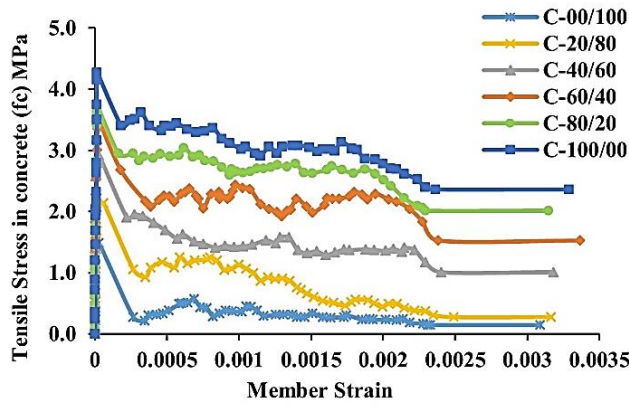
The maximum tensile stress of concrete in specimens was drastically reduced as the fly ash increased from the 0% to 100%. The maximum tensile stress of concrete at different fly ash to GGBFS ratios, i.e., 0/100, 20/80, 40/60, 60/40, 80/20, and 100/0, while in Mix-A were 0.93 MPa, 1.63 MPa, 2.39 MPa, 2.40 MPa, 2.6 MPa, and 2.41 MPa, while in Mix-B were 1.19 MPa, 1.80 MPa, 2.56 MPa, 3.46 MPa, 3.71 MPa, and 3.76 MPa, and in Mix-C 1.48 MPa, 2.14 MPa, 2.93 MPa, 3.52 MPa, 3.74 MPa, and 4.27 MPa were observed, respectively. Similar results were observed in this study when compared with the studies of Albitar [32] and Ganesan et al. [45, 46]. In the Albitar [32] study, the maximum tensile stress in concrete of 2.83 MPa was observed in fly ash-based GPC with a compressive strength of 35 MPa. Ganesan et al. [45] observed 2.5–3 MPa maximum tensile stress in plain FGPC of M40-grade concrete. Another Ganesan et al. [46] study observed 3–3.5 MPa maximum tensile stress in plain fly ash and GGBFS-based GPC containing M40 grade concrete. In the present study, specimens that achieved 40 MPa compressive strength had the maximum tensile stresses in concrete: 3.46 MPa, 3.71 MPa, and 3.76 MPa were observed in 60/40, 80/20, and 100/0 fly ash and GGBFS proportions in Mix-B mixes, respectively, and 3.52 MPa in 60/40 fly ash and GGBFS proportions in Mix-C mixes.



(a)



(b)



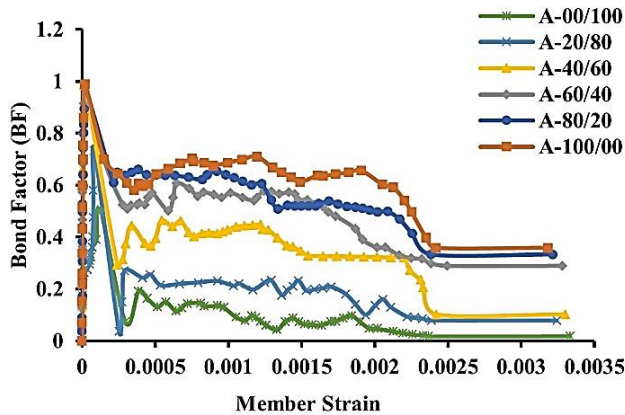
(c)

Fig. 8. Tensile stress in concrete vs Member strain at different GGBFS/Fly ash proportions (a) Mix-A, (b) Mix-B, and (c) Mix-C

#### 4.4 Bond Factor or Tension Stiffening Bond Factor

In this investigation, bond factor (BF) is calculated by taking the ratio of average load carried by the cracked concrete to load carried by concrete at first crack. It is represented by “ $\beta$ ” and its value generally varied between 0 to 1. In some cases, it may greater than 1. Better bond factor reveals that the better the member stiffness during the cracking of the member.

The bond factors of all mixes over member strain represented in Figures 9 (a), (b), and (c). In this context, if the bond factor is higher, which indicates that member stiffness is also higher, when compared to the remaining proportions in all the mixes, those mixes with 100% and 80% GGBFS content exhibited better bond factors. This indicates that the as the inclusion of fly ash in mixes, brittleness of member is decreased and enhance slightly the tension stiffening properties some extent. This is due to better bonding between concrete and steel. Since bond effects were primarily responsible for the tension stiffening effect in cracked R.C. members [29-31]. The bond factors dropped as fly ash content increases beyond 20%. This is due higher levels fly ash contents required better curing conditions and high molarity NaOH solutions. But in this investigation ambient curing and low molarity NaOH solutions are adopted.



(a)

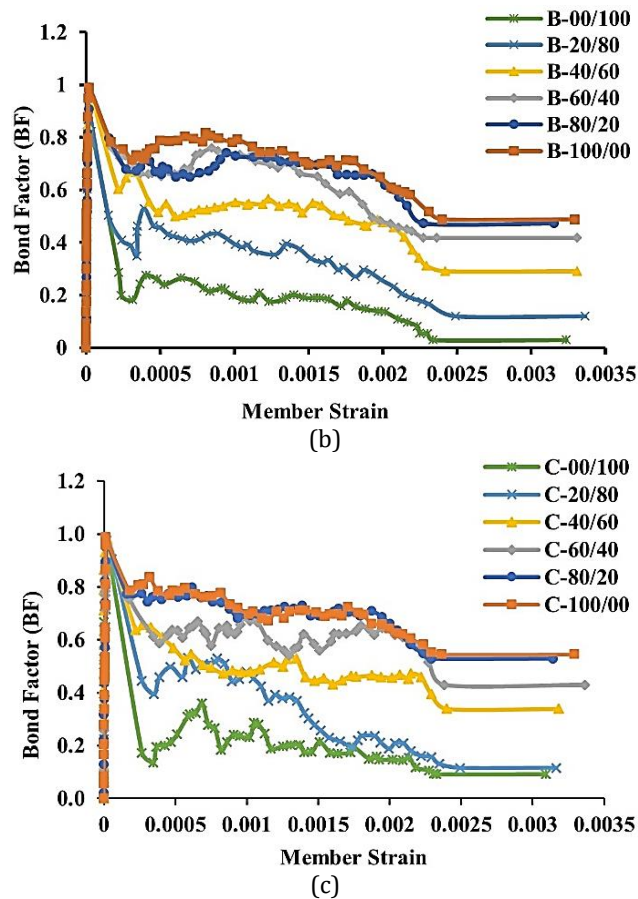


Fig. 9. Bond factor vs Member Strain at various GGBFS and Fly ash proportions (a) Mix-A, (b) Mix-B, and (c) Mix-C

The average bond factors improved as GGBFS content increased in all mixes. Among all the mixes, mix-C showed better average bond factor; these specimens indicated that there was better tension carrying capacity between the cracks after the first crack occurred. Similarly, all the mixes A, B, and C specimens having 60%–100% GGBFS had better bond factors and showed almost identical values at certain member strains. Mix-C specimens exhibited better average bond factors than mix-B and mix-A specimens, and mix-B specimens exhibited better average bond factors than mix-A. Overall, in all the mixes, the tension stiffening factor, or bond factor, varied from 0 to 1. Similar kinds of tension stiffening behaviour between the cracks (tension stiffening bond factor) were observed in this study when compared with the studies of Albitar [32] in fly ash-based GPC with a compressive strength of 35 MPa and plain FGPC of M40-grade concrete and plain fly ash and GGBFS-based GPC containing M40-grade concrete in Ganesan et al. [45, 46]. In Albitar [32] and Ganesan studies, the bond factors exist between 0 and 1. In Ganesan et al. [45, 46] studies, specimens having fly ash and the GGBFS combination exhibited better bond factors (tension stiffening behaviour between the cracks) compared to specimens having only fly ash. Similarly, in this study, specimens with fly ash and GGBFS combinations also exhibited better bond factors. Since better synergy existed between fly ash and GGBFS compared to fly ash as a sole binder.

### 4.5 Cracking Behavior

Cracking behavior is important in the limit state of serviceability of RC members. In this paper, an attempt is made to obtain a variation in the average crack spacing and the average maximum crack width as the load on the member increases and during the yield phase. Fig.10 illustrates the cracks formations and number of cracks of the tested prism. First crack formation was observed central region of the prism of most prisms, but two cracks also appeared at the same time in some members. The cracks that developed on all sides of the member were not uniform. When there is increasing in load, an increase in first crack width was observed.



Fig. 10. Crack patterns of the specimen

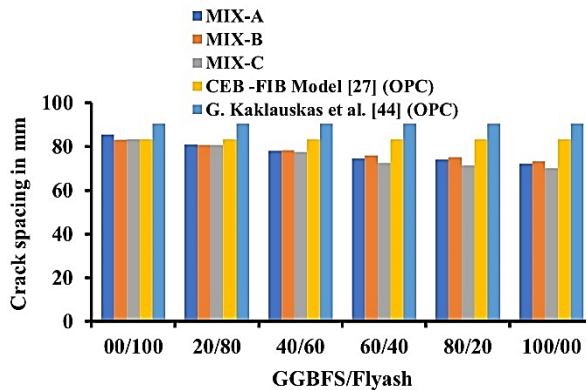


Fig. 11. Crack spacing comparison

Among all the mixes, minimum crack widths and reduced crack spacings were obtained at 100%, 80% and 60% GGBFS percentages. When GGBFS replacement exceeds 60%, both crack spacings as well as crack widths are increased. Fig.11 showed the average crack spacing in all the mixes, and these were compared with the CEB-FIB model code [27], as well as with proposed crack equations from G. Kaklauskas et al. [44]. The obtained values underestimated the CEB-FIB model code [27] and G. Kaklauskas et al. [44] equation some extent. But the variation observed between present experimental code and existed CEB-FIB model code [27] and G. Kaklauskas et al. [44] equation is below 10%. Ganesan et al. [45, 47] also reported that crack spacing for plain GPC consistent with CEB model code. Among all mixes, mixes containing 60% to 100% GGBFS had small crack spacing. This indicates that these mixes give better results from a serviceability point of view. Reduced crack spacing is frequently advantageous in terms of serviceability and plastic deformity aspect [47]. Closer results (crack spacings) were obtained in this study when compared with the studies of Ganesan et al. [45, 46], plain FGPC of M40-grade concrete, plain fly ash, and GGBFS-based GPC containing M40-grade concrete.

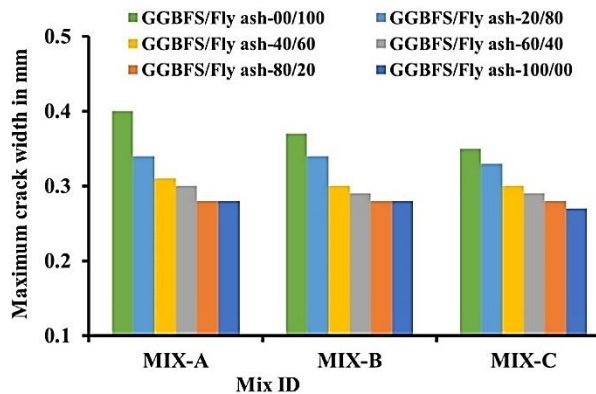


Fig. 12. Maximum crack width comparison

Ganesan et al. [45] observed 78.5 mm maximum average crack spacing in plain FGPC of M40-grade concrete. Another Ganesan et al. [46] study observed 73 mm maximum average crack spacing in plain fly ash and GGBFS-based GPC containing M40 grade concrete. In the present study, specimens that achieved 40 MPa compressive strength had the maximum average crack spacings in concrete: 83.1 mm, 80.76 mm, and 78.35 mm were obtained in 60/40, 80/20, and 100/0 fly ash and GGBFS proportions in Mix-B mixes, respectively, and 77.5 mm in 60/40 fly ash and GGBFS proportions in Mix-C mixes.

Fig.12 showed the maximum crack widths of all tested specimens. These crack width values were minimums in mixes having 100%, 80%, and 60% GGBFS compared to the remaining mixes. Reduced spacings and narrow crack widths are obtained, when the members have 60%-100% GGBFS compared to the remaining mixes. Replacing GGBFS with fly ash increases workability, reduces brittleness and thereby improves fresh, strength and cracking properties to some extent. And also, the better bonding between concrete and steel existed in these proportions. This implies that the synergy between fly ash and GGBFS binder is greater than the sole binder (fly ash or GGBFS-based). The obtained crack widths (mixes having 40%-100 % GGBFS) are within permissible limits specified by CEB-FIB model code [27] and Eurocode-2 [28]. The obtained maximum average crack widths are closer and more consistent with the results obtained in Ganesan et al. [45, 46] studies. But underestimated results were obtained by Albitar [32].

## 5. Conclusions

In this study, fresh, tension stiffening (strength), and cracking characteristics of AAC with different proportions of fly ash and GGBFS has been investigated. From this study, it was found that

- The workability of all mixes in terms of slump has decreased with an increase in GGBFS content in the total binder from 0% to 100%. But slump values decreased with increased GGBFS. When the GGBFS percentage was increased from 0% to 100%, slump values decreased by 54.17% in mix A, 60.17% in mix B, and 63.54% in mix C. An increase in GGBFS content from 0% to 100% increased the compressive, split tensile and flexural strength of the composites under ambient curing. Due to low concentration of alkaline solution and lack of heat curing, better hydration is not achieved in mixtures with high fly ash percentages, resulting in low compressive strength of those specimens. Maximum compressive strength 27.03 MPa in mix-a, 49.51 MPa in mix-B, and 65.81 MPa in mix-C were obtained when

100% GGBFS as used as binder. Maximum compressive strengths were achieved after 28 days curing in mix-A, mix-B, and mix-C at 100% GGBFS and 0% fly ash content, which are 27.03 MPa, 49.51 MPa, and 65.81 MPa in mix-A, B, and C respectively.

- From the load-member strain response, in most of the mixes, tension stiffening effect improved as the GGBFS rose from 0% to 100%. Tension stiffening effect is slightly similar when mixes have 100%-0% and 80%-20% of GGBFS-fly ash proportions compared to all mixes after first crack. Among all the mixes, mix-C showed better average bond factor; these specimens indicated that there was better tension carrying capacity between the cracks after the first crack occurred. In the present study, specimens that achieved 40 MPa compressive strength had a first crack load of 12.30 kN, 13.20 kN, and 13.40 kN in 60/40, 80/20, and 100/0 fly ash and GGBFS proportions of Mix-B mixes, respectively, and 12.50 kN in 60/40 fly ash and GGBFS proportions of Mix-C mixes.
- Minimum crack widths and reduced crack spacings were obtained at 100%, 80% and 60% GGBFS percentages compared to the remaining mixes. This is due to the improved synergy between fly ash and GGBFS than that of the sole binder (fly ash). The calculated crack spacings are in good agreement with CEB-FIB model, and the variations in crack spacings are below 10%.
- Hence, through this study, it can be concluded when fly ash and slag-based alkali activated concretes were prepared with solutions containing low NaOH concentrations and cured at room temperature, there was a rise in the tension stiffening (strength) and cracking properties with higher percentages GGBFS.
- However, from this study, it is recommended that there is a need for a detailed parametric study to predict equations for cracking and tensile characteristics of plain and R.C. alkali-activated geopolymer concrete tension members to assess the structural behaviour of members under ambient curing conditions in any environmental condition. The bond between steel bar and concrete can also be considered an influencing parameter in the behaviour of FSAAC.

## Acknowledgement

The authors acknowledge the support from NIT Warangal and the staff members of the material testing and Concrete Laboratory of the Department of Civil Engineering, NIT Warangal.

## References

- [1] Puertas F, Martínez-Ramírez S, Alonso S, Vázquez T. Alkali-activated fly ash/slag cements: Strength behaviour and hydration products. *Cement and concrete research*. 2000 Oct 1;30(10):1625-32. [https://doi.org/10.1016/S0008-8846\(00\)00298-2](https://doi.org/10.1016/S0008-8846(00)00298-2)
- [2] Thunuguntla CS, Gunneswara Rao TD. Appraisal on strength characteristics of alkali-activated GGBFS with low concentrations of sodium hydroxide. *Iranian journal of science and technology, transactions of civil engineering*. 2018 Sep; 42:231-43. <https://doi.org/10.1007/s40996-018-0113-4>
- [3] Mallikarjuna Rao G, Gunneswara Rao TD. Final setting time and compressive strength of fly ash and GGBS-based geopolymer paste and mortar. *Arabian journal for science and engineering*. 2015 Nov; 40:3067-74. <https://doi.org/10.1007/s13369-015-1757-z>
- [4] Mallikarjuna Rao G, Gunneswara Rao TD, Siva Nagi Reddy M, Rama Seshu D. A study on the strength and performance of geopolymer concrete subjected to elevated temperatures. In *Recent Advances in Structural Engineering, Volume 1: Select*



- Proceedings of SEC 2016 2019 (pp. 869-889). Springer Singapore. [https://doi.org/10.1007/978-981-13-0362-3\\_70](https://doi.org/10.1007/978-981-13-0362-3_70)
- [5] Karri SK, Ponnada MR, Veerani L. Development of eco-friendly GGBS and SF based alkali-activated mortar with quartz sand. Journal of Building Pathology and Rehabilitation. 2022 Dec;7(1):100. <https://doi.org/10.1007/s41024-022-00235-5>
- [6] Phoo-ngernkham T, Maegawa A, Mishima N, Hatanaka S, Chindaprasirt P. Effects of sodium hydroxide and sodium silicate solutions on compressive and shear bond strengths of FA-GGBFS geopolymer. Construction and Building Materials. 2015 Aug 30; 91:1-8. <https://doi.org/10.1016/j.conbuildmat.2015.05.001>
- [7] Singh SP, Murmu M. Effects of curing temperature on strength of lime-activated slag cement. International Journal of Civil Engineering. 2017 Jun; 15:575-84. <https://doi.org/10.1007/s40999-017-0166-y>
- [8] Bhowmick A, Ghosh S. Effect of synthesizing parameters on workability and compressive strength of fly ash based geopolymer mortar. International Journal of Civil & Structural Engineering. 2012;3(1):168-77.
- [9] Lee NK, Lee HK. Setting and mechanical properties of alkali-activated fly ash/slag concrete manufactured at room temperature. Construction and Building Materials. 2013 Oct 1; 47:1201-9. <https://doi.org/10.1016/j.conbuildmat.2013.05.107>
- [10] Hu Y, Tang Z, Li W, Li Y, Tam VW. Physical-mechanical properties of fly ash/GGBFS geopolymer composites with recycled aggregates. Construction and Building Materials. 2019 Nov 30; 226:139-51. <https://doi.org/10.1016/j.conbuildmat.2019.07.211>
- [11] Nath P, Sarker PK. Effect of GGBFS on setting, workability and early strength properties of fly ash geopolymer concrete cured in ambient condition. Construction and Building materials. 2014 Sep 15; 66:163-71. <https://doi.org/10.1016/j.conbuildmat.2014.05.080>
- [12] Fang G, Ho WK, Tu W, Zhang M. Workability and mechanical properties of alkali-activated fly ash-slag concrete cured at ambient temperature. Construction and Building Materials. 2018 May 30; 172:476-87. <https://doi.org/10.1016/j.conbuildmat.2018.04.008>
- [13] Beeby AW, Scott RH. Cracking and deformation of axially reinforced members subjected to pure tension. Magazine of concrete research. 2005 Dec;57(10):611-21. <https://doi.org/10.1680/macr.2005.57.10.611>
- [14] Chan HC, Cheung YK, Huang YP. Crack analysis of reinforced concrete tension members. Journal of Structural Engineering. 1992 Aug;118(8):2118-32. [https://doi.org/10.1061/\(ASCE\)0733-9445\(1992\)118:8\(2118\)](https://doi.org/10.1061/(ASCE)0733-9445(1992)118:8(2118))
- [15] Gupta AK, Maestrini SR. Tension-stiffness model for reinforced concrete bars. Journal of Structural Engineering. 1990 Mar;116(3):769-90. [https://doi.org/10.1061/\(ASCE\)0733-9445\(1990\)116:3\(769\)](https://doi.org/10.1061/(ASCE)0733-9445(1990)116:3(769))
- [16] Lee GY, Kim W. Cracking and tension stiffening behaviour of high-strength concrete tension members subjected to axial load. Advances in Structural Engineering. 2009 Apr;12(2):127-37.
- [17] Marti P, Alvarez M, Kaufmann W, Sigrist V. Tension chord model for structural concrete. Structural Engineering International. 1998 Nov 1;8(4):287-98. <https://doi.org/10.2749/101686698780488875>
- [18] Yankelevsky DZ, Jabareen M, Abutbul AD. One-dimensional analysis of tension stiffening in reinforced concrete with discrete cracks. Engineering Structures. 2008 Jan 1;30(1):206-17. <https://doi.org/10.1016/j.engstruct.2007.03.013>
- [19] Bischoff PH. Tension stiffening and cracking of steel fiber-reinforced concrete. Journal of materials in civil engineering. 2003 Apr;15(2):174-82. [https://doi.org/10.1061/\(ASCE\)0899-1561\(2003\)15:2\(174\)](https://doi.org/10.1061/(ASCE)0899-1561(2003)15:2(174))
- [20] Gribniak V, Mang HA, Kupliauskas R, Kaklauskas G. Stochastic tension-stiffening approach for the solution of serviceability problems in reinforced concrete:

- Constitutive modeling. Computer-Aided Civil and Infrastructure Engineering. 2015 Sep;30(9):684-702. <https://doi.org/10.1111/mice.12133>
- [21] Nayal R, Rasheed HA. Tension stiffening model for concrete beams reinforced with steel and FRP bars. Journal of materials in civil engineering. 2006 Dec;18(6):831-41. [https://doi.org/10.1061/\(ASCE\)0899-1561\(2006\)18:6\(831\)](https://doi.org/10.1061/(ASCE)0899-1561(2006)18:6(831))
- [22] Koeberl B, Willam K. Question of tension softening versus tension stiffening in plain and reinforced concrete. Journal of engineering mechanics. 2008 Sep;134(9):804-8. [https://doi.org/10.1061/\(ASCE\)0733-9399\(2008\)134:9\(804\)](https://doi.org/10.1061/(ASCE)0733-9399(2008)134:9(804))
- [23] Ian Gilbert R. Tension stiffening in lightly reinforced concrete slabs. Journal of Structural Engineering. 2007 Jun;133(6):899-903. [https://doi.org/10.1061/\(ASCE\)0733-9445\(2007\)133:6\(899\)](https://doi.org/10.1061/(ASCE)0733-9445(2007)133:6(899))
- [24] Kong KL, Beeby AW, Forth JP, Scott RH. Cracking and tension zone behaviour in RC flexural members. Proceedings of the Institution of Civil Engineers-Structures and Buildings. 2007 Jun;160(3):165-72. <https://doi.org/10.1680/stbu.2007.160.3.165>
- [25] Muhamad R, Ali MM, Oehlers DJ, Griffith M. The tension stiffening mechanism in reinforced concrete prisms. Advances in Structural Engineering. 2012 Dec;15(12):2053-69. <https://doi.org/10.1260/1369-4332.15.12.2053>
- [26] Abdulrahman H, Muhamad R, Azim MF. Tension stiffening behaviour of ordinary Portland and geopolymers concrete: A review. In AIP Conference Proceedings 2020 Oct 20 (Vol. 2284, No. 1). AIP Publishing. <https://doi.org/10.1063/5.0027322>
- [27] Code, CEB-FIP Model. "Comité euro-international du béton." Bulletin d'information 213 (1995): 46.
- [28] Eurocode 2 EN1992: Design of Concrete Structures (1992).
- [29] Fields K, Bischoff PH. Tension stiffening and cracking of high-strength reinforced concrete tension members. Structural Journal. 2004 Jul 1;101(4):447-56. <https://doi.org/10.14359/13330>
- [30] Bischoff PH. Effects of shrinkage on tension stiffening and cracking in reinforced concrete. Canadian Journal of Civil Engineering. 2001 Jun 1;28(3):363-74. <https://doi.org/10.1139/j00-117>
- [31] Kaklauskas G, Gribniak V, Bacinskas D, Vainiunas P. Shrinkage influence on tension stiffening in concrete members. Engineering structures. 2009 Jun 1;31(6):1305-12. <https://doi.org/10.1016/j.engstruct.2008.10.007>
- [32] Albitar M, Ali MM, Visintin P. Evaluation of tension-stiffening, crack spacing and crack width of geopolymer concretes. Construction and Building Materials. 2018 Jan 30; 160:408-14. <https://doi.org/10.1016/j.conbuildmat.2017.11.085>
- [33] IS: 12089-1987, Specification for Granulated Slag for The Manufacture of Portland Slag Cement.
- [34] IS 3812 (Part 1) :2003, Indian Standard Pulverized Fuel Ash Specification Part 1 for use as Pozzolana in Cement, Cement Mortar and Concrete.
- [35] IS 383, "Indian Standard Coarse and Fine Aggregate for Concrete," Bureau of Indian Standards, (2016)
- [36] IS 9103: 1999, Indian Standard Concrete Admixtures - Specification.
- [37] Thunuguntla CS, Gunneswara Rao TD. Mix design procedure for alkali-activated slag concrete using particle packing theory. Journal of Materials in Civil Engineering. 2018 Jun 1;30(6):04018113. [https://doi.org/10.1061/\(ASCE\)MT.1943-5533.0002296](https://doi.org/10.1061/(ASCE)MT.1943-5533.0002296)
- [38] IS:7320 - 1974, specification for concrete slump test apparatus.
- [39] IS: 516 - 1959, Indian Standard methods of tests for strength of concrete.
- [40] ASTM C-293-02, "Standard Test Method for Flexural Strength of concrete (using Simple Beam with Center-Point Loading)," International Standard Organization, (2002).
- [41] Diaz-Loya EI, Allouche EN, Vaidya S. Mechanical properties of fly-ash-based geopolymer concrete. ACI materials journal. 2011 May 1;108(3):300. <https://doi.org/10.14359/51682495>

- [42] Sofi M, Van Deventer JS, Mendis PA, Lukey GC. Engineering properties of inorganic polymer concretes (IPCs). *Cement and concrete research*. 2007 Feb 1;37(2):251-7. <https://doi.org/10.1016/j.cemconres.2006.10.008>
- [43] Khalfallah S, Guerdouh D. Tension stiffening approach in concrete of tensioned members. *International Journal of Advanced Structural Engineering*. 2014 Mar; 6:1-6. <https://doi.org/10.1007/s40091-014-0051-8>
- [44] Kaklauskas G, Ramanauskas R, Ng PL. Predicting crack spacing of reinforced concrete tension members using strain compliance approach with debonding. *Journal of Civil Engineering and Management*. 2019 May 2;25(5):422-30. <https://doi.org/10.3846/jcem.2019.9871>
- [45] Ganesan N, Indira PV, Santhakumar A. Influence of steel fibres on tension stiffening and cracking of reinforced geopolymer concrete. *Magazine of concrete research*. 2014 Mar;66(6):268-76. <https://doi.org/10.1680/macr.13.00273>
- [46] Ganesan N, Sahana R, Indira PV. Effect of hybrid fibers on tension stiffening of reinforced geopolymer concrete. *Advances in concrete construction*. 2017 Feb;5(1):075. <https://doi.org/10.12989/acc.2017.5.1.75>
- [47] Zwicky D. Bond and ductility: a theoretical study on the impact of construction details-part 1: basic considerations. *Advances in concrete construction*. 2013 Mar;1(1):103. <https://doi.org/10.12989/acc.2013.1.1.103>



## Experimental investigation and numerical optimization of sheet metal forming limits during deep drawing process of DD14 steel

Faouzi Hamza<sup>\*1,a</sup>, Ouzine Boussaid<sup>2,b</sup>, Hamid Hamadache<sup>3,c</sup>, Abdelmoumene Guedri<sup>4,d</sup>

<sup>1</sup>Department of Mechanical Engineering, Badji Mokhtar University, Annaba, Algeria

<sup>2</sup>Department of Mechanical Engineering, Badji Mokhtar University, Research Laboratory of Research on Industrial Risks, Control and Safety, Annaba, Algeria

<sup>3</sup>Department of Mechanical Engineering, Badji Mokhtar University, Research Laboratory of Advanced Technology in Mechanical Production (LRATPM), Annaba, Algeria

<sup>4</sup>Department of Mechanical Engineering, Med Chérif Messaadia University, Souk Ahras, Algeria

### Article Info

### Abstract

#### Article history:

Received 09 Dec 2023

Accepted 26 Feb 2024

#### Keywords:

DD14 steel;  
Experimental investigation;  
Numerical optimization;  
Forming limit curve;  
Deep drawing

This work aims to experimentally study the deep drawability of DD14 hot-rolled steel sheets and to optimize numerically the material formability. The material anisotropy was confirmed by metallographic analysis of the material and tensile tests on specimens taken in three orientations with respect to the sheet rolling direction. Where the stress-strain curves show a sensitivity of material to the Piobert-Lüders phenomenon. The die pressure and the blank holder were considered as controlling factors on plastic instability and the success of the deep drawing operation. The forming limit curves (FLC) were plotted to highlight the different deformation modes that the sheet metal underwent during the deep drawing process. The collected deep-drawn parts observation shows severe plastic instability, until fracture. The initial plastic anisotropy is determined by the Hill48 quadratic criterion and the work hardening by the Hollomon power law. It results, during the experimental tests, that the front bottom corners of the deep drawn part are the areas at high risk of damage. The various numerical simulation scenarios followed by comparisons with the experimental results, allowed us to confirm the optimum conditions that minimize the material's plastic instability risks, forming operation "Step" and BHP "Amplitude".

© 2024 MIM Research Group. All rights reserved.

## 1. Introduction

The forming processes make it possible to manufacture complex mechanical parts such as vehicle body components, household appliances, kitchen utensils and many others. The deep drawing being one of these processes is characterized by the plastic deformation of a sheet in order to obtain the desired shape. To do this, a stamping operation requires three main tools: the die, the blank holder and the punch. The blank is the sheet metal to be formed, positioned and held by the blank holder pressure. The forming operation is ensured by the action of the punch, which sinks into the blank until it matches the shape of the die. This action is carried out under penetration pressure at a certain speed to give the sheet the desired geometric shape. This process, difficult to master, depends on numerous criteria linked to the geometry of the finished product, the nature of the material and the working conditions.

The plastic instability of materials is one of the main causes of necking and mechanical fracture phenomena. This phenomenon is more increased in the case of deep drawing,

\*Corresponding author: [faouzi-hamza@hotmail.fr](mailto:faouzi-hamza@hotmail.fr)

<sup>a</sup> [orcid.org/0000-0002-2948-6281](https://orcid.org/0000-0002-2948-6281); <sup>b</sup> [orcid.org/0000-0002-5655-5676](https://orcid.org/0000-0002-5655-5676); <sup>c</sup> [orcid.org/0000-0002-3373-5738](https://orcid.org/0000-0002-3373-5738);

<sup>d</sup> [orcid.org/0000-0001-6406-8678](https://orcid.org/0000-0001-6406-8678)

DOI: <http://dx.doi.org/10.17515/resm2024.118me1209rs>

Res. Eng. Struct. Mat. Vol. 10 Iss. 3 (2024) 1321-1338

where it results in thinning and/or wrinkling of deep-drawn metal sheets. The anisotropy and friction of the material in the deep drawing device make the problem linked to its forming more complex. Several investigations have been carried out in this area. One of the difficulties of plastic instability is the material sensitivity to the Piobert-Lüders phenomenon, which manifests in the appearance of persistent sliding bands during the elastoplastic deformation. In the presence of this phenomenon, the tensile test curves show heterogeneity of the strain and a discontinuity of the elastic limit. We then witness two values of this property, higher and lower [1]. This discontinuity of  $R_e$  is more marked in mild steel and cast iron, in reason to the presence of small quantities of carbon or nitrogen [2].

It appears that the more random the distribution of carbides and more their forms are spheroidal, the more likely it is that the Piobert effect occurs. At large grain sizes,  $\epsilon_L$  becomes very small and the Lüders deformation bands disappear. However, other undesirable surface roughness makes the orange peel phenomenon appear. During sheet metal forming, differently oriented grains have the ability to deform independently, generating the formation of bands on the surface. Larger the grains more apparent the effect [3]. This phenomenon is undesirable for deep-drawing steel sheets because the deformation bands it causes are prominent on the surface after the sheets are deep-drawn [4].

The formation of the Piobert-Lüders phenomenon in ferritic mild steel has been the subject of several researches. In this context, Mazière et al. [5] studied by experimental and numerical analysis the Lüders phenomenon in low-carbon ferritic steel under simple shear load. Wenman and Chard-Tuckey [6] studied the Lüders deformation in ferritic steel tensile specimens by modeling and experimental material characterization and found some differences between the model responses when the level of plastic strain was lower than the Lüders strain presented by the material. Mao and Liao [7] studied the effects of ferrite grain size, pearlite volume fraction and pearlite interlamellar spacing on flow behavior. The study was carried out by modeling the elongation of the Lüders bands and hardening behaviors of two-phase ferrite-pearlite steels under tension. Further investigations into this phenomenon have been carried out by the finite element method [8-9].

Keeler [10] introduced the forming limit diagrams. These were constructed empirically to describe the deformation states known as the Keller-Goodwin curve, these curves show combinations of major and minor strains, from which a much-localized area of thinning or necking becomes visible on the sheet metal surface. Boudeau and Gelin [11] studied the influence of macroscopic and microscopic properties on the necking of metal sheets. Doege and El-Dsoki [12] Investigated by experimental and numerical simulation the initiation and propagation of cracks during the deep drawing process of X5 Cr Ni 18 9 steel. They were able to identify two different types of cracks which can lead to material failure. Jain et al. [13] determined experimentally the forming limit curve at necking and fracture, using a ductile fracture criterion to predict the fracture limit of aluminum sheets for automobiles.

The sensitivity of material plastic instability to the forming process parameters is also the subject of other studies. Where Kardan et al. [14] studied experimentally and by finite element method the influence of deep drawing parameters on the residual stresses evolution. Hamza et al. [15] studied by numerical simulation the deep drawing parameter's effect on the plastic strain evolution in the metal sheet during the forming operation. Habeeb et al. [16] studied how the Single-Point incremental forming process parameters impact the blank surface roughness. Rabia et al. [17] investigated how PVD coatings, lubrication conditions, and operating parameters impact tribological behavior, forming forces, and energy consumption when deep drawing is performed. An innovative test rig

will be utilized to record force-time variations, frictional interactions, and energy consumption under various conditions, such as lubrication and non-lubrication.

The blank material must be suitable for the deep drawing operation; Torkar et al. [18] determined the effect of the cementite particle/ferrite matrix interface on microcrack formation and its influence on the drawability of low-carbon steel. Some authors have proposed criteria and models as solutions to certain metal-forming problems. Ma et al. [19] proposed a ductile fracture criterion in order to predict the forming limit curve at fracture. Also, Butuc et al. [20] presented an experimental validation of a new prediction model of the forming limit curve under linear and complex deformation paths. Matin et al. [21] proposed a method for calculating the stress field corresponding to the local necking. The proposed method is designed to circumvent traditional difficulties associated with detecting and measuring strains at local necking regions of a forming limit in aluminum alloys. Stoughton and Yoon [22] determined the forming limit curve based on the stress-strain fields and discussed the parameters of the non-linear deformation. Several studies have been carried out to evaluate and analyze the formability of metal sheets. Li et al. [23] developed an analytical approach for predicting the forming limit with a non-linear strain path after pre-strained in uniaxial and biaxial tension for Aluminum alloy sheets. Kumar [24] studied the formability of different sheet materials, taking into account different parameters such as thickness, hardening coefficient and normal anisotropy. Aghaie-Khafri and Mahmudi [25] presented an analytical method to predict the forming limit curve of two aluminum alloys, with a theoretical and experimental analysis of the biaxial strain limit. Based on strains and stresses, Paul [26] contributed to the theoretical analysis of several instability criteria to construct a strain and stress-based forming limit diagrams, including the diffuse bifurcation analysis, the neck formation of through-thickness and the shear stress-based criteria onset of through-thickness necking. Paul, in review works, explains why HER (Hole Expansion Ratio) is currently an essential topic of engineering research [27], summarizes the factors affecting FLC comprehensively to help in decision-making in material selection and process design [28] and investigate how different tensile pre-straining methods affect the high cycle fatigue, low cycle fatigue, and notch fatigue performance of automotive grade dual phase steels. [29].

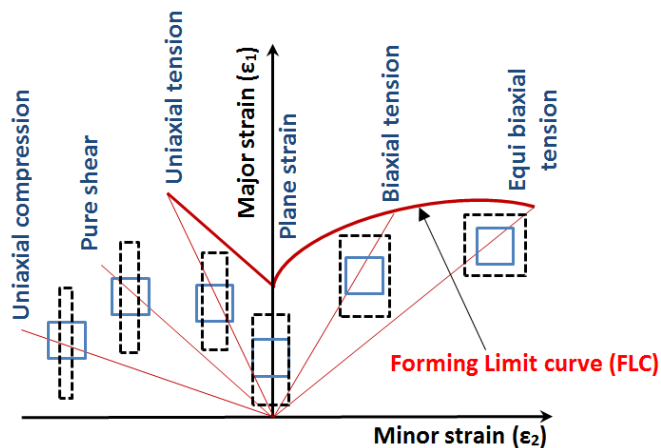


Fig. 1. Schematic representation of forming limit diagram (FLD) [26, 28, 29]

Often, the process technology varies according to the desired goal. The parameters affecting the formability of sheets are numerous and include among others: pressure, speed, thickness of the sheet, lubrication, or even the initial state of the material and the

thermal or mechanical treatment it has undergone. Furthermore, the output responses depend largely on the combination of the parameters between them and the resulting interactions. However, industrial deep drawing operations are based on the constancy of working conditions and parameters. Thus, in a technical-economic concern, the present work aims to study by experimental approach the influence of the blank holder pressure on the damages of the deep drawn parts of DD14 steel sheets and by numerical simulation the forming operation speed and the BHP amplitude on the material plastic instability, using an explicit finite element model from Abaqus/CAE software. The aim is to identify the optimum levels of process parameters that minimize the risk of necking and fracture during plastic instability of deep-drawn metal sheets. The anisotropy of the material was demonstrated from uniaxial traction tests carried out on specimens taken in three different directions. The FLC plots served as a fundamental tool for formability optimization. Finally, the practical execution and simulation of the deep drawing test made it possible to locate areas with high plastic instability.

## 2. Experimental Method

### 2.1. Material

The material studied is a mild steel grade DD14 complying with European standard EN 10111. The choice of this material is motivated by its large-scale use in the company's workshop GEMELEC El Kouif Tebessa, Algeria. The chemical composition mainly consists of 0.08%C, 0.35%Mn and 0.03%Si. The material is delivered in the hot-rolled, pickled and oiled state and has the mechanical properties given in Table 1.

Table 1. Tensile properties of DD14 steel

EN 10111	Mechanical characteristics		
DD14	Re (MPa) 220-280	Rm (MPa) 320-370	A90 % ≥ 33

The microstructure was revealed by surface chemical attack with Nital-based reagent, on previously coated and polished samples. Metallographic observation is made by a Nikon Eclipse LV100ND Microscope, with a magnification of 100x. revealed a ferritic microstructure hardened on the surface with different sizes of grains more or less elongated in the rolling direction (RD) likewise certain carbides (C) and sulfide inclusions (S) appeared at the grain boundaries (Fig. 2).

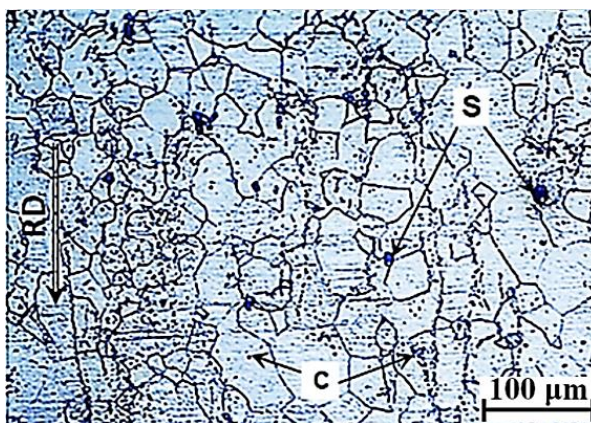


Fig. 2. Optical micrography of Microstructure of DD14 steel sample

## 2.2. Tensile Test

In order to highlight the material's anisotropy and its influence on mechanical behavior, uniaxial tensile tests were carried out on specimens taken in three directions (0°, 45° and 90°) with respect to the sheet's rolling direction (Fig. 3-a). The tests are carried out according to standard NF EN 10002-1 on a Zwick/Roell Z050 uniaxial tensile machine at room temperature, with a speed of 100 mm/min. Fig. 3-b shows the specimen geometry.

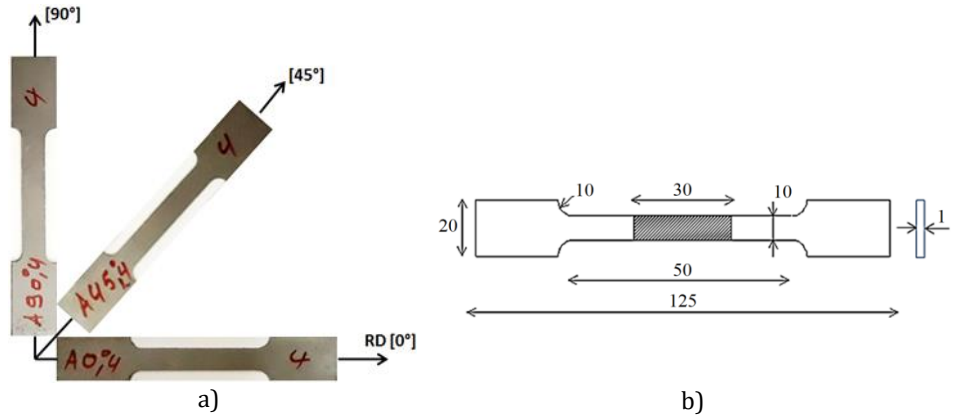


Fig. 3. Uniaxial tensile test specimen NF EN 10002, Sampling and geometry

Furthermore, the material's consolidation is supposed to obey Holloman's hardening law Eq (1) [30]. Thus, the hardening exponent ( $n$ ) and the strength coefficient ( $K$ ) of this law were estimated from the rational tensile curves.

$$\sigma_v = K \varepsilon_r^n \quad (1)$$

Where:  $\varepsilon_r$  and  $\sigma_v$  are true strain and true stress respectively.

## 2.3. Deep Drawing Test

The test was conducted industrially. Before submitting to the metal forming, a grid was drawn on the blank to be deep-drawn allowing the major and minor strains to be measured, to visualize their paths and to locate the most subjected areas to plastic strain for each test. In order to avoid unnecessary superposition and cluttering of experimental points on the FLC curve, squares of dimensions 50x50 mm<sup>2</sup> were chosen according to blank size and deep-drawn part geometry (Fig. 4).

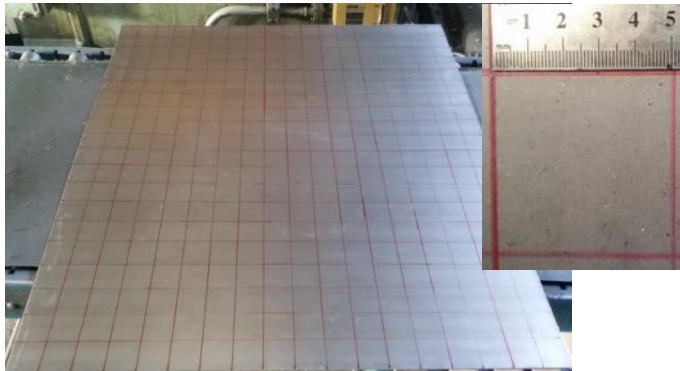


Fig. 4. Grid drawn on the blank



The tests were conducted with two main parameters, namely: die pressure (DP) and blank holder pressure (BHP). The forming action is obtained from the simultaneous displacement of the die and the blank holder, between them is held the blank, towards fixed punch on the press table. However, the blank holder pressure is the variable parameter in the tests.

#### 2.4. Modelling and Numerical Simulation

The material studied is characterized by anisotropic elastoplastic behavior. Anisotropy was taken into account in the numerical simulation through the Hill48 criterion [31]. This criterion states that the classical elastic function is the most important and frequently used method for metallic materials plastic anisotropy détermination. A rectangular Cartesian stress component can be used to express this extension of the isotropic Von Mises function, as follows Eq (2) [32]:

$$2f = F(\sigma_{yy} - \sigma_{zz})^2 + G(\sigma_{zz} - \sigma_{xx})^2 + H(\sigma_{xx} - \sigma_{yy})^2 + 2L\sigma_{yz}^2 + 2M\sigma_{zx}^2 + 2N\sigma_{xy}^2 = 1 \quad (2)$$

Where F, G, H, L, M and N are the Hill anisotropy coefficients, which can be expressed as follows Eq (3) [33]:

$$\begin{aligned} F &= \frac{1}{2} \left( \frac{1}{R_{22}^2} + \frac{1}{R_{33}^2} - \frac{1}{R_{11}^2} \right) \\ G &= \frac{1}{2} \left( \frac{1}{R_{11}^2} + \frac{1}{R_{33}^2} - \frac{1}{R_{22}^2} \right) \\ H &= \frac{1}{2} \left( \frac{1}{R_{11}^2} + \frac{1}{R_{22}^2} - \frac{1}{R_{33}^2} \right) \\ L &= \frac{3}{2R_{23}^2} \\ M &= \frac{3}{2R_{13}^2} \\ N &= \frac{3}{2R_{12}^2} \end{aligned} \quad (3)$$

Where R11, R22, R33 and R12 are the Hill anisotropy ratios that specify the material in the Abaqus FEM software.

These parameters can be expressed as follows in Eq (4) [33-34]:

$$\begin{aligned} R_{11} &= R_{13} = R_{23} = 1 \\ R_{22} &= \sqrt{\frac{r_{90}(r_0+1)}{r_0(r_{90}+1)}} \\ R_{33} &= \sqrt{\frac{r_{90}(r_0+1)}{(r_{90}+r_0)}} \\ R_{12} &= \sqrt{\frac{3r_{90}(r_0+1)}{(2r_{45}+1)(r_{90}+r_0)}} \end{aligned} \quad (4)$$

In the thin sheet metal forming process, the plane stress state is generally predominant. Consequently, only the four coefficients: F, G, H and N can be retained. These factors can be determined empirically from a monotonic tensile test following various sampling directions Eq (5) [35].

$$\begin{aligned}
 F &= \frac{r_0}{r_{90}(1+r_0)} \\
 G &= \frac{1}{1+r_0} \\
 H &= \frac{r_0}{1+r_0} \\
 N &= \frac{(r_0+r_{90})(2r_{45}+1)}{2r_{90}(1+r_0)}
 \end{aligned}
 \tag{5}$$

Where  $r_0$ ,  $r_{45}$  and  $r_{90}$  are the values of the anisotropy coefficient ( $r$ ) according to the directions,  $0^\circ$ ,  $45^\circ$  and  $90^\circ$  with respect to the rolling direction respectively.

The anisotropy coefficient ( $r$ ) is defined by the ratio of transverse strains Eq (6) [36]:

$$r = \frac{\varepsilon_2}{\varepsilon_3} = \frac{\ln \frac{b}{b_0}}{\ln \frac{t}{t_0}}
 \tag{6}$$

Where  $\varepsilon_2$  and  $\varepsilon_3$  are the strains in the width ( $b_0$ ) and thickness ( $t_0$ ) directions, respectively.

The stamping operation was simulated as performed industrially in the GEMELEC unit workshop. All experimental conditions were respected. The numerical deep drawing simulation model is run in 3D using Abaqus/CAE software. Fig. 5 shows the configuration of the forming tools and the blank. The geometry and mesh of the model are presented in the longitudinal section plane.

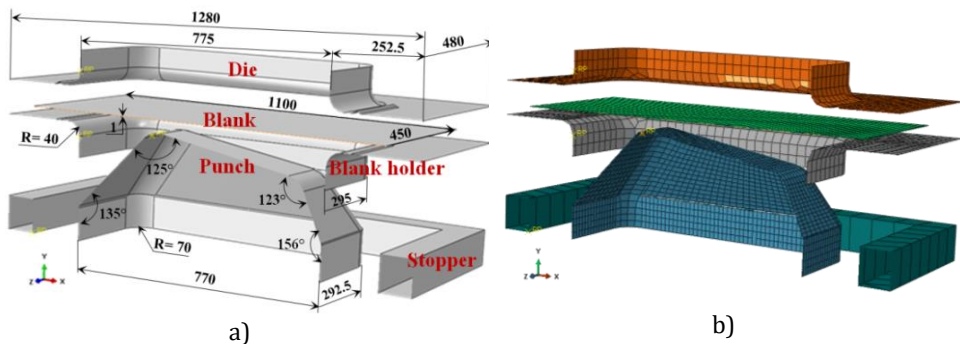


Fig. 5. Forming tools and blank, a) Drawing and b) Meshing

The boundary conditions for the simulation model have been derived from the different operations of the deep drawing manufacturing range (Fig. 6). The forming action is obtained by the die and the blank holder moving where between which the blank is maintained, compared to the fixed punch on the machine table. The die action takes place under controlled pressure until it reaches its final position once displaced 25mm.

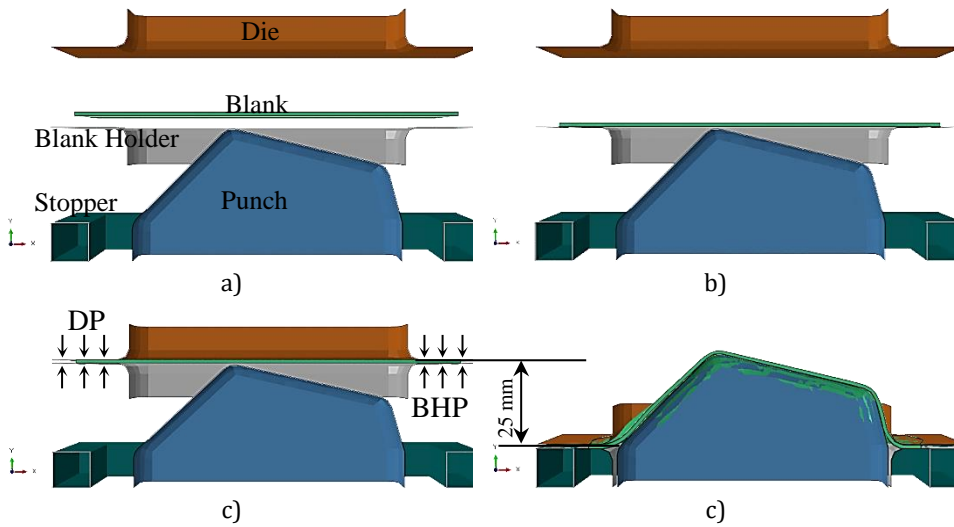


Fig. 6. Deep drawing manufacturing range; a) Initial position, b) Blank set-up, c) Die action and application of BHP and d) Final position after 25 mm stroke

### 3. Results and Discussion

#### 3.2. Tensile Test

Fig. 7 shows the true stress-true strain curve for the uniaxial tensile test. The sampling direction does not affect the material's behavior, as the curves show the same trends in both elastic and plastic deformation domains with presence of the Piobet-Lüders phenomenon. The slopes of the linear part of the three specimens seem to be confused, although Table 2 shows that tensile properties are weakest in the rolling direction and stiffness in terms of Young's modulus is highest when the material is tested in the 45° direction.

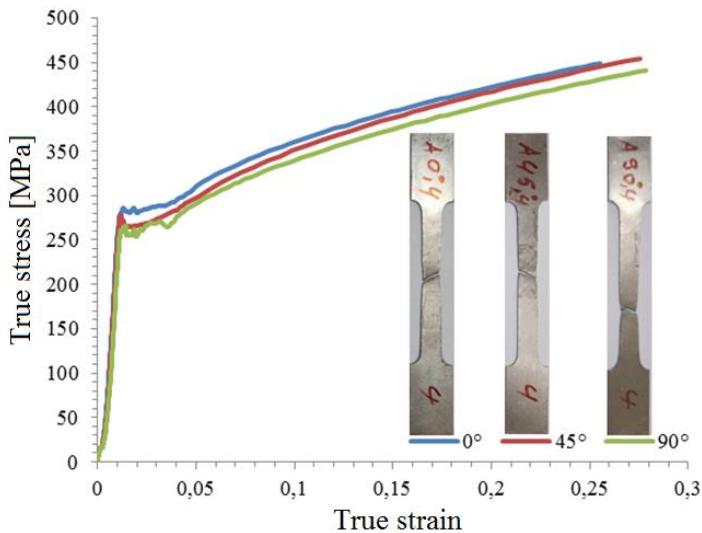


Fig. 7. Influence of sampling direction on true stress-true strain curves

This seems to be due to the material's low anisotropy ( $r_{45}=0.8$ ) in this direction. Rolling the sheet did not change the material's ability to undergo strain-hardening, whose coefficient ( $n=0.24$ ) remained constant regardless of the direction in which the specimen was taken, Table 2.

However, for all three samples tested, the curves show a discontinuity of  $R_e$ , which explains the material's sensitivity to the Piobet-Lüders phenomenon and consequently the appearance of two elastic limits ( $R_{eH}$  and  $R_{eL}$ ). The rolling direction is the most advantageous for this property and even offers the best tensile strength ( $R_m$ ) without sensitively affecting the material's elongation at fracture ( $A_{gt}(corr.) = 0.31\%$ ). The transverse direction ( $90^\circ$ ) is the least favorable for all tensile properties. The curve relating to this sampling direction shows the widest elastoplastic transition range and a more marked instability phenomenon (Necking) on the tensile specimen.

Table 2. Mechanical properties of DD14 steel

Direction	E (GPa)	$R_{eH}$ (MPa)	$R_{eL}$ (MPa)	$R_m$ (MPa)	$A_{gt}(corr.)$ %	r	n	K (MPa)
$0^\circ$	136,83	281,56	275,13	347,83	0.31	1,10	0.24	622,28
$45^\circ$	148,88	275,35	260,36	344,99	0.32	0,83	0.24	620.17
$90^\circ$	126,23	257,79	248,50	333,67	0.32	1,11	0.24	594.48

### 3.2. Deep Drawing Test

#### 3.2.1 Influence of Blank Holder Pressure

The evaluation of deformations was done by optical tracking. The observation made it possible to locate areas of necking or fractures, as well as the path of major and minor strains of each grid square. The measured values make it possible to plot the material's forming limit curve (FLC) (see section 3.2.2).

Fig. 8 shows an example of the deformation of the most solicited squares, in this case, the bottom front corners of the deep drawn part. The orientation of the grid lines enables us to determine the strain path and locate areas at risk of plastic instability. Under the deep drawing conditions shown in Fig. 8-a, the deformation path of the grid is indicated by the arrows oriented towards the front corners of the deep drawn part where the fracture is likely to occur.

These observations confirm those of Ref. [37], which show that due to excess material and/or a large difference between the corners, fractures initiate in the lower corners of the rectangular deep drawn part and then propagate diagonally.

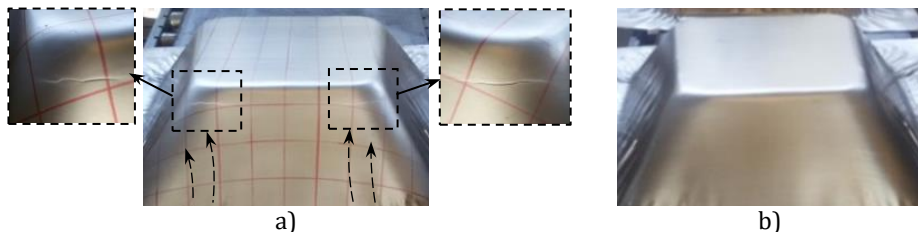


Fig. 8. Morphology of deep drawn parts under conditions; a) DP = 14 MPa, BHP = 10 MPa and b) DP = 14 MPa, BHP = 7 MPa

The extent of damage can be reduced or even spared if the deep drawing conditions are mastered. Figure 8-b shows that reducing the blank holder pressure gives a deep drawn part without necking and without fracture. However, this low pressure causes a slight increase in the wrinkle size which can affect the choice of the finished product quality.

Nevertheless, the phenomenon of wrinkling is not considered a reason for product rejection for the company. It is still necessary to optimize the deep drawing parameters to successfully complete the operation with the best quality.

### 3.2.2 Forming Limit Curve (FLC)

The FLC is a key result for judging sheet metal formability, both experimentally and in numerical simulation of the deep drawing process. The technique for plotting the FLC curve is inspired by Hecker's method of determining the limiting deformations; the simplicity of this method has led to its widespread use [38]. Therefore, for reasons of reducing the measures, only the most stressed squares and where the fracture could take place are taken into account (Fig. 9). For each numbered square, it is possible to locate and measure the deformations [39-41].

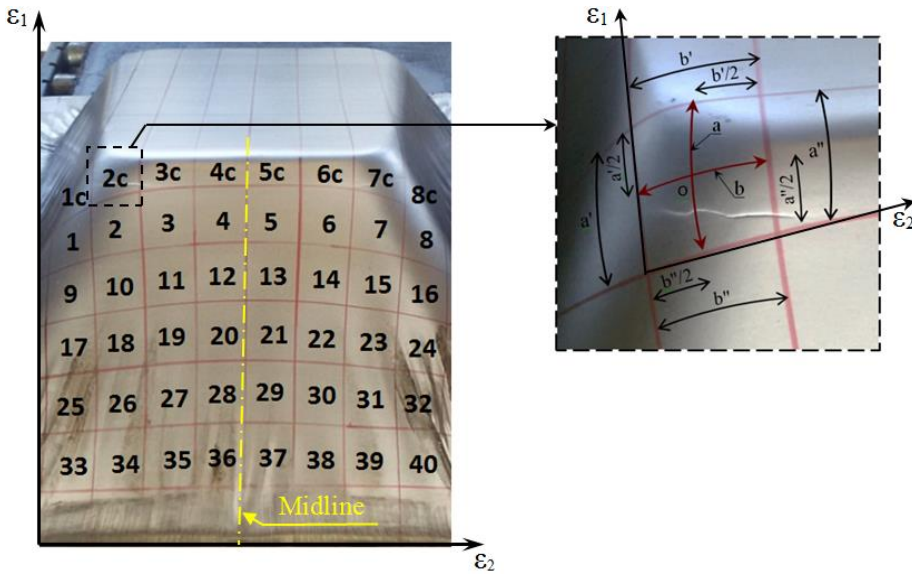


Fig. 9. Measuring method of grid deformations

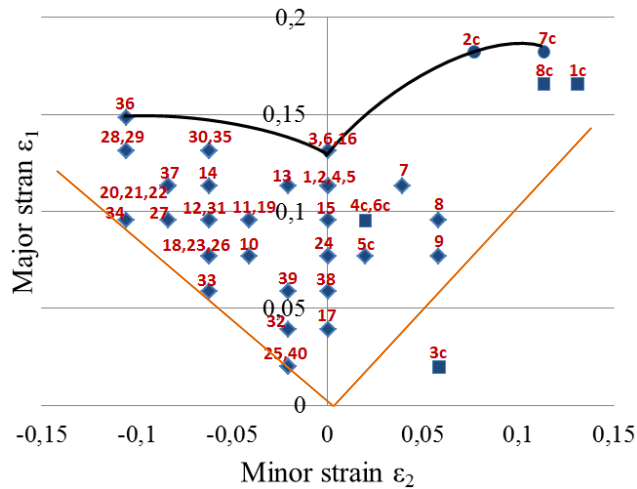
For better precision and to minimize random measurement errors, the dimensions of the deformed squares are evaluated relatively. To do this, the four sides ( $a'$ ,  $a''$ ,  $b'$ ,  $b''$ ) of the deformed square are measured individually. The final dimensions ( $a$  and  $b$ ) to be retained are measured between the centers of opposite sides two by two. The major and minor engineering strains are calculated as follows Eqs. (7)-(8) for evaluating the true major and true minor strains by Eq (9) [28].

$$e_1 = \frac{a-a_0}{a_0} \tag{7}$$

$$e_2 = \frac{b-b_0}{b_0} \tag{8}$$

$$\varepsilon_{1,2} = \ln (1 + e_{1,2}) \tag{9}$$

The graphic representation of the true strains in a reference frame ( $\varepsilon_1, \varepsilon_2$ ) makes it possible to trace the FLC (Fig. 10).



◆ Acceptable (4c, 5c et 1...40) ■ Necking (1c, 4c,6c et 8c) ● Fracture (2c, 7c)

Fig. 10. Experimental strains distribution during deep drawing of DD14 steel

It emerges from the analysis of this FLC curve that the limit points of strains (36, 3, 16, 2c and 7c) are those of the squares located at the deep drawn part bottom corners (2c and 7c) or at the edge of that (36, 16). In return, the majority of the squares were located in the uniaxial traction zone and some of them (25, 40, 32 and 33) located in the deep drawn part wall were deformed in the wrinkle form. Some grid elements traced on the sheet have undergone biaxial expansion (4c, 5c, 6c, 7, 8, 9) or insufficient traction (3c). The squares measured at the corners (1c, 2c, 7c and 8c) having suffered the fracture, are closest to the deep drawn part bottom where the sheet metal is more solicited to the balanced expansion, caused by the punch corner.

Some experimental points on the FLC curve were superimposed, which translates to the existence of deformation symmetry in areas equidistant from a midline between the frontal corners of the deep drawn part (Figure 8). The pairs of squares having undergone the same deformation during forming operation are located either on the front wall of the deep drawn part (3-6), (4-5), (18-23), (20-21) and (28-29) or on the corner of the latter, like pairs (1c-8c) and (2c-7c), with the exception of their minor strains which create a slight lack of symmetry. Generally, it was found that symmetry affects only 29.16% of the formed area, suggesting unstable elastoplastic behavior of the material during the deep drawing and that the tooling of the operation needs fine-tuning.

### 3.2.3 Modeling and Numerical Simulation

The anisotropy parameters (F, G, H, N) of the Hill 48 criterion and the anisotropy ratios (R11, R22, R33, R12, R13 and R23) are calculated from Eqs. (3)-(4). The obtained values in Table 3 are directly injected into the finite element calculation code Abaqus/CAE for numerical simulation of the deep drawing process.

Table 3. Anisotropic parameters for DD14 steel

Hill48 anisotropy coefficients				Anisotropy ratios			
F	G	H	N	R11 R13 R23	R22	R33	R12
0,468	0,475	0,524	1,260	1	1,003	1,029	1,091

A numerical simulation carried out under lubrication conditions with a coefficient of friction  $f=0.05$  and pressures  $DP= 14$  MPa,  $BHP= 10$  MPa provided a result almost identical to that of the experimental procedure (Fig. 11). Indeed, it can be seen that the major strain of the most solicited area is located at the front corners of the deep drawn part bottom.

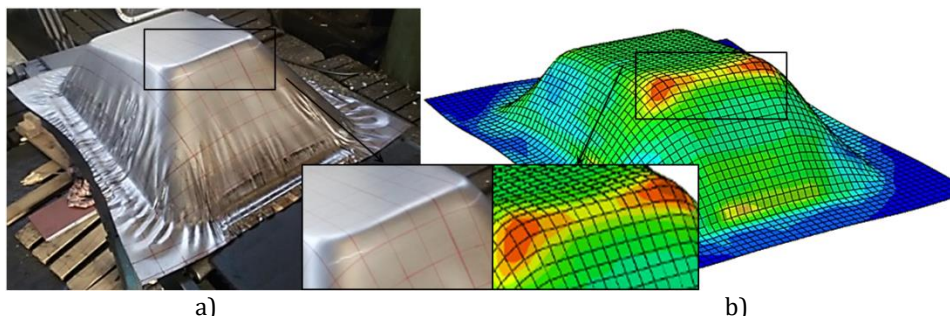


Fig. 11. Representation of deep-drawn, a) Experimental, b) Numerical simulation

For a deeper comparative analysis, the selected nodes for strain measurement were chosen in the same way as the experimental procedure (Fig. 12). The results of major and minor plastic strains measured at each node by the finite element code Abaqus/ CAE (PE22, PE11), allowed us to determine the true FLC curve according to Eq (9). Where PE11 is plastic strain component following the x-axis and PE22 is plastic strain component following the y-axis.

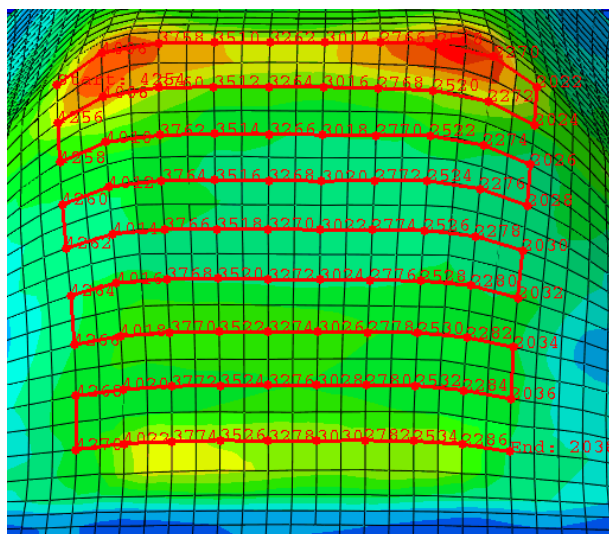


Fig. 12. Path of nodes concerned by the analysis

To adapt the operation time to the amplitude of the forming load, the simulation of the deep drawing operation was carried out by combining the "Step" module with "Load-Amplitude" in the finite element calculation code Abaqus/CAE. The numerical simulation took place in several scenarios, playing on the amplitude of the forming load and the execution time of the deep drawing operation. The best scenario results from a simulation conducted with  $DP=14$  MPa and  $BHP=10$  MPa (Fig. 13).

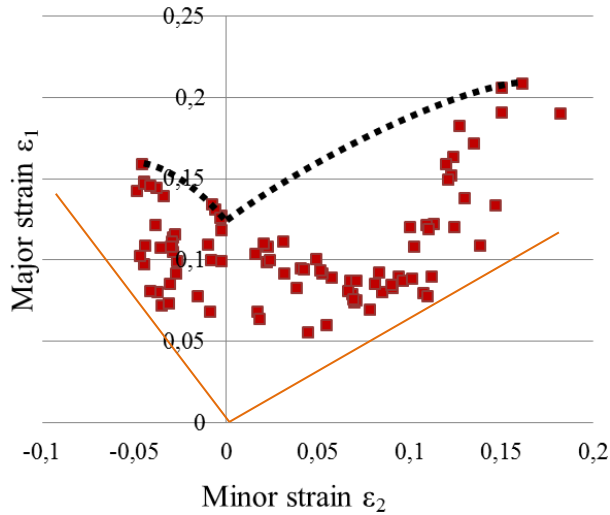


Fig. 13. Numerical simulation strains distribution during deep drawing of DD14 steel

Considering the maximum points for each deformation mode of the simulation FLC, respectively the uniaxial, planar and equi-biaxial modes, allowed us to determine the experimental-simulation comparative FLC curve.

The optimal FLC thus deduced shows the same trend as that obtained from the experimental test, though the material's formability range has expanded by 2% and 5% in terms of major and minor strains simultaneously (Fig. 14).

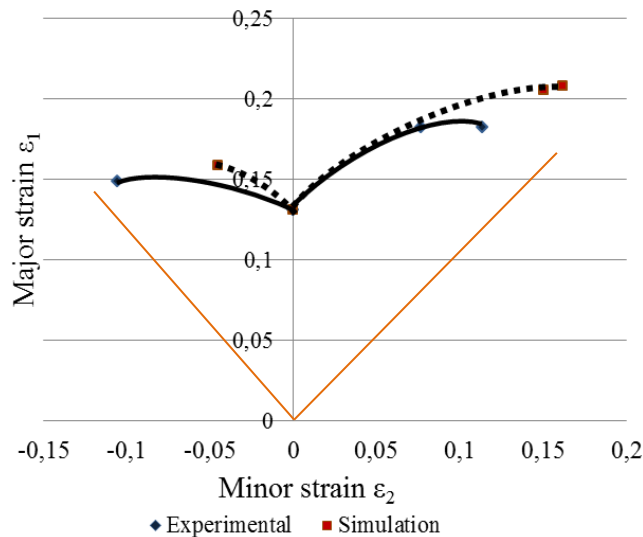


Fig. 14. Forming limit curve of DD14 steel

However, it should be noted that an adequate correlation between the amplitude of the forming load and the operation time enables the sheet to better adapt to equi-biaxial strain modes, according to the final geometry of the deep drawn part. These two factors are essential for optimizing formability. Numerical simulation, for its part, has shown that longer forming operation time can lead to uniform strain distribution in the sheet metal as a function of the applied load.



Comparatively with other results obtained in other similar studies, the punch corner or radius has a great influence on the damage of the deep drawn square parts. Where Fuh-Kuo et al. [42] studied the effect of punch radius in square-deep drawn parts. According to the findings, a larger punch radius enables a uniform material flow under the punch profile at corners, which delays the occurrence of fractures. Ravindra et al. [43] Confirmed, the punch-die corner region of a square cup has a smoother flow of material with an increase in the punch or die profile radius. As a result, the maximum width of the flange earring is decreased. Bouchaâla et al. [44] concluded that in the deep drawing process, the die shoulder radius and punch nose radius play a major role in force distribution and material flow during the forming operation, and so on...

#### 4. Conclusions

Plastic instability is manifested by a localization of plastic strain and is characterized by a weakening of the specimen section, leading to the fracture during the material forming. This study aims to better localize the phenomenon of plastic instability and reduce its undesirable effect during the deep drawing of DD14 steel sheets for a given geometry of deep-drawn parts. The following conclusions can be brought.

- The uniaxial tensile test provided a curve characterized by a discontinuity at the elastoplastic transition ( $R_e$ ), confirming the material's sensitivity to the Piobert-Lüders phenomenon. This phenomenon is more pronounced on specimens taken in the transverse direction ( $90^\circ$ ) compared to that of rolling.
- Hecker's method, more than being simple, allows us to accurately translate each strain measurement of grid squares into a well-identified experimental point in the FLC curve.
- The CLF of the material in the studied area shows the strain distribution, such that in the majority of cases, the strain cloud is in uniaxial and plane traction. Particularly, the located points in equi-biaxial deformation mode in the curve are the measured squares at the corners of the deep drawn part.
- The areas at a major risk of plastic instability were identified at the front corners of the deep drawn part bottom. Forming with low blank holder pressure leads to the appearance of wrinkles and makes it difficult for the material to flow. In return, high pressure causes fracture which begins in the sharp corners at the deep drawn part bottom where the diffuse necking is located at the end of the operation.
- Numerical simulation provided an FLC in good agreement with that deduced from the experimental test, through which the formability was optimized.
- Numerical simulation under various scenarios involving anisotropy, operation time and forming load amplitude has enabled us to predict the deformation modes experienced by the sheet to be deep drawn, risk areas to fracture and consequently to get a deep drawing optimal model.

This study could be extended to take into account all these factors, such as mechanical material behavior, punch corner radius, punch-die clearance, tool surface finish, friction and non-uniform blank thickness distribution, through a complete experimental test design to better surround the problem of plastic instability and make the deep drawing operation more successful.

## Nomenclature

• $A_{gt(\text{corr})}$	Total elongation for higher traction force
• $A_{90}$	Elongation at break in 90° direction (%)
• $K$	Strength coefficient
• $n$	Hardening coefficient
• $r$	Anisotropy coefficient
• $Re$	Yield strength (MPa)
• $Re_H$	Upper yield strength (MPa)
• $Re_L$	Lower yield strength (MPa)
• $Rm$	Tensile strength (MPa)
• BHP	Blank holder pressure (MPa)
• DP	Die pressure (MPa)
• $\sigma_v$	True stress (MPa)
• $\varepsilon_r$	True strain (%)
• $\varepsilon_1$	Major strain (%)
• $\varepsilon_2$	Minor strain (%)
• PE11	Plastic strain component following x-axis
• PE22	Plastic strain component following y-axis

## Abbreviations

• FLC	Forming Limit Curve
• FEM	Finite Element Method
• BHP	Blank Holder Pressure
• DP	Die Pressure

## Acknowledgment

We would like to thank the companies Sarl GEMELEC El Kouif- Tebessa, Anabib-tgt El malbioud- Tébessa and the metallurgy department of Badji Mokhtar University- Annaba (Algeria) for providing us with all the means available to succeed in this study.

## References

- [1] Hollomon JH. Tensile deformation. Aime Trans, 1945; 12: 1 - 22.
- [2] Cottrell AH, Bilby BA. Dislocation theory of yielding and strain ageing of iron. Proceedings of the Physical Society. Section A, 1949; 62 - 49.
- [3] Ebenberger P, Uggowitzer PJ, Kirnstötter S, Gerold B, Zaefferer S, Pogatscher S. Processing-controlled suppression of Lüders elongation in AlMgMn alloys. Scripta Materialia, 2019; 166: 64 - 67. <https://doi.org/10.1016/j.scriptamat.2019.02.047>
- [4] Hu H. Effect of solutes on Lüders strain in low-carbon sheet steels. Metallurgical Transactions A, 1983; 14: 85 - 91. <https://doi.org/10.1007/BF02643741>
- [5] Mazière M, Luis C, Marais A, Forest S, Gaspérini M. Experimental and numerical analysis of the Lüders phenomenon in simple shear. International Journal of Solids and Structures, 2017; 106: 305 - 314. <https://doi.org/10.1016/j.ijsolstr.2016.07.026>
- [6] Wenman MR, Chard-Tuckey PR. Modelling and experimental characterization of the Lüders strain in complex loaded ferritic steel compact tension specimens. International Journal of Plasticity, 2010; 26: 1013 - 1028. <https://doi.org/10.1016/j.ijplas.2009.12.005>
- [7] Mao B, Liao Y. Modeling of Lüders elongation and work hardening behaviors of ferrite-pearlite dual phase steels under tension. Mechanics of Materials, 2019; 129: 222 - 229. <https://doi.org/10.1016/j.mechmat.2018.11.015>

- [8] Tsukahara H, Iung T. Finite element simulation of the Piobert–Lüders behavior in an uniaxial tensile test. *Materials Science and Engineering: A*, 1998; 248: 304 - 308. [https://doi.org/10.1016/S0921-5093\(97\)00857-5](https://doi.org/10.1016/S0921-5093(97)00857-5)
- [9] Sun HB, Yoshida F, Ma X, Kamei T, Ohmori M. Finite element simulation on the propagation of Lüders band and effect of stress concentration. *Materials Letters*, 2003; 57: 3206 – 3210. [https://doi.org/10.1016/S0167-577X\(03\)00036-3](https://doi.org/10.1016/S0167-577X(03)00036-3)
- [10] Keeler SP. Forming Limit Criteria-Sheets. In *Advances in deformation processing*; Springer: Boston, MA, 1978; 127 - 157. [https://doi.org/10.1007/978-1-4613-4024-9\\_4](https://doi.org/10.1007/978-1-4613-4024-9_4)
- [11] Boudeau N, Gelin JC. Necking in sheet metal forming. Influence of macroscopic and microscopic properties of materials. *International Journal of Mechanical Sciences*, 2000; 42: 2209 - 2232. [https://doi.org/10.1016/S0020-7403\(00\)00003-5](https://doi.org/10.1016/S0020-7403(00)00003-5)
- [12] Doege E, El-Dsoki T. Deep-Drawing Cracks-Stretching Cracks: Two Different Types of Cracks in Deep-Drawing Processes. *Journal of Materials Processing Technology*, 1992; 32: 161 - 168. [https://doi.org/10.1016/0924-0136\(92\)90173-P](https://doi.org/10.1016/0924-0136(92)90173-P)
- [13] Jain M, Allin J, Lloyd JD. Fracture limit prediction using ductile fracture criteria for forming of an automotive aluminum sheet. *International Journal of Mechanical Sciences*, 1999; 41: 1273 - 1288. [https://doi.org/10.1016/S0020-7403\(98\)00070-8](https://doi.org/10.1016/S0020-7403(98)00070-8)
- [14] Kardan M, Parvizi A, Askari A. Influence of process parameters on residual stresses in deep-drawing process with FEM and experimental evaluations. *Journal of the Brazilian Society of Mechanical Sciences and Engineering*, 2018; 40: 157 - 169. <https://doi.org/10.1007/s40430-018-1085-9>
- [15] Hamza F, Boussaid O, Tadjine K. Study by Numerical Simulation of the Deep Drawing Parameters-Material during the Wheelbarrow Forming. *Materials Science Forum*. Trans Tech Publications Ltd, 2017; 895: 94-98. <https://doi.org/10.4028/www.scientific.net/MSF.895.94>
- [16] Habeeb HA, Jweeg MJ, Khleif AA. Effect of the Single-Point Incremental Forming Process Parameters on the Surface Roughness of Aluminum Alloy Al 2024-O Draw Pieces. *Advances in Science and Technology*. *Research Journal*, 2023; 17: 155-163. <https://doi.org/10.12913/22998624/174364>
- [17] Edis R, Sinmazcelik T, Erturk AT. Measuring applied force and energy consumption in deep drawing die Sets: An experimental and numerical analysis of CrN and CrTiN PVD coating effects. *Measurement*, 2024; 224: 113841. <https://doi.org/10.1016/j.measurement.2023.113841>
- [18] Torkar M, Tehovnik F, Podgornik B. Failure analysis at deep drawing of low carbon steels. *Engineering Failure Analysis*, 2014; 40: 1 - 7. <https://doi.org/10.1016/j.engfailanal.2014.02.003>
- [19] Ma B, Liu ZG, Jiang Z, Wu X, Diao K, Wan M. Prediction of forming limit in DP590 steel sheet forming: An extended fracture criterion. *Materials & Design*, 2016; 96: 401 - 408. <https://doi.org/10.1016/j.matdes.2016.02.034>
- [20] Butuc MC, Barlat F, Gracio JJ, da Rocha AB. A new model for FLD prediction based on advanced constitutive equations. *International journal of material forming*, 2010; 3: 191 - 204. <https://doi.org/10.1007/s12289-009-0667-6>
- [21] Matin PH, Smith LM, Petrusevski S. A method for stress space forming limit diagram construction for aluminum alloys. *Journal of materials processing technology*, 2006; 174: 258 - 265. <https://doi.org/10.1016/j.jmatprotec.2006.01.008>
- [22] Stoughton TB, Yoon JW. Path independent forming limits in strain and stress spaces. *International Journal of Solids and Structures*, 2012; 49: 3616 - 3625. <https://doi.org/10.1016/j.ijsolstr.2012.08.004>
- [23] Li H, Li G, Gao G, Zhang W, Wu X. A formability evaluation method for sheet metal forming with non-linear strain path change. *International Journal of Material Forming*, 2018; 11: 199 - 211. <https://doi.org/10.1007/s12289-017-1342-y>

- [24] Kumar DR. Formability analysis of extra-deep drawing steel. Journal of Materials Processing Technology, 2002; 130: 31 - 41. [https://doi.org/10.1016/S0924-0136\(02\)00789-6](https://doi.org/10.1016/S0924-0136(02)00789-6)
- [25] Aghaie-Khafri M, Mahmudi R. Predicting of plastic instability and forming limit diagrams. International Journal of Mechanical Sciences, 2004; 46: 1289 - 1306. <https://doi.org/10.1016/j.ijmecsci.2004.08.009>
- [26] Paul SK. Theoretical analysis of strain- and stress-based forming limit diagrams. The Journal of Strain Analysis for Engineering Design, 2013; 48: 177 - 188. <https://doi.org/10.1177/0309324712468524>
- [27] Paul SK. A critical review on hole expansion ratio. Materialia, 2020; 9: 100566. <https://doi.org/10.1016/j.mtla.2019.100566>
- [28] Paul SK. Controlling factors of forming limit curve: a review. Advances in Industrial and Manufacturing Engineering, 2021; 2: 100033. <https://doi.org/10.1016/j.aime.2021.100033>
- [29] Paul SK. Effect of forming strain on low cycle, high cycle and notch fatigue performance of automotive grade dual phase steels: A review. Forces in Mechanics, 2023; 100184. <https://doi.org/10.1016/j.finmec.2023.100184>
- [30] Sing WM, Rao KP. Role of strain-hardening laws in the prediction of forming limit curves. Journal of Materials Processing Technology, 1997; 63: 105-110. [https://doi.org/10.1016/S0924-0136\(96\)02608-8](https://doi.org/10.1016/S0924-0136(96)02608-8)
- [31] Rodney H. A theory of the yielding and plastic flow of anisotropic metals. Proceedings of the Royal Society of London. Series A. Mathematical and Physical Sciences, 1948; 1033: 281 - 297. <https://doi.org/10.1098/rspa.1948.0045>
- [32] Nguyen DT, Dinh DK, Thi Nguyen HM, Banh TL, Kim YS. Formability improvement and blank shape definition for deep drawing of cylindrical cup with complex curve profile from SPCC sheets using FEM. J. Cent. South Univ, 2014; 21: 27 - 34. <https://doi.org/10.1007/s11771-014-1911-x>
- [33] Chinara M, Paul SK, Chatterjee S, Mukherjee S. Effect of planar anisotropy on the hole expansion ratio of cold-rolled DP 590 steel. Transactions of the Indian Institute of Metals, 2022; 75: 535 - 543. <https://doi.org/10.1007/s12666-021-02444-x>
- [34] Yan Y, Wang H, Li Q. The inverse parameter identification of Hill 48 yield criterion and its verification in press bending and roll forming process simulations. Journal of Manufacturing Processes, 2015; 20: 46-53. <https://doi.org/10.1016/j.jmapro.2015.09.009>
- [35] Ghennai W, Boussaid O, Bendjama H, Haddag B, Nouari M. Experimental and numerical study of DC04 sheet metal behavior-plastic anisotropy identification and application to deep drawing. The International Journal of Advanced Manufacturing Technology, 2019; 100: 361 - 371. <https://doi.org/10.1007/s00170-018-2700-8>
- [36] Banabic D (ed.). Formability of metallic materials: plastic anisotropy, formability testing, forming limits. Springer Science & Business Media, 2000. <https://doi.org/10.1007/978-3-662-04013-3>
- [37] Tschätsch H. Metal forming Practise, translated by Koth a, 2006. <https://doi.org/10.1007/3-540-33217-0>
- [38] Banabic D. Sheet metal forming processes: constitutive modelling and numerical simulation, Springer Science & Business Media: Berlin Heidelberg, 2010. <https://doi.org/10.1007/978-3-540-88113-1>
- [39] Goodwin GM. Application of Strain Analysis to Sheet Metal Forming Problems in the Press Shop. Sae Transactions, 1968; 380 - 387. <https://doi.org/10.4271/680093>
- [40] Ramos GC, Stout M, Bolmaro RE, Signorelli JW, Serenelli M, Bertinetti MA, Turner P. Study of a drawing-quality sheet steel. II: Forming-limit curves by experiments and micromechanical simulations. International journal of solids and structures, 2010; 47: 2294 - 2299. <https://doi.org/10.1016/j.ijsolstr.2010.04.022>

- [41] Ke J, Liu Y, Zhu H, Zhang Z. Formability of sheet metal flowing through drawbead—an experimental investigation. *Journal of Materials Processing Technology*, 2018; 254: 283-293. <https://doi.org/10.1016/j.jmatprotec.2017.11.051>
- [42] Chen F, Huang T, Chang C. Deep drawing of square cups with magnesium alloy AZ31 sheets. *International Journal of Machine Tools and Manufacture*, 2003; 43: 1553-1559. [https://doi.org/10.1016/S0890-6955\(03\)00198-6](https://doi.org/10.1016/S0890-6955(03)00198-6)
- [43] Saxena R, Dixit P. Finite element simulation of earing defect in deep drawing. *The International Journal of Advanced Manufacturing Technology*, 2009; 45: 219-233. <https://doi.org/10.1007/s00170-009-1963-5>
- [44] Bouchaâla K, Ghanameh M, Faqir M, Mada M, Essadiqi E. Numerical investigation of the effect of punch corner radius and die shoulder radius on the flange earrings for AA1050 and AA1100 aluminum alloys in cylindrical deep drawing process. *Heliyon*, 2021; 7: 2405-8440. <https://doi.org/10.1016/j.heliyon.2021.e06662>

# Research on Structures



# Engineering Materials



<https://mimrg.net/>

